SOILS and ROCKS

An International Journal of Geotechnical and Geoenvironmental Engineering

Soils and Rocks publishes papers in English in the broad fields of Geotechnical Engineering, Engineering Geology, and Geoenvironmental Engineering. The Journal is published quarterly in March, June, September and December. The first issue was released in 1978, under the name *Solos e Rochas*, being originally published by the Graduate School of Engineering of the Federal University of Rio de Janeiro. In 1980, the Brazilian Association for Soil Mechanics and Geotechnical Engineering took over the editorial and publishing responsibilities of *Solos e Rochas*, increasing its reach. In 2007, the journal was renamed Soils and Rocks and acquired the status of an international journal, being published jointly by the Brazilian Association for Soil Mechanics and Geotechnical Engineering, by the Portuguese Geotechnical Society, and until 2010 by the Brazilian Association for Engineering Geology and the Environment.

Soils and Rocks

1978,	1 (1, 2)
1979,	1 (3), 2 (1,2)
1980-1983,	3-6 (1, 2, 3)
1984,	7 (single number)
1985-1987,	8-10 (1, 2, 3)
1988-1990,	11-13 (single number)
1991-1992,	14-15 (1, 2)
1993,	16 (1, 2, 3, 4)
1994-2010,	17-33 (1, 2, 3)
2011,	34 (1, 2, 3, 4)
2012-2019,	35-42 (1, 2, 3)
2020,	43 (1, 2, 3, 4)
2021,	44 (1, 2, 3, 4)
2022,	45 (1, 2, 3, 4)
2023,	46 (1, 2, 3, 4)

ISSN 1980-9743
ISSN-e 2675-5475 CDU 624.131.1

Soils and Rocks
An International Journal of Geotechnical and Geoenvironmental Engineering
ISSN 1980-9743 ISSN-e 2675-5475

Publication of
ABMS - Brazilian Association for Soil Mechanics and Geotechnical Engineering
SPG - Portuguese Geotechnical Society
Volume 46, N. 4, October-December 2023

Special Issue
8th Brazilian Conference on Slope Stability - COBRAE 2022

Guest Editors:
Roberto Quental Coutinho, Igor Fernandes Gomes
Universidade Federal de Pernambuco

Table of Contents

EDITORIAL

Soils and Rocks
v. 46, n. 4

Soils and Rocks
An International Journal of Geotechnical and Geoenvironmental Engineering
www.soilsandrocks.com
ISSN 1980-9743
ISSN-e 2675-5475

Introduction to the Special Issue of Soils and Rocks entitled "8th Brazilian Conference on Slope Stability – COBRAE 2022"

Roberto Quental Coutinho[1]*, Igor Fernandes Gomes[1]**

Editorial

This special issue includes the publication of 16 articles which were selected out of 235 papers presented at the 8th Brazilian Conference on Slope Stability - COBRAE 2022. The conference was held in Porto de Galinhas, PE, Brazil, between the 23rd and 26th of November 2022 and was attended by 500 people. The articles published in this special issue of Soils and Rocks are extended and improved versions of the papers originally published in the conference proceedings. The Willy Alvarenga Lacerda Conference, presented by Leonardo Cascini from the University of Salerno, Italy, is also included in this special issue.

The theme of the conference, "Slope stability in society and infrastructure", aimed at contributing to sustainable and resilient development. The conference featured a program and thematic areas that directly addressed different contexts covering central themes such as mass movement on slopes, geological-geotechnical investigations, geological mapping and risk management, slope and embankment behavior, engineering solutions, instrumentation and monitoring, submarine, and mining slopes. There was also a round table on "Disasters Associated with Gravitational Mass Movements", in a special session, and the II Reageo/INCT Workshop.

The relevance of this special issue of Soils and Rocks can be seen in its contribution to the development of technical and academic knowledge of geotechnical engineering in the face of the major mass movement events that have occurred in Brazil in recent years in cities such as Recife, Rio de Janeiro, Salvador and some places of the state of Santa Catarina and other regions, resulting from heavy rains and marked by landslides in inhabited risk areas. Also notable were the Mariana and Brumadinho disasters resulting from the collapse of mining tailings dams, which are directly linked to the topic of slope stability.

The organizing and scientific committees of the conference would like to thank all the authors and reviewers for their contribution to this special issue.

* Guest Editor
** Co-editor
[1] Universidade Federal de Pernambuco, Departamento de Engenharia Civil e Ambiental, Recife, PE, Brasil.

LECTURE

Soils and Rocks
An International Journal of Geotechnical and Geoenvironmental Engineering
www.soilsandrocks.com
ISSN 1980-9743
ISSN-e 2675-5475

The 1st Willy Alvarenga Lacerda lecture: New perspectives for landslide analysis and management

Leonardo Cascini[1#]

Lecture

Keywords
Landslides
Landslide triggering
Landslide evolution
Multidisciplinary approach
Multiscale approach
Landslide management

Abstract

Landslides are widespread all over the world, often causing significant consequences in terms of loss of life and property damage. This explains why many scientists from Geology and Geotechnics have long been engaged in solving complex problems of both theoretical and practical interest. Geologists have systematically investigated the common characteristics of landslides proposing several classification systems, while not providing general laws for the triggering and evolution stages. Geotechnical engineers have implemented models to quantitatively analyze these stages but not to develop a general framework for typical landslide behaviors. Aimed to bridge the scientific branches dealing with landslides and based on the past efforts of many researchers all over the world, this paper focuses on deep-seated landslides developing along an existing and/or a new slip surface and multiple shallow landslides that may involve large areas in short periods of time. Considering that these phenomena are often analyzed at one single topographical scale and through monodisciplinary approaches, the paper proposes a new vision that highlights the possibility of a landslide management modern and open to the advanced technologies.

1. Introduction

Many countries around the world are threatened by landslides that often cause significant consequences in terms of loss of life and property damage. Many datasets testify to the great diffusion and consequence of landslides and among these Froude & Petley (2018) and Kirschbaum et al. (2015) provide the necessary information on the subject. Another example is the landslide risk plans developed since 1998 at an intermediate scale (1:25,000) in Italy, that is the country with the highest landslide risk in Europe, which counts about 500,000 existing and potential landslides over an area of 301,230 km^2.

The diffusion and consequences of landslides explain the efforts of scientists and authorities to improve knowledge and to manage the related risk. Focusing on the scientific aspects, several disciplines (Geology, Geomorphology, Geography, Geotechnics, Geomechanics, Hydraulics, Hydrology, Social Sciences, etc.) deepen many topics from different perspectives and with different approaches. Among these, a leading role has been played, since the past, by Geology and Geomorphology, on the one hand, and Geotechnics and Geomechanics, on the other. All of them investigate, often on a monodisciplinary basis, such a variety of issues that their statement alone is beyond the scope of this paper. Referring to the topics covered in the following sections, it is worth noting that one of the main objectives of Geology and Geomorphology is to find common characteristics of landslides, while Geotechnics and Geomechanics essentially focus on their mechanical behavior.

As regards the common characteristics of landslides, the topic is so much debated that, to date, more than 100 classification systems have been proposed in the scientific literature; the best known has been developed by Varnes (1978) and the latest one by Hungr et al. (2014). While many of these proposals are extremely useful from a technical and scientific point of view, none of them can provide insight into the laws that regulate the triggering and evolution stages of landslides.

This topic is analyzed through a variety of equation-based methods that can be essentially grouped into two different categories. The first category implements limit equilibrium equations or develops coupled or uncoupled stress-strain finite-element analyses. These models are usually applied with an extended detailed dataset on: landslide stratigraphy, mechanical properties of landslide materials, pore water pressure regime, landslide displacements and so on. The second category implements mechanical models characterized by a low number of degrees of freedom to describe the external and internal forces acting on the landslide body. These models implement complex equation systems to capture the essence of the landsliding and, in many cases, an advanced dataset is not essential. Both categories of methods are extremely useful to solve scientific and technical questions, but they cannot be used to extend the knowledge from a single phenomenon to classes of similar mechanical behaviors.

#Corresponding author. E-mail address: cascinileonardo@gmail.com
1Laram School, Dipartimento di Ingegneria Civile, Salerno, Italia.

Submitted on March 17, 2023; Final Acceptance on October 7, 2023; Discussion open until February 28, 2024.

https://doi.org/10.28927/SR.2023.002723

This gap in scientific literature may lead one to believe that all landslides are unique and that it is impossible to identify common mechanical laws governing their dynamic equilibrium. In addition, the absence of a consistent bridge between the many disciplines dealing with landslides prevents the advancement of knowledge on many phenomena, especially those that often cause the worst consequences.

This paper aims to lay the foundations for progressing in the analysis and management of single deep-seated landslides, which develop along an existing and/or a new slip surface, and of multiple shallow instabilities that may involve, quite often as shallow landslides, large areas in a short period of time. To this end, the materials and methods used, the results achieved so far and the perspectives they open are discussed in the following sections.

2. Materials

Varnes (1978) classifies the landslides according to their instability features (fall, topples, slides, lateral spreads, flows, complex slides) and the materials involved in the landsliding (rock and soils). Hungr et al. (2014) provide more details on several factors, but the classification system is also based on a geomorphological description of the phenomena. This applies to many other proposals in the literature which, together with those mentioned above, represent the starting point for the geotechnical study of a single deep-seated landslide and multiple shallow instabilities. However, the predisposing and triggering factors, soil/rock properties and boundary conditions can be so different for both categories of instability phenomena as to suggest a detailed analysis for each case study to understand and model the triggering and evolution stages.

Leoroueil et al. (1996) hinted at the possibility of overcoming this vision for single deep-seated landslides. Later, the research activity developed at the University of Salerno (Italy), where the present author served as a professor of Geotechnics, has progressively outlined the possibility of passing from a heuristic to a mechanical evaluation of the landslide evolution stages. Similar attempts do not exist for multiple shallow instabilities, which encompass a wide range of phenomena often involving complex soil/rock materials.

For these two categories of landslides the following sections describe the input data implemented in the analyses, which derive from different case studies for deep-seated landslides and from a single case study for multiple shallow instabilities.

2.1 Input data for single deep-seated landslides

The landslides moving along an existing or new slip surface are divided by Leoroueil et al. (1996) into two sub-categories, which include respectively the first failure and the existing landslides. For each of them two different evolution stages are introduced, named pre-failure and post-failure for first failures and occasional reactivation and active landslides for the existing ones, Figure 1. During the failure stage, the authors hypothesize a very high velocity which decreases rapidly during the post-failure stage. For the existing landslides, they assume i) a moderately large velocity, when they are reactivated by exceptional triggering factors (i.e., earthquakes) or ii) a low velocity, if they are activated by recurring factors, such as seasonal rainfall.

As a general commentary, the authors observe that: "These four stages, with some modification depending on the type of movements, also apply to rock masses. Each of these four stages involves mechanical phenomena, controlling laws and parameters which are very different, so that Vaunat et al. (1994) came to the conclusion that it is necessary to separate these stages to understand, analyze and characterize the movements of the slopes".

These concepts have been deepened in a long-lasting research program started at the University of Salerno (Italy) in 2006 with the aim of filling the gap of knowledge for one of the most widespread type of landslides in the world. Without further relevant references in the literature, the research was developed in three key steps:

- Collecting case studies deeply investigated in the literature, regardless of the materials involved in the landsliding, the predisposing and triggering factors, the activity stages and the displacement values;
- Implementing a simple procedure to individuate common evolution stages among the landslides, apparently different from each other in the dataset;
- Finding the kinematic characteristics of the evolution stages, if any, with the aid of the fundamental laws of Mechanics and Physics.

The activities of the first step, discussed in this section, have been requiring a constant commitment which, to date, has led to identifying 18 case studies around the world, well documented in the scientific literature (Table 1).

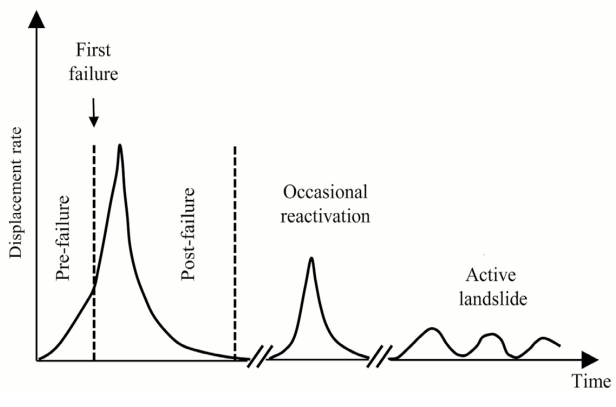

Figure 1. The landslide evolution stages introduced on a phenomenological basis [modified from Leoroueil (2001)].

Among them, 14 cases are from Europe (Italy 11, France 1, Switzerland 1, Spain 1), 3 in Asia (Japan 2, China 1), 1 in South America (Chile 1). Figure 2 provides an overview of two landslides that marked the recent history of the Italian territory as their evolution caused many casualties, huge economic damages, and the attention of mass-media over a long period of time.

The landslides in the dataset are classified according to Varnes (1978) as slides, translational slides, rotational slides, toppling, complex slides, avalanches. A similar variety of landslide triggering factors emerges from the references in Table 1 which, depending on the case, include rainfall, snow melt, rainfall and snow melt, water level fluctuation in a reservoir, excavations, earthquake. An even more marked variety is for the materials involved in the landsliding classified in the references as: rock and/or rock in different matrices, granitic gneisses, tuff, limestone, sandstones, debris, marly clay, stiff clays, clay schists, clay, volcanic grains, silt, etc. Finally, the length of the landslides (L) and the depth of the slip surface (H), Figure 3, vary in the ranges L = 340-2,000 m and H = 9.6-250 m. Often, the lowest values refer to a secondary sliding body of dimensions l and h, as schematized in the figure.

Aware that the equation-based methods (i.e., limit equilibrium methods, coupled or uncoupled stress-strain finite-element analyses, mechanical models characterized by a low number of degrees of freedom) could not be used to identify common characteristics among the selected landslides, the attention was focused on landslide displacements.

Table 1. The collected dataset (Scoppettuolo et al., 2020).

Landslide Name	Location	References
Bindo-Cortenova	Valsassina, Lecco, Italy	Secondi et al. (2011)
Castelrotto	Bolzano, Italy	Simeoni & Mongiovì (2007)
Chuquicamata	Andes, Chile	Voight & Kennedy (1979)
Fosso San Martino	Teramo, Italy	Bertini et al. (1986)
Kunimi	Japan	Shuzui (2001)
La Clapière	Southern Alpes, France	Helmstetter et al. (2004)
La Frasse	Aigle, Switzerland	Tacher et al. (2005)
La Saxe	Courmayeur, Valle d'Aosta, Italy	Crosta et al. (2014)
Montaldo di Cosola	Alessandria, Italy	Lollino et al. (2006)
Ohto	Japan	Suwa et al. (2010)
Porta Cassia	Orvieto, Italy	Tommasi et al. (2006)
Ragoleto	Licodia Eubea (Catanzaro, Italy)	Musso (1997)
Rosone	Orco river valley, Turin, Italy	Binet et al. (2007)
Ruinon	Valtellina, Sondrio, Italy	Crosta & Agliardi (2003)
Vallcebre	Pyrenees, Spain	Corominas et al. (2005)
Val Pola	Valtellina, Sondrio, Italy	Crosta et al. (2004)
Vajont	Erto e Casso, Pordenone, Italy	Nonveiller (1987)
Xintan	China	Keqiang & Sijing (2006)

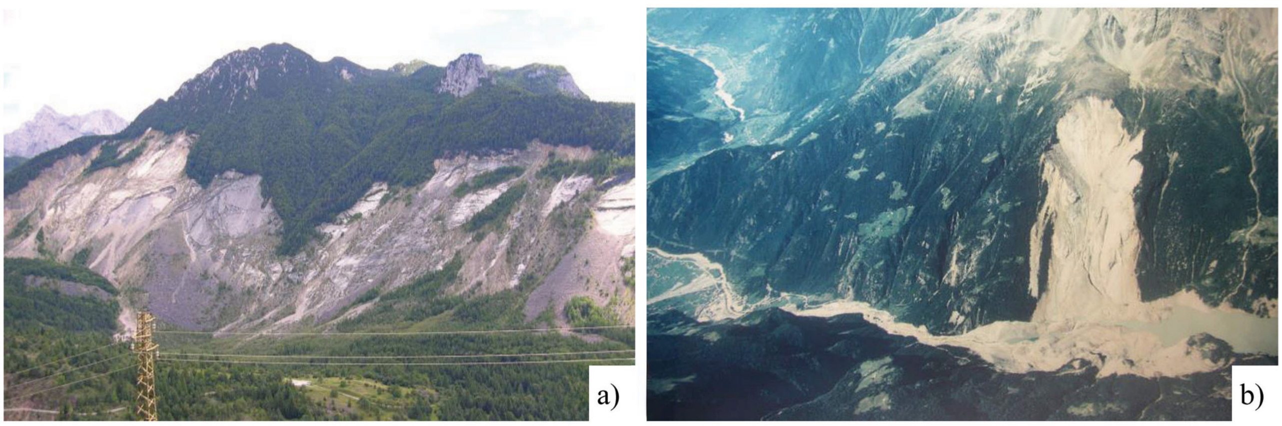

Figure 2. a) Vajont landslide (Wikipedia, 2023); b) Val Pola landslide [Studio Majone Ingegneri Associati (2023)].

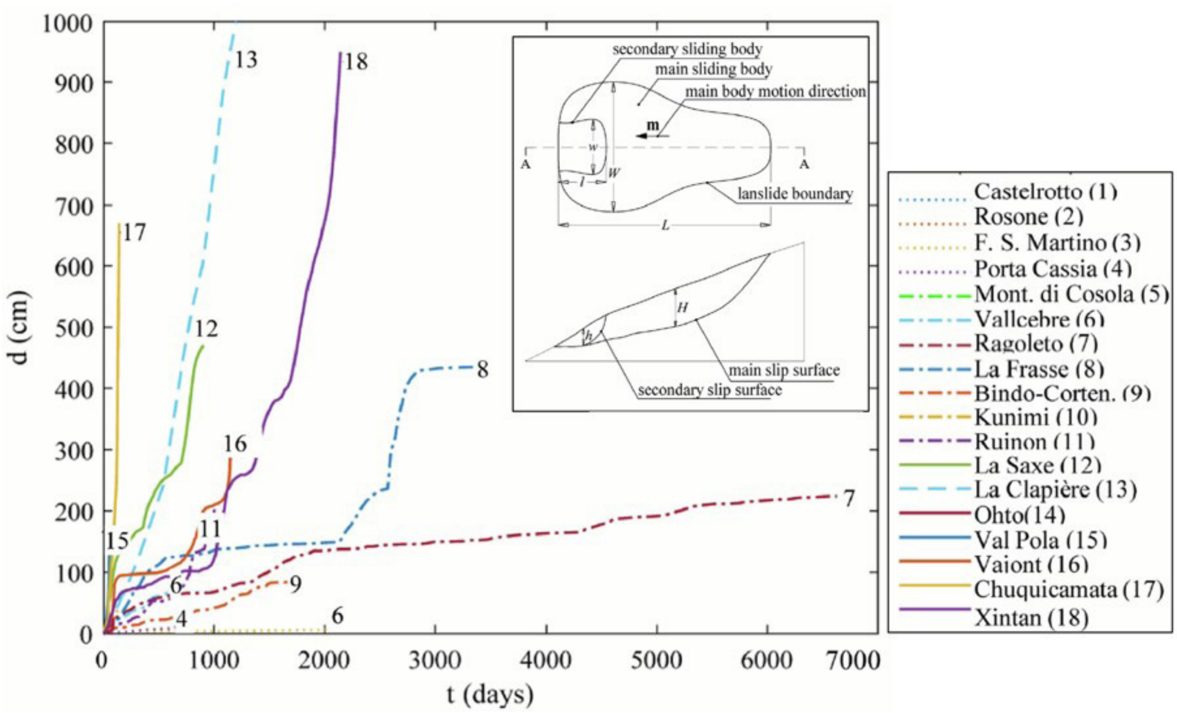

Figure 3. Geometry and dimensional displacements of the landslides in the dataset [modified from Cascini et al. (2022)].

This scientific investigation was started believing that the extent and types of displacements were linked also to the imbalance between the external and resistance forces acting on the landslide, regardless of the landslide type and the material involved. Indeed, the monitoring techniques, the historical time series, their significance and accuracy and anything else necessary for implementing the second and third key steps of the procedure were carefully analyzed before selecting each case study.

For information purposes it is noted that the displacements have been measured through: inclinometers (7), surface markers (4), extensometers (3), optical targets (2), distometer (1), crackmeters (1). In all the cases, the experimental devices are clearly described in the references (Table 1) which specify whether the measurements refer to the whole landslide body or to a part of it. The experimental data thus collected are plotted in Figure 3.

2.2 Input data for a case study of multiple shallow instabilities

This type of phenomena occurs in many geological contexts, often as shallow landslides threatening large areas in a short period of time. The slopes covered by ashy soils are among the most dangerous contexts due to the metastable behavior of these materials. However, despite the diffusion and consequences of such phenomena around the world (Cuomo, 2006), their analysis and management are far from being standardized due to: use of-monodisciplinary approaches usually implemented at a single topographical scale; oversimplification of the triggering mechanisms, predisposing factors and triggering causes; lack of historical data and input data for the geological and geotechnical analyses and so on.

This paper focuses on the case study of the Campania region (Southern Italy) currently threatened by the Vesuvius volcano, the only active volcano in the continental Europe, and in the past by other volcanic systems which both played a primary role in covering the slopes of the mountain basins in an area of about 3,000 km^2 (Figure 4a).

However, these mountain basins differ in soil covers, underlying bedrock, exposure of the slopes, geographical position, urbanization of the areas at the toe of the slopes, etc. Regardless of the differences, many mountain basins have been systematically affected in the past by catastrophic events, as that one in 1997 in Pozzano (Figure 4b), which caused four fatalities, and those in 1998 along the Pizzo d'Alvano massif (Figure 4c), responsible for 160 victims and economic damage amounting to 500 million euros.

Considering the limited knowledge at the time of the first event, detailed historical research was soon started. The first dataset on the past events was completed in the spring of 1998, almost concurrently with the second event which confirmed the very high risk threatening a large area of the Campania region. The echo of this second event in Italy and abroad, the commitment of the authorities, along with the scientific, technical and civil community made possible to acquire, during the emergency management of the event and in the following years, a large amount of data on many topics. Examples of the results achieved are provided in Figure 4d, as it concerns the historical events, and in Figures 5, 6, 7 regarding the in-situ and laboratory investigations.

Figure 5 refers to the Pizzo d'Alvano massif, for which the dataset contains the stratigraphical setting of the soil covers, the soil suction regime, the mechanical properties of the lithotypes, etc. Figure 6 refers to the Monte Albino massif, which threatens the municipality of Nocera Inferiore with various flow-like phenomena originated by shallow landslides or soil erosion due to runoff along the slopes. In detail, the figure shows the approximately 2,000 verticals investigated over an area of about 400 hectares to develop an accurate soil cover map all over the massif (Matano et al., 2016). Finally, Figure 7a refers to mountain basins of the Amalfi Coast systematically characterized by the presence of a village at the toe with the ancient ravine transformed in a paved culvert inside the urban area. The figure also provides an example of a soil cover map (Figure 7b), elaborated with the aid of the in-situ investigations, and of the analyzes that must be developed in these basins to evaluate, for the presence of the culvert, the cascading effects caused upstream by the slope instabilities triggered by critical rainfall (Figure 7c).

In conclusion, many investigations, often coordinated with each other, even if they were performed in different years and for different purposes, have made possible the investigation of many issues over a particularly vast territory. Among these issues it is worth mentioning: hydrology; soil stratigraphy relating the lithotypes to the eruption of the Vesuvius volcano; the trend of soil suction which, unlike in the past literature, links the season of the year, exposure of the slopes and bedrock underlying the soil cover into a unique framework; the mechanical properties of soils, in total and partial saturation conditions, which allow any standard or advanced geotechnical analysis; mechanisms and characteristics of the triggering and run out phenomena. It must be stressed that almost all these issues were addressed by the University of Salerno from a multidisciplinary and multiscale perspective which greatly facilitated the formulation of the proposal discussed in the following sections.

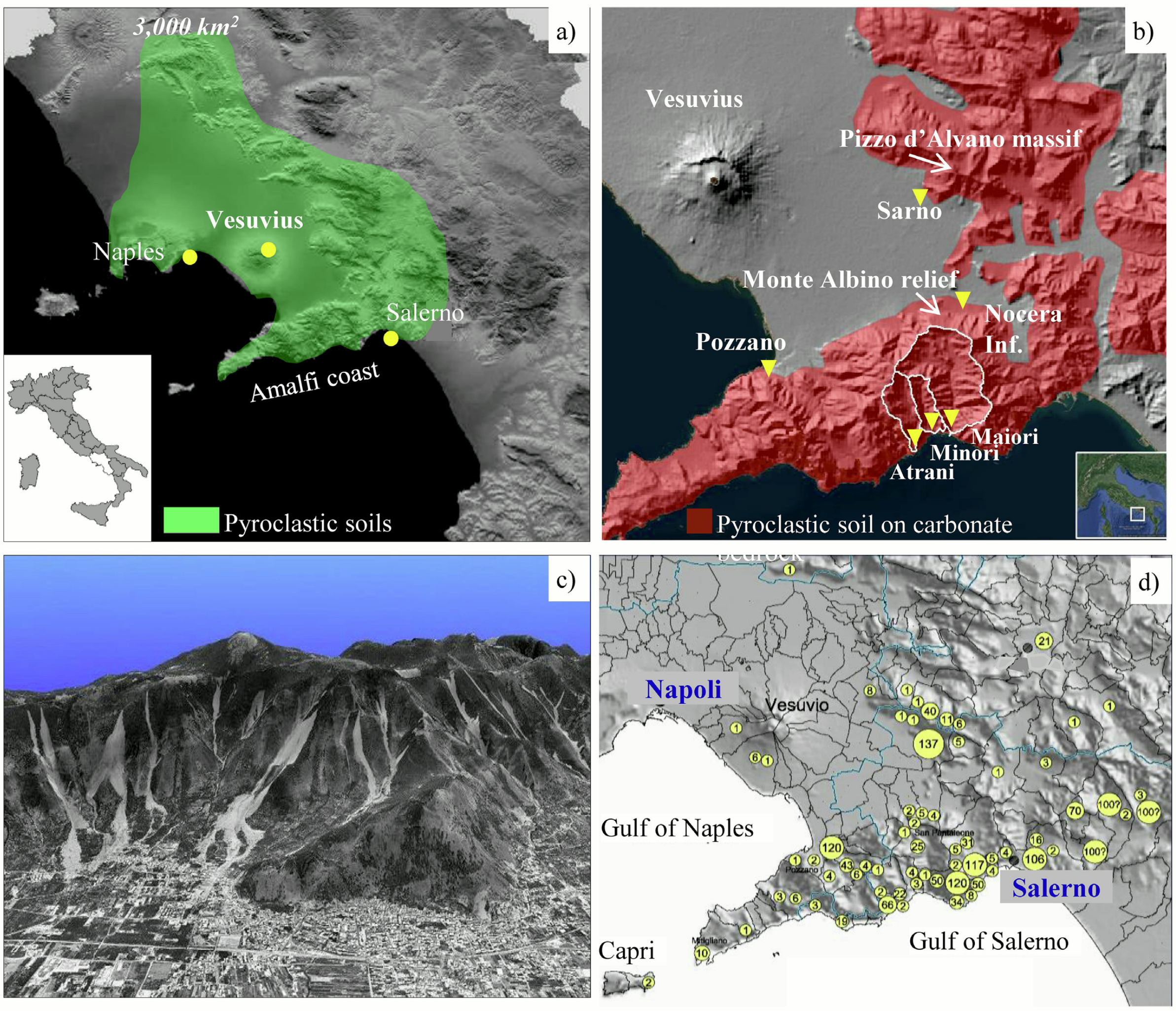

Figure 4. a) The area covered by pyroclastic soils in Campania Region (Southern Italy); b) in red the area where the pyroclastic soils cover a carbonate bedrock (Google Earth image); c) a view of the events that threatened the Sarno town [modified from Cascini (2004)]; d) victims recorded over the centuries where the pyroclastic soils mantle the carbonate bedrock [modified from Cascini (2004)].

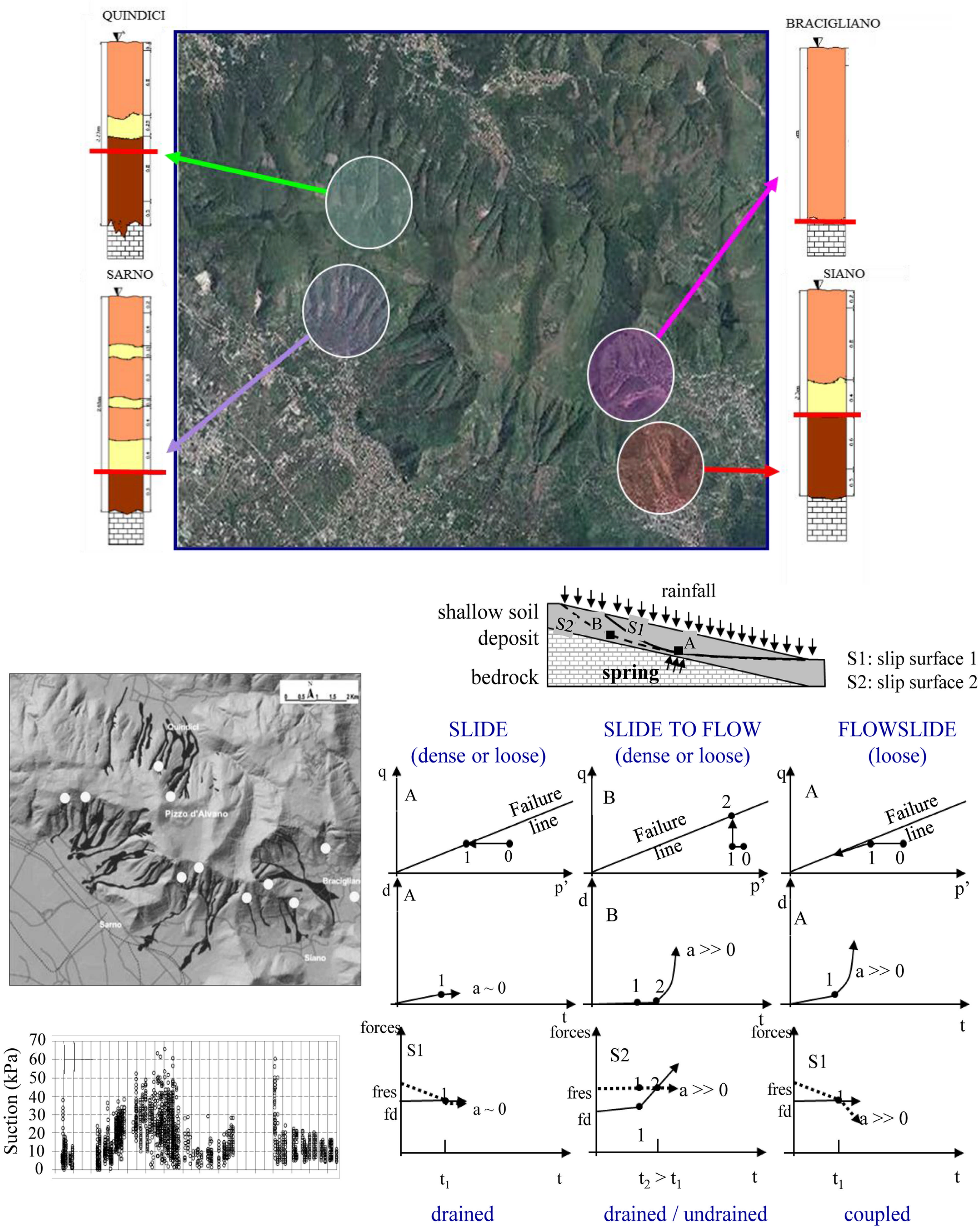

Figure 5. Examples of results provided by the in-situ and laboratory investigations at the Pizzo d'Alvano Massif [modified from Cascini (2004), Cascini et al. (2010) and Cuomo (2020)].

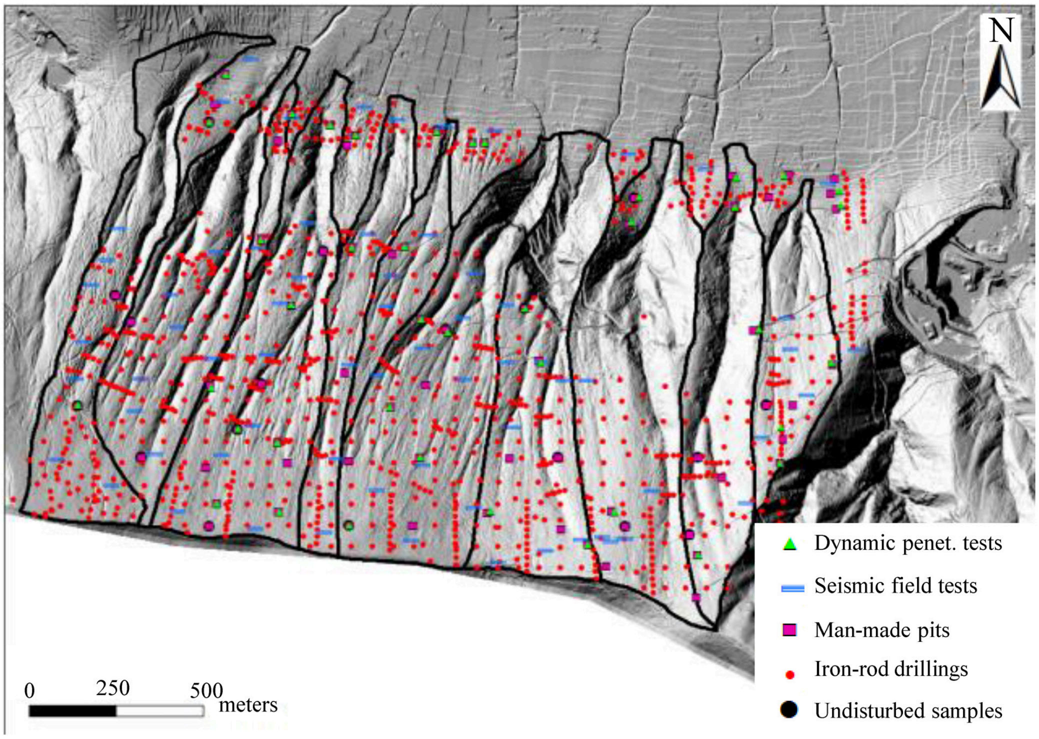

Figure 6. In-situ investigation carried out in the Monte Albino relief [modified from De Chiara (2014)].

3. Methods and results for single deep-seated landslides

The variability of the landslide displacement trends was evident from the early stages of the research, and it has grown further with the increase in the number of the selected case studies, Figure 3b. In the literature this variability is related to the difference in several factors such as: soil mechanical properties; groundwater regime; boundary conditions; landslide geometry; imbalance between external and resistance forces; and so on.

Given the inapplicability of the equation-based methods to tackle such a complex problem and confident that the landslide displacements could not have random trends, it was decided to investigate the deep essence of the problem through an innovative approach, simple schemes and consistent procedures, easily adaptable in case of partially unsatisfactory results.

Accordingly, the second and third key steps introduced in section 2.1 were addressed by grouping the displacement trend with the same prevailing evolution stage. Figure 8 collects the diagrams of landslides that, according to the references, have undergone a failure, those in which there is more than one occasional reactivation, and those in which the activity stages prevail.

These diagrams highlight i) a predominant concave shape where active stages prevail, ii) a convex shape for the other ones and iii) a totally different extent of the displacements, passing from the activity stages to occasional reactivations and failures. These observations prompted to isolate every single stage for the landslides in the dataset and this was carried out also with the aid of the triggering factors discussed in the references listed in Table 1.

The adopted procedure, explained with two examples (Figure 9), allowed the selection of 102 stages characterized by i) a linear displacement trend in correspondence with the minimum value of the triggering factors, ii) a concave trend for the active stages and iii) a convex one for occasional reactivations and first failures.

However, once the curves were distinguished in this way, the same activity stages of the landslides in the dataset were still not comparable due to the different time duration of each evolution stage and the magnitude of the displacements. Nevertheless, such a small number of displacement trends, their shape and values appeared to be non-random and potentially related to the extent of the imbalance between the external and resistance forces acting on the landslide body.

Indeed, it was decided to investigate this hypothesis through a simple procedure which, at the same time, did not obscure the essence of the problem. After several attempts, the comparison of similar stages became possible passing from dimensional to the dimensionless plan. Particularly, referring to a landslide characterized by N stages, assuming that the generic j-th activity stage is composed of n + 1 data, denoting by $d_{0,j}$ and $d_{n,j}$ the cumulative displacements at the initial and final times $t0_j$ and $t_{n,j}$ of the current stage, the dimensionless displacement $D_{i,j}$ and time $T_{i,j}$ were computed through the procedure shown in Figure 10a, $d_{i,j}$ being the displacement recorded at time $t_{i,j}$.

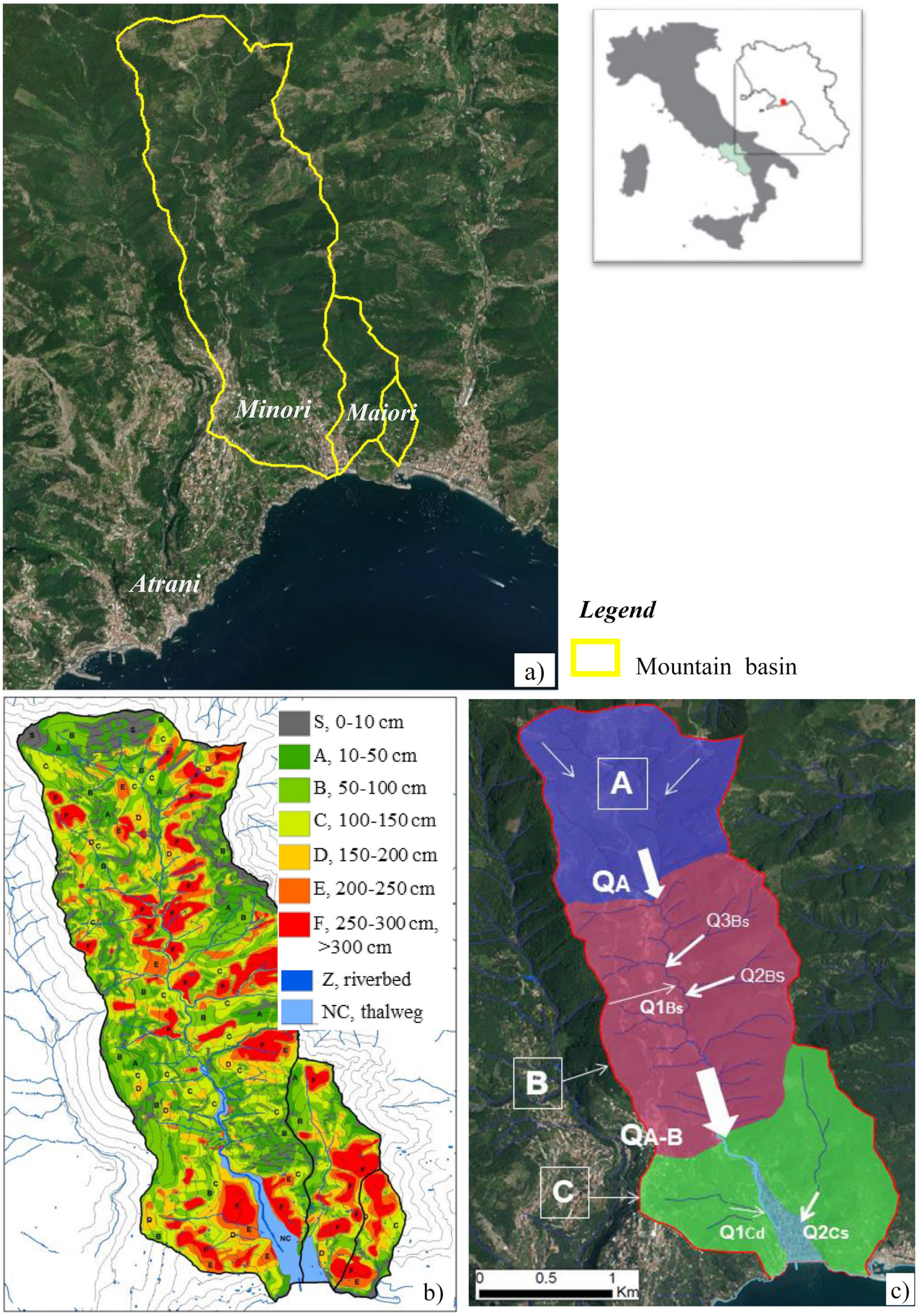

Figure 7. a) Mountain basins threatening the Minori village; b) soil cover map of the slopes in the mountain basins; c) reference scheme to analyze the cascading effects in these or similar basins.

The results obtained are plotted in Figure 10b showing that the 102 evolution stages in the dimensional plane are grouped into only 4 typical trends in the dimensionless one. Of these, 11 are linear (trend I), 66 concave (trend II), 20 convex as occasional reactivation (trend III) and 5 convex as failure (trend IV). Trend I is the diagonal of the diagram, trends II are placed above the diagonal, trends III and IV are below the diagonal being characterized by a different value of the convexity.

Scoppettuolo et al. (2020) show that the rescaled displacements defined as d/L, where d is the maximum displacement measured during a single stage and L the length of the landslide to which the experimental measures refer (Figure 3a), vary in the range from 2.5×10^{-7} to 1.4×10^{-3} for the active stages, from 2.7×10^{-5} to 2.8×10^{-2} for occasional reactivation, and are greater than 4.1×10^{-1} for failures.

It is interesting to observe that all these trends are consistent with both the landslide description in the references and the stages as defined in Figure 1. The only exception is the Vajont landslide, which according to some references [see, e.g., Alonso et al. (2010)] can be considered an existing landslide, that is a phenomenon for which Figure 1 indicates the possibility of active stages and occasional reactivations and not the failure.

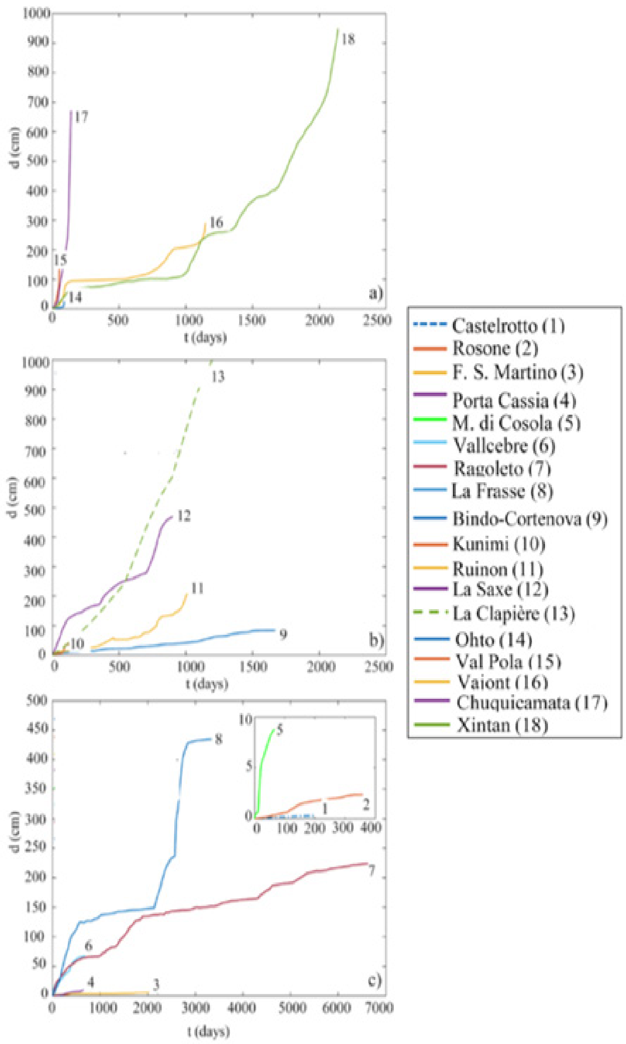

Figure 8. a) Failure events; b) occasional reactivations; c) active landslides [modified from Cascini et al. (2022)].

4. The stability chart

The existence of a small number of trends that well interpret the 102 evolution stages of the 18 landslides in the dataset (originally all different in the dimensional space) suggested the possibility to individuate well-defined laws of mechanics for them. The lack of the input data to implement traditional and/or advanced geotechnical models led to investigate these laws through the inverse approximation of the dimensionless displacements.

The implementation of this method required first the regularization of the experimental data with a continuous function and, among those tested, the power-law function was selected as it approximated all the available in-situ measurements with an error of less than 3%. Then, the mechanical characteristics of the trends were explored through the inverse approximation of displacement $d(t)$, velocity $\dot{d}(t)$, acceleration and jerk $\dddot{d}(t)$. Notice that the

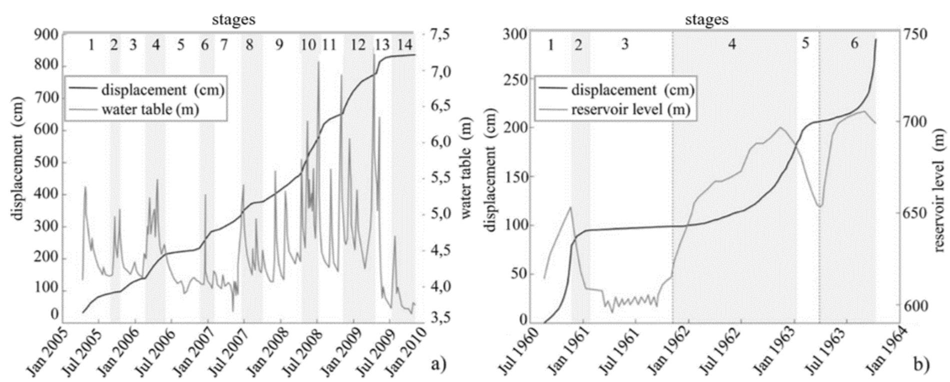

Figure 9. Isolating the activity stages through the shape of the displacement trend and the triggering factors for the case study of a) Bindo Cortenova and b) Vajont landslides [modified from Scoppettuolo et al. (2020)].

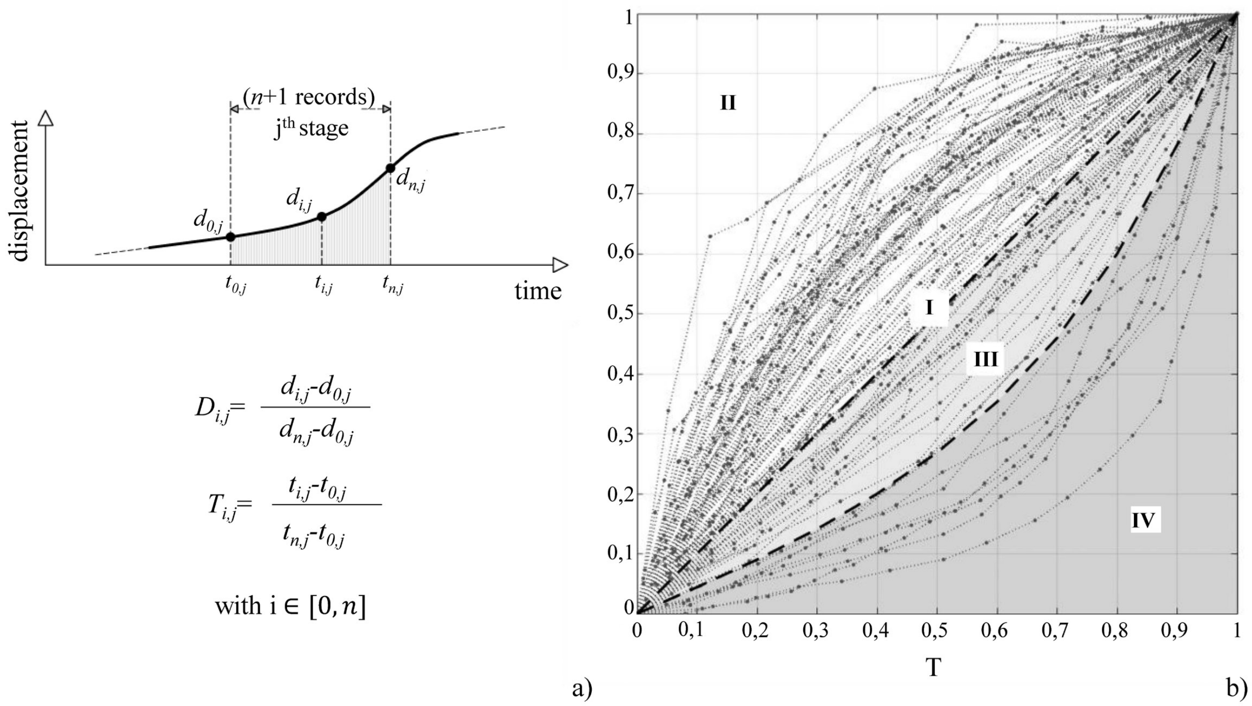

Figure 10. a) From dimensional to dimensionless displacement trends (Babilio et al., 2021); b) dimensionless displacement trends [modified from Scoppettuolo et al, (2020)].

displacement is recorded, and therefore it can be assumed to be known (and, similarly, its dimensionless counterpart), while its derivatives must be computed.

Displacements and velocities are systematically addressed in the literature. Acceleration is also analyzed by several authors, although its implementation in this paper follows an innovative approach (Babilio et al., 2021). As for the jerk, mentioned in economics and other technical fields, it is used for the first time in the study of landslides and among the first times in the resolution of Civil Engineering problems (Babilio et al., 2021).

The meaning of displacement and velocity is so clear that it does not require further comment. Acceleration and jerk have an equally clear meaning through the simple scheme in Figure 11 that allows writing:

$$\ddot{d}(t)=\frac{f_{ext}(t)-f_{res}(t)}{m(t)},\qquad \dddot{d}(t)=\frac{\dot{f}_{ext}(t)-\dot{f}_{res}(t)}{m(t)}-\frac{\dot{m}(t)}{m(t)}\ddot{d}(t) \tag{1}$$

where f_{ext} and f_{res} stand for external and resistance forces, whereas $\dot{f}_{ext}$ and $\dot{f}_{res}$ for their time derivatives. It is expected that $fres$ depends on both d (in case the sliding interface is characterized by either a hardening or a softening behavior) and $\dot{d}$ (viscous contribution).

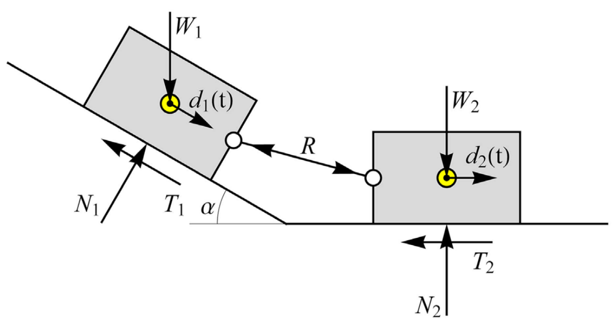

Figure 11. A reference scheme to interpret the results of the inverse analysis.

Indeed, acceleration describes at a given instant the value of the imbalance between the forces acting globally on the landslide and a positive value implies that the external forces exceed the internal resistance in the case of constant mass. In turn, the jerk defines the trend over time of the imbalance between these forces, still in the case of a constant mass. It follows that, knowing the trend of one of the two systems of forces, the other one can be deduced, and this allows evaluating the dynamic equilibrium of the landslide and its trend within each evolution stage.

The analysis of the 102 dimensionless trends is discussed in detail in Babilio et al. (2021) and numerical results are summarized in Table 2 and Figure 12.

Table 2. Kinematic characteristics of the evolution stages [modified from Babilio et al. (2021)].

Function name	Trend I	Trend II	Trend III	Trend IVa	Trend IVb
Displacement	$D > 0\uparrow$	$D > 0\uparrow$	$D > 0\uparrow$	$D > 0\uparrow$	$D > 0\uparrow$
Velocity	$\dot{D} > 0\leftrightarrow$	$\dot{D} > 0\downarrow$	$\dot{D} > 0\uparrow$	$\dot{D} > 0\uparrow$	$\dot{D} > 0\uparrow$
Acceleration	$\ddot{D} = 0\leftrightarrow$	$\ddot{D} < 0\uparrow$	$\ddot{D} > 0\downarrow$	$\ddot{D} > 0\uparrow$	$\ddot{D} > 0\uparrow$
Jerk	$\dddot{D} = 0\leftrightarrow$	$\dddot{D} > 0\downarrow$	$\dddot{D} < 0\uparrow$	$\dddot{D} > 0\downarrow$	$\dddot{D} > 0\uparrow$

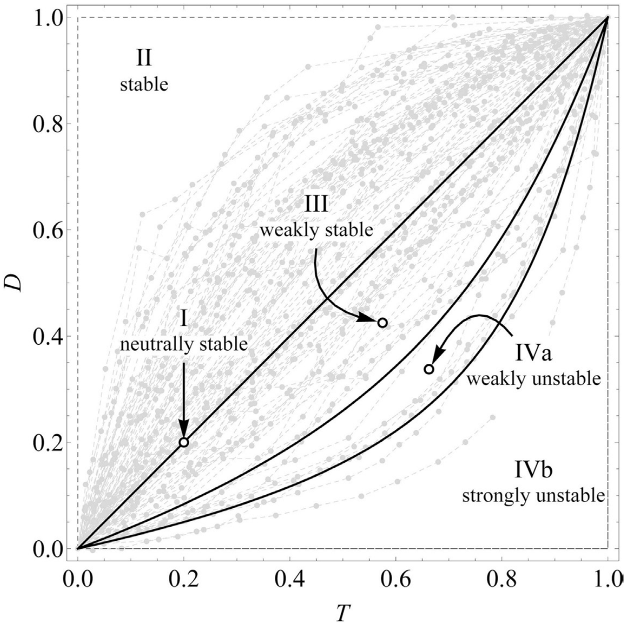

Figure 12. The stability chart [modified from Babilio et al. (2021)].

Together with the rescaled displacements provided in the previous section, the results obtained allow the following statements:

- Trend I is characterized by a positive constant velocity and zero acceleration and jerk, resulting from the perfect balance between external forces and the shear resistance mobilized along the slip surface. The exponent of the $D(T)$ function approximating the experimental data is equal to $x = 1$ that is the typical value of a landslide evolving in a neutrally stable condition.
- Trend II shows a positive decreasing velocity, a negative increasing acceleration and a positive decreasing jerk, testifying the prompt reaction of the landslide to the modification of the stress state induced by recurrent internal or external actions. The exponent of the $D(T)$ function is in between $0 < x < 1$ (concave shape of the displacement curve, testifying a typical stable condition).
- Trend III is characterized by a positive increasing velocity, a positive decreasing acceleration and a negative increasing jerk that testify the ability of the landslide to completely balance over time an exceptional and non-recurring external force. The exponent of the $D(T)$ function varies in the range $1 < x < 2$ (convex shape of the displacement curve evolving towards a concave shape, that is a weakly stable condition of the landslide).
- Trend IV is a failure condition due to the increasing value of acceleration caused by the imbalance over time between external and resistance forces. The jerk assumes a positive decreasing value for Trend IVa (the exponent of the function $D(T)$ is in the range $2 \leq x < 3$ and this highlights that the imbalance cannot exceed certain values) or a positive increasing value for Trend IVb (the exponent of the function $D(T)$ is $x \geq 3$, testifying an uncontrollable failure of the landslide that cannot be avoided by any external action).

This last trend explains the case of the Vajont landslide which, in 1960 and 1962, accelerated (stages 1 and 4 in Figure 9b) after the filling of the reservoir, and decelerated following its emptying (stages 2 and 5 in the same figure). In 1963, a third increase of the water level, slightly higher than the previous one, caused the disaster known to all (stage 6 in Figure 9b). The adopted procedure shows that the acceleration increases during all the stages while the jerk decreases in correspondence with the first two and increases during the last one. This explains why the lowering of the water level in the reservoir avoided failure during the first two stages, while disaster was unavoidable in the fatal third one. Pinyol & Alonso (2010) and Alonso et al. (2016) relate the collapse to the decay of the internal resistance caused by complex thermomechanical interaction along the slip surfaces. Hypothesis consistent with the increase in jerk and which also highlights the possible failure for an existing landslide under specific load and boundary conditions.

5. Methods and results for a case study of multiple shallow instabilities

5.1 The driving force of scientific activities

On 5-6 May 1998, over a period of approximately 10 hours, a sequence of flow-like phenomena caused 160 victims and significant economic consequences in the town of Sarno (Figure 4c) and in four other municipalities of the Campania region. The day after the disaster, the Department of National Civil Protection (DNCP) entrusted the scientific emergency management to the Geotechnical Group of the University of Salerno which, from the beginning, was supported by scientists, technicians and members of the authorities in charge of land use planning, which arrived in a few days from all over Italy (Cascini, 2003).

The extraordinary mobilization of technicians and researchers pushed the DNCP to request the zoning of the flow-like residual risk in the five municipalities, setting the deadline for the presentation on 18th May. Given the lack of experience and standards, in Italy and Europe, and the short time scheduled, it was decided to carry out essentially in-situ geological investigations and aerial photo interpretations.

The data collected were used to develop three maps, at a scale of 1: 25,000 and for the entire area of interest, respectively named the "*Geological and cover thickness map*", the "*Geomorphological Map*" and the "*May 1998 landslide map*". These maps highlighted the long run of the flows originated from shallow landslides or similar phenomena, due to the collapsibility of the soils mantling the slopes. Moreover, by overlapping these three maps (Figure 13a) it was clear that: the landslide source areas were almost all located at the same altitude along the massif; in the landslide source areas, the percentage of the mobilized soil cover was everywhere about 30% of the original one; a potential instability was evident in most of the soil covers still in place; the run out of the flow-like phenomena dated 1998 was sometimes the longest ever and sometimes not, comparing the recent with the ancient alluvial/colluvial fans.

Once the possibility of further instability phenomena in the landslide triggering areas was ascertained, it was prudently assumed that the future propagation may coincide with the areas bounded by the longest runout mapped at the base of each mountain basin (Figure 13b). It is interesting to observe that the zoning map thus elaborated (Figure 13c) confirmed its validity in the following two decades when the dataset allowed to apply more sophisticated numerical models than those implemented during the first 11 days of emergency management.

The day after the presentation of the residual risk zoning map, the DNCP asked for the zoning of the slopes susceptible to flow-like phenomena, similar to those occurred in May 1998, to be developed for the whole Campania Region (13,590 km^2) in the following three months. Not having the necessary data to provide a consistent answer to this further complex question, another working group was formed which, at the end of the activities, mapped the slopes threatening 212 municipalities in an area of 3,000 km^2 (Figure 4a) as susceptible to phenomena similar to those dated May 1998.

This high hazard in the Campania region had a so significant impact to induce the Central Government to issue the so-called "Sarno Law", which took its name from the municipality most damaged by the flows occurred in May 1998. The law imposed to all the Italian River Basin Autorities (AdB, acronym of the Italian name *Autorità di Bacino*) to zone the landslide and flood risk. This task was completed for the entire national territory in the following two years, thus allowing Italy to recover the gap accumulated over long time and to become one of the leading nations in Europe for the landslide risk zoning.

The Geotechnical Group of the University of Salerno coordinated and carried out many of these landslide-related activities in Southern Italy and, at the same time, systematically deepened many issues including the historical investigation started in 1997. This latter activity was developed through literary works, parish archives and Bourbon documents dating back to the nineteenth century (Cascini et al., 2002; Cascini & Ferlisi, 2003; Cascini et al., 2008c) which allowed the evaluation of the Societal Risk (Figure 14) in the area where the 212 municipalities are located.

The figure highlights that *i)* landslide risk is strictly related to the type of bedrock below the soil covers mantling the slopes and ii) the risk is so high in the geological context A1 as to make this area a national priority. Therefore, the University of Salerno has systematically investigated a variety of topics for the context A1, some of which are discussed below.

5.2 From practice to theory: the knowledge acquired through scientific activities

In the months following the emergency phase, the University of Salerno first identified the triggering mechanisms of the 1998 landslides through in-situ and desk investigations (Figure 15). The mechanism (M1) involved almost all the soil covers located in the so-called ZOB (Zero Order Basins) through a sequence of shallow landslides. M2, the second most widespread mechanism, was systematically caused by a small volume of soil that impacted the soil cover below causing a debris avalanche. M3 occurred in correspondence with the mountain tracks that locally increased the surface water runoff while the other three mechanisms (M4-M5-M6), partially or totally caused by erosion, have been less observed on the massif.

Once the mechanisms have been identified, the role played on M1 by the stratigraphy of the soil covering the massif and by the temporary springs, systematically recognized inside the ZOBs, was thoroughly analyzed, Figure 16. Cascini et al. (2003) and Cascini (2004) highlight that the Safety Factor (*SF*) provided by the limit equilibrium method is not significantly influenced by soil stratigraphy while it assumes the value $SF = 1$ only by implementing as input data the low flow rate measured for the temporary springs in the months following the events (Q = 2 L/min).

An equally relevant role of the temporary springs is demonstrated for the M2 and M3 mechanisms (Cascini et al., 2008b; Cascini et al., 2013) while the return period of the rainfalls before the event is not comparable to the slope

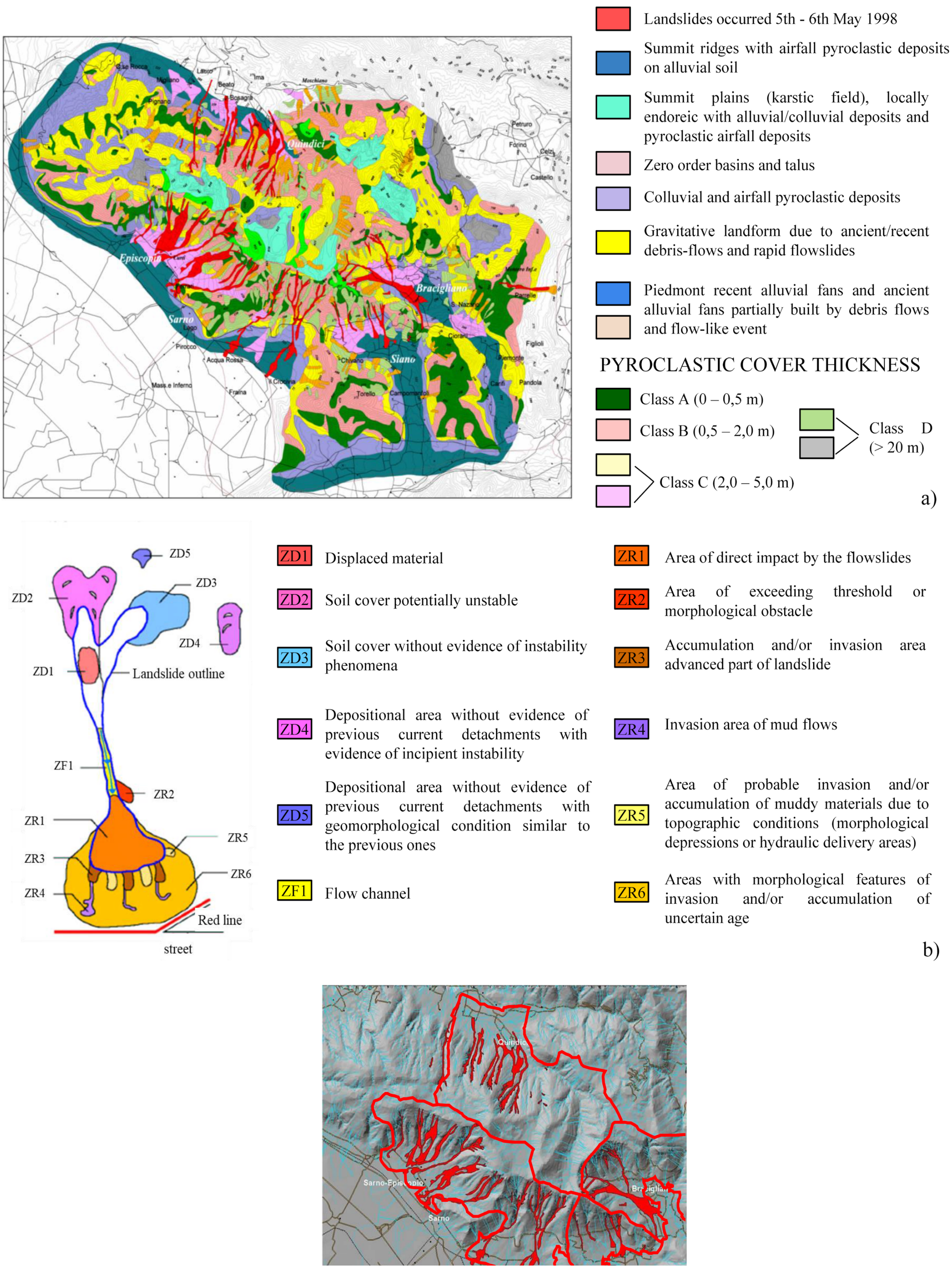

Figure 13. a) The synthesis map which overlaps the three geological maps developed with the data from the in-situ surveys [after Cascini (2004)], b) methodological scheme to zone the areas at residual risk of flowslides [after Cascini (2005)], c) the red line zoning the areas at flowslide residual risk [modified from Cascini (2004)].

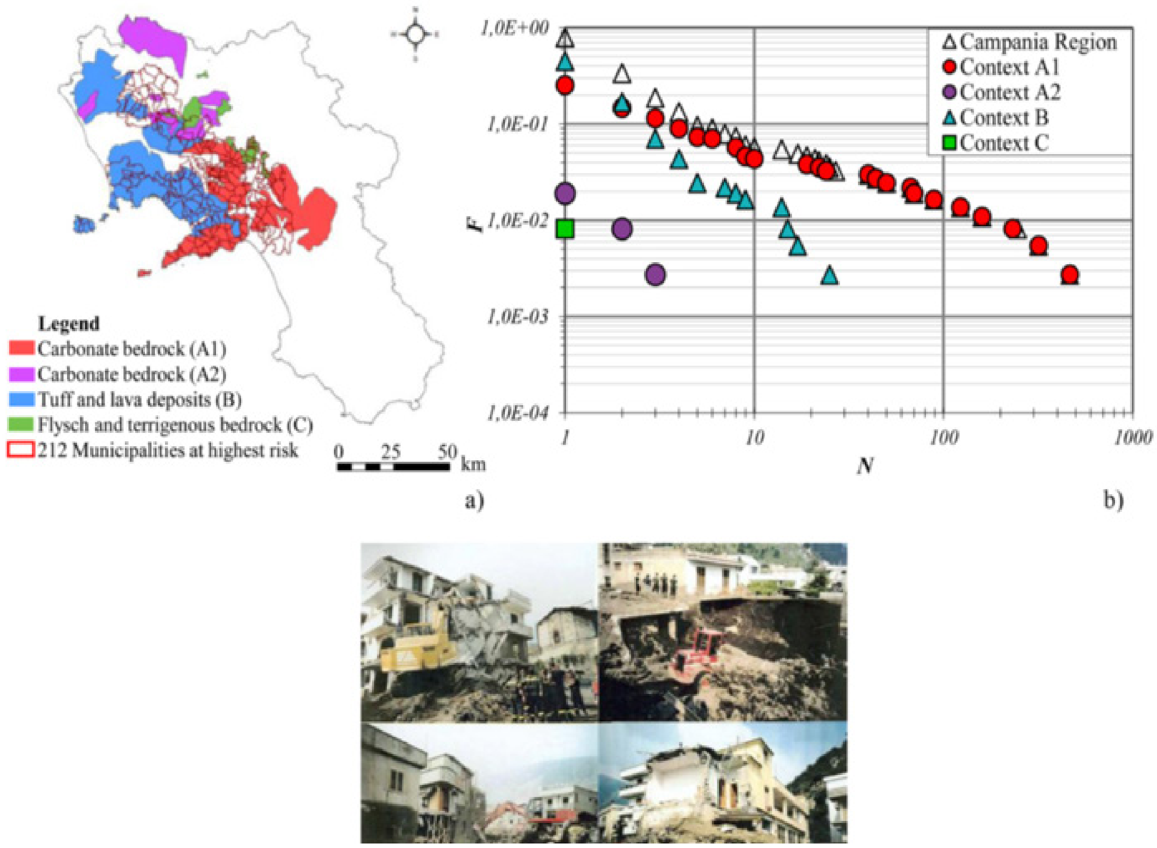

Figure 14. a) The bedrock in the area covered by pyroclastic soils, b) the Societal risk in the area of the pyroclastic soils, examples of damages to properties in the geological context A1 caused by c) the event dated 1998 along the Pizzo d'Alvano massif [modified from Cascini (2004)].

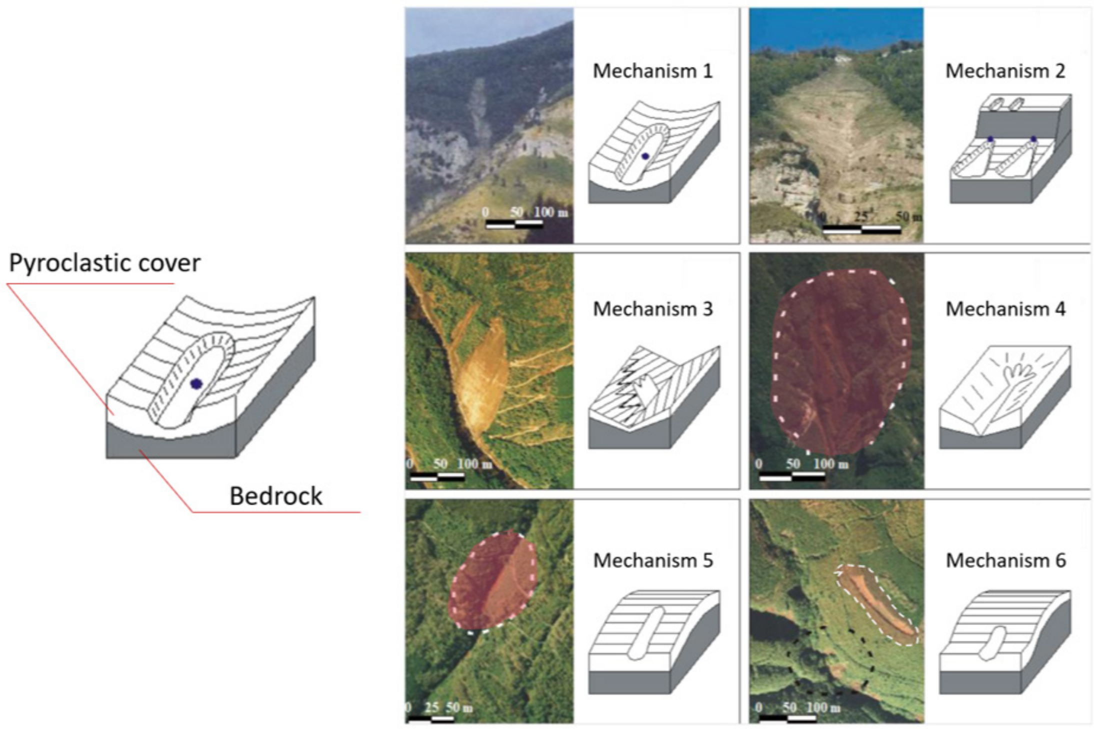

Figure 15. The triggering mechanisms along the massif affected by the event dated 1998 [modified from Cascini et al. (2008a)].

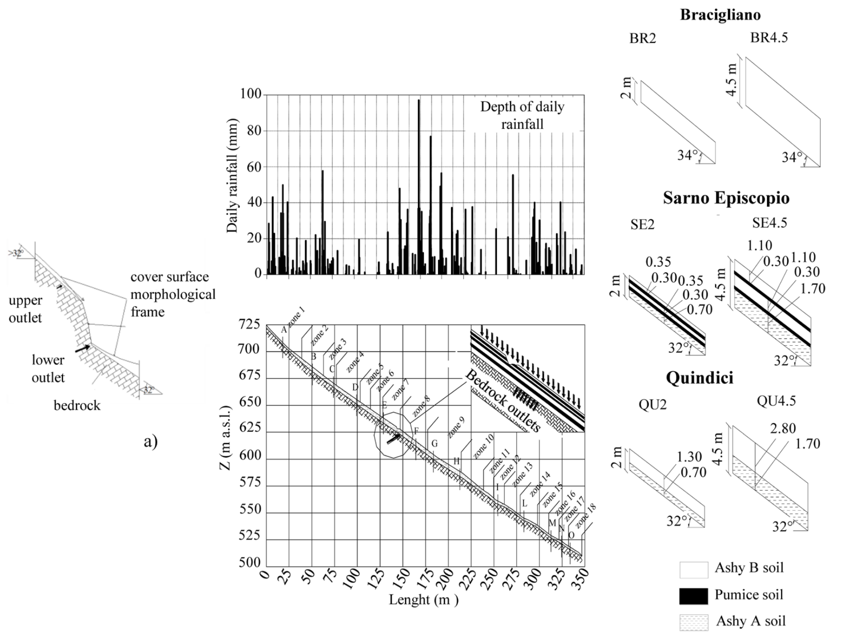

Figure 16. a) Outlets from the bedrock (Cascini, 2004), b) back-analysis of the mechanism M1 strongly influenced by the outlets in the landslide triggering areas (Cascini, 2004), c) parametric analysis of the triggering mechanisms M1 based on limit equilibrium approach [modified from Cascini (2005)].

instabilities and flow-like events, which never occurred with such intensity in the last three centuries. Together with the analysis of the hydrology of the previous years and the geological structure of the massif, this result delineates the possibility that the soil covers had been saturated from the top of the massif through the karst channels, which would have suddenly released a large amount of water accumulated in the previous years. Hypothesis, however, that is not demonstrable with engineering models.

On the contrary, the analyses demonstrate the need for a suitable model selection in order to correctly identify the areas affected by the first failure phenomena due to the mechanical and kinematic differences of the triggering mechanisms. This topic is discussed in Sorbino et al. (2010) who, back-analyzing the events dated May 1998 with distributed physically based models, compare the results obtained through two indexes that quantify the "success" and the "error" of each model in simulating the observed landslide source areas. The indexes highlight that these models can identify the areas where the mechanism M1 was observed while they fail for M2 and M3, whose characteristics cannot be captured by the differential equations they implement.

De Chiara (2014) and Ferlisi & De Chiara (2016) analyze a similar topic focusing on the Monte Albino relief, Figure 6, about 10 km far from the slopes of Sarno town, Figure 4. In such a case the detailed in-situ and laboratory investigations allowed identifying the hazards and mapping their source, evolution and deposition areas at 1:5,000 scale (Matano et al., 2016).

All the acquired elements were processed to analyze the occurrence of different mass movements (shallow landslides, erosion phenomena, etc.) which, depending on the characteristics of rainfall and the position of the triggering zones along the relief, originate flowslides, debris avalanches, hyperconcentrated flows and flash flood, so classified according to Coussot & Meunier (1996). The analyses were developed first by calibrating the rheology of the flowing masses through the back-analysis of the past events and then by estimating the hazard they originate at the toe of the slopes (Figure 17).

Moving from the Monte Albino relief to the slopes of the Amalfi coast (Figure 4a) historical data, in-situ surveys and numerical analyses show a further significant change of phenomena and consequence threatening the municipalities located at the toe of the mountain basins. The flowslides are almost completely absent and the flow-like phenomena are essentially represented by hyperconcentrated flows and flash floods, mainly occurring at the beginning of the rainy season (differently from the case of Pizzo d'Alvano massif). In almost all the municipalities, the discharge of water plus sediment originated by critical rainfalls causes the crisis of the culvert (see Section 2.2) with consequent flooding of the urban area above.

A case study testifying the serious consequences that these events may cause is dated 25 October 1954 when, starting from 1:00 p.m. and until night, more than 500 mm of rainfall were recorded, that is about half of the average yearly cumulated rainfall of the area. This extreme weather event caused 318 victims as well as severe damage in the City of Salerno and in

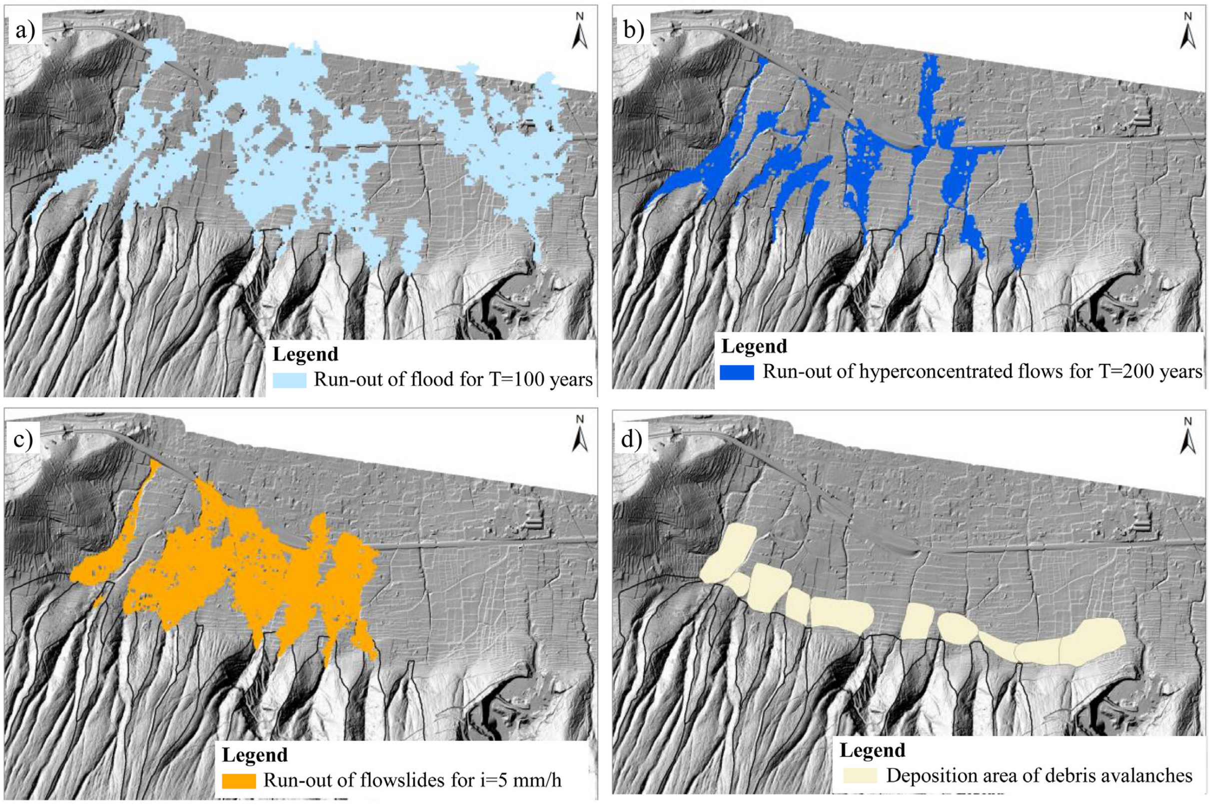

Figure 17. Numerical results provided by the propagation analysis of flow-like phenomena along the Monte Albino massif: a) flood, b) hyperconcentrated flows, c) flowslides, d) debris avalanches [modified from De Chiara (2014)].

many nearby municipalities of the Amalfi Coast. The erosive phenomena that affected the slopes of some mountain basins are analyzed in Cuomo et al. (2015), Cuomo & Della Sala (2015) while, due to the lack of many input data, the modeling of the flows that hit the inhabited centers was not developed.

However, the back-analysis of the event that occurred in 2010 in the Municipality of Atrani, Figure 4b, highlights that even not so critical rainfall can cause the flooding of the urban centre (Cascini et al., 2021). In such a case the estimated return period of the rainfall was about T = 50 years, to which correspond a cumulative water washout of 640,000 m^3 and a peak water discharge of 60 m^3/sec at the catchment outlet (Figure 18a). However, the in-situ surveys and cameras of eyewitnesses present in the area have shown that approximately 45,500 m^3 of sediments (i.e. only 7% of the water washout) were mobilized in less than 10 min (Figure 18b) by intense erosion along the slopes, originating the hyperconcentrated flow shown in Figure 18c. The combination of events increased the peak discharge of water plus sediments at the inlet section of the culvert up to the value of 180 m^3/sec (Cascini et al., 2021), equivalent to the effect expected from a rainfall with a return period of T = 200 years. As a result, the culvert was suddenly filled up and the excess volumes flooded the urban area above (Figure 18c), where caused damage and a victim.

6. Towards new frameworks for landslide analysis

While scientists from different disciplines attempt to provide general suggestions for either theoretical or applicative topics, the geotechnical community directs efforts to advance knowledge at slope scale rather than to identify classes of landslides having a similar behaviour. This is probably due to the young age of the basic principles of Geotechnics, established only 100 years ago, and to the idea that landslides require ever great insights to avoid the danger of undermining, with excessive simplifications, the reference framework built up to now with passion and competence.

The case studies discussed in this paper show that knowledge can be translated into general frameworks through a horizontal path in some cases and a vertical one in other. The path is here defined horizontal where the input data come from different case studies all analyzed in similar temporal conditions, with a monodisciplinary approach and at the same topographical scale. Vertical is instead a path for which the surveys, studies and analyses are developed with a multidisciplinary approach at different topographical scales, all correlated to each other and, where necessary, at different time scales. The benefits arising from this new analysis of landslides are discussed below.

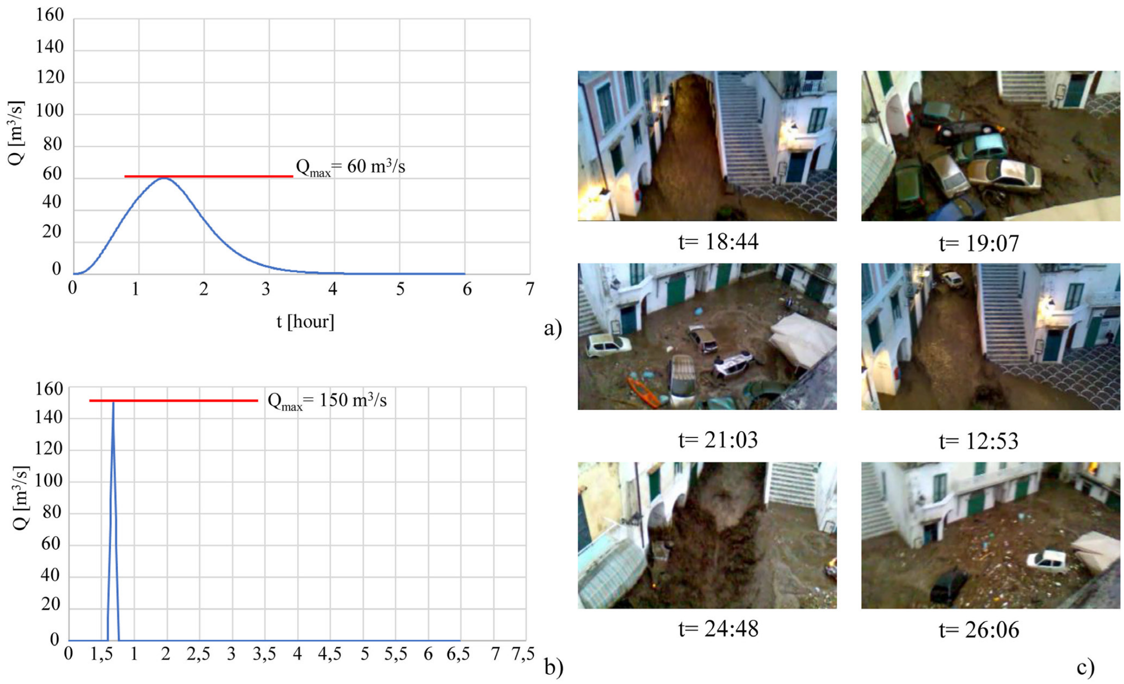

Figure 18. a) Estimated peak discharge of water and b) sediments; c) propagation in the urban area of the hyperconcentrated flow.

6.1 Single deep-seated landslides

The method proposed in Section 3, made possible by the efforts of many landslide researchers around the world, opens perspectives in practice and theory.

In practice, the identification of common dynamic characteristics of landslides allows the prediction of their evolution as described in Cascini et al. (2022) who propose two different procedures to achieve the goal. One directly processes the experimental curves while the other refers to the dimensionless displacements, as described in section 3.1. Two explanatory examples, one for each of the two proposed approaches, are reported below.

The first example is relative to the Vallcebre landslide (Corominas et al., 2005), a rainfall induced existing landslide characterized by a sequence of trends I and II. For trend II, systematically recorded during the wet season, Cascini et al. (2014a) compare the experimental measures with result from their approximation through the power law function. The comparison highlights that the first 7 data, i.e., 80 days in advance of the total duration of the activity stage, provide a satisfactory forecast of the entire set of displacements (Figure 19a).

The second example focuses on the Vajont landslide which has been analyzed through the dimensionless displacements (Figure 10b) and the stability chart (Figure 12) to estimate the equilibrium condition during each stage of the landslide evolution.

Figure 19b shows that during the first two increases of the water level in the reservoir the exponent of the power law function $D(T)$ approximating the experimental data, after a certain time, is in the range $2 \leq x < 3$, typical values of a weakly unstable condition (Figure 12 and Table 2) not evolved into failure by emptying the reservoir. The figure also shows that, during the third increase of the water level, the value of the exponent ($x > 3$) reveals, already 19 days before the disaster, the impossibility of avoiding the collapse due to the increase of both acceleration and jerk, a typical condition of a strongly unstable system (Figure 12 and Table 2).

From a theoretical point of view, the dimensionless displacement trends and the stability chart require identifying the basic governing principles and understanding whether landslides can be defined as "complex systems" as defined by Parisi (1999).

Regarding the first point, attention was focused on the approach proposed in Di Prisco & Flessati (2021) to verify whether the stability condition of these trends can be interpreted or not with Lyapunov's theory. Cascini et al. (2023) provide promising preliminary results but there is still a long way to go due to the complexity of the topic.

As it concerns the second point, this is not the place to go deeper into the subject nor does the writer have the skills to express an opinion on how to process input data in problems involving complex systems. Despite these limitations, it is useful to stimulate the discussion through three questions: can the landslides be considered a complex system? Can the individual evolution stages of landslides, as defined in Section 3, be assimilated to a complex system? Can a complex system or part of it be governed by the laws of Physics?

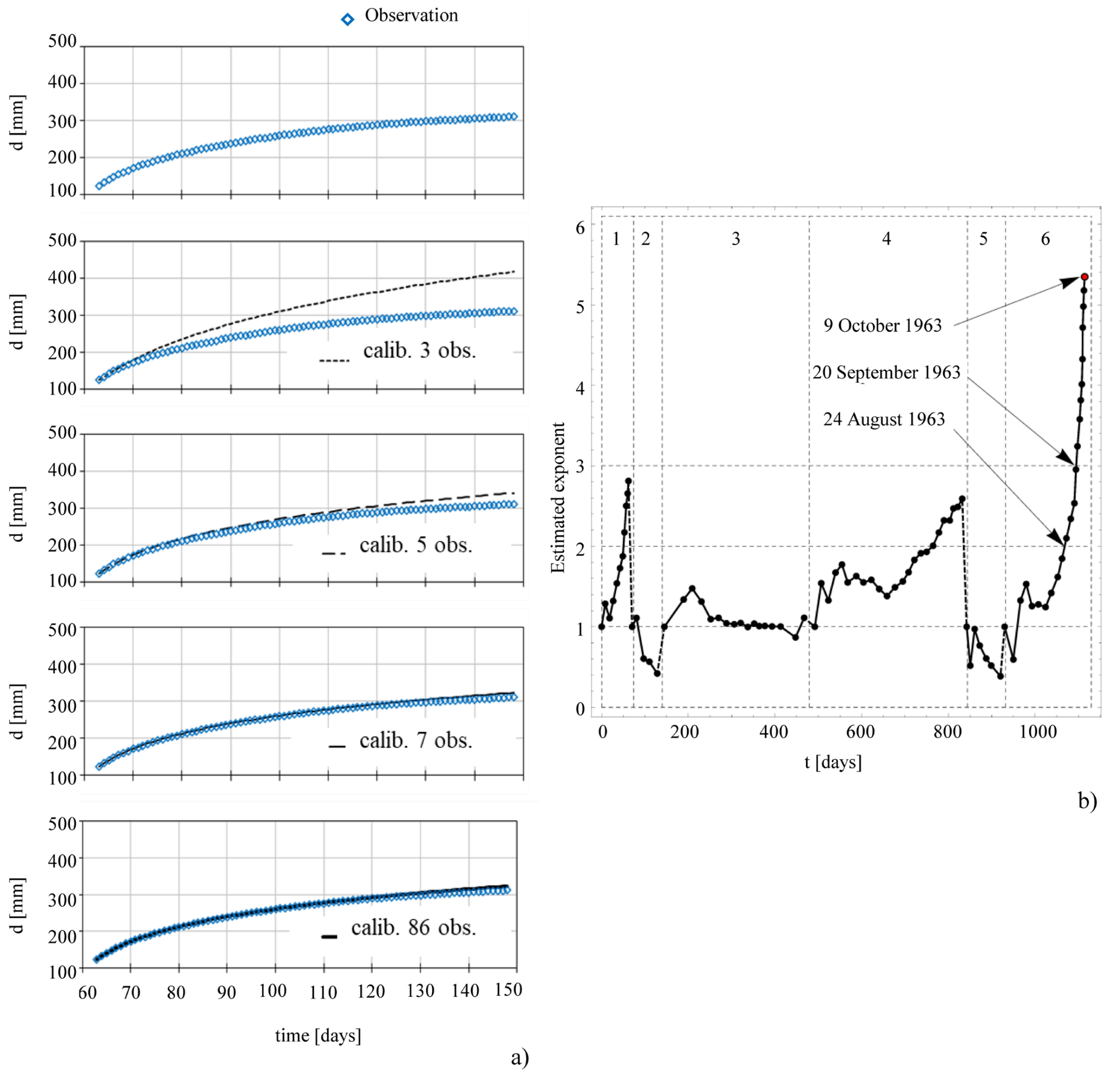

Figure 19. a) Forecasting the evolution of the Vallcebre landslide through the dimensional displacements (Cascini et al., 2014a), b) the exponent of the function approximating the dimensionless data for the last 1126 days before the collapse of the Vajont landslide [modified from Cascini et al. (2022)].

In the author's opinion, the first two questions can be answered positively since the evolution of landslides, over the years and within a single displacement trend, depends on many different interacting elements that determine their overall behavior not predictable from the study of the individual parts (Weisbuch, 1991).

The results discussed in Section 3 and simple considerations of Geology and Geotechnics indicate the possibility to provide a positive answer even to the third question, at least as regards the existing landslides. In fact, it is reasonable to hypothesize that the long geological history of these landslides has led to a geometric configuration which corresponds to a condition of stable equilibrium. Hypothesis supported by the residual shear strength systematically mobilized along the existing slip surfaces and by the linear displacements trend in the absence of external perturbations. It follows that the evolution stages represent the temporary or permanent variation of this stable equilibrium, induced by external perturbations and governed by the laws of Physics.

The author believes that the current knowledge is not sufficient to consider the previous answers exhaustive and, therefore, the questions are still open. However, it is already clear that their confirmation would furnish new theoretical perspectives for the study of landslides with extremely positive benefits as it concerns their analysis and management.

6.2 Multiple shallow instabilities

In the Campania region (Southern Italy) the risk zoning of flow-like phenomena was carried out at intermediate scale (1:25,000) with heuristic methods, i.e., the only ones capable of providing consistent replies within the mandatory deadlines set by the Authorities. Later, not having time constraints, the scientific studies were developed mainly at large (1:5,000) or detailed scale (1:1,000) implementing statistical and/or deterministic methods. In some cases, research has been developed at a small scale (<1:100,000), to complete knowledge on some issues not of direct interest to the Authorities.

In practice, the activities were carried out following the needs and objectives of the moment and, apparently, without a well-defined guiding thread. Therefore, the main questions are whether it is possible to follow a more rational path in the absence of external conditioning and which strategy to follow where these constraints exist.

With reference to the first question Cascini (2015) proposes two alternatives called respectively "bottom-up" and "top-down" approach. The first approach preliminarily analyses site-specific problems at large scale with the aid of deterministic methods; then, it generalizes knowledge to progressively larger areas through statistical or heuristic methods implemented at intermediate or small scales. The second approach follows the reverse path, initially framing the problems over large areas and at small scale with the aid of heuristic methods; then, the knowledge is deepened within sample areas of progressively decreasing extension that are usually analyzed through the statistical method at an intermediate scale and the deterministic ones at large/detailed scales.

The bottom-up approach starts from scientific-based evidence, progressively generalized through statistical and geological approaches, which gradually require an increasing expert judgment. The initial advantage is discounted with the time necessary to complete the entire path, which is generally long and, sometimes, unsustainable. An application of this approach is provided in Cascini (2015) who arrived at the generalization of the results after about 15 years.

The top-down approach certainly reduces the times of the entire process, but it requires the preliminary formulation of hypotheses whose validity must be progressively demonstrated with methods of increasing reliability. An application of this approach is illustrated in Cascini (2015) who demonstrate how it was possible to connect all the scales together in less than three years. These authors also provide guidelines to develop a consistent process that allows one to hit the target rather than progressively move away from it.

Where both approaches cannot be used, as in the case study described in the paper, it is recommended to develop, from the beginning, each step in a multiscale perspective to have, at the end of the path, a global and coordinated vision of all the issues, each analyzed with different materials and methods at different topographical scales. The framework resulting from a similar approach applied to the case study of the Campania region can be summarized as follows.

The pyroclastic covers mantling the slopes in an area of about 3,000 km^2 originate a high Societal risk in the geological context A1 systematically threatened over the centuries by events that caused victims and economic damages. The instability phenomena along the slopes of this area are triggered by critical rainfalls having different characteristics. In the hinterland the phenomena mainly occur during the wet season while moving along the coast the worst phenomena are recorded at the beginning of this season (Figure 20a). The rainfall intensity and the values of the soil suction during the hydrological year

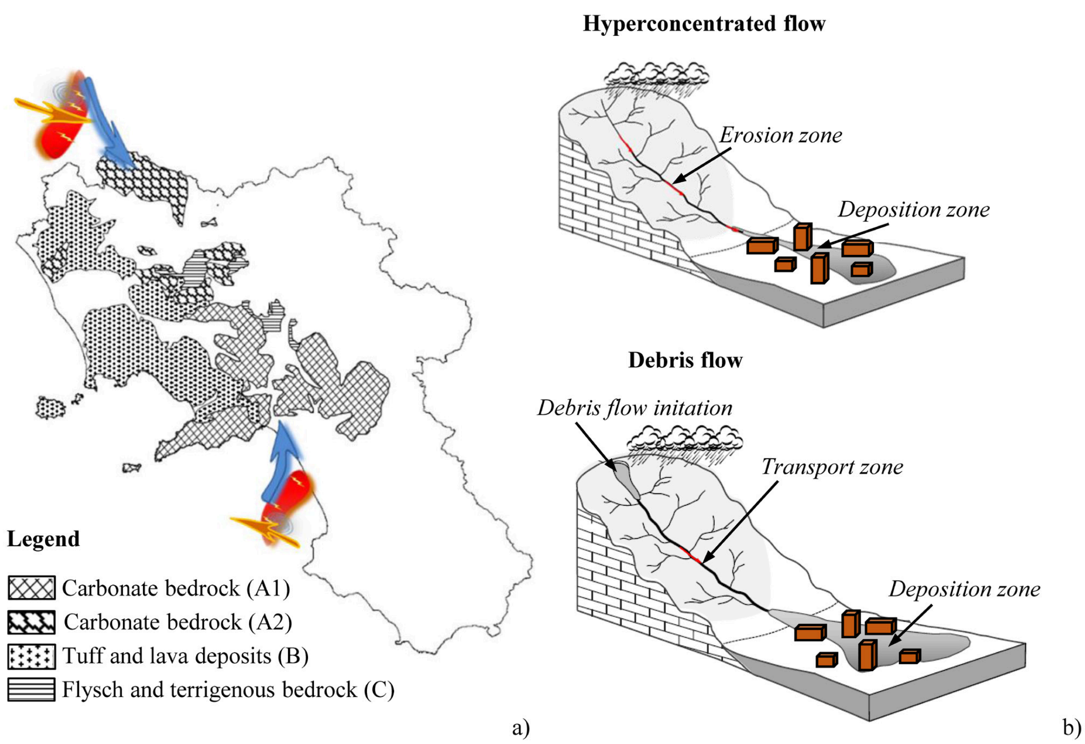

Figure 20. a) Different meteorological events causing the instability of the soil covers in the hinterland and along the Amalfi coast [modified from De Chiara (2014)]; b) different triggering and evolution mechanisms of the flows in the hinterland and along the Amalfi coast.

imply that: during the rainy season, in the hinterland, the rainfall infiltrates the soil covers originating shallow landslides that evolve into flowslides; along the coast, at the end of the dry season, erosive phenomena prevail originating flash floods or hyperconcentrated flows (Cascini et al., 2014b, 2021) with a peak discharge corresponding to a rainfall with a very high return period (Figure 20b).

In practice, this scientific evidence i) has made it possible the implementation of alarm systems, which have considerably reduced the risk to life all over the Campania region and ii) allows the mitigation of the risk to property that today appears to be only an economic problem, as the design of sustainable control works is possible thanks to the available know-how. Results, that at the beginning of the activities, were unimaginable and out of reach from a scientific and technical points of view.

7. Concluding remarks

The case studies, approaches and tools discussed in the paper show that attempts are possible to translate the impressive knowledge available on landslides into frameworks of general utility in practice, as is usually the case in much older scientific sectors than Geotechnics.

The study illustrated in Section 3 can give rise to one of these frameworks, as the evolution of single deep-seated landslides seems to be represented by a limited number of displacement trends, regardless of the geological contexts in which they occur, the soil properties of materials involved in the landsliding, the triggering factors and so on. This belief can be reinforced through the proposed method that is easy to apply and, as such, easy to use to further verify its reliability. This could establish a milestone for a class of landslides that are currently considered completely different from a mechanical point of view, while the obtained results indicate that the laws of Physics are the basis of their evolution stages.

The study outlined in Section 4 highlights the potential of the multiscale and multidisciplinary approach for studying multiple shallow instabilities that are too often analyzed in a monodisciplinary perspective. In particular, the paper proposes an approach able to connect materials and methods of different disciplines which, used together from the beginning of the cognitive process, can allow an unexpected advancement of knowledge. Moreover, sharing of knowledge, through consistent and physically based approaches, can make it possible to progress on phenomena for which the studies developed in a geological context are currently of limited interest to those carried out in another geological context.

In conclusion, the paper proposes a new vision for the analysis of landslides which, to be strengthened, requires the sharing of knowledge, implementation of coherent methods and, above all, further results to confirm some preliminary insights made possible by the efforts of a high number of researchers around the world.

Acknowledgements

The author is grateful to the many colleagues who shared complex research topics, as evidenced by the papers published in proceedings and journals. The author also thanks Enrico Babilio and Sabatino Cuomo who revised this paper and Giovanna De Chiara who made indispensable assistance in the overall organization of the manuscript.

Declaration of interest

The author has no conflicts of interest to declare. The author has observed and affirmed the contents of the paper and there is no financial interest to report.

Data availability

The datasets used in the current study are available from the author upon request.

List of symbols

d:	displacement
$\dot{d}$	velocity
$\ddot{d}$	acceleration
$\dddot{d}$	jerk
f_{ext}	external forces
f_{res}	resistance forces
f_d	driving forces
$\dot{f}_{ext}$	derivative of external forces
$\dot{f}_{res}$	derivative of resistance forces
h	depth of secondary slip surface
l	length of secondary sliding body
m	main body motion direction
p'	effective mean stress
q	deviatoric stress
t	time
w	width of secondary sliding body
D	dimensionless displacement
F	cumulative annual frequency of landslides
H	depth of main slip surface
L	length of main sliding body
N	number N of fatalities due to landslides
Q	discharge
SF	safety factor
T	dimensionless time
W	width of main sliding body

References

Alonso, E., Zervos, A., & Pinyol, N. (2016). Thermo-poro-mechanical analysis of landslides: from creeping. *Geotechnique*, *66*(3), 202-219. http://dx.doi.org/10.1680/jgeot.15.LM.006.

Alonso, E.E., Pinyol, N.M., & Puzrin, A.M. (2010). *Geomechanics of failures. Advanced topics*. Dordrecht: Springer. Catastrophic slide: Vaiont landslide, Italy, pp. 33-81. https://doi.org/10.1007/978-90-481-3538-7_2.

Babilio, E., Cascini, L., Fraternali, F., & Scoppettuolo, M.R. (2021). Investigating the evolution of landslides via dimensionless displacement trends. *Mathematics and Mechanics of Complex Systems*, *9*(3), 231-272. http://dx.doi.org/10.2140/memocs.2021.9.231.

Bertini, T., Cugusi, F., D'Elia, B., & Rossi-Doria, M. (1986). Lenti movimenti di versante nell'Abruzzo Adriatico: caratteri e criteri di stabilizzazione. In A.G.I. (Ed.), *Proceedings of the 16th National Conference* (Vol. 1, pp. 91-100). Padova, Italy: CLEUP.

Binet, S., Mudry, J., Scavia, C., Campus, S., Bertrand, C., & Guglielmi, Y. (2007). In situ characterization of flows in a fractured unstable slope. *Geomorphology*, *86*(1-2), 193-203. http://dx.doi.org/10.1016/j.geomorph.2006.08.013.

Cascini, L. (2004). The flowslides of May 1998 in the Campania region, Italy: the scientific emergency management. *Italian Geotechical Journal*, *38*(2), 11-44.

Cascini, L. (2003). Risk assessment of fast landslide – from theory to practice. General report. In L. Picarelli (Ed.), *Proceedings of the International Conference on "Fast Slope Movements — Prediction and Prevention for Risk Mitigation"* (Vol. 2, pp. 33-52). Bologna, Italy: Pàtron Editore.

Cascini, L. (2015). Geotechnics for urban planning and land use management. *Rivista Italiana di Geotecnica*, *49*(4), 7-62.

Cascini, L., & Ferlisi, S. (2003). Occurrence and consequences of flowslides: a case study. In L. Picarelli (Ed.), *Proceedings of the International Conference on "Fast Slope Movements — Prediction and Prevention for Risk Mitigation"* (pp. 85-92). Bologna, Italy: Pàtron Editore.

Cascini, L., Calvello, M., & Grimaldi, G.M. (2014a). Displacement trends of slow-moving landslides: classification and forecasting. *Journal of Mountain Science*, *11*(3), 592-606. http://dx.doi.org/10.1007/s11629-013-2961-5.

Cascini, L., Cuomo, S., & Guida, D. (2008a). Typical source areas of May 1998 flow-like mass movements in the Campania region, Southern Italy. *Engineering Geology*, *96*(3-4), 107-125. http://dx.doi.org/10.1016/j.enggeo.2007.10.003.

Cascini, L., Cuomo, S., & Pastor, M. (2008b). The role played by mountain tracks on rainfall-induced shallow landslides: a case study. In International Environmental Modelling & Software Society (Org.), *Proceedings of the 4th International Congress on Environmental Modelling and Software* (pp. 1484-1941). Barcelona: iEMSs.

Cascini, L., Cuomo, S., & Pastor, M. (2013). Inception of debris avalanches: remarks on geomechanical modelling. *Landslides*, *10*(6), 701-711. http://dx.doi.org/10.1007/s10346-012-0366-0.

Cascini, L., Cuomo, S., Di Mauro, A., Di Natale, M., Di Nocera, S., & Matano, F. (2021). Multidisciplinary analysis of combined flow-like mass movements in a catchment of Southern Italy. *Georisk*, *15*(1), 41-58. http://dx.doi.org/10.1080/17499518.2019.1674339.

Cascini, L., Cuomo, S., Pastor, M., & Sorbino, G. (2010). Modeling of rainfall-induced shallow landslides of the flow-type. *Journal of Geotechnical and Geoenvironmental Engineering*, *136*(1), 85-98. http://dx.doi.org/10.1061/(ASCE)GT.1943-5606.0000182.

Cascini, L., Di Prisco, C.G., Babilio, E., & Flessati, L. (2023). Creeping landslides. In L. Cascini, S. Cuomo, M. Calvello, S. Ferlisi & D. Peduto (Eds.), *Landslide risk assessment and mitigation: lessons learned from the International LARAM School* (Pt. IV). Switzerland: Springer Nature. Geoenvironmental Disaster Reduction. Retrieved in September, 2023, from https://www.springer.com/series/16107.

Cascini, L., Ferlisi, S., & Tagliafierro, G. (2002). Il contributo delle indagini storiche nella definizione del rischio da frana: un caso di studio. In AGI (Ed.), *Proceedings of the XXI Italian Geotechnical Congress* (pp. 135-142). Bologna, Italy: Pàtron Editore.

Cascini, L., Ferlisi, S., & Vitolo, E. (2008c). Individual and societal risk owing to landslides in the Campania region (southern Italy). *Georisk*, *2*(3), 125-140. http://dx.doi.org/10.1080/17499510802291310.

Cascini, L., Scoppettuolo, M.R., & Babilio, E. (2022). Forecasting the landslide evolution: from theory to practice. *Landslides*, *19*, 2839-2851. http://dx.doi.org/10.1007/s10346-022-01934-3.

Cascini, L., Sorbino, G., & Cuomo, S. (2003). Modelling of flowslides triggering in pyroclastic soils. In L. Picarelli (Ed.), *Proceedings of the International Conference on "Fast Slope Movements — Prediction and Prevention for Risk Mitigation"* (Vol. 1, pp. 93-100)., Italy: Pàtron Editore.

Cascini, L., Sorbino, G., Cuomo, S., & Ferlisi, S. (2014b). Seasonal effects of rainfall on the shallow pyroclastic deposits of the Campania region (southern Italy). *Landslides*, *11*, 779-792. http://dx.doi.org/10.1007/s10346-013-0395-3.

Corominas, J., Moya, J., Ledesma, A., Lloret, A., & Gili, J.A. (2005). Prediction of ground displacements and velocities from groundwater level changes at the Vallcebre landslide (Eastern Pyrenees, Spain). *Landslides*, *2*(2), 83-96. http://dx.doi.org/10.1007/s10346-005-0049-1.

Coussot, P., & Meunier, M. (1996). Recognition, classification and mechanical description of debris flows. *Earth-Science Reviews*, *40*, 209-227. http://dx.doi.org/10.1016/0012-8252(95)00065-8.

Crosta, G.B., & Agliardi, F. (2003). Failure forecast for large rock slides by surface displacement measurements. *Canadian Geotechnical Journal*, *40*(1), 176-191. http://dx.doi.org/10.1139/t02-085.

Crosta, G.B., Chen, H., & Lee, C.F. (2004). Replay of the 1987 Val Pola Landslide, Italian Alps. *Geomorphology*, *60*, 127-146. http://dx.doi.org/10.1016/j.geomorph.2003.07.015.

Crosta, G.B., Di Prisco, C., Frattini, P., Frigerio, G., Castellanza, R., & Agliardi, F. (2014). Chasing a complete understanding of the triggering mechanisms of a large rapidly evolving rockslide. *Landslides*, *11*, 747-764. http://dx.doi.org/10.1007/s10346-013-0433-1.

Cuomo, S. (2006). *Geomechanical modelling of triggering mechanisms for flow-like mass movements in pyroclastic soils* [PhD thesis, University of Salerno]. University of Salerno.

Cuomo, S. (2020). Modelling of flowslides and debris avalanches in natural and engineered slopes: a review. *Geoenvironmental Disasters*, *7*, 1-25. http://dx.doi.org/10.1186/s40677-019-0133-9.

Cuomo, S., & Della Sala, M. (2015). Large-area analysis of soil erosion and landslides induced by rainfall: a case of unsaturated shallow deposits. *Journal of Mountain Science*, *12*(4), 783-796. http://dx.doi.org/10.1007/s11629-014-3242-7.

Cuomo, S., Della Sala, M., & Novità, A. (2015). Physically based modelling of soil erosion induced by rainfall in small mountain basins. *Geomorphology*, *243*, 106-115. http://dx.doi.org/10.1016/j.geomorph.2015.04.019.

De Chiara, G. (2014). *Quantifying the risk to life posed by hyperconcentrated flows* [PhD thesis, University of Salerno]. University of Salerno.

Di Prisco, C., & Flessati, L. (2021). Progressive failure in elastic–viscoplastic media: from theory to practice. *Geotechnique*, *71*(2), 153-169. http://dx.doi.org/10.1680/jgeot.19.P.045.

Ferlisi, S., & De Chiara, G. (2016). Risk analysis for rainfall-induced slope instabilities in coarse-grained soils: practice and perspectives in Italy. In S. Aversa, L. Cascini, L. Picarelli & C. Scavia (Eds.), *Landslides and Engineered Slopes. Experience, Theory and Practice. Proceedings of the 12th International Symposium on Landslides* (Vol. 1, pp. 137-154). Boca Raton, United States: CRC Press.

Froude, M.J., & Petley, D.N. (2018). Global fatal landslide occurrence from 2004 to 2016. *Natural Hazards and Earth System Sciences*, *18*, 2161-2181. http://dx.doi.org/10.5194/nhess-18-2161-2018.

Helmstetter, A., Sornette, D., Grasso, J.R., Andersen, J.V., Gluzman, S., & Pisarenko, V. (2004). Slider block friction model for landslides: application to Vaiont and La Clapière landslides. *Journal of Geophysical Research*, *109*(B2), 1-15. http://dx.doi.org/10.1029/2002JB002160.

Hungr, O., Leroueil, S., & Picarelli, L. (2014). The Varnes classification of landslide types, an update. *Landslides*, *11*, 167-194. http://dx.doi.org/10.1007/s10346-013-0436-y.

Keqiang, H., & Sijing, W. (2006). Double-parameter threshold and its formation mechanism of the colluvial landslide: Xintan landslide, China. *Environmental Geology*, *49*(5), 696-707. http://dx.doi.org/10.1007/s00254-005-0108-x.

Kirschbaum, D., Stanley, T., & Zhou, Y. (2015). Spatial and temporal analysis of a global landslide catalog. *Geomorphology*, *249*, 4-15. http://dx.doi.org/10.1016/j.geomorph.2015.03.016.

Leoroueil, S. (2001). Natural slopes and cuts: movement and failure mechanisms. *Geotechnique*, *51*(3), 197-243. http://dx.doi.org/10.1680/geot.2001.51.3.197.

Leoroueil, S., Locat, J., Vaunat, J., Picarelli, L., Lee, H., & Faure, R. (1996). Geotechnical characterization of slope movements. In K. Senneset (Ed.), *Proceedings of the 7th International Symposium Landslides* (Vol. 1, pp. 53-74). Boca Raton, United States: CRC Press.

Lollino, G., Arattano, M., Allasia, P., & Giordan, D. (2006). Time response of a landslide to meteorological events. *Natural Hazards and Earth System Sciences*, *6*, 179-184. http://dx.doi.org/10.5194/nhess-6-179-2006.

Matano, F., De Chiara, G., Ferlisi, S., & Cascini, L. (2016). Thickness of pyroclastic cover beds: the case study of Mount Albino (Campania region, southern Italy). *Journal of Maps*, *12*(Suppl. 1), 79-87. http://dx.doi.org/10.1080/17445647.2016.1158668.

Musso, A. (1997). Limitazione nell'uso dei pendii con ridotto margine di sicurezza. In A. Pellegrino (Ed.), *Interventi di stabilizzazione dei pendii* (pp. 449-474).Udine: CISM. In Italian.

Nonveiller, E. (1987). The Vajont reservoir slope failure. *Engineering Geology*, *24*, 493-512. http://dx.doi.org/10.1016/0013-7952(87)90081-0.

Parisi, G. (1999). Complex systems: a physicist's viewpoint. *Physica A*, *263*(1-4), 557-564. http://dx.doi.org/10.1016/S0378-4371(98)00524-X.

Pinyol, N., & Alonso, E. (2010). Fast planar slides: a closed-form thermo-hydromechanical solution. *International Journal for Numerical and Analytical Methods in Geomechanics*, *34*(1), 27-52. http://dx.doi.org/10.1002/nag.795.

Scoppettuolo, M.R., Cascini, L., & Babilio, E. (2020). Typical displacement behaviours of slope movements. *Landslides*, *17*(5), 1105-1116. http://dx.doi.org/10.1007/s10346-019-01327-z.

Secondi, M., Crosta, G., Di Prisco, C., Frigerio, G., Frattini, P., & Agliardi, F. (2011), Landslide motion forecasting by a dynamic visco-plastic model. In F. Catani, C. Margottini, A. Trigila & C. Iadanza (Eds.), *The Second World Landslide Forum* (p. 332). Rome, Italy: FAO/ISPRA.

Shuzui, H. (2001). Process of slip-surface development and formation of slipsurface clay in landslides in Tertiary volcanic rocks, Japan. *Engineering Geology*, *61*, 199-220. http://dx.doi.org/10.1016/S0013-7952(01)00025-4.

Simeoni, L., & Mongiovì, L. (2007). Inclinometer monitoring of the Castelrotto landslide in Italy. *Journal of Geotechnical and Geoenvironmental Engineering*, *136*, 653-666. http://dx.doi.org/10.1061/(ASCE)1090-0241(2007)133:6(653).

Sorbino, G., Sica, C., & Cascini, L. (2010). Susceptibility analysis of shallow landslides source areas using physically based models. *Natural Hazards*, *53*, 313-332. http://dx.doi.org/10.1007/s11069-009-9431-y.

Studio Majone Ingegneri Associati. (2023). *Frana della Val Pola: 1987-2017, 30 anni dopo il tragico evento che colpi' la Valtellina*. Retrieved in September, 2023, from https://www.studiomajone.it/1987-2017-frana-val-pola-valtellina/

Suwa, H., Mizuno, T., & Ishii, T. (2010). Prediction of a landslide and analysis of slide motion with reference to the 2004 Ohto slide in Nara, Japan. *Geomorphology*, *124*(3-4), 157-163. http://dx.doi.org/10.1016/j.geomorph.2010.05.003.

Tacher, L., Bonnard, Ch., Laloui, L., & Parriaux, A. (2005). Modelling the behaviour of a large landslide with respect to hydrogeological and geomechanical parameter heterogeneity. *Landslides*, *2*(1): 3-14. https://doi.org/10.1007/s10346-004-0038-9

Tommasi, P., Pellegrini, P., Boldini, D., & Ribacchi, R. (2006). Influence of rainfall regime on hydraulic conditions and movement rates in the overconsolidated clayey slope of the Orvieto hill (central Italy). *Canadian Geotechnical Journal*, *43*(1), 70-86. http://dx.doi.org/10.1139/t05-081.

Varnes, D.J. (1978). Slope movement types and processes. In R.L. Schuster & R.J. Krizek (Eds.), *Landslides: analysis and control* (pp. 11-33). Washington: Transportation and Road Research Board/National Academy of Sciences. Special Report 176.

Vaunat, J., Leroueil, S., & Faure, R.M. (1994). Slope movements: a geotechnical perspective. In R. Oliveira (Ed.), *7th International Congress International Association of Engineering Geology* (pp. 1637-1646). Rotterdam: Balkema.

Violante, C. (2009). Rocky coast: geological constraints for hazard assessment. *Geological Society of London, Special Publications*, *322*, 1-31. http://dx.doi.org/10.1144/SP322.1.

Voight, B. & Kennedy, B. A. (1979). Slope Failure of 1967–1969, Chuquicamata Mine, Chile. In B. Voight (Ed.), *Developments in geotechnical engineering* (Chapter 17, Part B, Vol. 14, pp. 595-632). Amsterdam: Elsevier. https://doi.org/10.1016/B978-0-444-41508-0.50025-9.

Weisbuch, G. (1991). *Complex systems dynamics*. Boca Raton: CRC Press. https://doi.org/10.1201/9780429494031.

Wikipedia. (2023). *Vajont dam*. Retrieved in October 7, 2023, from https://en.wikipedia.org/wiki/Vajont_Dam

ARTICLES

Soils and Rocks
An International Journal of Geotechnical and Geoenvironmental Engineering
www.soilsandrocks.com
ISSN 1980-9743
ISSN-e 2675-5475

Soil surface-atmosphere interaction in a monitored embankment constructed with two compacted lime-treated soils

Katia Vanessa Bicalho[1#], Thiago Luiz Poleto[1], Yu-Jun Cui[2], Yasmina Boussafir[3]

Article

Keywords
Field monitoring
Soil suction
Soil moisture
Soil water evaporation
Soil-atmosphere interaction

Abstract

This study was carried out in an instrumented and monitored embankment divided into two symetrical sections and constructed with compacted treated soils (i.e., a silty soil and a clayey soil) exposed to the same atmospheric conditions in a continental climate, with oceanic influences. It aimed to investigate changes of bare soil surface moisture (w) and corresponding suction (s) as result of soil water evaporation processes on a monthly time scale. Seasonal variations in the w (and s) measurement in both soil surfaces show overall consistency with the meteorological measurement within the study area. The paper also examines the ability of four air temperature-based potential evaporation (*PET*) formulations to capture the process of evaporation at the site. Results indicated that soil water evaporation is controlled by both atmospheric and soil conditions. And, during the most significant drying time period, the measured s consistently increased and the corresponding w decreased suggesting a relatively significant water evaporation effect. However, the monthly predicted *PET* data varied from a maximum of over 120 mm/month to less than 50 mm/month during the drying time, depending on the used method. The continuously monitored soil surface suctions are used for discussing the variations of evaporation according to the predicted *PET* method and time period at the site.

1. Introduction

Geotechnical engineering works are subjected to soil moisture and corresponding soil suctions variations at both weather and climate timescales. Periodical drying-wetting cycles can alter soil seepage and stability analysis in earth works (Toll et al., 2011; Azizi et al., 2023). And, the knowledge of the effects of soil surface-atmosphere interaction (SAI) in earth engineering works can reduce faulty or very conservative engineering designs and deficient long-term performance of geo-structures (Bordoni et al., 2021). The SAI can be reflected by heat and water transfer in soil-plant-atmosphere continuum and described by the variations of soil surface boundary conditions (Blight, 1997; Elia et al., 2017; Sedighi et al., 2018; Toll et al., 2019).

In order to understand the dynamics and the variability of soil moisture in geotechnical engineering, it is crucial to well evaluate the main mechanisms related to water balances for the soil systems (Blight, 2003; Cui & Zornberg, 2008). Previous studies have shown that using only precipitation data for soil stability analysis provides insufficient information for assessment of landslide processes especially for clayey shallow soil (Toll et al., 2011; Bittelli et al., 2012; Bicalho et al., 2018; Fusco et al., 2022; Cui, 2022). Soil surface suctions (and moistures) respond directly to wetting by infiltration of rainfall or drying as a result of evapotranspiration. These changes in suction/moisture can take place independently of the main ground water table.

The amount of rainfall infiltration into the soil mass depends on external factors as well as intrinsic soil parameters, and the effect of rainfall infiltration on soil instabilities has been studied by many researchers (Wolle & Hachich, 1989; Springman et al., 2003; Rahardjo et al., 2005; Huang et al., 2009). Though forming a fundamental component on studies of soil water balance and applications, soil water evaporation is challenging to quantify in practice occurring in the form of combined liquid and vapor transport both at the depth and ground surface. Potential evaporation (*PET*), which represents the upper reference limit to the regional evaporative capacity in a given surface under given meteorological conditions (Lhomme, 1997; Zhou et al., 2020), is often estimated using

[#]Corresponding author. E-mail address: katia.bicalho@ufes.br
[1]Universidade Federal do Espírito Santo, Departamento de Engenharia Civil, Vitória, ES, Brasil.
[2]Ecole des Ponts ParisTech, Laboratoire Navier, Champs-sur-Marne, France.
[3]Université Gustave Eiffel, Champs-sur-Marne, France.

Submitted on April 8, 2023; Final Acceptance on October 25, 2023; Discussion open until February 28, 2024.
https://doi.org/10.28927/SR.2023.003523

climate models at multiple scales. Yet, soil water evaporation is controlled by atmospheric, vegetation and soil conditions (Wilson, 1990; Tran et al., 2016) with significant spatial variability (Niranjan & Nandagiri, 2023), and the suitability and accuracy of the *PET* empirical methods can be questioned.

Relative evaporation (i.e. the ratio of actual to maximum or potential evaporation, ET_a / *PET*) varies in time and space depending on soil-moisture conditions (Wilson, 1990), conceptual *PET* model, and measured data. The difference between the actual ET_a and the *PET* is considered negligible in humid regions or under wet conditions (e.g. precipitation greater than potention evaporation) but becomes increasingly large as the surface moisture availability decreases (Fetter, 1994). The local evaluation of the *PET* values is important for understanding soil atmosphere fluxes in the soil work performance over time and estimating the spatial and temporal change in the actual evaporation. *PET* values may vary significantly in both, time, and space, and exist different ways and definitions in use for identifying the model and parameter to estimate potential evaporation (Kay & Davies, 2008; Kalma et al., 2008; Hu et al., 2021). The selection of appropriate *PET* method for analysis of the data depends on input data availability, and the required accuracy of the estimated *PET* values in the investigated site and period.

Changes of the soil surface suction/moisture in an monitored nonvegetated embankment were examined considering the SAI in two lime treated fine-grained soils exposed to the same meteorological conditions (dry and wet seasons) in the Northeast of France. The field instrumentation included spatial and temporal changes of the soil suction/moisture at a predefined superficial locations within the embankment, as well as measurements of meteorological data, collected between Spring and Fall in 2011 (the first-year-old embankment building). In the cold period of a year, the evaporation estimated by different methods vary considerably due to the specificity of each adopted methodology. The air temperature can have negative values in the cold period in determined regions with very small calculated values of evaporation. The study was carried out using different meteorological data and soil conditions to examine the comparison among field monitoring soil surface suctions at specific location and calculated *PET* values determined using four common empirical expressions obtained from in-situ recorded meteorological observations over dry months.

2. Materials and methods

2.1 Description of the study area and data collection

A monitored full-scale embankment constructed with compacted lime treated soils in the Northeast of France is investigated herein. The site in Hericourt, Haute-Saône, France, is located at Latitude 47° 34’ 39” North, Longitude 06° 45’ 42” East and average altitude of 413 m. It is exposed to a continental climate, with oceanic influences. The embankment (107m long by about 5m high with side slopes of 1 on 2) was divided into two symmetrical sections, constructed with two natural soils (a silty soil and a clayey soil) treated with cement and/or lime in different dosages (Froumentin, 2012). As the soils were treated with different binders (lime or cement) and with different dosages, for the purpose of comparison, only the points with lime-treated soil have been selected for analysis in this study. According to the unified soil classification system, the two soils were classified as: CL, an inorganic clay with low plasticity, and CH, an inorganic clay with high plasticity. Soil and meteorological conditions on the test plots at the embankment have been monitored since the construction in 2010. A system of runoff measurement was also installed to monitor the runoff from the side slope (An et al., 2017).

The investigations and analysis were divided into two parts. The first part analyzes the potential evaporation calculations in the study site in 2011. A site-specific meteorology station on the top surface was used to record the meteorological data every 30 min, including precipitation, relative humidity, air temperature, net radiation and wind speed. The year of 2011 had a cumulative precipitation (rainfall) at local weather station (773 mm) above average annual precipitation (619 mm) in France. The air temperature and relative humidity were recorded at 0.5 m and 1.5 m above the soil surface in 2011. The second part investigates the monitoring data of matric suction and volumetric water content at predefined locations over time within the embankment. The instrumentation layout was symmetrical for the two sections of the embankment. The embankment consists of 17 layers made of the two fill materials compacted to optimum water contents (Standard Proctor tests). At each layer, the gravimetric water content and soil density were measured at various positions before and after construction, and the measurement variations were quite small. No leachate of lime or cement with rainfall was observed in the monitored area. A layer of the slope, approximately at mid-slope, was selected for the investigations and analyses in this paper. The selected layer, located at about 1.8 m from the embankment base, is instrumented with sensors, for measuring soil suction (s) and volumetric water content (w), located close to allow estimation of the in-situ s - w relationship at the specific position over time.

Time Domain Reflectometry (TDR) method, a measurement technique for electrical properties is used to monitor the volumetric soil water content changes at the investigated embankment. The used sensors are TRIME-PICO 64, of IMKO Micro GmbH, in Germany, which are capable of simultaneously measuring soil temperature and inferring the volumetric water content. The TDR method was used to monitor the soil volumetric water content, together with the soil temperature. The probes installed were linked to a control panel and data acquisition system, which allowed regular measurements. Watermark soil suction sensors connected to a data acquisition system was used to monitor the soil superficial suction changes over time at the embankment. The used sensor is an indirect, calibrated method of measuring soil suction. It is an electrical resistance type sensor. These "Granular Matrix Sensors" electronically read the amount of moisture absorbed through a special "granular matrix", or mix of precisely composed materials. This special mix buffers the sensor against the effects of different salinities and ensures a lifetime much longer than the traditional "gypsum blocks". The readings were calibrated to reflect the same values that would be generated by a Tensiometer.

2.2 Description of the adopted potential evaporation (*PET*) calculation methods

Evapotranspiration represents the combined evaporation from the soil surface and transpiration from plants. Actual evaporation (ET_a) indicates the amount of water evaporated through the bare soil surface while conceptually potential evaporation (*PET*) represents the maximum possible evaporation rate and is the rate that would occur under given meteorological conditions from a continuously saturated surface (Donohue et al., 2010). The regional evaluation of the maximum or potential evaporation is important for understanding soil atmosphere fluxes in the embankment system performance over time and estimating the spatial and temporal change in the actual evaporation ($ET_a < PET$).

Many methods have been proposed to evaluate *PET* calculations based on standard meteorological observations (Xu & Singh, 1998, 2001; Donohue et al., 2010; Tu & Yang, 2022). *PET* methods should be used for open water or fully water saturated soil surfaces. A large variability can be observed on the *PET* methods based on meteorological local date considering different assumptions, input data, and specific climatic regions (Lemaitre-Basset et al., 2022). Actual rates of evaporation from unsaturated soil surfaces are generally greatly reduced relative to the potential rate of evaporation.

Solar radiation, air temperature, air relativity humidity and wind speed are climatological input data to consider when assessing the evaporation process. In this study, the *PET* was estimated using four formulations applied in the year 2011 when the weather data were directly measured in the study area. The four *PET* methods (Thornthwaite, 1948; Blaney & Criddle, 1950; Kharrufa, 1985; Romanenko, 1961) are briefly summarized here (Table 1) and the cited references are suggested for a detailed discussion. The mean monthly net radiation and wind speed measured values in the region remained essentially unchanged during the evaluation period; therefore, it may be reasonable to make the assumption of no influence of the net radiation and wind speed on the evaporation considered by the used methods for the region in 2011.

Thornthwaite (1948) formulation is highly used, even though the empirical method is not recommended for areas that are not climatically similar to the developed area, in the eastern region of USA, where sufficient moisture water

Table 1. Equations for estimating potential evaporation (*PET*) according to air temperature-based methods (Thornthwaite, 1948; Blaney & Criddle, 1950; Kharrufa, 1985), and a combination of air temperature and air relative humidity-based method (Romanenko, 1961).

Method	Required inputs	Equation (*PET*)	Variable definition
Thornthwaite (1948)	average air temperature, and latitude	$16\left(10\frac{T}{I}\right)^{a}$	$i = \sum_{1}^{12}\left(\frac{T}{5}\right)^{1.514}$
			$a = 6.75x10^{-7} I^3 \; -7.71x10^{-5} I^2 + 1.7912x10^{-2} I \; +0.4939$
		$0 \le T \le 26°C$	$I =$ annual heat index, given by the sum of the 12 monthly values of i, monthly heat index
			$T =$ average air temperature
Blaney & Criddle (1950)	average air temperature, latitude, coefficient dependent on the vegetation type, location, and season	$\ddot{u} \quad (0.46 \quad +8.13)$	$k =$ crop coefficient (plantation). It is obtained from curves based on field measurements. In Blaney & Criddle (1962) an extensive table is presented with the values of k for several states of the Western USA.
			$p =$ monthly average percentage of light hours.
			$T =$ average air temperature
Kharrufa (1985)	average air temperature, and latitude	$0.34\, pT^{1.3}$	$p =$ monthly average percentage of light hours.
			$T =$ average air temperature
Romanenko (1961)	average air temperature, and average relative humidity of air	$0.0018\left(25+T\right)^2 A$	$R_h =$ air relative humidity
			$T =$ average air temperature
			$A = \left(100 - R_h\right)$

was available to maintain active transpiration. The original equation is misused in arid and semi-arid irrigated areas (Xu & Singh, 2001). Moreover, one should be aware that the soil temperature fluctuates daily and yearly mainly by changes in air temperature and solar radiation. Often, one chooses a model to estimate *PET* based on the available data to calculate the model. Generally, more sophisticated models require larger input files, and obtaining the necessary input data can be time consuming and difficult. The air temperature-based equations are evaluated in this paper due to the advantage that the methods allow calculating *PET* by using only the monthly average air temperature and the locations of the geographic coordinates.

Atmosphere water balance refers to the balance of the inflow and outflow of atmosphere moisture. An atmosphere water balance (*B*) is tied to an overall balance through the processes of precipitation (*P*), and evaporation (*ET*) at a given local and time scale (Blight, 1997, 2003). The actual evaporation (ET_a) differs from the potencial evaporation (*PET*) under most circumstances. For assessing four common air temperature-based *PET* methods, a dependency between ET_a and *PET* values is assumed in this study. And, *B* values are estimated using *PET* instead of ET_a:

$$B = P - PET \tag{1}$$

During the period of excess water (*B* positive), there is moisture available for ground-water recharge and runoff. The runoff were monitored for the investigated embankment. And, the runoff remained quite low (<0.1 mm/h) when the precipitation was lower than about 11 mm/h, and became significant beyond 11 mm/h precipitation (Cui, 2022).

Net water fluxes are a function of the infiltration entering the soil cover due to precipitation and exfiltration leaving the soil cover due to atmospheric evaporation. The uncertainties regard to the potential evaporation value, which depends on the model structure and input data, might result in different *B* values. The results of Equation (1) were estimated using four air temperature-based equations (Thornthwaite, 1948; Blaney & Criddle, 1950; Kharrufa, 1985; Romanenko, 1961) of *PET* values (see Table 1). Romanenko (1961) method is based on a combination of air temperature and air relative humidity data. Table 1 presents a summary of the required inputs, equation and variable definition used for determining *PET* values at site specific meteorology station on the top surface of the monitored embankment.

3. Results and discussions

The bare soil surface moisture/suction in unsaturated region can be changed under two main mechanisms: infiltration or evaporation. Many factors affect soil evaporation. In this study, the spatial and temporal field measured variations of the soil surface suction/moisture in two lime-treated soils (a silty soil and a clayey soil) due to local environmental conditions are compared to the potential evaporation calculations based upon the assumptions that the *PET* data were dependent only upon meteorological conditions and ignored the effect of soil conditions.

3.1 Prediction of *PET* data from the local recorded meteorological observations

Figure 1a illustrates the mean monthly recorded precipitation, *P*, and the calculated *PET* (mm/month) values according to air temperature-based methods (Thornthwaite, 1948; Blaney & Criddle, 1950; Kharrufa, 1985), and a combination of air temperature and air relative humidity-based method (Romanenko, 1961) from May to October in 2011, at Hericourt, France. The air temperature *T* and relative humidity R_h values were recorded at 0.5 m and 1.5 m above the soil surface at the site. The air temperatures are approximately constant at the measured heights, and a small difference (5-10%) was observed in the R_h values recorded at 0.5 m and 1.5 m above the surface. The air close to the soil surface is warmer than it is higher up from April to August in 2011. The same trend is not observed in the months with lower temperatures (October and November 2011).

Wind speeds between 0 and 5.5 m/s were recorded in 2011 at the site. The mean monthly wind speed was about 1.0 m/s for the monitored period. Wind speed is important because stronger winds cause more evapotranspiration. But rate of transpiration may decrease with increasing wind speeds (Schymanski & Or, 2016). It is also presented in Figure 1a, the *PET* values calculated by using Romanenko (1961) formulation and the mean month R_h values recorded at 0.5 m and 1.5 m above the ground surface, *PET* - R1 and *PET* - R2, respectively, at the site in 2011. The difference of about 5-10% observed in the R_h recorded at the measured heights resulted in calculated *PET* variations over 20 mm / month in June 2021 according to Romanenko (1961) *PET* - R1 and *PET* - R2 results. Fluctuations observed in the estimated *PET* (mm/month) values according to the recorded air temperature-based methods (Thornthwaite, 1948; Blaney & Criddle, 1950; Kharrufa, 1985) in the site in 2011 indicated a wide variation in the calculated *PET* data depending on the used method and considered time period. June (J) and August (A) in 2011 were the hottest investigated months, with the highest values of evaporation estimated by air temperature-based methods in the investigated site. The analysis of *PET* (mm/month) values identified that the highest values of evaporation were estimated by Blaney & Criddle (1950) and Kharrufa (1985) formulations (see Figure 1a). *PET* values by Thornthwaite (1948) were underestimated (over 40 mm/month in June 2021) concerning the Blaney & Criddle (1950) and Kharrufa (1985) formulations. Variation of evaporation depending on the estimation method and the time period of the recorded meteorological data. Higher differences between estimated values using the selected ways were identified in

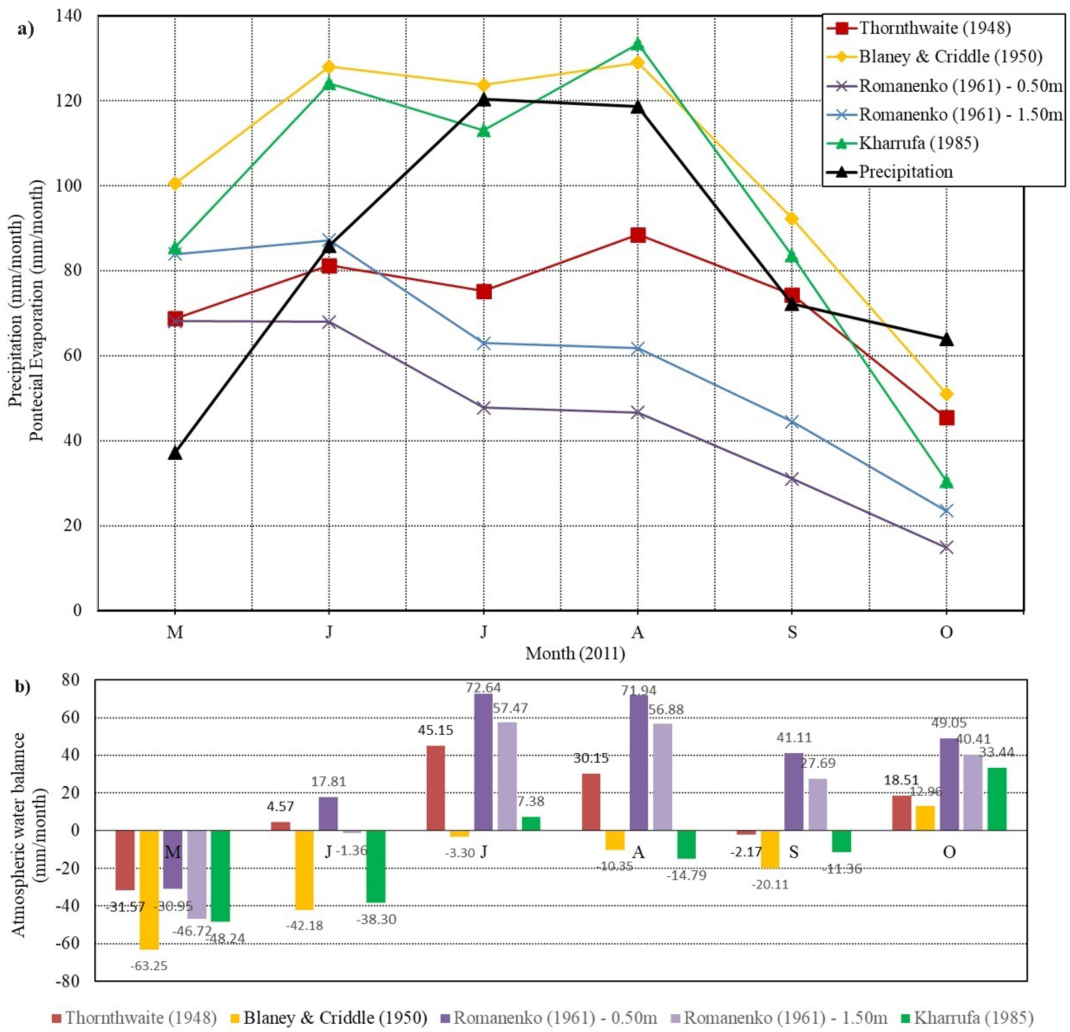

Figure 1. Variation of the measured (a) monthly precipitation and the calculated *PET* (mm/month) values (Thornthwaite, 1948; Romanenko, 1961; Blaney & Criddle, 1950; Kharrufa, 1985), and (b) calculated *B* values from May (M) to October (O) in 2011 in the investigated site.

the hottest months (i.e., July and August 2011) and lower in the coldest month (i.e., October 2011) of the evaluated period at the site.

Potential evaporation is an important component in the atmospheric water balance equation (*B*). It can be seen from Figure 1b, the comparison between the four methods clearly highlights the influence of the considered *PET* formulation on the predicted *B* values (Equation 1). The results show that May 2011 is a month of water deficit (*B* negative), and from June to September 2011, *B* values may be negative or positive depend on the adopted *PET* formulation. In October 2011, *B* is positive (water surplus) according to the four adopted *PET* methods. In June 2011, *B* varies from approximately –40 mm/month according to Blaney & Criddle (1950) and Kharrufa (1985) to approximately +20 mm/month by using Romanenko (1961) - R1. The difference observed in the formulations can be attributed to variations of the conceptual *PET* model, and measured input data (i.e., air relative humidity). The consideration of the runoff term in Equation 1 may prevent large positive anomalies of soil wetness (Delworth & Manabe, 1988). But there were no particularly intense rainfall events (>11 mm/h) during the significant water deficit period characterized by increasing soil surface suctions in the late spring (May and June in 2011) suggesting a relatively small amounts of runoff for the time period and site.

Thornthwaite (1948) considered only the mean monthly air temperature and sunlight as input data while Romanenko (1961) used the air temperature and relative humidity as input data. The mean monthly measured solar radiation and wind speed in the region remained essentially unchanged in 2011; therefore, it may be reasonable to assume no influence of the solar radiation and wind speed on the evaporation considered herein. Thornthwaite (1948) equation may underestimates the measured evapotranspiration (Blight, 1997) or overestimates *PET* where climate is relatively humid, while for arid and semiarid parts of China it produces an underestimation (Chen et al., 2005). The Blaney & Criddle (1950) method for estimating *PET* values is well known in the western USA and has been widely used elsewhere also (Xu & Singh, 2001).

3.2 Comparison between field measured soil surface suction/moisture and predicted potential evaporation data

Both infiltration and evaporation processes can have impacts on changing soil moisture and suction distribution in unsaturated soil surfaces. Changes of soil water evaporation are relatively expressive during significant periods of water deficit (*B* negative) at a site. Even though the relative contribution of soil evaporation to the amount of soil suction is not well defined. To investigate the effects of soil surface suction/moisture observations on predicted soil water evaporation, the measured in-situ soil surface suctions in the two bare treated fine-grained soils exposed at the same atmospheric conditions over dry months are compared to the simulated *PET* values (Thornthwaite, 1948; Blaney & Criddle, 1950; Kharrufa, 1985; Romanenko, 1961) determined from recorded meteorological observations at the investigated time period and site. *PET* - R1 and *PET* - R2 are the *PET* values calculated by using Romanenko (1961) formulation and the R_h recorded at 0.5 m and 1.5 m above the ground surface, respectively.

Figure 2 shows the comparisons of the mean monthly measured soil surface suction and corresponding volumetric water content values (about -0.25 m from slope face) in the two lime-treated soil (i.e., CL + 2% CaO and CH + 4% CaO) sections from April to November 2011 (dry and wet seasons). The layer of the slope located at about 1.8 m from the embankment base, approximately at mid-slope, was selected for the investigations and analysis because it is symmetrically instrumented with the sensors for measuring soil suction (*s*) and volumetric water content (*w*) located close to allow the estimation of the in-situ *s*-*w* relationship at the specific position over time. The data show consistency in the suctions determined by using watermark soil suction sensors and the volumetric water contents (and soil temperatures) determined by using TRIME-PICO 64 sensors, of IMKO

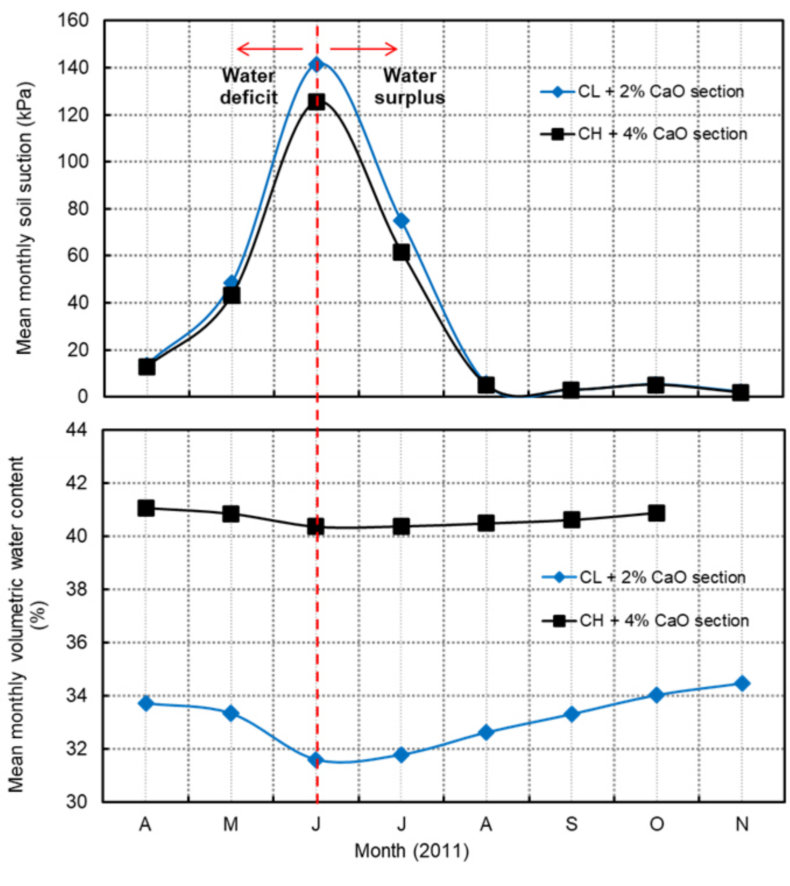

Figure 2. Comparison among mean monthly measured (a) soil suctions, (b) volumetric water contents, at mid-slope in the two treated soil sections from April (A) to November (N) in 2011.

Micro GmbH, variations trend in the two treated soils. Comparison between the lime-treated silty soil and the clayey soil (Figure 2a) showed that the variations of soil surface suction were more expressive in the silty soil in the late spring and summer, between June and August 2021. This confirmed that the hydraulic conductivity is an important factor in the response of soil to atmospheric conditions and the silty soil had a higher hydraulic conductivity, thus its suction changed more under the effects of infiltration / evaporation (Bicalho et al., 2015; Cui, 2022). During the most significant water deficit period in 2011 in the two lime-treated soils (i.e., from April to June), the mean monthly measured soil surface suctions have consistently increased and the corresponding water contents decreased. As can be seen in Figure 2, the responses of soil suction are usually less than 200 kPa (i.e., limit of the working range of each soil suction sensor). The simplified atmospheric water balance based on mean monthly potential evaporation calculated according to the adopted air temperature-based methods Blaney & Criddle (1950) and Kharrufa (1985) formulations, and, presented in Figure 1b (negative *B* values), illustrate well the period of water deficit observed in the responses of the mean monthly soil surface suction/moisture measurements (May and June) at the site. The same trend was not observed by using Thornthwaite (1948) and Romanenko (1961).

Figure 3 shows a graphical relationship for the mean monthly measured soil surface suction, *s* (kPa) versus the predicted potential evaporation *PET* (mm/month) for the two treated soils from April to June 2011 (i.e., a period of water deficit according to a relatively significant increase in the mean monthly measured soil surface suctions for the two lime-treated soils during the year at the site, Figure 2). *PET* (mm/month) values were calculated for the four methods from local recorded meteorological observations at the investigated site over the dry months in 2011 (i.e., April, May and June). It was joined straight lines through the measured / calculated points. Comparison between the silty soil and the clayey soil (Figure 2a) showed that the variations of suction were more significant for the more permeable soil (i.e., the silty soil). Knowing the responses of soil suction (and corresponding moisture) in association with soil water evaporation is important because soil suction is recognized as an important stress-state variable governing the behavior of unsaturated soils. Soil suction should be viewed as an environmental variable (Gens, 2010). Soil water evaporation is controlled by both atmospheric and soil conditions, and the comparison of the measured soil suction changes versus predicted potential evaporation (*PET*) changes can be used for evaluating the suitability and accuracy of the *PET* formulation. Changes of soil evaporation defined by predicted *PET* methods are related directly to soil suction (s) measurements during the investigated dry period.

The *s* (kPa) - *PET* (mm/month) relationship from April to June 2011 for the predicted air temperature-based *PET* methods proposed by Blaney & Criddle (1950) and Kharrufa (1985) exhibited a more substantial increase evaporation with soil suction increase. And, during the most significant drying time period, between May and June 2011, the measured *s*

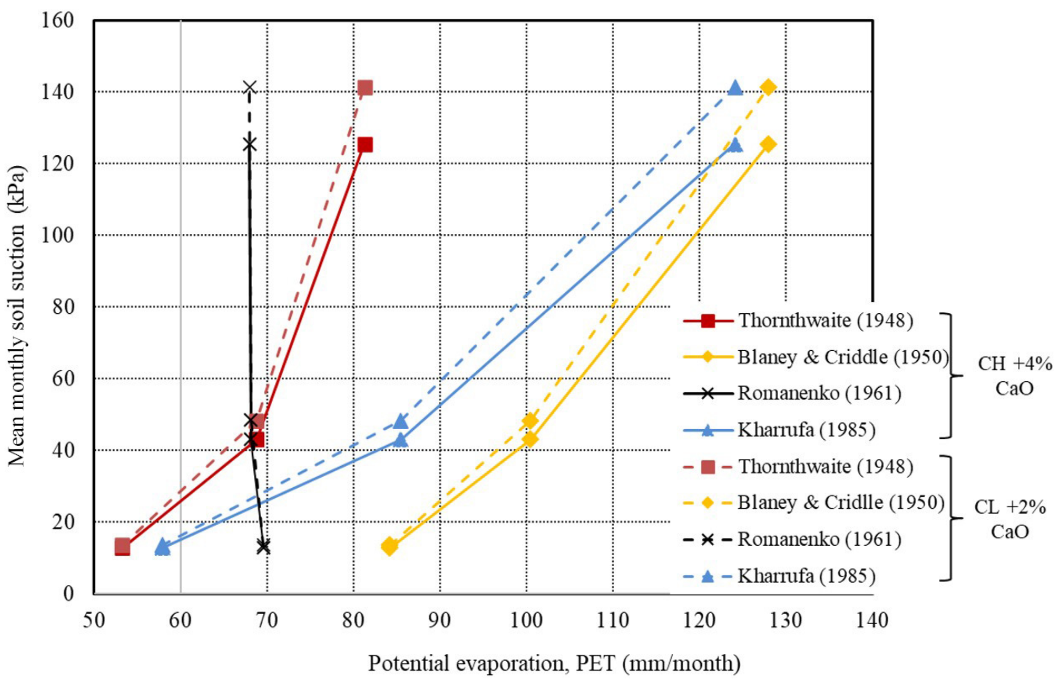

Figure 3. Comparison among mean monthly measured soil suctions at mid-slope in the two treated soil sections and different potential evaporation methods (Thornthwaite, 1948; Blaney & Criddle, 1950; Kharrufa, 1985; Romanenko, 1961) obtained solely by meteorological observations at the investigated site from April (A) to June (J) in 2011.

consistently increased and the corresponding *w* decreased suggesting a relatively significant water evaporation effect. The monthly predicted *PET* data varied from a maximum of over 120 mm/month (Blaney & Criddle, 1950) to less than 50 mm/month (Romanenko, 1961) depending on the used method during June 2011. The continuously monitored soil surface suctions were used for discussing the variations of evaporation according to the predicted *PET* method and time period at the site. The variations in the measured *s* and predicted *PET* by Blaney & Criddle (1950) and Kharrufa (1985) are more significant between May and June 2011. A similar trend is not observed with predicted *PET* proposed by Romanenko (1961) using mean monthly air temperature and air relative humidity, such that no significant difference in *PET* values were observed from April to June 2011. Moreover, the atmospheric water balances (*B*) calculated from measured precipitation (*P*) and predicted *PET* for the four methods from April to May indicate that May 2011 is a month of water deficit (*B* negative), and in June 2011, *B* values may be negative or positive depend on the adopted *PET* formulation and the position of the recorded input data. Calculated *B* values vary from approximately –40 mm/month (Blaney & Criddle, 1950; Kharrufa,1985) to approximately +20 mm/month (Romanenko, 1961). The difference observed in the formulations can be attributed to variations of the conceptual *PET* model and measured input data. Some previous studies have pointed out a decreasing trend in evaporation despite an increasing trend in air temperature, due to soil moisture limitation (Jung et al., 2010; Lemaitre-Basset et al., 2022). This result demonstrates the importance of previous critical analysis of *PET* formulations based upon the assumption that *PET* was dependent only upon meteorological conditions and empirical basis. Air relative humidity should not be used as input variable because atmosphere moisture is a function of soil moisture (Fetter, 1994). Moisture in the atmosphere is continually changing its physical state and the changes are all related to temperature. Air temperature is considered the most stable input parameter because it is a function of both solar radiation and water availability conditions (Wilson, 1990).

4. Conclusions

This paper examines changes of bare soil surface moistures (*w*) and corresponding suctions (*s*) at mid-slope of an embankment as result of soil water evaporation processes on a monthly time scale during drying period. The study also evaluates four commonly used air temperature-based formulations on predicting potential evaporation (*PET*) data at the site. Analysis of the monitoring data (both soil surface and atmosphere) of the two-lime treated fine-grained soils exposed to continuous soil drying period, in the embankment subjected to a continental climate, with oceanic influences, permit the following main conclusions:

- The measured suctions (*s*) using sensors Watermark and volumetric water contents (*w*) using quasi-TDR based TRIME PICO 64 in the two treated soil surfaces show overall consistency with local seasonal meteorological data variations. The mean month field measured *w* values gradually decreased and the corresponding *s* values increased as the water moved down into the soil or evaporated in the summer time at the investigated site. Mean month soil surface suctions are greater in the lime-treated silty soil at the same atmospheric conditions. This could be explained by the higher hydraulic conductivity of the silty soil;
- Soil water evaporation is controlled by both atmospheric and soil conditions. The continously measured *s* have consistently increased and the corresponding *w* decreased suggesting a relatively significant water evaporation effect during the most significant water deficit period at the site. The results of the predicted *PET* data determined on the basis of climatic conditions varied by about 80 mm/month in the most significant water deficit period depending on the used method. Some predicted *PET* data did not describe adequately the atmosphere water balance during the investigated drying period;
- The *s-PET* relationships for the adopted air temperature-based *PET* methods show a large variability according to the adopted *PET* method, and the differences given by the increased *PET* values during drying period were significant. The predicted monthly *PET* data varied from a maximum of over 120 mm/month to less than 50 mm/month depending on the used method during the hottest month. No significant difference in *PET* values calculated using mean monthly air temperature and air relative humidity, such that no significant difference in *PET* values were observed during the investigated period and site. This result indicates the importance of previous critical analysis of potential evaporation formulations based upon the assumption that *PET* was dependent only upon meteorological conditions and empirical basis;
- While the adopted air temperature-based *PET* methods assumptions are not correct, the methods are still useful for preliminary studies. To propose a calibrate suitable *PET* estimation method based on field measured of soil surface suctions/moistures and local meteorological data for wider applications, more studies within large and representative data for various atmospheric conditions are required. However, the approach of comparions between field measurements of soil surface suctions/moistures during evaporation and simple *PET* methods based on disponible local meteorological data may be used as an indicative of either a gross error in the used *PET* method (input data) or a violation of the assumption of a closed water balance.

Acknowledgements

This work has been performed within a part of the French Projet TerDOUEST ANR-07-PCGU-006-10. Great acknowledgments to the Cerema team of CER Rouen for the professionalism they demonstrated during embankment construction, sensors placement and data retrieval during these years. All in situ data are coming from Cerema's work. The authors acknowledge the constructive comments from the anonymous reviewers and the editor. The first author is also grateful to the financial support from the Brazilian agency CNPq (Research Productivity grant).

Declaration of interest

The authors have no conflicts of interest to declare. All co-authors have observed and affirmed the contents of the paper and there is no financial interest to report.

Authors' contributions

Katia Vanessa Bicalho: conceptualization, supervision, review and approval. Thiago Luiz Poleto: discussion, writing, reviewing and editing. Yu-Jun Cui: conceptualization, discussion, reviewing and editing. Yasmina Boussafir: project administration, discussion.

Data availability

All data produced or examined in the course of the current study are included in this article.

List of symbols

a	Index that adjusts to each region (Thornthwaite, 1948)
i	Heat index monthly (Thornthwaite, 1948)
k	Crop coefficient (plantation). It is obtained from curves based on field measurements. In Blaney & Criddle (1962) an extensive table is presented with the values of k for several states of the western USA.
p	Monthly average percentage of light hours
w	Soil surface moisture
s	Soil surface suction
B	Atmosphere water balance
ET	Evaporation
ET_a	Actual evaporation
I	Annual heat index, given by the sum of the 12 monthly values of i
P	Precipitation
PET	Potential evaporation
R_h	Air relative humidity
T	Average air temperature

References

An, N., Hemmati, S., Cui, Y.J., & Mercadier, D. (2017). Assessment of rainfall runoff based on the field measurement on an embankment. *Geotechnical Testing Journal*, 40(1), 20160096. http://dx.doi.org/10.1520/GTJ20160096.

Azizi, A., Kumar, A., & Toll, D.G. (2023). Coupling cyclic and water retention response of a clayey sand subjected to traffic and environmental cycles. *Geotechnique*, 73(5), 401-417. http://dx.doi.org/10.1680/jgeot.21.00063.

Bicalho, K.V., Boussafir, Y., & Cui, Y.J. (2018). Performance of an instrumented embankment constructed with lime-treated silty clay during four-years in the Northeast of France. *Transportation Geotechnics*, 17, 100-116. http://dx.doi.org/10.1016/j.trgeo.2018.09.009.

Bicalho, K.V., Vivacqua, G.P.D., Cui, Y.J., Froumentin, M., Mercadier, D., & Tang, A.M. (2015). Experimental Investigation of Soil-Atmosphere Interaction in an Instrumented Embankment constructed with two treated clays. *Soils and Rocks*, 38(2), 149-162. http://dx.doi.org/10.28927/SR.382149.

Bittelli, M., Valentino, R., Salvatorelli, F., & Pisa, P.R. (2012). Monitoring soil-water and displacement conditions leading to landslide occurrence in partially saturated clays. *Geomorphology*, 173–174(1), 161-173. http://dx.doi.org/10.1016/j.geomorph.2012.06.006.

Blaney, H.F., & Criddle, W.D. (1950). *Determining water requirement in irrigated areas from climatological data* (Soil Conservation Service Technical Publication, No. 96, 48 p.). Washington DC, US Department of Agriculture.

Blaney, H.F., & Criddle, W.D. (1962). *Determining consumptive use and irrigation water requirements* (Technical Bulletins, No. 171000). Washington, D.C.: Department of Agriculture, Economic Research Service.

Blight, G.E. (1997). Interactions between the atmosphere and the earth. *Geotechnique*, 47(4), 715-767.

Blight, G.E. (2003). The vadose zone soil-water balance and transpiration rates of vegetation. *Geotechnique*, 53(1), 55-64. http://dx.doi.org/10.1680/geot.2003.53.1.55.

Bordoni, M., Bittelli, M., Valentino, R., Vivaldi, V., & Meisina, C. (2021). Observations on soil-atmosphere interactions after long-term monitoring at two sample sites subjected to shallow landslides. *Bulletin of Engineering Geology and the Environment*, 80(10), 7467-7491. http://dx.doi.org/10.1007/s10064-021-02334-y.

Chen, D., Gao, G., Xu, C.-Y., Guo, J., & Ren, G. (2005). Comparison of the Thornthwaite method and pan data with the standard Penman-Monteith estimates of reference evapotranspiration in China. *Climate Research*, 28(1), 123-132. http://dx.doi.org/10.3354/cr028123.

Cui, Y.J. (2022). Soil–atmosphere interaction in earth structures. *Journal of Rock Mechanics and Geotechnical Engineering*, 14(1), 35-49. http://dx.doi.org/10.1016/j.jrmge.2021.11.004.

Cui, Y.J., & Zornberg, J.G. (2008). Water balance and evapotranspiration monitoring in geotechnical and geoenvironmental engineering. *Geotechnical and Geological Engineering*, 26(6), 783-798. http://dx.doi.org/10.1007/s10706-008-9198-z.

Delworth, T.L., & Manabe, S. (1988). The influence of potential evaporation on the variabilities of simulated soil wetness and climate. *Journal of Climate*, 1(5), 523-547. http://dx.doi.org/10.1175/1520-0442(1988)001<0523:TIOPEO>2.0.CO;2.

Donohue, R.J., McVicar, T.R., & Roderick, M.L. (2010). Assessing the ability of potential evaporation formulations to capture the dynamics in evaporative demand within a changing climate. *Journal of Hydrology*, 386(1-4), 186-197. http://dx.doi.org/10.1016/j.jhydrol.2010.03.020.

Elia, G., Cotecchia, F., Pedone, G., Vaunat, J., Vardon, P., Pereira, C., Springman, S.M., Rouainia, M., Van Esch, J., Koda, E., Josifovski, J., Nocilla, A., Askarinejad, A., Stirling, R., Helm, P., Lollino, P., & Osinski, P. (2017). Numerical modelling of slope-vegetation-atmosphere interaction: an overview. *Quarterly Journal of Engineering Geology and Hydrogeology*, 50(3), 249-270. http://dx.doi.org/10.1144/qjegh2016-079.

Fetter, C.W. (1994). *Applied hydrogeology* (3rd ed., 616 p.). New York: Macmillan College Publishing.

Froumentin, M. (2012). *Rapport de construction de l'ouvrage expérimental RD438 Héricourt Project TerDOUEST – ANR-07-PCGU-006-10*. Paris: Ministère de l'Ecologie, du Développement durable, des Transports et du Logement (in French).

Fusco, F., Bordoni, M., Tufano, R., Vivaldi, V., Meisina, C., Valentino, R., Bittelli, M., & De Vita, P. (2022). Hydrological regimes in different slope environments and implications on rainfall thresholds triggering shallow landslides. *Natural Hazards*, 114(1), 907-939. http://dx.doi.org/10.1007/s11069-022-05417-5.

Gens, A. (2010). Soil-environment interactions in geotechnical engineering. *Geotechnique*, 60(1), 3-74. http://dx.doi.org/10.1680/geot.9.P.109.

Hu, X., Shi, L., Lin, G., & Lin, L. (2021). Comparison of physical-based, data-driven and hybrid modeling approaches for evapotranspiration estimation. *Journal of Hydrology*, 601, 126592. http://dx.doi.org/10.1016/j.jhydrol.2021.126592.

Huang, C.C., Ju, Y.J., Hwu, L.K., & Lee, J.L. (2009). Internal soil moisture and piezometric responses to rainfall induced shallow slope failures. *Journal of Hydrology*, 370(1), 39-51.

Jung, M., Reichstein, M., Ciais, P., Seneviratne, S.I., Sheffield, J., Goulden, M.L., Bonan, G., Cescatti, A., Chen, J., de Jeu, R., Dolman, A.J., Eugster, W., Gerten, D., Gianelle, D., Gobron, N., Heinke, J., Kimball, J., Law, B.E., Montagnani, L., Mu, Q., Mueller, B., Oleson, K., Papale, D., Richardson, A.D., Roupsard, O., Running, S., Tomelleri, E., Viovy, N., Weber, U., Williams, C., Wood, E., Zaehle, S., & Zhang, K. (2010). Recent decline in the global land evapotranspiration trend due to limited moisture supply. *Nature*, 467(7318), 951-954. http://dx.doi.org/10.1038/nature09396.

Kalma, J.D., McVicar, T.R., & McCabe, M.F. (2008). Estimating land surface evaporation: A review of methods using remotely sensed surface temperature data. *Surveys in Geophysics*, 29(4-5), 421-469. http://dx.doi.org/10.1007/s10712-008-9037-z.

Kay, A.L., & Davies, H.N. (2008). Calculating potential evaporation from climate model data: a source of uncertainty for hydrological climate change impacts. *Journal of Hydrology*, 358(3-4), 221-239. http://dx.doi.org/10.1016/j.jhydrol.2008.06.005.

Kharrufa, N.S. (1985). Simplified equation for evapotranspiration in arid regions. *Beiträge zur Hydrologie*, 5(1), 39-47.

Lemaitre-Basset, T., Oudin, L., Thirel, G., & Collet, L. (2022). Unraveling the contribution of potential evaporation formulation to uncertainty under climate change. *Hydrology and Earth System Sciences*, 26(8), 2147-2159. http://dx.doi.org/10.5194/hess-26-2147-2022.

Lhomme, J.P. (1997). Towards a rational definition of potential evaporation. *Hydrology and Earth System Sciences*, 1(2), 257-264. http://dx.doi.org/10.5194/hess-1-257-1997.

Niranjan, S., & Nandagiri, L. (2023). Performance evaluation of simpler reference crop evapotranspiration estimation equations with and without local calibration. *Journal of Applied Water Engineering and Research*. In press. http://dx.doi.org/10.1080/23249676.2023.2230894.

Rahardjo, H., Lee, T.T., Leong, E.C., & Rezaur, R.B. (2005). Response of a residual soil slope to rainfall. *Canadian Geotechnical Journal*, 42(5), 340-351. http://dx.doi.org/10.1139/t04-101.

Romanenko, V.A. (1961). *Computation of the autumn soil moisture using a universal relationship for a large area* (No. 3). Kiev: Ukrainian Hydrometeorological Research Institute.

Schymanski, S.J., & Or, D. (2016). Wind increases leaf water use efficiency. *Plant, Cell & Environment*, 39(7), 1448-1459. http://dx.doi.org/10.1111/pce.12700.

Sedighi, M., Hepburn, B.D.P., Thomas, H.R., & Vardon, P.J. (2018). Energy balance at the soil atmospheric interface. *Environmental Geotechnics*, 5(3), 146-157. http://dx.doi.org/10.1680/jenge.15.00054.

Springman, S.M., Jommi, C., & Teysseire, P. (2003). Instabilities on moraine slopes induced by loss of suction: a case history. *Geotechnique*, 53(1), 3-10. http://dx.doi.org/10.1680/geot.2003.53.1.3.

Thornthwaite, C.W. (1948). An approach toward a rational classification of climate. *Geographical Review*, 38(1), 55-94. http://dx.doi.org/10.2307/210739.

Toll, D.G., Lourenço, S.D.N., Mendes, J., Gallipoli, D., Evans, F.D., Augarde, C.E., Cui, Y.J., Tang, A.M., Rojas, J.C., Pagano, L., Mancuso, C., Zingariello, C., & Tarantino, A. (2011). Soil suction monitoring for landslides and slopes. *Quarterly Journal of Engineering*

Geology and Hydrogeology, 44(1), 23-33. http://dx.doi.org/10.1144/1470-9236/09-010.

Toll, D.G., Rahim, M.S.M., Karthikeyan, M., & Tsaparas, I. (2019). Soil–atmosphere interactions for analysing slopes in tropical soils in Singapore. *Environmental Geotechnics*, 6(6), 361-372. http://dx.doi.org/10.1680/jenge.15.00071.

Tran, D.T.Q., Fredlund, D.G., & Chan, D.H. (2016). Improvements to the calculation of actual evaporation from bare soil surfaces. *Canadian Geotechnical Journal*, 53(1), 118-133. http://dx.doi.org/10.1139/cgj-2014-0512.

Tu, Z., & Yang, Y. (2022). On the estimation of potential evaporation under wet and dry conditions. *Water Resources Research*, 58(4), e2021WR031486. http://dx.doi.org/10.1029/2021WR031486.

Wilson, G.W. (1990). *Soil evaporative fluxes for geotechnical engineering problems* [Doctoral thesis, University of Saskatchewan]. University of Saskatchewan's repository. Retrieved in April 8, 2023, from https://harvest.usask.ca/handle/10388/etd-07102008-083937

Wolle, C.M., & Hachich, W.C. (1989). Rain-induced Landslides in South-eastern Brazil. In *Proceedings of 12th International Conference on Soil Mechanics and Foundation Engineering* (pp. 1639-1644), Rio de Janeiro. London: ISSMGE.

Xu, C.Y., & Singh, V.P. (1998). A review on monthly water balance models for water resources investigations. *Water Resources Management*, 12(1), 20-50. http://dx.doi.org/10.1023/A:1007916816469.

Xu, C.Y., & Singh, V.P. (2001). Evaluation and generalization of temperature-based methods for calculating evaporation. *Hydrological Processes*, 15(2), 305-319. http://dx.doi.org/10.1002/hyp.119.

Zhou, J., Wang, Y., Su, B., Wang, A., Tao, H., Zhai, J., Kundzewicz, Z.W., & Jiang, T. (2020). Choice of potential evapotranspiration formulas influences drought assessment: a case study in China. *Atmospheric Research*, 242, 104979. http://dx.doi.org/10.1016/j.atmosres.2020.104979.

Soils and Rocks
An International Journal of Geotechnical and Geoenvironmental Engineering
www.soilsandrocks.com
ISSN 1980-9743
ISSN-e 2675-5475

Numerical analysis of the breakwater failure at the Sergipe Terminal Port

Pedro Oliveira Bogossian Roque[1#], Celso Romanel[1],
Celso Antero Ivan Salvador Villalobos[1], Jackeline Castañeda Huertas[1]

Article

Keywords
Numerical analysis
Embankment on soft soils
Incremental construction
Breakwater
Slope failure

Abstract

The breakwater failure at the Sergipe Harbor is a well-known event among the Brazilian geotechnical community, which provided great knowledge about the behavior of embankments on soft soils, although some questions still remain, since the back analysis diverged from the field outcome. In this context, this work aims to carry out a numerical analysis of the construction of the breakwater using the finite element method to understand the mechanisms of failure. A fully coupled flow-deformation analysis was performed in Plaxis 2D software, using the Soft Soil Creep and Mohr-Coulomb constitutive soil models. The Volume Method was also applied to estimate the stability of the slopes, from the calculated numerical displacements. The interpretation of the results allowed to verify that the analysis simulated behaviors that had been raised as responsible for the failure. High excess pore pressure levels were generated in the phase at which failure occurred, in addition to a strain softening behavior, which, alongside the progressive failure, could justify why the back analysis considering unrealistic gains in undrained strength, calculated by the increase of the vertical effective stresses, had provided missed factors of safety. Although shear deformations and horizontal displacements were verified for both sides of the breakwater, the "shared failure" assumption could not be verified, since the shear stress was mobilized in the rockfill.

1. Introduction

The failure of the Sergipe Port Terminal (TPS) breakwater is one of the most well-known events among the Brazilian geotechnical community. Occurred in the late 1980s, the case was the subject of several works published in the national and international literature, discussing both the foundation slide failure in the initial design of the rockfill structure (Sandroni et al., 2018) as well as the modeling of the redesigned TPS (Brugger et al., 1998) constructed in the early years of 1990s. The rockfill structure, composed of a geotechnical berm 5.0 m thick and a hydraulic berm, was intended to protect the port pier, located more than 2.0 km from the shore, due to the large volume of sediment carried along the beach, and was placed on a soil profile with a surface layer of sand over a deposit of 7.0 m of soft soil (Figure 1).

The construction of the geotechnical berm was carried out with a side dump vessel from the temporary loading port. After an interval of about 6 months due to weather conditions, the construction of the hydraulic berm was started in August 1989 from the access bridge to the breakwater and, on October 12th of the same year, it failed. Studying the accident provided a great deal of learning about the construction of embankments on soft soils. However, despite the knowledge acquired, some doubts about the failure of the breakwater's original design remained, since the back analyses carried out both in terms of total and effective stresses, resulted in Factors of Safety greater than unity.

Some hypotheses were raised to explain the event such as: (a) the occurrence of progressive rupture in the soft clay, with loss of post-peak resistance and redistribution of shear stresses; (b) developing of excess pore pressure along the failure surface, reducing the effective acting stresses; (c) the occurrence of the shared failure phenomenon, based on the shear strength has not been completely developed in the rockfill body due to the failure mechanism.

Thus, the main objective of this work is to carry out a numerical back-analysis using the finite element method (FEM) to understand the mechanisms that led the breakwater of the TPS to rupture.

#Corresponding author. E-mail address: pedro_roque_93@yahoo.com.br
[1]Pontifícia Universidade Católica do Rio de Janeiro, Departamento de Engenharia Civil e Ambiental, Rio de Janeiro, RJ, Brasil.

Submitted on May 15, 2023; Final acceptance on October 25, 2023; Discussion open until February 28, 2024.

https://doi.org/10.28927/SR.2023.005223

To reach the proposed objective, a study was carried out using the finite element software for geotechnical problems Plaxis 2D v2020 considering a fully coupled flow-deformation analysis, using both the Soft Soil Creep (SSC) and the Mohr-Coulomb (MC) models in the soft clay layer of the foundation. The parameters used in the analyses were estimated based on the interpretation of geotechnical field and laboratory investigations in the foundation of the breakwater.

Additionally, an assessment of the stability of the breakwater was carried out using the Volume Method (Sandroni et al., 2004) based on the results of vertical and horizontal displacements obtained from the FEM analyses.

2. Geotechnical characteristics of Sergipe's soft soil

The breakwater was built over a four-meter surface sand layer, with SPT blow count (N_{SPT}) from 6 to 15 blows/30 cm on a 7-meter layer of very soft clay. Below the clay layer, there were clayey sand and sandy clay deposits, with N_{SPT} increasing with depth (Figure 2). This profile had great lateral homogeneity throughout the entire area of the work. To characterize the materials, notably the soft clay layer, several test campaigns were carried out by different institutions, many of them were published in the technical literature (Ladd & Lee, 1993; Sandroni et al., 1997; Brugger, 1996).

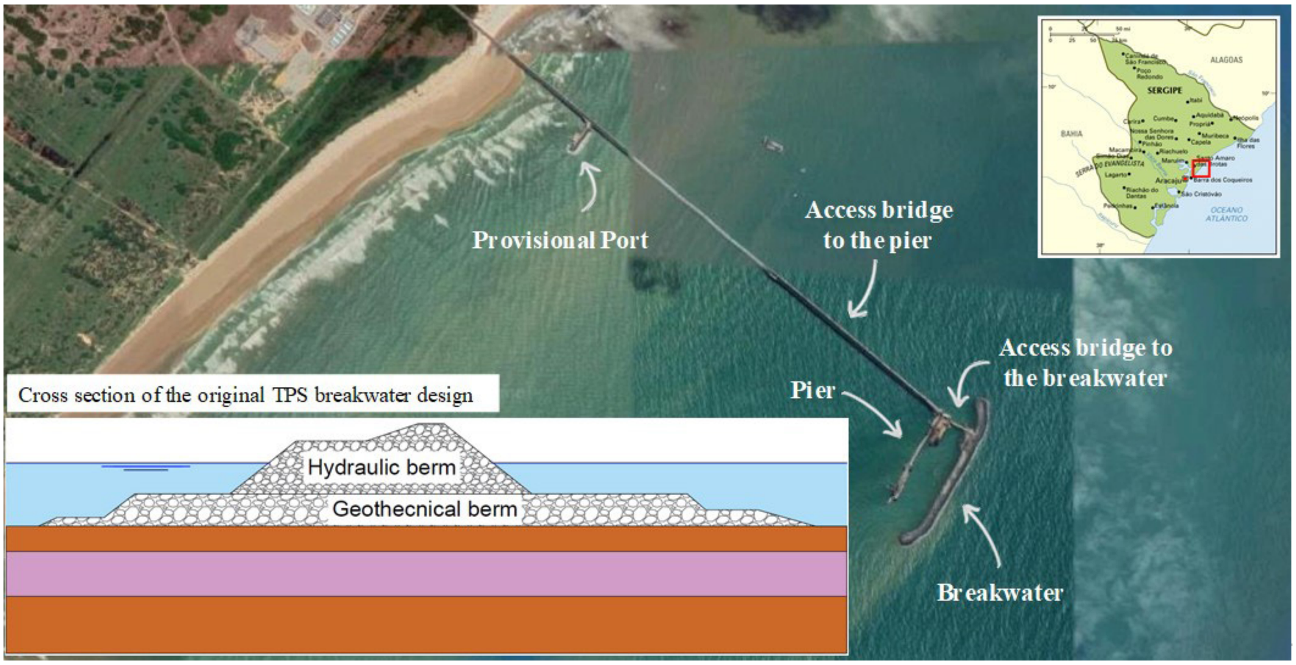

Figure 1. Location and typical cross-section of the original TPS breakwater design.

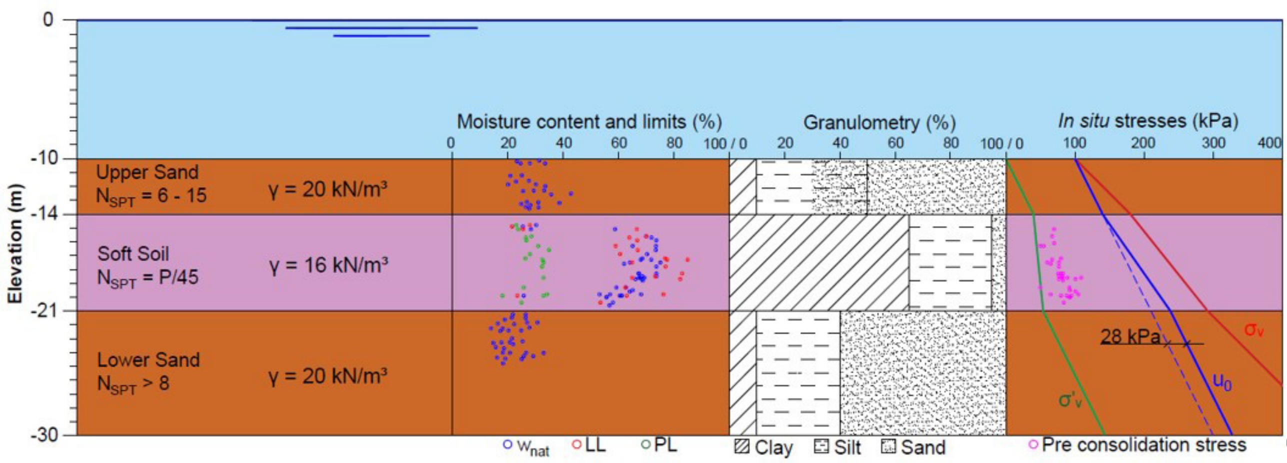

Figure 2. Typical stratigraphy of the TPS breakwater foundation materials showing variation of moisture content (w_{nat}), liquidity limit (LL), plasticity limit (PL), granulometry, in situ stresses and pre-consolidation stress.

According to the characterization process, the sand layers had a moisture content w_{nat} between 20 and 30% and the soft clay had an average moisture content between 54 and 72%, a plasticity limit *PL* between 24 and 35% and a liquidity limit *LL* between 58 and 85% (Ribeiro, 1992), although at some points *LL* was greater than 1.0, which could explain a metastable behavior of the soft clay (Sandroni et al., 1997).

Field geotechnical investigations, as well as piezometers installed in the clay, indicated a probable artesianism of approximately 28 kPa due to a freshwater aquifer in the lower sand layer, confined by the low permeability clay layer. This condition would be causing an upward freshwater flow in the clay, inducing the leaching of salts in its pores, in addition to reducing the effective stresses and increasing the sensitivity of the material.

Consolidation tests allowed verifying the Sergipe clay slightly pre-consolidated condition ($1 < OCR < 2$), with higher *OCR* at the top, lower between -16.0 m and -1.0 m elevations and then increasing with depth, indicating that artesianism dates to a geological age after the deposition of the material.

To determine the strength parameters of the clay, both field tests (vane tests and piezocone) and special laboratory tests (triaxial CIU and CK_0U and direct single shear tests DSS) results were evaluated. For laboratory tests with axial compression path, the values of undrained shear resistance as a function of the confining stress were equal to 0.30 for the CIU test, 0.24 for the CK_0U test and 0.22 for the DSS test. In the stress paths of the compression triaxial tests, the Skempton pore water pressure parameter A was greater than 1.0, confirming the sensitivity of the material.

The results of the Vane Tests indicated an increasing $Su,_{VT}$ profile with depth, with values close to 15 kPa at the top of the clay and reaching about 25 kPa at the base of the layer. These values do not consider the Bjerrum (1973) correction factor (μ), equal to 0.8 for Sergipe's clay (Sandroni, 2012 apud Schnaid & Odebrecht, 2012). The results of the CPTu tests allowed the construction of the N_{KT} profile, decreasing with depth, ranging from 16 at the top to 12 at the bottom (Brugger, 1996; Sandroni et al., 1997).

Based on the results of oedometric consolidation tests, it was also possible to define profiles of initial void ratios (e_0), compression (C_c) and swelling (C_s) indexes as a function of depth. The interpretation of the results were made by Geoprojetos (1992), Ladd & Lee (1993) and Brugger (1996), the last one adopted as initial values for the interactive process during the numerical analysis of the present research.

3. Numerical simulation of the construction of the breakwater

3.1 Finite element method

The numerical simulation of the rupture of the TPS breakwater was performed using the Plaxis 2D v.2020 software based on the Finite Element Method (FEM). The problem was represented in the plane strain state and discretized into 15-node triangular finite elements, automatically generated by the program with mesh refinement optimization.

The constructive sequence was adopted according to the time-path diagram of the construction stages presented by Sandroni (2016). The loading and consolidation of the geotechnical berm totaled 175 days. Loading the hydraulic berm took 55 days and was divided into 8 phases in the simulation. The loading phases were of the fully coupled flow and deformation type, used when there is a need to simultaneously evaluate the evolution of deformations and pore pressures in saturated or partially saturated soils.

The breakwater foundation clay was divided into 7 sublayers of 1.0 m thick each and represented using both the Mohr-Coulomb (MC) and the Soft Soil Creep (SSC) models. This distinction was necessary since, in the SSC model, undrained analysis is available only in terms of effective stresses.

For the analysis in terms of total stresses, the values of *Su* of the vane test were adopted with and without Bjerrum correction, with and without a resistance gain due to the loading of the geotechnical berm. The gain was calculated as a function of the variation of the effective vertical stresses calculated from the analysis and evolution of the steps of the numerical model.

The SSC model is applied to soft soils of high compressibility, suitable for compressive stress paths, as is the case of embankment construction. The model is a variation of the Soft Soil model, which is based on the Modified Cam-Clay model considering a logarithmic relationship between the mean effective stress p' and the volumetric strain instead of the void ratio.

Table 1 presents the geotechnical parameters considered for the clay sublayers based on the results of field and laboratory tests, where c_k represents the variation of the initial vertical permeability coefficient k_{v0} with the void ratio. It was also assumed, based on field and laboratory tests, a horizontal anisotropy ratio $k_h/k_v = 2$. The value of φ_{cv} was determined by means of analysis of stress versus deformation curves determined in COPPE and PUC-Rio laboratory tests. An attempt was made to obtain agreement between the experimental curves and the model's theoretical curves by calibrating the curves using the SoilTest tool in Plaxis 2D, finally obtaining the value $\varphi_{cv} = 18º$.

Sand and rockfill layers were simulated using the MC model. For the cohesionless sand layers, the saturated unit weight γ_{sat} was 20 kN/m^3 and the permeability coefficient *k* was 10^{-6} m/s. The effective friction angle φ' adopted for the upper sand layer was equal to 32º and for the lower sand layer it was equal to 35º. For the rockfill, γ_{sat} was 18 kN/m^3 and φ' was 51º.

3.2 Volume method

The Volume Method (Sandroni et al., 2004) is an empirical method for evaluating the stability of embankments executed on soft soils based on variations of volume of vertical and horizontal displacements, ΔV_v and ΔV_h, measured during construction.

Due to the lack of field records, in this research the numerical displacements were applied, assuming them to be representative of the field conditions. The basic criterion of the method proposes that:

- $\Delta V_v / \Delta V_h > 6$ for stable condition.
- $3 \leq \Delta V_v / \Delta V_h \leq 6$ for the intermediate condition of stability.
- $\Delta V_v / \Delta V_h < 3$ for unstable condition.

Figure 3 shows a schematic representation of the volumes of vertical and horizontal displacements, for both sides (sea and coast) of the TPS breakwater. The parameter $=V_{h1} / V_{h2}$, defined as the ratio between the volumes of horizontal displacements towards the side of the sea (V_{h1}) and towards the side of the coast (V_{h2}), was numerically calculated from the FEM analysis. This parameter thus enables the estimation of the volumes of vertical displacements for each side of the breakwater, in each of the loading phases, according to Equations 1 and 2.

$$V_{v1} = \frac{V_v \beta}{(1+\beta)} \tag{1}$$

$$V_{v2} = \frac{V_v}{(1+\beta)} \tag{2}$$

Although Equations 1 and 2 were proposed by Sandroni et al. (2004) for cases in which there is variation in the width of the berm only, the volume method has been applied to situations considering the variation of the height of the embankment also (Dienstmann, 2011; Cobe, 2017; Sandroni et al., 2018; Cordeiro, 2019).

4. Analysis and results

4.1 Finite element method

4.1.1 Vertical displacements

Figure 4 presents the calculated vertical displacements along the base of the breakwater in each of the phases of the numerical simulation.

It is possible to observe a gradual increase in vertical displacements at the base of the breakwater with increasing its height. In Phase 10 of the simulation, the proximity of the failure is evident, with the maximum vertical displacement close to the structure axis and the occurrence of an uplift near the foot of the embankment. This movement was verified in field investigations carried out after the accident to identify the position of the breakwater berms (Sandroni et al., 2018).

4.1.2 Horizontal displacements

The horizontal displacements calculated in the model were compared with the results of the inclinometer installed in the instrumented station STA1, located on

Table 1. Geotechnical parameters determined for clay sublayers.

General parameters					Mohr-Coulomb model				Soft Soil Creep model				
Sub-layer	γ_{sat} (kN/m³)	k_{v0} (m/s)	e_0	c_k	E' (kPa)	ν'	$S_{u,VT}$ (kPa)	μS_u (kPa)	λ^*	κ^*	μ^*	K_o^{NC}	OCR
Clay 1	16.0	1.5×10^{-9}	1.7	0.85	5800	0.25	15.5	12.4	0.16	0.032	0.006	0.69	1.70
Clay 2			1.8	0.90	6000		15.5	12.4	0.16	0.032		0.69	1.55
Clay 3			1.9	0.95	6400		16.8	13.4	0.15	0.030		0.69	1.50
Clay 4			1.9	0.95	6700		19.3	15.4	0.15	0.030		0.65	1.50
Clay 5			1.8	0.90	7000		21.8	17.4	0.15	0.030		0.65	1.55
Clay 6			1.7	0.85	7200		23.0	18.4	0.15	0.030		0.65	1.55
Clay 7			1.6	0.80	7500		23.0	18.4	0.15	0.030		0.69	1.60

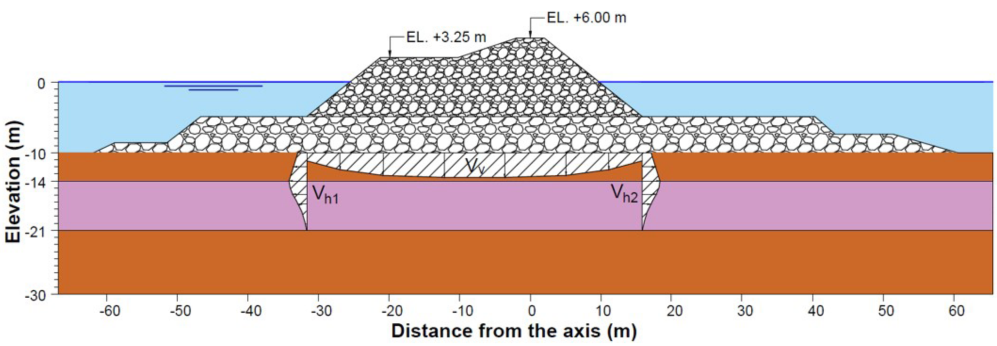

Figure 3. Schematic representation of the volumes of vertical and horizontal displacements.

the coast-side of the breakwater. Growing movements in this direction were noticed until the date of the failure. The comparison is shown in Figure 5, but the agreement between the numerical analysis and the instrumentation results was not satisfactory.

In the numerical analyses, the horizontal displacements calculated in the phases close to the moment of breakwater rupture were closer to the measured ones. Some questions have been raised about these measurements with inclinometers.

There were uncertainties about the exact position of the inclinometer and the distance at which it was located and about the dates the measurements were taken. Additionally, this inclinometer tube was spiraled (Sandroni, 2016), so that the available displacement profiles were corrected.

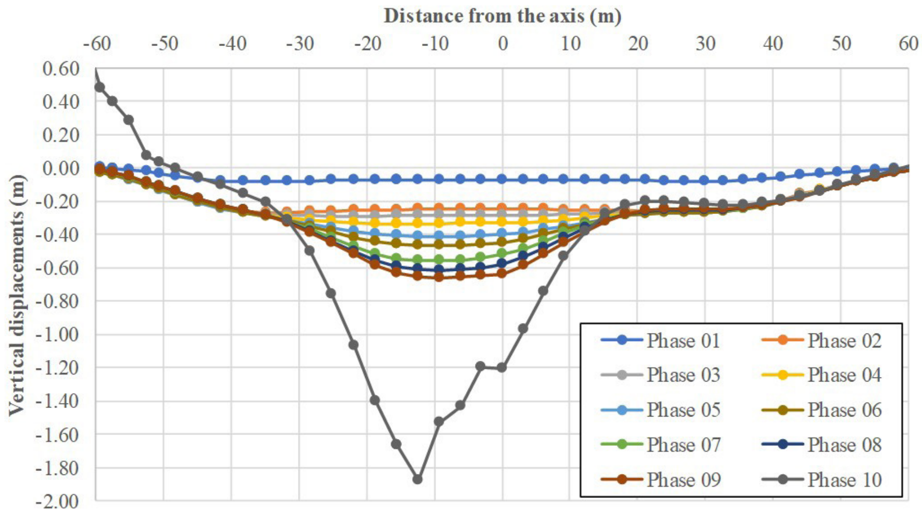

Figure 4. Vertical displacements at the base of the breakwater at the end of each loading phase.

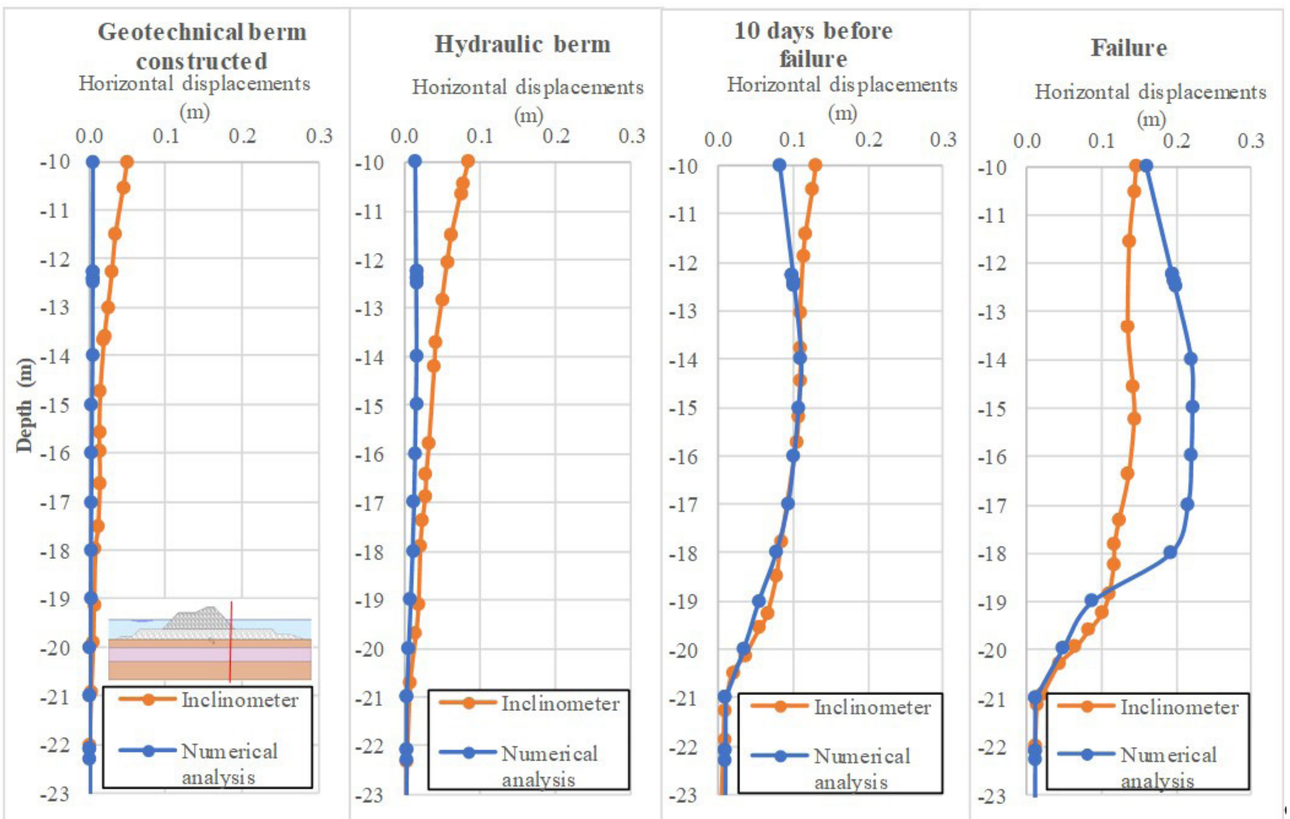

Figure 5. Profiles of horizontal displacements measured by the STA1 inclinometer and numerically calculated at different times for the TPS breakwater.

In the authors' opinion, the profile of inclinometer readings was anomalous for the configuration of the foundation and the geometry of the breakwater structure. The profile of horizontal displacements obtained in the numerical analyses seems to be more consistent with the behavior observed in other cases of embankments built on soft soils.

4.1.3 Pore pressures

The pore pressures calculated in the numerical simulation were consistent with the expected results, occurring an increase in pore pressures in the loading phases and dissipation in the consolidation phase of the geotechnical berm. This dissipation was greater along the draining boundaries and smaller in the central clay layers. Figure 6 shows excess pore pressure as a function of time. It is possible to observe that excess pore pressure was generated along the failure surface (green line), reducing the effective stresses acting on it.

4.1.4 Incremental shear strains

The failure mechanism can be followed by evaluating incremental shear strains ($\Delta\gamma_s$) in each of the loading phases of the model, as shown in Figure 7.

From these results, it is possible to observe that $\Delta\gamma_s$ was restricted only to the borders of the clay layer during the first phases of loading. The geometry of the breakwater, with the slopes of the hydraulic berm more inclined and a shorter distance from the foot to the end of the geotechnical berm, favored the development of a failure surface, caused by the concentration of shear deformations during the construction.

As of Phase 06, in which the hydraulic berm is 7.0 m high, the interpretation of the results indicates the formation of two potential failure surfaces. However, the magnitude of $\Delta\gamma_s$ is greater towards the side of the sea, as is the extent of the potential rupture surface.

In the last loading phase (Phase 10), the failure surface is well developed towards the sea. The failure surface calculated in the numerical simulation is similar to the surface verified in field investigations after failure of the structure.

However, the fact that it was observed the formation of two potential failure surfaces does not imply that shear strength was not mobilized in the rockfill. The analysis of the calculated effective stress path for a point in this material indicates that the maximum deviation stresses were mobilized (Figure 8a). Figure 8b presents the contours of relative shear stresses (τ_{rel}) given by the ratio between mobilized stresses (τ_{mob}) and maximum admissible stresses (τ_{max}) in the penultimate phase of the numerical simulation. It is possible to observe that, even before the failure, the relative stresses were equal to 1.0 in great part of the breakwater body.

4.1.5 Effective stress paths

Figure 9 presents the effective stress paths of some selected points, for all phases of the numerical simulation during the construction of the breakwater. The initial effective stress state is determined as a function of the unit weight, the buoyancy coefficient at rest and the *OCR* of the breakwater foundation materials.

In each graph are shown the Mohr-Coulomb failure envelope (in black), the critical state line CSL (in red) and the ellipse p_{eq} that defines the initial cap yield surface (in gray) of each point.

The effective stress paths follow the expected behavior according to the loading condition imposed by the construction of the breakwater. In general, the loading of the geotechnical berm generated effective stress increases like the stress paths imposed by triaxial compression tests with the generation of positive excess pore pressure.

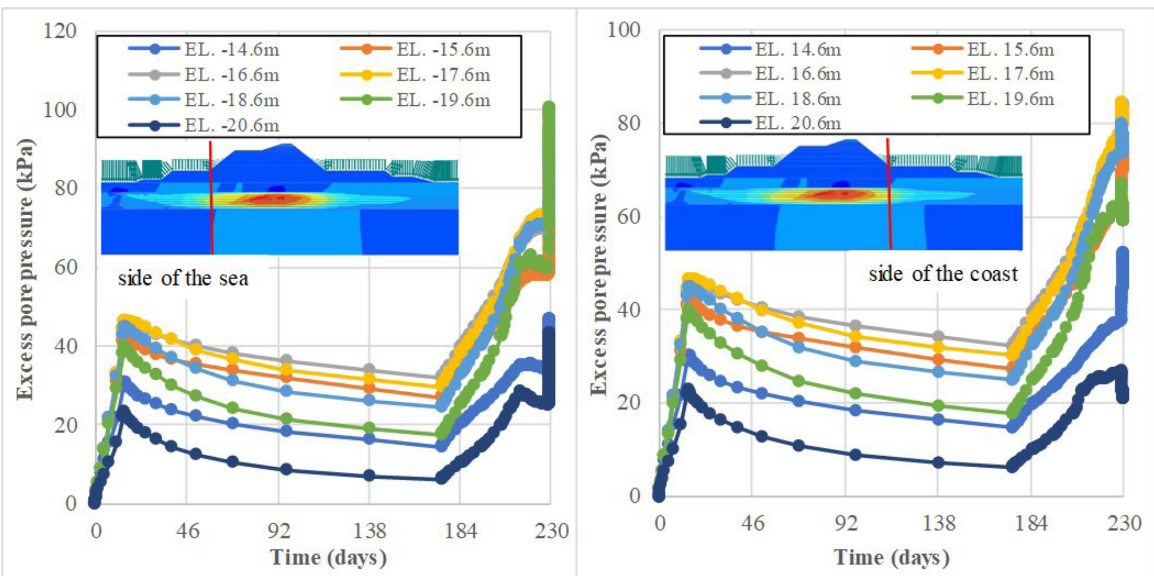

Figure 6. Excess pore pressure at different depths of the clay layer as a function of time.

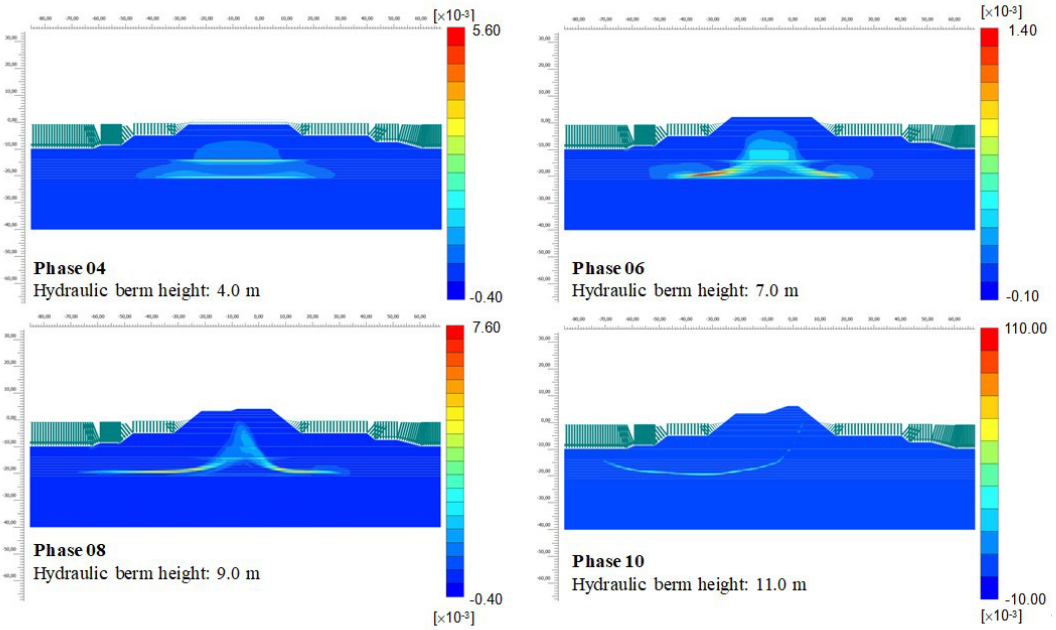

Figure 7. Contours of incremental shear strains in different phases of numerical simulation.

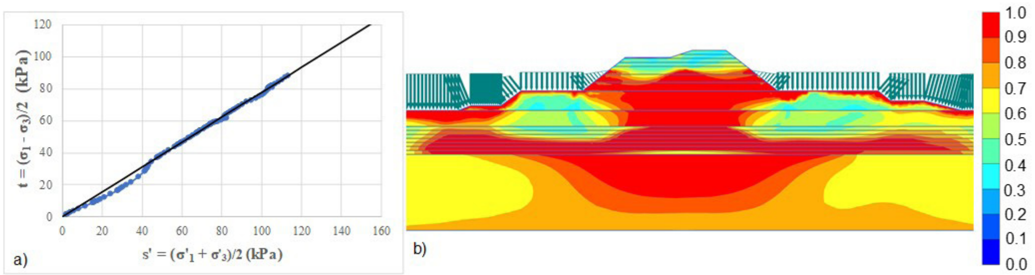

Figure 8. a) Effective stress path in the rockfill of the breakwater; b) contours of relative shear stress in Phase 09 in numerical simulation. The region in strong red indicates $\tau_{rel} = 1.0$.

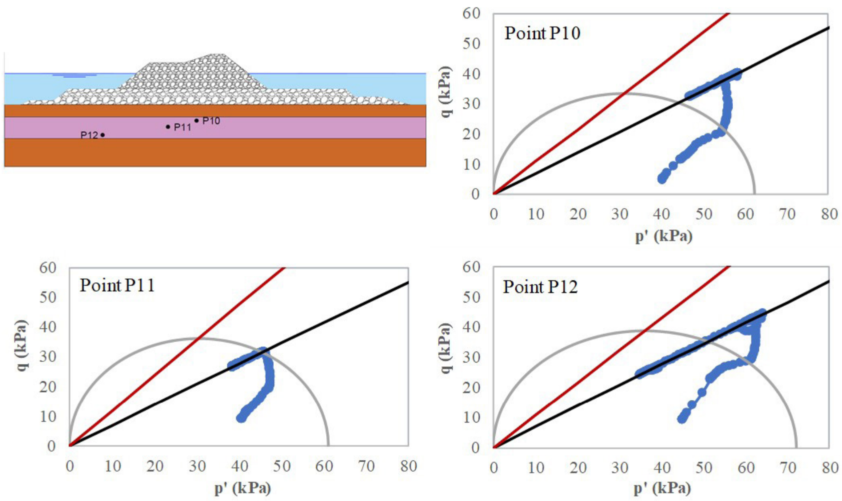

Figure 9. Effective stress paths at selected points in the clay layer located on the failure surface.

The first loading phases of the hydraulic berm already caused elastoplastic strains since the clay was already in the normally consolidation condition. After rupture, the effective stress paths followed the Mohr-Coulomb envelope towards the origin, indicating a strain softening behavior of the material, which represents a sensitivity of the material. This behavior, combined with the redistribution of shear stresses, is closely linked to the phenomenon of progressive failure in slopes (Leroueil et al., 2012).

4.1.6 Factors of safety

Figure 10 presents the undrained Factors of Safety (*FoS*) obtained in the numerical analyses as a function of the height of the breakwater, in each of the loading phases of the hydraulic berm. In addition to the results using the SSC model, where the soft clay was represented as an undrained material in terms of effective stresses, the clay layers were also modeled by the MC model in undrained condition in terms of total stresses.

In undrained analyses with the MC model with resistance gain (ΔSu), the *FoS* of the breakwater were greater than unity, with values in the last phase equal to 1.41 for analysis using *Su* from vane tests (VT) and 1.26 using corrected undrained strength (μ**Su*). The results were higher than those obtained in a limit equilibrium analysis (Sandroni, 2016), with stress increases calculated by using pore pressures measured in piezometers installed a few meters from the breakwater axis, while in the present numerical analysis the variation of effective vertical stresses was determined under the axis of the structure. In addition, the resistance gains were calculated in each of the increment phases of the breakwater construction, generating in the last phase, *Su* values higher than those used in stability analyses by the limit equilibrium method.

This may indicate that the clay of the foundation of the breakwater did not show resistance gain due to the consolidation process of the geotechnical berm, or that the resistance gain was much lower than that calculated in the traditional way, presenting a UU triaxial-like behavior.

Another hypothesis, suggested by Sandroni et al. (2018) would be that, despite this gain in strength, the sensitivity of the clay would cause a decrease in shear strength. According to Lacerda & Almeida (1995), the Sergipe clay would have sensitivity values from 4.0 to 6.0. This condition, verified in compression triaxial tests through the evaluation of the pore pressure parameter A after failure, is not simulated by the MC model.

In the analysis without resistance gain, considering or not the Bjerrum correction in *Su*, the *FoS* obtained were lower, and the values calculated for the last phase of the simulation were similar to those determined with the limit equilibrium method. For the analysis without correction, the *FoS* in the last phase was equal to 1.12, while for the one that used corrected *Su*, the failure occurred in the penultimate calculation phase, with a value equal to 1.00.

The analysis with the SSC model presented the most consistent results, with *FoS* values decreasing with the increase of the hydraulic berm until failure in the last loading phase, with a *FoS* equal to 0.99. The result differed considerably from the back analyses carried out by limit equilibrium.

This difference can be explained by the fact that the FEM generated higher values of excess pore pressure, mainly along the failure surface, which reduced the effective stresses and, consequently, the admissible shear stresses. Another

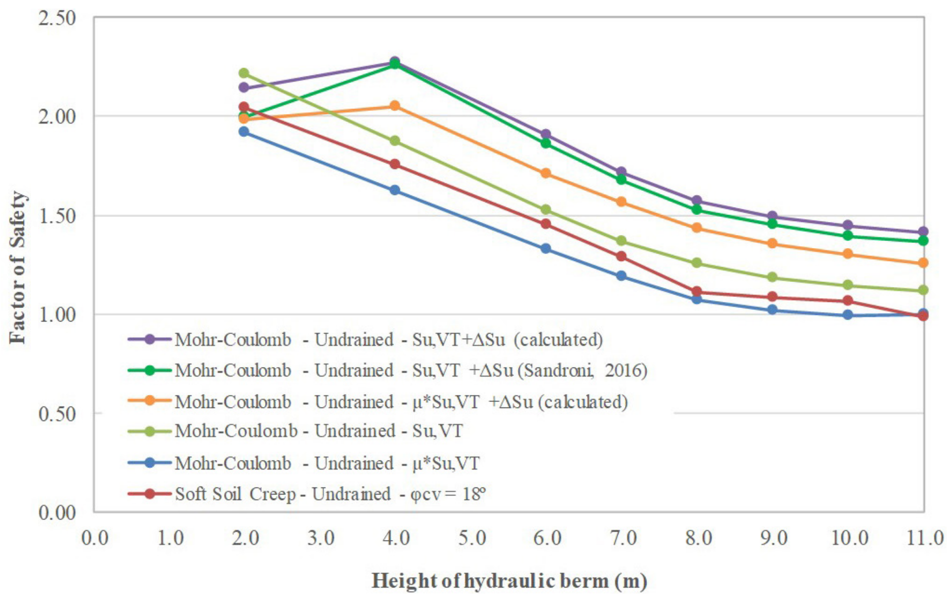

Figure 10. Factor of Safety obtained as a function of the height of the hydraulic berm for each analysis.

difference is the simulation of the strain softening behavior of the material after rupture, for the effective stress paths of the points located along the failure surface.

4.2 Volume method

Based on the displacement results obtained in the numerical simulation of the construction of the TPS breakwater, a stability assessment was carried out using the Volume Method (Sandroni et al., 2004) and comparing it with the *FoS* obtained in numerical stability analyses.

In the first loading phases of the berm, the β values varied between 1.0 and 1.5. After the outbreak of the rupture, an increase in β was observed due to the greater movements towards the side of the sea. Table 2 presents the displacement volumes and the calculation of $\Delta V_v / \Delta V_h$, for both sides of the breakwater (Figure 3), in each of the loading phases of the hydraulic berm.

Figure 11a shows calculated $\Delta V_v / \Delta V_h$ related to the embankment height of the hydraulic berm. It is possible to observe that, in the first loading phases of the hydraulic berm, the ratio $\Delta V_v / \Delta V_h$ is lower for the side of the coast when compared to the side of the sea, where the rupture occurred.

A comparison was also made between the results obtained by the Volume Method, for the side of the sea and the *FoS* obtained in the numerical simulation using the SSC model. Figure 11b shows, on the left vertical axis, the values of the *FoS* and, on the right vertical axis, the values of the ratio $\Delta V_v / \Delta V_h$ as a function of the height of the hydraulic berm.

From Phase 05 (height of the hydraulic berm equal to 6.0 m), the value of $\Delta V_v / \Delta V_h$ on the side of the sea showed a sharp decrease. Both curves kept below the range of $\Delta V_v / \Delta V_h = 3.0$ until the penultimate berm increment. In the last phase of the simulation, when the rupture was triggered towards the side of the sea, it occurred large horizontal displacements, taking the ratio between the displacement volume variations to values below 1.0. The ratio $\Delta V_v / \Delta V_h = 3$, as an indicator of an unstable condition, occurred when the corresponding factor of safety was *FoS* = 1.29 determined from the numerical analysis (Figure 10). For the side of the coast, however, there was an increase of $\Delta V_v / \Delta V_h$ to values greater than 3.0.

5. Conclusion

The numerical analysis of the construction of the original TPS breakwater aimed to better understand the mechanisms that led to the failure of the structure, using constitutive soil models and other finite element tools not available at the time of the accident. In this way, the results obtained in this research can be considered a contribution, since the main aspects of the problem were examined in the analyses, in terms of displacements, deformations, pore pressures and the stability of the structure itself. A numerical analysis considering the redesigned TPS breakwater, constructed in the early 1990s, was presented by (Brugger et al., 1998).

Table 2. Displacement volumes and the calculation of $\Delta V_v / \Delta V_h$ for both sides of the breakwater.

Phase	V_{h1} (m³/m)	V_{h2} (m³/m)	β	V_v (m³/m)	V_{v1} (m³/m)	V_{v2} (m³/m)	ΔV_{h1}	ΔV_{h2}	ΔV_{v1}	ΔV_{v2}	$\Delta V_{v1} / \Delta V_{h1}$	$\Delta V_{v2} / \Delta V_{h2}$
Phase 03	0.311	0.214	1.45	13.497	7.640	5.857	0.160	0.152	0.828	0.634	5.182	4.167
Phase 04	0.506	0.398	1.27	15.382	8.707	6.675	0.194	0.184	1.067	0.818	5.496	4.457
Phase 05	0.825	0.688	1.20	17.928	10.148	7.780	0.319	0.290	1.440	1.104	4.515	3.802
Phase 06	1.149	0.945	1.22	19.622	11.107	8.515	0.325	0.256	0.959	0.736	2.954	2.869
Phase 07	2.070	1.481	1.40	22.251	12.595	9.656	0.921	0.537	1.488	1.141	1.617	2.126
Phase 08	2.420	1.820	1.33	23.943	13.553	10.390	0.351	0.339	0.958	0.734	2.732	2.165
Phase 09	2.761	2.185	1.26	25.523	14.447	11.076	0.340	0.365	0.894	0.686	2.628	1.881
Phase 10	23.68	4.367	5.42	48.959	27.713	21.246	20.915	2.182	13.266	10.170	0.634	4.661

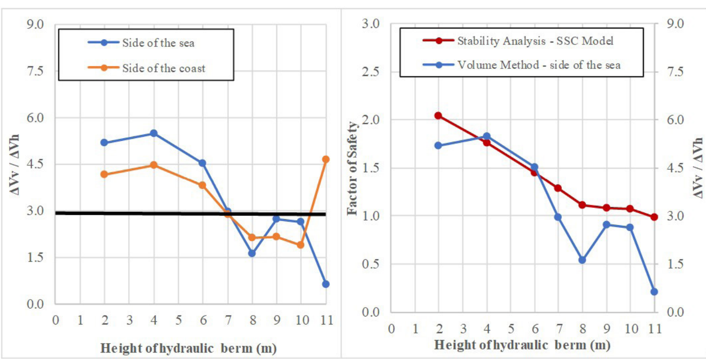

Figure 11. (a) $\Delta V_v / \Delta V_h$ as a function of the height of the hydraulic berm; (b) *FoS* and $\Delta V_v / \Delta V_h$ as a function of the height of the hydraulic berm.

From the analysis, it was possible to point out the hypothesis that the pressures acting on the clay layer at the moment of failure were higher than those adopted in former back analyses by the limit equilibrium method based on the readings of the piezometers.

The use of the SSC model allowed simulating a strain softening behavior, with loss of resistance after the peak. This property of geotechnical materials is important for the stability analysis, because when associated with the redistribution of shear stresses along the failure surface, it can cause a progressive rupture.

Analyses using the MC model, with different *Su* values, resulted in *FoS* similar to those obtained by the limit equilibrium method. The most plausible interpretation of these results indicates that, despite the gain in strength due to the consolidation of the clay layer, its sensitive behavior led to a mobilized shear strength much lower than the expected peak.

Although shear deformations and horizontal displacements of significant magnitude were observed for both sides of the breakwater, the shared failure hypothesis could not be properly demonstrated. The analysis of the stress paths and the relative shear stresses in the rockfill indicate that the shear resistance was mobilized in the rockfill body.

The analyses also indicated that the empirical Volume Method, originally proposed for monitoring works with field instrumentation, indicated that when the potentially unstable condition was reached (ΔV_v / ΔV_h = 3), the corresponding undrained factor of safety was *FoS* = 1.29 determined from the finite element analysis. Other applications of the Volume Method found in the literature, either applying results from field instrumentation (Cobe, 2017; Sandroni et al., 2018; Cordeiro, 2019) or numerical simulation (Dienstmann, 2011) indicate that this empirical method can be a useful tool for monitoring embankment constructions. In the authors' knowledge there is no published results relating the variation of the factor of safety against the volume ratio (ΔV_v / ΔV_h) as investigated in the present research. A generalization of this correspondence would imply the analysis of many other practical cases, including the verification of the stable and unstable ranges proposed by Sandroni et al. (2004).

Acknowledgements

To PUC-Rio and professors Sandro Sandroni and Willy Lacerda. This research was carried out with the support of the Coordenação de Aperfeiçoamento de Pessoal de Nível Superior – Brazil – Brazil (CAPES) – Financing Code 001.

Declaration of interest

The authors have no conflicts of interest to declare. All co-authors have observed and affirmed the contents of the paper and there is no financial interest to report.

Authors' contributions

Pedro Oliveira Bogossian Roque: conceptualization, data curation, writing – original draft. Celso Romanel: methodology, supervision, writing – review. Celso Antero Ivan Salvador Villalobos: validation, writing – review. Jackeline Castañeda Huertas: conceptualization, methodology, validation.

Data availability

The datasets generated analyzed in the course of the current study are available from the corresponding author upon request.

List of symbols

c_k	Change in permeability coefficient
e_0	Initial void ratio
C_c	Compression index
C_s	Swelling index
E'	Young's modulus
FoS	Factor of safety
K_0^{NC}	Coefficient of earth pressure at rest for normally consolidated soils
OCR	Overconsolidation ratio
$Su,_{VT}$	Undrained shear strength obtained by vane tests
V_h	Volume of horizontal displacements
V_v	Volume of vertical displacements
β	Asymmetry parameter, ratio between the volumes of horizontal displacements
γ_{sat}	Saturated unit weight
$\Delta\gamma_s$	Incremental shear strain
κ^*	Modified swelling index (Soft Soil model parameter)
λ^*	Modified compression index (Soft Soil model parameter)
μ	Bjerrum correction factor
μ^*	Modified creep index (Soft Soil Creep model parameter)
τ_{max}	Maximum admissible shear stress
τ_{mob}	Mobilized shear stress
τ_{rel}	Relative shear stress
ν'	Poisson's ratio
φ_{cv}	Critical-void friction angle

References

Brugger, P.J. (1996). *Análise de deformações em aterros sobre solos moles* [Doctoral thesis]. Instituto Alberto Luiz Coimbra de Pós-Graduação e Pesquisa de Engenharia, Universidade Federal do Rio de Janeiro (in Portuguese).

Brugger, P.J., Almeida, M.S.S., Sandroni, S.S., & Lacerda, W.A. (1998). Numerical analysis of the breakwater construction of Sergipe Harbour, Brazil. *Canadian Geotechnical Journal*, *35*(6), 1018-1031. Retrieved in May 15, 2023, from https://cdnsciencepub.com/doi/10.1139/t98-063

Bjerrum, L. (1973). Problems of soil mechanics and construction on soft clays. In *Proceedings of the 8th International Conference on Soil Mechanics and Foundation Engineering* (Vol. 3, pp. 111-159). Moscow.

Cobe, R.P. (2017). *Behavior of an embankment constructed on a soft clay foundation and its influence on the adjacent piles* [Master's dissertation, Pontifícia Universidade Católica do Rio de Janeiro]. Pontifícia Universidade Católica do Rio de Janeiro's repository (in Portuguese). https://doi.org/10.17771/PUCRio.acad.36574.

Cordeiro, R.F. (2019). *Avaliação do comportamento de aterro executado sobre depósito de argila mole na rodovia BR 470 em Gaspar/SC* [Master's dissertation, Universidade Federal de Santa Catarina]. Universidade Federal de Santa Catarina's repository (in Portuguese). https://repositorio.ufsc.br/handle/123456789/215088.

Dienstmann, G. (2011). *Projeto interativo dos molhes da Barra do Rio Grande – RS* [Doctoral thesis, Universidade Federal do Rio Grande do Sul]. Universidade Federal do Rio Grande do Sul's repository (in Portuguese). http://hdl.handle.net/10183/32005.

Geoprojetos. (1992). *Terminal Portuário de Sergipe – Relatório R-290592-137-39*. Geoprojetos Engenharia Ltda.

Lacerda, W.A., & Almeida, M.S.S. (1995). Engineering properties of regional soils: residual soils and soft clays – State-of-the-art lecture. In *Proceedings of the 10th Panamerican Conference on Soil Mechanics and Foundation Engineering* (Vol. 4, pp. 161-176). Guadalajara.

Ladd, C.C., & Lee, S.M. (1993). *Engineering properties of sergipe clay: TPS Progress Rept. No. 4. Research Rept R93-07*. MIT Department of Civil and Environmental Engineering.

Leroueil, S., Locat, A., Eberhardt, E., & Kovacevic, N. (2012). *Landslides and engineered slopes: protecting society through improved understanding*. CRC Press. Progressive failure in natural and engineered slopes, pp. 31-46.

Ribeiro, L.F.M. (1992). *Ensaios de laboratório para determinação das características geotécnicas da argila mole de Sergipe* [Master's dissertation]. Pontifícia Universidade Católica do Rio de Janeiro (in Portuguese).

Sandroni, S.S. (2016). *Willy Lacerda: doutor no saber e na arte de viver*. Geobrugg. Novo Projeto do quebra-mar de Sergipe depois da ruptura durante a construção, pp. 326-336.

Sandroni, S.S., Brugger, P.J., Almeida, M.S.S., & Lacerda, W.A. (1997). Geotechnical properties of Sergipe clay. In *Proceedings of the International Symposium on Recent Developments on Soil and Pavement Mechanics*, Rio de Janeiro: CRC Press, 271–277.

Sandroni, S.S., Lacerda, W.A., & Tassi, M. (2018). Landslide during construction of a rockfill breakwater in the coast of Sergipe, Brazil. In *Proceedings of the International Symposium on Field Measurements in Geomechanics,* Rio de Janeiro. Session 3.

Sandroni, S.S., Lacerda, W.A., & Brandt, J.R.T. (2004). Método dos volumes para controle de campo da estabilidade de aterros sobre argilas moles. *Solos e Rochas*, *27*, 25-35.

Schnaid, F., & Odebrecht, E. (2012). *Ensaios de campo e suas aplicações à engenharia de fundações* (2. ed.) Oficina de Textos.

Soils and Rocks

An International Journal of Geotechnical and Geoenvironmental Engineering

www.soilsandrocks.com

ISSN 1980-9743
ISSN-e 2675-5475

Hydro-geomorphological conditions for the classification of terrain susceptibility to shallow translational landslides: a geo-hydro ecological approach

Roberta Pereira da Silva[1#], Ana Luiza Coelho Netto[2], Willy Alvarenga Lacerda[3]

Article

Keywords
Shallow landslide
Terrain susceptibility
Geomorphological parameters
Geo-hydroecological approach

Abstract

This work is part of the review of methodological procedures for the analysis and classification of terrain susceptibility to shallow translational landslides, following the geo-hydro ecological approach. The pilot area is located in Nova Friburgo (RJ), specifically in the D'Antas Creek basin (53 km^2). At this stage of the work, geomorphological parameters and indices were evaluated, including slope angle, curvature, drainage efficiency index (*DEI*) and topography position index (*TPI*), seen as relevant in regulating the hydrological and mechanical behavior of soils. The results obtained were intersected with an inventory of landslide scars (n = 382) referring to the extreme rainfall event in January 2011, which occurred in the highland region, called Região Serrana, of the state of Rio de Janeiro. This intersection allowed an evaluation between these parameters and the slopes rupture. The concentration of landslide area per class subsidized the establishment of weights for each of the adopted classes, based on the AHP method. A readjustment of the slope angle classes was proposed, as well as the inclusion of the standard curvature in the construction of the Hydro-Geomorphological Conditions Map. The results were promising, with a concentration of 88.74% (0.85 km^2) of the landslide areas in the class of high erosive potential.

1. Introduction

Several methodologies have been described in the literature for classifying landslides susceptibility, including probabilistic analyzes based on long inventories of cases (Casagli et al., 2004; Fell et al., 2008; Martha et al., 2014) and diagnoses based on the crossing of thematic maps (Coelho Netto et al., 2007; Akgun et al., 2008; Bortoloti et al., 2015; Abedini & Tulabi, 2018). The latter still prevails in Brazil, whose information has emphasized the role of the geological and/or geological-geotechnical categories. The inclusion of geomorphological parameters is usually limited to the adoption of slope angle as the main, and sometimes only parameter in terrain susceptibility assessments (Fernandes et al., 2001; Dias et al., 2021a), through a linear vision of its interference in the occurrence of this phenomenon.

Although landslide terrain susceptibility maps are increasingly used, in the way they are presented today, they still have limitations, mainly due to the scale of elaboration and availability of data in adequate quantity and quality. Identifying the factors that control the distribution and occurrence of landslides and determining their relative importance is complex. These phenomena can be triggered under multiple meteorological, geological, geomorphological, vegetation cover, and land use conditions (Guzzetti et al., 2008; Coelho Netto et al., 2013; Borgomeo et al., 2014). The relationship between landslide and triggering factors varies spatially and temporally. Furthermore, the circumstances under which one factor may dominate the others are difficult to assess.

The methodological procedures and the models for evaluating terrain susceptibility to landslides must be dynamic and need to be open to updates at time intervals compatible with the rate and variability of landscape transformations. For this reason, the geo-hydro ecological approach has been adopted for structuring the thematic bases, as well as in the integrated analysis of terrain susceptibility. This approach is based on empirical-analytical and integrative knowledge of indicators and categories relevant to the phenomenon in focus, as summarized in Coelho Netto et al. (2020).

[#]Corresponding author. E-mail address: pereira.roberta00@gmail.com
[1]Universidade Federal do Rio de Janeiro, Programa de Pós-graduação em Engenharia Civil, Rio de Janeiro, RJ, Brasil.
[2]Universidade Federal do Rio de Janeiro, Departamento de Geografia, Rio de Janeiro, RJ, Brasil.
[3]Universidade Federal do Rio de Janeiro, Departamento de Geotecnia, Rio de Janeiro, RJ, Brasil.

Submitted on May 15, 2023; Final Acceptance on October 25, 2023; Discussion open until February 28, 2024.

https://doi.org/10.28927/SR.2023.005623

The integrated analysis aimed at classifying terrain susceptibility involves geological-geotechnical, hydrogeomorphological, vegetation cover, and land use indicators. The systemic view of geographic space, based on multiple (spatial and temporal) scales of analysis, is essential for the geo-hydroecological approach (Coelho Netto et al., 2020).

In one of the methodological review and update stages for classifying terrain susceptibility to shallow landslides, in a detailed scale (between 1:5,000 and 1:10,000), the study by Silva et al. (2022) evaluated the relevant geotechnical parameters in the definition of geological-geotechnical units in the D'Antas Creek basin (53 km^2), in Nova Friburgo (RJ), Brazil. The method proposed by the authors was based on the integration of parameters and indices, such as granulometry, Atterberg limits (*LL, PL, PI, A*), aggregate stability index, void ratio, saturated hydraulic conductivity, c' (effective cohesion) φ' (internal effective friction angle) for the categorization of terrain units according to the mechanical and hydraulic behavior of the materials. This study enabled the regrouping of the six lithological units, defined by Avelar et al. (2016), in three geological-geotechnical units, based on a functional reading of the geotechnical behavior of soils.

The present work constitutes one more stage of revision of the methodology developed by GEOHECO-UFRJ/Geo-Hydro Ecology and Risk Management Laboratory (COPPETEC/SMAC-RJ, 2000; Coelho Netto et al., 2007; COPPETEC/SEA -RJ, 2010 and Coutinho, 2015). Now, the focus lies on the functional categorization and improvement of hydro-geomorphological indicators related to the detonation of shallow landslides. An improvement of the tools available in the Geographic Information System (GIS) used in this study was sought, to obtain parameters, such as slope angle and curvature, which were more adequate to the analysis.

2. Materials and methods

To define the hydro-geomorphological conditions, the parameters, and indices were integrated and weighted on a functional basis. The latest reviews of these terrain conditions, prepared by Coutinho (2015) and Coelho Netto et al. (2014), considered a synthesis of the parameters related to the variable set of slopes angles within the landslide scars, however, not discriminating the mean slope angle of each scar. The topography position index (*TPI*) and the drainage efficiency index (*DEI*) were not changed. The curvature of the slopes was not considered. In the early work by Coelho Netto et al. (2007), the hydro-geomorphological map corresponds to the integration of the *DEI* with other functional parameters, including critical slope angles and curvature, combined in the following classes: concave/0–10°, convex-straight/0–10°, concave/10–20°; convex–straight/10–20°; concave/20–35°; convex–straight/20–35°; concave/>35°; convex–straight/>35°.

From these three works, in this research the incorporation of the curvature parameter as another terrain condition was proposed. Despite the recognized importance of curvature (plan and profile) and the gradual insertion of this parameter in models of susceptibility zoning, the curvature remains underestimated as a geomorphological parameter (Catani et al., 2005; Kayastha et al., 2013; Meirelles et al., 2018). The present study was developed in the same study area used by Coutinho (2015), which allowed the use of some formerly produced data, applying the necessary adjustments to adapt to the current proposal.

2.1 Study area

The D'Antas Creek basin (53 km^2) located in Nova Friburgo, a municipality in the highland region of the state of Rio de Janeiro (Figure 1), was defined as a pilot area given the occurrence of hundreds of landslides and the high losses and damages of a social, economic and environmental nature in the last catastrophic event in January 2011. Coelho Netto et al. (2013) identified 3,622 landslide scars, in an area of 421 km^2 (Figure 1b), largely inserted in the municipality of Nova Friburgo and including small areas of Teresópolis and Sumidouro municipalities, out of which more than 80% were concentrated in Nova Friburgo.

Since 2012, GEOHECO-UFRJ has been developing research on the conditions of shallow translational landslides, prevalent in the region. It is a 5th order basin (Strahler, 1952), with altitude varying between 840 m and 2,054 m, according to the Hipsometric model (Coutinho, 2015). The D'Antas Creek is a tributary of the Bengalas River, which drains to the Grande River, a tributary of the Dois Irmãos River. The latter runs into the right bank of the Paraíba do Sul River (regional collector).

High-altitude tropical climate predominates in the Região Serrana, with an annual average temperature of 16ºC, varying between 37º and -2ºC (Coelho Netto et al., 2013). The region's climate is influenced by the Atlantic Tropical air mass, which causes high rainfall, especially in summer. Nova Friburgo is pointed as one of the cities with the highest rainfall rates in the state, with average annual precipitation (1977–2000) around 2500 mm in the highest areas, decreasing progressively in the northern area down to 1,300 mm (Coelho Netto et al., 2008).

The region's characteristic biome is Atlantic Forest, currently fragmented and highly degraded. According to Ribeiro et al. (2009), more than 80% of the forest fragments have less than 50 ha and are more than 1 km apart. The authors claim that these forest remnants occupy from 11.4% to 16% of this region. The vegetation originally present in the study area is included in the phytogeographic classification of Montana Dense Ombrophilous Forest which, according to Veloso et al. (1991), covers the mountains and plateaus between 500 m and 1,500 m high.

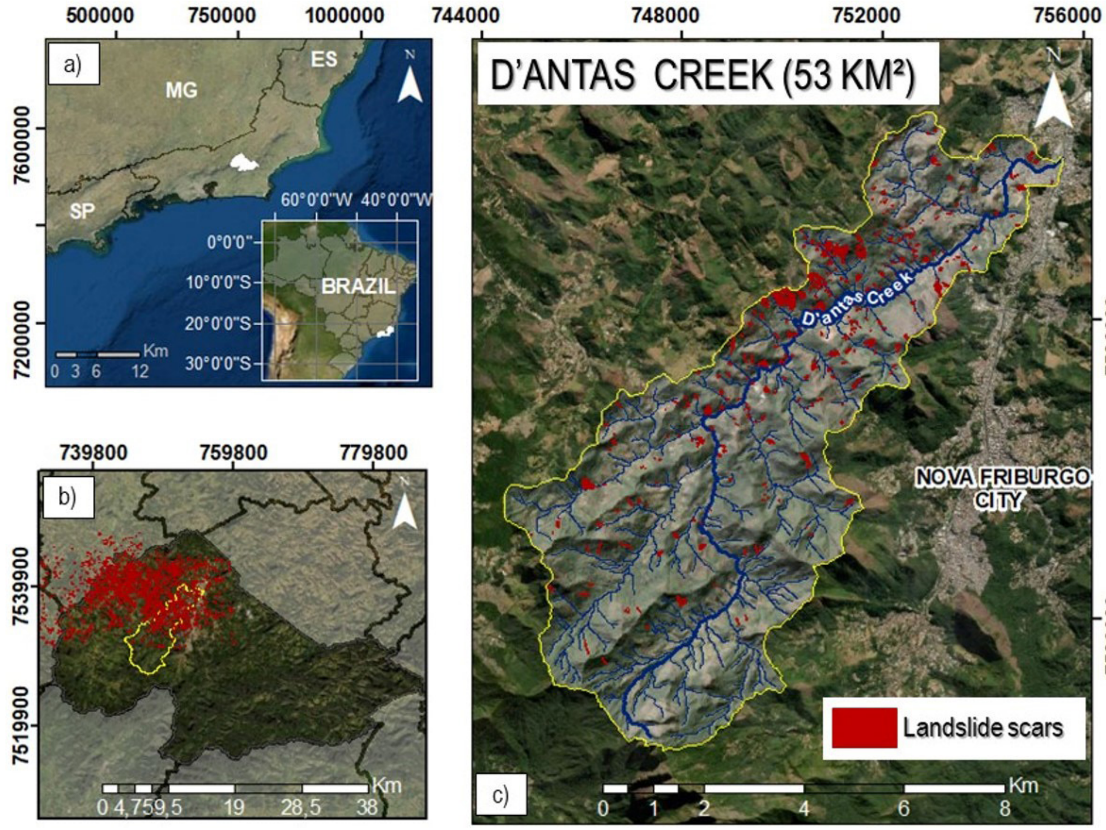

Figure 1. Location map of the D'Antas Creek basin. a) Location of the municipality of Nova Friburgo; b) Location of the D'Antas Creek basin in the context of the municipality. In red, there are the landslide scars mapped in an area of 421 km^2 by Coelho Netto et al. (2013); c) D'Antas Creek basin and the indication of landslide scars used in the present study.

With the opening and paving of the highway RJ-130, which connects Nova Friburgo to Teresópolis, in the 1970s, a process of transition from rural to urban in the basin area began. The region came to be considered an area of industrial expansion, a fact that accelerated population growth. Currently, the basin comprises eight neighborhoods (D'Antas Creek, Alto Floresta, Dois Esquilos, Ponte Preta, Cardinot, Solaris, Venda das Pedras and Jardim California), with a population of approximately 23,000 people (11% of the population of the municipality) (Coutinho, 2015).

2.2 Landslide Inventory

Based on the landslide inventory from the January 2011 extreme rainfall event prepared by Silva et al. (2016), there was a new visual interpretation of the scars. Using a Geoeye satellite image of high spatial resolution (0.5 m) obtained shortly after the event (May/2011), the contour lines at a scale of 1:5,000 and images provided by *Google Earth Pro* (dated 01/19/2011 and 06/05/2011), the scars were reclassified with a focus on shallow translational landslides and a prioritization of detonation and transport zones.

The landslides previously classified as complex (a combination of two or more types of movements), according to the definition by Varnes (1978), were dismembered to highlight the surfaces of ruptures or erosion zone (Figure 2a). Scars with an elongated shape and incised in the axes of concavities were classified as debris flow at their origin (Figure 2b) and were excluded from this analysis. Scars related to shapes with a wider base were associated with shallow translational slips (Figure 2c).

Considering these new criteria for mapping shallow translational landslide scars, 382 scars with areas between 50 m^2 and 60,000 m^2 were counted, totaling around 958,220 m^2 (0.96 km^2) of the landslide area. Despite the great variability in sizes between the mapped polygons, approximately 73% (280) of the scars had an area of up to 2,000 m^2 and 51% (197) an area of up to 1,000 m^2.

Based on the distribution of scars, the landslide potential of each class was defined, as observed in the works by Gao (1993), Larsen & Torres-Sánchez (1998), Catani et al. (2005), Nakileza & Nedala (2020), among others. The landslide inventory was used to validate the hydro-geomorphological conditions map, a process through which one sought to define the reliability, robustness, degree of adjustment, and forecasting ability of the proposed model.

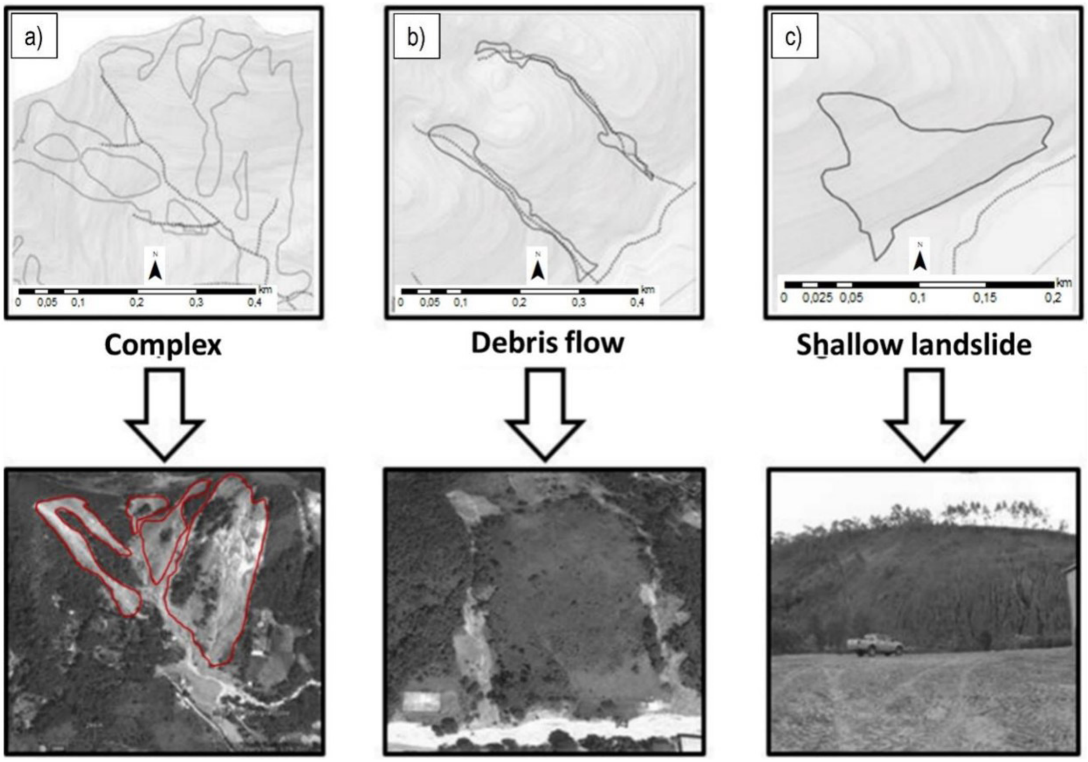

Figure 2. Types of gravitational mass movements considered in the scar inventory produced by Silva et al. (2016); a) Complex movement, which was dismembered from erosion and transport zones by the present study, as indicated by the red polygons; b) Debris flows associated with relief concave compartments, disregarded by this analysis; c) Shallow translational landslide, type of mass movement in focus (Adapted from Silva et al., 2016).

2.3 Hydro-geomorphological conditions

2.3.1 Drainage Efficiency Index (*DEI*)

Data referring to the Drainage Efficiency Index (*DEI*) used in this research were produced by Coutinho (2015). The channel network was traced with the support of the *ArcHydro* tool (ArcGis 10.2) and through field observations, especially in the low hierarchical order sub-basins (up to 2nd order). The higher hierarchical order basins, as well as the lateral slopes that drain directly into the main river channels, were adjusted to the adjacency pattern with the closest neighbors that went through the classification process (Coutinho, 2015). Initially, this author classified the numerical products of the *DEI* as "natural breaks[1]" into four classes (very high, high, medium, and low). However, in the present study, the option was the use of three *DEI* classes: high, medium and low, as proposed by Coelho Netto et al. (2007).

[1]The "natural breaks" method adjusts the limits of the classes according to the distribution of the data, identifying breakpoints between the classes from a statistical analysis based on the variability of the data, aiming to minimize the sum of the variance within each of the classes (Jenks, 1977).

Higher values of *DEI* tend to favor the rainwater flow of surface and subsurface, which converges to the topographic concavity axis, channeled or not (Coelho Netto et al., 2007). The increase in drainage efficiency tends to favor the incision of erosive channels whose incision and regressive growth can destabilize the steep slope and trigger landslides (positive feedback). Like the drainage density parameter, this index translates the time or response capacity of the basin which, together with the topographic gradient of the contribution basin, configures the drainage efficiency, as seen in Equation 1 proposal by Coelho Netto et al. (2007), where:

$$DEI = HDd \times G = \frac{\sum_1^n L_h + \sum_1^n L_c}{A_b} \times \frac{\Delta Z}{L} \qquad (1)$$

where: *HDd* is the Hollow-Drainage density, *G* is the basin gradient (non-dimensional), L_h is the total length of hollow axis, L_c is the total length of channels, ΔZ is the basin elevation, *L* is the basin length and A_b is the basin area.

2.3.2 Slope angle

The slope angle values were extracted from the Digital Terrain Model (DTM) (1:5,000), using the *Slope* tool

(ArcGis 10.7). The generated file was reclassified using the *Reclassify* tool within the same software. The works by Gao (1993), D'Amato Avanzi et al. (2004), Coelho Netto et al. (2007, 2014), Cevasco et al. (2013), Coutinho (2015) were used as a base for the definition of these classes. They discuss the role of slope angle in the detonation of shallow landslides and helped define the following class intervals:

i) 0° to 10°: considered as a potential area for deposition;
ii) 10° to 20°: low potential for landslides, considered an area of use permitted by law;
iii) 20° to 30°: medium landslide potential; area with legal restrictions for human use;
iv) 30º to 45º: critical angles of slope stability rupture, that is, with high potential for landslides;
v) > 45º: unstable slopes, generally with thin soil or rocky cliffs.

The files were converted from raster to vector (polygon) format, using the *Raster to polygon* tool. To define the intervals that best fit the critical angles of the basin, the DTM was extracted from the landslide scar polygons of January 2011 using the *Extract by mask* tool. To this file, containing elevation information only within the polygons of scars, the *Slope* tool was applied. The generated file was reclassified (*Reclassify*) one by one grade (through the manual classification method) covering all slope angles recorded inside the scars, which in this case was from 0° to 69°.

The landslide scars were evaluated individually concerning the mean, maximum, minimum, standard deviation, and frequency of distribution of slope values per scar. Mean slope angle values were assumed to be representative of the polygons. Figure 3 shows an example of how the reading of slope angle values was performed in each scar.

2.3.3 Curvature

The curvature of the slopes was also obtained from the DTM, using the *Curvature* tool (ArcGis 10.7). It was decided to work with the standard curvature, due to the greater possibility of understanding the role played by the concave portions of the relief in the convergence of superficial and shallow subsurface flows and consequent instability of the slopes.

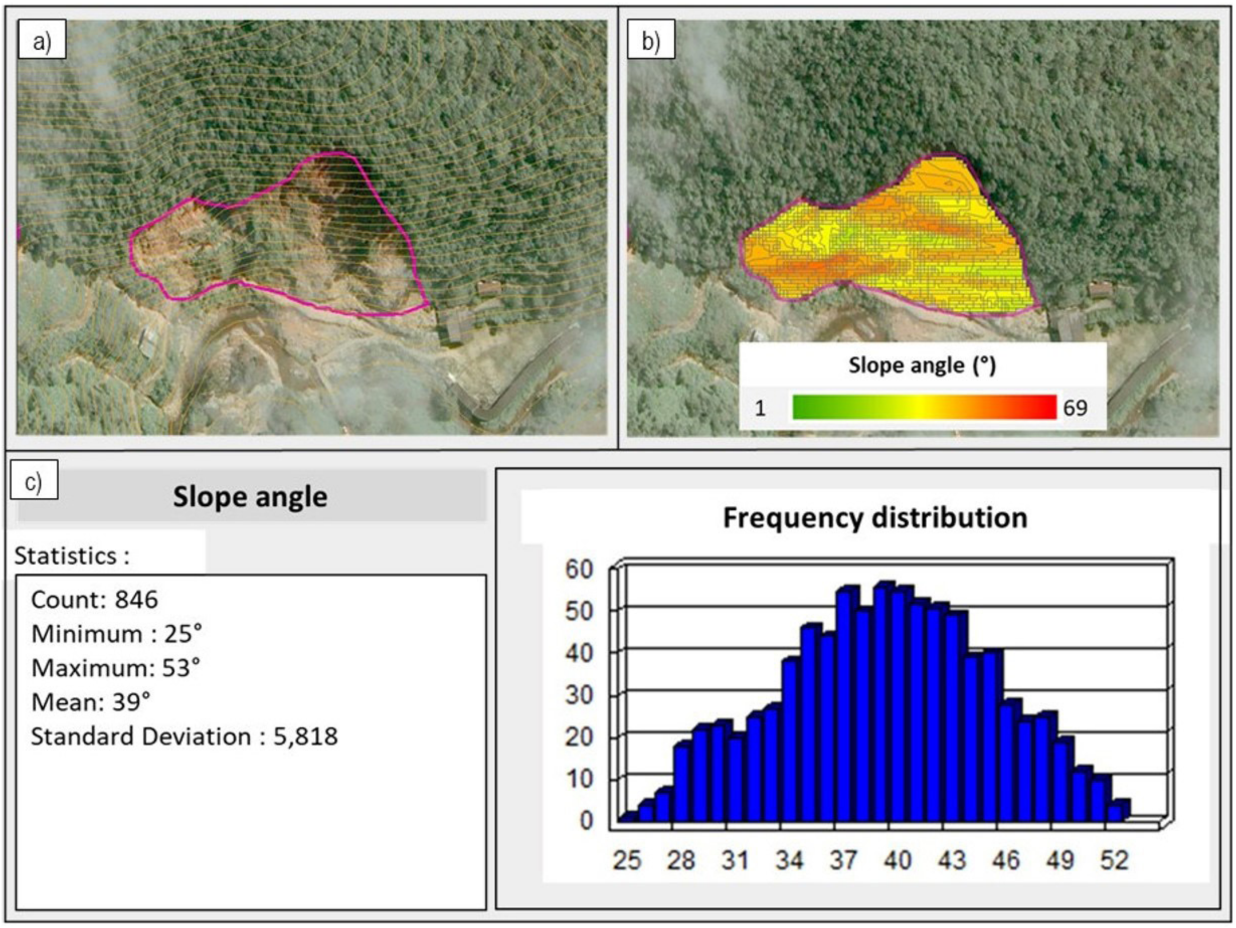

Figure 3. Morphological and topographical analysis of slipping scars. a) Example of scar demarcation with contour line (1:5,000); b) Example of data analysis referring to the distribution of slope angle values along the scar; c) Adapted model of how data is processed and presented by the software used (ArcGis 10.7).

Different intervals were tested in search of the best adjustment of this parameter to the reality of the study area. Initially, the tests were based on the values predefined in the literature (Valeriano, 2008; Tagil & Jenness, 2008; Bortoloti et al., 2015; Wang et al., 2015; ESRI, 2019; Dias et al., 2021b; Nohani et al., 2019), however, none of them proved to be adjusted to the study area.

In general, it was observed that the automated data were overestimating the convex-divergent areas and underestimating the rectilinear-planar areas. This problem was also pointed out by Valeriano (2008). According to the author, there is a need to admit a margin of values greater than zero so that planar slopes can be highlighted. Among the ranges tested, those that best fit the conditions of the D'Antas Creek basin were: values < -0.1 associated with concave-convergent slopes, values between -0.1 and 3.5 related to rectilinear -planar slopes, and values > 3.5 assumed as representative of convex-divergent slopes. These data were extracted from the DTM prior to the occurrence of the landslides. When necessary, supervised revisions were performed to better fit the model to the terrain conditions.

The judgment of the suitability of intervals was based on the mapping of landslide scars about the type of slope curvature, based on visual interpretation. With the aid of a *Geoeye* satellite image with a high spatial resolution (0.5 m), contour lines on a scale of 1:5,000, and a visualization scale between 1:5,000 and 1:3,000, this mapping proved to be essential to define the intervals of curvature. However, it is necessary to highlight that threshold adjustments need to be made depending on local conditions, mapping scale, and type of input data.

2.3.4 Topography Position Index (*TPI*)

The *TPI* has been used to determine the terrain susceptibility to landslide, as presented by Tagil & Jenness (2008), Seif (2014), and Nseka et al. (2019), among others. According to Weiss (2000), many physical and biological processes that act on the landscape are highly correlated with the topographic position. The *TPI* becomes relevant for the analysis of slope stability, as it helps to identify the preferential zones for the occurrence of landslides through the automation of relief classification (Tagil & Jenness, 2008; Seif, 2014).

The data referring to the *TPI* used in this research were produced by Coutinho (2015), based on the criterion defined by Weiss (2000) and the tool proposed by Jenness (2006). These data were generated at a scale of 1:5,000, with a spatial resolution of 2.5 m and radii of 12.5 m, 25 m, 50 m, and 100 m, as presented by Coutinho (2015). Adjustments related to the radii need to be made based on the local conditions of the study area and the scale of analysis. The results were classified using the "*Natural breaks*" method into five classes: i) Ridge; ii) Upper slope; iii) Middle slope; iv) Lower slope; v) Valley bottom (Coutinho, 2015).

2.3.5 Hydro-geomorphological map

Assuming that the forms mirror the processes that gave rise to them, in understanding the geomorphological evolution of the landscape, as advocated by Gilbert (1877), the hydro-geomorphological conditions listed for this study result from the integration of geomorphological indices and parameters, including *DEI*, slope angle, curvature and *TPI*. Figure 4 summarizes the parameters and synthesis indices used to build this mapping and their respective classes.

For the integration of the parameters and synthesis indices that make up the hydro-geomorphological conditions, weights were assigned to the classes and maps of each terrain condition according to their erosive potential. The generated mappings were intersected, using the Intersect tool (ArcGis 10.7), with the landslide scars inventory shape, and the results supported the establishment of weights for each class, based on the AHP method.

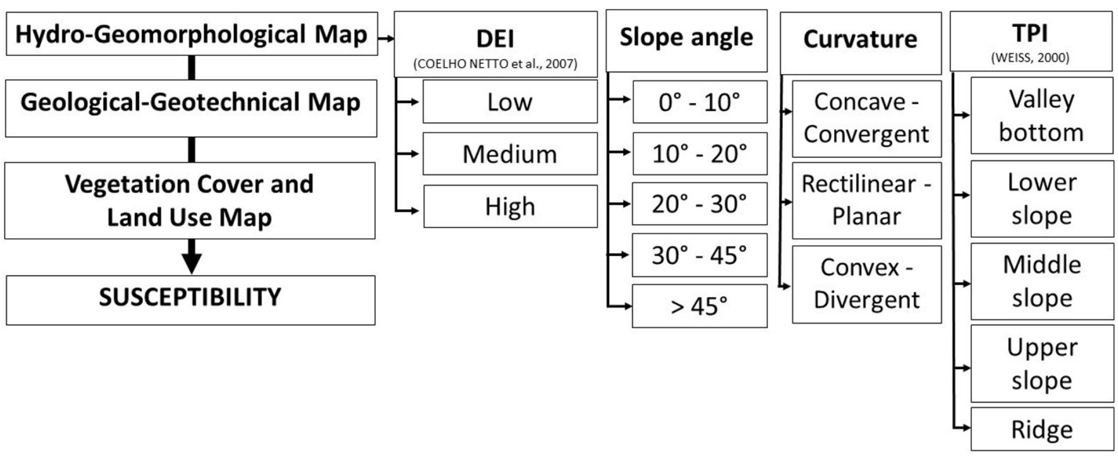

Figure 4. Methodological structure of the geo-hydroecological approach for terrain susceptibility zoning, focusing on the parameters considered relevant for the establishment of Hydro-geomorphological Conditions and the respective classes adopted in this research.

The incidence, which consists of the ratio between the slid area (%) in each class and the area occupied by this class in the basin, was used as a support for establishing weights in the AHP matrix for paired comparison.

The Analytical Hierarchical Process (AHP) was integrated into the geo-hydro-ecological approach to help determine the criteria and weights of each variable used in the crossings. Using the selected criteria, a paired comparison matrix was created to represent the relative importance of classes, based on the attribution of weights and the establishment of priorities. These weights were determined from the Saaty Fundamental Scale, which ranges from 1 to 9, where the value 1 is equivalent to equal importance between the factors and the value 9, the extreme importance of one factor over the other (Saaty, 1994).

In addition to the weight attributed to each class and map, the final weight of the classes (*Pf*) is calculated, which corresponds to the multiplication between the weight of the class (*Pclass*) and the weight of the map (*Pmap*), as shown in Equation 2:

$$Pf = Pclass \times Pmap \tag{2}$$

The shapes corresponding to the *DEI*, slope angle, curvature, and *TPI* were grouped using the *Union* tool (*ArcGis 10.7*). The final weight of the classes was added to obtain the synthesis values, which made it possible to classify the hydro-geomorphological conditions, as suggested by Coutinho (2015). In this sense, the equation applied to obtain the values of hydro-geomorphological conditions was as follows:

$$Pf\ CH = Pf\ Curvature + Pf\ DEI + Pf\ TPI + Pf\ Slope \tag{3}$$

It was decided to work with three classes of erosion potential: Low, Medium, and High, as proposed by Coelho Netto et al. (2007, 2014). The grouping of classes was initially conceived based on the "*Natural breaks*". However, when necessary, adjustments were made according to the characteristics of the terrain.

After the class definition step, the area of the polygons generated from the combination of shapes was calculated. All polygons smaller than 200 m^2 were merged with neighboring polygons with a larger area or a longer shared border, using the Eliminate tool. This minimum area value was assumed after tests had been carried out with all polygons and with the elimination of polygons with areas < 100 m^2, < 150 m^2, < 200 m^2, < 300 m^2, and < 400 m^2 (Figure 5).

The shape including all the generated polygons, in addition to containing many features (> 287,000), presented polygons with very small areas and not representative for the analysis, such as the approximately 44,000 features with an area of less than 1m^2. The elimination of polygons with areas < 100 m^2 and < 150 m^2 showed similar behavior about the distribution of classes, but still with the presence of unrepresentative polygons for mapping.

The elimination of polygons with an area < 200 m^2 presented a more stimulating result, considering the reduction in the number of features (maintenance of approximately 20% of the initial number of polygons) and the maintenance of the proportion of areas occupied by each class in the basin when compared to the previous tests. The tests carried out with the elimination of polygons < 300 m^2 and < 400 m^2 showed a more significant change in the areas occupied by each class, based on the overestimation of the high erosion potential class, to the detriment of the others.

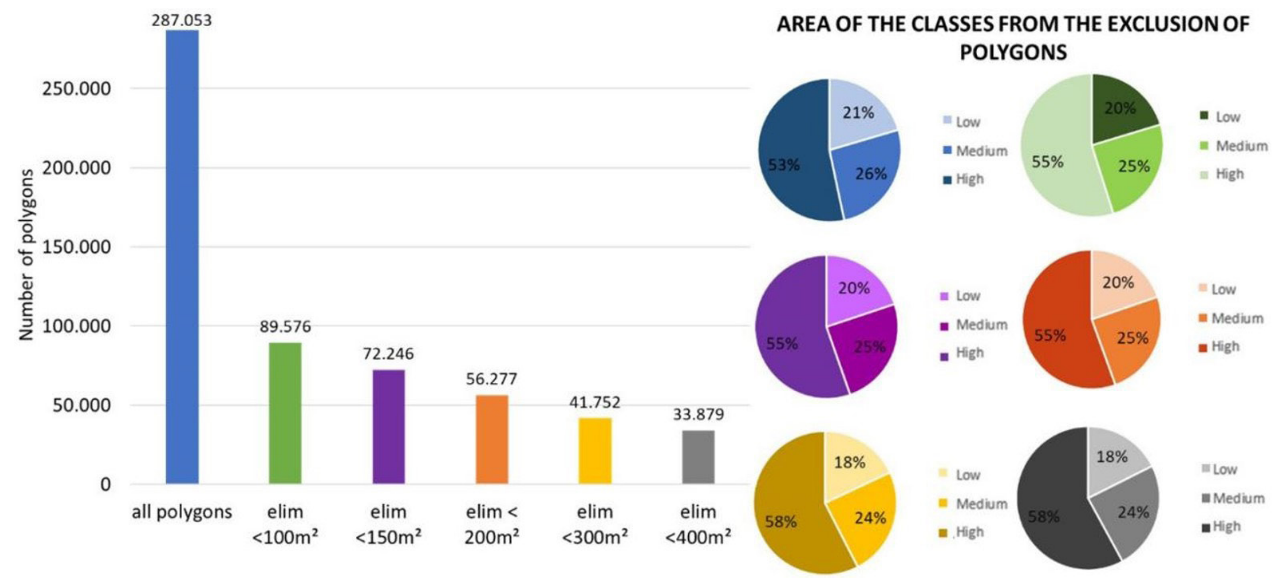

Figure 5. Number of polygons contained in each shape and the area occupied by each class of hydro-geomorphological conditions, from the elimination of polygons depending on the area or maintenance of all polygons generated with the union of the shapes.

Polygons < 200 m^2 were also eliminated from the curvature, slope angle and *TPI* shapes. It should be noted that, for each area of study and scale of analysis, these values must be revised. Tests need to be carried out so that the elimination of polygons does not lead to an inconsistent reading of the generated files.

3. Analysis and results

3.1 Drainage Efficiency Index (*DEI*)

The results were distributed into three class intervals: low (20.98%), medium (22.65%), and high (56.36%), as shown in Table 1. The low *DEI* class recorded the lowest incidence of landslides (0.40), with a landslide area of 8.37%. The medium *DEI* class concentrated 13% of the slid area and had an incidence of 0.57. The highest percentage of landslides (78.62%) occurred in the high *DEI* class (Table 1; Figure 6), as well as the highest incidence of landslides: 1.39. This class is usually associated with basins with a high topographic gradient and high density of drainage axes and/or concave up topographic hollows.

In the extreme rainfall event of January 2011, the detonation of translational landslides fed other debris flows at the bottom of slope valleys and along the trajectory of river channels. These articulated mass movements constitute a type of complex movement, integrating the processes acting on the slopes with the network of channels that drain the basins at their different hierarchical levels.

In the mountain massif of Tijuca (RJ, Brazil), as well as on the steep slopes of Serra do Mar, in the municipality of Angra dos Reis (RJ, Brazil), Coelho Netto et al. (2007, 2014, respectively) observed that areas with high susceptibility to landslides are associated with the high *DEI* class, in interaction with other geomorphological indices synthesized in the hydro-geomorphological map.

The incidence was used as a support for establishing weights in the AHP matrix for paired comparison (Table 2). An association was sought between the weight of classes and the concentration of landslide area per class (%). For this reason, the high *DEI* class (0.76) assumed the greatest weight, followed by the medium (0.16) and low (0.08) classes. Figure 6 shows the spatialization of the *DEI* in the D'Antas Creek basin.

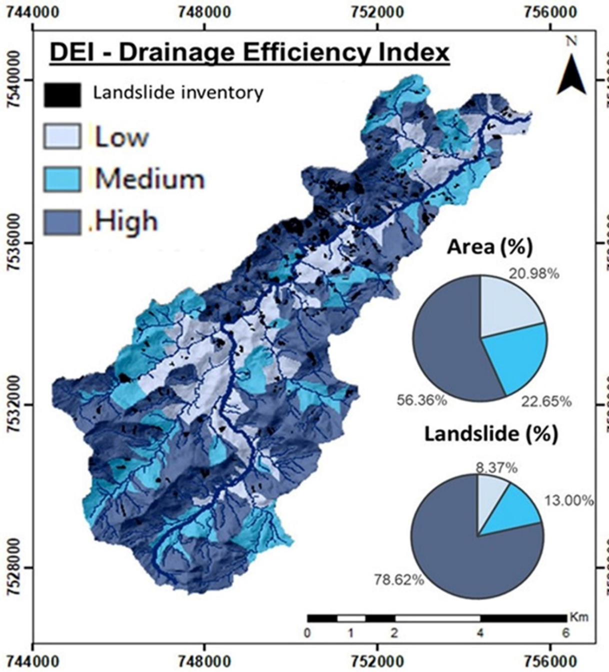

Figure 6. Drainage efficiency index map indicating the area (%) that each class occupies in the basin (adapted from Coutinho, 2015) and the landslide area (%) per class from the inventory of landslides that occurred during the extreme rainfall event in January 2011.

Table 1. Total area in the basin and slid area of each class used in the construction of the Drainage Efficiency Index (*DEI*).

Classes	Class area		Landslide area		Incidence
	km^2	%	km^2	%	
Low	11.16	20.98	0.08	8.37	0.40
Medium	12.05	22.65	0.12	13.00	0.57
High	29.98	56.36	0.75	78.62	1.39
Total	53.19	100	0.96	100	-

Table 2. AHP matrix of paired comparison between Drainage Efficiency Index (*DEI*) classes.

Classes	High	Medium	Low	Weight
High	1	5	9	0.76
Medium	1/5	1	2	0.16
Low	1/9	1/2	1	0.08

Consistency ratio = 0.001 (< 0.10 consistent).

3.2 Slope angle

The results were distributed into five slope angle classes: 0°–10° (11%); 10°–20° (24.06%); 20°–30° (33.34%); 30°–45º (27.74%); > 45° (3.85%). Crossing the slope angle classes with the landslide inventory showed that 73.04% (279) of the landslide scars had a mean value of slope angle between 30° and 45° (Table 3; Figure 7). The second group with the highest concentration of landslide scars was between 20° and 30° (21.47%; n = 82). The classes from 0° to 10°, from 10° to 20° and > 45° were less expressive in the analysis of the mean slopes; when added together, they represented less than 6% (21) of the total number of scars.

How the mean slope of the scars was read enabled a more precise definition of the critical angle in the basin. Although it is difficult to establish precise limits for the critical slope of so-called unstable slopes, values above 30º proved to be highly susceptible to the occurrence of shallow translational landslides in the D'Antas Creek basin. D'Amato Avanzi et al. (2004) in work carried out in the Cardoso basin in northwest Tuscany (Italy) indicate that 84.5% (547) of the assessed landslides occurred on slopes with slope angles between 31° and 45°, among which 35.6% had a gradient of inclination from 36° to 40°. Coelho Netto et al. (2007, 2014), based on Lacerda (1997, 2007) who indicate the critical friction angle for slopes in southeastern Brazil to be around 38°, assume as a critical angle slope angle values greater than 35°.

Cevasco et al. (2013) reported that shallow translational landslides triggered by episodes of intense rain in mountainous areas occur predominantly on slopes with slope angles between 30° and 45°. Steeper slopes generally have little material available for mobilization. Similar results were obtained by Fernandes et al. (2004), based on the analysis of the extreme rainfall event that occurred in the city of Rio de Janeiro in 1996, on the slopes of the Massif of Tijuca (RJ), observed a concentration of shallow landslides in the class between 30º and 55º. In the basins studied by the authors (Quitite and Papagaio), steeper slopes were associated with shallow soils, which could have been slipped previously, suggesting the existence of a threshold angle of inclination for the triggering of landslides.

In the analysis of the landslide area per class, the results assumed the same pattern found with the number of scars. The highest incidence of the slipped area occurred in the class from 30° to 45° (1.99), followed by classes 20° to 30° (1.01), > 45° (0.78), 10°–20° (0 .32), 0°–10° (0.01) as seen in Table 3. Coutinho (2015), when correlating the inventory of landslide scars (n = 244) with the slope angle classes (0°–10°; 10°–20°; 20°–35°; > 35°), obtained a concentration of 52.33% of the slid area in the 20°–35° class. However, how the slope angle values were obtained (through polygons representing a class interval) is not representative of the mean value of the landslide scar.

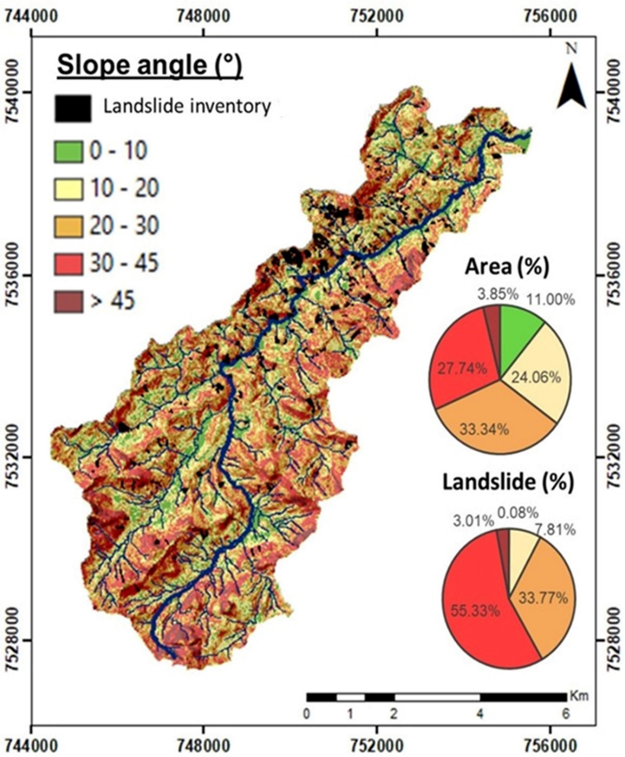

Figure 7. Slope angle map indicating the area (%) that each class occupies in the basin and the landslide area (%) per class from the inventory of landslides that occurred during the extreme rainfall event in January 2011.

Table 3. Total area in the basin and slid area of each class used in the slope analysis.

Classes (°)	Class area		Landslide area		Incidence	Distribution of landslide scars	
	km²	%	km²	%		no.	%
0–10	5.85	11.00	0.00	0.08	0.01	4	1.05
10–20	12.80	24.06	0.07	7.81	0.32	8	2.09
20–30	17.73	33.34	0.32	33.77	1.01	82	21.47
30–45	14.76	27.74	0.53	55.33	1.99	279	73.04
> 45	2.05	3.85	0.03	3.01	0.78	9	2.36
Total	53.19	100	0.96	100	-	382	100

The results obtained for the D'Antas Creek basin are in line with those reported for mountainous domains: extreme rainfall induced landslides tend to occur mainly on slopes angles between 30° and 45°. For this reason, in the AHP paired comparison matrix, the 30°–45° class (0.54) received the highest weight, followed by the 20°–30° class (0.21), as can be seen in Table 4. These two classes together concentrated approximately 90% (0.85 km^2) of the landslide area and 361 (94.50%) landslide scars. Figure 7 presents the slope angle map with the spatial distribution of the classes in the basin and the indication of the percentage of area occupied by each class and landslide area.

3.3 Curvature

The results obtained in an automated mode allowed the definition of three classes: concave-convergent (64.13%), convex-divergent (19.19%), and rectilinear-planar (16.68%). The highest concentration and incidence of landslide areas occurred in the concave-convergent class (75.59%; 1.18), followed by the rectilinear-planar classes (13.42%; 0.80) and convex-divergent (10.81%; 0.56), as observed in Table 5. The visual interpretation of the image also indicates the concave-convergent class as the one with the highest concentration of scars, around 66% (n = 252), followed by the rectilinear-planar class with 22.25% (n = 85) of scars, and the convex-divergent class (11.78%; n = 45).

This result was considered consistent, given the difference in the scale used in each assessment. While the visual interpretation was performed with the aid of contour lines at a scale of 1:5,000, the automated data generation process was based on the pixel value, which represents the smallest unit of measurement in the image. However, both results indicate a strong correlation between this slope geometry and the spatial concentration of shallow landslides. Figure 8 presents the curvature map and the indication of the percentage of occupied area and landslide area in each class.

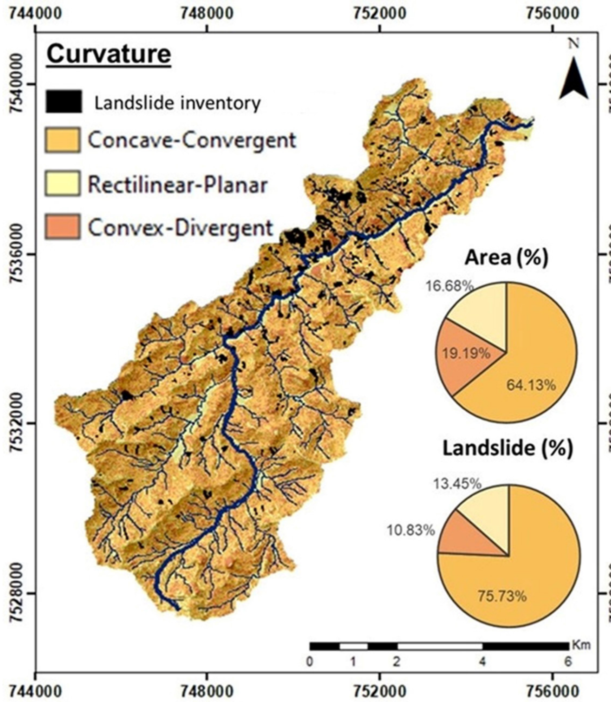

Figure 8. Curvature map indicating the area (%) that each class occupies in the basin and the landslide area (%) per class from the inventory of landslides that occurred during the extreme rainfall event in January 2011.

Table 4. AHP matrix of paired comparison between slope angle classes.

Classes (°)	30–45	20–30	>45	10–20	0–10	Weight
30–45	1	4	7	5	9	0.54
20–30	1/4	1	3	2	7	0.21
>45	1/7	1/3	1	2	3	0.11
10–20	1/5	1/2	1/2	1	3	0.09
0–10	1/9	1/7	1/4	1/5	1	0.04

Consistency ratio = 0.090 (< 0.10 consistent).

Table 5. Area of slope curvature classes, in addition to the slipped area accounted for by the automated mode and number of scars based on visual interpretation.

Classes	Automated Mode					Visual Interpretation (image May/2011)	
	Class area		Landslide area		Incidence	Number of landslide scars	%
	km^2	%	km^2	%			
Concave-Convergent	34.11	64.13	0.73	75.73	1.18	252	65.97
Convex-Divergent	10.21	19.19	0.10	10.83	0.56	45	11.78
Rectilinear-planar	8.87	16.68	0.13	13.45	0.80	85	22.25
Total	53.19	100	0.96	100	-	382	100

The role played by the concave relief compartments in the convergence of surface and subsurface flows has been attested since the studies by Hack & Goodlett (1960), Anderson & Burt (1978), Coelho Netto (1985), Dietrich & Dunne (1993), among others. Hack & Goodlett (1960) defined the concavity axes as the wettest part of the slope system, being able to present channeled flow, especially during rainy periods. This convergence of flows contributes to the development of saturation conditions in soils (Anderson & Burt, 1978). Nseka et al. (2019), in studies in the Kigezi region (southwest Uganda), point out that flow convergence zones (concave shapes), associated with moderately steep slope angles, medium/low slope, high humidity index and flow power index interact and induce the occurrence of landslides.

Research carried out in the southeastern region of Brazil also state that the concave slopes have a dynamic associated not only with the occurrence but also with the recurrence of landslide on the high slopes and accumulation of materials towards the axis of the concavities (Fernandes et al., 2001; Coelho Netto et al., 2016). Coelho Netto et al. (2016) showed this recurrence pattern in a colluvial cone located at the base of a rocky step (height = 10m), in the axis of a concave and steep slope (32º); through a thick sequence of colluviums rich in organic matter (3.5 meters), with radiocarbon ages ranging from 8,990 ± 100 years BP (10,374 to 9,779 cal years BP) at the base to 3,860 ± 100 (4,321 to 3,837 cal years BP) in a layer close to the surface. Studies in the Massif of Tijuca (Rio de Janeiro, RJ) by Fernandes et al. (2004) indicate that the concave shape of the slope presents a potential for failure about three times greater than that obtained in the convex and rectilinear features.

The concave-convergent areas were classified in the paired comparison matrix as being highly susceptible to shallow landslide detonation (0.75). The rectilinear-planar areas assumed a weight of 0.18 since they are the shapes that precede the concavities; therefore, they are subject to the occurrence of shallow landslides (Table 6). The convex-divergent areas, in their turn, were given the lowest weight (0.07) as they disperse water flows, favoring lower pore pressures and terrain stability.

The complexity associated with establishing thresholds adjusted to the study area may explain the low weights attributed to curvature in landslide susceptibility models. Catani et al. (2005), in their landslide susceptibility model (Arno River basin, Italy), state that the curvature, together with lithology and slope gradient, influences the volume and velocity of landslides. However, in the five evaluated areas, the authors point out that the land use (47.3%–10.9%) and the slope gradient (39.6%–14.6%) configure the highest degrees of susceptibility, followed by lithology (23.7%–8.4%), contribution area (30%–1.9%) and curvature (14.4%–2.8%).

Kayastha et al. (2013), evaluating the Tinau watershed (western Nepal), also attributed less weight to the curvature (0.0496) of the slope than to other geomorphological parameters, such as slope angle (0.1703) and aspect (0.0965). The work by Meirelles et al. (2018), developed in the Paquequer River basin (Teresópolis-RJ), points to the shape of the curvature (13.8%) as the third variable in importance to trigger landslides, preceded by slope angle (22.7%) and land use (16.3%). In their turn, Catani et al. (2013) highlight the importance of curvature, as the only variable that is not discarded in the scales evaluated for defining susceptibility models.

The inclusion of the curvature variable in the construction of the hydro-geomorphological conditions map proved to be relevant. The relationship between the forms and processes that gave rise to them constitutes an important precept in understanding the geomorphological evolution of the landscape (Gilbert,1877). Any alteration in the process will be reflected in the forms of the landscape through the readjustment of the parameters, categories, or synthesis indices in search of a new balance. Changes in the forms also influence the regulation of processes and the way they occur.

3.4 Topography Position Index (*TPI*)

The results were distributed into five *TPI* classes: ridge (12.07%), upper slope (13.18%); middle slope (48.45%), lower slope (21.05%), and valley bottom (5.24%). The middle slope class concentrated most of the landslide area, about 57% (0.55 km^2) of the total, representing an incidence of 1.18 of the landslide scars; followed by the upper slope (1.04), lower slope (0.87), ridge (0.76) and valley bottom (0.29), as shown in Table 7. In Figure 9, it is possible to observe the spatialization of the *TPI* classes in the basin, in addition to the landslide area.

Coutinho (2015) also attributed a higher concentration of landslides to the middle slope (49.58%) for the D'Antas Creek basin. Studies conducted by Coelho Netto et al. (2014), in the central area of Angra dos Reis, also indicate that areas with middle slopes, associated with slope angles greater than 35°, are the most susceptible to landslides. Nseka et al. (2019) also point out that in southeastern Uganda landslides are also concentrated (58%) on the middle slope.

Table 6. AHP matrix of paired comparison between the standard curvature classes.

Classes	Concave-convergent	Rectilinear-planar	Convex-divergent	Weight
Concave-convergent	1	3	7	0.75
Rectilinear-planar	1/3	1	3	0.18
Convex-divergent	1/7	1/3	1	0.07

Consistency ratio = 0.03 (< 0.10 consistent).

Although the landslides inventory used for crossing with the terrain conditioning parameters focused on the erosive domain of the scar and did not consider the depositional part (< 10°), there was a concentration of landslides in the lower slope class. Regarding this point, Coelho Netto et al. (2012) call attention to the variation of the geomorphological aspects involved in the rainfall events of 1996 and 2010, which occurred in the city of Rio de Janeiro. While in 1996 the landslides were concentrated from the ridge zone and intermediate interfluves to the valley bottoms, in the 2010 event, detonation prevailed on middle and lower slopes (approximately 60%) (Coelho Netto et al., 2012).

The authors showed that the detonation of landslides can occur in topographically different positions depending on the characteristics of the rainfall event. While in 1996 landslides were associated with steep and elongated slopes, which favored the propagation of mobilized materials and convergence towards valley bottoms, feeding debris flows; in the 2010 event, the high number of occasional landslides (45%) associated with the roads stands out, whether due to high and steep cuts or drainage outlets close to the road's curvatures (Coelho Netto et al., 2012).

These results guided the attribution of weights to the topography position classes (Table 8). The middle slope assumed greater importance (0.54), followed by the upper slope (0.24) and lower slope (0.13) classes. Ridge (0.06) and valley bottom (0.03) had the lowest weights in the paired comparison matrix, due to their little influence on the triggering of shallow landslides.

3.5 Hydro-Geomorphological Map

A synthesis analysis was carried out, attributing the *DEI* (0.38) the greatest importance among the hydro-geomorphological conditions (Table 9). It is an index that synthesizes a set of parameters from a functional reading of the landscape concerning the concentration and direction of flows and humidity on the slopes, which influence the potential for detonation of landslides.

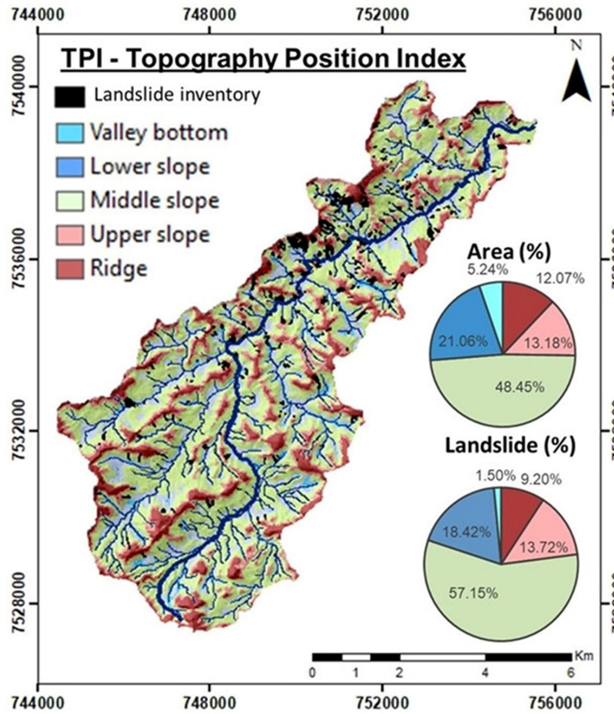

Figure 9. Topography position index map indicating the area (%) that each class occupies in the basin (adapted from Coutinho, 2015) and the landslide area (%) per class from the inventory of landslides that occurred during the extreme rainfall event in January 2011.

Table 7. Total area in the basin and slid area of each class used in the construction of the Topography Position Index (*TPI*).

Classes	Class area		Landslide area		Incidence
	km^2	%	km^2	%	
Ridge	6.42	12.07	0.09	9.20	0.76
Upper slope	7.01	13.18	0.13	13.72	1.04
Middle slope	25.77	48.45	0.55	57.15	1.18
Lower slope	11.20	21.05	0.18	18.42	0.87
Valley Bottom	2.79	5.24	0.01	1.50	0.29
Total	53.19	100	0.96	100	-

Table 8. AHP matrix of paired comparison between Topography Position Index classes.

Classes	Middle slope	Upper slope	Lower slope	Ridge	Valley Bottom	Weight
Middle slope	1	4	6	8	9	0.54
Upper slope	1/4	1	3	5	7	0.24
Lower slope	1/6	1/3	1	3	5	0.13
Ridge	1/8	1/5	1/3	1	3	0.06
Valley Bottom	1/9	1/7	1/5	1/3	1	0.03

Consistency ratio = 0.071 (< 0.10 consistent).

The slope angle (0.27), which is normally assigned as the main geomorphological parameter in the analysis of terrain susceptibility (Dias et al., 2021a), assumed a similar weight to the curvature (0.22), as both reflect the shape of the slope, based on the gravitational component and the concentration of water flows, respectively (Table 9). The *TPI* was assigned a lower weight (0.13) because it constitutes an approximate measure and delimitation, with a greater degree of generalization of the information.

The terrain conditions adopted and the weights assigned to each of them proved to be adjusted to the conditions of the basin. The data obtained from the inclusion of the curvature in the definition of the erosion potential of the study area were promising, since 88.74% (0.85 km^2) of the landslide area was associated with the class of high erosive potential (Table 10), against 80.05% (0.77 km^2) of landslide area at the intersection between slope angle, *DEI*, and *TPI*, without including slope curvature (Table 11).

The medium class (22.88%) of erosive potential concentrated 7.86% (0.08 km^2) of the landslide area, while the low class (21.03%) erosion potential presented a concentration of 3.40% (0. 03 km^2) of the landslide area. Figure 10 provides an integrated view of the parameters and synthesis indexes that were used to build the hydro-geomorphological conditions map.

The results obtained highlight the importance of using parameters and synthesis indexes of a geomorphological nature in the analysis and classification of the terrain susceptibility. Digital Terrain Models and derived datasets (slope angle, curvature, aspect, surface area, hydrographic pattern, among others) have been highly exploited to obtain geomorphological parameters. However, these parameters need to be inserted in the mappings functionally; that is, allowing one to understand how the processes contribute to the evolution of the landscape and to evaluate how the forms condition the processes at different spatial scales.

It is also important to point out that for each model, the values (or ranges of values) of the input parameters should be adjusted to allow agreement between field observations and automated operations. When adjusted to the conditions of the study area and scale of analysis, the geomorphological parameters are highly promising for the classification of terrain susceptibility to shallow landslides.

Table 9. AHP matrix of paired comparison between hydro-geomorphological conditions.

Classes	*DEI*	Slope angle	Curvature	*TPI*	Weight
DEI	1	2	2	2	0.38
Slope angle	1/2	1	2	2	0.27
Curvature	1/3	1/2	1	2	0.22
TPI	1/5	1/3	1/2	1	0.13

Consistency ratio = 0.081 (< 0.10 consistent).

Table 10. Total area in the basin and landslide area of each class used in the construction of the map of hydro-geomorphological conditions.

DEI, Slope angle, Curvature, *TPI*					
Classes	Class Area		Landslide Area		Incidence
	km^2	%	km^2	%	
Low (0.05795–0.188692)	11.18	21.03	0.03	3.40	0.16
Medium (0.188693–0.376064)	12.17	22.88	0.08	7.86	0.34
High (0.376065–0.662033)	29.84	56.10	0.85	88.74	1.58
Total	53.19	100	0.96	100	-

Table 11. Mapping of hydro-geomorphological conditions without using the curvature parameter.

DEI, Slope angle, *TPI*					
Classes	Class Area		Landslide Area		Incidence
	km^2	%	km^2	%	
Low (0.034660–0.142448)	11.66	21.91	0.04	4.01	0.18
Medium (0.142449–0.263714)	17.9	33.64	0.15	15.94	0.47
High (0.263715–0.513428)	23.64	44.44	0.77	80.05	1.80
Total	11.66	21.91	0.04	4.01	-

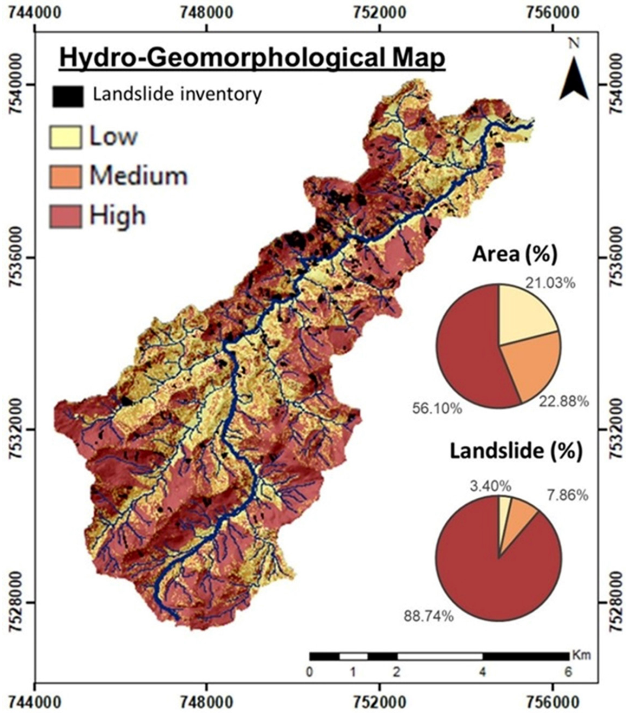

Figure 10. Hydro-geomorphological conditions map indicating the area (%) that each class occupies in the basin and the landslide area (%) per class from the inventory of landslides that occurred during the extreme rainfall event in January 2011.

4. Conclusions

The study of geomorphological parameters has been shown to be highly relevant in integrated analyzes of terrain susceptibility to shallow translational landslides. The functional methodology adopted, integrative of terrain conditions, presents a systemic foundation and organization of the database in a SIG environment. This base remains open for updates, as new functional parameters are identified as relevant, favoring updated diagnoses to guide territorial (re) ordering aimed at preventing, mitigating, and/or adapting human occupation.

How mean slope angle values were obtained for each landslide scar proved to be a significant adjustment for determining the critical slope. The inclusion of the curvature as another condition for the definition of the erosive potential also presented a satisfactory result, with the concentration of more than 87% of the landslide areas in the high erosive potential class. It should be noted that it was not just the inclusion of one more parameter, based on pre-established models, that was conducted. Ranges of values related to curvature were tested in search of a better fit between field observations and automated operations.

The attribution of weights (degree of importance) for each terrain condition was based on a previous analysis that evaluated the behavior of each class of parameters and synthesis indices, considered relevant for the crossing of hydro-geomorphological conditions. The results indicated a significant adjustment between terrain conditions and landslide areas (km^2) and the number of landslide scars. The main objective of this methodological step was to seek ways to bring forecast models closer to the reality of the study area. For this, the AHP method was integrated into the geo-hydro-ecological approach. From a mathematical basis, which allows organizing and examining the relative importance of the criteria, the AHP helped to reduce the inconsistencies of the model.

It is important to point out that the analysis and classification of terrain susceptibility is a continuous process that should be open to updates at time intervals compatible with the pace and variability of landscape transformations. Data concerning the frequency and spatial distribution of landslide should also be permanently open to revision and expansion. The occurrence of new landslides or the reactivation of old ones can provide important information on the rupture mechanisms and/or on the relationship between the occurrence of the movement and the terrain conditions.

Therefore, it is essential that the methodological bases for building and validating these models are available and that they are improved as knowledge advances. Understanding which mapping should be used in each territory, by the public administration, is essential to ensure coherent territorial management in the face of the needs of the population. The use of the resulting map as a planning and territorial management tool should be associated with knowledge of the potentialities and limitations of the generated product.

The questions in this research were stimulated not only by the relevance of landslides in the pattern of evolution of mountainous domains but mainly by the high applied value of this knowledge, since these areas are occupied by cities with a high population contingent, in addition to their socio-environmental, economic and cultural valuations. In this way, the aim is to contribute to a better equation of the risk of disasters.

Acknowledgements

The authors are grateful for the invitation of the scientific committee of VIII COBRAE for the publication of this article. The authors are also grafeful to INCT-REAGEO, the National Council for Scientific and Technological Development (CNPq) and the Carlos Chagas Filho Foundation for Research Support in the State of Rio de Janeiro (FAPERJ), which made this study financially viable.

Declaration of interest

The authors have no conflicts of interest to declare. All co-authors have observed and affirmed the contents of the paper and there is no financial interest to report.

Authors' contributions

Roberta Pereira da Silva: conceptualization, methodology, formal analysis, writing – original draft. Ana Luiza Coelho Netto: conceptualization, methodology, formal analysis, supervision, writing – review & editing. Willy Alvarenga Lacerda: conceptualization, methodology, formal analysis, supervision, writing – review & editing.

Data availability

The data generated and used for the analyzes presented throughout this article are available for scientific use upon request to the authors.

References

Abedini, M., & Tulabi, S. (2018). Assessing LNRF, FR, and AHP models in landslide susceptibility mapping index: a comparative study of Nojian watershed in Lorestan province, Iran. *Environmental Earth Sciences*, *77*, 1-13. http://dx.doi.org/10.1007/s12665-018-7524-1.

Akgun, A., Dag, S., & Bulut, F. (2008). Landslide susceptibility mapping for a landslide-prone area (Findikli, NE of Turkey) by likelihood frequency ratio and weighted linear combination models. *Environmental Geology*, *54*, 1127-1143. http://dx.doi.org/10.1007/s00254-007-0882-8.

Anderson, M.G., & Burt, T.D. (1978). The role of topography in controlling throughflow generation: a reply. *Earth Surface Processes and Landforms*, *3*(4), 331-344. http://dx.doi.org/10.1002/esp.3290030402.

Avelar, A.S., Vinagre, R. & Lacerda, W.A. (2016). Influências Geológicas, Geomorfológicas e Geotecnicas Geotécnicas nos Movimentos de Massa ocorridos nos dias 11 e 12 de janeiro de 2011, em Nova Friburgo, Rio de Janeiro, Brasil. In: *15º Congresso Nacional de Geotecnia e 8º Congresso Luso-Brasileiro de Geotecnia*, Porto, Portugal, 12 p.

Borgomeo, E., Hebditch, K.V., Whittaker, A.C., & Lonergan, L. (2014). Characterising the spatial distribution, frequency and geomorphic controls on landslide occurrence, Molise, Italy. *Geomorphology*, *226*(1), 148-161. http://dx.doi.org/10.1016/j.geomorph.2014.08.004.

Bortoloti, F.D., Castro Junior, R.M., Araújo, L.C., & Morais, M.G.B. (2015). Preliminary landslide susceptibility zonation using GIS-based fuzzy logic in Vitória, Brazil. *Environmental Earth Sciences*, *74*, 2125-2141. http://dx.doi.org/10.1007/s12665-015-4200-6.

Casagli, N., Catani, F., Puglisi, C., Delmonaco, G., Ermini, L., & Margottini, C. (2004). An inventory-based approach to landslide susceptibility assessment and its application to the Virginio River Basin, Italy. *Environmental & Engineering Geoscience*, *10*(4), 203-216. http://dx.doi.org/10.2113/10.3.203.

Catani, F., Casagli, N., Ermini, L., Righini, G., & Menduni, G. (2005). Landslide hazard and risk mapping at catchment scale in the Arno River basin. *Landslides*, *2*, 329-342. http://dx.doi.org/10.1007%2Fs10346-005-0021-0.

Catani, F., Lagomarsino, D., Segoni, S., & Tofani, V. (2013). Landslide susceptibility estimation by random forests technique: sensitivity and scaling issues. *Natural Hazards and Earth System Sciences*, *13*(11), 2815-2831. http://dx.doi.org/10.5194/nhess-13-2815-2013.

Cevasco, A., Pepe, G., & Brandolini, P. (2013). The influences of geological and land use settings on shallow landslides triggered by an intense rainfall event in a coastal terraced environment. *Bulletin of Engineering Geology and the Environment*, *73*(3), 859-875. http://dx.doi.org/10.1007/s10064-013-0544-x.

Coelho Netto, A.L. (1985). *Surface hydrology and soil erosion in a tropical mountainous rainforest drainage basin, Rio de Janeiro* [Doctoral thesis]. Katholieke University Leuven.

Coelho Netto, A.L., Avelar, A.S., Fernandes, M.C., & Lacerda, W.A. (2007). Landslide susceptibility in a mountainous geoecosystem, Tijuca Massif, Rio de Janeiro: the role of morphometric subdivision of the terrain. *Geomorphology*, *87*(3), 120-131. http://dx.doi.org/10.1016/j.geomorph.2006.03.0.

Coelho Netto, A.L., Avelar, A.S., Fernandes, M.C., Coutinho, B., & Freitas, L. (2008). *Relatório Técnico da Qualidade Ambiental do Estado do Rio de Janeiro (1:100.000): subsídios para o zoneamento econômico-ecológico*. Secretaria de Meio Ambiente do Governo do Estado do Rio de Janeiro.

Coelho Netto, A.L., Avelar, A.S., Sato, A.M., Dias, M.A., & Negreiros, A.B. (2012). Vulnerabilidade em geoecossistemas montanhosos e desastres causados por deslizamentos na interface florestal-urbana: controles geológicos, geomorfológicos e geoecológicos. In W.L. Lacerda, E.M. Palmeiras, A.L. Coelho Netto & M. Ehrlich (Eds.), *Desastres naturais: susceptibilidade e riscos, mitigação e prevenção, gestão e ações emergenciais*. COPPE/UFRJ.

Coelho Netto, A.L., Avelar, A.S., Sato, A.M., Fernandes, M.C., Oliveira, R.R., Vinagre, R., Barbosa, L., Lima, P.H., & Lacerda, W.L. (2014). Landslide susceptibility and risk zoning at Angra dos Reis, Rio de Janeiro state, southeast Brazil: a quali-quantitative approach at 1:5000 scale. In In W.L. Lacerda, E.M. Palmeiras, A.L. Coelho Netto & M. Ehrlich (Eds.), *Extreme rainfall induced landslides: an international perspective* (pp. 262-296). Oficina de Textos.

Coelho Netto, A.L., Facadio, A.C., & Silva, R.P. (2020). Geomorfologia do Estado do Rio de Janeiro e zona de fronteira: uma abordagem geo-hidroecológica. In M.E. Dantas, J.M. Morais, M.A. Ferrassoli, M.Q. Jorge & V. A. Hilquias (Eds.), *Geodiversidade do Estado do Rio de Janeiro - Programa Geologia do Brasil - Levantamentos da Geodiversidade* (1. ed., Vol. 1, pp. 125-186). Serviço Geológico do Brasil - CPRM.

Coelho Netto, A.L., Sato, A., Avelar, A.S., Vianna, L.G., Araújo, I., Ferreira, D., Lima, P., Silva, A., & Silva, R.P. (2013). January 2011: The Extreme Landslide Disaster in Brazil. In C. Margottini, P. Canuti & K. Sassa (Eds.), *Landslide science and practice* (pp. 377-384). Springer-Verlag Berlin Heidelberg.

Coelho Netto, A.L., Silva, R.P., Facadio, A.C., & Lima, P.H. (2016). Movimentos gravitacionais de massa e evolução das encostas montanhosas em regiões tropicais: estudos em Nova Friburgo, RJ. In A.L.L.S. Nunes, C.F. Mahler, F.A.B. Danziger, F.J.C.O. Castro, F.R. Lopes, F.T.S. Aragão, I.S.M. Martins, L.M.G. Motta, M.S.S. Almeida, M.C. Barbosa, M. Ehrlich (Eds.), *Willy Lacerda: doutor no saber e na arte de viver* (pp. 235-241). Outras Letras.

COPPETEC/SEA-RJ. (2010). *Mapeamento (Escala 1:5 000) de áreas de riscos, frente aos escorregamentos de encostas no município de Angra Dos Reis, RJ*. Fundação Coordenação de Projetos, Pesquisas e Estudos Tecnológicos/Secretaria de Estado do Meio Ambiente – Governo do Estado do Rio de Janeiro.

COPPETEC/SMAC-RJ. (2000). *Diagnóstico/Prognóstico sobre a Qualidade Ambiental do Geoecossistema do Maciço da Tijuca - subsídios à regulamentação da APARU do Alto da Boa Vista*. Fundação Coordenação de Projetos, Pesquisas e Estudos Tecnológicos/Secretaria de Estado do Meio Ambiente - Prefeitura da Cidade do Rio de Janeiro.

Coutinho, B.H. (2015). *Indicadores geo-hidroecológicos de suscetibilidade das encostas frente a erosão e movimentos de massa em região montanhosa tropical úmida: suporte metodológico para zoneamentos de riscos em diferentes escalas de análise espacial* [Doctoral thesis]. Universidade Federal do Rio de Janeiro. (in Portuguese)

D'Amato Avanzi, G., Giannecchini, R., & Puccinelli, A. (2004). The influence of the geological and geomorphological settings on shallow landslides, An example in a temperate climate environment:the June 19, 1996 event in north-western Tuscany (Italy). *Engineering Geology*, *73*(3-4), 215-228. http://dx.doi.org/10.1016/j.enggeo.2004.01.005.

Dias, H., Hölbling, D., & Grohmann, C. (2021a). Landslide Susceptibility Mapping in Brazil: a review. *Geosciences*, *11*(10), 1-15. http://dx.doi.org/10.3390/geosciences11100425.

Dias, H.C., Gramani, M.F., Grohmann, C.H., Bateira, C., & Vieira, B.C. (2021b). Statistical-based shallow landslide susceptibility assessment for a tropical environment: a case study in the southeastern Brazilian coast. *Natural Hazards*, *108*, 205-223. http://dx.doi.org/10.1007/s11069-021-04676-y.

Dietrich, W.E., & Dunne, T. (1993). The channel head. In K. Beven & M.J. Kirkby (Eds.), *Channel network hydrology* (pp. 175-219). John Wiley & Sons.

ESRI. (2019). *Curvature function*. ArcGis. Retrieved in October 10, 2022, from https://desktop.arcgis.com/en/arcmap/10.7/manage-data/raster-and-images/curvature-function.htm.

Fell, R., Corominas, J., Bonnard, C., Cascini, L., Leroi, E., & Savage, W.Z. (2008). Guidelines for landslide susceptibility, hazard and risk zoning for land use planning. *Engineering Geology*, *102*(3-4), 85-98. http://dx.doi.org/10.1016/j.enggeo.2008.03.022.

Fernandes, N.F., Guimarães, R.F., Gomes, R.T.A., Vieira, B.C., Montgomery, D.R., & Greenberg, H. (2001). Condicionantes geomorfológicos dos deslizamentos nas encostas: avaliação de metodologias e aplicação de modelo de previsão de áreas susceptíveis. *Revista Brasileira de Geomorfologia*, *2*(1), 51-71. [in Portuguese]

Fernandes, N.F., Guimarães, R.F., Gomes, R.T.A., Vieira, B.C., Montgomery, D.R., & Greenberg, H. (2004). Topographic controls of landslides in Rio de Janeiro: field evidence and modeling. *Catena*, *55*(2), 163-181. http://dx.doi.org/10.1016/S0341-8162(03)00115-2.

Gao, J. (1993). Identification of topographic settings conducive to landsliding from dem in Nelson county, Virginia, U.S.A. *Earth Surface Processes and Landforms*, *18*(7), 579-591. http://dx.doi.org/10.1002/esp.3290180702.

Gilbert, G.K. (1877). *Report on the geology of the Henry mountains*. U.S. Department of the Interior. https://doi.org/10.3133/70039916.

Guzzetti, F., Ardizzone, F., Cardinali, M., Galli, M., Reichenbach, P., & Rossi, M. (2008). Distribution of landslides in the Upper Tiber River basin, central Italy. *Geomorphology*, *96*(1-2), 105-122. http://dx.doi.org/10.1016/j.geomorph.2007.07.015.

Hack, J.T., & Goodlett, J.C. (1960). *Geomorphology and forest ecology of a mountain region in the central Appalachians - Professional Paper 347*. U.S. Department of the Interior. https://dx.doi.org/10.3133/pp347.

Jenks, G.F. (1977). *Optimal data classification for choropleth maps*. Lawrence, KS: University of Kansas, Department of Geography, 24 p.

Jenness, J. (2006). *Topograhic Position Index (tpi_jen.avx) extensión for ARCView 3.X, v.1.3a*. Jennes Enterprises. Retrieved October 10, 2022, from http://www.jennessent.com/arcview/tpi.htm.

Kayastha, P., Megh Raj, D., & De Smedt, F. (2013). Application of the Analytical Hierarchy Process (AHP) for landslide susceptibility mapping: a case study from the Tinau watershed, west Nepal. *Computers & Geosciences*, *52*, 398-408. http://dx.doi.org/10.1016/j.cageo.2012.11.003.

Lacerda, W.A. (1997). Stability of natural slopes along the tropical coast of Brazil. In *Proceedings of the Internacional Symposium on Recent Developments in Soil and Pavement Mechanics* (pp. 17-39). Rio de Janeiro. Balkema.

Lacerda, W.A. (2007). Landslide initiation in saprolite and colluvium in southern Brazil: field and laboratory observations. *Geomorphology*, *87*(3), 104-119. http://dx.doi.org/10.1016/j.geomorph.2006.03.03.

Larsen, M.C., & Torres-Sánchez, A.J. (1998). The frequency and distribution of recent landslides in three montane tropical regions of Puerto Rico. *Geomorphology*, *24*(4), 309-331. http://dx.doi.org/10.1016/s0169-555x(98)00023-3.

Martha, T.R., Roy, P., Govindharaj, K.B., Kumar, K.V., Diwakar, P.G., & Dadhwal, V.K. (2014). Landslides triggered by the June 2013 extreme rainfall event in parts of Uttarakhand state, India. *Landslides*, *12*(1), 135-146. http://dx.doi.org/10.1007/s10346-014-0540-7.

Meirelles, E., Dourado, F., & Castilho da Costa, V. (2018). Análise multicritério para mapeamento da suscetibilidade a movimentos de massa na bacia do rio Paquequer-RJ. *Geo UERJ*, *33*, 1-22. https://dx.doi.org/10.12957/geouerj.2018.26037.

Nakileza, B.R., & Nedala, S. (2020). Topographic influence on landslides characteristics and implication for risk management in upper Manafwa catchment, Mt Elgon Uganda. *Geoenvironmental Disasters*, *7*(27), 1-13. http://dx.doi.org/10.1186/s40677-020-00160-0.

Nohani, E., Moharrami, M., Sharafi, S., Khosravi, K., Pradhan, B., Pham, B.T., Lee, S.M., & Melesse, A. (2019). Landslide susceptibility mapping using different gis-based bivariate models. *Water (Basel)*, *11*(1402), 1-22. http://dx.doi.org/10.3390/w11071402.

Nseka, D., Kakembo, V., Bamutaze, Y., & Mugagga, F. (2019). Analysis of topographic parameters underpinning landslide occurrence in Kigezi highlands of southwestern Uganda. *Natural Hazards*, *99*, 973-989. http://dx.doi.org/10.1007/s11069-019-03787-x.

Ribeiro, M.C., Metzger, J.P., Martensen, A.C., Ponzoni, F.J., & Hirota, M.M. (2009). The Brazilian Atlantic Forest: how much is left, and how is the remaining forest distributed? Implications for conservation. *Biological Conservation*, *142*(6), 1141-1153. http://dx.doi.org/10.1016/j.biocon.2009.02.021.

Saaty, T.L. (1994). How to make a decision: the analytic hierarchy process. *Interfaces*, *24*, 19-43. http://dx.doi.org/10.1287/inte.24.6.19.

Seif, A. (2014). Using Topographic Position Index for landform classification (Case study: Grain Mountain). *Bulletin of Environment, Pharmacology and Life Sciences*, *3*, 33-39.

Silva, R.P., Lacerda, W.A., & Coelho Netto, A.L. (2022). Relevant geological-geotechnical parameters to evaluate the terrain susceptibility for shallow landslides: nova Friburgo, Rio de Janeiro, Brazil. *Bulletin of Engineering Geology and the Environment*, *81*, 1-18. http://dx.doi.org/10.1007/s10064-021-02557-z.

Silva, R.P., Lima, P.H.M., Facadio, A.C., & Coelho Netto, A.L. (2016). Condicionantes geomorfológicos e geológicos relacionados à deflagração de movimentos gravitacionais de massa: bacia do Córrego Dantas, Nova Friburgo – RJ. In *Anais do XI Simpósio Nacional de Geomorfologia* (pp. 1-7). Maringá. UGB.

Strahler, A. (1952). Dynamic Basis of Geomorphology. *Geological Society of America Bulletin*, *63*(9), 923-993. http://dx.doi.org/10.1130/0016-7606(1952)63[923:DBOG]2.0.CO;2.

Tagil, S., & Jenness, J. (2008). GIS-Based automated landform classification and topographic, landcover and geologic attributes of landforms around the Yazoren Polje, Turkey. *Journal of Applied Sciences*, *8*(6), 910-921. http://dx.doi.org/10.3923/jas.2008.910.921.

Valeriano, M.D.M. (2008). *Topodata: guia para utilização de dados*. INPE. Retrieved in October 10, 2022, from http://urlib.net/ibi/8JMKD3MGP8W/33EPEBL.

Varnes, D.J. (1978). Slope movement types and processes. In R.L. Schuster & R.J. Krizek (Eds.), *Landslides: analysis and control* (pp. 11-33). National Academy of Sciences. Retrieved in November 12, 2023, from https://onlinepubs.trb.org/Onlinepubs/sr/sr176/176-002.pdf.

Veloso, R.B., Rangel Filho, A.L.R., & Lima, J.C.A. (1991). *Classificação da vegetação brasileira, adaptada a um sistema universal*. IBGE. Retrieved in October 10, 2022, from https://jbb.ibict.br/handle/1/397.

Wang, Q., Li, W., Chen, W., & Bai, H. (2015). GIS-based assessment of landslide susceptibility using certainty factor and index of entropy models for the Qianyang County of Baoji city, China. *Journal of Earth System Science*, *124*, 1399-1415. http://dx.doi.org/10.1007/s12040-015-0624-3.

Weiss, A.D. (2000). *Topographic position and landforms analysis*. Jenness Enterprises. Retrieved in October 10, 2022, from http://www.jennessent.com.

Soils and Rocks
An International Journal of Geotechnical and Geoenvironmental Engineering
www.soilsandrocks.com
ISSN 1980-9743
ISSN-e 2675-5475

Hydro-mechanical numerical analysis of fault reactivation due petroleum production as trigger for submarine slope stability

Tasso Carvalho da Silva[1#], Igor Fernandes Gomes[1], Tiago Siqueira de Miranda[2], Julliana de Paiva Valadares Fernandes[3], José Antônio Barbosa[4], Leonardo José do Nascimento Guimarães[5]

Article

Keywords
Submarine slopes
Fault reactivation
Petroleum reservoir
Hydro-geomechanical analysis

Abstract

Oil production in offshore regions involves the transportation of oil and gas in submarine pipelines, which are vulnerable to geological processes triggered by subsurface oil production like fault reactivation. The fault reactivation process can lead to phenomena that impact the seabed, like subsidence and fluid exudation, and can trigger instability of submarine slopes, which can result in environmental and economic damage. The present work addresses a coupled hydromechanical numerical modeling of a hypothetical case involving fault reactivation caused by oil reservoir production and its impact on an overlying submarine slope. The hypothetical case was simulated using a finite element model. The case involves a reservoir which is cut by a fault zone that reaches the seabed. The slope instability studied was induced by the injection and production of fluids in the reservoir. The fault zone is assumed to be a sealing region and a geomechanical and pressure field discontinuity within the reservoir. Int this work was used the Mohr-Coulomb elastoplastic model with Perzyna viscoplastic regularization to represent the behavior of the fault zone and the overlying submarine slope. Results showed that the fault reactivation, caused by the reservoir production, developed shear stress and shear plastic strain along the fault and through the submarine slope, causing horizontal and vertical displacements in the slope mass and acting as a trigger factor for slope stability. Pore pressure increase at the bottom of the slope structure correlated with the injection pressure artificially increased into the reservoir.

1. Introduction

The injection and production of fluids in oil and gas reservoirs can cause significant changes to the stress state of the rocks, resulting from changes in the pore pressure. Reservoir interventions can lead to the concentration of shear stresses in fault zones in the reservoir or nearby, and cause reactivation.

Geological faults form discontinuity regions and damage zones between blocks of rocks, and are characterized by the parallel movement of broken parts (Peacock et al., 2017). Faults are characterized by the parallel movement of the rupture surface, and the fault plane can be flat or curved. Faults with sealing capacities (very low permeability zones) are important to forming hydrocarbon traps by preventing fluid migration through porous media. Fault zones consist of two main regions: a fault core, and a fault damage zone (Billi et al., 2003; Gudmundsson, 2004; Mitchell & Faulkner, 2009; Choi et al., 2016; Fossen, 2016; Celestino et al., 2020; Souza et al., 2022). Each region in a damage zone has specific shear strength and stiffness, porosity, permeability, and other properties heterogeneously distributed along its length and depth (Choi et al., 2016).

A damage zone is the network of subsidiary structures that involves the fault core and can increase the permeability of the fault zone in relation to the core and the undeformed protolith. Fault-related subsidiary structures in damage zones include small faults, veins, fractures, cleavages, and

[#]Corresponding author. E-mail address: tasso.carvalho@ufpe.br
[1]Universidade Federal de Pernambuco, Departamento de Engenharia Civil e Ambiental, Recife, PE, Brasil.
[2]Universidade Federal de Pernambuco, Departamento de Geologia, Recife, PE, Brasil.
[3]WALM BH Engenharia, Belo Horizonte, MG, Brasil.
[4]Universidade Federal de Pernambuco, Departamento de Geologia, GEOQUANTT, Recife, PE, Brasil.
[5]Universidade Federal de Pernambuco, Departamento de Engenharia Civil e Ambiental, Recife, PE, Brasil.

Submitted on June 10, 2023; Final Acceptance on October 25, 2023; Discussion open until February 28, 2024.
https://doi.org/10.28927/SR.2023.006523

folds that contribute heterogeneity and anisotropy to the permeability structure and elastic properties of the fault zone (Matsumoto & Shigematsu, 2018). Large damage zones can indicate multiple slipping episodes and the overprinting of successive deformation events (Caine et al., 1996; Choi et al., 2016; Torabi et al., 2020).

Studies of fault zones show how properties differ significantly, depending on the region analyzed, from the fault core to the undamaged rock. Cappa & Rutqvist (2011) argue that the fault core is a region of low permeability with small intergranular porosity, while the damage zone is more permeable, but less permeable than the reservoir, as a result of its macroscopic fracture network.

Gudmundsson (2004) showed how the development of the fault core and the damage zone can affect the mechanical properties, in particular the Young's modulus, of the host rock. The author also demonstrated an example regarding the distribution of the elastic modulus (Young) across the fault zone, from the undamaged host rock to the fault core.

Myers (1999) studied a fault zone in an outcrop of the Aztec sandstone located in the Valley of Fire State Park, USA. The fault consists of five structural elements with distinct characteristic permeabilities. The damage zone is formed by joints, sheared joints, fault cores, and slip surfaces, which are embedded in the undisturbed host rock.

The fault reactivation process can be characterized by shear strains and loss of the sealing characteristic due to dilation, which is the increase in volume associated with the shear deformation. Several works have addressed the numerical hydro-mechanical modeling of fault reactivation problems, such as Khan et al. (2020), Quevedo et al. (2017), Yang et al. (2021), Rutqvist et al. (2007), Soltanzadeh & Hawkes (2008) and Guimarães et al. (2009, 2010).

Fault reactivation can lead to seabed deformation and exudation of fluids on the seabed surface. Interventions during reservoir production can affect geological faults and destabilize submarine slopes. Submarine slope instability can lead to landslides, and hence tsunami (Gue, 2012; Ma et al., 2013), damage to offshore pipelines (Zhang et al., 2019) and offshore wind towers (Bakhsh et al., 2021), and extensive environmental and economic damage.

There are few and important studies on the risks and effects of submarine slope instability, the failure, and effects like landslide as Masson et al. (2010), Gue (2012), Urgeles & Camerlenghi (2013), Katz et al. (2015) and Scarselli et al. (2016). Scarselli (2020) provided a general view of key factors related to submarine landslides such as classification schemes, architectural elements, preconditioning, and triggering factors. The author studied the causes of submarine slope failure and the environments of occurrence, finding trigger factors such as increased pore pressure due to fluid migration and seepage, and the slope steepening due to faulting, folding, and diapirism.

Yincan (2017) discussed several topics related to submarine landslide theme, like classification and instability mechanisms and methods for analyzing stability. These authors treated statistical data of submarine slope instability events and their triggering factors like earthquake and fault activities, shallow gas or natural gas hydrate exudation, human activities, and erosion effects.

Various stability analysis methods for submarine slope have been commonly used, such as the limit equilibrium method, and analytical and numerical methods, as proposed by Leynaud et al. (2004), ten Brink et al. (2009), Quinn et al. (2011, 2012), Puzrin et al. (2015), Dey et al. (2016). Numerical analysis allows prediction of the stress state and displacement field for the slope structure and the surrounding structures below the submarine slope. This type of analysis adopts constitutive models, which allows the definition of the stress-strain inelastic (regarding a rate-dependent or independent plasticity) behavior. Finite element methods are commonly used to represent small-strain (Lagrangean) or large-strain (Eulerian) related mechanical phenomena (Dey et al., 2016; Stoecklin et al., 2021). Methods like the material point and the discrete element approach are also commonly used, especially for post-failure simulation. The analysis of total or effective stress of submarine slopes can be treated through numerical simulations with reliable results and it allows to reduce risks.

Overall, the study of fault reactivation impact on submarine slope stability scarcely regards the contexts of oil and gas production or CO_2 storage. The hypothesis of this work is that the geological faults and the related kinematics are impacted by the increase in pore pressure created by fluid flow along the fault structure, which can trigger fault reactivation and slope instability. The present work uses a novel approach to analyze a hypothetical case study on submarine slope stability, considering the scenario of a geological fault reactivation as the trigger. The scenario involves a shallow offshore reservoir production and a normal fault that cut the reservoir.

The study uses a coupled hydromechanical numerical simulation of fluid flow in the context of oil reservoir production with the possibility of fault reactivation. The simulation is able to demonstrate the impact of the fault reactivation process on the stress-strain response of a submarine slope above the reservoir, through the Mohr-Coulomb viscoplastic model, and viscous Perzyna regularization (Perzyna, 1966). The model is simplified by treating the fault zone and the core as a homogeneous, continuous medium. The simulation was carried out using in-house finite element code (Olivella et al., 1995; Guimarães et al., 2007; Silva et al., 2021; Souza et al., 2022), and a 2D finite strain analysis was considered. The post-failure slope behavior was not investigated here.

2. Mathematical modeling

Soils and rocks are complex porous media which need adequate constitutive models to describe each type of material. Thus, elastoplastic constitutive models are used to represent the elastic and plastic behavior as a response to stresses to which the material is submitted. The model describes the material strain in two parts, elastic vs plastic, and reversible vs irreversible. In this work, the hydro-mechanical simulation was formulated considering the governing equations for the mass and moment balance in each phase. The geomechanical problem presents the stress-strain behavior of the rock, which depends on the state of the stresses and the pore pressure field. For simulating the hydraulic effects, the permeability and porosity of the porous media are updated at each time step. Infinitesimal (small) strain effects, and constant-temperature equations were considered for the calculations, regarding the mechanical problem defined by the Cauchy equilibrium equation (Equation 1). This approach considered constitutive laws and complementary equations, and the hydraulic problem is characterized by the mass balance of the fluid phase using Darcy's law (Equation 2).

$$\nabla\sigma + b = 0 \tag{1}$$

where ∇ is the divergence operation on the stress tensor σ, and b is the volumetric vector of the body forces. The phase mass balance is represented by:

$$\frac{\partial \phi \rho_l}{\partial t} + \nabla.\left(\rho_l q_l\right) + \rho_l \phi \nabla \dot{u} + f_l = 0 \tag{2}$$

where ρ_l is the density of the fluid phase, ϕ is the porosity of the rock, q_l is the Darcy's flux vector, and f_l is a source/sink mass term of the fluid phase. The invariants of the problem are the nodal displacement vector $\dot{u}$, and the nodal fluid pressure p_l. The main constitutive equation for the hydraulic problem is Darcy's Law; in this work, only a single-phase fluid flow is considered:

$$q_l = \left(\frac{K}{\mu_l}\right)(\nabla p_l + \rho_l g) \tag{3}$$

where K is the intrinsic permeability tensor of the porous medium, μ_l is the viscosity of the fluid phase, and g is the gravity vector.

2.1 ElastoViscoplastic constitutive model

It was adopted the Mohr-Coulomb elastoplastic model with viscous regularization by Perzyna's model (Perzyna, 1966; Simo & Hughes, 1998), where the stress and strain increments are described as follows:

$$d\sigma' = D^e d\varepsilon = D^e(d\varepsilon^e + d\varepsilon^{vp}) \tag{4}$$

In which $d\sigma'$ is the effective stress increment, D^E is the elastic constitutive tensor and the variables $d\varepsilon$, $d\varepsilon^E$, $d\varepsilon^{VP}$ are, respectively: the increment of total, elastic and viscoplastic strains. The stress vector is determined by the effective stress principle, where the stress state is a function of a change in the fluid pressure field p_l:

$$d\sigma' = d\sigma + m dp_l \tag{5}$$

where $d\sigma$ is the total stress increment and m is an identity tensor. The Perzyna viscoplastic model allows the modeling of the effects of the time rate in the plastic strain process. In a mechanical analysis, the resulting stresses and strains are time dependent, and a viscoplastic multiplier $\dot{\lambda}$ is applied to the plastic flow rule, as shown in (Equation 6):

$$\dot{\varepsilon}^{vp} = \frac{\langle\left(F\left(\sigma,h\right)\right)\rangle}{\eta}\frac{\partial F\left(\sigma,h\right)}{\partial\sigma} \tag{6}$$

Therefore, the viscoplastic multiplier is a function of a penalty parameter $1/\eta$ and consider a monotonic function $\Phi(F(\sigma,h))$, and $\Phi(F(\sigma,h)) = 0 \Leftrightarrow F(\sigma,h) = 0$, where $F(\sigma,h)$ is the creep function and h are the internal variables for the plasticity model. Applying the flow rule (Equation 4) makes it possible to relate the state of stress with the strain via a viscoplastic constitutive tensor, D^{VP}. The creep function of the Mohr-Coulomb plasticity model is written in terms of the three stress invariants: p', J and θ, defined as the mean effective stress, deflection stress and Lode angle, respectively:

$$F\left(\sigma',h\right) = J - \left(\frac{c'}{tan\varphi'} + p'\right)G\left(\theta\right) = 0 \tag{7}$$

where σ' is the effective stress, c' the effective cohesion and ϕ' is the effective friction angle.

2.2 Hydromechanical coupling

This work used a formulation that allows for coupling between changes in porosity and intrinsic permeability. The porosity variation is calculated using the solid equilibrium equation:

$$\frac{D\phi}{Dt} = \frac{\left(1-\phi\right)}{\rho^s}\frac{D\rho^s}{Dt} + \left(1-\phi\right)\dot{\varepsilon}_v \tag{8}$$

where $\dot{\varepsilon}_v$ is the volumetric strain rate. The determination of permeability with the change in the rock strain is a complex function that depends on the elastic or inelastic regime of the material. The Mohr-Coulomb viscoplastic model uses a linear law that relates the variation in permeability to the evolution of plastic shear strain, which is directly related to volumetric plastic strain at a given dilation angle (Guimarães et al., 2009).

3. Methodology

The simulation was carried out in a hypothetical bi-dimensional model describing a shallow reservoir cut by a fault. The simulation considered the oil reservoir production process, which involved operation of wells for injection and production of fluids. The fault zone was considered as a sealing region, a low permeability, geomechanical discontinuity within the reservoir. The fault is connected to a submarine slope over the reservoir, which was considered in equilibrium of stress. The model, described in Figure 1a, consists of a reservoir interval, a cap rock zone (overburden) with seal capacity, and an underlying interval (underburden). The sea level is 110 m above the overburden interval and the submarine slope (over the foot wall). The normal fault ends below the submarine slope which is formed by an overlying bed 130 m thick. The slope is located over the topographic displacement formed by the fault throw. The sea level depth over the hanging wall is −150 m, the base level of the submarine slope. The model is 1560 m wide, with a maximum thickness of 640 m in the slope region. The cap interval and underburden interval are both 270 m thick, and the reservoir interval is 80 m thick. The fault zone thickness is 10 m. The fault throw is 20 m (Figure 1).

The model was implemented as an unstructured finite element mesh of linear triangle elements (Figure 1b) with 8523 nodes and 16853 elements. The model contains 5 different materials which represent the slope, the reservoir interval, the cap interval and the overlying interval, and the fault zone. Each material is characterized by its mechanical and hydraulic properties—the modulus of elasticity E, cohesion c', and effective friction angle ϕ', porosity n, permeability k (materials were assumed to be isotropic), and Perzyna's viscous parameter $\eta / \Delta t$—summarized in Table 1.

The reservoir simulation involved two wells: an injector on the left side of the model, and a producer on the right side. The injector well is 155 m from the fault (left side) with a depth of 308 m, and the production well is located 20 m from the fault (right side), at a depth of 315 m. The bottomhole pressure (BHP) in the injector well is 4.2 MPa, above the reservoir pressure; at the production well, the pressure is 4.0 MPa, below the reservoir pressure. The mechanical and hydraulic boundary conditions are shown in Figure 2. The boundary conditions related to the movement restriction are applied horizontally, to limit lateral displacement, and vertically at the base of the model. Effective stress σ' is prescribed as zero at the surface of the seabed, the applied liquid pressure P_l corresponds to the equivalent to a water level P_w. The compressibility of the injection fluid and its density are 1.0×10^{-4} MPa^{-1} and 1001.7 kg/m^3, respectively. The simulation assumes a plane strain state.

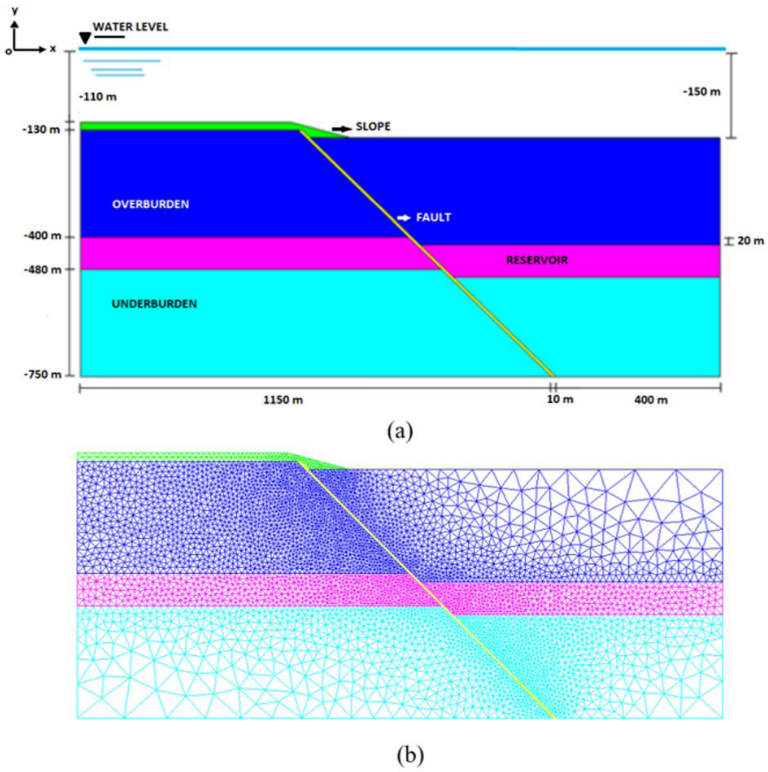

Figure 1. Details of the problem modeled: (a) geometries and materials; (b) FEM mesh.

Table 1. Property of materials.

Layer	E (MPa)	c' (MPa)	ϕ' (°)	k (m^2)	n	η / Δt
Slope	5	0,10	10	$1x10^{-16}$	0.48	10^4
Overburden	6780	2.30	26	$1x10^{-25}$	0.01	-
Underburden	10800	3.60	26	$1x10^{-25}$	0.01	-
Fault	8000	0.80	23	$5x10^{-22}$	0.1	10^4
Reservoir	15860	5.80	30	$5x10^{-12}$	0.2	-

Adapted from Pereira et al. (2014).

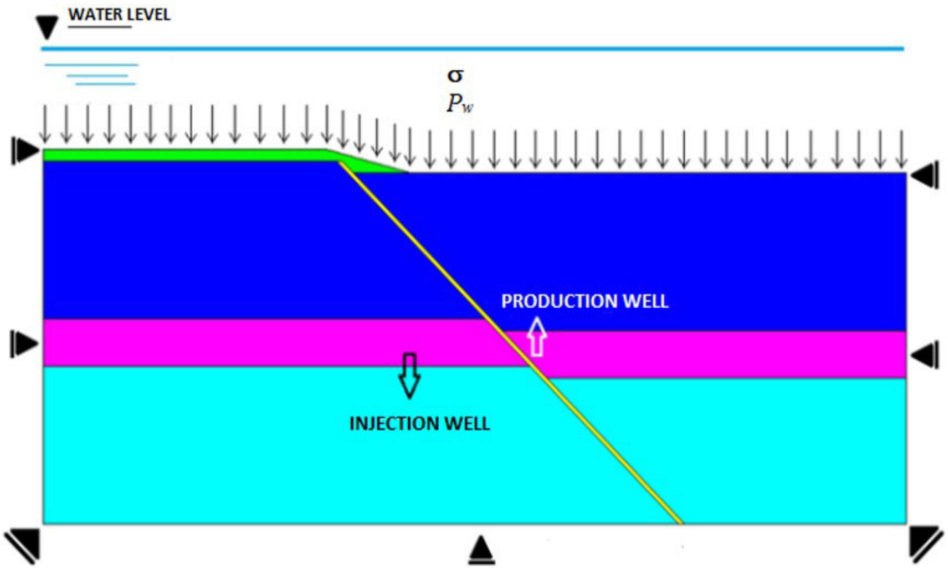

Figure 2. Initial and boundary conditions.

4. Results

The influence of the injection well was analyzed in the left region of the fault, close to the slope, observing the impact of the secondary oil recovery in the reservoir and the fault reactivation process.

The first variable to be considered is the pore pressure field, which changes due to well operation, leading to changes in the stress state variations inside the reservoir and for surrounding and cap rocks and geological structures. This can result in reactivating the fault structure through the shearing process, and increasing the permeability of damage zones and core fault, leading to fluid flow to the fault and increased pore pressure. Figure 3 shows the pore pressure distribution along the fault for an intermediate (Figure 3a) and final (Figure 3b) time step of the simulation process. The pressure increase inside the fault is evidence of reactivation and migration of the fluid.

Figure 4 shows the vectors indicating fluid flow from the reservoir through the fault. They reach the submarine slope base at top of field, indicating exudation at the seabed. These results show an important aspect to the slope stability process due to pressurizing the slope layer for a high pore pressure level.

The main fault reactivation indicators are the viscoplastic shear strain $\dot{\varepsilon}_d^{vp}$ (Figures 5a and b) and the consequent permeability fault increase (Figures 5c and d) as function of $\dot{\varepsilon}_d^{vp}$. The evolution of the shear plastic strain is a consequence of the stress path which reaches the Mohr-Coulomb yield surface, leading to a plastification process. Due the linear relation between the permeability changes and the shear plastic strain, as discussed in section 2.2, the fault permeability increases with plastification, opening the fault pores in a dilatancy process to fluid migration from the reservoir as explained above. This response has been widely observed, e.g. by Langhi et al. (2010) who realized a three-dimensional numerical simulation of the fault reactivation problem for a complex, sealed set of geological faults, accounting for hydro-mechanical coupling. This study considered shear strains and dilation as well as fluid flux as determining factors of fault leakage. Similar conclusions were presented in Guimarães et al. (2009, 2010), Rutqvist et al. (2007).

Pereira et al. (2014) presented a fault reactivation study for oil production scenario, applying methodology similar which was used in this study. They modeled a hydro-mechanical coupling and uncertainty analysis for fault properties, focusing on determining the maximum bottom hole pressure (BHP) without fault reactivation in which the plastic work (associated

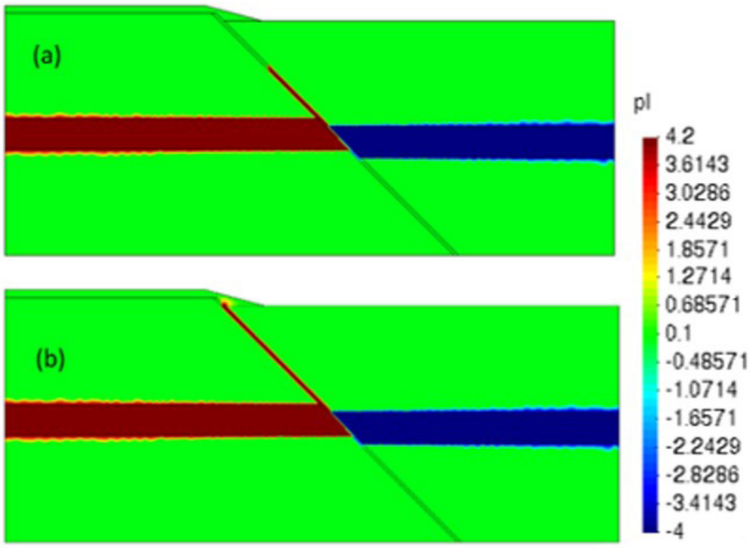

Figure 3. Pore pressure (MPa) at fault reactivation analysis: (a) pore pressure distribution at intermediary simulation time; (b) final distribution. Negative values indicate a drop in initial pore pressure, and positive values are related to increase because effective stress analysis.

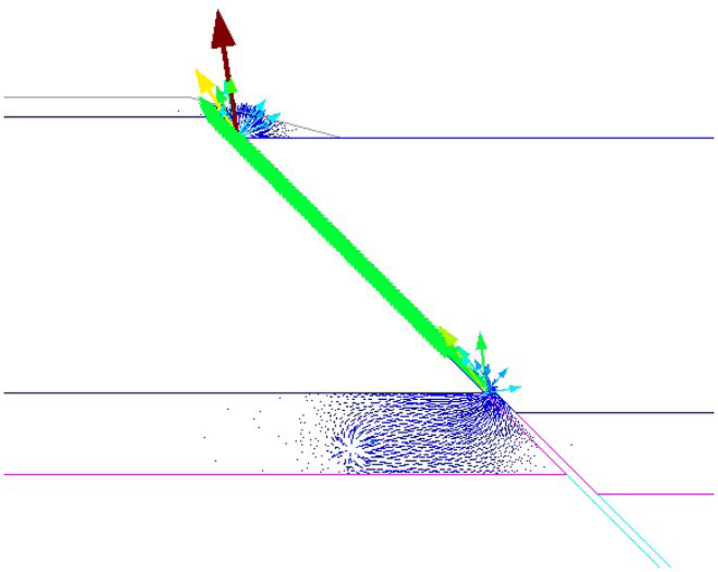

Figure 4. Distribution of fluid flow vectors to final time.

with shear plastic strain) and permeability increase, via the reactivation indicators as we describe in the present work. It is noteworthy that the permeability measure is in m^2 and is expressed on a negative log scale.

The pressurization of the fault structure during the reactivation process, associated with the change in the state of stress, causes differential displacements, especially at the top of the field where an expressive vertical displacement in the submarine slope is observed. This process occurs due to the ground uplift caused by the increased reservoir pore pressure as a function of well injector activity, which changes the initial stress state and pore pressure field. Then, the fluid injection in the compartmented reservoir causes volumetric expansion through hydro-mechanical coupling. Similar behavior has been presented as discussed by Khan et al. (2020), where the authors conducted a numerical investigation of CO_2 storage in reservoirs, analyzing the effects of pressure changes in the fault, reservoir, and surrounding rocks. The authors discussed the effects of reservoir size and boundary conditions on pore pressure buildup, on the ground uplift, and on fault reactivation and indicate the occurrence of fault reactivation and round uplift

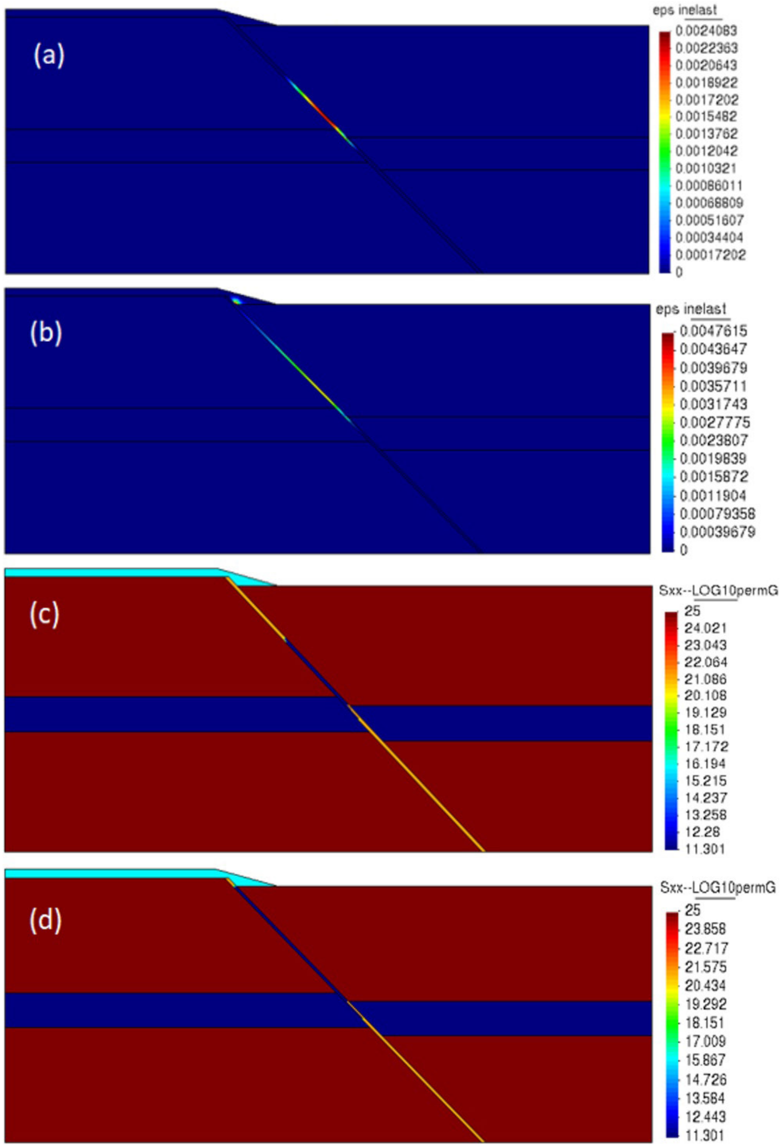

Figure 5. Fault reactivation indicators: (a) viscoplastic shear strain at intermediary simulation time; (b) final distribution of viscoplastic shear strain; (c) -log permeability change at intermediary simulation time; (d) final distribution of increased -log fault permeability.

associated with increased pore pressure of reservoir due to CO_2 injection. Then, the same hydro-mechanical behavior is observed as in the present work.

These aspects can be observed in Figures 6a and 6b that show the final distribution of vertical and horizontal displacements of the field. The figures show a greater positive displacement on the slope; in the region where the fault meets, a dilatation process occurs due to the injection of the fluid, as shown in Figure 6. For horizontal displacements, it is possible to identify a discontinuous displacement field in the surrounding rocks for two sides of the fault, showing the shearing effect of the structure.

Following the above general analysis of the oilfield and geological fault, showing the reactivation process discussions, the mechanical analysis of the submarine slope is now carried out, analyzing the consequences of reservoir pressurization and fault reactivation effects.

Initially, is intended aim to analyze the pore pressure increase, shear stress and shear plastic strain occurrence in the slope layer as a function of the fault reactivation that led to fluid flow from the reservoir to the base of slope as observed in Figure 7. The slope shearing follows the top of the fault movement and presents irreversible (plastic) strains (Figure 7b), indicating loss of shear strength and susceptibility to failure. Increasing the pore pressure (Figure 7a) to a high level to inject fluid pressure in the reservoir promotes an expressive unstable condition of the soil, conducive to slope movement. Additional evidence of slope failure is the pattern and level of shear stress band localized at the slope, showing a failure surface (Figure 7c).

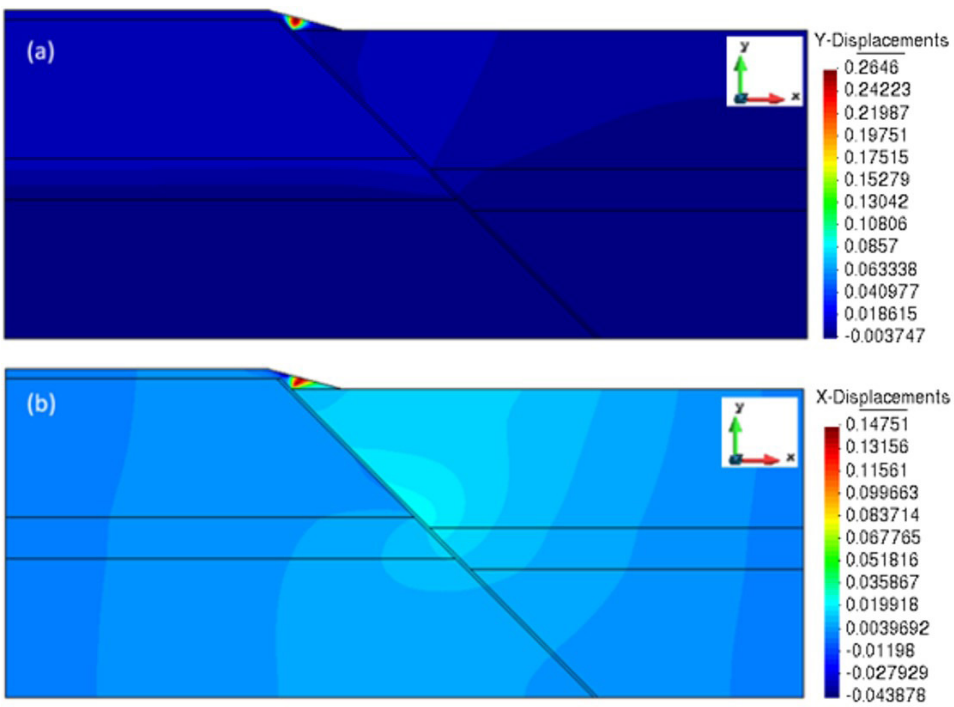

Figure 6. Final distribution of displacements: (a) vertical displacements; (b) horizontal displacements.

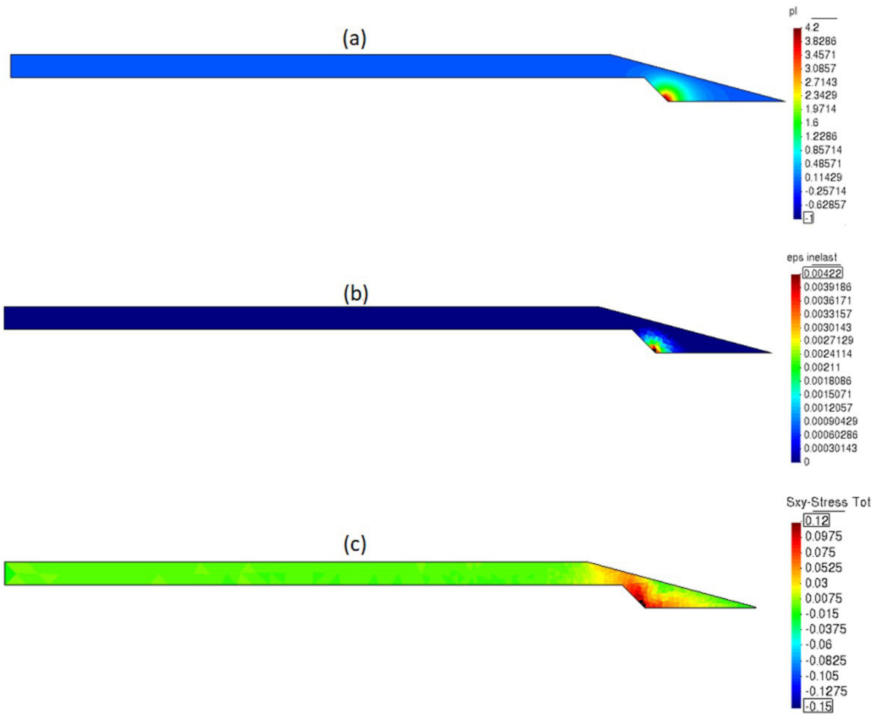

Figure 7. Submarine slope analysis – final distribution: (a) pore pressure (MPa); (b) shear plastic; (c) shear strain stress (MPa).

The evolution of shear plastic strain and pore pressure for a selected point can be observed in Figure 8. Focusing on this point makes it possible to identify the evolution of pore pressure with the soil plastification and the stabilization of pore pressure under expressive increase of shear plastic strain indicating two failures, possibly associated with fault movement history. The stabilization of pore pressure for these instants can be associated with the sudden increase in permeability which leads to fast fluid percolation reaching the pore pressure value.

The slope soil presents an initial and low permeability, and it shows an expressive and faster increase as shown in Figure 9. The permeability measure considered is in m^2 and expressed logarithmically, and the reduction of *y*-axis values is related to the exponent, indicating an increase in 3 orders of magnitude.

After a time, the shearing process in a dilatant behavior continues and the permeability is increased gradually followed by an increase in pore pressure. Similar behavior is observed in an analysis of dilatant response through the analysis of permeability and porosity evolution as shown in Figure 9. It is possible to observe a few increases of porosity with change in permeability indicating a volumetric inelastic strain. The curve contours are like the response observed in

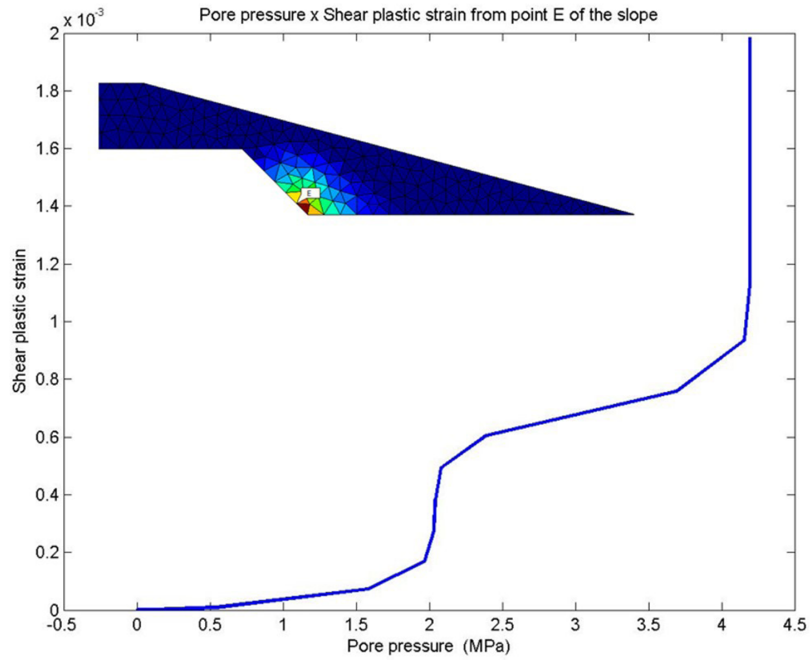

Figure 8. Submarine slope analysis – shear plastic strain vs pore pressure (MPa) at point E (contact between slope layer and fault).

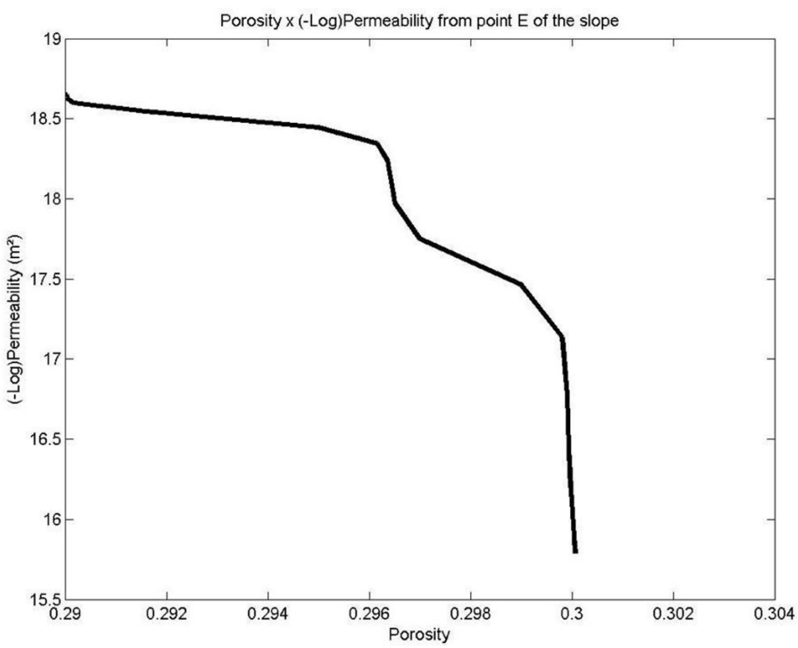

Figure 9. Submarine slope analysis: -log of permeability (m^2) vs porosity at point E (contact between slope layer and fault).

the relation between shear plastic strain and pore pressure (Figure 8).

Both horizontal and vertical displacement occurred on the slope, as shown in Figures 10a and 10b, respectively. The horizontal displacement where the fault touches the slope was approximately 14 cm. There was a displacement in expansive subsidence (ground uplift) of about 26 cm, pushing the slope laterally, therefore, the instability is caused by pressurization and plastic strain in the slope.

Finally, to investigate the relationship between the slope displacements and the development of fault reactivation, two mesh elements were selected at different regions on the slope layer, and the evolution of displacements over time was evaluated (Figure 11), associating them with the evolution of shear plastic strains mapped at points on the geological fault (Figure 12). It is verified that the displacements at the different points of the slope occur from the process of fault reactivation, indicating a progressive movement of the slope in the downstream direction. A greater intensification of the reactivation process is observed by the increase of plastic strains, between 9 and 10 days. This process causes a change in the pattern of slope displacements, with an increasing trend at point A (foot of the slope), and with an inflection point at the top node of the slope, point B, for a negative displacement associated with the shearing process and ground uplift at the top of the fault. A time-dependent behavior of the soft clay of the slope is verified, indicating an adequate application of the viscoplastic model.

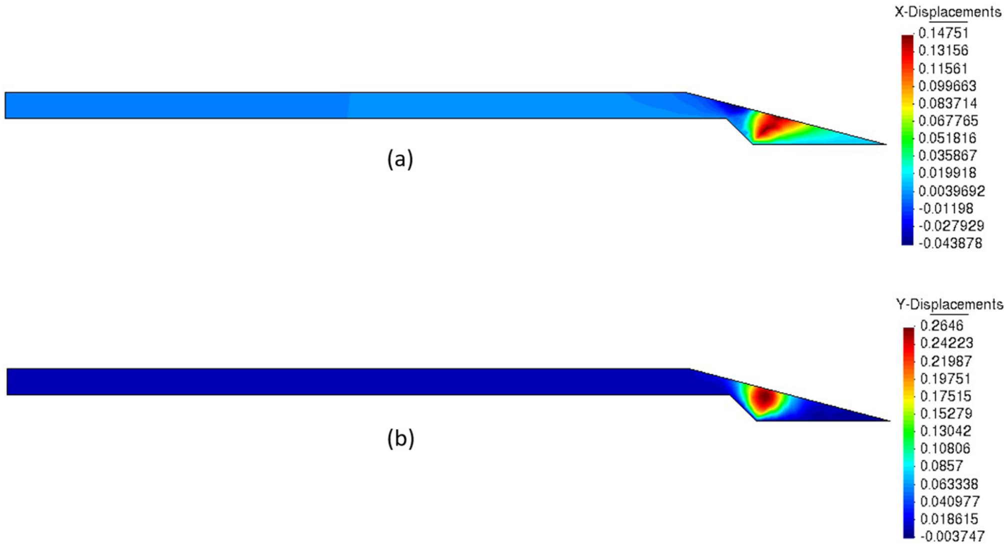

Figure 10. Submarine slope analysis – final distribution: (a) horizontal displacements (m); (b) vertical displacements (m).

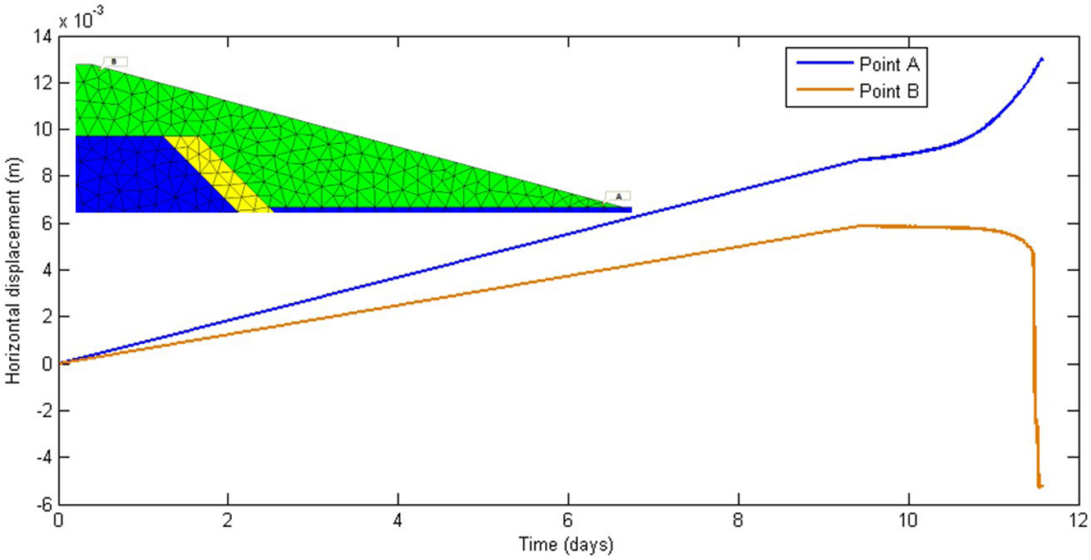

Figure 11. Submarine slope analysis – horizontal displacements (m) evolution of two analysis points: base and top of submarine slope.

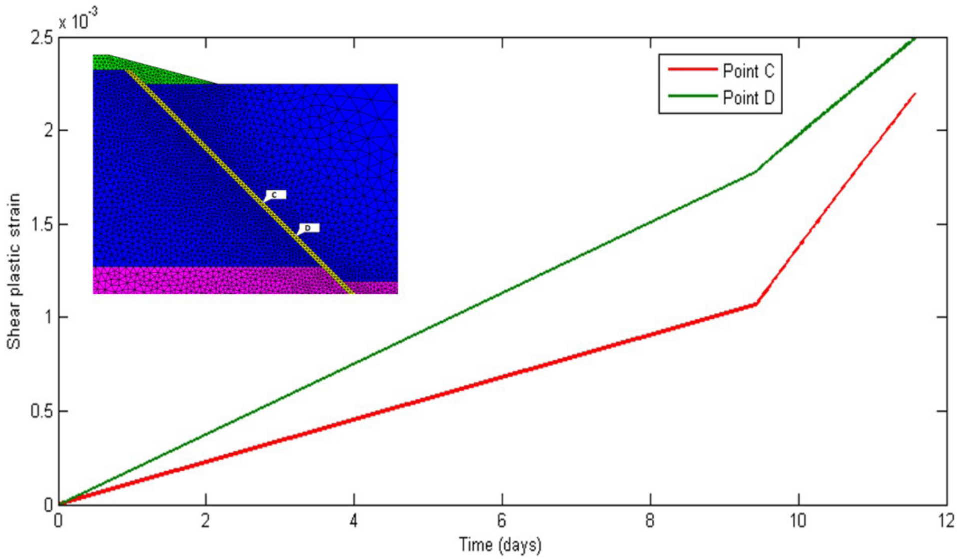

Figure 12. Analysis of the shear plastic strain at two different fault points analysis.

5. Discussion

Adopting shear plastic strain for slope stability analysis and the evolution of shear stress localization were previously discussed in studies like Dey et al. (2016), where a slope stability problem was modeled for large strain using a finite element approach analysis to study shear plastic strain localization and associated displacements. The authors comment that a finite element analysis performs well because initiation and progressive evolution of the weak shear zones in the submarine slopes cannot be simulated by the limit equilibrium method. They also observe, importantly, the relation between decreased shear strength in the initiated failure zone and factors such as geological activities, pore pressure increase, earthquake, and plastic shear deformation. The results obtained by the present study showed similar relations between the effects that trigger the instability and the conditions which led to the slope failure.

Numerical analysis by Zhang & Puzrin (2022), demonstrated how an initial failure surface evolves to a large submarine landslide, and they quantified the different phases. For these authors, the failure zone formation for submarine slope is associated with loss of soil strength due to shearing (shear stress development) and because the pore pressure increases, which is similar to the effects described in this study. Urgeles & Camerlenghi (2013), compiled a catalog of submarine slope failure events in the Mediterranean Sea, and discussed the trigger mechanisms and relationship with fluid flow. They indicate that, amongst various factors, the increase in shear stress on the slope is the most common cause of failure.

Shan et al. (2022) discusses how earthquake, high sedimentation rate and diapirism are the most common triggers for submarine slope stability, suggesting more analyses that account for the hydro-mechanical coupling and consider seismicity, pore pressure changes and water turbidity as warning factors for slope stability risk. In the present study, we indicate that the fault reactivation led to increased pore pressure in the submarine slope, and we consider this result as a trigger factor by which fault reactivation can lead to seismicity. Rutqvist et al. (2013) studied potential fault reactivation due to fluid injection in a hydraulic fracturing operation and the associated induced seismicity. The authors showed that the fault reactivation presents a relation with micro-seismic events and, when faults are present in the field, it is possible that the occurrence of large seismic events depends on factors such as initial fault permeability, in situ stress state, and shear strength properties of faults.

6. Conclusions

For the scenario analyzed, subject to a few simplifications in geometries and the homogeneity of the geological fault and submarine slope properties, the work showed a clear influence of the oil production process on the mechanical behavior of the submarine slope, due to fault reactivation. The reservoir pressure variation was the trigger for fault reactivation, and the overlying submarine slope. This was evidenced by through the development of shear plastic strains, permeability change, shear stress and pore pressure increase for fault and slope materials as well as by the displacement observed in the slope. This stress-strain response is relevant because displacement reached up to 26 cm, which should be contextualized by the fact that the slope is also under water pressure.

The pore pressure increase is directly associated with the increase in the soil and rock permeability, as a function of shear plastic strain. A numerical simulation with hydro-mechanical coupling is an adequate way to analyze this kind of problem. Furthermore, it is suggested using different types of constitutive models for the evaluation of the submarine slope stability.

The methodology used in this work can be applied to real oil reservoir problems, given adequate information about submarine slope geometries and important attributes such as declivity and seabed relief.

It is of great importance to investigate the impact of oil and gas production in faulted reservoirs, considering the need to assess the risk of reactivation and its effect on the stability of submarine slopes with implications for environmental and economic damage, since slope instability can lead to damage to pipelines, and offshore wind towers, and catastrophic hydrocarbon leakage.

It is suggested that a geomechanical analysis to predict reactivation risks is highly necessary because it can define the safe levels of fluid injection pressure for operating reservoirs that present faults connected to shallow regions of the sedimentary column and submarine slopes.

Additionally, submarine landslides can occur due to post-failure slope conditions, remobilizing and displacing large volumes of sediments. This type of simulation needs a large-strain analysis, different from the approach presented here, where the interest was the pre-failure and failure occurrence caused by fault reactivation as the triggering mechanism.

Acknowledgements

The work presented in this paper has been supported by FACEPE, National Council for Scientific and Technological Development – CNPq and Energi Simulation.

Declaration of interest

The authors have no conflicts of interest to declare. All co-authors have observed and affirmed the contents of the paper and there is no financial interest to report.

Authors' contributions

Tasso Carvalho da Silva: conceptualization, methodology, data analysis, writing – original draft. Igor Fernandes Gomes: conceptualization, methodology, data analysis, writing – original draft, supervision, review & editing, funding acquisition. Tiago Siqueira de Miranda: conceptualization, review & editing. Julliana de Paiva Valadares Fernandes: writing – review & editing. José Antônio Barbosa: conceptualization, review & editing. Leonardo José do Nascimento Guimarães: review & editing, funding acquisition.

Data availability

The datasets generated analyzed in the course of the current study are available from the corresponding author upon request.

List of symbols

b	volumetric vector of body forces
c'	effective cohesion
f_l	fluid phase source/sink mass term
g	gravity vector
h	hardening parameter
k	permeability
m	identity tensor
n	porosity
p'	effective mean stress
p_l	fluid pressure
q_l	Darcy flow vector
$\dot{u}$	nodal displacement
D^E	elastic constitutive tensor
D^{VP}	viscoplastic constitutive tensor
E	Young's modulus
F	fluency function
J	deviator stress
K	permeability tensor
$\dot{\varepsilon}^{vp}$	viscoplastic strain rate
$\dot{\varepsilon}_v$	volumetric strain rate
ε	total strain
ε^E	elastic strain
ε^{VP}	viscoplastic strain
$\dot{\varepsilon}_d^{vp}$	viscoplastic shear strain
∇	divergent operator
η	Perzyna's viscous regularization parameter
θ	Lode's Angle
$\dot{\lambda}$	viscoplastic multiplier
μ_l	fluid phase viscosity
ρ_l	fluid phase density
ρ^s	solid phase density
σ	stress tensor
σ'	effective stress tensor
ϕ	rock porosity
ϕ'	effective friction angle

References

Bakhsh, T.T., Simpson, K., & Lapierre, T. (2021). Potential geo-hazard to floating offshore wind farms in the US pacific. In *Proceedings of the ASME 2021 3rd International Offshore Wind Technical Conference (IOWTC 2021)*. New York: American Society of Mechanical Engineers.

Billi, A., Salvini, F., & Storti, F. (2003). The damage zone-fault core transition in carbonate rocks: implications for fault growth, structure, and permeability. *Journal of*

Structural Geology, 25(11), 1779-1794. http://dx.doi.org/10.1016/S0191-8141(03)00037-3.

Caine, J.S., Evans, J.P., & Forster, C.B. (1996). Fault zone architecture and permeability structure. *Geology*, 24(11), 1025-1028. http://dx.doi.org/10.1130/0091-7613(1996)024<1025:FZAAPS>2.3.CO;2.

Cappa, F., & Rutqvist, J. (2011). Modeling of coupled deformation and permeability evolution during fault reactivation induced by deep underground injection of CO_2. *International Journal of Greenhouse Gas Control*, 5(2), 336-346. http://dx.doi.org/10.1016/j.ijggc.2010.08.005.

Celestino, M.A., Miranda, T.S., Mariano, G., Alencar, M.L., Carvalho, B.R.B.M., Falcão, T.C., Topan, J.G., Barbosa, J.A., & Gomes, I.F. (2020). Fault damage zones width: implications for the tectonic evolution of the northern border of the Araripe Basin, Brazil, NE Brazil. *Journal of Structural Geology*, 138, 104116. http://dx.doi.org/10.1016/j.jsg.2020.104116.

Choi, J.H., Edwards, P., Ko, K., & Kim, Y.S. (2016). Definition and classification of fault damage zones: a review and a new methodological approach. *Earth-Science Reviews*, 152, 70-87. http://dx.doi.org/10.1016/j.earscirev.2015.11.006.

Dey, R., Hawlader, B.C., Phillips, R., & Soga, K. (2016). Numerical modelling of submarine landslides with sensitive clay layers. *Geotechnique*, 66(6), 454-468. http://dx.doi.org/10.1680/jgeot.15.P.111.

Fossen, H. (2016). *Structural geology* (2nd ed., 524 p.). Cambridge: Cambridge University Press.

Gudmundsson, A. (2004). Effects of Young's modulus on fault displacement. *Comptes Rendus Geoscience*, 336(1), 85-92. http://dx.doi.org/10.1016/j.crte.2003.09.018.

Gue, C.S. (2012). *Submarine landslide flows simulation through centrifuge modeling* [Doctoral thesis]. University of Cambridge, Cambridge.

Guimarães, L.J.N., Gens, A., & Olivella, S. (2007). Coupled thermo-hydro-mechanical and chemical analysis of expansive clay subjected to heating and hydration. *Transport in Porous Media*, 66(3), 341-372. http://dx.doi.org/10.1007/s11242-006-0014-z.

Guimarães, L.J.N., Gomes, I.F., & Fernandes, J.P.V. (2009). Influence of mechanical constitutive model on the coupled hydro-geomechanical analysis of fault reactivation. In *Proceedings of the SPE Reservoir Simulation Symposium* (SPE-119168-MS), The Woodlands, Texas, USA.

Guimarães, L.J.N., Gomes, I.F., Barbosa, J.A., & Almeida, R.P.M. (2010). Numerical modelling of CO2 flow through deformable aquifers with the possibility of fault reactivation. In *Proceedings of the 6th International Congress on Environmental Geotechnics*, New Delhi, India.

Katz, O., Reuven, E., & Aharonov, E. (2015). Submarine landslides and fault scarps along the eastern Mediterranean Israeli continental-slope. *Marine Geology*, 369, 100-115. http://dx.doi.org/10.1016/j.margeo.2015.08.006

Khan, S., Khulief, Y.A., & Al-Shuhail, A.A. (2020). Effects of reservoir size and boundary conditions on pore-pressure buildup and fault reactivation during CO_2 injection in deep geological reservoirs. *Environmental Earth Sciences*, 79(12), 294. http://dx.doi.org/10.1007/s12665-020-09040-0.

Langhi, L., Zhang, Y., Gartrell, A., Underschultz, J., & Dewhurst, D. (2010). Evaluating hydrocarbon trap integrity during fault reactivation using geomechanical three-dimensional modeling: an example from the Timor Sea, Australia. *AAPG Bulletin*, 94(4), 567-591. http://dx.doi.org/10.1306/10130909046.

Leynaud, D., Mienert, J., & Nadim, F. (2004). Slope stability assessment of the Helland Hansen area offshore the mid-Norwegian margin. *Marine Geology*, 213(1–4), 457-480. http://dx.doi.org/10.1016/j.margeo.2004.10.019.

Ma, G., Kirby, J.T., & Shi, F. (2013). Numerical simulation of tsunami waves generated by deformable submarine landslides. *Ocean Modelling*, 69, 146-165. http://dx.doi.org/10.1016/j.ocemod.2013.07.001.

Masson, D.G., Wynn, R.B., & Talling, P.J. (2010). Large landslides on passive continental margins: processes, hypotheses, and outstanding questions. In D.C. Mosher, R.C. Shipp, L. Moscardelli, J.D. Chaytor, C.D.P. Baxter, H.J. Lee & R. Urgeles (Eds.), *Submarine mass movements and their consequences* (pp. 153-165). Cham: Springer.

Matsumoto, N., & Shigematsu, N. (2018). In-situ permeability of fault zones estimated by hydraulic tests and continuous ground water-pressure observations Earth. *Earth, Planets, and Space*, 70(1), 13. http://dx.doi.org/10.1186/s40623-017-0765-5.

Mitchell, T.M., & Faulkner, D.R. (2009). The nature and origin of off-fault damage surrounding strike-slip fault zones with a wide range of displacements: A field study from the Atacama fault system, northern Chile. *Journal of Structural Geology*, 31(8), 802-816. http://dx.doi.org/10.1016/j.jsg.2009.05.002.

Myers, R.D. (1999). *Structure and hydraulics of brittle faults in sandstone* [Doctoral thesis]. Stanford University, Stanford, CA.

Olivella, S., Carrera, J., Gens, A., & Alonso, E.E. (1995). Numerical formulation for a Simulator (CODE_BRIGHT) for the coupled analysis of saline media. *Engineering Computations*, 7, 87-112.

Peacock, D.C.P., Dimmen, V., Rotevatn, A., & Sanderson, D.J. (2017). A broader classification of damage zones. *Journal of Structural Geology*, 102, 179-192. http://dx.doi.org/10.1016/j.jsg.2017.08.004.

Pereira, L.C., Guimarães, L.J.N., Horowitz, B., & Sánchez, M. (2014). Coupled hydro-mechanical fault reactivation analysis incorporating evidence theory for uncertainty quantification. *Computers and Geotechnics*, 56, 202-215. http://dx.doi.org/10.1016/j.compgeo.2013.12.007.

Perzyna, P. (1966). Fundamental problems in viscoplasticity. *Advances in Applied Mechanics*, 9, 243-377. http://dx.doi.org/10.1016/S0065-2156(08)70009-7.

Puzrin, A.M., Gray, T.E., & Hill, A.J. (2015). Significance of the actual nonlinear slope geometry for catastrophic failure in submarine landslides. *Proceedings - Royal Society. Mathematical, Physical and Engineering Sciences*, 471(2175), 20140772. http://dx.doi.org/10.1098/rspa.2014.0772.

Quevedo, R., Ramirez, M., & Roehl, D. (2017). 2D and 3D numerical modeling of fault reactivation. In *Proceedings of the 51st U.S. Rock Mechanics/Geomechanics Symposium*, San Francisco, CA, USA.

Quinn, P.E., Diederichs, M.S., Rowe, R.K., & Hutchinson, D.J. (2011). A new model for large landslides in sensitive clay using a fracture mechanics approach. *Canadian Geotechnical Journal*, 48(8), 1151-1162. http://dx.doi.org/10.1139/t11-025.

Quinn, P.E., Diederichs, M.S., Rowe, R.K., & Hutchinson, D.J. (2012). Development of progressive failure in sensitive clay slopes. *Canadian Geotechnical Journal*, 49(7), 782-795. http://dx.doi.org/10.1139/t2012-034.

Rutqvist, J., Birkholzer, J., Cappa, F., & Tsang, C.F. (2007). Estimating maximum sustainable injection pressure during geological sequestration of CO_2 using coupled fluid flow and geomechanical fault-slip analysis. *Energy Conversion and Management*, 48(6), 1798-1807. http://dx.doi.org/10.1016/j.enconman.2007.01.021.

Rutqvist, J., Rinaldi, A.P., Cappa, F., & Moridis, G.J. (2013). Modeling of fault reactivation and induced seismicity during hydraulic fracturing of shale-gas reservoirs. *Journal of Petroleum Science Engineering*, 107, 31-44. http://dx.doi.org/10.1016/j.petrol.2013.04.023.

Scarselli, N. (2020). Chapter 16 - Submarine landslides – architecture, controlling factors and environments: a summary. In N. Scarselli, J. Adam, D. Chiarella, D.G. Roberts & A.W. Bally (Eds.), *Regional geology and tectonics* (2nd ed., pp. 417-439). Amsterdam: Elsevier.

Scarselli, N., McClay, K., & Elders, C. (2016). Seismic geomorphology of cretaceous megaslides offshore Namibia (Orange Basin): insights into segmentation and degradation of gravity-driven linked systems. *Marine and Petroleum Geology*, 75, 151-180. http://dx.doi.org/10.1016/j.marpetgeo.2016.03.012.

Shan, Z., Wu, H., Ni, W., Sun, M., Wang, K., Zhao, L., Lou, Y., Liu, A., Xie, W., Zheng, X., & Guo, X. (2022). Recent technological and methodological advances for the investigation of submarine landslides. *Journal of Marine Science and Engineering*, 10(11), 1728. http://dx.doi.org/10.3390/jmse10111728.

Silva, J.P., Gomes, I.F., Santos, R.F.V.C., Miranda, T.S., Guedes, R.P., Barbosa, J.A., Guimarães, E.X., Beserra, L.B., & Guimarães, L.J.N. (2021). Topological analysis of fracture networks integrated with flow simulation models for equivalente fracture permeability estimation. *Journal of Structural Geology*, 147, 104338.

Simo, J.C., & Hughes, T.J.R. (1998). Integration algorithms for plasticity and viscoplasticity. In J.C. Simo & T.J.R. Hughes (Eds.), *Computational Inelasticity* (pp. 113-151). New York: Springer.

Soltanzadeh, H., & Hawkes, C.D. (2008). Semi-analytical models for stress change and fault reactivation induced by reservoir production and injection. *Journal of Petroleum Science Engineering*, 60(2), 71-85. http://dx.doi.org/10.1016/j.petrol.2007.05.006.

Souza, F.M., Gomes, I.F., Nogueira, F.C.C., Vasconcelos, D.L., Canabarro, B.M., Souza, J.A.B., Guimarães, L.J.N., & Beserra, L.B.S. (2022). 2D modeling and simulation of deformation bands' effect on fluid flow: implications for hydraulic properties in siliciclastic reservoirs. *Journal of Structural Geology*, 158, 104581. http://dx.doi.org/10.1016/j.jsg.2022.104581.

Stoecklin, A., Trapper, P., & Puzrin, A.M. (2021). Controlling factors for post-failure evolution of subaqueous landslides. *Geotechnique*, 71(10), 879-892. http://dx.doi.org/10.1680/jgeot.19.P.230.

ten Brink, U.S.T., Lee, H.J., Geist, E.L., & Twichell, D. (2009). Assessment of tsunami hazard to the U.S. East Coast using relationships between submarine landslides and earthquakes. *Marine Geology*, 264(1-2), 65-73. http://dx.doi.org/10.1016/j.margeo.2008.05.011.

Torabi, A., Ellingsen, T.S.S., Johannessen, M.U., Alaei, B., Rotevatn, A., & Chiarella, D. (2020). *Fault zone architecture and its scaling laws: where does the damage zone start and stop?* (Special Publications Series, No. 496, pp. 99-124). London: Geological Society. http://dx.doi.org/10.1144/SP496-2018-151.

Urgeles, R., & Camerlenghi, A. (2013). Submarine landslides of the Mediterranean Sea: trigger mechanisms, dynamics, and frequency-magnitude distribution. *Journal of Geophysical Research. Earth Surface*, 118(4), 2600-2618. http://dx.doi.org/10.1002/2013JF002720.

Yang, P., Guanghui, W., Perach, N., Ai Duc, N., Yongquan, C., Shuai, Y., Yue-xing, F., Zhanli, R., & Jian, Z. (2021). In situ LA-ICPMS UPb dating and geochemical characterization of fault-zone calcite in the central Tarim Basin, northwest China: implications for fluid circulation and fault reactivation. *Chemical Geology*, 568, 120125. http://dx.doi.org/10.1016/j.chemgeo.2021.120125.

Yincan, Y. (2017). Submarine landslides. In Y. Yincan (Ed.), *Marine geo-hazards in China* (chap. 6, pp. 179-267). Amsterdam: Elsevier.

Zhang, W., & Puzrin, A.M. (2022). How small slip surfaces evolve into large submarine landslides—insight from 3D numerical modeling. *Journal of Geophysical Research: Earth Surface*, 127(7), e2022JF006640. https://doi.org/10.1029/2022JF006640.

Zhang, Y., Wang, Z., Yang, Q., & Wang, H. (2019). Numerical analysis of the impact forces exerted by submarine landslides on pipelines. *Applied Ocean Research*, 92, 101936. http://dx.doi.org/10.1016/j.apor.2019.101936.

Soils and Rocks

An International Journal of Geotechnical and Geoenvironmental Engineering

www.soilsandrocks.com

ISSN 1980-9743
ISSN-e 2675-5475

Shear strength reduction factor used in critical state models with hardening

Isabella Maria Martins de Souza[1], Daniela Toro Rojas[1#], Ana Carolina Gonzaga Pires[1], Márcio Muniz de Farias[1], Manoel Porfírio Cordão Neto[1]

Article

Keywords
Shear strength reduction
Strength reduction factor
Critical state models
Safety factor

Abstract

The slope stability analyses are important to predict environmental, financial, and human life impacts. The Limit Equilibrium Method (LEM) is commonly used to estimate a slope's Safety Factor (*SF*). However, the Finite Element Method (FEM) is increasingly applied to slope stability analyses, using different approaches, among which the technique of Shear Strength Reduction (SSR) is commonly used in perfectly plastic elastic models. The objective of this study is to present a discussion about these two methodologies, using critical state models with or without hardening will be used to model the stress-strain behavior of the soil mass. The results obtained in the case study presented, using LEM and FEM considering critical state models with and without hardening are consistent and allowed verifying the stability condition of the slope. Also, the reduction factors are smaller when compared to the results using perfectly plastic elastic models.

1. Introduction

Geotechnical accidents involving natural slopes or large structures such as dams and embankment in general can seriously impact society. The failure of these structures can result in significant financial, environmental, and human losses. Therefore, verifying the stability condition of a slope is of utmost importance to prevent the occurrence of catastrophic accidents.

In general, slope failure is caused by processes that increase internal shear stresses, such as external loads and the removal of materials that provide support at the toe of slope. In addition, some factors may reduce the soil's shear strength, such as the increase of pore pressure and changes caused by weathering and physical-chemical activity.

There are several methods to analyze the stability of slopes, among them the methods based on the Limit Equilibrium Method (LEM). This method divides the slope into "n" slices, each subjected to a set of forces. However, it is necessary to formulate some hypotheses to make the problem determined. In addition, LEM makes some hypotheses that may compromise the accuracy of the response, such as the need to predefine a failure surface, stresses are determined only on the failure surface and between slices, the safety factor is the same for both friction and cohesion strength components, the same safety factor value is applied to all slices, and the material is considered rigid and perfectly plastic (Fredlund & Rahardjo, 1993, 2012; Duncan et al., 2014).

The Finite Element Method (FEM), introduced by Clough & Woodward (1967), is also a commonly used tool for solving geotechnical problems and can be applied to verify the stability condition and estimate the safety factor of a structure. The FEM consists of discretizing the soil mass into regions called finite elements, which are interconnected by common nodes. This method calculates displacements, pore pressures, and other variables in each finite element and, thus, allows for solving geotechnical problems with more accuracy, such as the stability of slopes and settlement of foundations, among others (Dong et al., 2018).

The Finite Element Method can be used to analyze slope stability in two ways. The first one was proposed by Matsui & San (1992), and it is defined as the Shear Strength Reduction Method (SSR), which is the method used in this work. The second was proposed by Farias & Naylor (1998) and is called the Improved Limit Equilibrium Method. The later performs an analysis similar to the conventional Limit Equilibrium Method, however, the stresses along the failure surface are calculated from the stress and pore pressure fields arising from a finite element analysis.

The Shear Strength Reduction Method (SSR), introduced by Matsui & San (1992), can also be applied to verify the safety of a geotechnical structure. Numerically, SSR alters the shear strength parameters by repeatedly

[#]Corresponding author. E-mail address: dtr1593@gmail.com
[1]Universidade de Brasília, Programa de Pós-graduação em Geotecnia, Brasília, DF, Brasil.

Submitted on January April 27, 2023; Final Acceptance on October 25, 2023; Discussion open until February 28, 2024.
https://doi.org/10.28927/SR.2023.004123

applying a Strength Reduction Factor (*SRF*) until a critical *SRF* is found. The SSR can be applied in a finite element analysis and the critical *SRF* can be defined when the problem solution does not converge or the occurrence of excessive displacements, indicating the beginning of failure (Vardon et al., 2017).

The SSR method is commonly employed together with elastic perfectly plastic (EPP) models. However, this paper presents a discussion of this method using critical state models with or without hardening.

2. SSR and Critical State Models

The use of Critical State Models (Roscoe et al., 1958) with hardening when applying the Shear Strength Reduction Method (SSR) will be discussed below. It should be noted that the term "hardening" will be used in the context of isotropic hardening and can refer to both the increase in the yield surface as well as its contraction (softening).

As already mentioned, SSR alters the shear strength parameters and results in changes in the stress-strain constitutive matrix, which is used in the formation of the stiffness matrix K_{ij}:

$$\mathrm{K}_{ij} = \int B_{mi} D_{ml} B_{lj} \mathrm{dV} \tag{1}$$

where D_{ml} is the stress-strain constitutive matrix, and B_{lj} a matrix relating displacement and strains.

Thus, any change in the constitutive matrix reflects changes in the system's stiffness matrix, as can be easily visualized in Equation 1. Static equilibrium with external forces is given by:

$$\mathrm{F}_i = \mathrm{K}_{ij} u_j \tag{2}$$

where K_{ij} is the stiffness matrix, u_j is the displacement vector, and F_i represents external forces.

If the stiffness matrix changes due to the application of the *SRF*, an imbalance will occur that will be corrected with displacement increases, without the boundary conditions and external forces being changed. An illustration of what happens can be seen in Figure 1, where two "load-displacement" curves with different stiffness are presented. It should be noted that the stiffness illustrated in the figure is that of the system and not of a single element.

In Figure 2, point A represents a stress state that was within the elastic zone before the application of *SRF*, and after, it is located outside the reduced yield surface and violates the consistency law. Therefore, in the case of elastic perfectly plastic models without hardening, the violation of the consistency law is compensated by the appearance of plastic deformations, during some stress return algorithm to ensure consistency.

The stress-strain constitutive matrix (D_{ij}^{ep}) for elastic perfectly plastic models is given by:

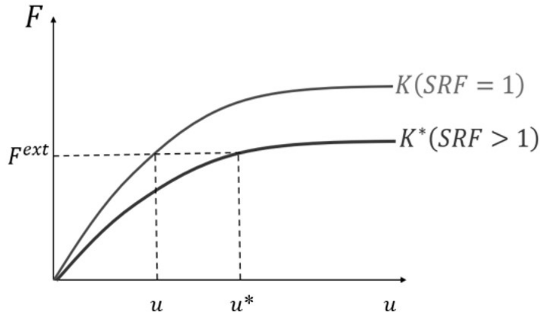

Figure 1. Effect of stiffness change due to *SRF* application, where K is the stiffness matrix for *SRF* equal to 1, K^* is the stiffness matrix for *SRF* less than 1, F^{ext} represents external forces, u is the initial displacement vector and u^* is the final displacement vector.

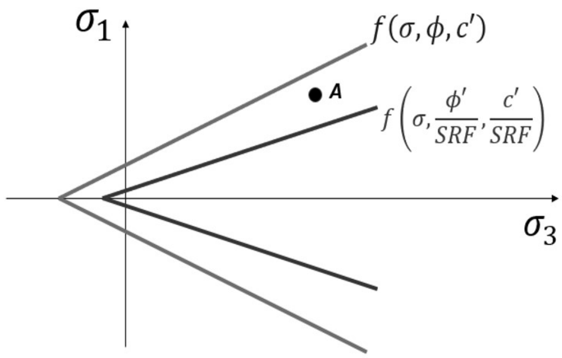

Figure 2. Yield surface before and after *SRF* application.

$$D_{ij}^{ep} = D_{ij}^{e} - \frac{\left(D_{im}^{e} b_m\right)\left(D_{jn}^{e} a_n\right)}{a_k D_{kl}^{e} b_l} \tag{3}$$

where D_{ij}^{e} is the elastic constitutive matrix, a_n is the vector normal to the yield function and b_m the normal to the plastic potential function. In models with associated flow rules, the plastic potential and the yield surfaces are the same, and therefore vector a_n and b_m are equal.

For points within the yield surface, the constitutive matrix is the elastic matrix D_{ij}^{e}. On the other hand, whenever a point touches or exceeds the plastic yield surface, the second term is activated and the constitutive matrix becomes D_{ij}^{ep}. In the case of these models, the matrix D_{ij}^{ep} always corresponds to a condition of lower stiffness than when the matrix D_{ij}^{e} is used.

Up to this point, the problem with using constitutive models that consider hardening is not evident. To illustrate the problem, Figure 3 will be used. Point A was located within the elastic region, but the consistency condition is violated after applying the reduction factor. However, for elastoplastic models that include hardening, such as critical state models, the matrix formulation is different.

In Figures 3 and 4, the yield surface (*f*) of the Modified Cam-Clay model is illustrate in the *p'*-*q* stress invariants space. The yield surface in this case is an ellipsis with major axes at p_0 (called over-consolidation stress), and the minor axes is delimited the critical state failure criterion, given by a straight line with inclination M, related to the soil's friction angle at the critical state (CS). In critical state models, plastic deformations generate an increase in the yield surface, that is, hardening, which can be observed in Figure 4.

For the Modified Cam-Clay model the stiffness matrix expression is given by

$$D_{ij}^{ep} = D_{ij}^{e} - \frac{\left(D_{im}^{e} b_m\right)\left(D_{jn}^{e} a_n\right)}{a_k D_{kl}^{e} b_l + Y} \tag{4}$$

where the additional term Y is a scalar related to the model's hardening law and give by:

$$Y = \frac{\partial F}{\partial p_0}\frac{\partial p_0}{\partial \varepsilon_v^p}\frac{\partial F}{\partial p} \tag{5}$$

in which p_0 is over-consolidation stress (the stress-like internal hardening variable of the MMC model), ε_v^p is plastic volumetric strain (the strain-like internal hardening variable of the MMC model), and Y is the corresponding hardening modulus.

In this way, the application of the SSR generates at the same time a reduction of the friction strength parameter M and the variation of the state parameter related to the size of the surface, p_0. For the process to be considered similar to that described for elastic perfectly plastic models, the parameter p_0 must be constant or at least to have a small variation.

However, the hardening modulus tends to zero when the ratio η = q/p› tends to M. This occurs because the last term of Equation 5, $\partial F/\partial p$, tends to zero while the others do not depend on η. Additionally, for stress states near the failure surface the ratio η values are close to M, and therefore, Y values tend to zero. On the other hand, points that tend to have more significant hardening tend to be far from the failure surface (Figure 5).

For other models, such as Norsand (Jefferies, 1993; Jefferies & Shuttle, 2002; Cheng & Jefferies, 2020), the hardening modulus will also tend towards zero, even though the mathematical formulation may be different. Figure 6 shows the influence of the parameter M on the yield surface of the Norsand model, and it is easy to see that the statements proposed for the Modified Cam-Clay model are also valid for Norsand.

Therefore, considering that the effect of applying the reduction factor is to flatten the surface, one can imagine that the points most affected by the reduction factor are precisely those with an η value close to M. The region formed by these points will be the region of the formation of a potential failure surface. Points that would be subject to higher hardening would be those farther away from the "failure zone".

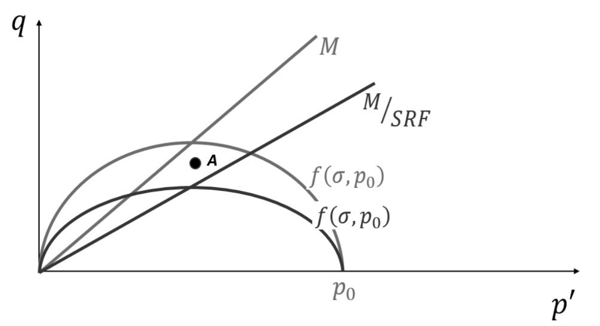

Figure 3. Effect of reduction factor in Cam-Clay type models.

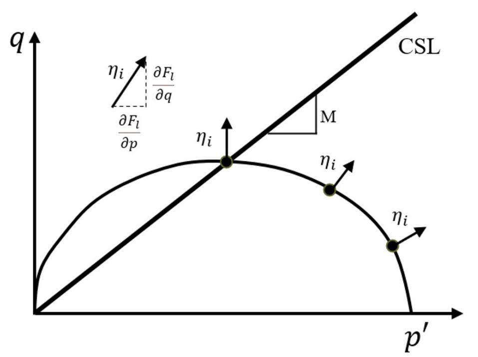

Figure 5. Surface normal vectors for different stress states.

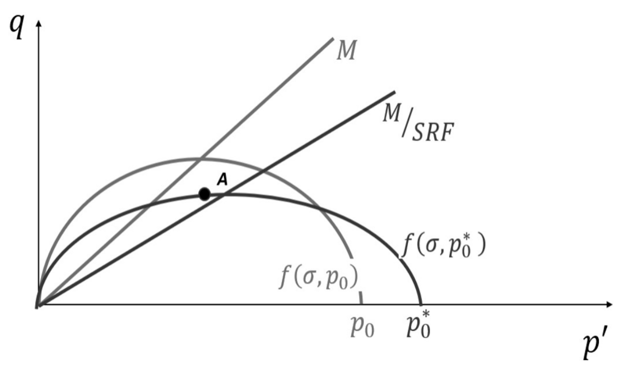

Figure 4. Evolution of the yield surface after *SRF* application.

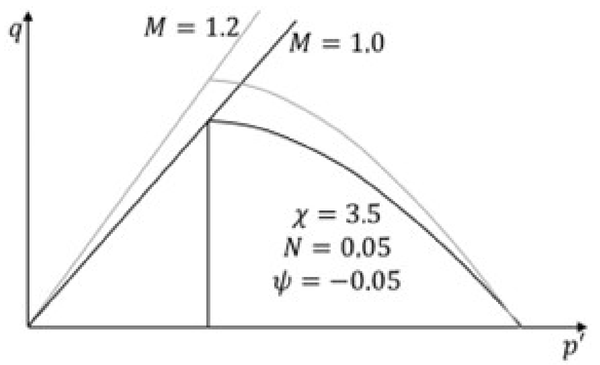

Figure 6. Effect of the MTC parameter on the yield surface of the Norsand model.

In the next items, it will be demonstrated how the reduction factor method can be used to evaluate the stability of geotechnical structures.

3. Application of the SSR

The case study in this work is a hypothetical natural slope representing highway slopes in Brasília, illustrated in Figure 7. The slope stability analysis will be carried out using two different methodologies, encoded in the SLOPE/W and SIGMA/W programs from GeoStudio (Geoslope International, Ltd, 2021). Initially, the Limit Equilibrium Method (LEM) will be applied using the Morgenstern-Price method to calculate the Factor of Safety (FS). Then, the Finite Element Method (FEM) will be employed using the shear strength reduction technique (SSR).

Furthermore, two constitutive models will be used to estimate the *SRF*: the elastic perfectly plastic model with Mohr-Coulomb failure criterion (MC) and the Modified Cam Clay (MCC). The first is a conventional model without hardening. The second is a critical state model that considers the isotropic hardening/softening of the flow surface (Roscoe et al., 1963, Roscoe & Burland, 1968).

The F.E. mesh consisted of 1722 quadrilateral elements with 4 nodes, with a length of 1 m on the face of the slope and 4 m elsewhere in the domain. Boundary conditions were applied that restricted only horizontal displacements on the sides and vertical displacements at the base of the geometry. The input data used is indicated in Table 1. It is worth noting that the values used in the Modified Cam Clay model and the Mohr-Coulomb failure criterion were obtained from triaxial tests carried out for a theoretical-experimental study of the behavior of tropical soils conducted by Futai (2002).

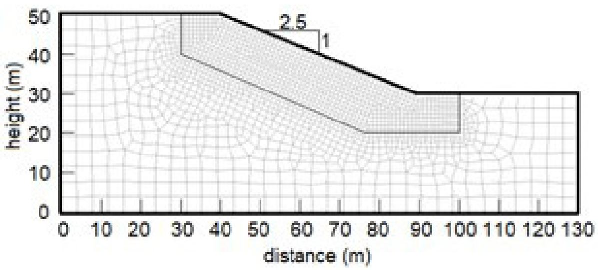

Figure 7. Case study geometry using the shear strength reduction (SSR) technique.

Using the Mohr-Coulomb failure criterion and the optimization of the SLOPE/W program to determine the critical failure surface, the safety factor value of 1.71 was obtained by the Limit Equilibrium Method. Figure 8 illustrates the failure surface resulting from this analysis.

In defining the critical *SRF* using the Mohr-Coulomb criterion, five points near the failure surface (P1 to P5) were monitored. Figure 9 illustrates the *xy* displacement for *SRF* values of 1.60 and 1.70. Figure 9a shows the slope on the verge of potential failure, as the monitored points exhibited displacements of more than 0.3 m. Figure 9b shows the potential failure zone, which is similar to the one obtained in the previously presented Limit Equilibrium Method.

Similar to the previous study, the aforementioned five points were also monitored in defining the critical *SRF* using the Modified Cam Clay model (MCC). Figure 10 illustrates the *xy* displacement for *SRF* values of 1.30 and 1.40. Figure 10a shows the structure on the verge of potential failure, as the monitored points exhibited displacements of more than 0.3 m. Figure 10b presents the formed failure surface.

The displacements at points P1 to P5 are presented in Figure 11 for a comparative analysis between the displacements of the five monitored points of the Modified Cam Clay model

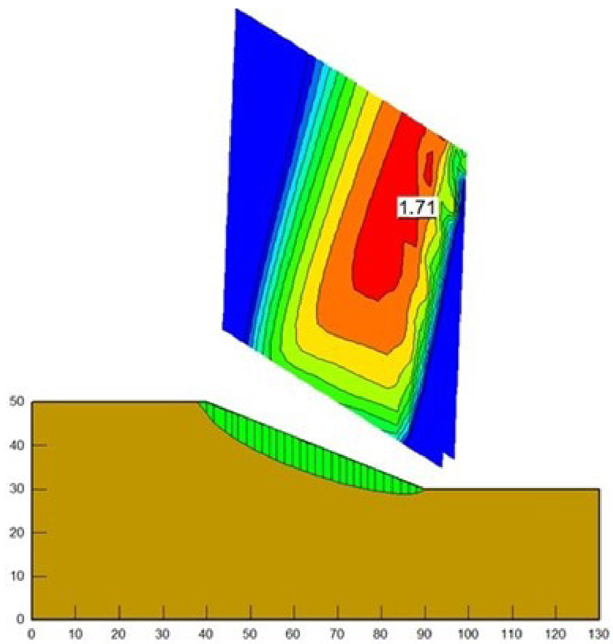

Figure 8. Result of LEM.

Table 1. Input data.

Constitutive model	γ (kN/m^3)	ν	E (MPa)	c (kPa)	ϕ (º)	e_i	κ	λ	M (initial)	OCR
Mohr-Coulomb	18	0.35	12	7	28	-	-	-	-	-
Modified Cam-Clay	18	0.35	-	-	-	0.80	0.02	0.17	1.14	1.20

Legend: see List of Symbols.

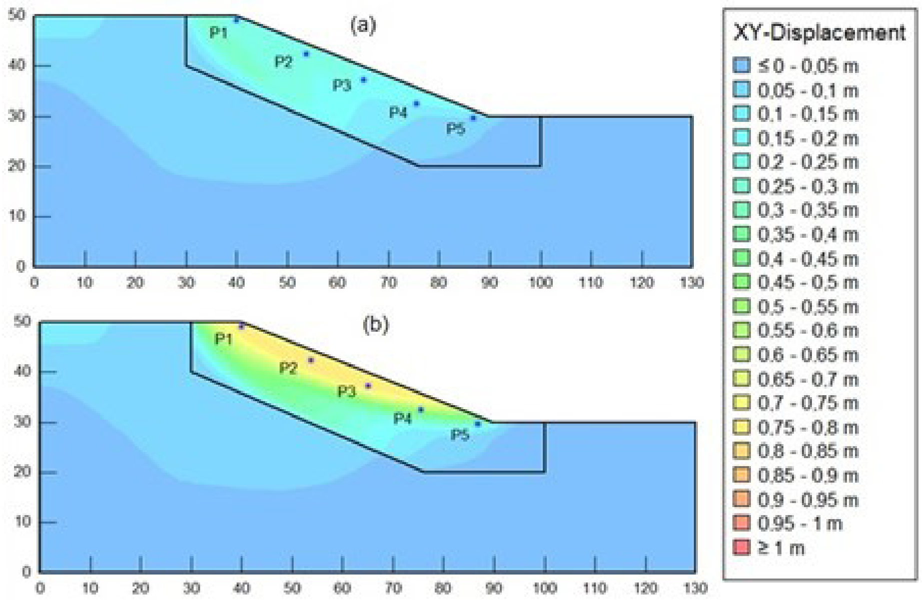

Figure 9. Result of the MC failure criterion, (a) *SRF* of 1.60 and (b) *SRF* of 1.70.

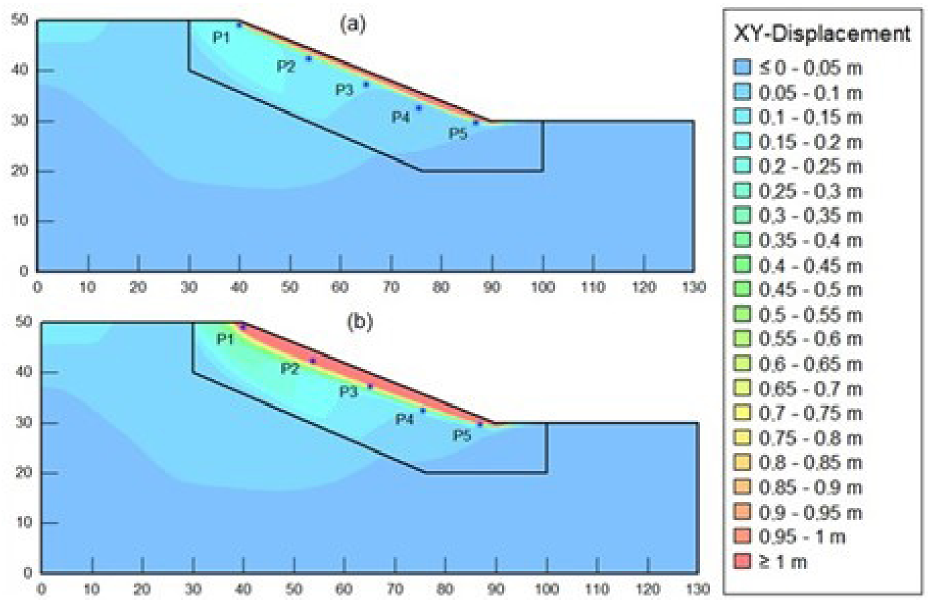

Figure 10. Result of the MCC model, (a) *SRF* of 1.30 and (b) *SRF* of 1.40.

(MCC) and the Mohr-Coulomb criterion (MC) as a function of the applied *SRF*. The curve in red corresponds to the average of the displacements of the five monitoring points.

The average displacement of the monitored points allowed for estimating the critical *SRF* between 1.60 and 1.70 for the MC model. At 1.60, the onset of slope instability in the analyzed slope can be inferred. For the second *SRF* value (1.70), a mean displacement of 1 m was found, representing a significant deformation of the structure of 5%. Similarly, the average displacement of the monitored points using the MCC model allowed for estimating the critical *SRF* between 1.30 and 1.40.

In addition, considering the average displacement values of the monitored points, a complementary comparison was made to determine the critical *SRF*. Figure 12 illustrates the derivative of the curve of average displacement values of the monitored points as a function of the applied *SRF* for the two models used. The results observed in Figure 12 confirmed the

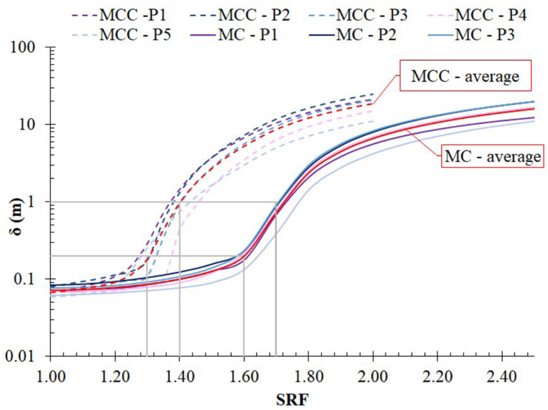

Figure 11. Comparison of the displacement (δ) between the MCC and MC models.

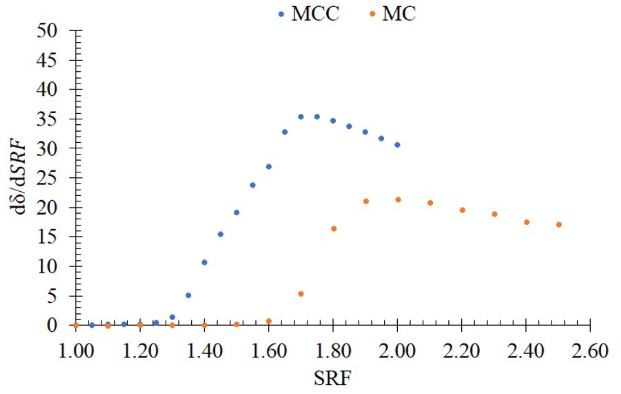

Figure 12. Derivative of each point on the curve of mean displacement values $d\delta / dSRF$ – Comparison between MCC and MC.

critical *SRF* value of 1.30 and 1.60 for the MCC and MC models, respectively. Furthermore, at these points, there is a significant increase in the displacements resulting from the applied *SRF*.

Another relevant point is the fact that the failure surface obtained by the MC criterion is different from the surface presented in the MCC model. The first surface presents lower values of displacements, but a more extensive failure surface is found, which encompasses a larger region. On the other hand, the second failure surface presents higher values of displacements, but these are concentrated on the surface face of the analyzed slope. This is because the Cam-Clay Model does not have a cohesion value like the Mohr-Coulomb model.

Knowing that for some soils, the value of the cohesive intercept is a consequence of the overconsolidation of the tested samples, analyzes were carried out to evaluate the effect of the overconsolidation ratio on the *SRF*. This assessment will be detailed in the next item.

4. Sensitivity analysis of the overconsolidation ratio

Complementarily, a sensitivity analysis of the value of the overconsolidation ratio (*OCR*) used in the analysis of shear strength reduction (SSR) with the Cam-Clay model was carried out. It is noteworthy that the geometry of the hypothetical slope was changed to reduce the computational cost of the analysis, with the aim of achieving the fastest critical *SRF*, which is illustrated in Figure 13. In the model, 1556 quadrilateral elements were generated with 4 nodes and length of 1 m on the face of the slope and 4 m on the rest of the domain. Boundary conditions were applied that restricted the horizontal displacements on the sides and the vertical displacements on the base of the geometry.

The methodology previously described was applied in a similar manner, where the displacements of six points were monitored, and the *OCR* value was assumed to be 1.00, 1.50, 2.00, 4.00, and 8.00. During the sensitivity analysis, no significant changes in results were observed for overconsolidation ratios greater than one (*OCR* > 1). Therefore, a comparison of results will be presented for *OCR* values of 1, normally consolidated soil, and 8 highly overconsolidated soil.

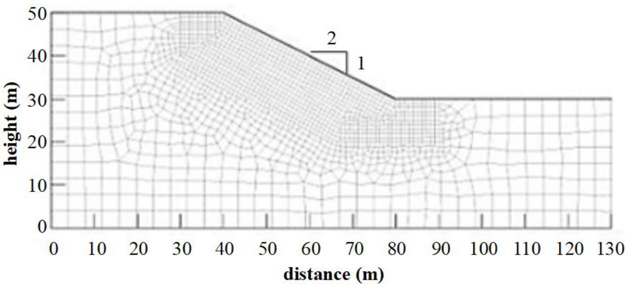

Figure 13. New geometry for overconsolidation ratio sensitivity analysis.

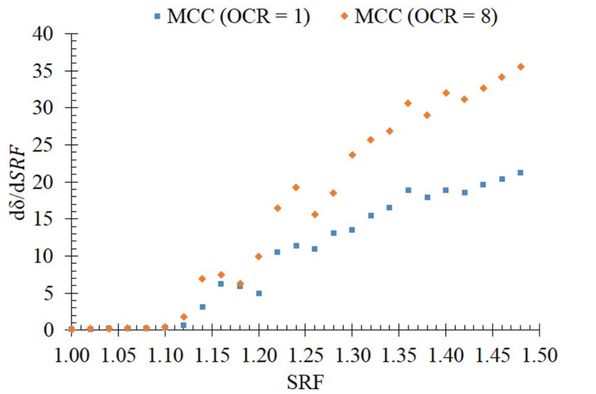

Figure 14. Derivative of each point on the curve of mean displacement values $d\delta / dSRF$ - Comparison between *OCR* = 1 and *OCR* = 8.

The value of 1.12 was considered for the critical *SRF* in both cases since the derivative of the mean displacement values of the monitored points as a function of the applied *SRF* indicates an abrupt increase in displacement, an indication of the beginning of rupture (Figure 14).

Figure 15 illustrates the monitored points and indicate the displacements obtained for an *SRF* of 1.12 for normally compacted soil (*OCR* = 1) and pre-consolidated soil (*OCR* = 8).

The failure surface obtained is similar in both cases and the critical *SRF* of 1.12 can also be considered for both cases. However, the pre-consolidated material (*OCR* = 8) showed slightly higher displacement values at the monitored points, one hypothesis would be the different stress paths. Figure 16 illustrates the difference in the displacement value obtained in both cases for each applied *SRF* value.

In addition, Figure 17 shows the derivative of each point of the displacement curves ($d\delta / dSRF$) illustrated in Figure 16 for values of *OCR* = 1 and *OCR* = 8. It can be observed that the critical *SRF* of 1.12, for the monitored points P1, P2, P3, and P4, can be considered for both normally consolidated material (*OCR* = 1) and overconsolidated material (*OCR* = 8). The points P5 and P6 indicate higher

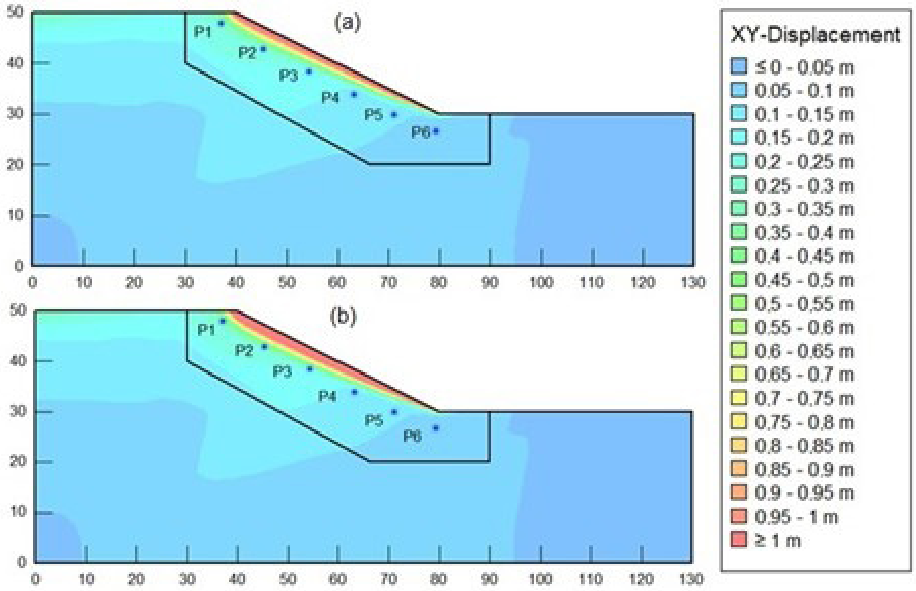

Figure 15. Sensitivity analysis for SRF = 1.12, (a) *OCR* = 1 and (b) *OCR* = 8.

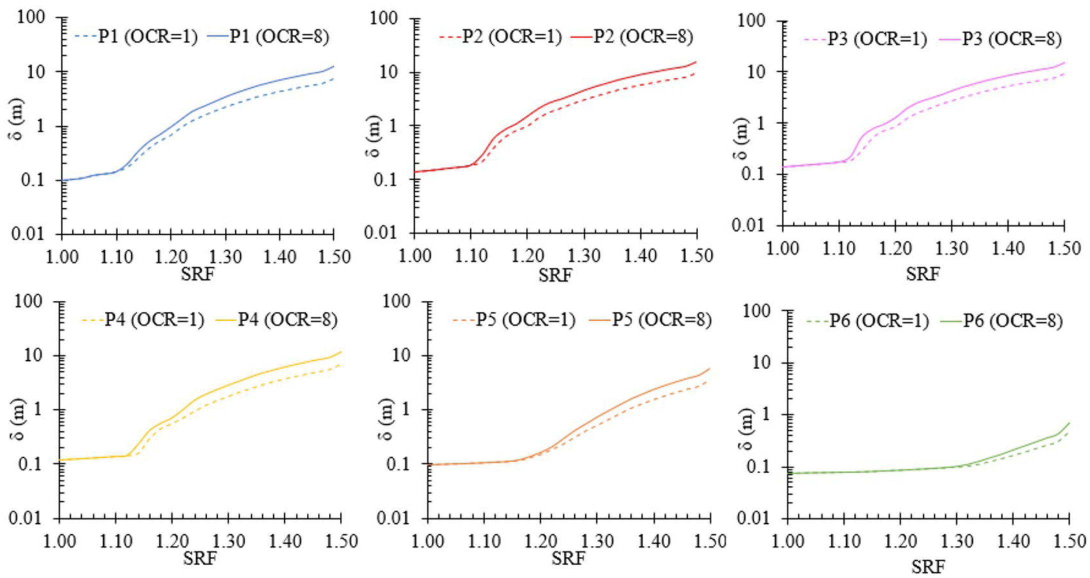

Figure 16. Offset comparison (δ) between *OCR* = 1 and *OCR* = 8.

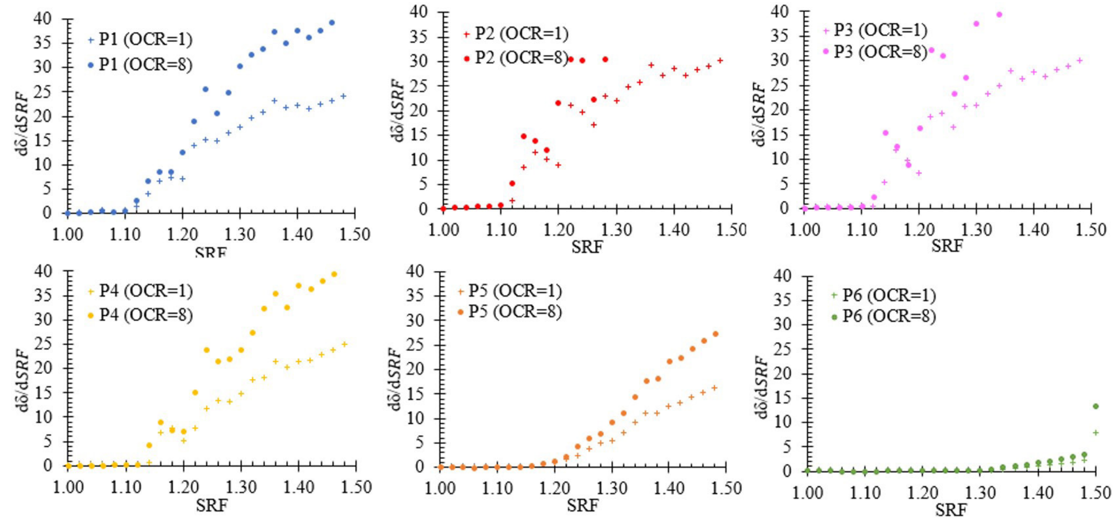

Figure 17. Derivative of each point of the displacement curves $d\delta / dSRF$ - Comparison between OCR = 1 and OCR = 8.

critical *SRF*, but they also do not indicate any influence of the *OCR* value.

One hypothesis that explains the similarity in results is the fact that displacements and *SRF* depend more on the stress state ($\eta = q / p'$) than on the state parameters p_0 and its variation with increasing *SRF*. As discussed, points close to the surface would have values of η close to *M*, and thus, there would be no significant variations in the values of p_0.

5. Conclusions

The paper presents a discussion about the use of the Critical State Model with hardening when applying the Shear Strength Reduction Method (SSR). Considering the Modified Cam Clay model (MCC), the application of SSR generates a reduction in the slope of the critical state line (CSL) and a variation in the yield surface size. However, the stress state that tends to have the most significant hardening tends to be far from the failure surface, as presented in the MCC model formulation.

The case study presented in this article compared the application of SSR with a perfectly plastic elastic model without hardening with the MCC model, this is a critical state model that considers hardening/softening of the yield surface. The MCC model resulted in a lower *SRF* value, indicating that the model was more conservative when evaluating the slope stability condition.

Furthermore, an evaluation of the effect of pre-consolidation stress on the *SRF* was carried out. A similarity in the results was observed for materials with different overconsolidation ratio (*OCR*) values. One hypothesis that explains this similarity is the fact that the displacements and *SRF* depend more on the state of stress of the material than on the pre-consolidation stress, a parameter that controls the yield surface size.

For future work, it is suggested to assess the influence of geometry, material strength parameters, dilation angle, material stress state, and to use other constitutive models in order to corroborate the aforementioned hypotheses.

Acknowledgements

The authors would like to thank the Postgraduate Program in Geotechnics of the University of Brasilia and the National Council for Scientific and Technological Development ("CNPq" by Portuguese abbreviation) for the support of this research.

Declaration of interest

The authors have no conflicts of interest to declare. All co-authors have observed and affirmed the contents of the paper and there is no financial interest to report.

Authors' contributions

Isabella Maria Martins de Souza: conceptualization, data curation, methodology, writing – original draft. Daniela Toro Rojas: conceptualization, writing – original draft. Ana Carolina Gonzaga Pires: validation, writing - reviewing and editing. Márcio Muniz de Farias: validation, reviewing. Manoel Porfírio Cordão Neto: methodology, supervision, validation, writing – review & editing.

Data availability

All data produced or examined in the course of the current study are included in this article.

List of symbols

a_m	Normal to a yield surface
B_{lj}	Matrix that relates displacement and strains
b_m	Normal to the plastic potential function
CSL	Critical State Line
c	Cohesion
D_{ml}	Stress-strain constitutive matrix
D_{ij}^{e}	Elastic constitutive matrix
D_{ij}^{ep}	Elastic-plastic constitutive matrix
E	Young's Modulus
e_i	Initial void index
F	Yield surface
F_i	External forces
FEM	Finite Element Method
K_{ij}	Stiffness matrix
LEM	Limit Equilibrium Method
M	CSL slope in *p-q* space
MC	Mohr Coulomb
MCC	Modified Cam-Clay Model
η	Stress ratio (q/p')
p'	Mean effective stress
OCR	Overconsolidation ratio
p_0	Preconsolidation stress
q	Deviator stress
SF	Safety Factor
SRF	Strength Reduction Factor
SSR	Shear Strength Reduction
u_j	Displacement vector
Y	Plastic modulus
γ	Specific weight
δ	Displacement
ε_v^p	Plastic volumetric strain
ν	Poisson Coefficient
ϕ	Friction angle

References

Cheng, Z., & Jefferies, M. (2020). Implementation and verification of NorSand model in general 3D framework. In *Proceedings of the Geo-Congress 2020: Geotechnical Earthquake Engineering and Special Topics* (pp. 10-19). Reston: ASCE. https://doi.org/10.1061/9780784482810.

Clough, R.W., & Woodward, R. (1967). Analysis of embankment stresses and deformations. *Journal of the Soil Mechanics and Foundations Division*, *4*, 529-549. http://dx.doi.org/10.1061/JSFEAQ.0001005.

Dong, L., Wang, J., Li, X., & Peng, K. (2018). Dynamic stability analysis of rockmass: a review. *Advances in Civil Engineering*, *2018*, 1-22. http://dx.doi.org/10.1155/2018/4270187.

Duncan, J.M., Wright, S.G., & Brandon, T.L. (2014). *Soil strength and slope stability* (2nd ed.). John Wiley & Sons.

Farias, M.M., & Naylor, D.J. (1998). Safety analysis using finite elements. *Computers and Geotechnics*, *22*(2), 165-181. http://dx.doi.org/10.1016/S0266-352X(98)00005-6.

Fredlund, D.G., & Rahardjo, H. (1993). *Soil mechanics for unsaturated soils*. John Wiley & Sons.

Fredlund, D.G., & Rahardjo, H. (2012). *Unsaturated soil mechanics in engineering practice*. John Wiley & Sons.

Futai, M.M. (2002). *Estudo teórico-experimental do comportamento de solos tropicais não-saturados: aplicação a um caso de voçoramento* [Doctoral thesis]. Universidade Federal do Rio de Janeiro (in Portuguese).

Geoslope International, Ltd. (2021). *Add-Ins programming guide and reference*. Geoslope International, Ltd.

Jefferies, M.G. (1993). NorSand: a simple critical state model for sand. *Geotechnique*, *43*(1), 91-103. http://dx.doi.org/10.1680/geot.1993.43.1.91.

Jefferies, M.G., & Shuttle, D.A. (2002). Dilatancy in general Cambridge-type models. *Geotechnique*, *52*(9), 625-637. http://dx.doi.org/10.1680/geot.2002.52.9.625.

Matsui, T., & San, K. (1992). Finite element slope stability analysis by shear strength reduction technique. *Soil and Foundation*, *32*(1), 59-70. http://dx.doi.org/10.3208/sandf1972.32.59.

Roscoe, K.H., & Burland, J.B. (1968). *Engineering plasticity*. Cambridge University Press. On the generalized stress-strain behaviour of wet clay, pp. 535-609.

Roscoe, K.H., Schofield, A.N., & Wroth, C.P. (1958). On the yielding of soils. *Geotechnique*, *8*(1), 22-53. http://dx.doi.org/10.1680/geot.1958.8.1.22.

Roscoe, K.H., Schofield, A.N.D., & Thurairajah, A. (1963). Yielding of clays in states wetter than critical. *Geotechnique*, *13*(3), 211-240. http://dx.doi.org/10.1680/geot.1963.13.3.211.

Vardon, P.J., Wang, B., & Hicks, M.A. (2017). Slope failure simulations with MPM. *Journal of Hydrodynamics*, *29*(3), 445-451. http://dx.doi.org/10.1016/S1001-6058(16)60755-2.

Soils and Rocks
An International Journal of Geotechnical and Geoenvironmental Engineering
www.soilsandrocks.com
ISSN 1980-9743
ISSN-e 2675-5475

Geotechnical site characterization by DMT and laboratory tests on an unsaturated tropical soil site for slope stability analysis

Breno Padovezi Rocha[1#], Jhaber Dahsan Yacoub[2], Jeferson Brito Fernandes[2], Roger Augusto Rodrigues[2], Heraldo Luiz Giacheti[2]

Article

Keywords
Site characterization
Slope stability
In situ tests
DMT
Unsaturated soils
Suction

Abstract

The slope stability is an important topic because it presents risks of socio-economic losses caused by eventual ruptures. It is necessary to identify the site profile, as well as obtaining soil strength parameters for the slope stability analysis. This paper presents and discusses the use of the Flat Dilatometer Test (DMT) in the geotechnical site characterization for slope stability analysis in an unsaturated tropical soil site. Six DMTs were performed to define the stratigraphical profile and estimate geotechnical parameters. Shear strength parameters were determined in the laboratory using saturated and unsaturated triaxial compression as well as soil water retention curves (SWRC) to support DMT data interpretation. A commercial software was used to perform the slope stability analysis a cut slope with 6.6 m height and a gradient around 55° to illustrate the application of DMT and triaxial test data. The DMT allowed the representative site profile to be identified, as well as estimating the design parameters that compared well to those interpreted from unsaturated triaxial test data for the in-situ soil suction. The DMT can be used as logging test in the preliminary characterization of studied site specially to define the stratigraphical profile, site variability, select the regions to collect disturbed and undisturbed soil samples and as the first attempt to estimate the geotechnical design parameters via correlations. It is important to emphasize that laboratory tests on undisturbed soil samples are essential in the slope stability analysis of unsaturated tropical soil profiles.

1. Introduction

Slopes can be natural or man-made, and their stability is a very important issue because of the risks of socio-economic losses caused by eventual failures. Slope failures can damage buildings, road infrastructure, as well as cause injury or death to people (Rahardjo et al., 2019). One of the relevant aspects that leads to the complexity of slope stability is that it can be formed by rock, soil, or both, requiring a proper understanding of the stress state and failure mechanisms.

The need for stabilization and adequate preventive measures for slope protection has gained great relevance in the context of sustainable development of urban areas, especially in times of climate change. In the light of the effects of climate change, longer periods of drought and higher intensity and shorter duration rainfall are expected in the future, and it is necessary to prevent future rain-induced slope failures for slope protection against rainfall.

Changes in rainfall patterns, in particular, will influence the boundary condition of flow at the ground surface. Changes in groundwater hydrology associated with extreme events at the soil-atmosphere interface demonstrate the complex nature of time-dependent problems such as slope stability that can only be best analyzed in the context of Unsaturated Soil Mechanics.

The behavior of unsaturated soils depends on the soil suction (Alonso et al., 1990). Changes in the water content and suction in an unsaturated soil occurs due to climate variations (Blight, 2003; Cui et al., 2008). Climate events (i.e., extreme precipitation and droughts) are dominated by soil-atmospheric interactions in which soil water content and soil suction can change seasonally (Rahardjo et al., 2019). The changes in soil suction could reduce the shear strength of soil that may result in rainfall-induced slope failures and consequent destructions and deaths (Cho & Lee, 2002; Ng & Shi, 1998; Tohari et al., 2007). Therefore, the effects of unsaturated soils should be considered in slope stability

[#]Corresponding author. E-mail address: breno.rocha@ifsp.edu.br
[1]Instituto Federal de Educação, Ciência e Tecnologia de São Paulo, Ilha Solteira, SP, Brasil.
[2]Universidade Estadual Paulista "Júlio de Mesquita Filho", Faculdade de Engenharia, Departamento de Engenharia Civil e Ambiental, Bauru, SP, Brasil.

Submitted on May 15, 2023; Final Acceptance on October 25, 2023; Discussion open until February 28, 2024.
https://doi.org/10.28927/SR.2023.005123

analyses for geotechnical designs (Alonso et al., 2003; Fredlund & Rahardjo, 1993; Ng et al., 2001).

It is necessary to determine unsaturated soil properties for a proper unsaturated slope stability analysis, such as unsaturated shear strength, hydraulic conductivity, and soil water retention curve (SWRC). So, suction-controlled, and conventional triaxial tests as well as tests to determine the soil water characteristic curves (SWRC) (i.e., suction-plate, pressure-chamber, and filter-paper) should be carried out on undisturbed soil samples. It is important to recognize the significant progress that suction control tests have brought to the understanding of unsaturated soils, especially Hilf's (1956) axis translation technique. It is important to mention, however, that suction control techniques are complex to use and expensive, which brings the need to search for more cost-effective alternatives.

In the slope stability analysis, it is necessary to identify the geomaterials in the site profile, their thicknesses, the ground water level position, as well as the strength parameters of each of these materials. Geotechnical site characterization can be carried out by means of in situ and laboratory tests. In situ tests, such as the Flat Dilatometer (DMT) can be used as an alternative to the traditional drilling, sampling, and laboratory testing, especially in sandy soils, where sampling is complex and does not always maintain the natural characteristics of the soil. Combining the use of a in situ profiling test with a specific determination of some indexes or properties is a modern approach to better characterize the site.

This paper presents and discusses the use of the Flat Dilatometer Test (DMT) in the geotechnical site characterization of an unsaturated tropical sandy soil profile, with emphasis on its application to the slope stability analysis. The classification of the soil profile and the estimative of strength parameters were done and compared with laboratory test data. In addition, the stability analysis on a cut slope in unsaturated sandy soil profile is presented and discussed.

2. Flat dilatometer test (DMT)

The Flat Dilatometer Test (DMT) is a simple and repeatable in situ test, and its data can be used to identify the soil type and estimate design parameters such as in situ coefficient of lateral earth pressure (K_0), undrained shear strength (S_u), friction angle (ϕ), overconsolidation ratio (OCR), and vertical drained constrained modulus (M_{DMT}) (Marchetti, 1980). The test can also be used to predict settlements of shallow foundations, monitoring densification (i.e., soil compaction), liquefaction analysis as well as in the detecting slip surfaces in overconsolidated clays slopes. Moreover, dissipation tests can be performed to estimate the in situ consolidation (coefficient of consolidation, c_h) and flow parameters (coefficient of permeability, k_h) (Marchetti et al., 2001; Marchetti & Monaco, 2018; Schmertmann, 1986).

The DMT has a flat stainless-steel blade with a 60 mm diameter steel membrane mounted flush on one side (Marchetti, 1980). The nominal dimensions of the blade are 95 mm width and 15 mm thickness, having a cutting edge angled between 24° and 32° to penetrate the soil (Marchetti et al., 2001). The blade is designed to safely withstand up to 250 kN pushing force. The other components are the control unit, pneumatic-electrical cable, and gas tank (Figure 1).

The blade is advanced quasi statically or dynamically into the ground. The penetration rate is usually equal to 20 mm/s as in the cone penetration tests. The calibration procedure to obtain ΔA and ΔB pressures, necessary to overcome membrane stiffness, must be done before each profile. A-Pressure (just begin to move the membrane into the soil) and B-Pressure (move the membrane center 1.1 mm against the soil) are typically recorded every 200 mm during the test and p_0 and p_1 pressures were calculated. C-Pressure can also be recorded. The DMT interpretation starts with the intermediate parameters (I_D, K_D and E_D) determination (Marchetti et al., 2001):

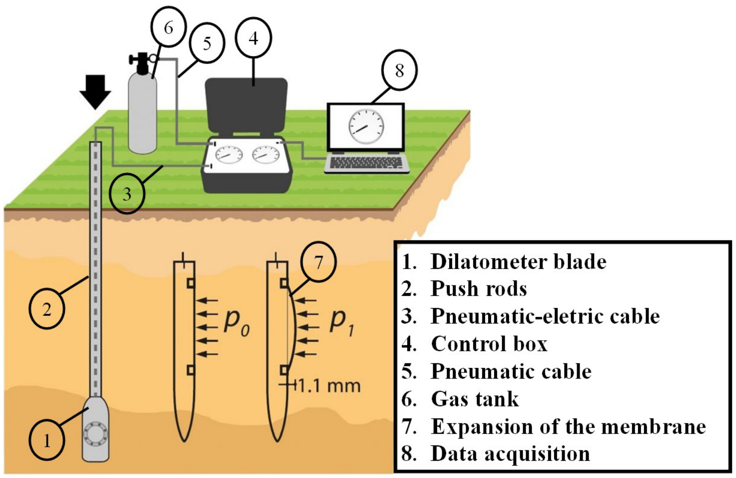

Figure 1. Schematic representation of DMT [adapted from Marchetti et al. (2001)].

$$I_D = \frac{p_1 - p_0}{p_0 - u_0} \quad (1)$$

$$K_D = \frac{p_0 - u_0}{\sigma'_v} \quad (2)$$

$$E_D = 34.7.(p_1 - p_0) \quad (3)$$

where u_0 is the hydrostatic pressure, and the σ'_v is the effective vertical stress.

I_D is calculated to identify soil type. In general, I_D provides an expressive profile of soil type and, in "normal" soils a reasonable soil description (Marchetti et al., 2001). The K_D provides the basis for several soil parameters correlations and is the key result of the dilatometer test (Marchetti et al., 2001). E_D in general should not be used as such, especially because it lacks information on stress history (Marchetti et al., 2001).

3. Study site

The study site is the experimental research area at the São Paulo State University (Unesp) - Bauru Campus and a typical cut slope (the case study) that occurs in this region. The schematic representation of the study site in the city of Bauru, state of São Paulo, Brazil, is shown in Figure 2, as well as the location of the cut slope (case study).

Several site characterization programs including SPT, SPT-T, S-SPT, DMT, PMT, SCPT, CH and DH tests were carried out at the study site. Sample pits were also excavated to retrieve undisturbed and disturbed soil blocks at 1.5, 3.0, 5.0, 7.0, and 9.0 m depth. Soil specimens from these blocks were tested in laboratory for soil characterization and determination of mechanical properties and parameters.

The site profile is a red clayey fine to medium sand identified based on SPT. MCT Classification System (Nogami & Villibor, 1981) classified the top 13 m as lateritic soil behavior (LA') followed by a non-lateritic soil behavior (NA'), as discussed Giacheti et al. (1998). The soil is classified in the Unified Soil Classification System as a SM Group soil. Some relevant geotechnical characteristics are summarized in Figure 3.

Figure 3a shows the typical site profile defined by SPT tests. Figure 3b shows that SPT *N* values increase almost linearly with depth. From CPT tests, the corrected cone resistance (q_t) and the sleeve friction (f_s) shows higher values at the top 1 m and tends to increase with depth leading to a friction ratio (R_f = (f_s/q_t)*100%) between 1.0 and 3.0%. Moreover, Figure 3 presents the variation of shear wave velocity (*Vs*) with depth (Figure 3e) measured by cross-hole (CH), SCPT and down-hole tests (DH 1 and DH2). The void ratio (*e*) at 1.0 m depth is equal to 0.72 and drops to about 0.60 at 16 m depth. The dry unit weight (γ_d) at 1.0 m depth is equal to 15.64 kN/m^3 and increase with depth (Figure 3f). The groundwater level was deeper than 30 m depth at this location.

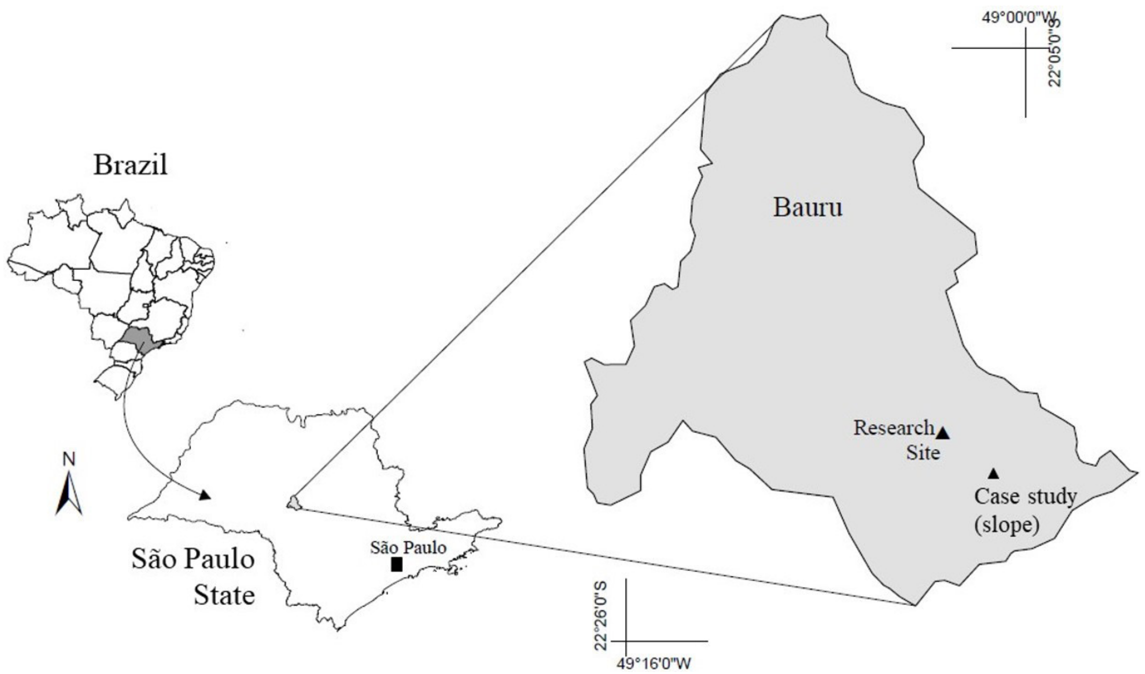

Figure 2. Schematic representation of the Unesp research site and the cut slope in the city of Bauru, São Paulo State, Brazil.

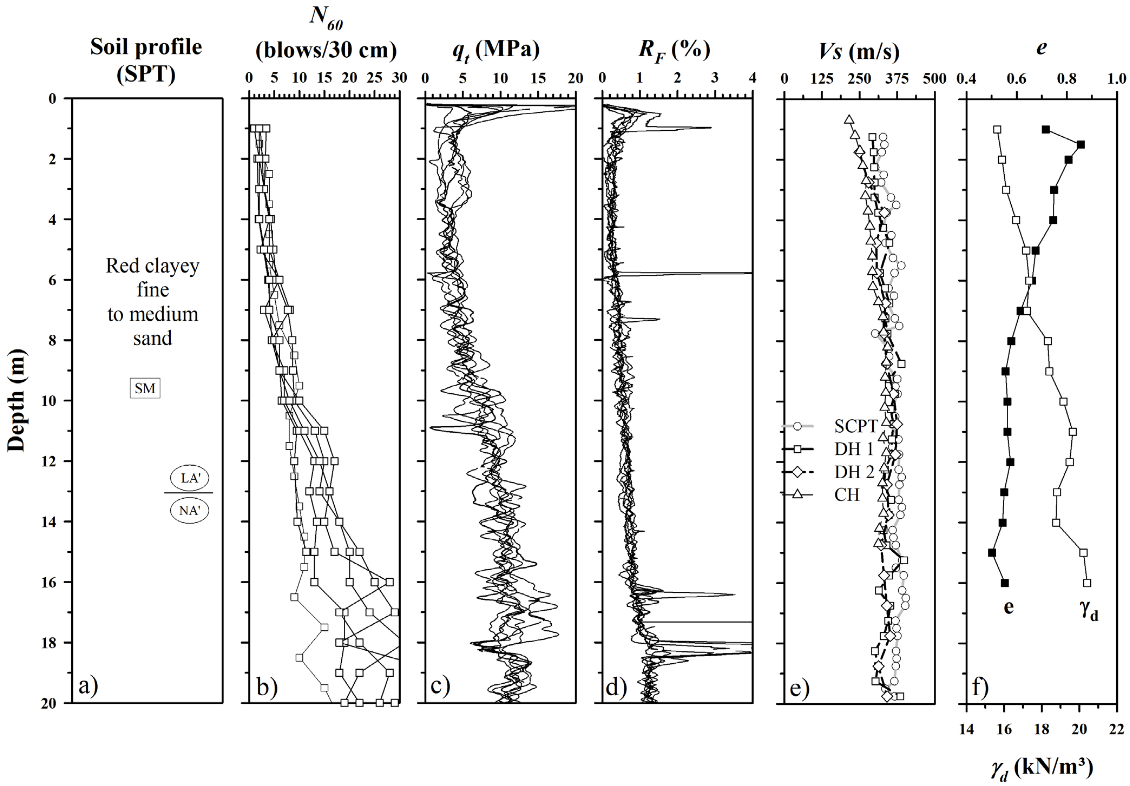

Figure 3. In situ and laboratory tests data for the experimental research site. The water level is deeper than 30 mat this location [adapted from Rocha & Giacheti (2018)].

4. Results and analysis

Six DMTs were carried out at the site and Figure 4 presents the DMT profiles in terms of I_D, K_D and E_D data plotted as an average profile as well as plus and minus one standard deviation (*SD*). The I_D, K_D and E_D parameters were calculated using Equations 1, 2, and 3, respectively (Marchetti, 1980).

From the interpretation of the laboratory and in situ tests (Figure 3) it is observed that the site profile is relatively homogeneous, and that possible variations observed in the mechanical parameters of the soil may be associated with soil suction, as well as its variation over time. In this sense, the interpretation of in situ tests, as well as the design of geotechnical works (e.g., slope stability) should consider the effect of soil suction.

Since the DMT does not provide soil sample, the soil type can be defined based on the material index (I_D) and by means of the chart proposed by Marchetti & Crapps (1981) relating I_D and E_D . Geotechnical parameters can be estimated by using classical correlations and these parameters can be compared with laboratory-determined reference values obtained by triaxial tests on undisturbed soil samples.

4.1 Soil classification

The first step of the site characterization in the slope stability analysis consists of defining the representative site profile. The definition of the soil type was done by means of grain size distribution tests in the laboratory. Tropical soils normally present a macroaggregate structure, due to the cementing action of iron and aluminum oxides and hydroxides. It is recommended to carry out grain size distribution tests with and without the use of dispersant, to have a textural classification of the soil in these two conditions to better understand how this aggregation occurs.

Figure 5 shows the particle size distribution curves with and without the use of dispersant for samples collected at 0.25 m, 3.50 m, 5.50 m, and 8.00 m depth using a helical auger. It can be seen in this figure a significant difference between the clay and silt fractions for these two conditions, with implications for the soil classification. For instance, the sample collected at 8 m depth is classified as a clayey sand (78% Sand; 5% Silt; 17% Clay) with the use of dispersant and as a silty sand (65% Sand; 35% Silt) without the use of dispersant. It is due to the action of iron and aluminum oxides and hydroxides, present in tropical soils, which produce agglutination of the clay fraction, leading to a macroaggregate structure.

The soil classification by means of the DMT uses the Material Index (I_D) and the Dilatometric Modulus (E_D) as proposed by Marchetti & Crapps (1981). The site profile is classified as a sandy silt by the DMT data, as shown in Figure 4 and Figure 6. This classification is not in agreement with the grain size of the soil obtained by the test with

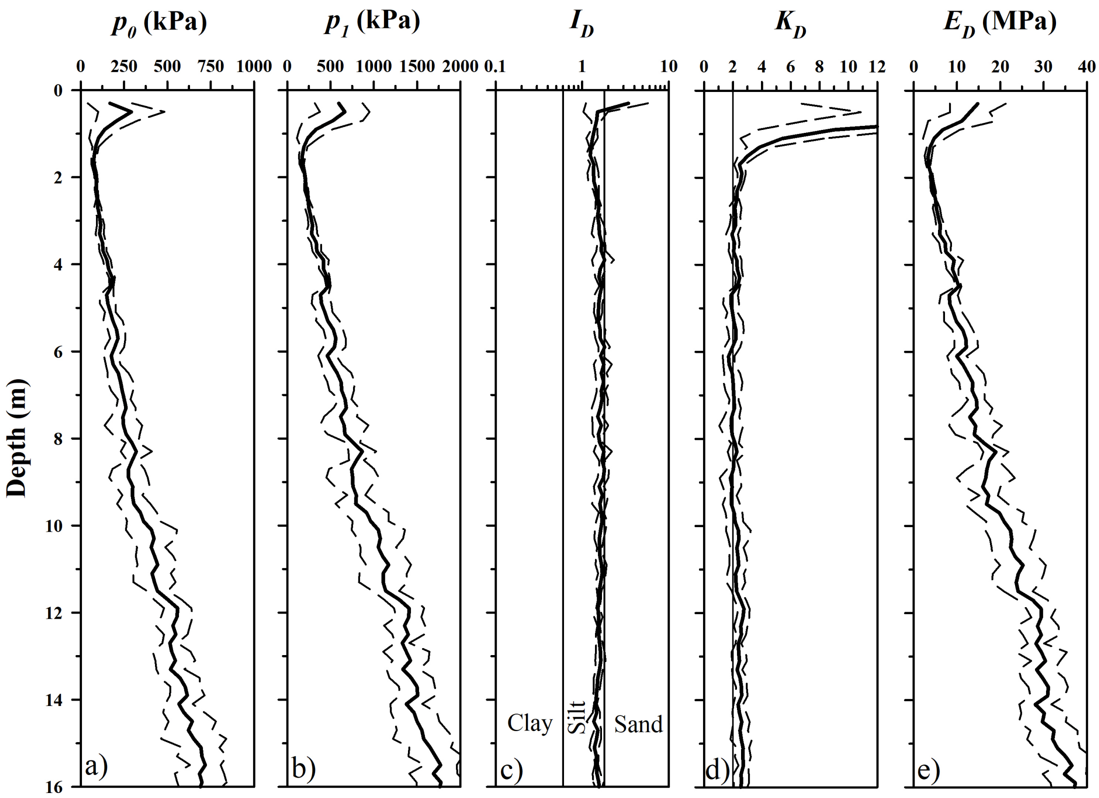

Figure 4. DMT data and interpretation for the study site. a) Corrected first reading, b) Corrected second reading, c) Material index, d) Horizontal stress index, e) Dilatometer modulus.

dispersant (Figure 5), which classifies the soil as a fine sand with little clay. However, the soil is classified as a silty sand when the grain size distribution curve is determined without the use of the dispersant. That classification is more consistent with the behavior identified by the DMT. It is important to note that the I_D index is a parameter that reflects the mechanical behavior of the soil, as a stiffness index, and not the grain size composition of the soil (Marchetti et al., 2001). Furthermore, the I_D index indicates that mixtures of sand and clay are usually classified as silts, as observed for the study site (Marchetti et al., 2001).

4.2 Geomechanical parameters

The geomechanical parameters estimative by means of the average profiles ± standard deviation of I_D, K_D and E_D was done considering the six DMTs. It is important to emphasize that the investigated profile is unsaturated. Thus, the mechanical soil parameters were determined by triaxial tests both in saturated and unsaturated condition for a soil suction equal to 50 kPa (Fernandes, 2022; Saab, 2016) through the axis translation technique (Hilf, 1956). This value was used in laboratory to represent the field condition as it was measured in situ by tensiometers and granular matrix sensors.

Figure 7 shows the profiles of total unit weight (γ_n), friction angle (ϕ), and cohesion intercept (c) estimated by the DMT. These values were compared with reference values determined in laboratory from undisturbed samples (Fagundes & Rodrigues, 2015; Fernandes, 2022). The γ_n values were estimated by Schmertmann (1986)'s equation (Equation 4) while friction angle was estimated by equation suggested by Marchetti (1997). The cohesion intercept values were calculated from Equation 6 proposed by Cruz & Viana Da Fonseca (2006). It is worth noting that the proposed equation was developed for a residual silty sand from Granite.

$$\frac{\gamma_n}{\gamma_w} = 1.12 \cdot \left(\frac{E_D}{p_a}\right)^{0.1} \cdot \left(I_D\right)^{-0.05} \tag{4}$$

$$\phi = 28 + 14.6 \cdot \log K_D - 2.1 \cdot \log^2 K_D \tag{5}$$

$$c = 0.376 \cdot v_{OCR} + 3.08 \tag{6}$$

γ_w is the specific weight of water, p_a is the atmospheric reference pressure (100 kPa), and v_{OCR} is the virtual overconsolidation ratio obtained from Marchetti & Crapps (1981) approach.

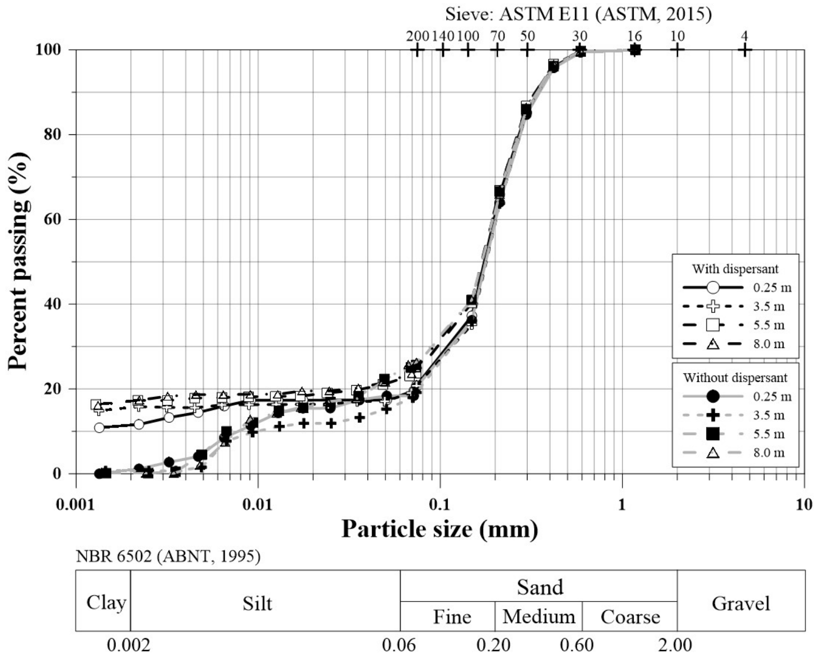

Figure 5. Grain size distribution curves with and without dispersant for the soil samples collected at 0.25, 3.50, 5.50, and 8.00 m depth [adapted from Rocha (2018)].

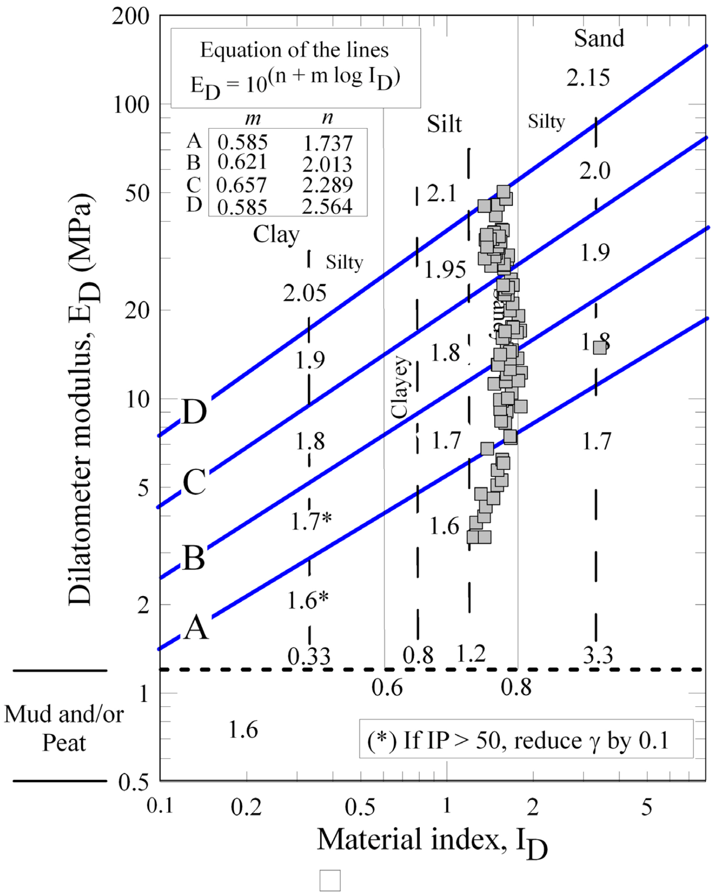

Figure 6. Soil classification for the soils from the study site in the DMT chart [adapted from Marchetti & Crapps (1981)].

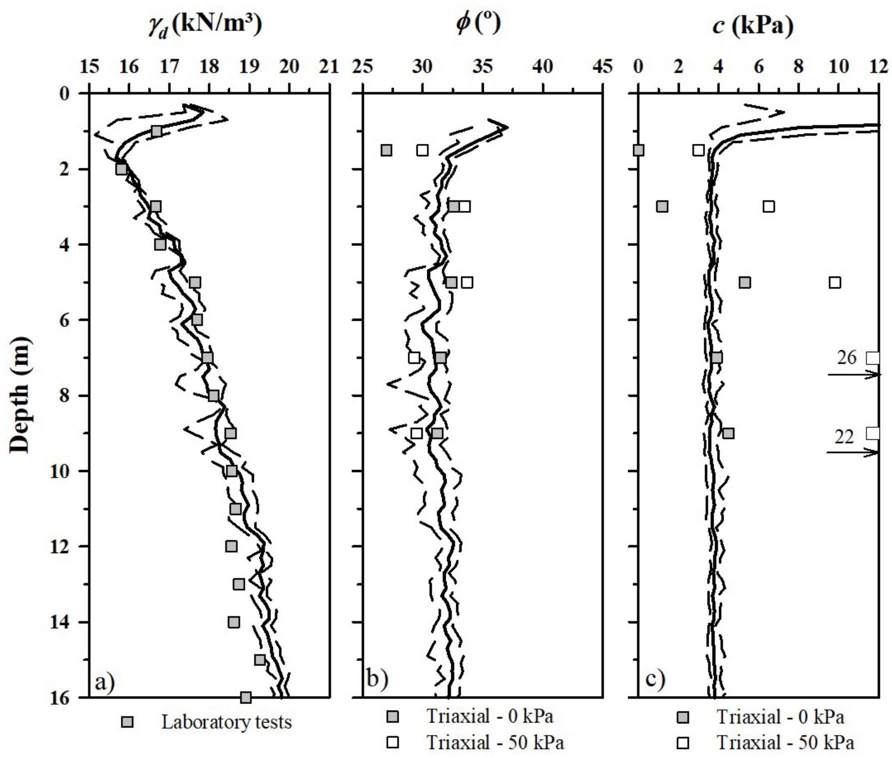

Figure 7. Estimated parameters from DMT for the study site and reference values determined by triaxial tests.

Figure 7a shows that the density values estimated by Equation 4 are in good agreement with those determined from undisturbed soil samples, especially between 1 and 11 m depth. The ϕ value varied from 27.0º for 1 m depth to 31.2º for 9 m depth at the saturated condition and varied from 30.0º for 1 m depth to 29.5º for 9 m depth at the unsaturated condition (Figure 7b and Table 1). So, an average ϕ value equal to 30.9º in the saturated condition, and 31.2º in the unsaturated condition were calculated from the triaxial tests. The ϕ values determined from the average profiles of I_D, $K_{D,}$ and E_D agree relatively well with the reference values from triaxial tests below 2 m depth. It did not occur above 2 m depth, and it could be related to the effect of high soil suction values, which increased p_0 and p_1 values, mainly in the topsoil due to the soil-atmosphere interaction, which reflect in the estimative of geomechanical parameters by DMT (Giacheti et al., 2019; Rocha, 2018; Rocha et al., 2021).

Cohesion intercept values estimated from the DMT were compared with those determined in the laboratory by triaxial tests on undisturbed soil samples (Figure 7c). It should be mentioned that a soil suction value equal to 20 kPa to estimate the cohesion intercept from the DMT. This suction value was assumed from moisture content profiles and soil water retention curves available for the site and will be discussed latter on. The cohesion intercept values increased with depth and with soil suction (Table 1). The cohesion value was equal to 0 kPa in the saturated condition, and 3.0 kPa for 50 kPa suction for the sample collected at 1.5 m depth. The cohesion intercept was equal to 4.5 kPa in the saturated condition, and 22 kPa for 50 kPa suction for the sample collected at 9.0 m depth.

It is important to mention that the cohesion intercept for tropical sandy soils is mainly related to the cementing structures and the effect of the unsaturated condition and this parameter varies seasonally depending on the rainfall regime and water infiltration in the soil mass.

5. Slope stability analysis

The stability analysis of a cut slope in the city of Bauru, São Paulo state, which has a site profile and mechanical parameters like those found in the experimental research site at the Unesp, will be performed. DMT (Figure 4) and the triaxial tests (Table 1) previously presented will be used in these analyses.

The slope is 6.6 m high and has an approximate slope gradient of around 55°. The slope geometry was defined from planialtimetric surveys, and the groundwater was assumed at the slope foot, based on SPT data carried out at this location. No groundwater flow was considered in the stability analysis. Figure 8 shows the defined geometry and the assumed groundwater position for the slope stability analysis.

Table 1. Strength parameters obtained by triaxial tests for different test depth for saturated and unsaturated conditions (Fernandes, 2022; Fernandes et al., 2022).

Depth (m)	Cohesion intercept (kPa)		Friction angle (°)	
	s = 0 kPa	s = 50 kPa	s = 0 kPa	s = 50 kPa
1.5	0.0	3.0	27.0	30.0
3.0	1.2	6.5	32.6	33.5
5.0	5.3	9.8	32.4	33.7
7.0	3.9	26.0	31.5	29.3
9.0	4.5	22.0	31.2	29.5

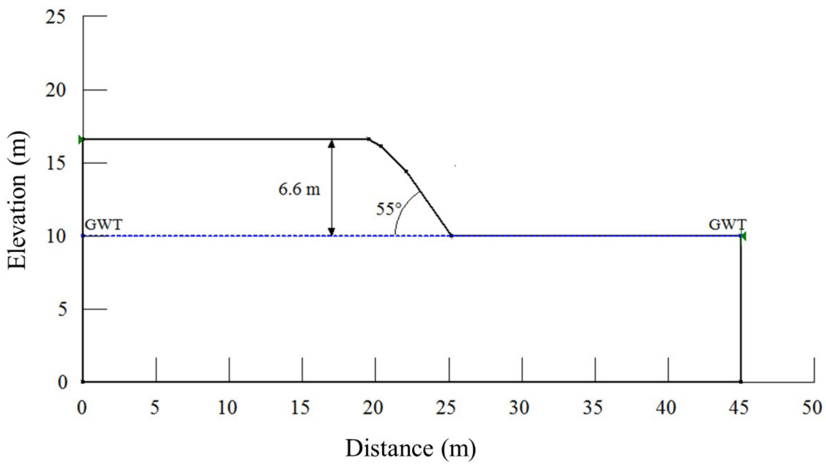

Figure 8. Slope geometry.

The GeoStudio software was used to perform the slope stability analysis using the Simplified Bishop's stability method. The shear strength criterion is that one proposed by Fredlund et al. (1978) for the unsaturated soil.

5.1 The analysis with DMT data

At the time the DMTs were carried out, disturbed soil samples were taken using a helical auger to determine the moisture content profiles (Figure 9a) to estimate the soil suction. The moisture content profile ranges from 4.0 to 11.2%, and the estimated soil suction varies from 4.2 to 50 kPa, with an average value equal to 20 kPa. These values were estimated from the soil water retention curves (SWRCs) determined from undisturbed samples collected at 1, 3, 5, and 7 m depth (Figure 9b) by Fernandes (2022). Table 2 presents the input parameters for the stability analyses by DMT and triaxial tests. In these analyses, the suction was assumed not to affect the internal friction angle (ϕ) of the soil.

Figure 10 presents the safety factor (*FS*) equal to 0.943, as well as the possible rupture surfaces considering the soil parameters obtained by DMT. This value is lower than one, i.e., the slope is in an unstable condition for the assumed boundary conditions, stresses, and soil parameters. It is worth noting that the geomechanical parameters (c and ϕ) were obtained using empirical correlations, and they may not adequately represent the mechanical behavior of the studied unsaturated tropical soil.

5.2 The analysis with triaxial test data

To compare the *FS* values calculated from the interpretation of DMT data, the cohesion intercept value determined using the triaxial test data for the same field suction value (i.e., 20 kPa) was estimated. For this, the model of Fredlund et al. (1978) was used to estimate the unsaturated cohesion for 20 kPa of suction (Equation 7), which resulted in a cohesion intercept value equal to 4.7 kPa.

In order to apply Equation 7 the values of cohesion intercept versus suction (Table 1) were reinterpreted to define ϕ^B that resulted in the value of 5.10° (tg $\phi^b = 0.089$). Hence, the calculated *FS* was equal to 1.035, close to that found from the interpretation of the DMT data (Figure 11).

$$c = c_{sat} + \left(u_a - u_w\right) . \tan \phi^b \tag{7}$$

where c_{sat} is the saturated cohesion, $u_a - u_w$ is the soil suction and ϕ^b is the angle indicating the increase in shear strength due to soil suction.

Following the same approach, another stability analysis was performed considering an average cohesion value obtained for the suction condition equal to 50 kPa (Table 1). In this case, the calculated *FS* was 2.161 (Figure 12).

Table 2. Average soil parameters assumed for slope analysis stability by DMT and triaxial tests for different soil suctions.

Type of test	Soil parameters		
	γ (kN/m³)	c (kPa)	ϕ (°)
DMT *s* = 20 kPa	16.8	3.7	32.0
Triaxial *s* = 20 kPa	16.8	4.7	32.5
Triaxial *s* = 50 kPa	16.8	13.4	32.5

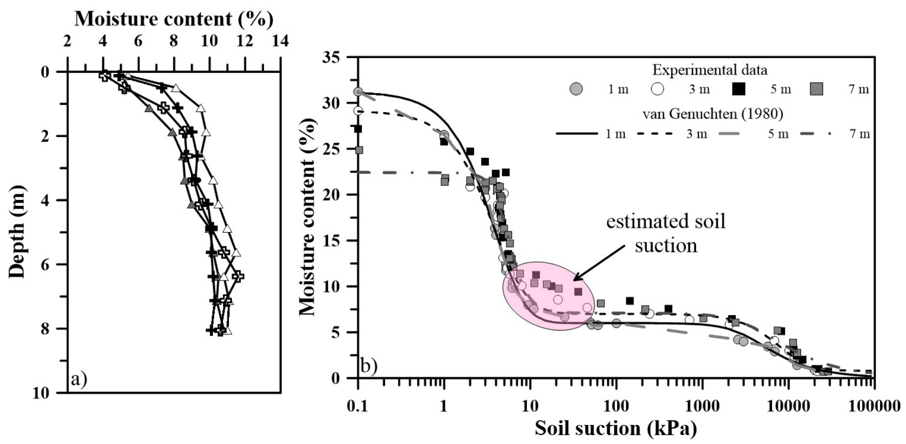

Figure 9. Moisture content profiles (a) and the soil water retention curves (b) [adapted form Fernandes (2022)].

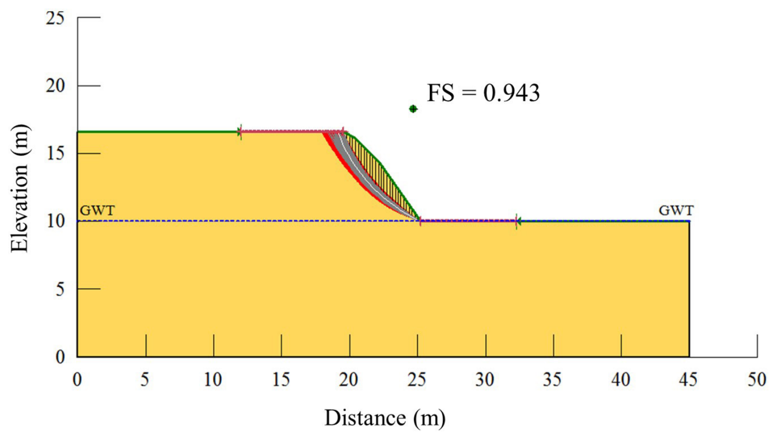

Figure 10. Minimum safety factor (*FS*) and slip surfaces tested assuming shear strength parameters by DMT.

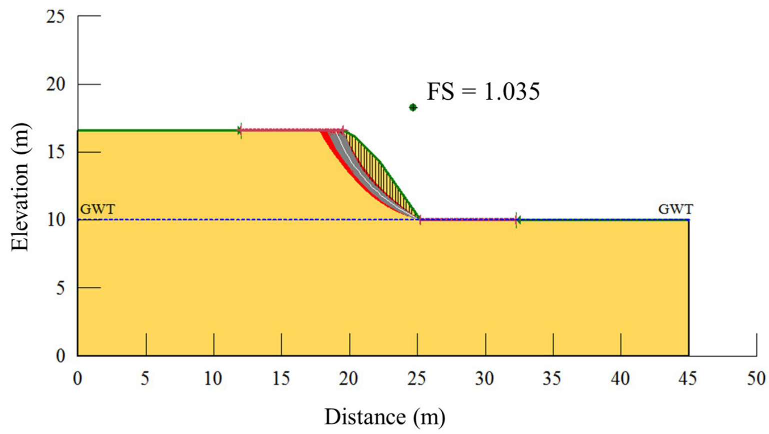

Figure 11. Minimum safety factor and slip surfaces tested assuming shear strength parameters from the unsaturated triaxial tests with a suction value equal to 20 kPa.

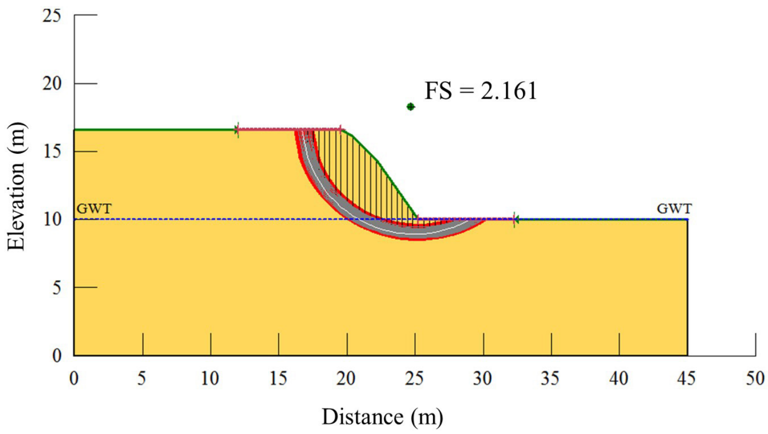

Figure 12. Minimum safety factor and slip surfaces tested assuming shear strength parameters from the unsaturated triaxial tests with a suction value equal to 50 kPa.

Figure 13. The slope after failure [adapted from Vieira (2021)].

The results of this and other similar studies have led to a general consensus that unsaturated condition, with its associated soil suction, tend to increase slope stability due to increase in apparent cohesion (Dai et al., 2022; Kang et al., 2020; Sivakumar Babu & Murthy, 2005).

5.3 Slope failure back analysis

Vieira (2021) performed the back analysis of similar shear slope slides by integrating data from laboratory tests and numerical modeling. The author analyzed a rupture that occurred after a 124.7 mm rainfall. Figure 13 shows the slope after rupture. The GeoStudio software (SLOPE/W and SEEP/W) was used to perform the numerical simulations in a time-dependent analysis. The approach adopted considered the Simplified Bishop's stability method, as well as the Mohr-Coulomb criterion that incorporates the effect of the saturated condition, as proposed by Fredlund et al. (1978). The slope geometry and the failure surface were obtained from planialtimetric surveys. The rainfall history of the region during the slope failure period was obtained from a meteorological station near the slope. The slope failure back analysis was performed by combining the cohesion intercept and friction angle values to obtain them, considering the unitary safety factor (*FS* = 1) at the time of the 124.7 mm rain that caused the slope failure.

It is worth noting that slope stability analyses that use geomechanical parameters determined by triaxial compression tests with controlled suction in numerical simulations that incorporate the hydraulic properties of the soil, and flow conditions to simulate rainfall and its interaction with the soil mass are unusual in the practice of geotechnical jobs.

6. Conclusion

The main conclusions are:

- The DMT allowed to define the site profile and to give a preliminary estimative of the strength parameters of the soils;
- The natural specific weight profile (γ_n), friction angle (ϕ) and the cohesion intercept (c) presented reasonable agreement with the reference values;
- The DMT was an interesting tool in defining the site profile for the case study as well as for estimating the strength parameters required in the slope stability analyses in the preliminary design phase;
- The slope stability analyses performed considering the geometry, stresses and parameters estimated by the DMT and by the triaxial tests for a suction value of 20 kPa indicated that the slope is at the eminence of rupture ($FS \approx 1$). In addition, the slope was found to be stable for a suction value of 50 kPa based on the triaxial test data, since the factor of safety in this case is greater than 2.0 ($FS \approx 2.2$);
- The back analysis of a slope with similar characteristics to those in this study confirms that the failure occurs due to the reduced contribution to soil shear strength by the effect of rainfall and its interaction with the soil mass;
- The DMT can be used as logging test in the preliminary site characterization of unsaturated tropical soil sites specially to define the stratigraphical profile, site variability, select the regions to collect disturbed and undisturbed soil samples and as the first attempt to estimate the geotechnical design parameters via correlations;
- The ideal condition is to characterize the site using a logging test like the SPT, CPT or DMT and refine it with triaxial compression tests with controlled suction to determine the shear strength parameters to have a better understanding of the suction effect during the lifetime of the slope considering the hydraulic properties of the soil and the influence of rainfall regime, infiltration and drainage conditions.

Acknowledgements

The authors thank the São Paulo Research Foundation - FAPESP (Grants 2015/17260-0 and 2017/23174-5), the National Council for Scientific and Technological Development - CNPq (Grant 436478/2018-8), and the Coordination for the Improvement of Higher Education Personnel – CAPES, for supporting their research.

Declaration of interest

The authors have no conflicts of interest to declare. All co-authors have observed and affirmed the contents of the paper and there is no financial interest to report.

Authors' contributions

Breno Padovezi Rocha: conceptualization, data curation, visualization, formal analysis, investigation, methodology, writing – original draft, writing – review & editing. Jhaber Dahsan Yacoub: conceptualization, data curation validation, writing – review & editing. Jeferson Brito Fernandes: conceptualization, data curation validation, writing – review & editing. Roger Augusto Rodrigues: conceptualization, experimental supervision, methodology, writing – review. Heraldo Luiz Giacheti: conceptualization, methodology, supervision, funding acquisition, project administration, writing – review.

Data availability

The datasets generated during and/or analyzed during the current study are available from the corresponding author on reasonable request.

List of symbols

c	Cohesion
c_h	Coefficient of consolidation
c_{sat}	Saturated cohesion
e	Void ratio
f_s	Sleeve friction
p_a	Atmospheric reference pressure (100 kPa)
p_0	Corrected first reading
p_1	Corrected second reading
q_t	Cone resistance
s	Soil suction
A-	Pressure required to just begin to move the membrane into the soil
B-	Pressure required to move the membrane center 1.1 mm against the soil
C-	Pressure taken by slowly deflating the membrane immediately after *B-pressure* is reached
CH	Crosshole test
DH	Downhole test
DMT	Flat dilatometer tests
E_D	Dilatometer modulus
FS	Safety factor
I_D	Material index

K_D Horizontal stress index
K_h Coefficient of permeability
K_0 In situ coefficient of lateral earth pressure
LA' Lateritic soil behavior
M_{DMT} Vertical drained constrained modulus
NA' Non-lateritic soil behavior
OCR Overconsolidation ratio
PMT Pressuremeter tests
R_f Friction ratio
SCPT Seismic cone test
SM Silty sand
SPT Standard penetration tests
SPT-T Standard penetration tests with torque measurements
S-SPT Seismic SPT
SWRC Soil water retention curve
S_u Undrained shear strength
Vs Shear wave velocity
ϕ Friction angle
ϕ^b Angle indicating the increase in shear strength due to soil suction
γ_d Dry unit weight
γ_n Total unit weight
γ_w Specific weight of water
u_0 Hydrostatic pressure
$u_a - u_w$ Soil suction
v_{OCR} Virtual overconsolidation ratio
σ'_v Effective vertical stress
ΔA Calibration parameters used to correct the *A*, *B* pressure
ΔB Calibration parameters used to correct the *A*, *B* pressure

References

Alonso, E.E., Gens, A., & Delahaye, C.H. (2003). Influence of rainfall on the deformation and stability of a slope in overconsolidated clays: a case study. *Hydrogeology Journal*, *11*(1), 174-192. http://dx.doi.org/10.1007/s10040-002-0245-1.

Alonso, E.E., Gens, A., & Josa, A. (1990). A constitutive model for partially saturated soils. *Geotechnique*, *40*(3), 405-430. http://dx.doi.org/10.1680/geot.1990.40.3.405.

Blight, G.E. (2003). The vadose zone soil-water balance and transpiration rates of vegetation. *Geotechnique*, *53*(1), 55-64. http://dx.doi.org/10.1680/geot.2003.53.1.55.

Cho, S.E., & Lee, S.R. (2002). Evaluation of surficial stability for homogeneous slopes considering rainfall characteristics. *Journal of Geotechnical and Geoenvironmental Engineering*, *128*(9), 756-763. http://dx.doi.org/10.1061/(ASCE)1090-0241(2002)128:9(756).

Cruz, N., & Viana Da Fonseca, A. (2006). Portuguese experience in residual soil characterization by DMT tests. In *Proceedings of the Second International Conference on the Flat Dilatometer – DMT 2006* (pp. 359-364). Washington D.C.

Cui, Y.-J., Tang, A.-M., Mantho, A.T., & De Laure, E. (2008). Monitoring field soil suction using a miniature tensiometer. *Geotechnical Testing Journal*, *31*(1), 100769. http://dx.doi.org/10.1520/GTJ100769.

Dai, G., Zhang, F., & Wang, Y. (2022). Stability analysis of layered slopes in unsaturated soils. *Frontiers of Structural and Civil Engineering*, *16*(3), 378-387. http://dx.doi.org/10.1007/s11709-022-0808-2.

Fagundes, L.S., & Rodrigues, R.A. (2015). Shear strength of a natural and compacted tropical soil. *The Electronic Journal of Geotechnical Engineering*, *20*, 47-58.

Fernandes, J.B. (2022). *Strength and deformability study of an unsaturated tropical soil profile* [Doctoral thesis, São Paulo State University]. São Paulo State University's repository (in Portuguese). https://repositorio.unesp.br/handle/11449/217501

Fernandes, J.B., Saab, A.L., Rocha, B.P., Rodrigues, R.A., Lodi, P.C., & Giacheti, H.L. (2022). Geomechanical parameters in the active zone of an unsaturated tropical soil site via laboratory tests. *Soils and Rocks*, *45*(4), 1-15. http://dx.doi.org/10.28927/SR.2022.000422.

Fredlund, D.G., & Rahardjo, H. (1993). *Soil mechanics for unsaturated soils*. John Wiley & Sons.

Fredlund, D.G., Morgenstern, N.R., & Widger, R.A. (1978). The shear strength of unsaturated soils. *Canadian Geotechnical Journal*, *15*(3), 313-321. http://dx.doi.org/10.1139/t78-029.

Giacheti, H.L., Bezerra, R.C., Rocha, B.P., & Rodrigues, R.A. (2019). Seasonal influence on cone penetration test: an unsaturated soil site example. *Journal of Rock Mechanics and Geotechnical Engineering*, *11*(2), 361-368. http://dx.doi.org/10.1016/j.jrmge.2018.10.005.

Giacheti, H.L., Coelho, V., & Carvalho, D. (1998). Caracterização geotécnica de dois perfis de solos tropicais com base em ensaios de laboratório. In *Anais do XI Congresso Brasileiro de Mecânica dos Solos e Engenharia de Fundações – COBRAMSEG* (pp. 195-202). São Paulo: ABMS.

Hilf, J.W. (1956). *An investigation of pore-water pressure in compacted cohesive soils*. Faculty of the Graduate School, University of Colorado.

Kang, S., Lee, S.-R., & Cho, S.-E. (2020). Slope stability analysis of unsaturated soil slopes based on the site-specific characteristics: a case study of Hwangryeong Mountain, Busan, Korea. *Sustainability*, *12*(7), 2839. http://dx.doi.org/10.3390/su12072839.

Marchetti, S. (1980). In situ tests by flat dilatometer. *Journal of the Geotechnical Engineering Division*, *106*(3), 299-321. http://dx.doi.org/10.1061/AJGEB6.0000934.

Marchetti, S. (1997). The flat dilatometer: design applications. In *Proceedings of the. Third International Geotechnical Engineering Conference - ICSMGE* (pp. 421-448). Cairo.

Marchetti, S., & Crapps, D. K. (1981). *Flat dilatometer manual*. Internal Report of G.P.E. Inc.

Marchetti, S., & Monaco, P. (2018). Recent improvements in the use, interpretation, and applications of DMT and

SDMT in practice. *Geotechnical Testing Journal*, 41(5), 20170386. http://dx.doi.org/10.1520/GTJ20170386.

Marchetti, S., Monaco, P., Totani, G., & Calabrese, M. (2001). The Flat Dilatometer Test (DMT) in soil investigations. In *Proceedings of the International Conference on in situ Measurement of Soil Properties – IN SITU 2001* (41 p.). Indonesia.

Ng, C.W., & Shi, Q. (1998). A numerical investigation of the stability of unsaturated soil slopes subjected to transient seepage. *Computers and Geotechnics*, *22*(1), 1-28. http://dx.doi.org/10.1016/S0266-352X(97)00036-0.

Ng, C.W., Zhang, L.M., & Ho, K.K. (2001). Influence of laterally loaded sleeved piles and pile groups on slope stability. *Canadian Geotechnical Journal*, *38*(3), 553-566. http://dx.doi.org/10.1139/t00-109.

Nogami, J.S., & Villibor, D.F. (1981). Uma nova classificação de solos para finalidades rodoviárias. In *Anais do Simpósio Brasileiro de Solos Tropicais em Engenharia* (pp. 30-41). Rio de Janeiro. ABMS.

Rahardjo, H., Kim, Y., & Satyanaga, A. (2019). Role of unsaturated soil mechanics in geotechnical engineering. *International Journal of Geo-Engineering*, *10*(1), 8. http://dx.doi.org/10.1186/s40703-019-0104-8.

Rocha, B.P. (2018). *Geotechnical Characterization of Unsaturated Tropical Soils by In situ tests* [Doctoral thesis, University of São Paulo]. University of São Paulo's repository (in Portuguese). https://doi.org/10.11606/T.18.2018.tde-03122018-103909

Rocha, B.P., & Giacheti, H.L. (2018). Site characterization of a tropical soil by in situ tests. *Dyna*, *85*(206), 211-219. http://dx.doi.org/10.15446/dyna.v85n206.67891.

Rocha, B.P., Rodrigues, R.A., & Giacheti, H.L. (2021). The flat dilatometer test in an unsaturated tropical soil site. *Geotechnical and Geological Engineering*, *39*(8), 5957-5969. http://dx.doi.org/10.1007/s10706-021-01849-1.

Saab, A.L. (2016). *Influence of suction on the compressibility parameters of an unsaturated soil* [Master's dissertation, São Paulo State University]. São Paulo State University's repository (in Portuguese). https://repositorio.unesp.br/bitstream/handle/11449/148696/saab_al_me_bauru.pdf?sequence=3

Schmertmann, J.H. (1986). Suggested method for performing the flat dilatometer test. *Geotechnical Testing Journal*, *9*(2), 93. http://dx.doi.org/10.1520/GTJ11035J.

Sivakumar Babu, G.L., & Murthy, D.S. (2005). Reliability analysis of unsaturated soil slopes. *Journal of Geotechnical and Geoenvironmental Engineering*, *131*(11), 1423-1428. http://dx.doi.org/10.1061/(ASCE)1090-0241(2005)131:11(1423).

Tohari, A., Nishigaki, M., & Komatsu, M. (2007). Laboratory rainfall-induced slope failure with moisture content measurement. *Journal of Geotechnical and Geoenvironmental Engineering*, *133*(5), 575-587. http://dx.doi.org/10.1061/(ASCE)1090-0241(2007)133:5(575).

Vieira, R.H.M. (2021). *Back-analysis of the slide of a planar slope of an unsaturated tropical sandy soil from Bauru-SP*. [Master's dissertation, São Paulo State University]. São Paulo State University's repository (in Portuguese). https://repositorio.unesp.br/handle/11449/215781

Soils and Rocks

An International Journal of Geotechnical and Geoenvironmental Engineering

www.soilsandrocks.com

ISSN 1980-9743
ISSN-e 2675-5475

Back-analyses of soft soil failure with "strain-softening" behavior by the "equivalent sensitivity" concept

Lennon de Souza Marcos da Silva[1#], Marcus Peigas Pacheco[1]

Article

Keywords
Finite elements
Soft soils
Slope stability
Strain-softening
Equivalent sensitivity

Abstract

Stability analyses of slopes in soft soils are usually affected by strain-softening, resulting in unrealistic (unconservative) safety factors. The loss of post peak strength cannot be accounted for by classic limit equilibrium analyses. In practice, however, the overall loss of soil strength is generally approximated by Bjerrum correction factor $\mu \leq 1$, which is believed to account for the different failure velocities during the field tests (usually vane tests) and the actual failure in the field, in addition to anisotropy (Schnaid & Odebrecht, 2012). The objective of this work is to demonstrate that strain-softening reduces the overall safety factor to a value nearly equivalent to the application of Bjerrum's correction factor. To accomplish this, a simple constitutive model (Mohr-Coulomb with residual stress) is used for total stress finite element analyses by means of the concept of "equivalent sensitivity" proposed by Pereira Pinto (2017). The results showed that equivalent sensitivity can be a great instrument to simulate the strain-softening behavior of soft soils.

1. Introduction

Low permeability soils mobilize the undrained strength when the load is applied at a rate greater than the ability of the soil to allow for dissipation of pore pressure excess. Existing techniques for pore pressure predictions in effective stress finite element analyses estimate the pore pressure by the product of the elastic volumetric strains by the bulk modulus of the water. This procedure seems to produce acceptable values mostly for stress paths under dominant volumetric strains, such as in prediction of settlements for embankments on soft clays. Unfortunately, under dominant shear distortions (as in slope stability analyses) the prediction of pore pressures is generally unreliable, as it depends strongly on the small (positive or negative) volumetric strains produced, which are generally difficult to predict (Boyce, 1978; Duncan & Wright, 2005).

In addition to difficulties to correctly predicting pore pressures, neglecting strain-softening can severely overestimate safety factors either in limiting equilibrium or FE analyses if the post-peak loss of strength is disregarded. This is demonstrated by the case history presented in this paper.

A relevant difficulty to model strain-softening is the negative stiffness produced after peak, which causes the results to be affected by the discretization of the FE mesh in the most common geotechnical software, which are based on the classic continuum of Cauchy. This means that different mesh discretizations will produce different results. More up to date software based on the generalized continuum of Coserat can address adequately negative stiffness. Unfortunately, despite the ability to model strain-softening with no dependence of mesh discretizations, these modern softwares are still prone to numerical instabilities, thus making it difficult the use on routine basis.

Strain-softening can be accommodated by correcting the undrained shear strength of the soil (S_u), determined in field or laboratory tests, by a reduction factor called Bjerrum's correction factor $\mu \leq 1$ (Bjerrum, 1972), which is correlated to the plasticity index *PI* (Cheng & Lau, 2014; Chowdhury et al., 2010). Bjerrum´s correction factor was conceived by comparing the measured undrained strength in field or laboratory tests to the strength needed to produce failure in the field, considering that the strength measured was generally higher than the true strength in the field. Therefore, according to Bjerrum (1972), the higher *PI*, the smaller the true strength. Soft soils holding high *PI* values are more susceptible to strain-softening. However, the correlation between μ and *PI* produces such a high scatter that estimating the reduction factor is prone to a great deal of uncertainty. Experience with Brazilian soft clays indicates that $\mu = 0.6$

[#]Corresponding author. E-mail address: lennon.engciv@gmail.com
[1]Universidade do Estado do Rio de Janeiro, Programa de Pós-graduação em Engenharia Civil, Rio de Janeiro, RJ, Brasil.

Submitted on May 15, 2023; Final Acceptance on October 25, 2023; Discussion open until February 28, 2024.
https://doi.org/10.28927/SR.2023.005323

to 0.8 produces generally better results regardless of the correlation with *PI*. Furthermore, in the case history presented in this paper, *PI* is very low, suggesting $\mu \cong 0$, whereas the ratio *FS* (no strain-softening)/*FS* (strain-softening) $\cong \mu$ is the range above, as typical of Brazilian clays.

In this paper, a simplified procedure to model strain-softening in undrained FE analyses is presented. As a result of strain-softening, the undrained shear strength decays to the residual value individually, in each element, as the maximum peak stress is exceeded, gradually propagating to neighboring elements by progressive rupture.

2. The equivalent sensitivity concept

Both RS2 and RS3 geotechnical software provide the option of Mohr-Coulomb constitutive model with residual stress to simulate the instantaneous loss of strength shown in Figure 1. To overcome well-known numerical limitations to handle the post peak negative stiffness shown by the dashed curve in Figure 1, Pereira Pinto (2017) proposed the concept of equivalent sensitivity (S_t^*), according to Equation 1.

$$S_t^* = \frac{S_{u,p}}{S_{u,r}^*} \qquad (1)$$

Similarly to the classical definition of soil sensitivity, the equivalent sensitivity * is given by the ratio of the peak undrained stress $S_{u,p}$ to the equivalent undrained residual stress $S_{u,r}^*$. As shown in Figure 1, strain-softening depends on the limiting strain $\epsilon_{u,p}$ above which the material softens and, therefore, the concept cannot be extended to limit equilibrium analyses. As show in this work, the equivalent residual stress $S_{u,r}^*$ is determined by back analyses of previous failures (*FS* = 1), provided that the peak strength $S_{u,p}$ and the undrained stiffness E_u are known. Accordingly, $S_{u,r}^*$ is increased gradually from $S_{u,r}^* = 1$ until failure (*FS* = 1) is achieved numerically.

For the soft soils found on the banks of the Amazon River, Pereira Pinto (2017) found an equivalent sensitivity of approximately 1.4 in 2-D finite element analyses. More recently, Silva (2021) obtained an equivalent sensitivity of 1.6 in 3-D finite element simulations, which is compatible to the value obtained in 2-D simulations. From the Authors experience in other slope stability analyses in soft soils, an equivalent sensitivity of 1.5 accommodates satisfactorily for both 2-D and 3-D analyses in most Brazilian soft clays.

3. Case study

The case study is a slope on the banks of the Amazon River, in the municipality of Santana, in the State of Amapá, Brazil. In January 2013, a catastrophic failure occurred in the river port in the vicinity of the city of Santana, resulting in human and material losses, in addition to extensive environmental damage due the spill of a large amount of iron ore into de river. After the failure, an extensive site investigation was carried out to determine the most likely mechanisms of failure.

The port activities initiated in the 50's where, at the time, the site investigation (only SPT tests) identified a deposit of quaternary soft soil on the banks of the river, as well as a more resistant tertiary material upstream (Barreiras Formation). A safety strip 140 m wide was then delimited between the riverbank and the limiting resistant soil, for which there could be no storage of ore. The original port structure was composed of a floating pier connected to the site by two steel trusses, which allowed the pier to oscillate as the tide swayed. The trusses, being close to the extremities, were called East and West. In the central portion there was a conveyor belt, which assisted in transporting the ore from the storage area (on resistant soil) to the floating pier.

In 1993 a first landslide occurred in the vicinity of the east truss, in the submerged portion of the slope, which displaced about 30,000 m³ of mass towards the bed of the

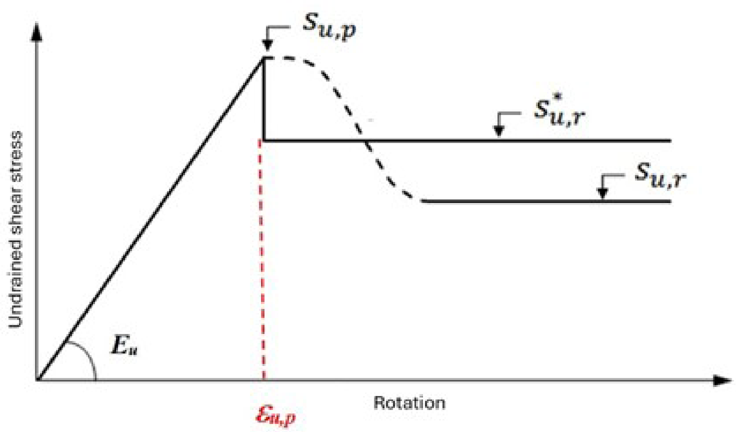

Figure 1. Equivalence between stress vs. rotation curve of the abrupt loss model and the real behavior in vane test (Pereira Pinto, 2017).

Amazon River. Figure 2 shows the scenario of the riverbank after the failure of 1993.

In 2008, a new soil investigation was carried out, which consisted of SPT, CPTu and vane tests, in addition to Atterberg limits and grain size analyses. The alluvial soft soil strip was confirmed, and the storage restrictions were strictly enforced.

In January 2013, the stack reclaimer failed, resulting in unplanned changes in ship loading. The ore began to be transported to the ships in trucks and loaders directly to the ship holds. During the period between January and March 2013, the storage position of the stacks changed continuously, sometimes advancing inadvertently the safety range of 140 m, thus allowing the placement of stockpiles on the weak soft soil. Figure 3 shows the overlapping of all identified stacks by satellite images, after failure of the stack reclaimer and before the slope failure, according to the forensic report published and discussed in Public Audience (Brasil, 2014).

In March 2013 the slope failed suddenly, with no previous warning, as typical of progressive failure triggered by

Figure 2. Scenario of the 1993 failure: 1) west truss; 2) stack reclaimer; 3) conveyor belt; and 4) east truss (Pacheco et al., 2014).

Figure 3. Overlapping of stacks between January and March 2013. The boxes in red indicate the boundary between the soft soil and the resistant soil, according to forensic studies (Pacheco, 2017).

strain-softening. The movement generated a wave about 5 to 6 meters high, comprising a collapsed area of approximately 16,000 m^2 and a detached mass volume of approximately 750,000 m^3, followed by 20,000 tons of ore that slid towards the bed of the Amazon River. The post-failed scenario is shown in Figure 4.

Figures 5 to 7 show records of the post-failure scenario and the presence of stockpiles on the strip of weak alluvial soil. Such evidence corroborates and complements what was presented in Figure 3.

A new site investigation was carried out after the accident, consisting of SPT, CPTu and vane tests. Grain size analysis and Atterberg Limit tests were also performed. Grain size analysis indicated the soft soil with about 55% silt and 25% clay particles. The Atterberg limits indicated a material of medium to high plasticity, with a medium

Figure 4. Post-failure scenario, highlight for the remaining stockpile (modified from Brasil, 2014).

Figure 5. View of the post-failure scenario, highlight for the remaining stockpile, East side (modified from Brazil, 2014).

Figure 6. Post-failure scenario, both West and East sides. Highlight for the remaining ore Stack (adapted from Pacheco, 2017).

Figure 7. Detail of the remaining stockpile at the eastern side, indicating that the failure occurred for a stack height of 6 m (Pacheco et al., 2014).

value of plasticity index (*PI*) about 25%, and with liquidity index values higher than unit at some. Figure 8 presents the distribution of the Plasticity Index with depth. Figure 9 shows the result of one vane test from the site that reproduces the strain-softening behavior, with a sensitivity value about 2.4, and Figure 10 shows the sensitivity values obtained from CPTu tests with the additional data from vane tests. CPTu soil sensitivity values calibrated from vane tests ranged between 1.5 and 4, classifying the soil sensitivity as medium to low (Pacheco et al., 2014; Pereira Pinto, 2017). Figure 11 shows the basic CPTu data (q_c, f_s and u) for one borehole that is representative of the entire deposit.

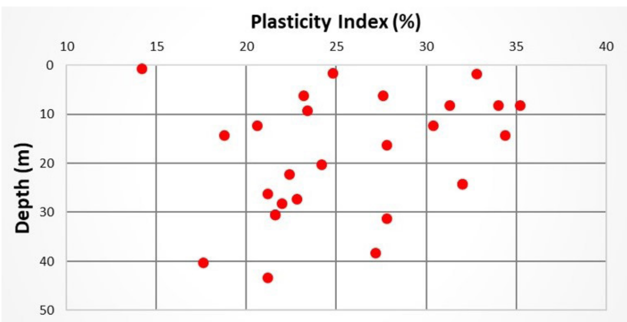

Figure 8. Spatial distribution of the Plasticity Index (*PI*) with depth.

For the sake of stability analysis, the undrained response of the material was confirmed by CPTu classification index values shown in, Figures 12 and 13. Table 1 presents the strength parameters and unit weight values used in the stability analyses. The undrained model was assumed as $E_u = 50.S_u$ for all soft soil layers.

Table 1. Strength parameters and unit weight values for stability analyses (Pereira Pinto, 2017, apud Silva, 2021).

Material	c (kPa)	$\phi(^\circ)$	$\gamma\left(\frac{kN}{m}\right)$
Fill	10	35	19
Soft soil 1	46	0	16
Soft soil 2	36	0	16
Soft soil 3	46	0	16
Soft soil 4	56	0	16
Soft soil 5	64	0	16
Resistent soil	10	35	17

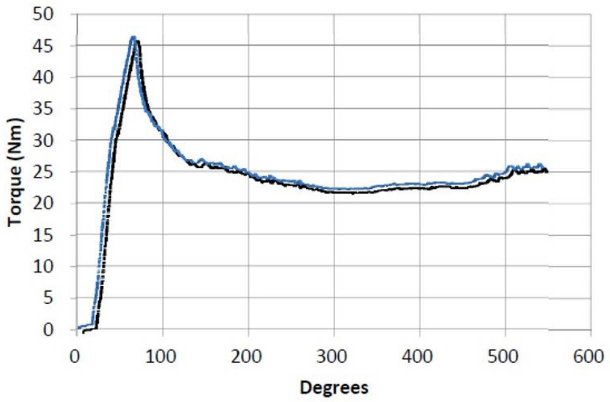

Figure 9. Typical vane test plot from the site (Pacheco et al., 2014).

4. Bidimensional stability analyses

Pacheco et al. (2014) processed 2-D stability analyses by the limit equilibrium method, with the aid of the software Slide 2. The analyses were processed using two main cross sections, also called East and West. Strain-softening was clearly identified by vane tests, according to the sensitivity values shown in Figures 9 and 10.

Pacheco et al. (2014) performed undrained analyses considering mean strength parameters reduced by Bjerrum's correction factor $\mu = 0{,}7$. The value of Bjerrum's correction factor used by Pacheco et al. (2014) was adopted considering the Brazilian experience from the literature. As can be seen in Figure 8, the spatial distribution of the plasticity index can result in several values of correction factor. However, the higher values of plasticity index seem to justify the use of the correction factor. Figure 14 shows a comparison of Brazilian values (Almeida et al., 2008; Azzouz et al, 1983; Bello, 2004; Magnani, 2006; Massad, 1999; Oliveira, 2000; Oliveira & Coutinho, 2000; Sandroni, 1993; Silva et al., 2022; Tabajara, 2021) for Bjerrum's correction factor. Considering only the medium value of the plasticity index of the deposit (PI = 25%), the correspondent value of correction factor is about 0.95, what would result in no change in the undrained shear strength. Pacheco et al. (2014) concluded that, for the Brazilian soils, the correction factor should be studied

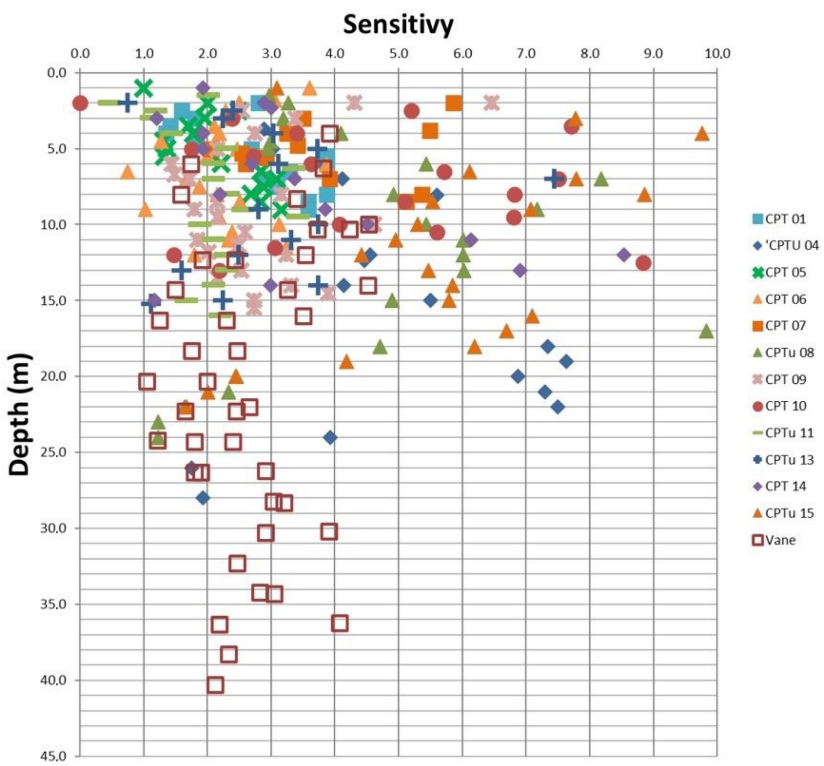

Figure 10. Soil sensitivity obtained by vane tests and correlation with CPTu tests (adapted from Pacheco et al., 2014).

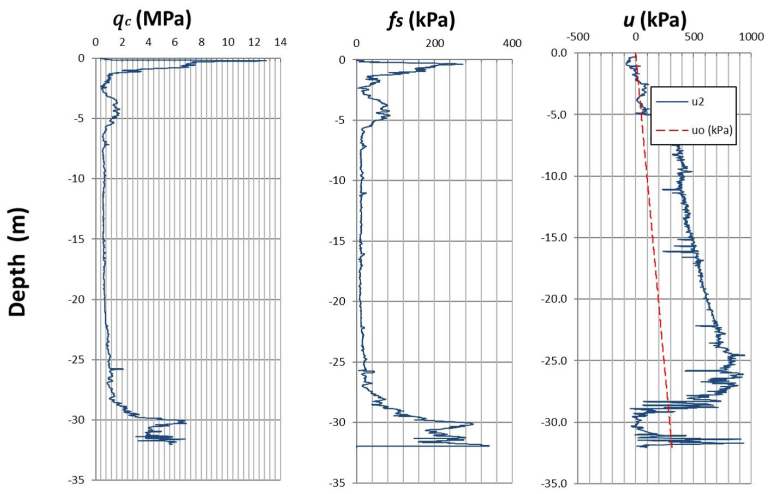

Figure 11. Basic CPTu data for one borehole - q_c, f_s and u.

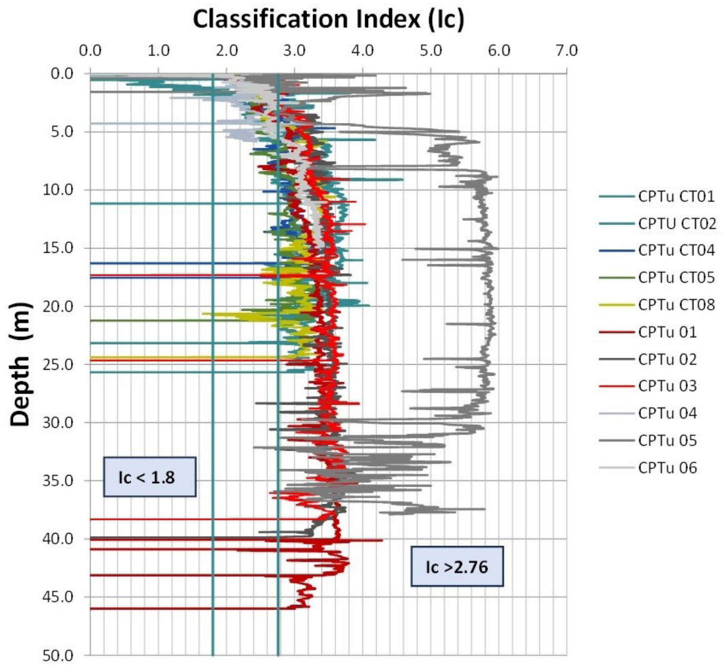

Figure 12. Classification index, West side (Pereira Pinto, 2017).

carefully and individually. Stability scenarios were also verified with and without the presence of ore stacks.

Pereira Pinto (2017), with the aid of software RS2 conducted 2-D finite element stability analyses. The East and West cross sections were again used, in addition to the same scenarios without loading and with loading simulating the ore stacks. Pereira Pinto (2017) used his proposed method of equivalent sensitivity to simulate strain-softening and found nearly the same safety factors as Pacheco et al. (2014) for undrained strength corrected by $\mu = 0{,}7$: *(i)* $FS \cong 1{,}4$ (no stockpiles) and *(ii)* $FS = 0.98$ (with stockpiles).

5. Three-dimensional stability analyses

Three-dimensional analyses were performed with the aid of the RS3 software, aiming at verifying the influence and applicability of the concept of equivalent sensitivity (Pereira Pinto, 2017) to 3D modelling, as well as to cross checking the most likely failure scenario.

The analyses were processed in two modalities, *(i)* analyses without loading, with the objective of verifying only the influence of strain-softening and *(ii)* analyses simulating the loads from the ore stacks, to check the joint interaction of the ore stacks and strain-softening.

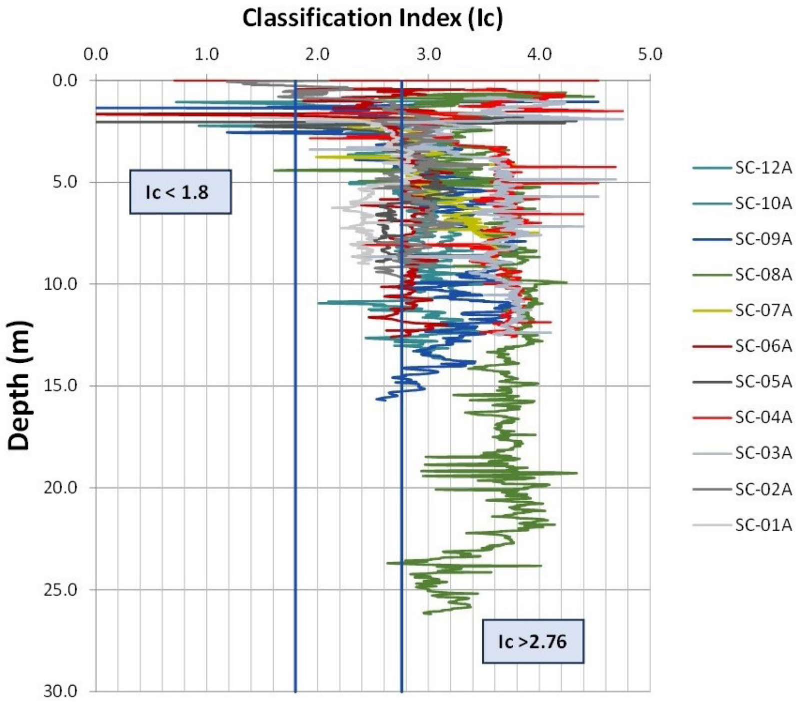

Figure 13. Classification index, East side (Pereira Pinto, 2017).

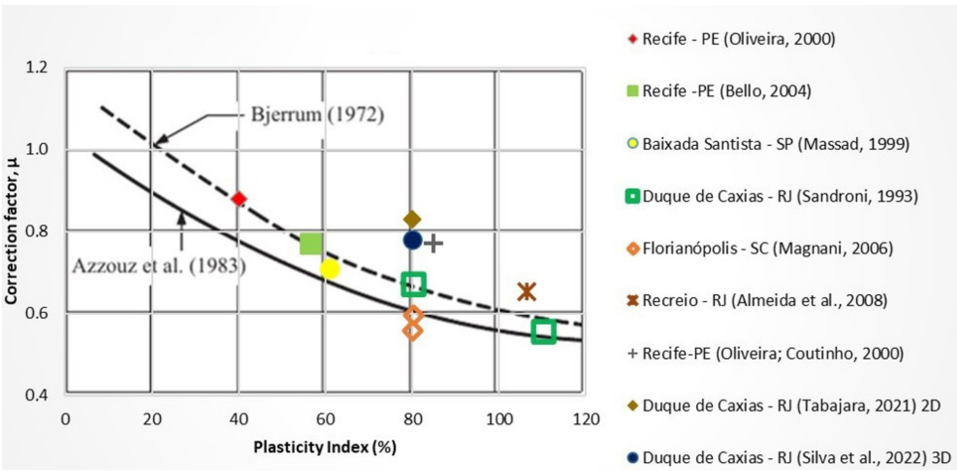

Figure 14. Undrained shear strength correction factor and plasticity index considering international and Brazilian experience (adapted from Schnaid & Odebrecht, 2012).

The three-dimensional model (Silva, 2021) used twenty-four different cross sections representing the entire area of interest, instead of only two cross sections (East and West) used by Pacheco et al. (2014) and Pereira Pinto (2017). The cross sections were drawn from the bathymetric survey of 2007, the only one available before the 2013 accident, thus representing the geometric shape of the slope before the 2013 failure and accounting for the remaining scar of the landslide of 1993. The three-dimensional model is shown in Figure 15.

The East and West cross sections shown in Figures 16 and 17 are the same used by Pacheco et al. (2014) and Pereira Pinto (2017).

Regarding the stockpile loading, a circular uniform load of 150 kPa was adopted, corresponding to the 6 m high ore stack shown in Figure 7. The distributed load was applied in three different loading stages, with increasing radius. The variation in the size of the loaded area had the objective of simulating the increasing variation of the ore stacks, considering part of the stack stored in resistant soil and part inadvertently stored within the safety range of soft soil.

The 3-D finite element analyses processed without ore stacks and without strain-softening, indicated a safety factor close to 1.8 (Silva, 2021), whereas the corresponding 2-D analyses by Pereira Pinto (2017) indicated a safety factor of the order of 1.4. For slopes with geometrically uniform cross-section, the difference between 2-D and 3-D safety factors is generally smaller than 10%, where 3-D safety factors are usually higher than 2-D. In the present analyses, however, this difference is about 28%, indicating the tridimensional effect of the concave scar produced by the 1993 failure. In Table 2, for $S_t^* = 1$ (stockpile loading and no strain-softening), $FS = 1.54$.

Table 2 shows safety factors obtained for each equivalent sensitivity considered in the back-analysis. According to Figure 1, the equivalent sensitivity is lower than the medium sensitivity values obtained by field tests.

The results above seem on first thought to indicate reasonably safe stability conditions. However, when strain-softening is incorporated into the analyses, the results processed with stack loading indicated $FS = 1$ for $S_t^* = 1.6$, according to the back-analysis shown in Table 2, thus simulating the failure scenario in Figure 18.

Validation of the critical failure surface is provided by observation of the contours of maximum shear strains (Bradley & Vandenberge, 2015). Accordingly, the maximum shear strain contours in Figure 18 indicate a deep failure throughout the soft soil region, propagating progressively from the riverbank towards the upstream resistant soil, as verified in the field, denoting the triggering scenario of the failure.

For comparison, Figures 19 and 20 present the contours of maximum shear strains for an auxiliary cross-section located under the ore stacks. The failure scenario is shown in Figure 20.

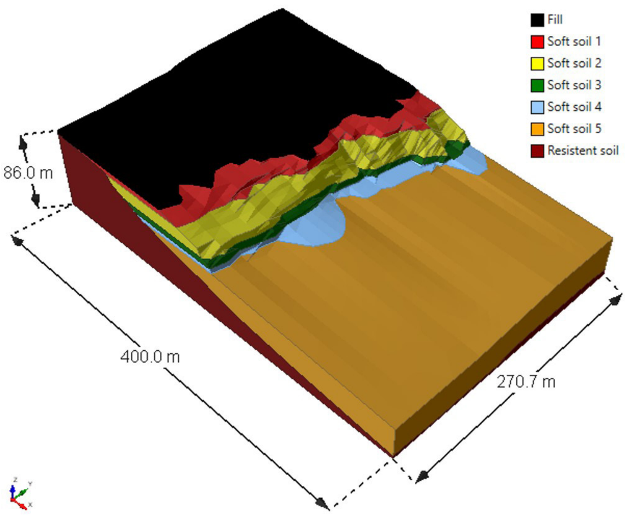

Figure 15. Three-dimensional slope model (adapted from Silva, 2021).

Table 2. Safety factors for back analyses with load and post-peak strength loss.

Equivalent sensitivity (S_{t^*})	*FS*
1.0*	1.54
1.4	1.13
1.5	1.08
1.6	1.0

*No strain-softening.

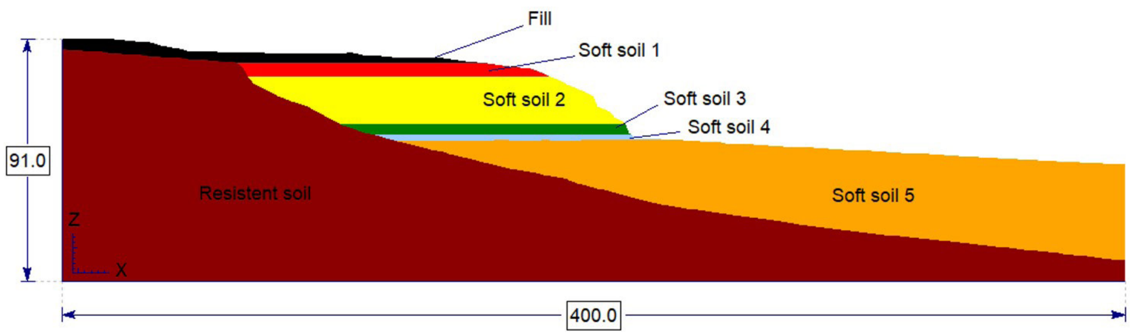

Figure 16. East cross section, drawn from the three-dimensional model.

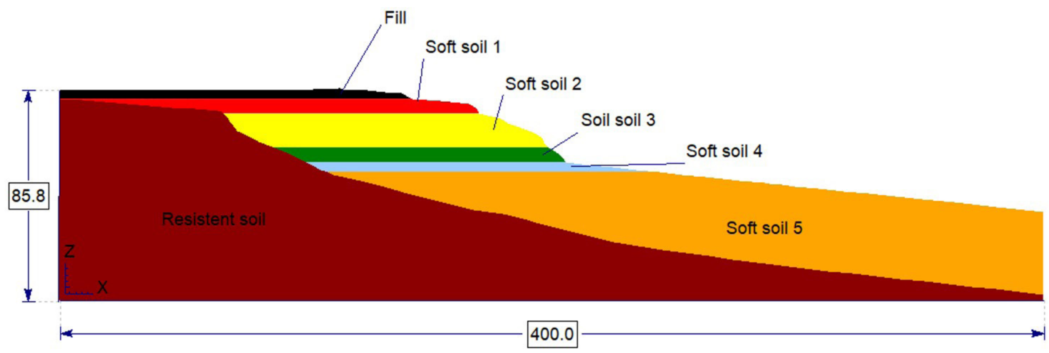

Figure 17. West cross section, drawn from the three-dimensional model.

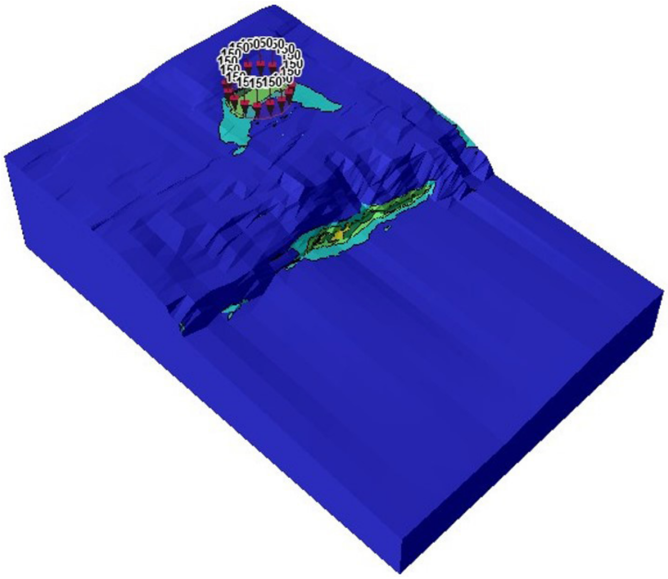

Figure 18. Contours of maximum shear strains at failure, for the analysis with stockpile loading and strain-softening (Silva, 2021).

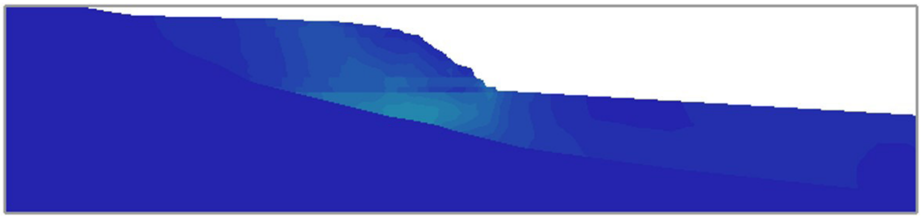

Figure 19. Maximum shear strains - no loading and no strain-softening, *FS* = 1.8 (Silva, 2021).

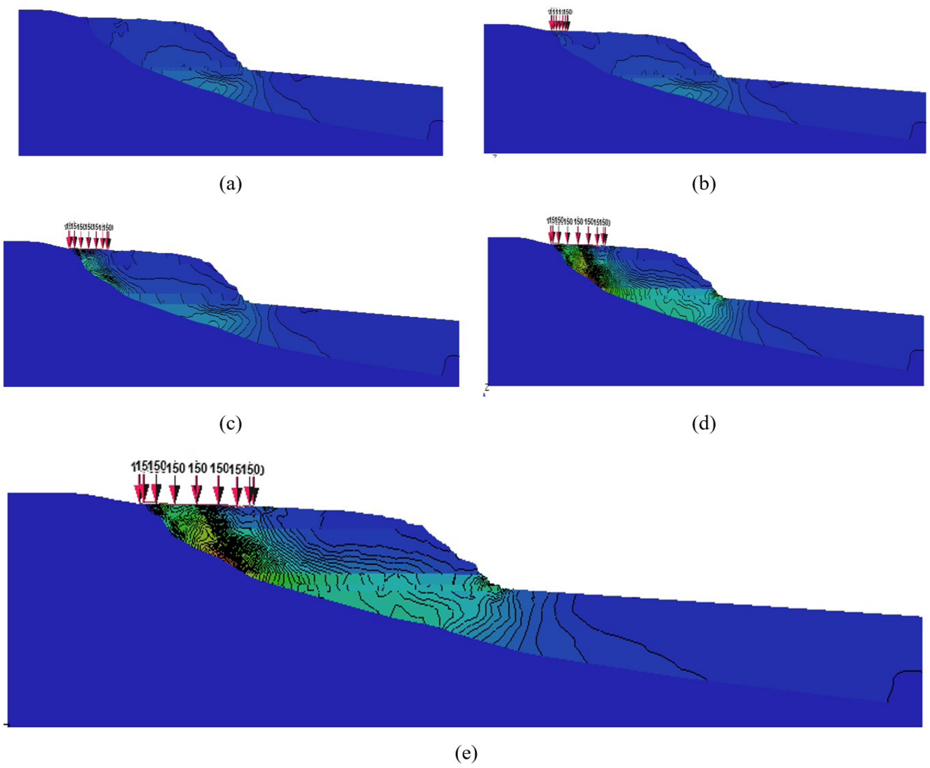

Figure 20. Maximum shear strains as loading increases: (a) initial condition, no load; (b) load with radius of 7.5 m; (c) load of radius of 17.5m; (d) load of radius of 25 m; (e) load with radius of 50 m (Silva, 2021).

6. Conclusions

The three-dimensional analyses presented by Silva (2021) validate the concept of equivalent sensitivity for Brazilian soft soils of low to medium sensitivity proposed by Pereira Pinto (2017) in bidimensional analyses. The equivalent sensitivity obtained by Silva (2021), in the three-dimensional model (S_{t^*}= 1.6), is compatible with the value obtained by Pereira Pinto (2017), in the two-dimensional model (S_{t^*} = 1.4). For practical purposes, an equivalent sensitivity (S_{t^*}= 1.5) seems satisfactory in both the 3-D and 2-D models.

Both 2-D and 3-D analyses show that significant unconservative errors are obtained in stability analyses that neglect strain-softening on medium to low sensitivity clays commonly found in Brazil, leading to unrealistic and excessively high safety factors.

For the 3-D analyses presented in this work, it is concluded that ratio between *FS* (strain-softening)/*FS* (no strain-softening) = 1/1.54 = 0.65 is approximately the stress reduction corresponding to Bjerrum correction factor. Further research is needed to determine the corresponding contribution of strain-softening, difference of shear velocity and anisotropy on the shear stress reduction in the field.

Realistic safety factor values can be obtained from conventional limit equilibrium analysis with application of the Bjerrum's correction factor (1972) to correct (reduce) the mean undrained resistance of the soft soils obtained in laboratory and field tests. However, Bjerrum's correction factor should be selected with good engineering judgment, due to the high uncertainty in selecting appropriate μ values as a function of the Plasticity Index (*PI*). From the Authors experience, values of the correction factor should be in the range of 0.6 to 0.8 regardless of *PI*, for Brazilian soft soils of medium to low sensitivity.

The equivalent sensitivity model proposed by Pereira Pinto (2017) coupled to the Mohr-Coulomb constitutive model with residual stresses provides a simple and stable numerical processing, independent of the discretization of the finite element mesh.

Acknowledgements

The authors are grateful to the State University of Rio de Janeiro for the financial support provided by the research program PROCIENCIA.

Declaration of interest

The authors have no conflicts of interest to declare. All co-authors have observed and affirmed the contents of the paper and there is no financial interest to report.

Authors' contributions

Lennon de Souza Marcos da Silva: M. Sc. Dissertation (conceptualization, methodology, writing – original draft).

Marcus Peigas Pacheco: Dissertation Advisor (supervision, writing – reviewing and editing).

Data availability

The datasets generated analyzed during the current study are available from the corresponding author upon request. All data produced or examined during the current study are included in this article.

List of symbols

c	Cohesion
CPT_u	Cone Penetration Test with pore pressure measurement
E_u	Undrained stiffness
FS	Safety Factor
PI	Plasticity Index
SPT	Standard Penetration Test
SRF	Strength Reduction Factor
S_u	Undrained Shear Strength
$S_{u,p}$	Peak undrained shear strength
$S_{u,r}$	Residual undrained shear strength
$S_{u,r}^*$	Equivalent residual shear strength
S_{t^*}	Equivalent sensitivity
γ	Specific weight of soil
$\epsilon_{u,p}$	Undrained limiting strain
μ	Bjerrum's correction factor
ϕ	Angle of internal friction of soil
ϕ_u	Undrained angle of internal friction of soil

References

Almeida, M.S.S.A., Marques, M.E.S., Lima, B.T., & Alves, F. (2008). Failure of a reinforced embankment on an extremely soft peat clay layer. In *Proceedings of the 4th European Geosynthetics Conference*, Edinburgh.

Azzouz, A.S., Baligh, M.M., & Ladd, C.C. (1983). Corrected field vane strength for embankment design. *Journal of the Geotechnical Engineering Division*, 109(5), 730-734.

Bello, M.I.M.C. (2004). *Estudo de ruptura em aterro sobre solos moles: aterro do galpão localizado na BR-101 – PE* [Master's dissertation, Federal University of Pernanbuco]. Federal University of Pernambuco's repository (in Portuguese). Retrieved in April 30, 2023, from https://repositorio.ufpe.br/handle/123456789/5692

Bjerrum, L. (1972). Embankments on soft ground. In *Proceedings of the ASCE Specialty Conference on Performance of Earth and Earth Supported Structures* (Vol. 2, pp. 1-54), West Laffayette. Purdue University.

Boyce, S.C. (1978). *Total stress vs effective stress stability analysis of embankments on soft clays* [Master's thesis, Massachusetts Institute of Technology]. Massachusetts Institute of Technology's repository. Retrieved in April 30, 2023, from https://apps.dtic.mil/sti/citations/ADA070839

Bradley, N., & Vandenberge, D.R. (2015). *Beginner's guide for geotechnical finite element analyses*. Blacksburg, VA: Virginia Polytechnic Institute and State University.

Brasil. Câmara dos Deputados. (2014). *Reconstrução do porto de minério da ICOMI no Amapá: Audiência Pública Ordinária.* Retrieved in April 30, 2023, from https://www2.camara.leg.br/atividade-legislativa/comissoes/comissoes-temporarias/externas/54a-legislatura/reconstrucao-do-porto-de-minerio-da-icomi-no-amapa/audiencias-publicas/RelatriodeRegulacaoAngloAmericanMaio2014Edicao1.pdf

Cheng, Y.M.; & Lau, C. K. (2014). *Slope stability and stabilization: new methods and insight.* London: Taylor & Francis.

Chowdhury, R., Bhattacharya, G., & Metya, S. (2010). *Geotechnical slope analysis*. Boca Raton: Taylor & Francis Group.

Duncan, J.M., & Wright, S.G. (2005). *Soil strength and slope stability* (1st ed.). Newark: John Wiley & Sons.

Magnani, H. (2006). *Comportamento de aterro reforçado sobre solos moles levado a ruptura* [Doctoral thesis, Federal University of Rio de Janeiro]. Federal University of Rio de Janeiro's repository (in Portuguese). Retrieved in April 30, 2023, from http://www.coc.ufrj.br/pt/teses-de-doutorado/150-2006/1071-henrique-magnani-de-oliveira

Massad, F. (1999). Baixada Santista: implicações na história geológica no projeto de fundações. *Solos e Rochas*, 22(1), 3-49 (in Portuguese).

Oliveira, A.T.J. (2000). *Uso de um equipamento elétrico de palheta em argilas do Recife* [Master's dissertation]. Federal University of Pernambuco (in Portuguese).

Oliveira, A.T.J., Coutinho, R.Q. (2000). Utilização de um equipamento elétrico de palheta de campo em uma argila mole de Recife. In *Anais do Seminário Brasileiro de Investigação de Campo (BIC'2000)*, São Paulo (in Portuguese).

Pacheco, M. (2017). *Estabilidade de solos moles e o acidente do Porto de Santana no Amapá.* Clube de Engenharia. Retrieved in September 20, 2020, from https://www.youtube.com/watch?v=pzHYglgPyrM

Pacheco, M., Gerscovich, D.S., & Danziger, B.R. (2014). *Relatório técnico: parecer sobre a ruptura do talude do Porto de Santana – Amapá*. Rio de Janeiro: Universidade do Estado do Rio de Janeiro (in Portuguese).

Pereira Pinto, G. (2017). *A influência da sensibilidade na estabilidade de solos moles brasileiros* [Master's dissertation, State University of Rio de Janeiro]. State University of Rio de Janeiro's repository (in Portuguese). Retrieved in April 30, 2023, from http://www.labbas.eng.uerj.br/pgeciv/nova/index.php?menu=dissertacoes

Sandroni, S.S. (1993). Sobre o uso dos ensaios de palheta no projeto de aterros sobre argilas moles. *Solos e Rochas*, 16(3), 207-213(in Portuguese).

Schnaid, F., & Odebrecht, E. (2012). *Ensaios de campo e suas aplicações à engenharia de fundações*. São Paulo: Oficina de Textos.

Silva, L.S.M. (2021). *Análise tridimensional de taludes em solos moles* [Master's dissertation, State University of Rio de Janeiro]. State University of Rio de Janeiro's repository (in Portuguese). Retrieved in April 30, 2023, from http://www.labbas.eng.uerj.br/pgeciv/nova/index.php?menu=dissertacoes

Silva, L.S.M., Tabajara, J.B., Gerscovich, D.M.S., & Pacheco, M.P. (2022). Análise tridimensional de um aterro sobre argila mole levado à rupture. In *Anais da VIII Conferência Brasileira sobre Estabilidade de Encostas* (pp. 87-93), Porto de Galinhas (in Portuguese).

Tabajara, J.B. (2021). *Avaliação das abordagens em termos de tensão total e efetiva em estudos de estabilidade de aterro sobre solos compressíveis* [Master's dissertation, State University of Rio de Janeiro]. State University of Rio de Janeiro's repository (in Portuguese). Retrieved in April 30, 2023, from http://www.labbas.eng.uerj.br/pgeciv/nova/index.php?menu=dissertacoes

Soils and Rocks
An International Journal of Geotechnical and Geoenvironmental Engineering
www.soilsandrocks.com
ISSN 1980-9743
ISSN-e 2675-5475

Influence of the degree of saturation and the wetting front on the stability of cliffs: a case study on a cliff located on the beach of Tabatinga-RN-Brazil

Allan Benício Silva de Medeiros[1#], Romário Stéffano Amaro da Silva[1], Valteson da Silva Santos[2], Olavo Francisco dos Santos Junior[2], Ricardo Nascimento Flores Severo[3], Osvaldo de Freitas Neto[2], Bruna Silveira Lira[4]

Article

Keywords
Slope stability
Limit-equilibrium methods
Stress analysis methods
Barreiras formation

Abstract

Coastal zones are of great interest in civil engineering due to their economic relevance and active geological dynamics. In Brazil, the development of these regions is related to the use of their geomorphological features in the landscape, among which the cliffs stand out. Although there are studies that consider the influence of the wetting front in stability analysis with cliffs, in general, the studies only consider extreme saturation situations (dry and saturated). In this sense, the present study aims to understand the influence of the wetting front and the degree of saturation reached by the materials in the stability of cliffs composed of Barreiras Formation soil. The stability analyses were carried out using the limit equilibrium method and stress analysis, varying the degrees of saturation of the materials and wetting fronts of a model of a cliff located at Praia de Tabatinga, State of Rio Grande do Norte, Brazil. Failures were identified, in different wetting fronts, by the limit equilibrium method from degrees of saturation around 20%, and by the stress analysis method around 40%. Thus, it was concluded that the variation in the degree of saturation has a preponderant effect on the destabilization of a cliff, since partial saturations are already enough to trigger significant mass movements. It was also noticeable that the wetting front is a relevant effect on instability, although conditioned to the degree of saturation reached, which may enhance the order of magnitude of the identified failures.

1. Introduction

Due to the active dynamics of coastal regions, the study of slope stability conditions in these regions, as well as the monitoring of mass movements that occur on these slopes, is a relevant topic for society (Collins & Sitar, 2008; Epifanio et al., 2013; Marques et al., 2013; Martino & Mazzanti, 2014; Barbosa et al., 2020; Prémaillon et al., 2021). In Rio Grande do Norte, the economy of the coastal regions is usually linked to the development of tourism, which is related to the scenic beauty associated with the presence of cliffs. The term coastal cliff refers to a vertical, or nearly vertical surface angle, formed from the meeting of the continent with the ocean. Cliffs are geomorphological features that occur at all latitudes along about 80% of the world's coastlines (Emery & Kuhn, 1982). In general, the stability of a cliff cannot be guaranteed, since retreat movements and increases in the continental line are continuous in the long term, being a cyclical process of failure and temporary stabilization (Richards & Lorriman, 1987; Silva et al., 2020). Within this cyclical process, the cliffs become unstable when the mobilizing stresses in the massif reach the limit of the mechanical strength of the material. This condition can be reached by the intervention of internal or external agents. In this context, one can highlight the increase in the degree of saturation of the materials.

It is common in engineering, especially in project development, that the soil is considered only under saturated

[#] Corresponding author. E-mail address: allan.medeiros.702@ufrn.edu.br
[1] Universidade Federal do Rio Grande do Norte, Programa de Pós-Graduação em Engenharia Civil e Ambiental, Natal, RN, Brasil.
[2] Universidade Federal do Rio Grande do Norte, Departamento de Engenharia Civil, Natal, RN, Brasil.
[3] Instituto Federal de Educação, Ciência e Tecnologia do Rio Grande do Norte, Natal, RN, Brasil.
[4] Universidade Federal do Piauí, Departamento de Recursos Hídricos, Geotecnia e Engenharia Sanitária, Teresina, PI, Brasil.

Submitted on May 15, 2023; Final Acceptance on October 25, 2023; Discussion open until February 28, 2024.
https://doi.org/10.28927/SR.2023.005423

condition. However, the suction present in situations of lower saturation causes increases in the mechanical strength of the soil, in the form of apparent cohesion. This increment may be sufficient, for example, to stabilize a natural slope (Fredlund et al., 2012).

Due to their coastal location, coastal cliffs, especially those in tropical regions, tend to show intermediate degrees of saturation over time. The intermediate saturations are justified due to the natural seasonality of the contact between the waves and the cliffs, and the rainfall patterns in these regions. The increase in the degree of saturation in the profile of soils that make up a cliff can trigger mass movements (Duperret et al., 2002; Hampton, 2002; Collins & Sitar, 2008; Barbosa et al., 2020). Thus, aiming at a better understanding of cliff stability conditions, it is rational to realize the importance of considering saturation gradually. Associated to this thougth, it is important to identify under which material range saturation will occur, since it is in this area that there will be a decrease in strength.

Therefore, although the importance of this gradual variation in the saturation of coastal cliffs is perceived, in general, the dry and/or saturated horizons are considered in the development of stability analysis (Pacheco et al., 2006; Barbosa et al., 2020). In view of the above, this study aims to evaluate how the variation in the degree of saturation and the increase in the wetting front can influence the stability of a cliff, based on the case study of a cliff located in northeastern Brazil.

2. Materials

In several stretches of the Brazilian coast, the presence of cliffs is the result of the meeting of the sea with the Barreiras Formation. The edge of the coastal tablelands in contact with the sea through continental and marine erosion processes originate the cliffs that appear as abrupt changes in terrain. The cliff evaluated in the present study is the same one studied by Silva (2019) and Morais et al. (2020). This cliff can be found along the coastline of Barra de Tabatinga Beach, located on the southern coast of the state of Rio Grande do Norte, Brazil, as shown in Figure 1. It is composed of layered sediments from the Barreiras Formation. The Barreiras Formation has an origin dated between the Miocene and the Pliocene, and extends from Rio de Janeiro to Amapá. This geological unit consists of a sedimentary cover, with intercalated layers of claystones, siltstones and sandstones, presenting in its composition different contents of silt, clay, and conglomeratic sandstones. (Santos Júnior et al., 2015).

To determine the geotechnical characteristics of the sediments that make up the cliff, it was divided into three distinct layers, called Top, Middle and Bottom layers. The geotechnical characteristics were necessary for the implementation of numerical models applied to the cliff. The Top and Middle layers are approximately 15 meters thick, while the Bottom layer is approximately 10 meters thick, as shown in Figure 2. The materials that make up this cliff are stratified sediments of the Barreiras Formation,

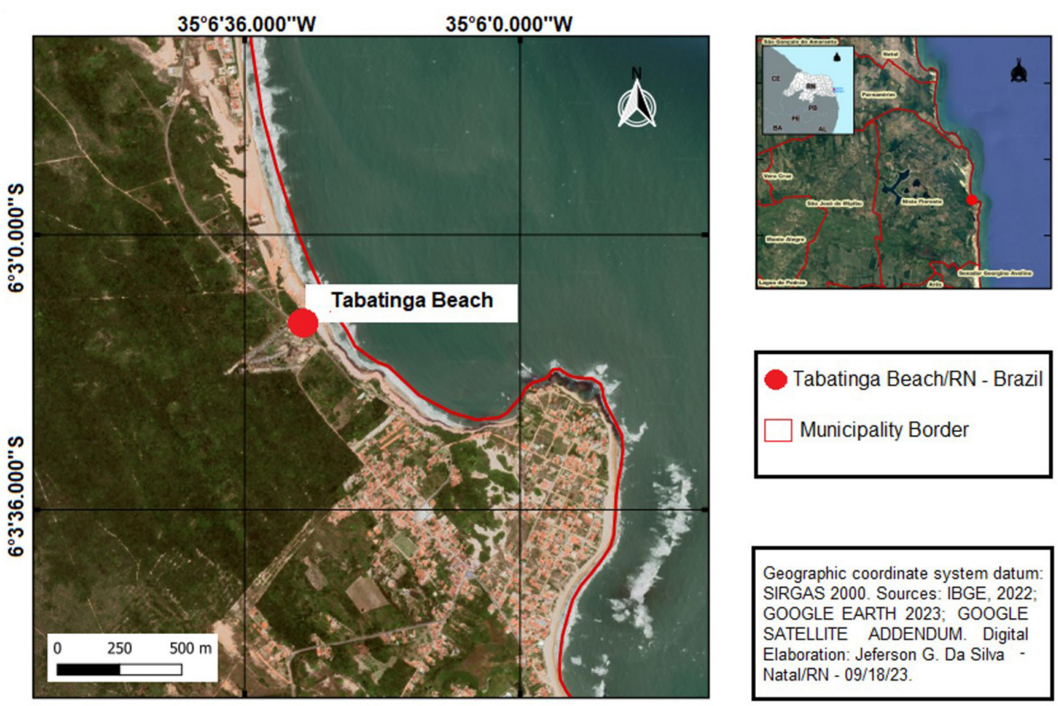

Figure 1. Location of the study area.

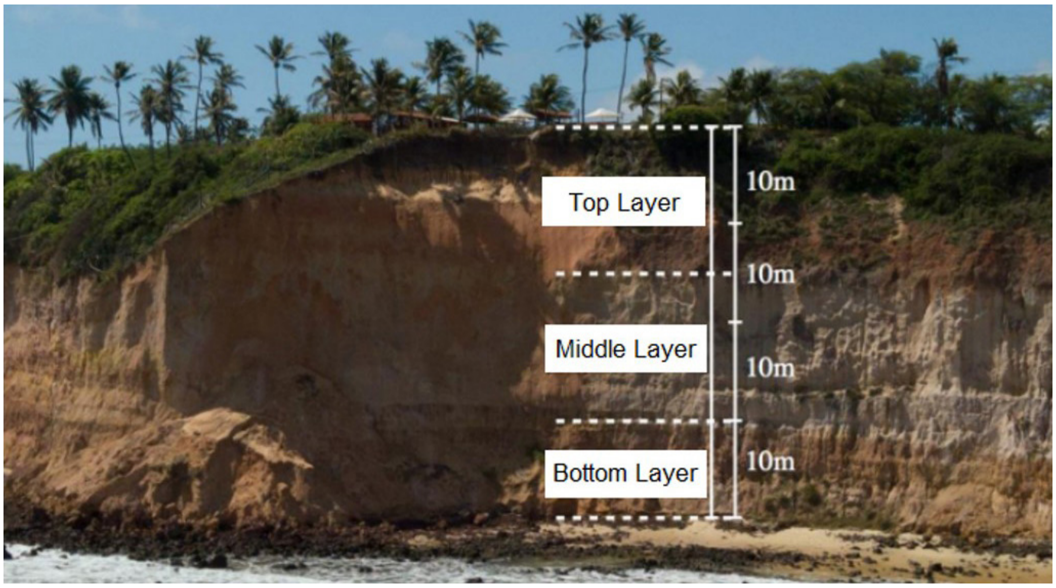

Figure 2. Typical profile and height of the sediment layers that make up the cliff (Adapted from Silva, 2019).

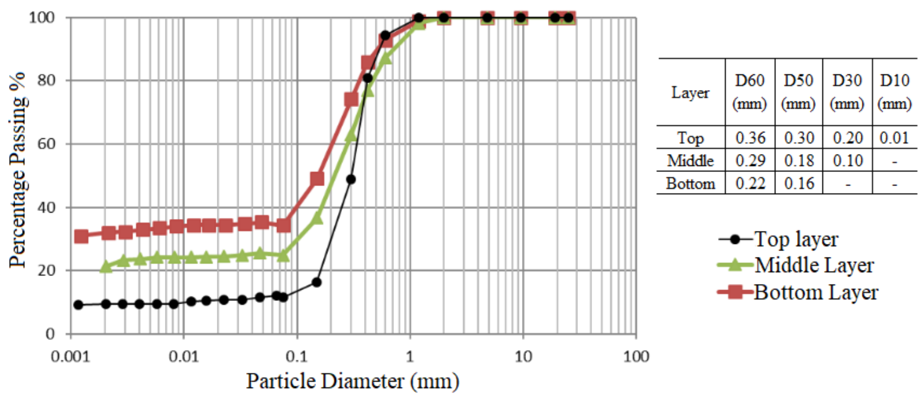

Layer	D60 (mm)	D50 (mm)	D30 (mm)	D10 (mm)
Top	0.36	0.30	0.20	0.01
Middle	0.29	0.18	0.10	-
Bottom	0.22	0.16	-	-

Figure 3. Granulometric Curve of materials (Adapted from Morais et al., 2020).

predominantly sandy, and present different levels of natural cementation. The occurrence of tension cracks on the top of the cliff resulting from the concentration of tensile stresses in this region, and incisions at its base resulting from maritime action were observed (Silva, 2019).

Morais et al. (2020) carried out geotechnical characterization and mechanical strength tests from undisturbed samples collected from each of the three cliff layers. These results were used as input parameters for the stability analysis performed in this study.

The material present in the bottom layer of the cliff is quite heterogeneous, predominantly yellow in color, with rusty reddish-purple veins. It presents a higher degree of consolidation among the studied samples. The material present in the middle layer of the cliff is white or gray in color. Like the bottom layer, it has reddish veins, although to a lesser extent. This material presents an intermediate level of consolidation among the studied materials. The component material of the top layer of the cliff presents greater homogeneity among those studied, having a reddish color and the absence of ferruginous veins. It presents easy disintegration and a lower degree of consolidation among the studied materials. The results of the characterization tests obtained by Morais et al. (2020) are shown in both Figure 3 and Table 1.

The authors experimentally determined soil-water characteristic curves using both the filter paper and tensile table methods. These curves were adjusted by the equations proposed by Van Genuchten (1980), when unimodal, and Durner (1994), when bimodal. Furthermore, the authors conducted CU (Consolidated Undrained) and CD (Consolidated Drained) triaxial tests to assess the saturated condition, and CW (Constant Water Content) triaxial tests to assess the unsaturated condition, resulting in the determination of friction angles and cohesive intercepts.

Table 1. Results of characterization tests of the sediments that make up the cliff (Adapted from Morais et al., 2020).

Layer	γ_s (kN/m³)	γ_d (kN/m³)	γ_{sat} (kN/m³)	Void Ratio	*LL* (%)	*PL* (%)	SUCS
Top	26.3	16.5	20.3	0.60	N.L.	N.P.	SP
Middle	26.3	17.6	20.9	0.50	18	15	SM
Bottom	26.6	18.8	21.7	0.41	25	19	SM-SC

Table 2. Sediment strength parameter (Adapted from Morais et al., 2020).

Layer	Saturated Condition		Unsaturated Condition	
	φ'(°)	c' (kPa)	φ'(°)	c'_{ap} (kPa)
Top	30.7	4.65	35.67	65.48
Middle	29.7	12.01	37.92	120.93
Bottom	30.2	17.8	42.74	276.38

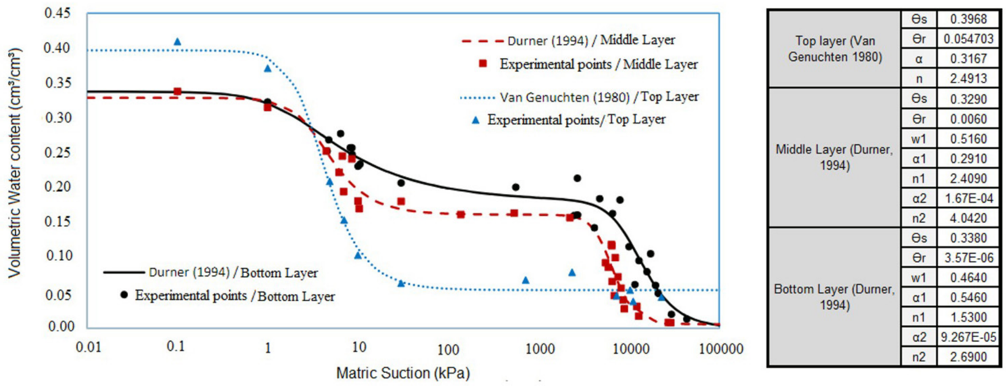

Figure 4. Soil-water characteristic curves and adjustments used (Adapted from Morais et al., 2020).

The average moisture content obtained in the test specimens for the apparent cohesion are 2.47% for the Bottom Layer, 0.47% for the Middle Layer and 2.01% for the Top Layer (Morais, 2019). The experimental retention curves and their respective adjustments are shown in Figure 4, and the strength parameters are shown in Table 2.

3. Methods

Stability analysis were performed using the Morgenstern-Price method (Morgenstern & Price, 1965), based on the concept of limit equilibrium, using the Mohr-Coulomb failure criteria. Furthermore, was used the stress analysis method proposed by Collins & Sitar (2011). According to Barbosa et al. (2020), in order to study an unfavorable condition of stability, a geometry was adopted for the cliff that has a basal incision one meter high and three meters deep. The geometry model is shown in Figure 5. The GeoStudio software library was used employing Slope/W for the limit equilibrium analysis and Sigma/W for the stress analysis.

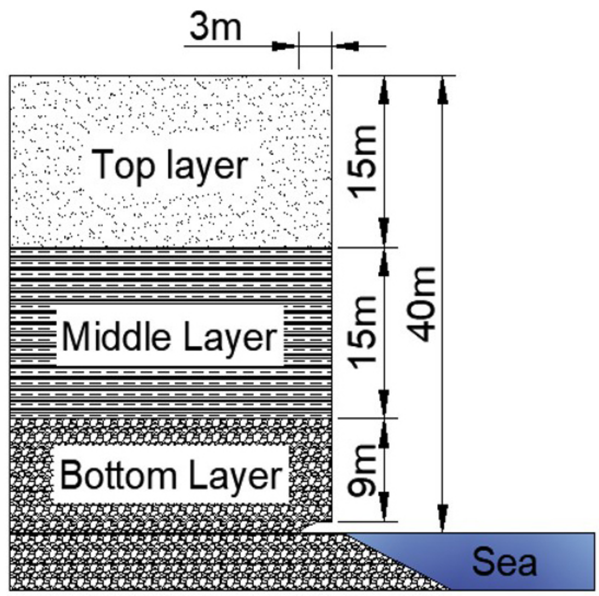

Figure 5. Geometry of the cliff used for stability analysis.

3.1 Limit equilibrium analysis methodology

Seven hypotheses were considered to simulate the variation of the wetting front, as shown in Figure 6. The regions of the massif not specified as wet/humid were considered completely dry, while those considered wet/humid had their degree of saturation varied.

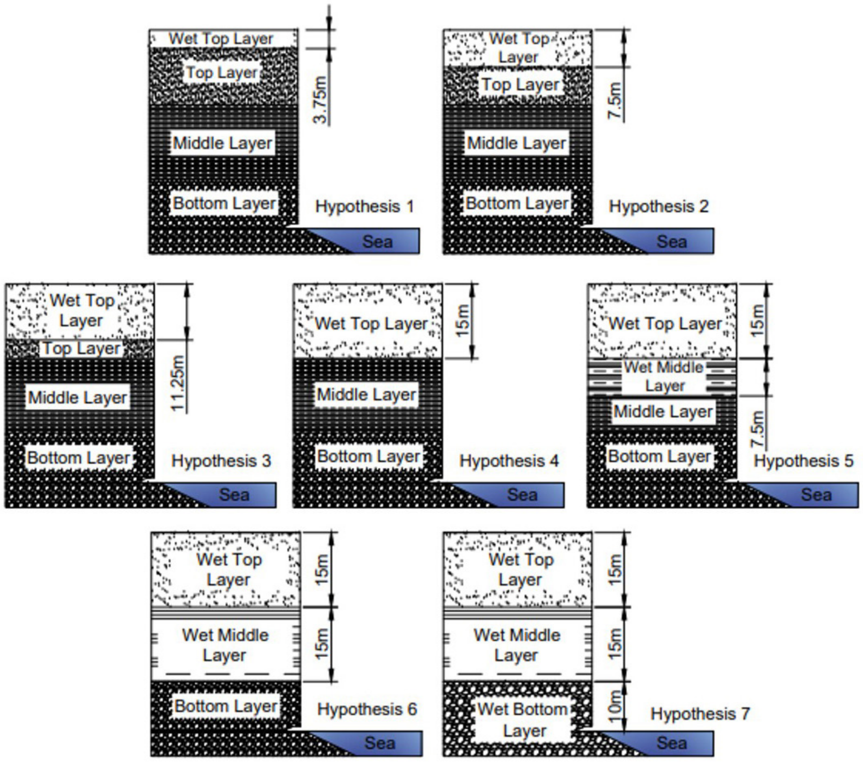

Figure 6. Wetting front depth assumptions used in limit equilibrium analysis.

Table 3. Variation of cohesion and specific weight according to the degree of saturation (Adapted from Morais et al., 2020).

Layer	S (%)	0%	10%	17.5%	20%	40%	47.5%	48.5%	60%	80%	100%
Top	c' (kPa)	65.2	65.1	22.3	15.3	8.04	7.35	7.27	6.58	5.65	4.65
	γ (kN/m^3)	16.5	16.9	17.2	17.3	18	18.3	18.3	18.8	19.5	20.3
Middle	c' (kPa)	120.2	118.7	118	117.9	116	97.6	38	16.7	14.2	12
	γ (kN/m^3)	17.6	17.9	18.2	18.3	18.9	19.2	19.2	19.6	20.3	20.9
Bottom	c' (kPa)	276.1	275.8	268.7	268	261.8	260.9	260.5	243	24. 1	17.8
	γ (kN/m^3)	18.8	19.1	19.3	19.4	20	20.2	20.2	20.5	21.1	21.7

For each wetting front condition, 10 different degrees of saturation were applied to the wetted fractions. The friction angles of the saturated condition obtained by Morais et al. (2020) were used in the analysis, as shown in Table 2. The degrees of saturation applied in the limit equilibrium analysis were 0%, 10%, 17.5%, 20%, 40%, 47.5%, 48.5%, 60%, 80% and 100%. The determination of the degrees of saturation used for the development of the stability analysis was made from an evaluation of the sensitivity of the apparent cohesion. Cohesion variation was performed according to the prediction of active cohesion using Vilar (2007) hyperbolic model. The hyperbolic adjustments were calibrated according to the soil-water characteristic curves and strength parameters obtained by Morais et al. (2020). Due to the bimodal format of the soil-water characteristic curves, as shown in Figure 4, it was noticed that the ranges with saturation between 10% and 20% and between 40% and 60%, present a more sensitive variation in the c parameter, therefore intermediate values were adopted in these cases. Variations in cohesion and specific weights depending on the degrees of saturation are shown in Table 3. The Bottom, Middle and Top Villar's hyperbolic envelopes as showed in the Figure 7.

3.2 Stress analysis methodology

The methodology adopted for stress analyses, as presented by Collins & Sitar (2011), consists of determining the state of stress in the massif using a numerical model based on the finite element method and comparing the acting stresses with the values of mechanical strength of the soil components of the cliff. Two situations related to wetting fronts were considered for this analysis. The first occurred from the wetting of the Bottom layer only, this situation being related to the increase in the degree of saturation caused by the effect of the tides and/or the water table. The second situation aimed to represent the effects of rainfall, from the cliff in all layers.

Aiming to facilitate the understanding with regard to the influence of the variation in the degree of saturation,

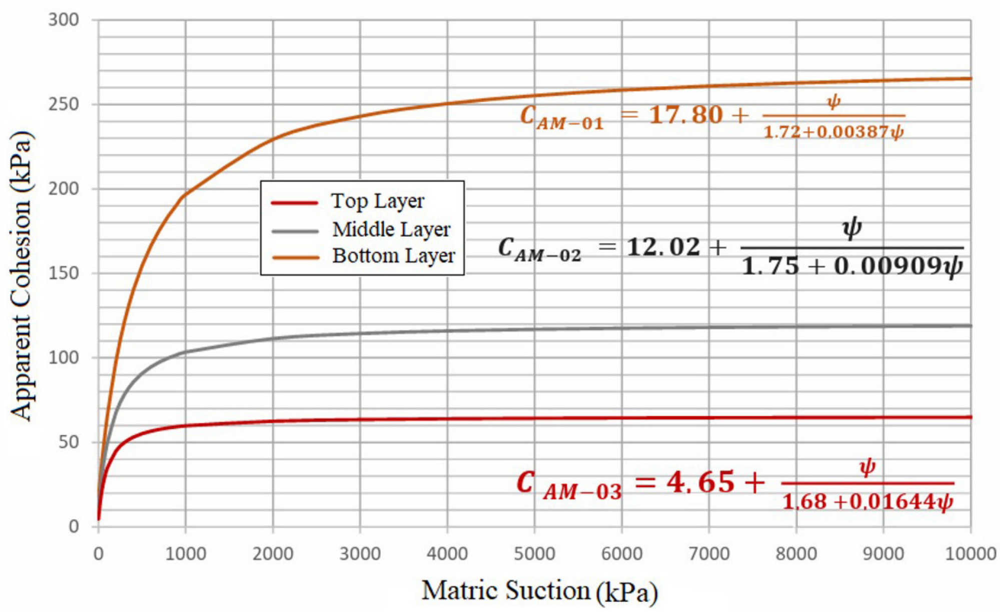

Figure 7. Villar's hyperbolic envelopes (Adapted from Morais, 2019).

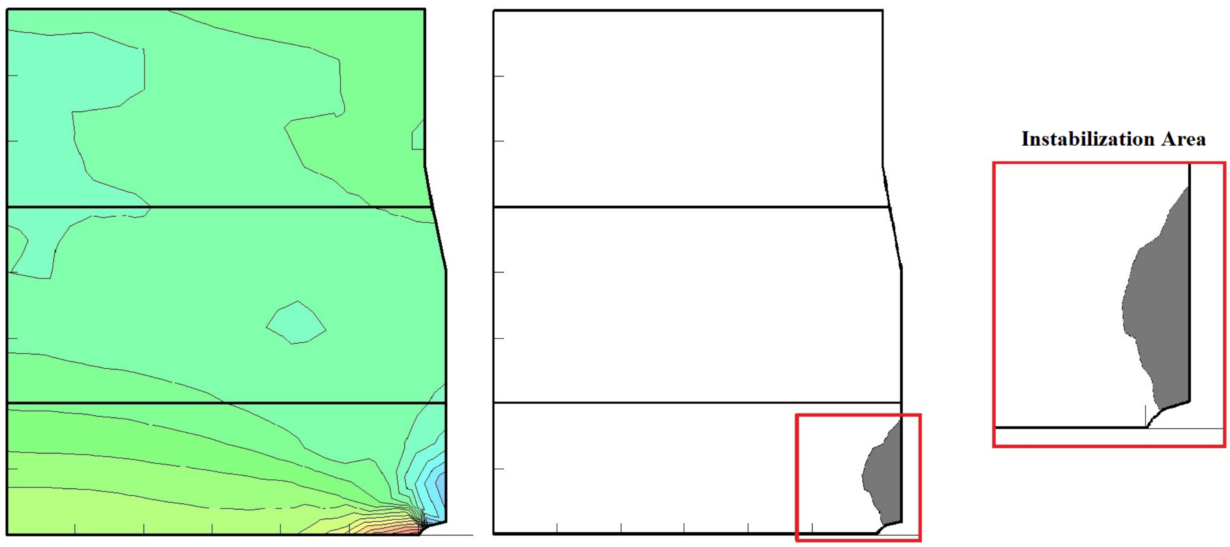

Figure 8. Representation of the definition of a mobilization area by tensile stresses.

areas of instability were defined. The areas of instability refer to regions where, upon evaluating the stress distribution map, resulted in stress analyzes using the finite elements net. The tensile stresses greater than or equal to the soil's tensile strength in the analyzed situation were identified. The process for determining an area of instability is illustrated in Figure 8. In hypothetical scenarios involving deep areas of instability, such as extreme saturation situations, regions with a maximum depth of 3 meters (constrained by the length of the basal incisions) and with simplified geometries, nearly parallel to the slope faces, were defined.

The acting stresses and areas of instability were evaluated for each of the following degrees of saturation in the wetting fronts: 0%, 10%, 20%, 40%, 60%, 80% and 100%. The variation of the degree of saturation in these regions provokes the variation of the acting stresses and of the tensile strength of the soils. A Poisson's coefficient of 0.3 and a deformability modulus of 30 MPa were adopted, which are the same values used by Barbosa (2017), in accordance with the findings of Severo (2011). The parameters used to model the Top, Middle, and Bottom sediments, as obtained from diametral compressive tests conducted by Morais et al. (2020), are summarized in Table 4.

4. Analysis and results

4.1 Results of stability analysis by the Morgenstern-Price method

Table 5 displays safety factors obtained using the Morgenstern-Price method (Morgenstern & Price, 1965). In cases of identified failures characterized by a safety factor less than 1, the critical slip surfaces only developed through the Top layer, as illustrated in Figure 9. No critical slip surfaces were identified passing through the Middle or Bottom layers.

The material that composes the Top layer shows greater variations in apparent cohesion in relation to small increments in the degree of saturation. Thus, before higher degrees of saturation are reached and/or the wetting front reaches lower layers, superficial mass movements occur, which alter the geometry of the cliff and create a new situation to be evaluated, as highlighted by Silva et al. (2020). Aligning with this, Río et al. (2009) observed behaviors similar to those indicated in Table 5 in failures that occurred on the coast of Spain. The authors justify that the rotational landslides studied by them are related to the contrast between the local stratigraphic layers, occurring because of the saturation of the upper layer after intense rainfall.

For this type of analysis, the degree of saturation is the factor with the greatest influence on the stability of the cliff. Degrees of saturation in the order of magnitude of 20% in the Top layer can destabilize the studied cliff, leading to the occurrence of localized failures in this layer. For this type of analysis, the increase in the wetting front was perceived

Table 4. Parameters used in stress analysis (Morais et al., 2020).

Layer	Degree of Saturation (%)	0%	10%	20%	40%	60%	80%	100%
Top	Tensile Strength (kPa)	38	28	19	0	0	0	0
Middle	Tensile Strength (kPa)	90	74	59	28	0	0	0
Bottom	Tensile Strength (kPa)	116	102	87	59	30	1	0

Table 5. Slip safety factors determined by the Morgenstern-Price method.

Hypothesis	Degree of Saturation									
	0%	10%	17,5%	20%	40%	47.5%	48.5%	60%	80%	100%
1	1.255	1.250	1.202	1.194	1.178	1.176	1.176	1.170	1.162	1.161
2	1.255	1.246	1.152	1.118	<1	<1	<1	<1	<1	<1
3	1.255	1.243	1.024	<1	<1	<1	<1	<1	<1	<1
4	1.255	1.240	<1	<1	<1	<1	<1	<1	<1	<1
5	1.255	1.234	<1	<1	<1	<1	<1	<1	<1	<1
6	1.255	1.230	<1	<1	<1	<1	<1	<1	<1	<1
7	1.255	1.230	<1	<1	<1	<1	<1	<1	<1	<1

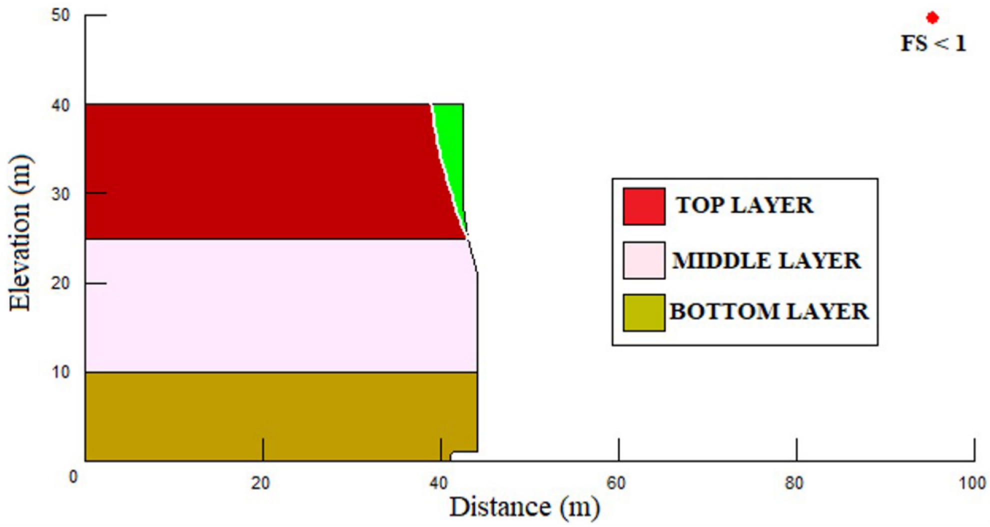

Figure 9. Representive rupture surface on the Top Layer using the Morgenstern-Price method.

as having less relevance for stability. For lower degrees of saturation, the increase in wetting range can trigger, or even potentialize, failures.

This methodology was not able to predict deep failures and, therefore, was not able to assess the effects of the presence of the basal incision on the stability of the cliff. Studies such as Hampton (2002), Collins & Sitar (2011) and Barbosa et al. (2020) point to the existence of limitations in the ability of methods based on the concept of limit equilibrium to predict all the real equilibrium conditions of cliffs with incisions at the base. This observation justifies the adoption of other methods of analysis, in a complementary way.

4.2 Results of stability analysis by the stress analysis method

In the first wetting front hypothesis, the variation in the degree of saturation was considered only in the base material of the cliff. For all degrees of saturation adopted, only variations in tensile stresses were noticed. As for these stresses, increments of up to 12 kPa were identified at some points. This variation in the magnitude of stresses results from the direct relationship between the specific weight of the soil and the degree of saturation.

Thus, only the stress maps are presented, in the "X" and "Y" directions (Figures 10a and 10b, respectively), for the situation of the completely saturated base material of the cliff. This situation was chosen because it is the most unfavorable in terms of cliff stability.

In this study the tensile stresses were considered as negative and the compressive stresses were considered positive. Analyzing Figure 10, it can be seen that the highest tensile stresses observed tend to act on the cliff face of the Middle and Base layers, considering the stresses in the X direction (Figure 10a). In the Y direction (Figure 10b), the tensile stresses have smaller magnitudes, and are concentrated primarily in the top layer. As described in the methodology, comparisons were made between the applied tensile stresses and the tensile strength of the layers, to determine the mobilization areas.

The stresses that were identified on the face of the Middle layer, the higher being applied on the cliff face of the layer, are always smaller than the tensile stresses of the completely dry material, so that there is no generation of mobilization areas in this layer for this saturation condition. Therefore, these efforts were not considered. The tensile stresses acting in the Y direction also did not generate mobilization areas due to their distribution on the top of the cliff. Therefore, they too were not considered. Table 6 shows the results of the applied maximum tensile stresses, tensile strengths of the bottom layer and the calculated mobilized areas, varying according to the degree of saturation adopted.

Tensile stresses mobilized in the X direction (Figure 10a), as they are distributed along the cliff face, are responsible for causing failures. As shown in Table 6, it was noticed that increases in the degree of saturation, although causing little increase in applied tensile stresses (maximum 12 kPa), considerably reduced the tensile strength of the base material. In this context, failure situations were identified only in the base layer. This decrease in strength justifies the variations in the areas of mobilization. The application of degrees of saturation from 40% trigger the appearance of areas of instability. Therefore, before the situation of total saturation is reached, significant mass movements occur on this cliff.

As seen in Figure 10, tensile stresses occur in the Y direction (Figure 10b). However, these tensile stresses, as seen in the stress distribution, do not occur significantly along the cliff face, since they remain concentrated in the top region. In this way, the stresses mobilized in the Y direction do not create situations in which regions of imminent failure are identified according to the stress analysis method, although these stresses can justify the appearance of tensile cracks,

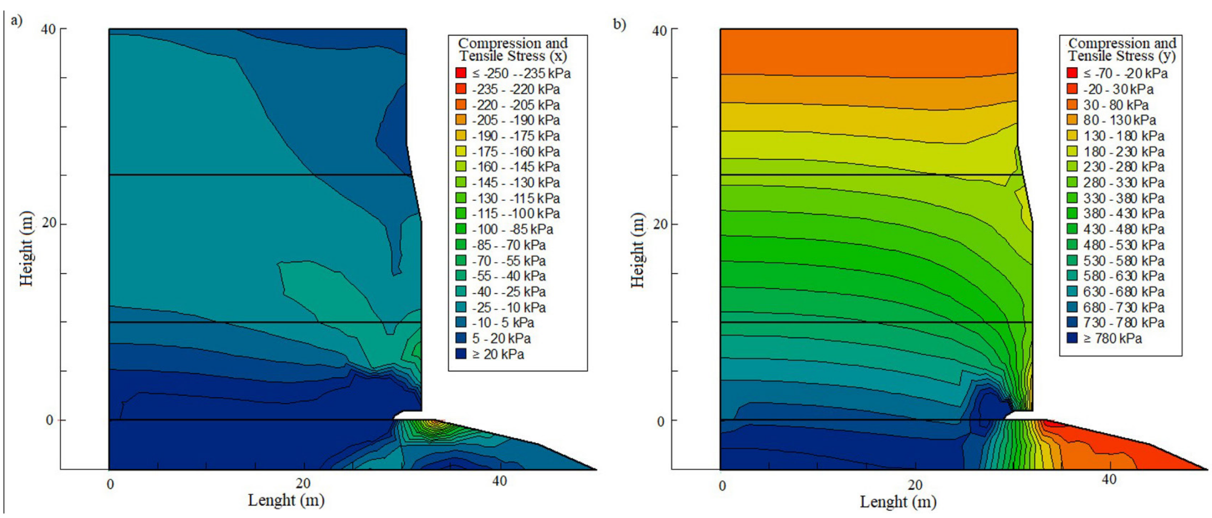

Figure 10. Maps of stresses acting on the cliff with only the base saturated in the X (a) and Y (b) directions.

Table 6. Results of stress analysis with the wetting front acting only from the bottom layer.

Degree of Saturation (%)	0%	10%	20%	40%	60%	80%	100%
Bottom Layer Tensile Strength (kPa)	116	102	87	59	30	1	0
Maximum Tensile Stress (x)	-210	-211	-212	214	-217	-219	-222
Mobilization Area X (m^2)	0	0	0	0.79	11.61	12.38	12.60

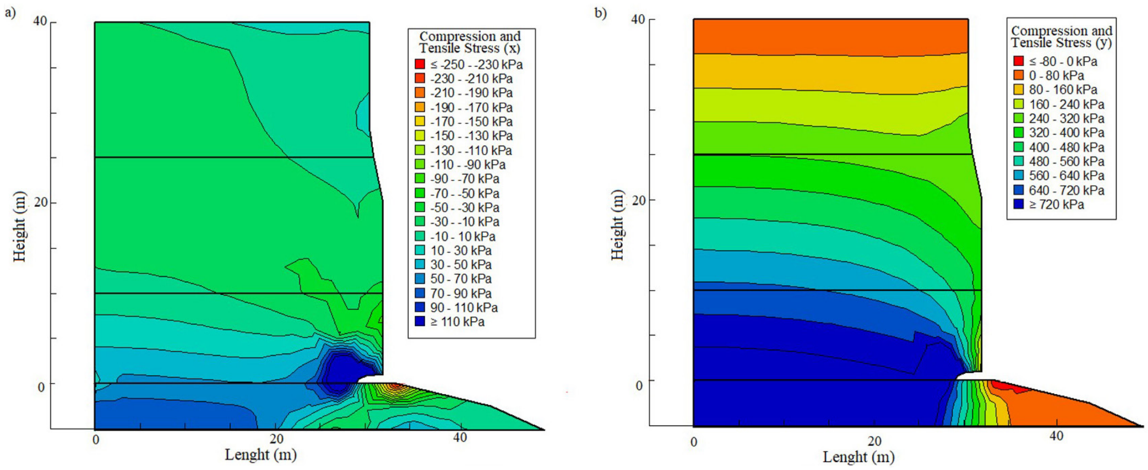

Figure 11. Map of stresses acting on the cliff with all layers saturated in the X (a) and Y (b) directions.

perceived in the studied cliff, as reported by Silva (2019). The appearance of tensile cracks in surface regions of cliffs, especially when filled with water, may be related to another type of failure, triggering block toppling.

In the second hypothesis of the wetting front studied, all layers of sediments are wet. As in the previous hypothesis, the shape of the stress distribution inside the cliff does not change significantly with the increase in the degree of saturation. For this case, increments of a maximum of 40 kPa were observed in tensile stresses, comparing extreme saturation situations. Figure 11 shows the distribution maps for the most critical situation (completely saturated sediments) in the X (a) and Y (b) directions.

The stress maps shown in Figure 11 indicate that, with the increase in the layers' own weight, there is the occurrence of more significant regions of tensile stress on the cliff face along the three layers. However, it was observed that for the top layer, the tensile stresses in the X direction (Figure 11a), as well as those identified in the Y direction (Figure 11b), did not generate significant mobilized areas on the cliff face. Thus, these results were disregarded in the analyses. It is important to point out that, as in the previous hypothesis, these stresses can generate the appearance of tensile cracks, which may consequently trigger another type of failure mechanism.

Comparisons were made between the applied tensile stresses and the tensile strength of the layers, to determine the mobilization areas, as defined in the methodology. Table 7 shows the results of the maximum tensile stress applied in the X direction, the tensile strength of the Base and Middle sediments and the mobilized areas, which varied according to the variation in the degree of saturation.

Based on Table 7, it can be seen that the increase in the degree of saturation in all layers causes a more relevant increase in the maximum acting tensile stresses, when compared to the situation of saturation variation only in the base material. Failures passing through more than one layer (Base and Middle) are identified in Table 7, with magnitude depending on the applied stresses and the degree of saturation acting. When analyzing the development of the increase in the mobilization area, it is noticed that this increase occurs in an equivalent way to that observed in the previously analyzed situation.

Situations of imminent failure are identified in degrees of saturation of 40% and become more representative when the component materials of the layers reach a degree of saturation in the order of 60%, similarly to the wetting front in which variation was imposed in the degree of saturation only at the base. However, it is worth mentioning that the total magnitude of the failures found is higher, due to the development of ruptures in two layers. Even with the saturation of the top layer, the occurrence of tensile failures passing through it was not noticeable.

Therefore, it is possible to state that for both wetting front hypotheses, the degree of saturation of the layers plays a fundamental role in the destabilization of the massif, with considerable failures being developed from degrees of saturation in the order of 40%, regardless of the adopted wetting front. It is also possible to note that, in stress analyses, as well as for the limit equilibrium method, the wetting front has a

Table 7. Results of stress analysis with the wetting front acting on all cliff layers.

Degree of Saturation	0%	10%	20%	40%	60%	80%	100%
Maximum Tensile Stress (x)	210	214	218	226	234	246	250
Middle Layer Tensile Strength (kPa)	89.7	74.2	58.8	27.9	0	0	0
Mobilizated Area in the Middle Layer (m^2)	0	0	0	1.2	26.3	26.2	25.8
Base Layer Tensile Strength (kPa)	115.9	101.6	87.2	58.5	29.9	1.2	0
Mobilizated Area in the Bottom Layer (m^2)	0	0	0	0.7	10.1	12.2	12.2
Total Mobilizated Area (m^2)	0	0	0	1.9	36.4	38.4	38.4

secondary effect and is only responsible for enhancing the effects caused by the variation in the degree of saturation, increasing the failure area.

It is important to point out that the materials that make up the cliffs, due to natural coastal dynamics, infiltration and capillarity processes, spend a good part of their time subjected to situations of partial saturation. In this context for the studied cliff, developing analysis only under extreme saturation conditions (dry and saturated) would not be plausible. It was noticed, from the two analysis methodologies, the occurrence of relevant ruptures in conditions related to intermediate degrees of saturation. These failures related to partial saturation tend to create new geometries, which condition new stress distributions, which lead to a tendency for progressive failure processes to occur. Therefore, real situations in which the soil layers reach saturation are improbable.

5. Conclusion

In the present study, through slope stability analyses, the way the degree of saturation and the wetting front interfere in the stability of a cliff located on Tabatinga beach, in the Northeast Region of Brazil, were evaluated. Analyses were carried out using a method based on the concept of limit equilibrium and a method based on stress analysis. The wetting fronts and the geotechnical properties that make up the cliff were varied, according to the degree of saturation applied to each layer, which varied between 0% and 100%.

The stability analyses by the Morgenstern-Price method applied to the cliff studied, showed only superficial ruptures passing through the Top layer. Thus, it is concluded that, for this type of analysis, the degree of saturation of the layers is an extremely crucial factor for stability. Low degrees of saturation applied to the top layer, in the order of magnitude of 20%, are capable of triggering ruptures. Another conclusion is that the wetting front can be a crucial factor in the decrease in stability, however, only in the superficial layers and being conditioned by the degree of saturation applied.

Regarding the stress analyses, for both wetting fronts studied, values of saturation degrees around 40% in the middle and/or base layers are capable of triggering failures. Thus, it is possible to see that this is an extremely crucial factor in the analysis of stability. It was also noticed the appearance of surface tensile stresses, which can trigger the occurrence of tensile cracks, which can cause the blocks to tip over.

For the studied cliff, the use of different wetting fronts also becomes a relevant factor for the stability analysis, since, for this type of method, the wetting front will define the layers where the failures develop and may enhance the mobilized areas. Due to the natural dynamics of this region, it is common to see partial saturation conditions on coastal cliffs made up of soils from the Barreiras Formation. The results of this study point to the occurrence of ruptures in these conditions of partial saturation.

It is concluded that the consideration of the wetting front is important for the stability of cliffs with soils from the Barreiras Formation, enhancing failures, and should be implemented in stability analyses. And that, more strikingly, the consideration of the gradual variation in the degree of saturation, commonly adopted only at its extremes (saturated and completely dry soil), is not sufficient for the most credible simulation of the stability condition of a coastal cliff.

Acknowledgements

Acknowledgements to CAPES and the Graduate Program in Civil and Environmental Engineering at the Federal University of Rio Grande do Norte for their support during the development of the study.

Declaration of interest

The authors have no conflicts of interest to declare. All co-authors have observed and affirmed the contents of the paper and there is no financial interest to report.

Authors' contributions

Allan Benício Silva de Medeiros: conceptualization, data curation, visualization, writing – original draft. Romário Stéffano Amaro da Silva: supervision, validation, writing – review & editing. Valteson da Silva Santos: supervision, validation, writing – review & editing. Olavo Francisco dos Santos Junior: conceptualization, data curation, methodology, supervision, validation, writing – original draft. Ricardo Nascimento Flores Severo: supervision, validation, writing – review & editing. Osvaldo de Freitas Neto: supervision, validation, writing – review & editing. Bruna Silveira Lira: supervision, validation, writing – review & editing.

Data availability

The datasets generated analyzed in the course of the current study are available from the corresponding author upon request.

List of symbols

c'	Effective cohesion
c'_{ap}	Apparent cohesion
LL	Liquidity limit
LP	Plasticity limit
SP	Poorly graded sand
SM	Silty sand
SM-SC	Silt-clay sand
SUCS	Unified Soil Classification System
NL	The material has no liquidity limit
NP	The material has no plasticity limit
D_{10}	Diameter at which 10% of the soil mass passes the sieve
D_{30}	Diameter at which 30% of the soil mass passes the sieve
D_{50}	Diameter at which 50% of the soil mass passes the sieve
D_{60}	Diameter at which 60% of the soil mass passes the sieve
S	Degree of saturation
φ'	Effective friction angle
γ_s	Specific weight of solids
γ_d	Dry specific weight
γ_{sat}	Saturated specific weigh

References

Barbosa, N., Taquez, D., Santos Junior, O., Freitas Neto, O. & Scudelari, A. (2020). The effect of basal erosion on sea cliff stability. *Journal of Coastal Research*, *95*, 362-366. http://dx.doi.org/10.2112/SI95-070.1.

Barbosa, N.M. (2017). *Analysis of the stability of the sea cliffs of Barreira do Inferno - RN* [Master's thesis]. Federal University of Rio Grande do Norte repository (in Portuguese). https://repositorio.ufrn.br/jspui/handle/123456789/23446.

Collins, B.D., & Sitar, N. (2008). Processes of coastal bluff erosion in weakly lithified sands, Pacifica, California, USA. *Geomorphology*, *97*(3-4), 483-501. http://dx.doi.org/10.1016/j.geomorph.2007.09.004.

Collins, B.D., & Sitar, N. (2011). Stability of steep slopes in cemented sands. *Journal of Geotechnical and Geoenvironmental Engineering*, *137*(1), 43-51. http://dx.doi.org/10.1061/(ASCE)GT.1943-5606.0000396.

Duperret, A., Genter, A., Mortimore, R.N., Delacourt, B., & De Pomerai, M.R. (2002). Coastal rock cliff erosion by collapse at Puys, France: the role of impervious marl seams within chalk of NW Europe. *Journal of Coastal Research*, *18*(1), 52-61.

Durner, W. (1994). Hydraulic conductivity estimation for soils with heterogeneous pore structure. *Water Resources Research*, *30*(2), 211-223. http://dx.doi.org/10.1029/93wr02676.

Emery, K.O. & Kuhn, G.G. (1982). Sea cliffs, their processes, profiles, and classification. *Geological Society of America Bulletin*, *93*(7), 644-654. http://dx.doi.org/10.1130/0016-7606(1982)93<644:SCTPPA>2.0.CO;2.

Epifanio, B., Zezere, J.L., & Neves, M. (2013). Identification of hazardous zones combining cliff retreat rates with landslide susceptibility assessment. *Journal of Coastal Research*, *65*(sp 2), 1681-1686. http://dx.doi.org/10.2112/SI65-284.1.

Fredlund, D.G., Rahardjo, H., & Fredlund, M.D. (2012). *Unsaturated soil mechanics in engineering practice*. Ney Jersey: John Wiley & Sons, Inc.

Hampton, M.A. (2002). Gravitational failure of sea cliffs in weakly lithified sediment. *Environmental & Engineering Geoscience*, 8(3), 175-191. http://dx.doi.org/10.2113/8.3.175.

Marques, F.M.S.F., Matildes, R., & Redweik, P. (2013). Sea cliff instability susceptibility at regional scale: a statistically based assessment in the southern Algarve, Portugal. *Natural Hazards and Earth System Sciences*, *13*, 3185-3203. http://dx.doi.org/10.5194/nhess-13-3185-2013.

Martino, S., & Mazzanti, P. (2014). Integrating geomechanical surveys and remote sensing for sea cliff slope stability analysis: the Mt. Pucci case study (Italy). *Natural Hazards and Earth System Sciences*, *14*, 831-848. http://dx.doi.org/10.5194/nhess-14-831-2014.

Morais, A. D., Santos Junior, O. F. & Freitas Neto, O. (2020). Propriedades geotécnicas de sedimentos da formação barreiras nas falésias de Barra de Tabatinga litoral oriental do Rio Grande do Norte/Brasil. *Holos*, *36*(7), 1-20. https://doi.org/10.15628/holos.2020.9560.

Morais, A.D. (2019). *Propriedades Geoténicas de Sedimentos da Formação Barreira e Análise de Estabilidade de Falésias Considerando a Condição Não Saturada: Estudo de Caso em Barra de Tabatinga/RN* [Master's thesis]. Federal University of Rio Grande do Norte repository (in Portuguese). https://repositorio.ufrn.br/jspui/handle/123456789/29508.

Morgenstern, N.R., & Price, V.E. (1965). The analysis of the stability of general slip surfaces. *Geotechnique*, *15*(1), 79-93.

Pacheco, G. H. S., Freitas Neto, O. & Severo, R.N.F. (2006). Análise da estabilidade das falésias de Tibau do Sul por métodos de equilíbrio-limite. *Holos*, *22*, 78-100. https://doi.org/10.15628/holos.2006.98.

Prémaillon, M., Dewez, T.J.B., Regard, V., Rosser, N.J., Carretier, S., & Guillen, L. (2021). Conceptual model of fracture-limited sea cliff erosion: erosion of the seaward tilted flyschs of Socoa, Basque Country, France. *Earth Surface Processes and Landforms*, *46*(13), 2690-2709. http://dx.doi.org/10.1002/esp.5201.

Richards, K.S., & Lorriman, N.R. (1987). Basal erosion and mass movement. In M.G. Anderson & K.S. Richards (Eds.), *Slope stability: geotechnical engineering and geomorphology* (648 p.). Chichester: John Wiley. https://doi.org/10.1177/030913338801200415.

Río, L.D., Gracia, F.J., & Benavente, J. (2009). Mass Movements and Cliff Retreat along the SW Spanish Coast. *Journal of Coastal Research*, 717-721. Retrieved in May 15, 2023, from http://www.jstor.org/stable/25737672

Santos Júnior, O.F., Coutinho, R.Q., & Severo, R.N.F. (2015). Propriedades geotécnicas dossedimentos da formação barreiras no litoral do Rio Grande do Norte - Brasil. *Geotecnia*, *134*, 87-108. https://doi.org/10.24849/j.geot.2015.134.05.

Severo, R.N.F. (2011). *Caracterização Geotécnica da Falésia da Ponta do Pirambu em Tibau do Sul - RN considerando a Influência do Comportamento dos Solos nos Estados Indeformado e Cimentado Artificialmente* [Doctoral thesis]. Federal University of Pernambuco (in Portuguese).

Silva, B.M.F. (2019). *Probabilistic seacliffs stability analysis in Rio Grande do Norte State, NE Brazil* [Master's dissertation]. Federal University of Rio Grande do Norte repository (in Portuguese). https://repositorio.ufrn.br/jspui/handle/123456789/28024.

Silva, B.M.F., Santos Júnior, O.F., Freitas Neto, O., & Scudelari, A.C. (2020). Erosão em falésias costeiras e movimentos de massa no Rio Grande do Norte, Nordeste do Brasil. *Geociências*, *39*(2), 447-461. http://dx.doi.org/10.5016/geociencias.v39i2.14233.

Van Genuchten, M.Th. (1980). A closed from equation for predicting the hydraulic conductivity of unsaturated soil. *Soil Science Society of America Journal*, *44*(5), 892-898. http://dx.doi.org/10.2136/sssaj1980.03615995004400050002x.

Vilar, O.M. (2007). An expedite method to predict the shear strengh of unsatured soils. *Soils and Rocks*, *30*(1), 51-61. http://dx.doi.org/10.28927/SR.301051.

Soils and Rocks

An International Journal of Geotechnical and Geoenvironmental Engineering

www.soilsandrocks.com

ISSN 1980-9743
ISSN-e 2675-5475

Modeling of a soft clay gentle slope with sand layer in centrifuge under seismic loading: PIV and strain rate analysis

Lucas Chinem Takayassu[1#], Cristian Yair Soriano Camelo[2], Marcio de Souza Soares de Almeida[1], Maria Cascão Ferreira de Almeida[3], Santana Phani Gopal Madabhushi[4], Ricardo Garske Borges[5]

Article

Keywords
Centrifuge modeling
PIV
Gentle slopes
Layered profile
Seismic response
Strain rate effect

Abstract

Dynamic soil parameters such as the shear modulus suffer degradation while damping in soil increases under dynamic loading. These can be determined from various tests such as element tests, field tests and centrifuge experiments. Most of the studies about dynamic soil characterization have focused on evaluating these parameters assuming horizontal ground conditions without considering the effect of static shear stresses induced by ground inclination. This paper presents a dynamic centrifuge test conducted on a layered gentle slope comprising clay and sand, to obtain experimental data in terms of shear modulus and damping for various shear strains. Particle Image Velocimetry (PIV) was employed to measure the displacements and to calculate accelerations due to seismic loading at various depths throughout the slope model. The results suggest that the static shear stress caused by the profile inclination causes a more pronounced degradation of the shear modulus when compared to flat ground conditions. Moreover, the damping during the centrifuge test exhibited larger values than expected, following a similar behavior observed in other experimental programs. The strain rate analysis revealed the mobilization of shear stresses higher than the monotonic shear strength for the clay layers during the seismic shaking.

1. Introduction

Evaluation of dynamic soil parameters is essential to understand how sites will respond during an earthquake event. To simulate the dynamic response of soil sites, numerical models employ shear modulus degradation and damping variation curves. Families of curves have been developed for different materials based on element tests (Kokusho, 1980; Vucetic & Dobry, 1991; Darendeli, 2001; Vucetic & Mortezaie, 2015), field investigations (Chang et al., 1989; Zeghal et al., 1995; Yang et al., 2017).

Most of the reported literature on dynamic centrifuge testing employed for the estimation of stiffness and damping parameters has considered horizontal or level ground profiles in sand, clay and a combination of both (Elgamal et al., 1996; Brennan et al., 2005; Rayhani & El Naggar, 2007; Li et al., 2013). However, there are few reported data on the evaluation of the stiffness and damping for canyons (Tarazona et al., 2019) and sloping grounds (Soriano Camelo et al., 2022). In particular with small inclinations ranging between 1° to 5° (Masson et al., 2006), which are characteristic of continental slopes. As those slopes are under static shear stresses due to ground inclination, this effect has not been addressed before in the measurement of the shear modulus and damping in clay and sandy soils.

Additionally, in centrifuge modeling, small-scale models are subjected to increasing acceleration levels to match a particular prototype stress level. Since the physical centrifuge models are smaller than the prototype by a scale factor, N, events like earthquakes will occur more rapidly in the model than in the prototype (Sathialingam & Kutter, 1989). In dynamic centrifuge testing, during the simulation of earthquakes, the time is scaled by a factor equal to N. This means that the rate of change of stresses and strains occurs N-times faster in the model than in the prototype. The dynamic response of soils is closely related to the rate

[#]Corresponding author. E-mail address: lucas.takayassu@coc.ufrj.br
[1]Universidade Federal do Rio de Janeiro, Instituto Alberto Luiz Coimbra, Rio de Janeiro, RJ, Brasil.
[2]Université Gustave Eiffel, CG-lab, Nantes, France.
[3]Universidade Federal do Rio de Janeiro, Escola Politécnica, Rio de Janeiro, RJ, Brasil.
[4]University of Cambridge, Cambridge, United Kingdom.
[5]Petrobras, Centro de Pesquisa e Desenvolvimento, Rio de Janeiro, RJ, Brasil.

Submitted on April 5, 2023; Final Acceptance on October 25, 2023; Discussion open until February 28, 2024.
https://doi.org/10.28927/SR.2023.003223

of strain, and can be studied by analyzing experimental data obtained from centrifuge tests. Specifically, the displacements and accelerations observed during these tests can provide valuable insights into the effect of strain rate on soil behavior.

This paper aims to evaluate the shear modulus and damping variation of clay in an inclined ground profile or gentle slope. To achieve this, a centrifuge test was carried out in a layered soil profile consisting on a sand layer between two soft clay layers. Stress-strain data was measured to obtain modulus and damping data points at various level of shear strains by measurements of accelerations and displacements by means of Particle Image Velocimetry (PIV) at various locations in the slope. The PIV measurements were validated on the basis of recorded data of accelerometers and displacement transducers also installed in the slope model. A set of earthquakes with varying amplitudes and frequency content were applied to the model using a shaking table. Typically, in centrifuge experiments, a dense array of accelerometers is employed. However, this arrangement can interfere in the soil response if the soil layer is too thin. Moreover, an accelerometer malfunction could interfere with the calculation of dynamic soil parameters when using the methodology of downhole arrays. The PIV methodology can overcome such constraints as it employs a non-intrusive methodology, providing complementary data with a greater number of normalized shear modulus points. At the end, a strain rate analysis evaluates its effect on shear strength.

2. Materials and methods

A layered gentle slope model, with an inclination of three degrees, was tested at an acceleration level of 60-g on the 10 m diameter beam centrifuge at the Schofield Centre, University of Cambridge (Schofield, 1980; Madabhushi, 2014). The slope model was built inside a laminar box and then subjected to a set of earthquakes by means of a shaking table driven by a servo hydraulic actuator (Madabhushi et al., 2012).

2.1 Materials and model preparation

Three soil layers compose the model profile: two clay layers and an intermediate Hostun sand layer, as shown in Figure 1. For the clay layers, Speswhite kaolin was employed (Almeida, 1984, Vardanega et al., 2012), with the following properties (Lau, 2015): liquid limit, $LL = 63\%$; plastic limit, $PL = 30\%$; plasticity index $PI = 33\%$; and specific gravity, $G_s = 2.60$. The intermediate soil layer was composed of Hostun Sand (Colliat et al., 1986; Chian et al., 2014). For the present study, the values adopted were (Azeiteiro et al., 2017): critical state friction angle, $\phi_{crit} = 31.5°$; specific gravity, $G_s = 2.64$; minimum void ratio, $e_{min} = 0.66$; maximum void ratio, $e_{max} = 1.00$.

The clay was mixed with water, under vacuum, with a water content (w) of around 120%. This material was placed in a consolidation box (500 mm length x 250 mm height) and a consolidation pressure of 250 kPa was applied (Soriano Camelo et al., 2021). After two weeks under constant final stress the clay block was removed from the box and cut horizontally in two parts: the lower layer with 150 mm and the upper layer with 80-90 mm. The sand layer was prepared in two plastic boxes measuring 250 x 250 x 50mm. The containers were filled with deaired water. With the help of an adapted nozzle and a controlled drop height, a relative density (RD) of 45% (void ratio, $e = 0.85$) was achieved. The sand blocks were then stored in freezers for 24 hours to obtain a solid material to enable manipulation and positioning of the sand layer over a lower clay layer and subsequent placement of the top clay layer. This resulted in a three-layer block which was covered by a rubber bag to

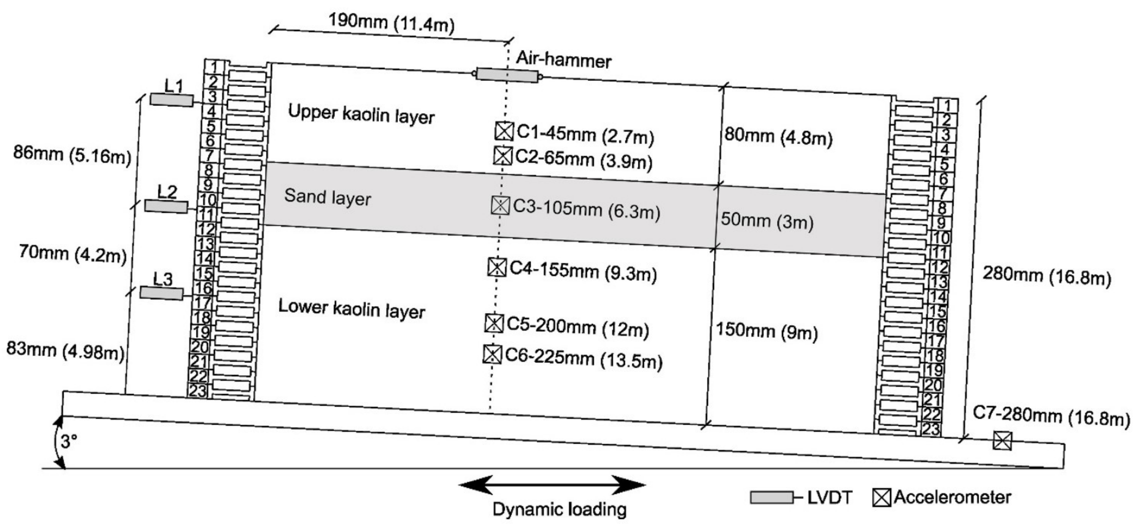

Figure 1. Centrifuge instrumented model, column (C1-C6) and base (C7) accelerometers with respective depths in millimeters. Model scale, prototype scale in parentheses.

avoid the leakage of water. In the sequence, the frames of the laminar container were installed one-by-one across the layered block until reaching the final height of the model (Soriano Camelo et al., 2021). The final soil profile is presented in Figure 1, composed of a superficial layer of clay with a thickness of 80 mm, a central 50 mm sand layer and finally the lower clay layer with a thickness of 150 mm.

After the preparation of the layered profile, the model was instrumented with seven piezoelectric accelerometers (C1 to C7 in Figure 1), three linear variable differential transformers (LVDTs, L1 to L3 in Figure 1) and an air hammer placed at the surface of the model to obtain shear wave velocity data points. For the PIV analysis, a set of markers were glued to each lamina of the model container, and a high-speed camera was placed in front of the model (Soriano Camelo et al., 2021).

2.2 Particle Image Velocimetry setup

Particle Image Velocimetry (PIV) technique was used in the centrifuge test during the earthquake loading. A high-speed camera (MotionBLITZ EoSens mini2 by Mikrotron GmbH) was employed to monitor the dynamic response of the model (Soriano Camelo et al., 2021). The images were recorded at a resolution of 1504 x 1050 pixels with an acquisition rate of 953 Hz. A total of 1354 frames were defined for each earthquake to capture the condition of the model before, during and after the application of the shaking. An external trigger started the camera, and it was set to generate footage with 15% of the frames recorded before the earthquake and the remaining frames to record the seismic shakings applied to the model.

To capture the movements of the soil/laminar box system, circular fiducial markers were used for PIV analysis. The placement of the markers is shown in Figure 2 and are referred to in this study by the letter "M" followed by the number of the layer to which they were attached. The markers identified as Fixed 1 and Fixed 2 were employed to track the displacements associated with the input motion at the base of the model. Those markers were attached to a column fixed to the base of the model container. Due to space restrictions, the camera field of view covered only markers M3 to M17 and markers Fixed 1 and Fixed 2 as shown in Figure 2. The recorded photos were scaled from pixel dimensions to distance dimensions using a checkerboard sheet with a 20 mm x 20 mm pattern.

The XnConvert editing tool was used for batch processing of the images for the PIV analysis. Several adjustments were made to improve the contrast of the photo sequence. The marker displacements were tracked using an open-source software (Blender - Hess, 2010), employed for modeling, animation and video editing in 2D and 3D. The tracking routine was configured for "Location Only" motion capture function with a default correlation factor of 0.75.

2.3 Centrifuge test

The centrifuge was accelerated in increments of 10-g until reaching a level of 60-g. Afterwards, the model was kept in flight for around 1 hour for pore pressure equilibrium. Subsequently, a set of earthquakes of varying frequency content and amplitudes were applied to the model. Table 1 and Figure 3 present the characteristics and time histories of the applied ground motions. The earthquakes consisted of three sinusoidal (1 Hz) waves and one real scaled motion (Kobe, 1 Hz-4 Hz), this earthquake have been widely studied in literature (Lu & Hwang, 2019; Sahoo & Shukla, 2021) with Peak Ground Accelerations (PGA) varying between 0.06 g and 0.29 g and Significant Durations (D_{595}) varying between 4.69 s and 9.59 s.

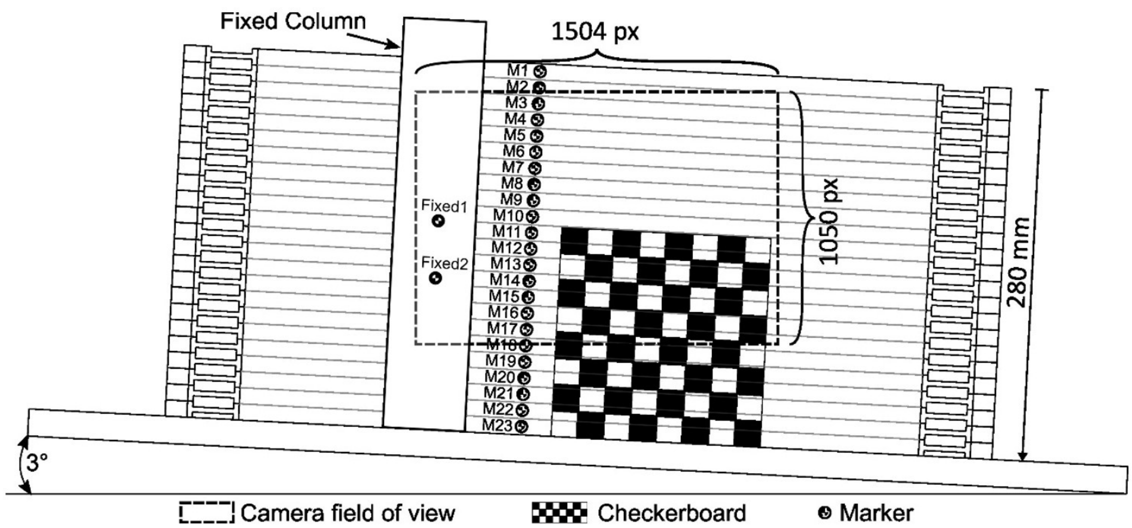

Figure 2. Position of the circular fiducial markers used for the PIV, camera field of view area and checkerboard sheet pattern.

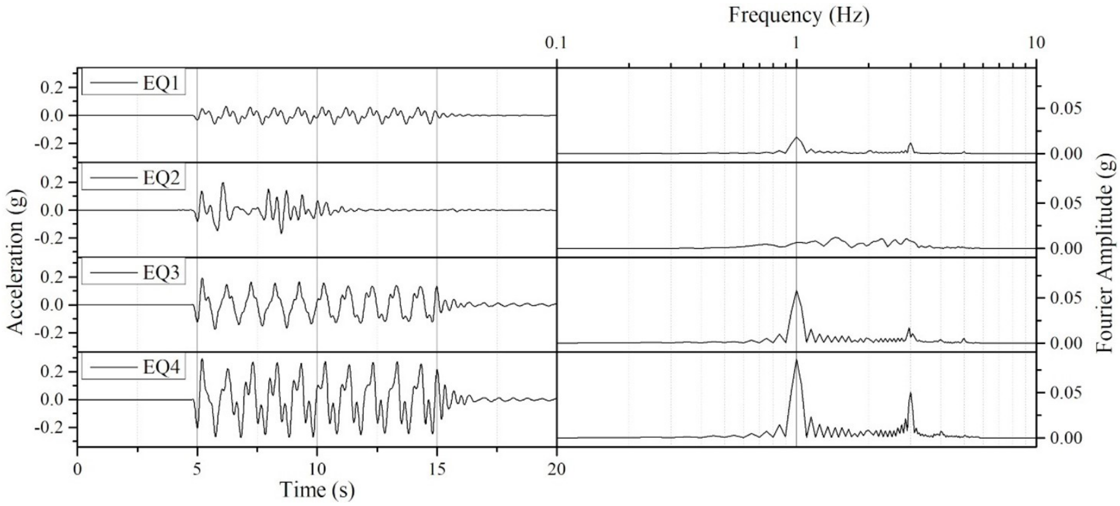

Figure 3. Ground motions at the base of the model: measured acceleration-time histories and Fourier amplitude (prototype scale).

Table 1. Input motions recorded at the base of the model, prototype scale.

Code	Input	PGA_{Base} [g]	D_{595} [s]	Frequency [Hz]
EQ1	Sinusoidal	0.06	9.05	1
EQ2	Kobe	0.2	4.69	1-4
EQ3	Sinusoidal	0.19	9.53	1
EQ4	Sinusoidal	0.29	9.59	1

2.4 In-flight characterization tests

In-flight characterization tests were carried out to obtain undrained shear strength and shear wave velocity profiles. Shear wave velocity data points were obtained by means of air hammer tests (Ghosh & Madabhushi, 2002). Arrival times of shear waves generated by the air hammer placed at the surface of the model were measured by the accelerometers placed in the central column of the model (Figure 1). The shear wave velocity data points at the middle depth between accelerometers were estimated based on the distance between the accelerometer and the arrival times (Figure 4a).

The central column of accelerometers (C1 to C6 in Figure 1) was used for the Air Hammer test (Ghosh & Madabhushi, 2002) to calculate the soil shear wave velocity values v_s and then the initial shear modulus G_0, calculated using Equation 1 and soil density (ρ), as shown in Figure 4a.

$$G_0 = \rho v_s^{\,2} \tag{1}$$

The theoretical initial shear modulus profile was obtained by the Equation 2 proposed by Hardin & Black (1969):

$$G_0 = Af\left(\mathrm{e}\right)\left(\frac{p'}{p_{\mathrm{r}}}\right)^m OCR^k \tag{2}$$

where:
G_0 – Initial shear modulus [MPa]
p' – Average effective stress [kPa]
p_r – Reference stress (100 kPa)
OCR – Over consolidation ratio
A, f(e), k and m – Correlated parameters

The constants A, f(e), k and m are correlated parameters. The reference values used in this study are shown in Table 2.

The undrained shear strength (s_u) profile was obtained from a mini-Cone Penetration Test (CPT), using Equation 3 and a cone factor (N_{kt}) equal to 16 (Herreros, 2020), as shown in Figure 4b. The upper clay layer exhibited s_u values ranging from 8 to 26 kPa and the deeper clay layer presented an average s_u of 26 kPa.

$$s_{\mathrm{u}} = {q_{\mathrm{c}}}/{N_{\mathrm{kt}}} \tag{3}$$

where:
s_u – Undrained shear strength [kPa]
q_c – Measured cone tip resistance [kPa]

Theoretical values of s_u were estimated using Equation 4 (Wroth, 1984) with the parameters K = 0.23 and n = 0.62 proposed by Zhang et al. (2011) for Speswhite kaolin. The results presented a reasonable agreement with the experimental results for the upper clay layer (Figure 4b).

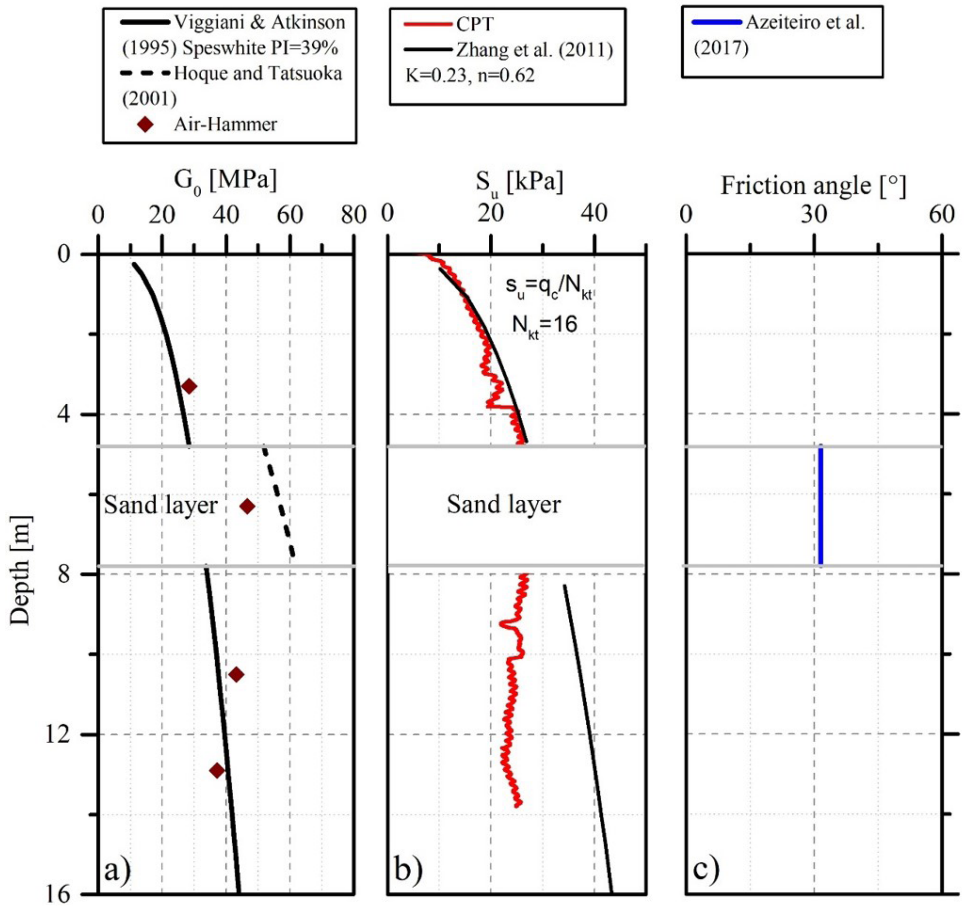

Figure 4. (a) G_0 profile and G points generated by "Air-hammer"; (b) Undrained shear strength, S_u; c) Friction angle of sand layer.

Table 2. Fitting constant values.

Soil	*A*	*f*(e)	*k*	*m*	Reference
Hostun Sand	80	$\frac{(2.17-e)^2}{1+e}$	0	0.47	Hoque & Tatsuoka (2000)
Speswhite Kaolin	750	1	0.25	0.83	Viggiani & Atkinson (1995) IP=39%

For the deeper layer, the empirical correlation exhibited higher values when compared with data obtained from the CPT.

$$s_u = K.\sigma_v^{'}\left(OCR\right)^n \quad (4)$$

where:
K – Normally consolidated strength ratio
$\sigma_v^{'}$ – Effective vertical stress [kPa]
OCR – Overconsolidation ratio
n – Plastic volumetric strain ratio

Figure 4c shows the value of the friction angle of the Hostun sand obtained by a series of triaxial test performed by Azeiteiro et al. (2017) for loose and moderately loose samples.

3. Results

By measuring seismic displacements throughout the slope model, the use of the PIV technique in this study aims to enable the generation of the shear modulus degradation and damping evolution curves. Therefore, some results are presented first to illustrate the validation of the PIV analysis. This is followed by a summary of the expected results of the normalized shear modulus for all the applied earthquakes.

3.1 Measured displacements

The displacements (u) obtained from the PIV analysis and LVDT readings for the EQ3 loading are compared in Figure 5. The position of each instrument and marker can be seen in Figure 1 and Figure 2. The superficial displacement transducer L1, in Figure 1, detached from the laminar container at the beginning of the test. Therefore, the results from L2 and L3 were used for comparison. Overall, it was observed a good agreement between the measured displacements measured by the LVDTs and the displacements obtained from PIV analysis.

3.2 Acceleration-time history and response spectra data

Acceleration (ü) time history values were obtained for each layer and show the results for the top (C1) and bottom (C7) accelerometers for the EQ3 loading (Figure 1 and Figure 6). Accelerometer data used a bandpass filter with cutoff frequencies [5-350] Hz, in prototype scale. For the PIV analysis, accelerations were obtained through double derivation of displacements plus a Savitzky–Golay filter, using a third-order polynomial and a window size of 11 points. This filter smooths the signal without distorting its trend.

Figure 6 shows good agreement between the PIV and acceleration data. Within the loading phase, the M4 and M5 markers display adequate similarity with the upper accelerometer (C1) signal, Figure 6a. The result obtained by the Fixed1 marker, presented a good phase correlation with the accelerometer result at the base (C7). The latter presented another frequency component outside the single-frequency sinusoidal load (Figure 6b), this characteristic can be better observed on response spectra results. As far as the response spectra (Kramer, 1996) data is concerned, the accelerometer at the base (Figure 7b) shows a second peak outside the loading period of the model. As presented by Brennan et al. (2005), dynamic loads applied by actuators in centrifuge tests do not necessarily contain only one frequency. Higher frequency harmonics may exist, not necessarily being signal noise.

3.3 Calculation of shear stresses and shear strains

For shear stress (τ) and shear strain (γ) calculations, groups of three adjacent markers were employed. For each loading and group of markers (Figure 8), shear stress calculations were done by implementing trapezoidal integration with shear strains obtained through a second order approximation (Brennan et al., 2005). For these calculations, the markers were divided into two groups: the first corresponding to the clay layers and the second, corresponding to the sand layer to obtain data points for each type of material. An advantage of using the PIV methodology, with a laminar box, was the larger number of points for obtaining the shear strains and shear stresses in the slope when compared with an analysis only employing the accelerometers installed in the model. For the calculations, six groups of markers were employed in the in the clay layers and two groups in the sand layer.

Figure 9 shows an example of a shear stress versus shear strain plot for the bottom clay layer covered by markers M12, M13 and M14 for input motion EQ3. According to Biscontin & Pestana (2006), in a slope, even with a few degrees, there is a static shear stress (τ_s) applied within the soil in the downslope direction of the model. Elgamal et al. (1996) expresses this steady loading as $\tau_s = \rho g z \sin(\alpha)$, with mass density ($\rho$), gravity ($g$), depth ($z$) and slope angle ($\alpha$). During dynamic loading, this shear stress generated a

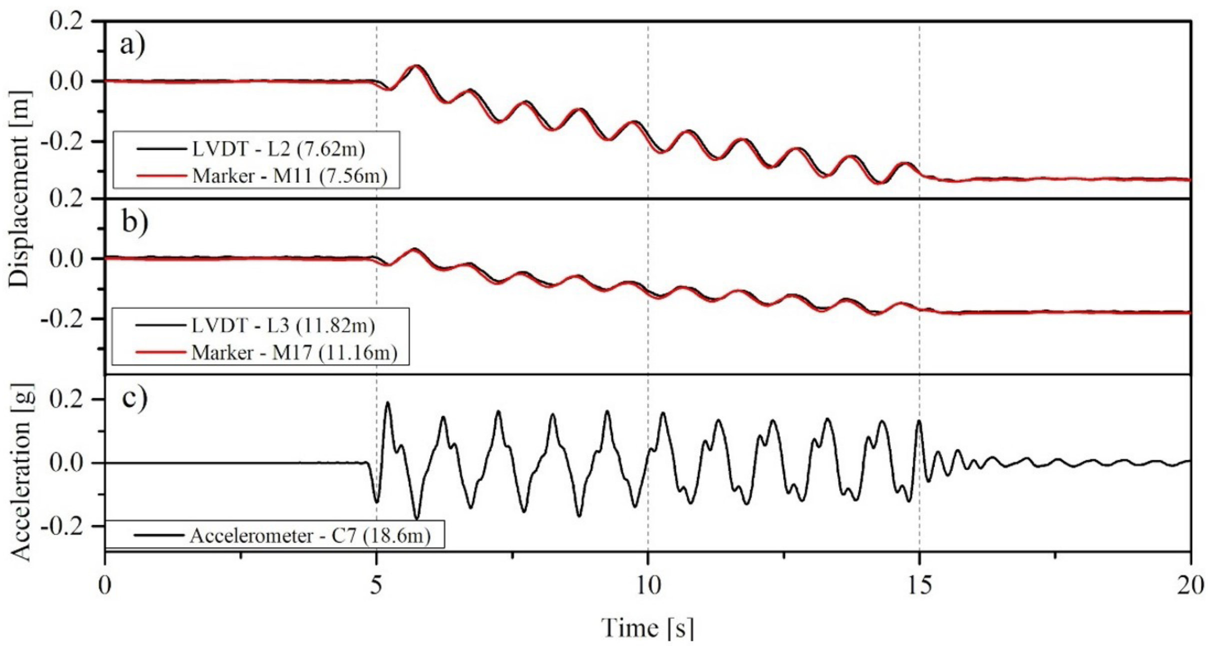

Figure 5. Comparison of EQ3 displacements, generated by PIV and LVDTs, values in prototype values: (a) L2 (7.62 m) and M11 (7.56 m); (b) L3 (11.82 m) and M17 (11.16 m); (c) Accelerations at the base of the model (C7).

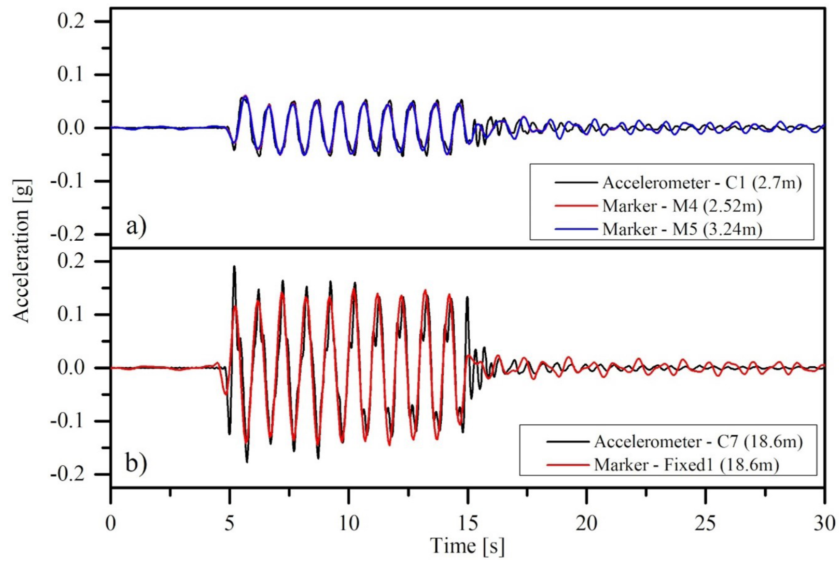

Figure 6. Comparison of EQ3 accelerations (prototype scale), between accelerometer and PIV. Depths in parentheses. (a) Top accelerometer (C1) with closest markers (M4 and M5); (b) Base accelerometer (C7) with base marker (Fixed1).

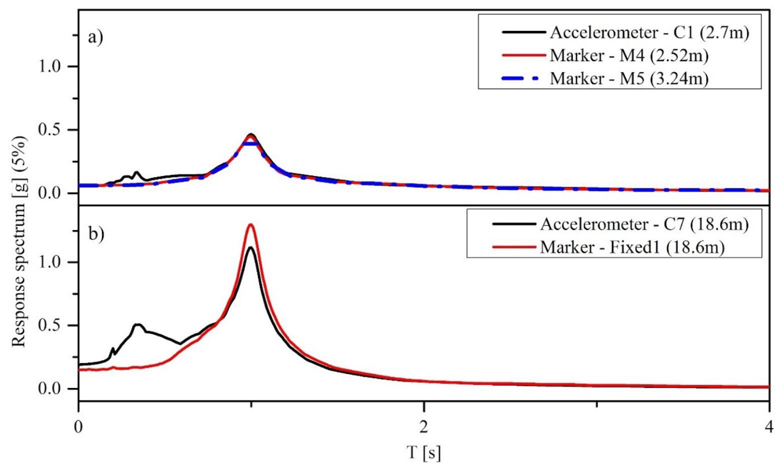

Figure 7. Response spectra comparison for EQ3, obtained from accelerometer and PIV: (a) Top accelerometer with closest markers; (b) Base accelerometer with base marker.

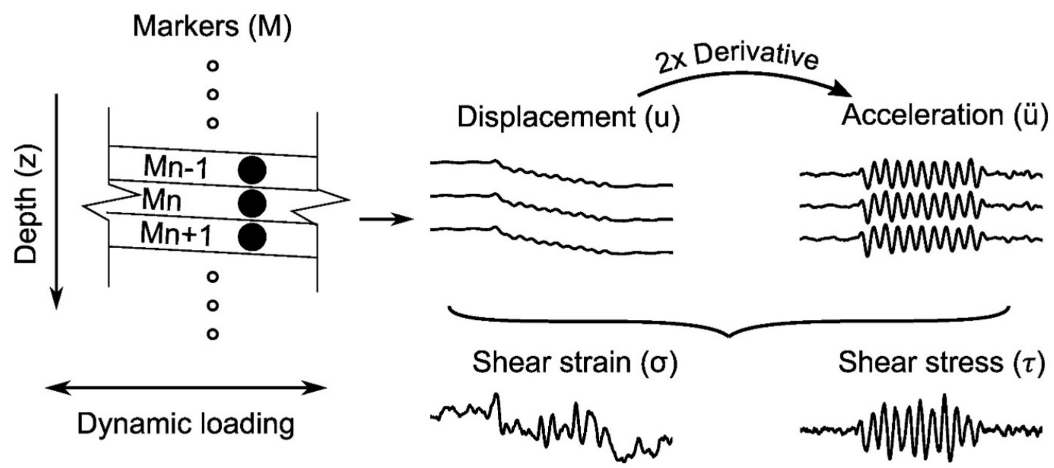

Figure 8. Acceleration conversion from PIV displacement.

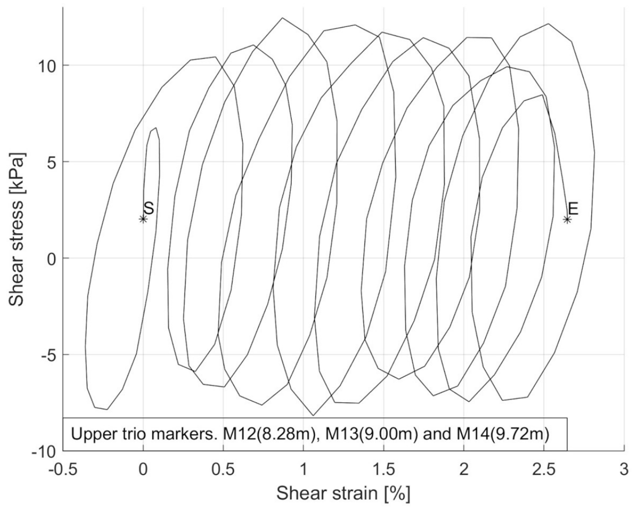

Figure 9. Shear stress versus shear strain for loading EQ3 and markers M12, M13 and M14. Prototype depths in parentheses.

shear strain accumulation, caused by the superposition of the static shear stresses with that generated by the dynamic loading, as found by Elgamal et al. (2002). As the signal passes through the soil, a permanent strain can be observed. Strain stress loops starts (S) at around zero strain and a 2.5 kPa static stress. At the end (E) of loading, static stress continues around 2.5 kPa and strain accumulation reaches values above 2.5%.

3.3.1 Experimental shear modulus and damping data points

For each applied earthquake, shear stress/strain loops at different depths in the model were obtained. The secant shear modulus was calculated, for each loop, through the tangent line generated by maximum and minimum points. In this way, each trio of markers generates several pairs of secant shear modulus ($_{\text{sec}}$) and shear strain (γ). Normalized shear modulus ($G_{\text{norm}} = G_{\text{sec}} / G_0$) at various shear strains was determined using values for G_0 at different depths (Figure 4). The area for each loop was calculated and used to find damping (Afacan et al., 2014).

Figure 10a summarizes the shear modulus values G_{norm} for the applied input motions. The results are separated according to the type of material (kaolin clay and hostun sand). A distinct behavior was observed between the sand and the clay layers, where the granular material showed a lower shear strain, due to lower degradation in shear resistance during the shaking. The dynamic damping exhibited dispersed values, not indicating a trend, a similar response has been reported in the literature (Tarazona et al., 2019; Afacan et al., 2014; Tsai & Hashash, 2009).

There was a difference in behavior between the upper and lower clay layers (Figure 10b). The deeper layer presented, on average, a higher normalized shear modulus and strains greater than 1%. The dynamic response of the clay does not depend on the confining stress and the identical material was employed for both clay layers; therefore, normalized shear module (G_{norm}) for the upper and lower clay layer should present a similar value. Figure 10b shows the lower layer with values higher than the topmost layer and strains above 1%. One possible explanation for this difference is the increase in the static shear stress with depth, higher static shear stresses may accelerate the shear modulus degradation process. Another probable explanation is the presence of the sand on the wave propagation in the model, acting as a “filter”. To illustrate this, Figure 11 shows the displacement profiles during seismic shaking EQ4 at the location of the PIV markers. Nearly at the beginning of loading (Figure 11a), the markers show no major horizontal displacement. Five seconds later (Figure 11b), there is not a significant variation of values between neighboring points in the sand layer, indicating a probable attenuation of the signal. While the lower clay layer presents greater shear deformations, the upper clay layer and the sand layer present a more rigid behavior. Figure 11c and 11d show similar behavior for the two upper layers, when compared to Figure 11b the increment of strain accumulation in the lower layer is noticeable.

3.3.2 Input comparison

Figure 12 presents representative shear modulus reduction curves for clay and sand (Darendeli, 2001) adjusted by means of the GQ/H model (Groholski et al., 2016), compared with the data points obtained from PIV for all input motions analyzed. The centrifugal (experimental) results appear below the reference curves. The empirical curves (Darendeli, 2001) are based on Resonant Column Torsional Shear tests (RCTS), which in turn are unable to evaluate some characteristics present in the centrifuge test under study, such as the slope profile (Soriano Camelo et al., 2021) and heterogeneous layers (Rayhani & El Naggar, 2007). Overall, depending on the type of soil, the range of mobilized shear strains varies. For the sand layer (Figure 12b), the mobilized shear strains reached values up to 0.3% during the application of the earthquakes to the model. Regarding the clay layers, depicted in Figure 12a and Figure 12c, larger shear strains were mobilized with maximum values around 2%. The data points for the sand layer and the clay layers seem to be offset when compared with the reference curves. This has an important implication in the definition of the modulus degradation curves because the effects of the static shear stresses of the sloping ground should be considered, given that there is a more pronounced shear modulus degradation due to the superposition of the dynamic and static shear stresses. All experimental damping, shown in Figure 12, present higher values compared to the reference curves. Strain accumulation favors one direction of movement over the other, for this reason the area enveloped by the shear stress-strain loops employed for the damping

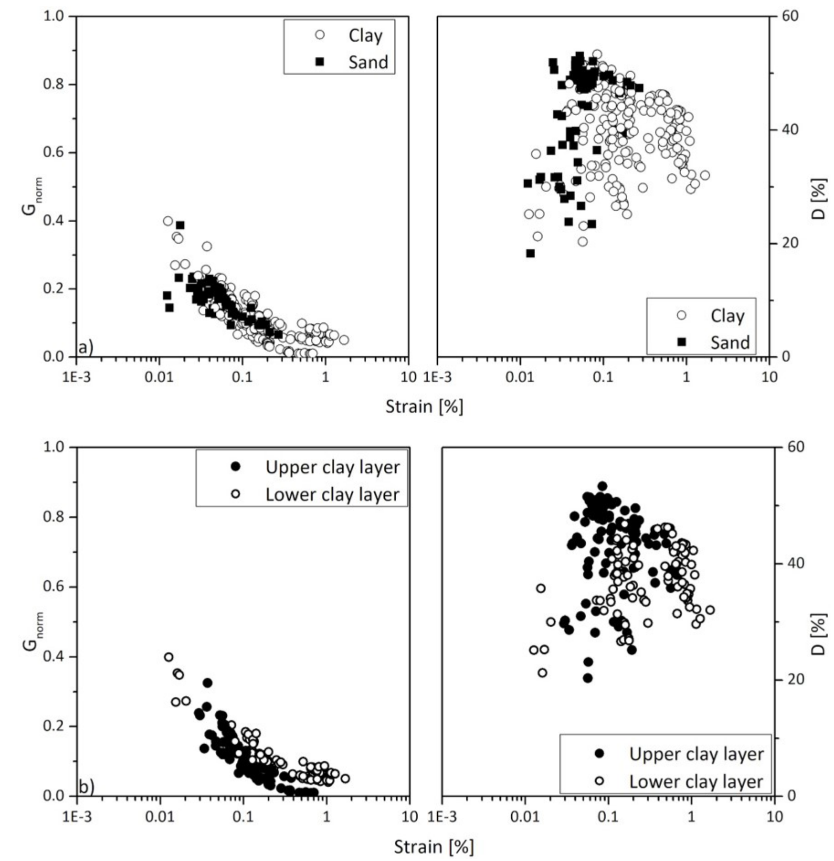

Figure 10. Normalized shear modulus and damping versus strain: (a) Difference between sand and clay data; (b) Difference of results between the upper and lower clay layers.

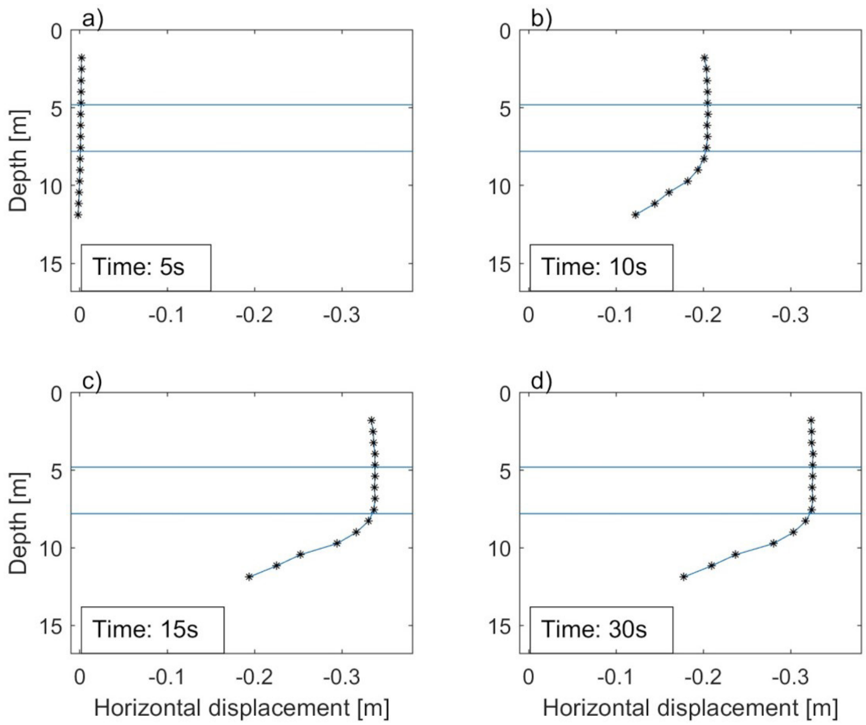

Figure 11. Horizontal displacement for EQ4 and all PIV markers, at different loading moments (prototype scale): (a) 5 s; (b) 10 s; (c) 15 s; (d) 30 s. Division between layers marked with a blue line.

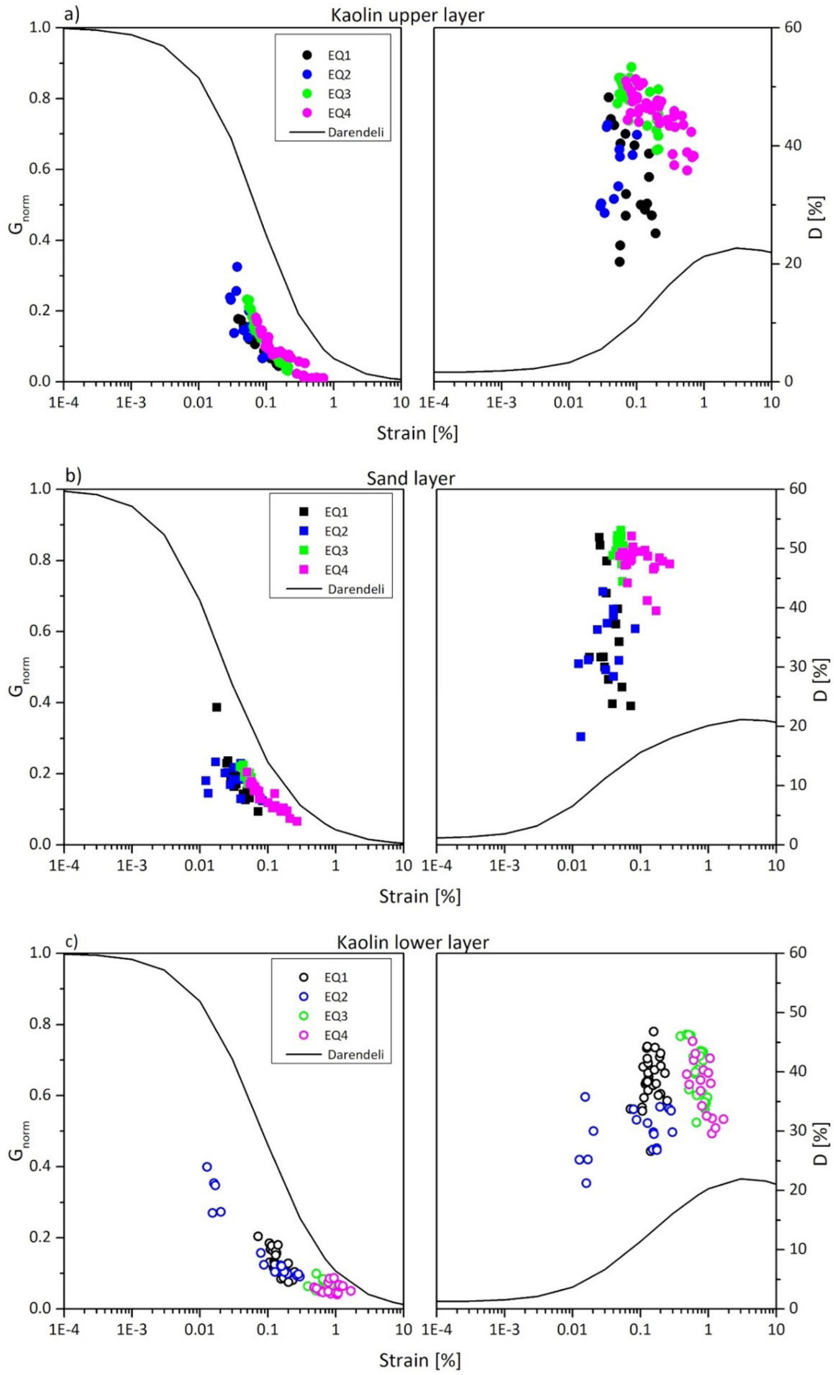

Figure 12. Shear modulus degradation and damping variation: (a) Clay upper layer; (b) Sand layer; (c) Clay lower layer.

calculations increases leading to values larger than the reference ones. It is important to note that the reference curves (Darendeli, 2001) were based on a different type of test with some unrelated conditions.

3.3.3 Strain rate effect

Multiple authors observed a correlation between the dynamic response of soil with the strain rate ($\dot{\gamma}$) generated during each log cycle. Sheahan et al. (1996) summarize numerous percent changes in s_u per log cycle, varying between 0% - 17%. Quinn et al. (2012) performed a series of triaxial tests on kaolin samples, at strain rates from 1%/h to 180,000%/h. They found that the rate effects not only change with the log cycle with a specific fractional increase, in reality, follows a backbone curve. It was also pointed out that soil type influences strain rate effects.

Due to its single frequency nature, sinusoidal signals are simple and predictable. Further calculations were limited for this load. A relation between the strain rate compatible shear strength ($(s_u)_d$) and undrained shear strength (s_u) was calculated for each trio of markers using Equation 5 (Afacan et al., 2014).

$$\left(s_u\right)_d \Big/ s_u = \left(1+\lambda\right)^{\log_{10}\left(\dot{\gamma}/\dot{\gamma}_{ref}\right)} \tag{5}$$

where:

$\left(s_u\right)_d$ – Strain rate compatible shear strength [kPa]

s_u – Undrained shear strength [kPa]

λ – Fractional increase of normalized shear strength per log cycle

$\dot{\gamma}$ – Strain rate [%/s]

$\dot{\gamma}_{ref}$ – Reference strain rate [%/s]

For each input, the average strain rate ($\dot{\gamma}_{average}$) was calculated by dividing the accumulated strain by the input duration (model scale). The fractional increase per log cycle (λ = 0.09) was obtained from Sheahan et al. (1996), and the reference strain rate ($\dot{\gamma}_{ref}$ = 0.006%/s) was taken from Afacan et al. (2014). Figure 13a shows the shear strength profile obtained from CPT, as well as the strain rate compatible shear strength. Larger values were observed at greater depths, where larger deformations occurred. This adjustment increased soil resistance by 12% to 41% compared to the CPT value. Figures 13b and 13c display the backbone stress strains curve (Darendeli, 2001) and the normalized shear stress versus the average shear strain (γ_a) for each loop. In Figure 13b, the cyclic shear strength ($\tau_{f,cy}$, Equation 6) normalized with s_u, reached values above unity, whereas in Figure 13c, cyclic shear strength

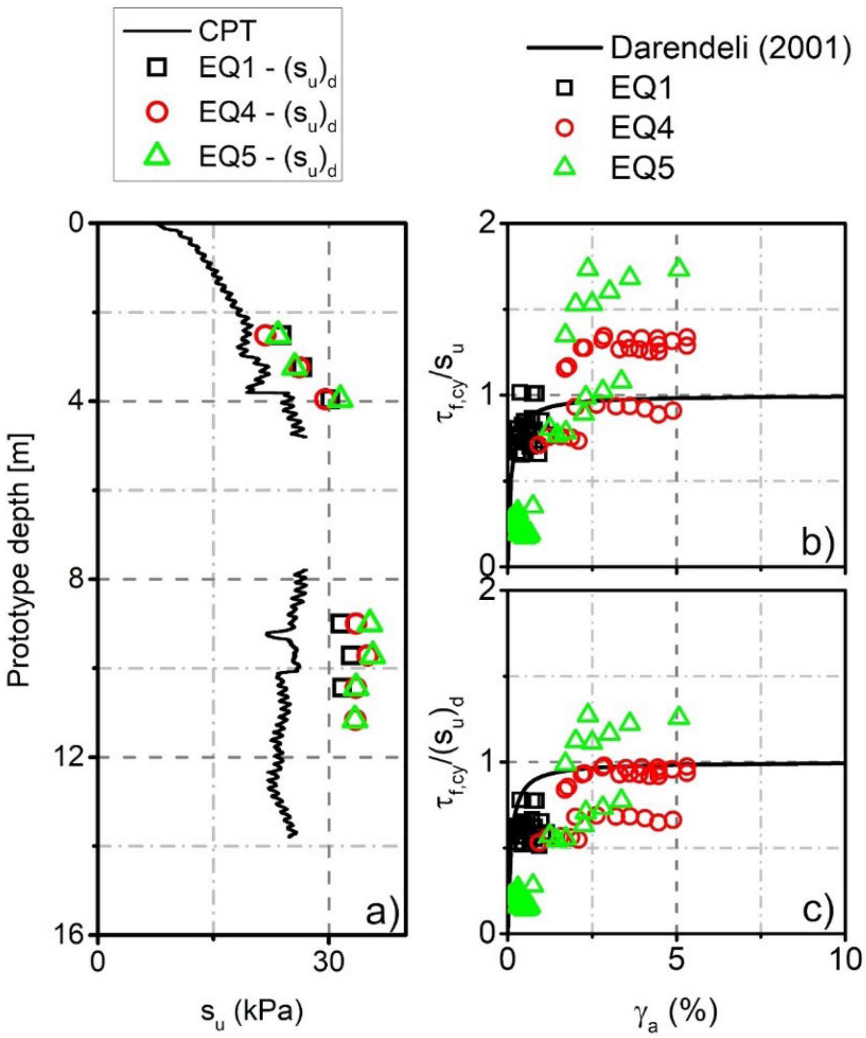

Figure 13. Strain rate effect. (a) Measured undrained shear strength and strain rate compatible shear strength profile; (b) Normalized cyclic shear stress by the measured undrained shear strength; (c) Normalized cyclic shear stress by the strain rate compatible shear strength. Model scale.

normalized with the strain rate compatible shear strength ($\tau_{f,cy} / \left(s_u\right)_d$) exhibited points around unity. This statement highlights the importance of applying strain-rate corrections to shear strengths for site-response problems. It is observed that strain rates mobilized in centrifuge models are higher than those expected for prototype conditions.

$$\tau_{f,cy} = \tau_s + \tau_{cy} \tag{6}$$

$\tau_{f,cy}$ – Cyclic shear strength [kPa]
τ_s – Static shear stress [kPa]
τ_{cy} – Cyclic shear stress [kPa]

The normalized shear modulus (G_{norm}), explained previously, is used for evaluating the dynamic behavior of soil and has been used to evaluate degradation curves in numerical modeling programs such as DEEPSOIL (Hashash et al., 2016) and OpenSEES (McKenna et al., 2010) for nonlinear analyses. Undrained shear strength is also important for the calibration of numerical models. To match the undrained shear strength of clay layers, a strain rate correction actor must be applied to reflect the larger shear stresses that can be mobilized during seismic shaking. This effect is more pronounced in centrifuge testing, where there is no compatibility between strain rates at the model and the prototype. Figure 13 demonstrates the importance of considering strain rate effects for calibrating numerical models, where strain rate corrected values of shear stress were compatible with the expected values.

As discussed earlier, the calculation of average strain rate ($\dot{\gamma}_{average}$) involves dividing the accumulated strain by the input duration. This parameter is summarized in Figure 14a by the inclination of the dotted line. However, a more detailed analysis was performed by calculating the strain rate for each loop ($\dot{\gamma}_{loop}$), which is defined as the inclination of the line that passes through the maximum and minimum values of time and shear strain for each loop, as shown in Figure 14b. Notably, for the sinusoidal input, the average inclination of each loop differs from the overall average, indicating that the strain rate varies throughout the test. This information is essential for understanding the dynamic behavior of the material under different loading conditions and for developing accurate numerical models to simulate this behavior.

Figure 15 presents the strain rate compatible normalized shear stress versus strain rate for each distinct strain stress loop ($\dot{\gamma}_{loop}$) obtained from Figure 9, at different depths. Despite the sinusoidal inputs at different depths yielding strain rates of up to 60.6%/s in Equation 5, the strain rates calculated for each loop exceeded 100%/s, suggesting that $\dot{\gamma}$ may have been underestimated. The normalized shear stress increase with strain rate until stabilizing. This behavior is in line with the backbone curve described by Quinn et al. (2012).

Figure 16 compares the normalized shear stress calculated using the average strain rate ($\dot{\gamma}_{average}$) with the strain rate evaluated for each strain-stress loop ($\dot{\gamma}_{loop}$), color-coded based on $\dot{\gamma}_{loop}$. On average, the values of strain rate compatible undrained strength, adjusted for each load/unload loop were higher than those calculated using $\dot{\gamma}_{average}$. The difference between the two methods was more pronounced at higher shear stress values due to the increase in strain rate for each loop with shear stress. In Figure 16, it is presented all points below 50%/s (blue) yielded normalized shear stress values below 0.8, whereas all data points above 100%/s (orange) had $\tau_{f,cy} / \left(s_u\right)_d$ above 0.9.

Table 3 presents the maximum values of the average strain rate ($\dot{\gamma}_{average}$) for each input used to calculate $\left(s_u\right)_d$, the maximum strain rate calculated for each loop, the corresponding values of normalized shear strength, and the percentile increase. Shear strain rates calculated using accumulated strain and input duration can underestimate soil solicitation during dynamic motion, as show in Figure 16. However, for the strain rate range studied, the increase resulting from using the strain rate calculated for each loop is negligible, amounting to a maximum increase of 5.8%. Higher strain rates may result in a greater difference between the normalized rates and justify calculating the strain rate for each loop.

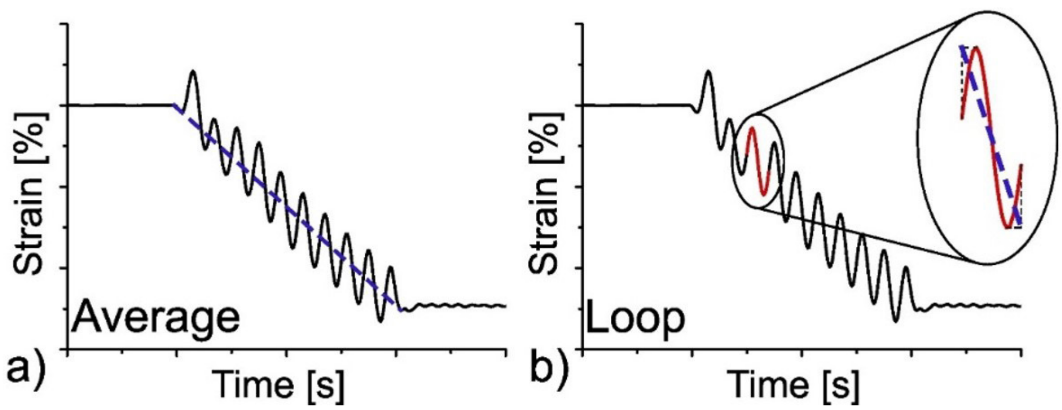

Figure 14. Time history shear strain, strain rate calculation. (a) Strain rate calculated by the average; (b) Strain rate calculated for each loop.

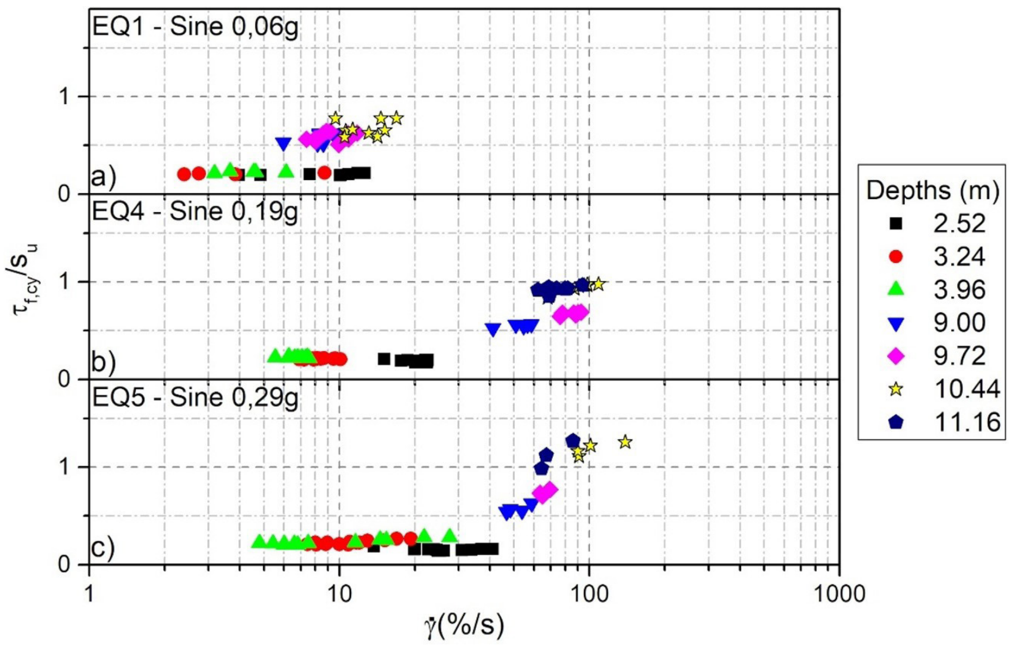

Figure 15. Strain rate compatible normalized shear stress versus strain rate. Model scale.

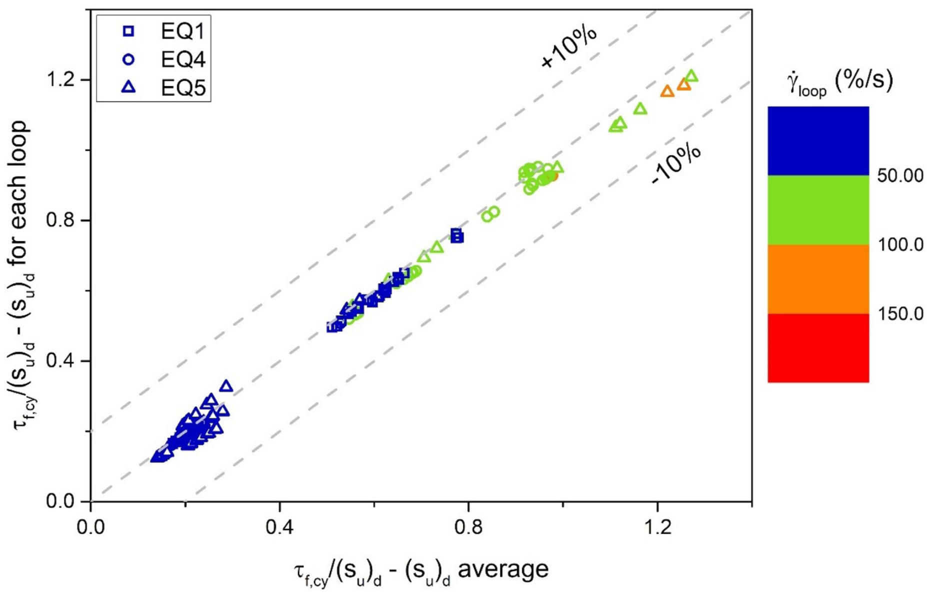

Figure 16. Strain rate compatible normalized shear stress versus strain rate.

Table 3. Shear strain rate, average and for each loop.

	$\dot{\gamma}_{\text{average}}\ (\%/s)$	$\dfrac{(s_u)_{\text{d, average}}}{s_u}$	$\dot{\gamma}_{\text{loop}}\ (\%/s)$	$\dfrac{(s_u)_{\text{d, loop}}}{s_u}$	$\dfrac{(s_u)_{\text{d, loop}}}{(s_u)_{\text{d, average}}}(\%)$
EQ1	7.0	1.30	16.9	1.35	3.8
EQ4	29.5	1.37	108.6	1.45	5.8
EQ5	60.6	1.41	139.2	1.46	3.5

4. Conclusions

In this study, Particle Image Velocimetry (PIV) analysis was used to evaluate the results of a centrifuge test of a gentle slope consisting of a sand layer sandwiched between two clay layers. The PIV analysis was validated by comparing it with data from accelerometers and LVDTs, yielding good agreement. By accurately measuring lateral displacements of soil profiles, PIV enables the evaluation of dynamic soil parameters in physical modelling while accounting for shear strain accumulation.

The shear stress versus shear strain graph revealed an accumulation of strains during loading, consistent with previous findings in the literature (Biscontin & Pestana, 2006). A decline in the shear modulus (G) and increase in damping were also observed.

The results showed lower values of modulus degradation than those reported in the literature for clay and sand. This behavior may be due to the increased reduction in the normalized shear modulus (G_{norm}) resulting from the action of the static shear stress generated by the slope. Further investigation could be conducted to adjust a new set of modulus degradation curves to account for the slope angle.

Each of the three soil layers in the study displayed distinct behavior. The sand layer showed lower strain due to its higher resistance to strength degradation. On the other hand, the upper clay layer had lower normalized shear modulus values compared to the deeper layer. This can be attributed to the increase in static shear stress with depth. The lower layers exhibited more pronounced shear modulus degradation curves, which could potentially be corrected for slope angle effects.

Strain rate analysis for the clay layers supported previous findings in the literature (Afacan et al., 2014; Quinn et al., 2012). Undrained shear strength was found to increase with strain rate and should be accounted for in dynamic tests, particularly in centrifuge tests where the model/scale factor for strain rate depends on the centrifuge acceleration. Although the strain rate calculated for each loop yielded higher than $\dot{\gamma}_{average}$, this increase was insignificant and did not justify the refinement. However, higher shear stress could generate sufficient strain rates that to sustain such analysis.

Acknowledgements

The authors express their gratitude to the staff of the Schofield Centre at the University of Cambridge for conducting the testing program presented in this study. This research work is part of a collaborative effort between PETROBRAS and the Federal University of Rio de Janeiro, under a Cooperation Agreement aimed at investigating ‘Seismic Centrifuge Modelling of Gentle Slopes’ (Contractual Instrument 2017/00259-5). This project has also received partial funding from the Rio de Janeiro State Research Foundation (FAPERJ) and the National Institute of Science and Technology – REAGEO

Declaration of interest

The authors have no conflicts of interest to declare. All co-authors have observed and affirmed the contents of the paper and there is no financial interest to report.

Authors’ contributions

Lucas Chinem Takayassu: formal analysis, software, visualization, writing – original draft. Cristian Yair Soriano Camelo: conceptualization, data curation, methodology, writing – original draft. Marcio de Souza Soares de Almeida: conceptualization, project administration, writing – review & editing. Maria Cascão Ferreira de Almeida: conceptualization, project administration, writing – review & editing. Santana Phani Gopal Madabhushi: data curation, methodology, writing – review & editing. Ricardo Garske Borges: supervision, review & editing.

Data availability

The datasets generated analyzed in the course of the current study are available from the corresponding author upon request.

List of symbols

e	Void ratio
e_{max}	Maximum void ratio
e_{min}	Minimum void ratio
g	Gravity
k	Fitting function (Hardin & Black, 1969)
m	Fitting function (Hardin & Black, 1969)
n	Plastic volumetric strain ratio
p'	Average effective stress
p_r	Reference stress
q_c	Measured tip resistance
s_u	Undrained shear strength
$(s_u)_d$	Strain rate compatible shear strength
$(s_u)_{d,\ average}$	Strain rate compatible shear strength, calculated with $\dot{\gamma}_{average}$
u	Horizontal displacement
$\ddot{u}$	Horizontal acceleration
v_s	Shear wave velocity
w	Water content
z	Depth
A	Fitting function (Hardin & Black, 1969)
CPT	Cone Penetration Test
D_{595}	Significant Durations
F(e)	Fitting function
G_0	Initial shear modulus

G_{norm}	Normalized shear modulus
G_s	Specific Gravity
G_{sec}	Secant shear modulus
K	Normally consolidated strength ratio
LL	Liquid Limit
LVDT	Linearly Varying Differential Transformers
N_{kt}	Cone factor
OCR	Overconsolidation ratio
PGA	Peak Ground Accelerations
PI	Plasticity Index
PIV	Particle Image Velocimetry
PL	Plastic Limit
RCTS	Resonant Column Torsional Shear
RD	Relative density
α	Slope angle
γ	Shear strains
$\dot{\gamma}$	Strain rate
$\dot{\gamma}_{average}$	Average reference strain rate
$\dot{\gamma}_{loop}$	Reference strain rate, calculated for each loop
$\dot{\gamma}_{ref}$	Reference strain rate
λ	Fractional increase of normalized shear strength per log cycle
ρ	Soil density
σ'_v	Effective vertical stress
τ	Shear stress
τ_{cy}	Cyclic shear stress
$\tau_{f,cy}$	Cyclic shear strength
τ_s	Static shear stress
ϕ_{crit}	Critical state friction angle

References

Afacan, K.B., Brandenberg, S.J., & Stewart, J.P. (2014). Centrifuge modeling studies of site response in soft clay over wide strain range. *Journal of Geotechnical and Geoenvironmental Engineering*, 140(2), 04013003. http://dx.doi.org/10.1061/(ASCE)GT.1943-5606.0001014.

Almeida, M.S.S. (1984). *Stage constructed embankments on soft clay* [Doctoral thesis]. Churchill College.

Azeiteiro, R.J.N., Coelho, P.A.L.F., Taborda, D.M.G., & Grazina, J.C.D. (2017). Critical state–based interpretation of the monotonic behavior of hostun sand. *Journal of Geotechnical and Geoenvironmental Engineering*, 143(5), 04017004. http://dx.doi.org/10.1061/(ASCE)GT.1943-5606.0001659.

Biscontin, G., & Pestana, J.M. (2006). Factors affecting seismic response of submarine slopes. *Natural Hazards and Earth System Sciences*, 6(1), 97-107. http://dx.doi.org/10.5194/nhess-6-97-2006.

Brennan, A.J., Thusyanthan, N.I., & Madabhushi, S.P. (2005). Evaluation of shear modulus and damping in dynamic centrifuge tests. *Journal of Geotechnical and Geoenvironmental Engineering*, 131(12), 1488-1497. http://dx.doi.org/10.1061/(ASCE)1090-0241(2005)131:12(1488).

Chang, C.Y., Power, M.S., Tang, Y.K., & Mok, C.M. (1989). Evidence of nonlinear soil response during a moderate earthquake. In *Proc. 12th Int. Conf. on Soil Mechanics and Foundation Engineering*, Rio de Janeiro, Brazil, Vol. 3. Retrieved in April 5, 2023, from https://www.issmge.org/uploads/publications/1/33/1989_03_0105.pdf

Chian, S.C., Tokimatsu, K., & Madabhushi, S.P.G. (2014). Soil liquefaction–induced uplift of underground structures: physical and numerical modeling. *Journal of Geotechnical and Geoenvironmental Engineering*, 140(10), 04014057. http://dx.doi.org/10.1061/(ASCE)GT.1943-5606.0001159.

Colliat, J.L., Desrues, J., & Flavigny, F. (1986). Avantages et inconvénients de l'utilisation d'un système d'antifrettage dans l'essai triaxial de compression. *Revue Française de Géotechnique*, 34, 41-55. http://dx.doi.org/10.1051/geotech/1986034041.

Darendeli, M.B. (2001). *Development of a new family of normalized modulus reduction and material damping curves* [Doctoral thesis]. University of Texas.

Elgamal, A., Yang, Z., & Parra, E. (2002). Computational modeling of cyclic mobility and post-liquefaction site response. *Soil Dynamics and Earthquake Engineering*, 22(4), 259-271. http://dx.doi.org/10.1016/S0267-7261(02)00022-2.

Elgamal, A., Zeghal, M., Taboada, V., & Dobry, R. (1996). Analysis of site liquefaction and lateral spreading using centrifuge testing records. *Soil and Foundation*, 36(2), 111-121. http://dx.doi.org/10.3208/sandf.36.2_111.

Ghosh, B., & Madabhushi, S.P.G. (2002). An efficient tool for measuring shear wave velocity in the centrifuge. In *Proceedings of the International Conference on Physical Modeling in Geotechnics: ICPMG'02* (pp. 119-124). St. John's, New Foundland, Canada: CRC Press / Balkema.

Groholski, D.R., Hashash, Y.M.A., Kim, B., Musgrove, M., Harmon, J., & Stewart, J.P. (2016). Simplified model for small-strain nonlinearity and strength in 1D seismic site response analysis. *Journal of Geotechnical and Geoenvironmental Engineering*, 142(9), 04016042. http://dx.doi.org/10.1061/(ASCE)GT.1943-5606.0001496.

Hardin, B.O., & Black, W.L. (1969). Closure to "Vibration Modulus of Normally Consolidated Clay". *Journal of the Soil Mechanics and Foundations Division*, 95(6), 1531-1537. http://dx.doi.org/10.1061/JSFEAQ.0001364.

Hashash, Y.M.A., Musgrove, M.I., Harmon, J.A., Groholski, D.R., Phillips, C.A., & Park, D. (2016). *DEEPSOIL 6.1: User Manual*. Deepsoil.

Herreros, J.P. (2020). *Dynamic soil-structure interaction of pile foundations: experimental and numerical study* [Doctoral thesis]. École centrale de Nantes.

Hess, R. (2010). *Blender foundations: the essential guide to learning Blender 2.6*. Focal Press/Elsevier.

Hoque, E., & Tatsuoka, F. (2000). *Kinematic elasticity of a granular material*. In *Paper presented at the ISRM International Symposium*, Melbourne, Australia. Retrieved in April 5, 2023, from https://onepetro.org/

ISRMIS/proceedings-abstract/IS00/All-IS00/ISRM-IS-2000-231/50956.

Kokusho, T. (1980). Cyclic triaxial test of dynamic soil properties for wide strain range. *Soil and Foundation*, 20(2), 45-60. http://dx.doi.org/10.3208/sandf1972.20.2_45.

Kramer, S.L. (1996). *Geotechnical earthquake engineering*. Prentice Hall.

Lau, B.H. (2015). *Cyclic behaviour of monopile foundations for offshore wind turbines in clay* [Doctoral thesis]. University of Cambridge.

Li, Z., Escoffier, S., & Kotronis, P. (2013). Using centrifuge tests data to identify the dynamic soil properties: application to Fontainebleau sand. *Soil Dynamics and Earthquake Engineering*, 52, 77-87. http://dx.doi.org/10.1016/j.soildyn.2013.05.004.

Lu, C.-C., & Hwang, J.-H. (2019). Nonlinear collapse simulation of Daikai Subway in the 1995 Kobe earthquake: necessity of dynamic analysis for a shallow tunnel. *Tunnelling and Underground Space Technology*, 87, 78-90. http://dx.doi.org/10.1016/j.tust.2019.02.007.

Madabhushi, G. (2014). *Centrifuge modelling for civil engineers.* CRC Press/Taylor & Francis.

Madabhushi, G.S.P., Haigh, S.K., Houghton, N.E., & Gould, E. (2012). Development of a servo-hydraulic earthquake actuator for the Cambridge Turner beam centrifuge. *International Journal of Physical Modelling in Geotechnics*, 12(2), 77-88. http://dx.doi.org/10.1680/ijpmg.11.00013.

Masson, D. G., Harbitz, C. B., Wynn, R. B., Pedersen, G., & Løvholt, F. (2006). Submarine landslides: processes, triggers and hazard prediction. *Philosophical Transactions of the Royal Society A: Mathematical, Physical and Engineering Sciences*, *364*(1845), 2009-2039. https://doi.org/10.1098/rsta.2006.1810

McKenna, F., Scott, M.H., & Fenves, G.L. (2010). Nonlinear Finite-Element Analysis Software Architecture Using Object Composition. *Journal of Computing in Civil Engineering*, 24(1), 95-107. http://dx.doi.org/10.1061/(ASCE)CP.1943-5487.0000002.

Quinn, T.A.C., Robinson, S., & Brow, M.J. (2012). *High strain rate characterisation of kaolin and its application to rapid load pile testing.* In *Proc. Kanazawa. 9th Int. Conf. on Testing & Design Methods for Deep Foundations*, Kanazawa. Retrieved in April 5, 2023, from https://www.researchgate.net/publication/304282658_High_strain_rate_characterisation_of_kaolin_and_its_application_to_rapid_load_pile_testing.

Rayhani, M.H.T., & El Naggar, M.H. (2007). Centrifuge modeling of seismic response of layered soft clay. *Bulletin of Earthquake Engineering*, 5(4), 571-589. http://dx.doi.org/10.1007/s10518-007-9047-0.

Sahoo, P.P., & Shukla, S.K. (2021). Time-history analysis of soil slope subjected to seismic loadings. *Soil Mechanics and Foundation Engineering*, 58(2), 130-137. http://dx.doi.org/10.1007/s11204-021-09717-z.

Sathialingam, N., & Kutter, B. L. (1989). *The effects of high strain rate and high frequency loading on soil behavior in centrifuge model tests (NCEL Contract Report).* California Univ Davis, from: https://apps.dtic.mil/sti/citations/ADA212089.

Schofield, A.N. (1980). Cambridge geotechnical centrifuge operations. *Geotechnique*, 30(3), 227-268. http://dx.doi.org/10.1680/geot.1980.30.3.227.

Sheahan, T.C., Ladd, C.C., & Germaine, J.T. (1996). Rate-dependent undrained shear behavior of saturated clay. *Journal of Geotechnical Engineering*, 122(2), 99-108. http://dx.doi.org/10.1061/(ASCE)0733-9410(1996)122:2(99).

Soriano Camelo, C.Y., Almeida, M.C.F., & Almeida, M. (2022). Centrifuge modeling of the seismic behavior of soft clay slopes. *Journal of Geotechnical and Geoenvironmental Engineering*, 148(11), 04022089. http://dx.doi.org/10.1061/(ASCE)GT.1943-5606.0002884.

Soriano Camelo, C.Y., Almeida, M.C.F., Madabhushi, S.P.G., Stanier, S.A., & Almeida, M. (2021). Seismic centrifuge modeling of a gentle slope of layered clay, including a weak layer. *Geotechnical Testing Journal*, 45(1), 20200236. http://dx.doi.org/10.1520/GTJ20200236.

Tarazona, S.F.M., Almeida, M.C.F., Bretschneider, A., Almeida, M.S.S., Escoffier, S., & Garske, R.B. (2019). Evaluation of seismic site response of submarine clay canyons using centrifuge modelling. *International Journal of Physical Modelling in Geotechnics*, 172, 1-38.

Tsai, C.-C., & Hashash, Y.M. (2009). Learning of dynamic soil behavior from downhole arrays. *Journal of Geotechnical and Geoenvironmental Engineering*, 135(6), 745-757. http://dx.doi.org/10.1061/(ASCE)GT.1943-5606.0000050.

Vardanega, P.J., Lau, B.H., Lam, S.Y., Haigh, S.K., Madabhushi, S.P.G., & Bolton, M.D. (2012). Laboratory measurement of strength mobilisation in kaolin: link to stress history. *Géotechnique Letters*, 2(1), 9-15. http://dx.doi.org/10.1680/geolett.12.00003.

Viggiani, G., & Atkinson, J.H. (1995). Stiffness of fine-grained soil at very small strains. *Geotechnique*, 45(2), 249-265. http://dx.doi.org/10.1680/geot.1995.45.2.249.

Vucetic, M., & Dobry, R. (1991). Effect of soil plasticity on cyclic response. *Journal of Geotechnical Engineering*, 117(1), 89-107. http://dx.doi.org/10.1061/(ASCE)0733-9410(1991)117:1(89).

Vucetic, M., & Mortezaie, A. (2015). Cyclic secant shear modulus versus pore water pressure in sands at small cyclic strains. *Soil Dynamics and Earthquake Engineering*, 70, 60-72. http://dx.doi.org/10.1016/j.soildyn.2014.12.001.

Wroth, C.P. (1984). The interpretation of in situ soil tests. *Geotechnique*, 34(4), 449-489. http://dx.doi.org/10.1680/geot.1984.34.4.449.

Yang, Z., Yuan, J., Liu, J., & Han, B. (2017). Shear modulus degradation curves of gravelly and clayey soils based on kik-net in situ seismic observations. *Journal of Geotechnical and Geoenvironmental Engineering*, 143(9), 06017008. http://dx.doi.org/10.1061/(ASCE)GT.1943-5606.0001738.

Zeghal, M., Elgamal, A.-W., Tang, H.T., & Stepp, J.C. (1995). Lotung downhole array. II: evaluation of soil nonlinear properties. *Journal of Geotechnical Engineering*, 121(4), 363-378. http://dx.doi.org/10.1061/(ASCE)0733-9410(1995)121:4(363).

Zhang, C., White, D., & Randolph, M. (2011). Centrifuge modeling of the cyclic lateral response of a rigid pile in soft clay. *Journal of Geotechnical and Geoenvironmental Engineering*, 137(7), 717-729. http://dx.doi.org/10.1061/(ASCE)GT.1943-5606.0000482.

CASE STUDIES

Soils and Rocks
An International Journal of Geotechnical and Geoenvironmental Engineering
www.soilsandrocks.com
ISSN 1980-9743
ISSN-e 2675-5475

Development of a risk mapping along a railway

Felipe Gobbi[1#], Alvaro Pereira[1], Bruno Denardin[1], Fabiano Madrid[1], Karine Liboreiro[2], Adoniran Coelho[2]

Case Study

Keywords
Risk mapping
Semi-empirical method
RHRS
Railway risk

Abstract

The Ramal Trem Turístico (RTT), a 17 km long railway between Ouro Preto and Mariana, a centenary line, currently in operation as a tourist attraction with historical importance. The railroad was built along a steep region, with hundreds of slopes, and eventually slope instabilities compromised the tour. In linear infrastructure projects, a risk assessment is an important tool for risk management, mapping it is the first step. After slope instabilities in 2019, a risk map was elaborated early 2021 for RTT. Risk is obtained by multiplying the probability of a certain event to occur by its consequences. Define its value in a quantitative way demands geotechnical investigation, for precise failure probability. Regardless of its importance, its determination needs high resources, specially for linear infrastructure in a region with heterogeneous geology and pedology. Therefore, for the risk mapping of the RTT, a semi-empirical methodology was adopted, based on the Rockfall Hazard Rating System (RHRS), originally developed for rocky slopes, and adapted for the registration of slopes in soil and in landfill. The aim of the method is to register a series of slope characteristics to be assigned a specific score, framing the slopes within pre-defined risk classes. This methodology was applied to this 17 km railway and identified 286 slopes. In January 2022 extreme rainfall triggered slopes instabilities at RTT. A critical analysis of this event shows a satisfactory result for the applied methodology. Risk mapping is an important tool for risk management, helping to prioritize investments in mitigation measures.

1. Introduction

The cities of Marina and Ouro Preto, both located in the state of Minas Gerais, Brazil, are connected by a century-old railway line, which in the past served as the main commercial and passenger route between both municipalities. The construction of the railway line was an engineering challenge at the time, as the region's geomorphology is extremely rough, passing through different geological formations along its 17 km length. With the evolution of road and truck transportation, the railway ended up losing relevance in the region, and after a significant period of neglect, it was converted by private initiative into a tourist attraction, offering people a journey through the secular history of these two municipalities.

Although the extension is not significant, this railway work structure required the execution of cuts, embankments, and tunnels in order to keep the track inclination restricted, mainly due to the limitations of the locomotives of the time. Therefore, along the stretch, hundreds of slopes are observed, consisting of different geotechnical materials and with different geometries.

The rainy season of 2019/2020 in the state of Minas Gerais was extremely intense, with hundreds of millimeters of precipitation recorded in very short time intervals (hours and days), representing very high return periods. These extreme events were responsible for thousands of instabilities throughout the state, including the slopes that make up the section of the old railway between Ouro Preto and Mariana, resulting in the circulation interruption of the tourist attraction.

After assessing the magnitude of the ruptures, it was found that in addition to the triggered events, many slopes presented a critical stability condition. Therefore, the managers of the tourist train operation chose to close the attraction in order to ensure operational safety and the safety of its users.

For the resumption of activities, it was defined that the region should not be subject to a high level of geotechnical risk, meaning that risk mitigation measures would be implemented to ensure the safety of the users. However, even in a short extension, there are hundreds of slopes that can potentially be mobilized, and it is necessary to direct the resources following their degree of criticality, in order to allow the resumption of operation in the shortest possible time, already with the mitigated risk.

[#]Corresponding author. E-mail address: felipe@fgs.eng.br
[1]FGS Geotecnia, Porto Alegre, RS, Brasil.
[2]VALE, Belo Horizonte, MG, Brasil.

Submitted on May 15, 2023; Final Acceptance on October 25, 2023; Discussion open until February 28, 2024.

https://doi.org/10.28927/SR.2023.005523

To define the priority order e the rationalization of the resources, it was decided to develop a geotechnical risk mapping of the slopes present in the entire railway line of the Tourist Train Branch, the RTT. The geotechnical risk map aims to evaluate, define and identify the classes of geotechnical risk of each slope, categorizing them as: very high, high, medium and low risk, enabling a more assertive risk management approach.

Geotechnical risk is defined as the product of the probability of occurrence of a certain event by the consequence of this event. Equation 1 defines a numerical value for the risk:

$$R=H.E.V \tag{1}$$

where: R = risk; H = hazard; E = elements subjected to risk (individuals or infrastructure); and V = vulnerability.

Calculating the risk in quantitative terms demands a significant amount of resources and time, as it requires a detailed geotechnical investigation to support slope stability analyses and the appropriate definition of the probability of failure. In addition, the elements at risk, their spatial variability and frequency, as well as their vulnerability must be determined. Depending on the scale of the problem, this can create a demand for resources and time that are incompatible with the expectations of the parties involved in the problem.

There are simplified methodologies that aim to define the terms of the aforementioned expression qualitatively or quantitatively based on secondary data or the product of field inspections. As an example, the methodology for mapping risk areas published by Instituto de Pesquisas Tecnológicas (IPT) and widely used for mapping and classifying the risk of cities in Brazil can be mentioned. This methodology, Brasil (2007) is fundamentally qualitative and aims to classify risk sectors and areas into groups that fit specific characteristics indicated in that methodology. This type of methodology has a significant advantage over the time of application because the classification is obtained practically immediately after the field visit. However, it has as a negative point the implicit subjectivity arising from the personal judgment of the technicians involved in the mapping.

For this study, the quantitative approach was not feasible due to the extent of the analyzed railway and the deadline for generating the risk classification. Therefore, a semi-empirical methodology was employed for the risk classification, with parameters obtained primarily from the field visit and physical data of the slope but classified according to the variation of the importance of each parameter. This definition of several topics to be evaluated in the inspection, with well-defined classes and aiming to cover all occurrences related to local geomorphology, and its main objective is the reduction of subjectivity in the evaluation, reducing the influence of the technician's judgment involved in the field mapping.

In this study, the development of the geotechnical risk mapping was mainly based on the well-established and widely spread methodology, the Rockfall Hazard Rating System (RHRS). This method was developed by the Oregon Department of Transportation, USA (Pierson et al., 1990; cited in Hoek, 2006), and is a risk classification system for rock mass instabilities applied to roadways. Its basic parameters were adjusted to allow for use on both embankment slopes and natural and cut slopes. This adjustment has already been employed by the authors in linear highway works, and the version presented in this study was adapted and applied to this railway section.

This article aims to present a detailed description of the study area, the adaptations implemented in the RHRS, and the main mapping results. In addition, a comparison was made between the risk map results and different terrain characteristics (slope, materials, orientations) as well as information from open and free sources, in order to establish a correlation between the results obtained by the detailed analysis and these more comprehensive data.

2. Location and geological characterization

2.1 Location

The railway section, spanning approximately 17 kilometers, is located between the municipalities of Ouro Preto and Mariana, in the state of Minas Gerais. Known as the Tourist Train, this section can be characterized as an important tourist route, mainly due to its historical value for the state of Minas Gerais and the country. The ride provides rich historical and cultural knowledge, as well as beautiful landscapes, of the ancient gold route. Figure 1 shows a satellite image with the approximate position of the railway section.

2.2 Geological characterization

The Ouro Preto - Mariana railway is located in the context of the Iron Quadrangle (Romano & Rezende, 2017; Lobato, 2005), which is composed of an archean basement and archean and paleoproterozoic metasedimentary units, with some volcanic contribution. Figure 2 shows a cutout of the most recent geological mapping of the Iron Quadrangle, where according to Endo et al. (2019), intercalations of metasedimentary rocks are expected in the presented groups and formations, with quartzites, schists, itabirites, and phyllites commonly described along this railway stretch.

Regarding pedology, according to Embrapa (2006), the entire study region is located in areas of haplic cambisoil - soil characterized by the presence of an incipient B horizon (therefore, the soil as a whole is not usually very deep) - and, being a poorly developed soil, its characteristics vary according to the origin material.

Figure 1. Railway alignment and pluviometry stations i) Santo Antônio; ii) County of Soares; iii) Bauxita e iv) Highway Melo Frando (Image from *Google Earth*).

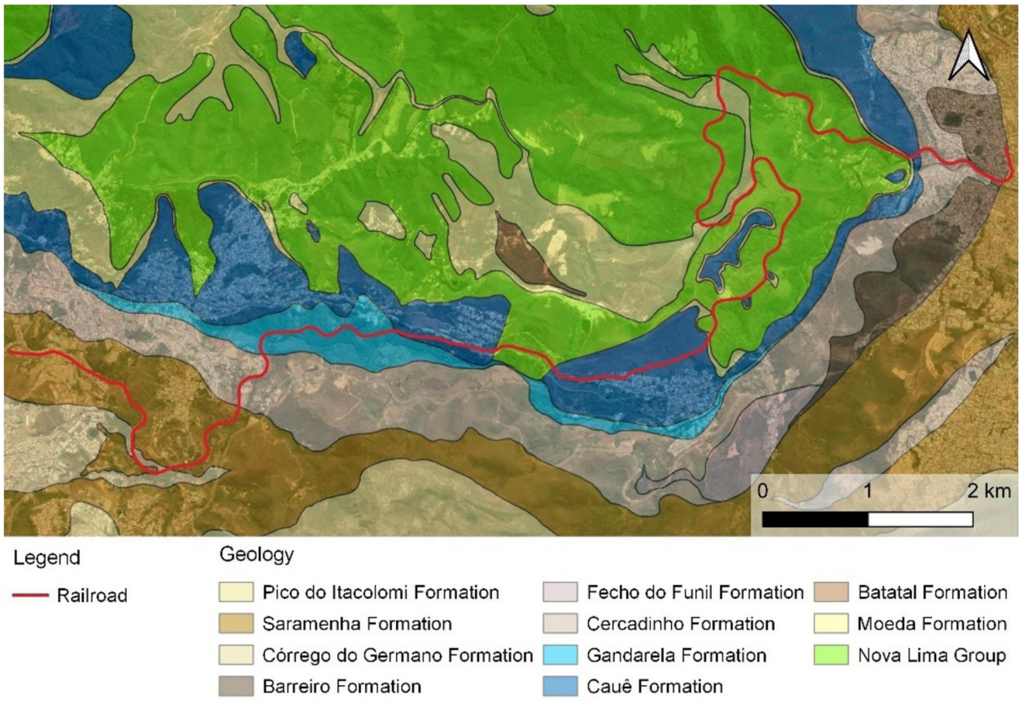

Figure 2. Geological map of the area (adapted from Endo et al., 2019).

With the basic geological and pedological characterization, it was possible to predict which materials are present in the railway section, and thus, basic geotechnical models of the railway slopes were constructed for subsequent refinement with the field survey information to be conducted.

Along this section, it was possible to evaluate the presence of cut, fill, and mixed slopes, executed according to the topographic and geometric variation of the railway, which were classified according to the main material as: fill slopes, cut slopes in rocky masses, cut slopes in soil masses, and natural slopes. This classification is fundamental for the application of the risk classification methodology defined in the project.

Initially, a visit to the region was made with the objective of a general reconnaissance of the area as well as to delineate the general characteristics of the materials to subsidize the following phases of the study.

There was no available information such as boreholes or material classification maps, and thus, for the development, it was necessary to consider that all materials within the same group are similar, assigning a specific classification according to the field observations. In addition to the type of material, this preliminary inspection aimed to preliminarily evaluate the possible instability mechanisms that can affect the local slopes.

3. Risk classification methodology

Geotechnical risk is a function of the product between the probability of an instability event and the consequence of that event, as presented in equation 1, and determining these components requires defining the properties and characteristics of each evaluated slope, a level of detail that makes application in linear sections impractical (especially in terms of time and cost). To overcome this situation, it was necessary to adopt a semi-empirical classification methodology, using an approach to quantify the risk in each mapped slope.

It was defined that the numerical risk is obtained by summing individual scores for a series of pre-established criteria, a procedure established by the Rockfall Hazard Rating System (RHRS) method, due to the large number of successful historical cases of application. As the name suggests, the RHRS was developed to assess the risk of rock fall, so it was necessary to adapt the methodology to the scenario where different materials and rupture mechanisms are present, as well as the specificities of the railway. Note that in this methodology, both the probability component of a certain event occurring and the consequence generated by it are evaluated in terms of specific parameters and scores assigned to local conditions, as will be presented below, meaning that the final score already takes into account the HxC (product presented above).

3.1 Risk classification parameters

The original methodology was used to define the concept that risk is composed of the sum of classification parameters, which indirectly represents the product of the probability and consequence of the event, in other words, a semi-empirical classification methodology. A classification table was established for soil/embankment/rock slopes, and 11 classification parameters were defined for each one, with scores growing exponentially by 3, 9, 27, and 81. The overall score for each slope is obtained by adding up the parameters, a sum that varies between 33 and 891, and the assigned risk is a function of the overall sum. Table 1 and Table 2 indicates the main concepts adopted for defining the classification parameters.

3.2 Table for risk assessment

Above, all the information that constitutes the field parameter criteria was presented and defined. Based on the above criteria, a table was developed for each of the geotechnical materials, which determine the nomenclatures of the parameters, field descriptions, as well as the score assigned to each item.

On Table 3, Table 4 and Table 5 are shown below. Based on these tables, a field mapping was carried out, which consisted of a walking inspection along the entire length of the railway, with a team consisting of a geologist and a geotechnical engineer. In addition to the information indicated in the tables, complementary records were made, mainly related to the drainage system and existing containment structures. Field inspections were restricted to the railway's right-of-way.

To facilitate field activities, these tables were loaded into a GIS environment (software QGIS), allowing all information to be recorded and the polygon of the slope area to be defined during the field inspection, generating an electronic classification table. On the field all the data was collected using a tablet, where all the presented tables were preloaded.

Table 1. Classification parameters for Consequences.

Consequence	Definition
Element and number of exposed people	Building, people, drainage
Vulnerability	Depends on the size of event, energy, potential damage
Time of exposure	Time probability of presence the exposed element at the exact moment of failure

Table 2. Classification parameters for Probabilities.

Probability	Definition
Slope type and geometry	Defines the mechanisms, energy levels, height and slope inclination
Railway geometry	Evaluates: curves, driver time of response, setback of the slope
Slope structure and signs of instabilities	Structural condition of the rockface, erosion signs, tension cracks, etc..
Drainage	Evaluate the correlation between drainage system and stability
Historical cases	Evaluates the historical data of events

Table 3. Classification parameters for rock slopes.

Risk Classification System for Rock Slopes						
CATEGORIA			Classification and scoring criteria			
			3 Points	9 Points	27 Points	81 Points
1.1 Elements at risk: People			Psychological effects	Minor injuries	Serious injuries	Fatality
1.2 Elements at risk Environment			No impact	Punctual impact	Local impact	Regional Impact
1.3 Elements at risk: Financial			>US$10M-US$100 M	>US$ 100M-US$1bi	>US$ 1 bi-US$3bi	>US$ 3 bi
2. Exposure Time			25% of the time	50% of the time	75% of the time	100% of the time
3. Slope height			>7.5 m	>15 m	>25 m	>30 m
4. Presence and effectiveness of ditches			Good containment	Moderate containment	Limited containment	No containment
5. Driver decision distance			Enough for breaking	Enough for speed reduction	Insufficient	Nonexistent
			D>1 km	0.75<D<1.0 km	D<750 m	D<250 m
6. Distance from slope to exposed element			>13 m	Up to 10.80 m	Up to 8.40 m	<6 m
7. Geological conditions	**Case 1**	**Structural condition**	discontinuous fractures	discontinuous fractures	discontinuous fractures	Continuous fractures
			Favorable orientation	Random orientation	Unfavorable orientation	Unfavorable orientation
		Rock friction	Rough, irregular	Wavy	Flat	Clay fill, slickensides
	Case 2	**Points of erosion**	No erosion	Isolated points	Many Points	Large areas
		Variation on erosion	Small variation	Moderate variation	Large variation	Extreme variation
8. Block size			0.3 m	0.6 m	0.9 m	1.2 m
9. Block volume			V<3.00 m^3	3.0<V< 6.00 m^3	6<V<9.00 m^3	>9.00 m^3
10 Movement history			Rare	Occasional	Recurrent	Frequent
11. Water presence/ drainage system			Dry	Isolated wet points	Large areas with water, dripping	Large areas with water flow
			Drainage in perfect condition	Drainage in good condition	Drainage partially functional	Drainage compromised
12.1 Social Impact			No Impact on local communities/culture	Impact on local community	Impact on nearby municipalities	Impact on several municipalities
12.2 Reputation Impact			No impact to image	Local repercussion	National repercussion	International repercussion

Table 4. Classification parameters for soil slopes.

Risk Classification System for Soil Cuts						
CATEGORIA			Classification and scoring criteria			
			3 Points	9 Points	27 Points	81 Points
1.1 Elements at risk: People			Psychological effects	Minor injuries	Serious injuries	Fatality
1.2 Elements at risk Environment			No impact	Punctual impact	Local impact	Regional Impact
1.3 Elements at risk: Financial			>US$10M-US$100 M	>US$ 100M-US$1bi	>US$ 1 bi-US$3bi	>US$ 3 bi
2. Exposure Time			25% of the time	50% of the time	75% of the time	100% of the time
3. Slope height			>7.5 m	>15 m	>25 m	>30 m
4. Presence and effectiveness of ditches			Good containment	Moderate containment	Limited containment	No containment
5. Driver decision distance			Enough for breaking	Enough for speed reduction	Insufficient	Nonexistent
			D>1 km	0.75<D<1.0 km	D<750 m	D<250 m
6. Distance from slope to exposed element			>13.20 m	Up to 10.80 m	Up to 8.40 m	<6 m
7. Geotechnical conditions	**Case 1**	Anisotropy Condition	Favorable orientation	Random orientation	Adverse orientation	Unfavorable orientation
		Anisotropy Inclination	i < 15º	15º<i<30º	30º<i<45º	i>45º
	Case 2	Probability of movement	Unlikely	Likely	Very Likely	Imminent
		Points of erosion	No erosion	Isolated points	Many Points	Large areas
8. Unstable Thickness			t< 0.50 m	0.50<t<1.0	1.00<t<2.00	t>2.00
9. Volume			V<2.50 m^3	2.50<V< 5.00 m^3	5.0<V<10.0 m^3	>10.00 m^3
10 Movement history			Rare	Occasional	Recurrent	Frequent
11. Susceptibilities to saturation / drainage system			Very little susceptible	little susceptible	Susceptible to saturation	Very susceptible to saturation
			Drainage in perfect condition	Drainage in good condition	Drainage partially functional	Drainage compromised
12. Slope Inclination			i < 30º	30º<i<45º	45º<i<60º	i>60º
13.1 Social Impact			No Impact on local communities/culture	Impact on local community	Impact on nearby municipalities	Impact on several municipalities
13.2 Reputation Impact			No impact to image	Local repercussion	National repercussion	International repercussion

Table 5. Classification parameters for embankments.

Risk Classification System for embankments				
CATEGORIA	Classification and scoring criteria			
	3 Points	9 Points	27 Points	81 Points
1.1 Elements at risk: People	Psychological effects	Minor injuries	Serious injuries	Fatality
1.2 Elements at risk: Environment	No impact	Punctual impact	Local impact	Regional Impact
1.3 Elements at risk: Financial	>US$10M-US$100 M	>US$ 100M-US$1bi	>US$ 1 bi-US$3bi	>US$ 3 bi
2. Exposure Time	25% of the time	50% of the time	75% of the time	100% of the time
3. Slope height	>7.5 m	>15 m	>25 m	>30 m
4. Embankment foundation condition	No signs of problems	Containment structure in good condition	Signs of problems, Containment structure in good condition	Visible problem Containment structure precarious
5. Driver decision distance	Enough for breaking	Enough for speed reduction	Insufficient	Nonexistent
	D>1 km	0.75<D<1.0 km	D<750 m	D<250 m
6. Distance from edge of road to embankment crest	>10.00 m	Up to 7.50 meters	5.00 meters	<2.50 meters
7. Embankment Condition – **Longitudinal Cracks** – Length	No cracks	Small and isolated (Up to 1.00m)	Medium and connected (1,00 à 5,00 m)	Long and connected (>5,00m)
7. Embankment Condition – **Longitudinal Cracks** – Thickness	No cracks	Up to 1 cm	Up to 5 cm	>5cm
7. Embankment Condition – **Subsidence** – Length	Nonexistent	P Small and isolated (Up to 1.00 m)	Medium and continuum (1.00 à 5.00 m)	Long and connected (>5.00m)
7. Embankment Condition – **Subsidence** – Depth	Nonexistent	Up to 10 cm	Up to 50 cm	>50cm
8. Erosion processes	No erosion	Isolated points	Many Points	Large areas
9. Impact on road in case of failure	No impact	Reaches outer edge	Partial destruction	Total destruction
10 Movement history	Rare	Occasional	Recurrent	Frequent
11. Susceptibilities to saturation / drainage system	Very little susceptible	little susceptible	Susceptible to saturation	Very susceptible to saturation
	Drainage in perfect condition	Drainage in good condition	Drainage partially functional	Drainage compromised
12.1 Social Impact	No Impact on local communities/culture	Impact on local community	Impact on nearby municipalities	Impact on several municipalities
12.2 Reputation Impact	No impact to image	Local repercussion	National repercussion	International repercussion

This technique allowed the field teams to do a rapid data acquisition, and most important, as this information were digitalized it was possible to automatically exported all the registered slopes and polygons, simplifying and assisting all the data analysis and interpretation of the results.

3.3 Risk classification based upon a GIS approach

In addition to the risk analysis of each point, the polygons registered in the mapping along the railway were analyzed in a GIS environment, in order to determine a possible relationship between the defined risk class and: (i) the local lithology; (ii) the terrain slope. This analysis would allow a preliminary evaluation and direction of geoprocessing mapping for new areas. To approach the data along the railway axis, the risk classification and the limit of influence polygons of each point were considered according to the field survey and risk map analysis, the regional geological map, and the digital elevation model (DEM) based on ALOS PALSAR satellite data, which has a spatial resolution of 12.5 m.

4. Obtained results

Based on the methodology used and the results obtained through field surveys, it was possible to determine the risk classes, considered according to the recommendations indicated in AGS (2000, 2007) manual and the IPT (Brasil, 2007) Ministry of Cities manual, defining 4 risk classes, R1-R4, according to the score presented in Table 6.

The mapping along the railway resulted in the registration of 286 slopes (polygons in Figure 3), which were grouped according to the risk classes. The distribution of the risk levels (Table 6) of all registered elements is presented succinctly in Figure 3, graphically, by the distribution of slopes according to the risk class assigned to each of them and a map.

4.1 Results based upon the GIS approach

According to the position of the points and the regional geological map, the points within each risk class were grouped according to the lithological occurrences, indicating the percentage (%) of points registered in each unit, which are presented in Table 7

Looking at the percentage distribution in Table 7, it can be observed that the majority of high-risk polygons are located in the Barreiro and Córrego do Germano formations, while the high-risk polygons are found in the Saramenha and Moeda formations. These units are characterized by the occurrence of metasedimentary rocks such as quartzites, schists, and phyllites, with the latter two being the main lithologies found in the high-risk areas.

However, another parameter that needs to be evaluated is the spatial representativeness of each lithology. For this analysis, the occurrence of each lithology along the 18km stretch of the tourist train railway was verified. For quantitative purposes, a 30m width strip was considered, representing the same width as the risk polygons on both sides of the railway.

Table 6. Risk classes based on AGS (2007) and Brasil (2007).

Risk	Risk	Score
Low	R1	0-300
Medium	R2	300-500
High	R3	500-700
Very High	R4	>700

The table below shows the area in square meters of each lithology, as well as the percentage of the total surveyed strip area.

To eliminate the impact of spatial representativeness of each lithology, the risk by lithology index (*RL*) was evaluated using the following expression:

$$RL = \frac{\sum AR_{nl}}{\sum A_l} \tag{2}$$

where: RL = risk by lithology; AR_{nl} = area in m^2 of a specific risk class (*n*) in a specific lithology (*l*); and A_l = área in m^2 for a specific lithology (*l*) along the railway.

Table 8 presents the lithology of the total area along the railway and the risk areas by the different classes.

The chart presented in Figure 4 show the *RL* parameter for each lithology to the present study.

Based on the satellite Digital Elevation Model (MDE), a slope map in percentage was generated, with classifications following the recommendations of Embrapa (1979). Based on the geoprocessing values, the maximum, minimum, and average slopes were extracted, as well as the range for each risk class. The MDE with the percentage distribution per risk class is presented in Figure 5.

Table 7. Relation between risk and litology.

Name / Risk	Very High	High	Medium	Low
Moeda Formation	5.0%	20.0%	55.0%	20.0%
Cauê Formation	2.7%	5.4%	35.1%	56.8%
Gandarela Formation	0.0%	12.5%	33.3%	54.2%
Nova Lima Group	3.2%	16.1%	53.2%	27.4%
Cercadinho Formation	0.0%	4.8%	47.6%	47.6%
Barreiro Formation	20.0%	0.0%	40.0%	40.0%
Saramenha Formation	4.2%	22.9%	56.3%	16.7%
Córrego do Germano Formation	14.3%	14.3%	28.6%	42.9%

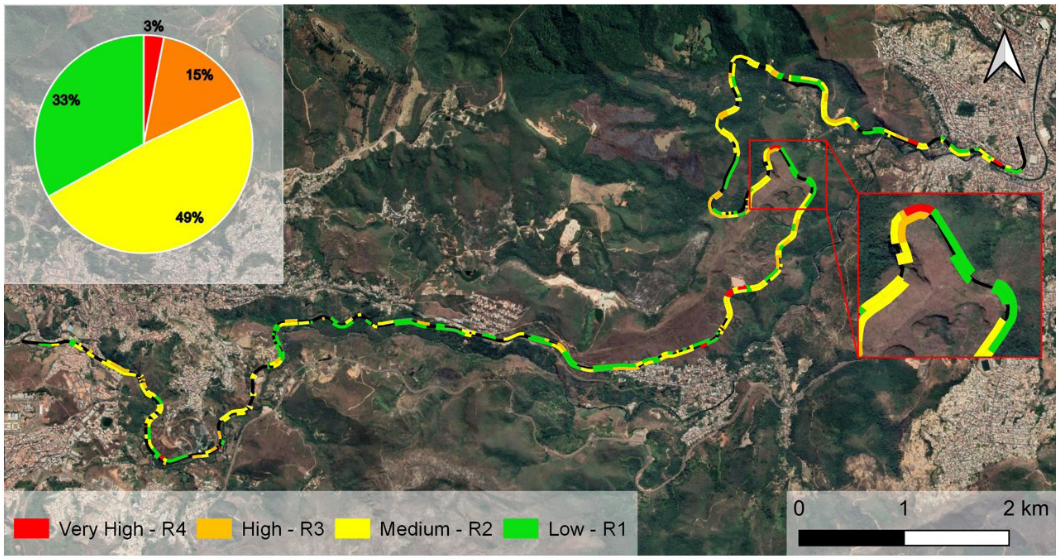

Figure 3. Risk classification of the slopes (numbers and percentage) and the risk map.

Table 8. Spatial distribution of risk and lithology.

Lithology	Total lithology area along the railway (m^2)	Total R1 area (m^2)	Total R2 area (m^2)	Total R3 area (m^2)	Total R4 area (m^2)
Moeda Formation	334,572.64	93,502.38	170,066.75	60,273.45	10,730.06
Cauê Formation	43,136.34	6,805.43	25,254.10	8,427.97	2,648.85
Gandarela Formation	113,727.29	66,109.95	34,182.09	11,314.03	2,121.21
Nova Lima Group	50,712.79	28,629.75	17,386.87	4,696.17	0,00
Cercadinho Formation	11,025.86	4,034.34	4,235.25	0.00	2,756.26
Barreiro Formation	40,648.81	17,391.93	21,280.12	1,976.75	0,00
Saramenha Formation	12,866.81	7,046.33	4,879.30	480.78	460.41
Córrego do Germano Formation	96,676.57	19,239.01	58,859.57	17,239.38	1,338.62

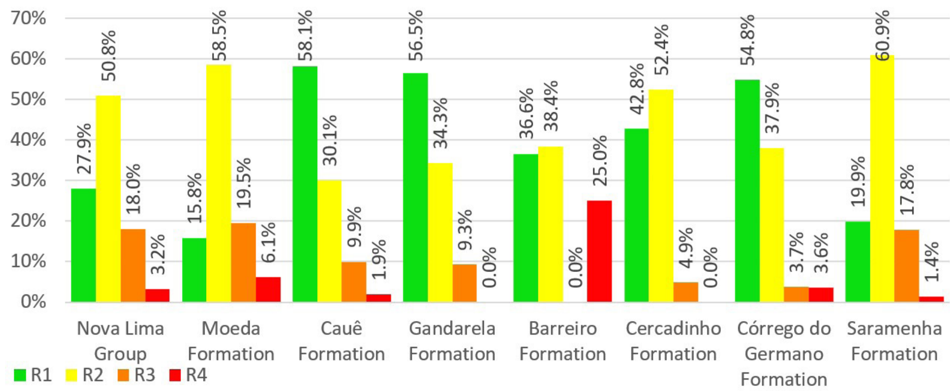

Figure 4. Chart with the lithology vs risk along the railway.

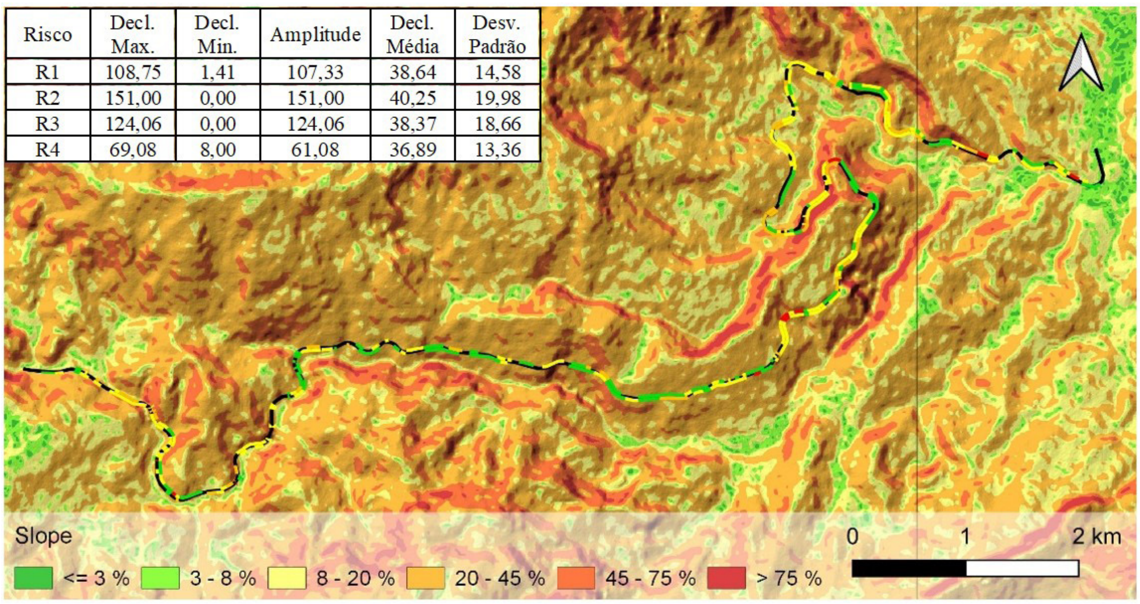

Figure 5. Slope map and % with the risk polygon on the railway.

When analyzing the statistical summary of the slope averages, it can be noted that the maximum values increase and the minimum values decrease as the risk decreases, resulting in a significant increase in the slope range. In other words, there is an increase in the variation of possible slopes according to the change in risk. This factor may be directly related to the higher occurrence of lower-risk classes. The graphic results of this analysis are presented in Figure 6.

The average of the slopes remains relatively constant, around 38%. When observing the distribution of the maximum and minimum values, it is noticed that the results do not suggest a strict pattern of relationship between the topography and the risk areas. This could be due to two factors: a) these estimates did not provide conclusive results due to the local nature of the areas, and the resolution of the available data may not be detailed enough for the level of detail in this

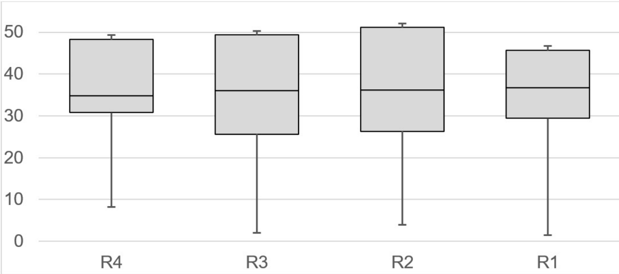

Figure 6. Boxplot chart illustrating the slop distribution for each risk class.

study; or b) the risk factors are better conditioned by the specific lithology found point by point.

4.2 Risk map evaluation after occurrence of new failures

During the rainy season of 2021/2022, specifically from January 7th to 10th, 2022, there was a period of high precipitation (return period of approximately 50/100 years), resulting in some new slope failure along the railway. To assess the accuracy of the risk map, one of the first actions taken was to evaluate the precipitation that occurred. Observational data shows that during the first half of January alone, the four pluviometry stations recorded accumulated rainfall that exceeded the historical monthly average for the month, which ranges from 300-350mm. The consulted data from the stations i) Santo Antônio with 445 mm; ii) Subdistrict of Soares with 469 mm; iii) Bauxita with 446 mm; and iv) Rodovia Melo Frando with 469.31 mm, according the CEMADEN. The rainfall data shows consistency in the spatial distribution of rainfall in the area of interest, which allows extrapolating this rainfall to the railway region. As can be seen between the 7th and 10th of January, the period when the failures occurred, there was a significant accumulation of precipitation, with daily rainfall reaching approximately 180 mm in 24 hours.

A new inspection along the entire stretch of the railway was carried out by two geotechnical engineers to identify and locate unstable points. After mapping these new points, they were cross-checked with the risk map that had been previously conducted and reclassified. Photographic records were taken for all points and compared with previous records, and the description of each point in the risk map and the current description of instability were retrieved. Additionally, actions that could be implemented were indicated for each point. Table 9 presents the results of the inspection carried out after the rainy period of 2021/2022, including the initial classification of the polygons, the reclassification of each instability point, the justification for each point's alteration, and the severity of impact on the railway. The severity was classified as low, medium, or high. Low severity means that the volume that reached the railway would not be sufficient to cause a disruption in the line, medium severity means that the volume would temporarily halt the line but could be cleared within a few hours (i.e., < 10 m^3), and high severity refers to volumes exceeding 10m^3. If the instability did not reach the railway, the severity was classified as null.

Based on the assessment of the points recorded and presented in Table 9 a total of 32 instability points were identified: 9 in high-risk areas, 18 in medium-risk areas, and 4 in low-risk areas. Two of the points occurred in locations where retaining walls were present, which had been excluded from the initial risk map. After the site visit, the points were reclassified based on the changed local conditions, it can be observed that there is a convergence between the classification assigned to the instability points and the characteristics of the actual events recorded at the site. Overall, the significant change was the escalation of medium-risk points to high risk. Only one low-risk point moved to the high-risk category, and one high-risk point moved to very high risk. It is worth noting that the two points related to retaining walls were not classified in the risk map, as it was assumed (during the development of the risk mapping) that the constructed containment structures were designed and built to withstand the predicted events throughout the structure's lifespan.

It is important to revisit the conceptual difference between risk and susceptibility. Susceptibility refers to the probability of a specific event (in this case, instabilities) occurring, while risk is the product of this susceptibility and the resulting consequence (in this case, the impact on the railway). In other words, points with records of occurrences that did not affect the railway do not indicate high-risk points but rather high susceptibility. This difference is crucial to understand to avoid misinterpretation of the relationship between the recorded events and the existing risk mapping. In other words, small events that did not impact the railway did not pose a risk to its operation. For a quantitative assessment in this regard, severity classes of the events were defined as mentioned earlier. Excluding points with null severity, there were 9 instabilities recorded in areas pre-classified as high risk, 10 in areas pre-classified as medium risk, and 1 instability in an area previously mapped as low risk.

5. Conclusion

A risk mapping of a 17 km railway section between the cities of Ouro Preto and Mariana was presented. This study identified 286 risk areas classified as low, medium, high, and very high. This risk mapping was used for railway risk management, including planning, stabilization projects, construction works, and monitoring.

Less than a year after the completion of the mapping, an intense rainfall event struck the state of Minas Gerais and caused a series of instabilities in this railway section. The instabilities occurred in high, medium, and low-risk areas: 9 in high-risk areas, 18 in medium-risk areas, 3 in low-risk areas, and 2 were not classified because the slopes already had containment structures. Locations with a high probability of an event occurrence but without significant consequences are categorized as low risk. This situation was identified in most

Table 9. Analysis results.

Point	Initial Risk	Risk post event	Hazard of railway impact	Reason to risk alteration
04	Low	Medium	Low	No field evidence was found for an event of this magnitude, suggesting that it was possibly caused by the overflow of the upstream street drainage system.
06	Medium	High	Medium	Mobilization of a previously occurred event, with the contribution of the upstream drainage system failure.
09	High	High	High	Unchanged
10	Medium	Medium	Low	Unchanged
11	Medium	Medium	Null	Unchanged
12	Medium	Medium	Medium	Unchanged
33	Medium	High	Low	Change in local conditions, after the rains and the occurrence of the rupture (which did not reach the railway), a crack was triggered, and a second event could now affect the railway, thereby altering the risk at the site.
40	Low	Low	Null	Unchanged
-	Not classified	High	Low	Unclassified because of a retaining wall existing
42	High	Very High	High	An expected critical event was predicted; however, the magnitude of the recorded event is greater than initially anticipated.
45	High	High	Low	Unchanged
46	High	High	Low	Unchanged
150	Medium	Medium	Low	Unchanged
151	Medium	High	Low	The obstruction of the drainage system at the crest of the slope
160	Medium	High	Null	As a result of the identification of a tension crack
183	High	High	Low	Unchanged
192	Medium	Medium	Low	Unchanged
193	Low	Low	Null	Unchanged
198	High	High	Low	Unchanged
213	Medium	Medium	Null	Unchanged
214	Medium	Medium	Low	Unchanged
215	Medium	Medium	Low	Unchanged
218/219	High	High	Low	Unchanged
220	Medium	Medium	Null	Unchanged
221	Medium	Medium	Null	Unchanged
226	High	High	Low	Unchanged
227	Medium	Medium	Null	Unchanged
236	Low	Low	Null	Unchanged
239	Medium	Medium	Null	Unchanged
248	High	High	Low	Unchanged
250	Medium	Medium	Null	Unchanged
256	Medium	Medium	Low	Unchanged
-	Not classified	High	Medium	Unclassified because of a retaining wall existing

of the instabilities recorded in medium and low-risk areas. Excluding points with null severity, the results were 9 in high-risk areas, 8 in medium-risk areas, and 1 in low-risk area.

The crossing of risk areas with lithology indicated that the Barreiro Formation, followed by the Córrego do Germano Formation, had the highest occurrence in the R4 class. The Saramena Formation and Moeda Formation represented the highest proportion in the R3 and R2 classes, respectively. Regarding the lowest risk class, R1, the Cauê and Gandarela Formations from the Itabira Group were the predominant lithologies.

The crossing of risk areas and slope did not show a strong correlation between topography and risk areas. This result may indicate that the topographic base does not have a resolution compatible with the detail scale of the mapping or that the predominant factor is related to lithology.

The analysis of correlations highlights that specific local factor of each slope (e.g., geometry, materials, drainage conditions) and human activities on the terrain are sometimes masked due to the scale of the available information. The higher the level of detail in the provided information, the greater the accuracy of the risk mapping.

Finally, the analysis conducted after a high rainfall event and a large number of instabilities indicated that the risk mapping showed satisfactory convergence. Additionally, a risk map is a management tool used to allocate resources and identify areas to be further studied in subsequent stages. It should be constantly updated as new information becomes available.

Acknowledgements

The authors would like to express their gratitude to VALE for their support in conducting this work, which led to the publication.

Declaration of interest

The authors have no conflicts of interest to declare. All co-authors have observed and affirmed the contents of the paper and there is no financial interest to report.

Authors' contributions

Felipe Gobbi: Field Mapping, original draft, Project administration, Methodology, Validation; Formal Analysis. Alvaro Pereira: Field Mapping, Conceptualization; Writing – review & editing; Formal Analysis. Bruno Denardin: Formal Analysis, Field Mapping, Writing – review & editing, Methodology. Fabiano Madrid: Formal Analysis, Software, GIS analysis; Field support. Karine Liboreiro: Funding acquisition; Project administration, resource acquisition for field mapping, result analysis and discussions. Adoniran Coelho: Funding acquisition; Project administration, resource acquisition for field mapping, result analysis and discussions.

Data availability

The datasets generated analyzed in the course of the current study were collected during the development of the present study, and all data produced or examined in the course of the current study are included in this article.

References

Australian Geomechanics Society – AGS. (2000). Landslide risk management concepts and guidelines. *Journal and News of the Australian Geomechanics Society*, 35, 49-92.

Australian Geomechanics Society – AGS. (2007). Landslide risk management. *Journal and News of the Australian Geomechanics Society*, 42(1), 1-269.

Brasil. Ministério das Cidades. Instituto de Pesquisas Tecnológicas – IPT. (2007). *Mapeamento de riscos em encostas e margem de rios.* Brasília.

Empresa Brasileira de Pesquisa Agropecuária – Embrapa. (1979). *Manual de métodos de análise de solos.* Embrapa.

Empresa Brasileira de Pesquisa Agropecuária – Embrapa. (2006). *Sistema brasileiro de classificação de solos* (2. Ed.). Embrapa.

Endo, I., Galbiatti, H.F., Delgado, C.E.R., Oliveira, M.M.F., Zapparoli, A.C., Moura, L.G.B., Peres, G.G., Oliveira, A.H., Zavaglia, G., Danderfer Filho, A., Gomes, C.J.S., Carneiro, M.A., Nalini Junior, H.A., Castro, P.T.A., Suita, M.T.F., Tazava, E., Lana, C.C., Martins-Neto, M.A., Martins, M.S., Ferreira Filho, F.A., Franco, A.P., Almeida, L.G., Rossi, D.Q., Angeli, G., Madeira, T.J.A., Piassa, L.R.A., Mariano, D.F., & Carlos, D.U. (2019). *Mapa geológico do Quadrilátero Ferrífero, Minas Gerais, Brasil. Escala 1:150.000*. Ouro Preto: Departamento de Geologia, Escola de Minas, Centro de Estudos Avançados do Quadrilátero Ferrífero, Universidade Federal de Ouro Preto.

Hoek, E. (2006). *Pratical Rock Engineering* (341 p.). Evert Hoek Consulting Engineering Inc.

Lobato, L.M. (Coord.). (2005). *Projeto Geologia do Quadrilátero Ferrífero: integração e correção cartográfica em SIG com nota explicativa – Folha Mariana. Escala: 1:50.000* (Vol. 1). Belo Horizonte: CODEMIG.

Romano, A.W., & Rezende, L.F.S. (2017). *Projeto Triângulo Mineiro - Folha Ouro Preto SF.23-X-A-III. Escala 1:100.000*. Belo Horizonte: CODEMIG.

Soils and Rocks

An International Journal of Geotechnical and Geoenvironmental Engineering

www.soilsandrocks.com

ISSN 1980-9743
ISSN-e 2675-5475

3D numerical analysis of soil nailing in sedimentary soil with vertical inclusions

Max Gabriel Timo Barbosa[1#], Leonardo Rodrigues Ferreira[1], George Joaquim Teles de Souza[2], Renato Pinto da Cunha[1], Ennio Marques Palmeira[1]

Case Study

Keywords
Soil nailing
Sedimentary soil
Finite element method
3D
Displaceability
Excavation

Abstract

In this case study of a soil nail retaining wall, the measured horizontal displacement is of the order of 0.023% *H*, where *H* is the excavation depth, while the two-dimensional Finite Element Method (FEM) analysis suggests horizontal displacements of the order of at least 0.5% *H*. This study aims to understand which parameters influence such displacements through a Sensitivity Analysis. In addition, the study compares results obtained through two-dimensional and three-dimensional FEM analyses for this case. It concludes that Young's Modulus (E) and the in-situ earth pressure coefficient (K_0) are the two parameters that most influence such displacements. This study shows that Mohr Coulomb's perfectly plastic Elastic Constitutive Model is unsuitable for simulating this structure, which had minimal displacements in situ, suggesting the Hardening Soil model (Schanz et al., 1999) as a viable alternative. Compared to 3D analysis, 2D analysis showed significantly larger horizontal displacements. This led to the conclusion that 2D analysis in MEF is unsuitable for predicting lateral displacements unless a Reduction Factor (*FR*) ranging from 0.4 to 1.0 was applied.

1. Introduction

The technique called Soil Nailing, in which a metallic reinforcement is inserted into the soil and grouting the bar into the hole, is increasingly used worldwide. This technique, which derives from the New Austrian Tunneling Method (NATM), also uses shotcrete on the face of the excavation.

This technique was first applied in Brazil in a case in the Rodovia dos Imigrantes in 1972. Because it was a work located in a rural area, far from nearby constructions, the deformations of the retaining wall were not a concern, with priority being given only to the stability of the retaining wall. Many other cases followed this one, and for 20 years, most of the soil nailing applications were related to infrastructure constructions, with little concern for deformations due to excavation.

This generated an understanding that solutions using soil nailing deformed excessively, and its application should not be recommended in urban areas. Despite this, the technique continued to evolve to allow its use in urban works. Sectorized post-grouting was responsible for this evolution, reducing deformations in the excavation wall to acceptable, often negligible, values (Pitta et al., 2017).

The sectorized post-grouting technique has several advantages over the soil nailing performed without pressure, called gravity-grouted soil nails (Barbosa et al., 2022). This is due to soil densification, resulting in more significant confining stress and improving strength and deformability properties. The possible increase in the soil's local apparent cohesion is also an essential factor in improving these properties, together with the decrease in global permeability and homogenization of the improved soil. The difference in methods is portrayed in Figure 1.

In addition to this technique, introducing vertical inclusions before excavation also causes a stiffening of the excavation face and allows a quicker excavation. This technique avoids weighting of the cut during excavation, eliminating a step in the construction process and providing excellent safety for workers executing the retaining wall. Figure 2 illustrates the technique and the construction phase.

In order to illustrate the use of soil nailing in urban environments, the advantageous influence of the vertical inclusions prior to the excavation, and the accurate simulations of such structures in design scenarios considering sectorized post-grouting, a case study of an actual retaining wall was performed.

#Corresponding author. E-mail address: maxtimo@gmail.com
[1]Universidade de Brasília, Brasília, DF, Brasil.
[2]Solotrat, São Paulo, SP, Brasil.

Submitted on May 15, 2023; Final Acceptance on October 25, 2023; Discussion open until February 28, 2024.
https://doi.org/10.28927/SR.2023.005723

(a) (b)

Figure 1. Soil nail: (a) gravity-grouted; and (b) post-grouted (Pitta et al., 2017).

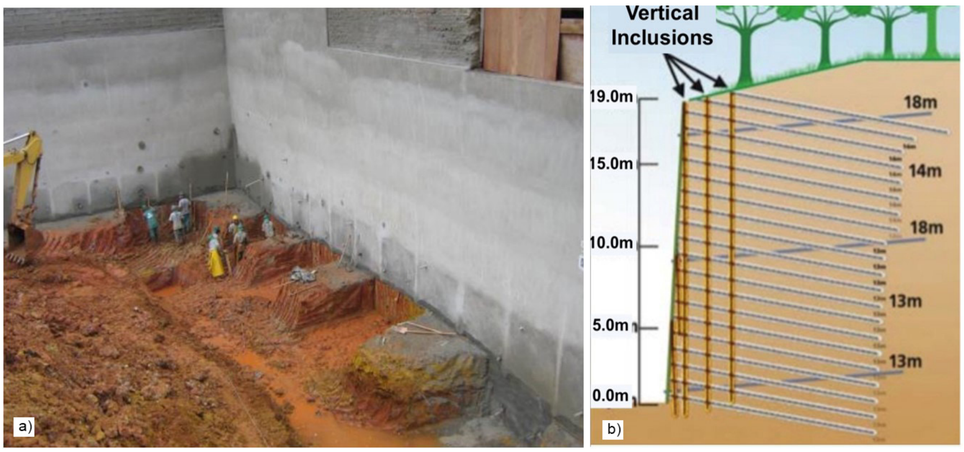

Figure 2. Constructive procedure: (a) using berms; and (b) vertical inclusions (adapted from Pitta et al., 2013).

2. Case study

2.1 Project description

The studied retaining wall is located at Rua Alfredo Pujol in São Paulo and is part of a commercial development. Its project foresaw two floors of underground garages, in which the excavated slopes were stabilized using the soil nailing technique. The excavation totalled a depth of almost 19.0 m and presented very low displacements, 0.02% of the depth.

The local sedimentary soil presents two main characteristic layers. The upper layer was located above the water level and consisted of alternated layers of fine sand and silty and sandy clay. The lower layer was below the water level and consisted of silty clay from the tertiary sediment of São Paulo (regionally known as "taguá clay").

Thus, the soil can be classified as the typical variegated occurring commonly in São Paulo. Futai et al. (2012) mentions that the variegated soil is characterized by layers of clay with little sand alternating with layers of fine sand with little clay, a stratigraphy similar to that found in the site. Engineering properties vary widely, and consistencies vary from medium to hard, but they behave like stiff and even hard soils.

2.2 Scenario description

Figure 3 summarizes the geometry of the analyzed area in the front view, plan, and section view. Vertical and horizontal spacing between nails was approximately 1 meter.

2.3 Field measurements

The same grout injection monitoring proposed by Ludemann et al. (2018) was used in the installed instrumentation, which allowed the analysis of various registers. The most used data are described below, starting with the excavation operations, followed by data from the inclinometer installed on the excavation face, data from the pullout test, and, finally, data from the N_{SPT} test.

The progress of excavation depth according to the schedule is shown in Figure 4.

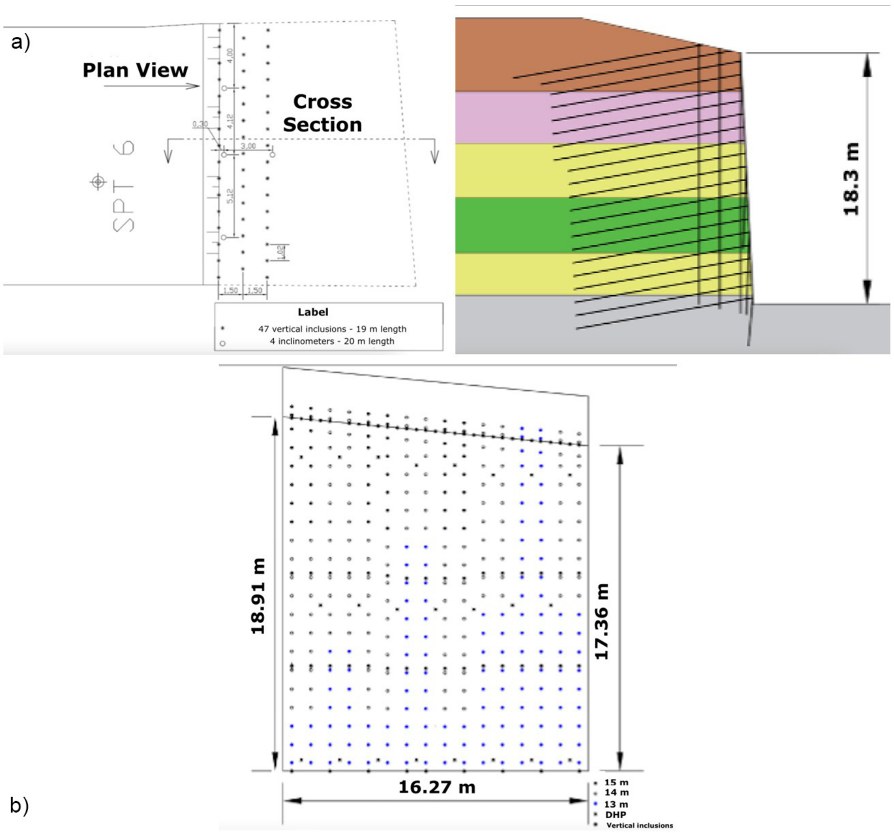

Figure 3. Area: (a) plan section; (b) front view.

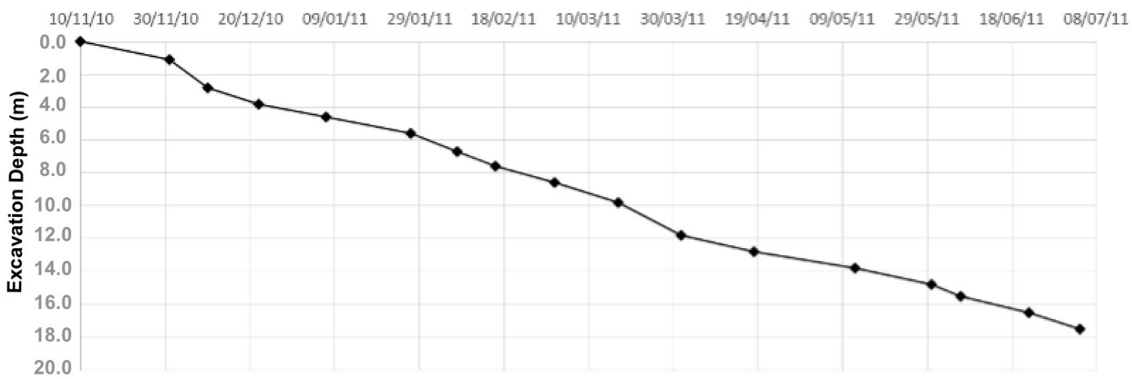

Figure 4. Work schedule.

The horizontal displacements measured by the inclinometers are shown in Figure 5 . The legend indicates the depth of the excavation at the time of reading.

Five pullout tests were performed in total, on different days and at different depths. The summary of the results is arranged in Table 1 .

It is known that the N_{SPT} test in Brazil transfers between 72% and 82.3% of the theoretical potential energy to SPT rods. Table 2 indicates N_{SPT} values obtained on site.

3. Description of simulation models

Three finite element simulation models were prepared to analyze the work, one of the models being two-dimensional and the other three-dimensional, as shown in Figure 6 . The third numerical model is a three-dimensional model adapted to analyze vertical inclusions.

As shown in Table 2, the soil mass was divided into seven layers, following the soil profile. The excavation was divided into nine stages of approximately 2 meters, and the water table was positioned at a depth of 15 meters, as predicted by the penetration test, considering the lowering to the bottom of the excavation.

The two-dimensional numerical model comprises 2,744 triangular elements of 15 and 22,089 nodes. Close to the excavation face, the elements are smaller and in greater quantity. The software used was Plaxis 2D.

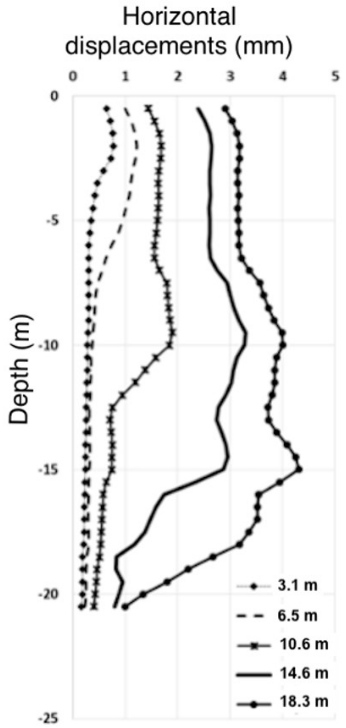

Figure 5. Inclinometer data.

The three-dimensional model is composed of 454,323 elements 611,084 nodes, and the elements are ten-node tetrahedrons. The software used was Plaxis 3D.

An adapted three-dimensional numerical model was also used to verify the influence of vertical inclusions: a 4-meter-long strip centered on the three-dimensional numerical model, as shown in Figure 7. This was necessary because the use of vertical inclusions in the original three-dimensional model generated very small elements and in a quantity superior to the computational capacity possessed. The constitutive model used was the *Hardening Soil*, elaborated by Schanz et al. (1999).

4. Analysis results

The analyses carried out on the two-dimensional numerical model allowed a sensitivity analysis to identify the relevant parameters in the model, which in turn allowed the calibration of the three-dimensional model. The sensitivity analysis indicated that the Young's Modulus (E) and the at-rest earth pressure coefficients (K_0) of the different layers are the most relevant parameters influencing the horizontal displacements of the soil nailing retaining wall.

The parameters used were determined from correlations with the N_{SPT} values obtained in the field and corrected by the aforementioned sensitivity analysis. These parameters are summarized in Table 3 .

The calibration process showed a significant increase in the Young's modulus of the soil mass since the displacements obtained by the instruments were very small (on the order of 0.02% H).

This increase is represented as "n" in Table 4, where E_i is the initial tangent Young's Modulus used in the calibrated model, and E_{i0} is the initial tangent Young's Modulus obtained by correlation with the N_{SPT}.

Table 1. Results of pullout tests.

Nail Depth (m)	Maximum pullout force– T_{Max} (kN)	Resistance per meter of nail (kN/m)	Pullout Resistance q_s (kPa)
6.0	35	17.5	73
	70	35	146
Averages 6.0	52.5	26.5	109.5
9.0	50	25	104
	40	20	84
	35	17.5	73
Averages 9.0	41.6	20.8	87

Table 2. SPT test result.

	Depth (m)	N_{SPT} 72	N_{SPT} 60	local stratigraphy
Layer 1	0 to 5	~5	~6	landfill
Layer 2	5 to 9	5 to 11	6 to 13	fine clayey sand
Layer 3	9 to 13	8 to 14	10 to 17	hard silty clay
Layer 4	13 to 17	6 to 12	7 to 14	fine clayey sand
Layer 5	17 to 20	13 to 16	16 to 19	silty clay
Layer 6	20 to 25	22 to 30	26 to 36	silty clay very tough
Layer 7	25	>30	>36	Impenetrable

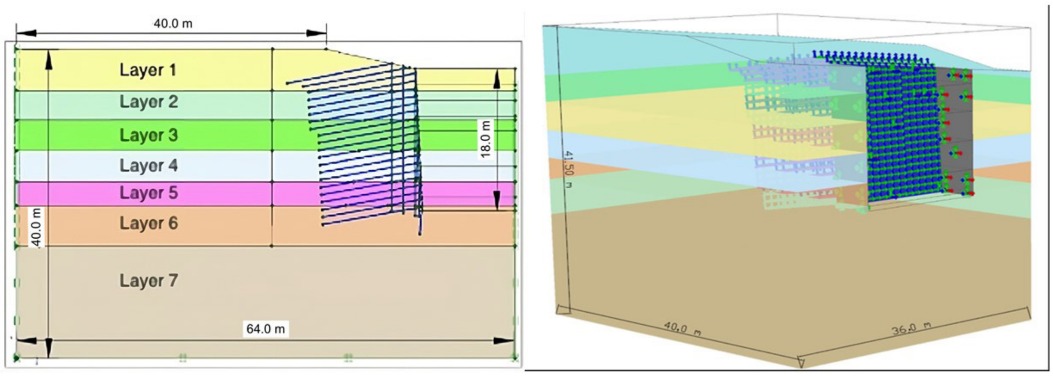

Figure 6. Geometry of the numerical models used, two-dimensional and three-dimensional.

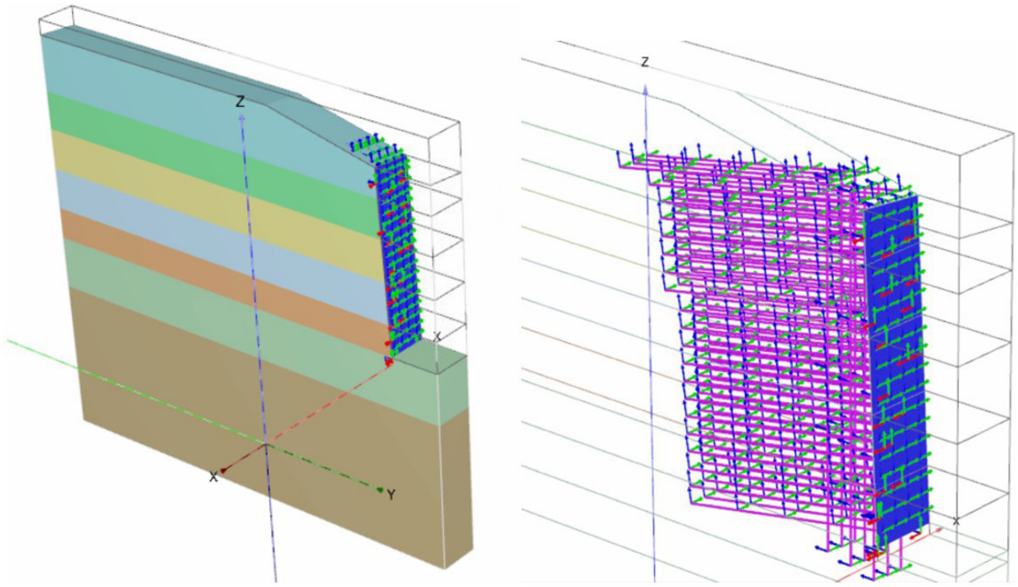

Figure 7. Three-dimensional numerical model adapted to consider vertical inclusions.

Table 3. Parameters used in the calibrated model.

Layer	Friction Angle (ϕ')	Cohesion (c') kPa	Poisson Coefficient (v)	At rest earth pressure (K_0)	Specific Weight (γ) - kN/m^3
1	32	40	0.3	0.7	16
2	34	25	0.25	0.7	17
3	25	50	0.33	1.5	17
4	34	25	0.25	1.5	17
5	23	45	0.33	1.5	18
6	30	60	0.33	0.86	18
7	-	1000	0.2	1	20

According to Falk (1998), when the soil is injected with cement grout under pressure (as in this case), there is a significant improvement in soil parameters, especially in stiffness and cohesion. The increase in stiffness proposed by the calibration is within the range Falk (1998) proposed in the injected soils, as indicated in Figure 8 .

The horizontal displacements calculated by the numerical model and obtained in the field are compared in Figure 9 .

4.1 Influence of vertical inclusions

With the model calibrated, the influence of the vertical inclusions was verified. The adapted three-dimensional model was used for this, with the parameters considered calibrated from the previous analysis.

The model was calculated four times: disregarding the vertical inclusions, considering only one row of inclusions,

Table 4. Parameters used in the calibrated model.

Layer	$Ei = n.Ei_0$	n	E_{50}^{ref} (MPa)	E_{oed}^{ref} (MPa)	E_{ur}^{ref} (MPa)
1	136	1.4	100	125	300
2	380	2.5	230	287	690
3	634	2.8	300	375	900
4	839	4.8	330	412	990
5	989	3.4	390	487	1170
6	888	2.0	400	500	1200
7	782	1.4	430	537	1290

considering two rows of inclusions, and considering three rows of inclusions. Figure 10 shows the results for the four calculated situations. The maximum horizontal displacements were evaluated in each excavation step and compared with those obtained in the model without vertical inclusions.

Table 5 summarizes the results obtained in each situation and the variation concerning the model without vertical inclusions.

It was observed that the vertical inclusions reduced the maximum horizontal displacements observed by up to 1%, maintaining an average of approximately 0.5% decrease in relation to the maximum displacements obtained without horizontal nails.

These values, especially when dealing with millimetric displacements, are insignificant for the magnitude of the excavation. It is considered, then, that the vertical inclusions did not influence the horizontal displacements, at least not as a structure, that is, using its own stiffness and strength to reduce displacements.

However, the effects of vertical inclusions on the increase in soil stiffness should be addressed since it is believed that the grout injection under pressure is directly related to the increase in soil stiffness in this case.

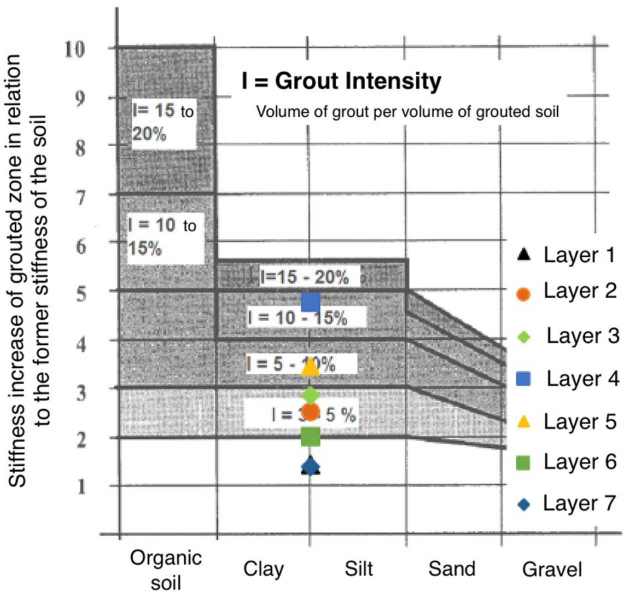

Figure 8. Increased stiffness due to soil injection by soil type (modified from Falk, 1998).

4.2 Comparison between 2D and 3D models

With the three-dimensional model calibrated, it was possible to create a relationship between the maximum displacements obtained by the two-dimensional model and the maximum displacements obtained by the three-dimensional model using the same parameters.

The comparison between the 2D and 3D models was based on the Maximum Horizontal Displacements obtained in each stage of the simulation, that is, in each stage of the excavation. Then, the horizontal displacements in the 3D model were made compatible with what happens in the field. This was done from model calibration. For comparison purposes, some principles were considered.

The first principle considered is exposed by Equation 1, which defines that the two- and three-dimensional models will present equal results when the excavation length is infinite.

$$\lim_{L \to \infty} \frac{H}{L} = 0 \tag{1}$$

The second principle considers that, with lateral restrictions in the excavation direction (as in the case study), the three-dimensional model should result in horizontal displacements smaller than the displacements calculated by the two-dimensional model.

Therefore, when calculating a horizontal displacement in a two-dimensional model considering plane deformations, the model will produce an overestimated result compared to a three-dimensional model, as observed in the simulations. A reduction factor can approximate such values to more realistic values.

As the most significant interest lies in the maximum horizontal displacement on the slope, the comparison is made by relating the Maximum Horizontal Displacement calculated by the 3D model (DMH_{3D}) to the Maximum Horizontal Displacement calculated by the 2D model (DMH_{2D}). In this way, the Reduction Factor (FR) is defined, as in Equation 2.

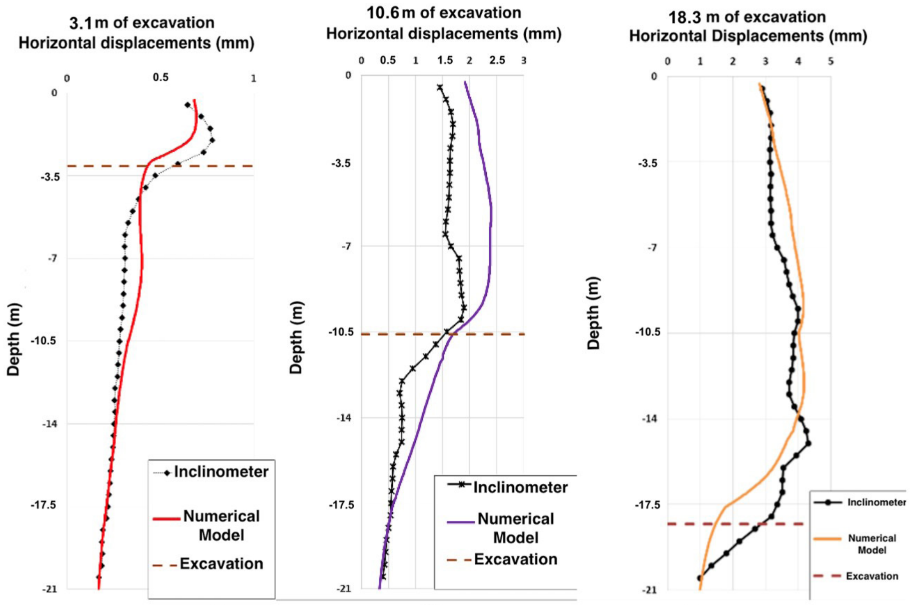

Figure 9. Horizontal Displacements at different excavation stages. (a) horizontal displacements at 3.1 m of excavation; (b) horizontal displacements at 10.6 m, c) horizontal displacements at 18.3 m.

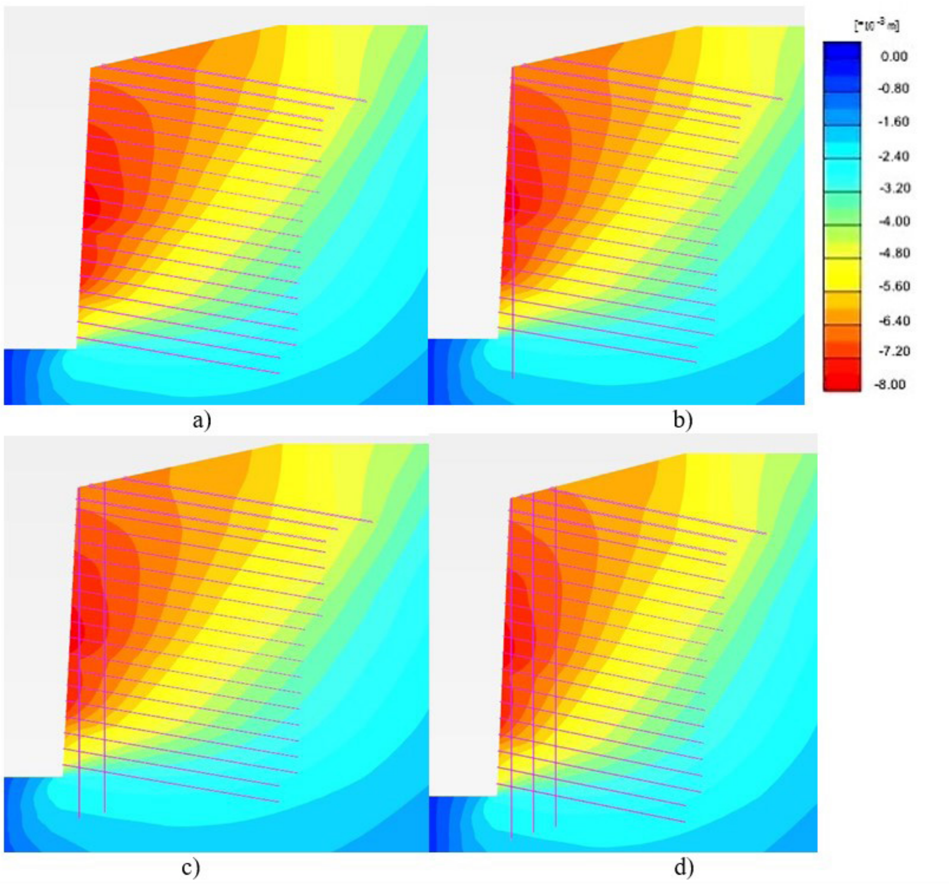

Figure 10. Horizontal displacements with the model adapted in four different situations. (a) Horizontal displacements in the simulation without vertical inclusions; (b) Horizontal displacements in the simulation with one row of vertical inclusions; (c) Horizontal displacements in the simulation with two rows of vertical inclusions; (d) Horizontal displacements in the simulation with three rows of vertical inclusions.

Table 5. Variation in maximum horizontal displacements due to the use of Vertical Inclusions.

Excavation Stage	Excavation depth (m)	Maximum Horizontal Displacement obtained with vertical inclusions (mm)	Maximum Horizontal Displacement obtained without vertical inclusions (mm)	Variation due to the use of vertical inclusions
One Row of Inclusions				
1	3.0	0.646	0.646	0%
3	6.1	1.522	1.524	-0.13%
5	10.6	3.580	3.587	-0.19%
7	14.6	5.966	5.979	-0.22%
9	18.3	7.875	7.900	-0.32%
Two Rows of Inclusions				
1	3.0	0.645	0.646	-0.16%
3	6.1	1.52	1.524	-0.26%
5	10.6	3.568	3.587	-0.53%
7	14.6	5.947	5.979	-0.54%
9	18.3	7.845	7.900	-0.70%
Three Row of Inclusions				
1	3.0	0.646	0.646	0%
3	6.1	1.517	1.524	-0.46%
5	10.6	3.553	3.587	-0.96%
7	14.6	5.927	5.979	-0.88%
9	18.3	7.818	7.900	-1.05%

$$FR = \frac{DMH_{3D}}{DMH_{2D}} \tag{2}$$

It is clear that at different excavation stages in the case studied, the *H/L* ratio varies since *H* (excavation depth) varies and *L* (excavation length) remains constant.

Disregarding the lack of symmetry in the three-dimensional model, the *H/L/FR* ratio was obtained, as shown in the graph in Figure 11 . The relationship was obtained through a plot with 6 well-established points, indicating scattering with consistent values obtained by the 2D and 3D models and validated with the inclinometer data.

Equation 3 relates *FR* and *H/L*, with a correlation coefficient (R^2) equal to 0.8971.

$$\frac{H}{L} = \frac{0.2266}{F.R^2} - 0.2017 \tag{3}$$

After making the necessary comparisons between the 2D and 3D models with the calibrated parameters, several values of Young 's Modulus, ranging from 25 MPa to 500 MPa, where the average Young 's Modulus ($\bar{E}$) of the soil mass was considered, as shown in Table 6 . This enabled the creation of a set of horizontal displacement results that allowed a better understanding of the 2D and 3D behavior when calculating the same problem.

However, by varying the Young's Modulus parameters using the Mohr-Coulomb constitutive model, many results can be considered outliers, as shown in the graph in Figure 12 . In this graph, the blue dots symbolize the Young's Modulus parameter range variations.

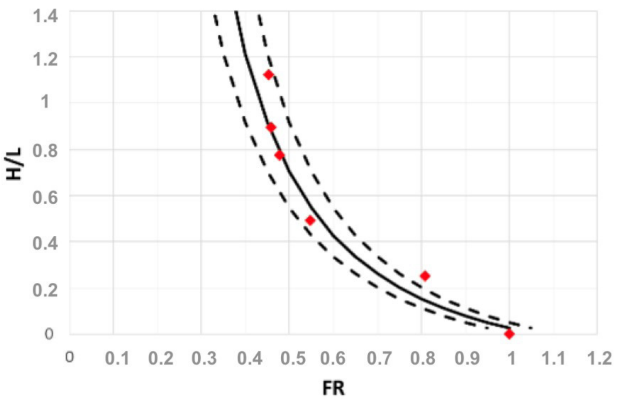

Figure 11. Possible relation of the Maximum Horizontal Displacements obtained by the 2D and 3D models, consistent with values obtained by the inclinometer.

With this Young's modulus range, the first relation proposed by Equation 3 seems to fit relatively well in the interval 0.8< (*H/L*) <1.2; however, the points deviate from this relation in the interval 0.2< (*H/L*) <0.8. Such scatter suggests a linear relationship between (*H/L*) and *FR*, given by Equation 4 in Figure 13 .

$$\frac{H}{L} = -2.2034.FR + 2.0354 \tag{4}$$

This new relation has a correlation coefficient of R^2=0.9688; the straight line adapted very well to the Young's modulus range. Using an average coefficient of variation (*CV*) equal to 0.4 on the Factor of Reductions axis, it can be seen

Table 6. Variation in Young's Modulus for better comparison between 2D and 3D models.

	$\bar{E}$ (MPa)					
	25	50	100	150	200	500
Layer	Young's modulus (E) of each layer (MPa)					
1	16	31	62	94	125	312
2	19	38	75	113	151	376
3	21	42	85	127	169	424
4	24	47	94	141	188	471
5	26	52	105	157	209	524
6	29	58	116	175	233	582
7	35	70	140	210	280	700

that more than 90% of the points are within the proposed range, as indicated by the distribution in Figure 13.

The main observations at this stage of the analysis are listed below:

1. No direct relationship was observed between the Young's Modulus and the Reduction Factor. The graphs suggest that, even with significant differences in soil stiffness, the reduction factor varies in a narrow range;
2. The relationships presented are valid only for the analyzed case study since there are uncertainties regarding the asymmetry of the site geometry, along with the influence of other soil parameters, the nails, and the constitutive model used;
3. When using the same geometry and the same soil layers, both in the 2D and 3D models, it is possible that the relationship between *H/L* and *FR* is linked to these characteristics;
4. The relationships may be adequate to the sedimentary soils of the metropolitan region of São Paulo, but more studies are needed to arrive at a more general conclusion;
5. The use of the linear relationship is safer in the interval $0.1 < H/L < 1.1$, being suggested in this range in similar cases;
6. No Reduction Factor value lower than 0.4 was obtained in the analyses, and such small values are not recommended in any practical context.
7. The existence of vertical inclusions does not significantly change the resulting relationships (as will be seen later).

The validation of such relations is of great interest since it allows the use of predictions of maximum horizontal displacements in two-dimensional FEM programs more straightforwardly and practically, which is very useful for everyday applications. Decreasing a maximum horizontal displacement prediction by a factor ranging from 10 to 60% can have the utmost effect on design, causing an approved or rejected soil nailing application.

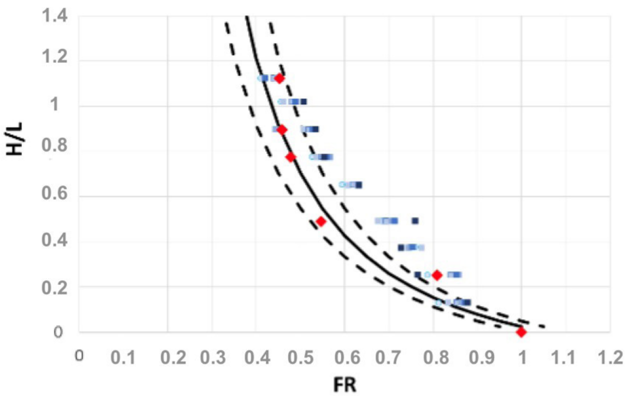

Figure 12. Relationship between the DMH obtained by the 2D and 3D models varying Young's Modulus.

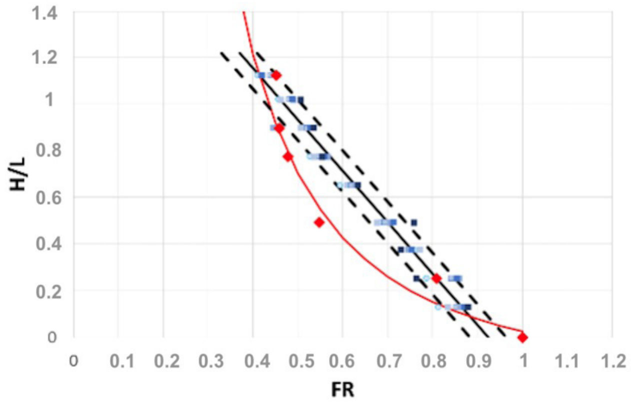

Figure 13. Apparent linear relationship between the Reduction Factor and (*H/L*).

5. Conclusion

From the displayed results, it was possible to reach the following conclusions:

- It is possible to predict the displacements in soil nailing works using the finite element method. A constitutive model that reached good results is the Hardening Soil Model.
- The parameter with the most significant influence on the displacements was the Young's Modulus. The non-linear behavior between soil stresses and deformations significantly impacts the determination of displacements since the soil has a higher deformability modulus for small deformations.

- Another parameter of great influence on the displacements was the at-rest earth pressure (K_0), a relatively high parameter in São Paulo soils (generally greater than 1).
- It is believed that the resistance parameters (cohesion and friction angle) did not significantly influence the displacements because the simulated situation was far from failure. Otherwise, concentrated plasticized regions in the simulated results would produce large and unacceptable horizontal displacements.
- The simulated analysis found a correlation between the Maximum Horizontal Displacement (*DHM*) estimated in the plan strain state (2D). The suggested correlation is linear and follows Equation 4, where (*H/L*) is the ratio of excavation depth (*H*) to the excavation length (*L*), and *FR* is a Reduction Factor.
- This correlation is probably the same for other soil nail applications in sedimentary soil masses in São Paulo. However, the results obtained so far are insufficient to confirm this behavior.
- The vertical inclusions did not significantly influence the maximum horizontal displacements according to the simulations results. However, the considerable increase in the initial Young's Modulus (E_i) in the simulations can be mainly explained by the injection of cement grout under pressure into the soil. The increase in grout injections into the soil allowed a significant reduction of horizontal displacements in soil nail solution. The vertical inclusions, therefore, help to increase the soil stiffness, significantly affecting the horizontal displacements measured on the site.
- Numerical simulation of vertical inclusions is not required for displacement calculation purposes. The inclusion of its stiffness increase is enough to consider the influence of these elements.

Acknowledgements

The authors thank MHosken for making the executive design available, especially Solotrat for providing the data from field instrumentation and for all the valuable support throughout the work. The authors also thank CNPq for funding this research.

Declaration of interest

The authors have no conflicts of interest to declare. All co-authors have observed and affirmed the contents of the paper, and there is no financial interest to report.

Authors' contributions

Max Gabriel Timo Barbosa: data curation, visualization, supervision, validation, writing – original draft. Leonardo Rodrigues Ferreira: conceptualization, data curation, methodology, writing – original draft. George Joaquim Teles de Souza: funding acquisition, data guidance, formal advice. Renato Pinto da Cunha: supervision, resources, software. Ennio Marques Palmeira: supervision, resources, software.

Data availability

The datasets generated and analyzed in the course of the current study are available from the corresponding author upon request.

List of symbols

c'	Cohesion intercept
q_s	pullout resistance per square meter of nail
CV	Coefficient of Variation
DMH_{2D}	Maximum Horizontal Displacement calculated by the 2D model
DMH_{3D}	Maximum Horizontal Displacement calculated by the 3D model
E	Young Modulus
E_i	Initial tangent Young's
E_{i0}	Initial tangent Young's Modulus obtained by correlation with the N_{SPT}
$\overline{E}$	Average Young Modulus of the soil mass
FR	Reduction Factor
I	Grout intensity
H	Excavation depth
K_0	At rest earth pressure coefficient
L	Excavation length
N_{SPT}	Number of blows per 30 cm in the Standard Penetration Test
R^2	Correlation coefficient
SPT	Standard Penetration Test
T_{Max}	Maximum pullout force
ϕ'	Friction Angle
γ	Specific Weight
v	Poisson Coefficient

References

Barbosa, M.G.T., de Assis, A.P., & da Cunha, R.P. (2022). An innovative post grouting technique for soil nails. *Geotechnical and Geological Engineering*, *40*(11), 5539-5546. http://dx.doi.org/10.1007/s10706-022-02231-5.

Falk, E. (1998). *Soil improvement by injection of solid material with hydraulic energy* [Doctoral thesis, Technische Universität Wien]. Institut für Grundau und Bodenmechanik, Technische Universität Wien.

Futai, M.M., Cecílio Junior, M.O., & Abramento, M. (2012). Resistência ao cisalhamento e deformabilidade de solos residuais da região metropolitana de São Paulo. In A.S. Dyminski, A. Negro, M.M. Futai, E. Salamuni, L.F. Vaz, V.L. Sanches, L. Decourt, M.E.G. Boscov, F. Massad, J.M.C. Barros, C. Benvenuto, A.S. Damasco, E.D. Avanzi, N.A. Nascimento, P.R. Chamecki, I. Grandis, M. Cepollina, C.M. Wolle, L.H.F. Olavo, E.S. Macedo, C.H. Daher & M.A.S. Romano (Eds.), *Twin cities: solos das regiões metropolitanas de São Paulo e Curitiba* (pp. 155-187). ABMS (in Portuguese).

Ludemann, S.M., Garcia, R.S., Barbosa, M.G.T., & Cavalcante, A.L.B. (2018). A contingency solution using jet grouting barrier for a dam under risk of piping in Brazil. *Soils and Rocks*, 41(1), 17. http://dx.doi.org/10.28927/sr.411017.

Pitta, C.A., Barbosa, M.V.R., Barbosa, M.G.T., & Assis, A.P. (2017). A injeção de maciços para obtenção de solo grampeado de deformações irrelevantes. In *Anais do Geocentro* (Vol. 4, pp. 231-236). Goiânia. ABMS (in Portuguese).

Pitta, C.A., Souza, G.J.T.D., & Zirlis, A.C. (2013, December). Alguns detalhes da prática de execução do solo grampeado. In *Anais da VI Conferência Brasileira de Encostas (COBRAE)* (pp. 1-24). São Paulo: ABMS (in Portuguese).

Schanz, T., Vermeer, P.A., & Bonnier, P.G. (1999). The hardening soil model: Formulation and verification. In R.B.J. Brinkgreve (Ed.), *Beyond 2000 in computational geotechnics* (pp. 281-290). Balkema.

Soils and Rocks
An International Journal of Geotechnical and Geoenvironmental Engineering
www.soilsandrocks.com
ISSN 1980-9743
ISSN-e 2675-5475

Mechanically stabilized wall (MSW) with geogrids as complement of partially executed anchored wall

Cristina Francischetto Schmidt[1#], Pedro Paulo Monteiro Soares dos Anjos[2], Ivan Steinmeyer[3], Mateus Cardoso Reis Cleto[1], Emília Mendonça Andrade[1]

Case Study

Keywords
Mechanically stabilized wall
Reinforced wall
Geogrid
Geosynthetic
Wrap around

Abstract

This article presents the case study of Wall C11 of Lot 1 in the ringroads of Caraguatatuba and São Sebastião job site, whose original design consists of an anchored retaining wall with a concrete face supported on root piles. At the time of its interruption, only a part of the job had been executed. The alternative solution, mainly aimed at speeding up the completion of the job, was the execution of reinforced backfill with geogrids behind the concrete wall, eliminating the need for the remaining anchors. The presence of the bedrock top very close to the face of the retaining wall at some points could compromise the anchorage length required for the geogrids. In the construction phase, tests were carried out to verify the elements already executed, specially, the anchors. During the execution of the reinforced soil and after its completion, the instrumentation followed the displacements in the concrete wall.

1. Introduction

The Tamoios Highway, between the cities of São José dos Campos, on the margins of Presidente Dutra Highway and Caraguatatuba on Rio-Santos Highway, is the main connection between the Paraíba Valley and the northern coast of the state of São Paulo. In 2015, it began to be managed by Concessionária Tamoios. On its arrival in Caraguatatuba, the Tamoios Highway will be connected to the Northern and Southern ringroads, also called the Caraguatatuba and São Sebastião Ringroads, with a total length of about 34 km. The works on the ringroads was halted in 2018 and restarted in October 2021, taken over by the Concessionária Tamoios. Once completed, they will form a modern and safe road complex in the region of Vale do Paraíba and the Northern Coast of São Paulo. When completed, the Tamoios-Ringroads Complex will relieve the flow of tourists travel through the beach region and increase the cargo capacity for the Port of São Sebastião, which only receives road cargo. In general, the original project consisted in embankments with concrete faces reinforced by soil with steel strips known in Brazil as “Terra Armada” system or in anchored walls. With the resumption of the ringroads works and the establishment of very tight deadlines for the conclusion of the new coastal road system, some original design solutions had to be reviewed, to minimize costs and reduce the execution deadlines, in order to meet the construction schedule. It should be noted that this region is located at the base of the Serra do Mar and is subject to heavy rainfall that could impact the construction schedule especially during Spring and Summer.

2. Wall C11 of Lot 1 - original design solution

Wall C11 of Lot 1 is 244.6 m long and has a maximum height of 14.3 m. Initially, it was expected that the backfill would be built in a reinforced soil system. However, when cleaning the vegetation layer of the surface, it was detected that the rocky top was outcropping, for a much greater extension than originally planned and with steeper slopes. Thus, it was necessary to change the solution from reinforced soil to an anchored wall, because the global stability did not reach the minimum safety factor of 1.5 for the long term situation, required by standard for this type of work.

The original design consists of a reinforced concrete-faced wall supported on a line of 31 cm nominal diameter root piles. The horizontal spacing of the piles was designed for a maximum compressive load of 800 kN, resulting in a maximum horizontal spacing of 3 m. For the rock sections, the allowable geotechnical loads were calculated considering the diameter reduction (telescoping) from 31 cm to 23 cm, with a minimum embedment of 5 m in slightly weathered or

#Corresponding author. E-mail address: cristina@huesker.com.br
1Huesker Ltda., São José dos Campos, SP, Brasil.
2Engetec Construções e Montagens S.A., Rio de Janeiro, RJ, Brasil.
3Steinsolos Engenharia Ltda., Barueri, SP, Brasil.

Submitted on May 9, 2023; Final Acceptance on October 25, 2023; Discussion open until February 28, 2024.
https://doi.org/10.28927/SR.2023.004623

sound rock. According to the geotechnical profile sections, the calculated pile lengths were estimated in the ranging from 11 m and 18 m, starting from the base. The wall consisted at most on four anchor lines per section with working loads of 400 kN, 600 kN or 800 kN and maximum spacing of 3 m, in a total of 289 anchors. At the time of the interruption of the services in 2018, the root piles and the reinforced concrete face were already fully completed, but only about 1/3 of the anchors had been executed, as well as part of the backfill behind the wall. Figure 1 illustrates the front view of the tallest part of the anchored retaining wall. Figure 2 shows the typical cross section of the original design of Wall C11.

3. Restart of construction - alternative solution

This wall was one of the critical structures for the restart of the work, as it corresponds to the only access for the execution of the tunnel ahead, and needed to be completed finish as quickly as possible so that the tunnel excavations could continue without trucks using the local streets. The alternative solution consisted in completing the embankment behind the reinforced concrete wall using the geogrid-reinforced soil technique and a wrapped around face with a lost metallic formwork, eliminating the need to execute most of the missing anchors and working with mixed sections, where the lower part includes the already existing anchors (and eventually a few new ones) and the upper part in geogrid-reinforced soil. One of the main advantages of this alternative solution was the significant reduction in time to finish the whole service, making according to the construction schedule, and with practically no need to interrupt access to the tunnel region.

In reinforced soils, the inclusion of geogrids as backfill reinforcement element provides an overall redistribution of stresses and strains, allowing the adoption of vertical face structures (walls) or steeper slopes, minimizing the volume of compacted backfill.

The presence of reinforcements in the retaining structure generates a resistant tensile force that acts to balance the embankment mass thrust that tends to surcharge the retaining structure. These reinforcements can consist of geogrids with mechanical properties suitable for this purpose, i.e., high tensile strength and low deformation and should be sized to ensure the stability of the wall immediately after its construction and throughout its life.

The stability of reinforced masses must also be ensured by soil-reinforcement interaction mechanisms, i.e., the anchoring capacity of the geogrid, which is a function of its geometric characteristics and the confining stress to which it is subjected.

The assembly of the system's panels is done simultaneously with the compaction of the backfill layers and the placement of the geogrid layers, with the panels being the very formwork of compaction, which brings a significant gain in terms of time and construction cost. The standard ABNT NBR 16920-1 (ABNT, 2021) specifies the requirements for design and execution of walls and slopes in reinforced continuous earth masses.

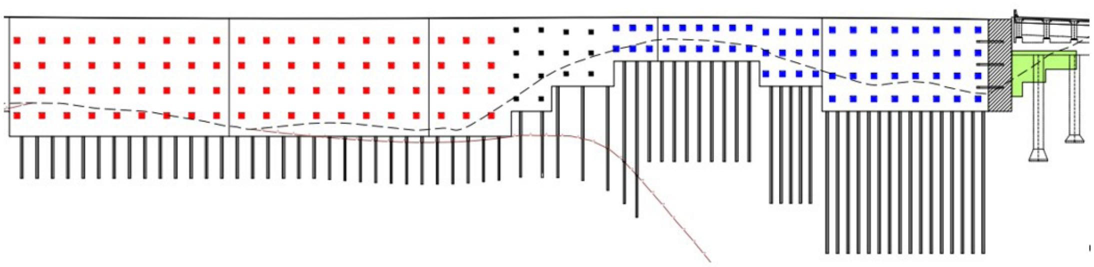

Figure 1. Part of the original design front view.

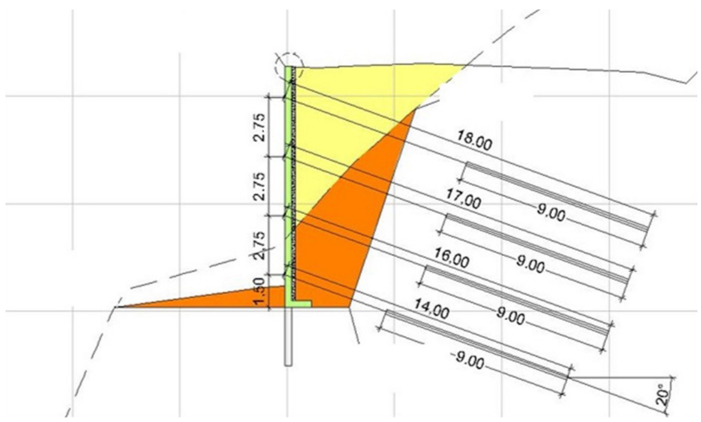

Figure 2. Typical cross section of the original design (units in meters).

One of the difficulties in using reinforced soil was the presence of the rock top very close to the wall face at some points, which could compromise the anchorage length of the geogrids. After a detailed field survey of the rock position, several global stability analyses were performed to verify the suitability of the solution under study using RocScience's Slide v. 6.0 software. In some cases, additional anchors were required.

Figure 3 shows part of the front view of the alternative mixed solution and Figure 4 shows the mixed cross section of the anchored wall and reinforced soil at the section close to pile 1106. Figure 5 presents one of the stability analyses performed.

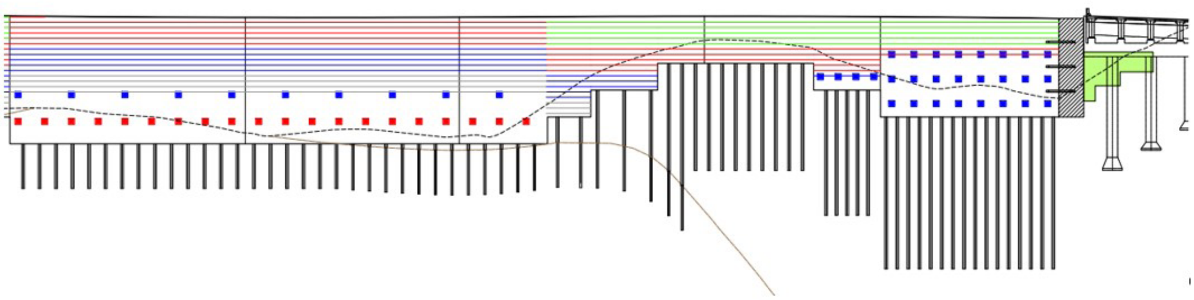

Figure 3. Partial front view of the alternative solution with mixed section (anchors in the lower part and geogrids in the upper part).

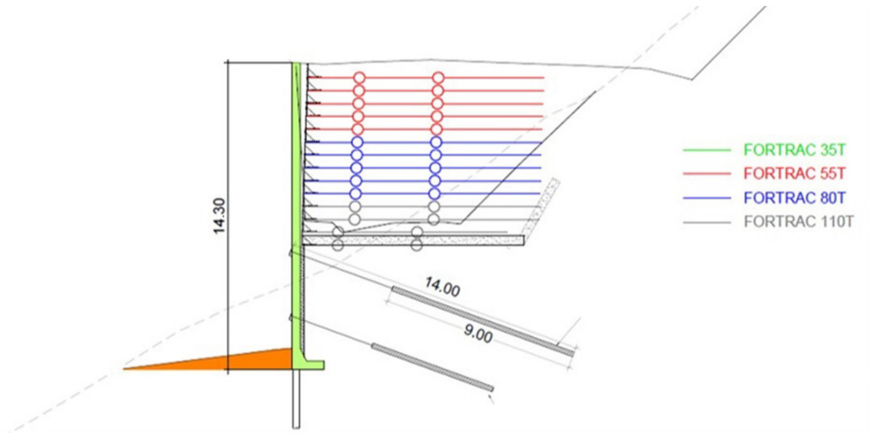

Figure 4. Section with anchors in the lower part and geogrid-reinforced soil in the upper part (units in meters).

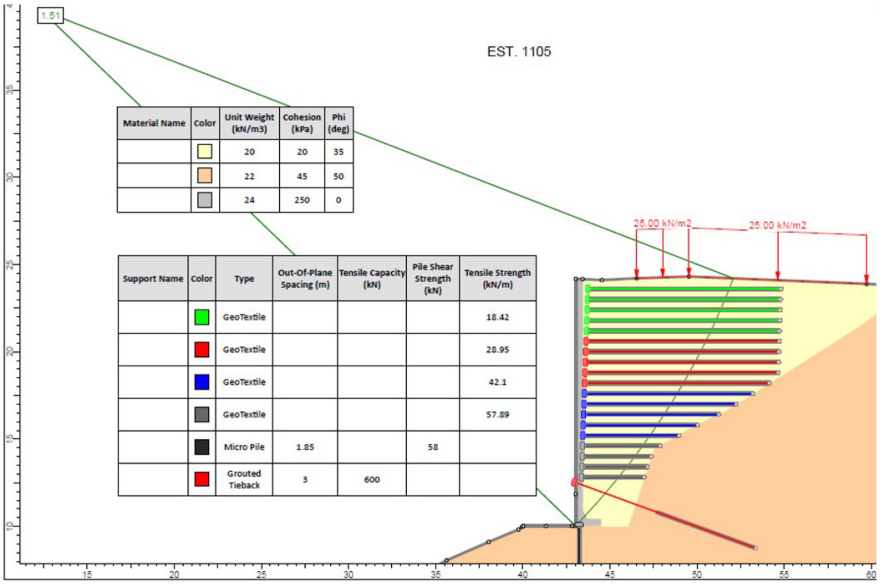

Figure 5. Global stability analysis of a mixed section – section closest to pile 1105.

4. Compacted backfill

For the compacted backfill, stone material produced from crushed material excavated from the site itself was used, with the following composition, based on ABNT NBR 6502 (ABNT, 2022), shown in Table 1 and Figure 6:

According to the characterization tests results provided, the maximum density of the soil reaches 21.7 kN/m^3. From the compaction tests, the optimum moisture is 6.6% corresponding to a density of 19.9 kN/m^3. The strength parameters found in the direct shear test for the soil in a condition close to the optimum water content attain a effective cohesion of 38 kPa and effective friction angle of 39° were obtained (CD test, moisture content of 6.6% and density of 19.9 kN/m^3). Although the shear strength tests of this material have presented higher values, conservative design parameters were adopted with effective cohesion of 20 kPa, effective friction angle of 35° and specific weight of 20 kN/m^3. Figure 7 shows the execution of compacted backfill.

Table 1. Backfill soil composition.

Type	Content
Coarse gravel	0%
Medium gravel	5.8%
Fine gravel	26.8%
Coarse sand	23.1%
Medium sand	18.3%
Fine sand	16.1%
Silt	9.5%
Clay	0.4%

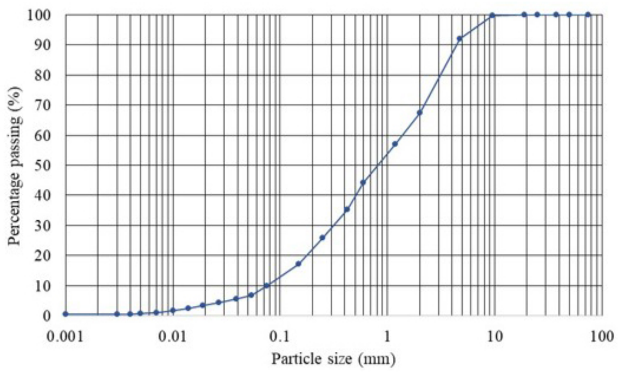

Figure 6. Particle size distribution curve of the material used in the compacted backfill.

Unlike reinforced soil with metallic strips, where the compacted backfill must be basically made of granular material, the geogrid reinforced soil can use soil from the construction site itself, even if it is of finer granulometry, as long as it meets the minimum requirements, according with those recommended by the standard rules.

5. Anchors

When the job activities were halted, Wall 11 had 135 anchors done, nearly 50% of the total number predicted in the original project. It was found that some anchors were without the bearing plate and anchor head and without the driving wedges unprotected tendons, among other mis occurrences.

With the resumption of the work in 2021, the conditions of the installed anchors were initially verified, evaluating if some would not attend the receipt and qualification tests recommended in ABNT NBR 5629 (ABNT, 2018), due to the degradation conditions of structural elements since the construction interruption. As a result, 12 anchors were considered inadequate and discarded.

For the execution of the hybrid solution in part of the anchored wall and geogrid reinforced soil, new stability analyses were performed. Additional 20 new anchors, 13 of 400 kN and 7 of 600 kN had to be included.

In the final design configuration, a total of 150 anchors were defined to compose the system below the geogrid reinforced soil, divided in sections with one row and others with two to three rows of anchors with varying spacing in

Figure 7. Execution of compacted backfill.

each section, being the minimum spacing of 2.5 m and the maximum spacing of 3 m.

Based on Annex D of ABNT NBR 5629 (ABNT, 2018), twelve ties were randomly chosen for receipt test (type A) and three ties were chosen for qualification test with creep measurement (type QF). The remaining tension specimens were tested with type B test, according to Table 2:

In the Type A test, the anchor is tensioned up to 1.75 times its expected working load; in the Type B test, the maximum load is 1.5 times the expected working load. In the QF test, the load of 1.75 times the expected working load is maintained, and the head displacements are measured with two strain gauges, installed diametrically opposite to the tie axis.

Through the conformity tests it was possible to identify some problems in the previously executed anchors:

- Throughout the test, the anchor bulb showed a displacement beyond predicted, requiring the replacement of the anchor.
- During the test, one or two tendons reached failure at loads lower than those foreseen for the end of the test, defining the anchor replacement.
- With the result of the graphs of load mobilization in the anchors, it was verified that the real deformation was not positioned between the range defining maximum and minimum acceptable values according to ABNT NBR 5629 (ABNT, 2018), concluding that they should be substituted.

For the eleven anchors that needed to be replaced, holes were drilled with a concrete extractor 50 cm away from the design point, with a diameter corresponding to 150 mm.

During the beginning of the execution of the reinforced soil behind the wall, a 400 kN tie rod was replaced by a new one.

Table 2. Summary of tested anchors - wall 11 Lot 01.

Expected working load	Test type	Quantities
400 kN	A	5
	B	61
	QF	1
600 kN	A	5
	B	52
	QF	1
80 kN	A	2
	B	22
	QF	1
	Total	150

6. Facing system

The reinforced soil facing was built with a 10V:1H slope, creating a free space behind the concrete wall, so as not to generate horizontal thrusts on the upper part of the wall.

The reinforced soil lost formwork system was composed of non-galvanized steel welded wire mesh, with 6 mm diameter bars spaced every 10 cm, folded in "L". Each module has a useful height of 60 cm and width of 2.5 m. Its stabilization is done through inclined rods, with seven units per module. In this specific case, the steel mesh is not galvanized and serves only as a formwork or temporary lost form. About 1,170 units of non-galvanized folded metallic template were used. The stability of the reinforced soil facing is achieved by wrapped around of the geogrid, as shown in the detail in Figure 8.

7. Geogrids

Polyester geogrids with nominal or characteristic tensile strengths of 35 kN/m, 55 kN/m, 80 kN/m and 110 kN/m and maximum deflection of 10% at nominal strength were used. These geogrids have an overall reduction factor lower than 1.84 for a design life of 120 years, according to certification issued by the British Board of Agrément (BBA). Approximately 28,000 m^2 of geogrids were used. The Figure 9 shows the tensile strength mobilization curve from the wide band test (CLR curve) and the isochronous curves of the geogrids used on site.

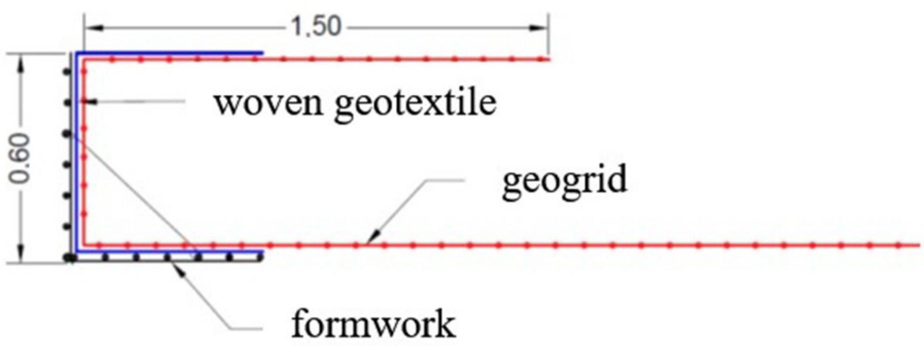

Figure 8. Facing system with non-galvanized metallic formwork and geogrid wrapped around.

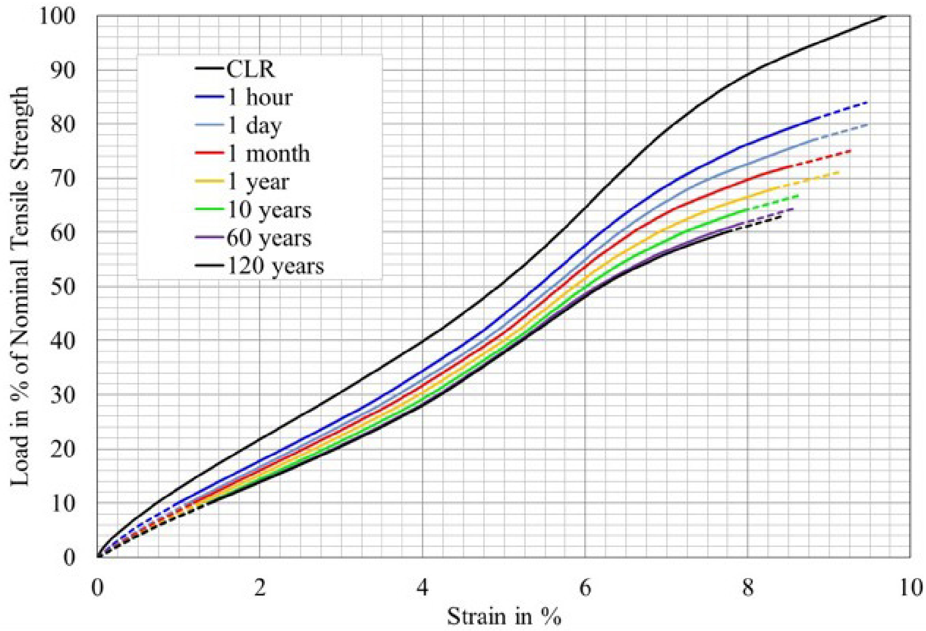

Figure 9. Geogrid tensile strength mobilization (CLR curve) and isochronous curves.

Figure 10. Drainage pipe in the reinforced soil base behind the concrete wall.

8. Drainage system

Due to the large water flow at the site, a robust internal drainage system for the compacted fill was executed, consisting of a gravel bed with a minimum thickness of 40 cm at the contact of the fill with the natural ground and at the base of the wall, associated with drainage pipes. Figure 10 shows the assembly of the drainage pipe in the metallic formwork behind the concrete wall.

9. Deformation monitoring

The substitution of upper lines of active anchors by passive reinforced soil is supposed to generate more deformation in the upper part of the structure and change the loads in the concrete wall. Throughout the execution of the reinforced soil and after its completion, the concrete wall was instrumented to verify the occurrence of any significant displacements generated by the construction of the reinforced

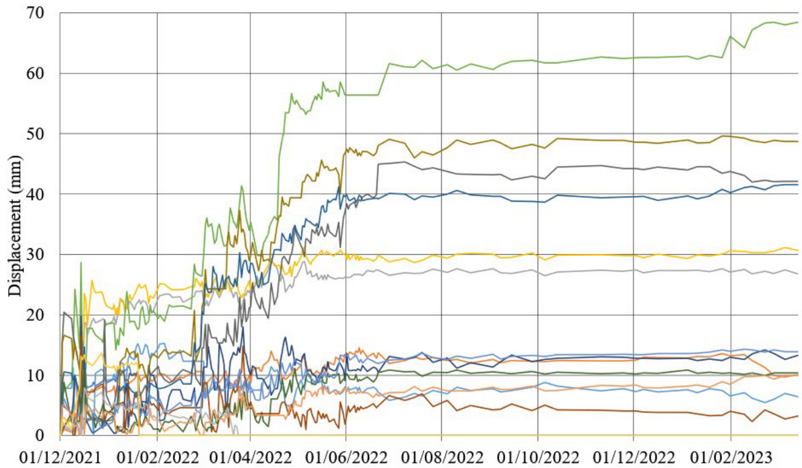

Figure 11. Overview of measured displacements in the concrete wall.

soil, which could indicate inadequate behavior. Thus, a system composed of prisms distributed along the wall was designed, with at least two prisms per section, one at the top and the other at the bottom of the wall. For sections of greater height three prisms were indicated.

The reading schedule was established as follows:

- Daily readings at the beginning of the day for 15 days.
- From day 16 onwards, a weekly reading in the morning until completion of the wall works.
- After completion of the work, monthly readings until release to traffic by the highway.
- After release to traffic, monthly readings for 6 months.
- From the 7th month on, one reading every 3 months for 1 year, then readings every 6 months.

The readings began on 01/12/2021 and the last, before the registers included in the present paper, were observed on 15/03/2023, as shown in Figure 11. During the reinforced backfill and anchors execution, as well as after the liberation for traffic on 15/12/2021, the horizontal displacements presented minimum value of 1.52 cm and maximum of 2.75 cm whereas vertical displacements varied from 0.06 cm to 0.27 cm for the prisms located at the top of the wall. The prisms on the face of the wall presented displacements ranging from 0.02 cm to 0.04 cm. These displacements were within the expected ranges for this type of work. No alteration was observed in the concrete face.

10. Alteration of the walls to the new solution

After the first successful experience with a geogrid-reinforced soil wall, the construction company decided that the retaining walls not yet in place would be redesigned and built with this system. Thus, several designs in the reinforced earth system were changed. Unlike the first site experience, where there was already a previously executed reinforced

Figure 12. Closed articulated and galvanized formwork.

concrete wall, which led to the adoption of a simple non-galvanized wire mesh form behind this wall, the new retaining walls were designed with an articulated and galvanized mesh face, with stone finishing.

To facilitate the transportation and handling of the wire mesh, the system has an exclusive rod that allows the mesh to be transported folded and installed on site in the final position through manual assembly, as shown in Figures 12 and 13.

In the execution of the system, there is no need for concreting, cutting, or bending of the metallic frames, which are just mounted in the definitive location and locked in place with steel hooks. No formwork or shoring is required.

The panels form modules of 250 cm wide by 60 cm high freeboard on the wall face when assembled. The vertical spacing between geogrids is also modulated by 60 cm by the height of the panels.

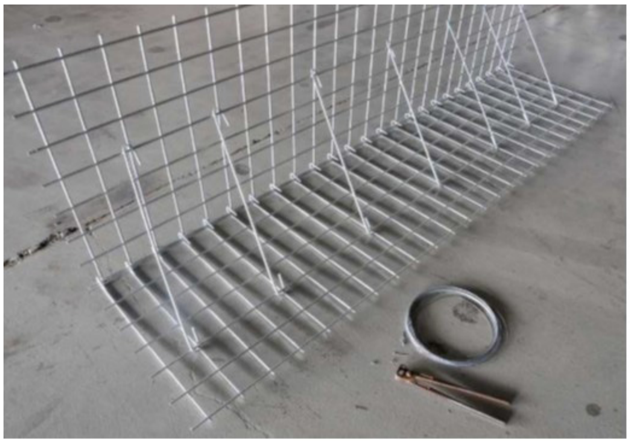

Figures 13. Open articulated and galvanized formwork.

Figure 14. Assembling the face modules.

Figure 15. Filling the face modules with small rocks.

Table 3. Main characteristics of the system.

Item	System
Vertical spacing between geogrids	60 cm
Facing elements	ϕ 8 mm welded mesh screen with 10 cm x 10 cm opening, hot dip galvanized - Larger bar diameter results in less susceptibility to face vandalism
Auxiliary formwork for face assembly	The face elements are self-supporting, requiring no auxiliary formwork for assembly
Maximum diameter of the face stone	20 to 25 cm
Filling the face element with stones	Basically mechanized - System productivity of about 30 m^2 to 50 m^2 of facing area per day depending on the wall geometry
Geogrids for soil reinforcement	Polyester with maximum deformation of 10% PVA with maximum deformation of 5%

PVA: polyvinyl alcohol.

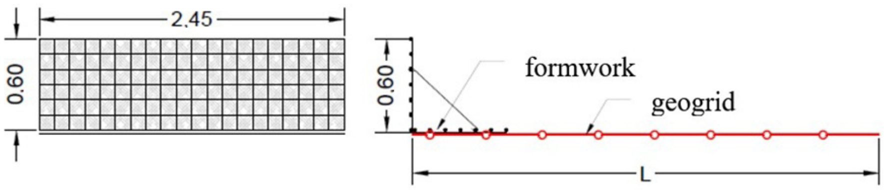

Figure 16. Facing modules and geogrid position.

The structure of the meshes consists of 8 mm diameter bars with 10 cm spacing in both directions on the front vertical panel of the containment, and 6 mm diameter bars with 10 cm spacing in both directions on the horizontal part of the panel that is buried between layers of reinforcement and compacted soil. The 8 mm diameter bar of the front screen presents less risk of damage from vandalism.

The entire wire mesh structure is hot-dip galvanized according to standard ABNT NBR 6323 (ABNT, 2016). Therefore, there is no need to coat the face with geogrid. The geogrid goes under the wire mesh and terminates “topside” at the wall face, as shown in Figure 14. The connection between geogrid and wire mesh is made by the interface friction of the two elements and by the interlocking of the facing stones, as shown in Figures 15 and 16.

Also, for these walls, stone material produced from crushed material excavated from the site itself was used in the compacted backfill. Table 3 presents the main characteristics of the system.

The walls were constructed with geogrids with a nominal or characteristic tensile strength between 55 kN/m and 150 kN/m. The walls were built by the construction company’s own teams. The supplier of the reinforced soil system provided a detailed installation manual with photographs and made an engineer available to guide the start of the execution of each wall. In addition, during the entire construction period, its engineers, its consultant, and its representative made regular visits to monitor the work. It is noticeable that there was an evolution of the assembly team over time regarding to the aesthetic quality and productivity.

11. Global warming potential (GWP) comparative assessment

In order to evaluate the performance of the solutions studied in terms of criteria related to sustainability, calculations were developed to estimate the Global Warming Potential (GWP) generated by the consumption of construction materials used in two alternative solutions for the execution of the walls: reinforced soil with geogrids and face in folding galvanized steel mesh and mechanically stabilized soils with face in concrete plates (“Terra Armada” system).

Studies carried out in the last decade, such as the publications by Stucki et al. (2011) and Corney et al. (2010), demonstrate a significant reduction in the environmental impact with the application of geosynthetic solutions in substitution of conventional solutions in civil engineering, especially in terms of greenhouse gas emissions and global warming potential.

For each of the alternatives studied in this case, the consumption of materials used in significant quantities for the composition of the structure was calculated, per square meter of wall face, considering a height of 9 m. Based on the consumption of materials and the reported values of global warming potential in the Environmental Product Declarations (EPDs) made available by suppliers of cement, steel, galvanization and geosynthetics, the total GWP for each m^2 of wall face, in kgCO2-eq., was evaluated. Other materials, such as sand and aggregates, had their GWP values adopted from the ICE Database (2011).

The GWP values collected for the materials are described in Table 4. For this study, the values reported for the “cradle to gate” boundaries were considered, corresponding to the materials production phase. This limitation was adopted due to the availability of data by suppliers, as not all of them have reports covering other phases of the product life cycle. Thus, to enable product comparison, transport to the site and installation work were not considered. Additionally, for simplification purposes, other materials and services, such as transportation and compaction of local soil, were not included in the comparative calculations, as they were taken as approximately equivalent for the two alternatives.

Thus, for each m^2 of wall face for the two alternative systems, it was possible to assign a GWP value related to the materials used for the construction of a wall with a height of up to 9 m.

As can be seen in Table 5, the results obtained show an important reduction in greenhouse gas emissions and global warming potential linked to the materials used in the solution with reinforced soil, compared to the solution with steel strips and concrete face. This difference is mainly due to the reduction in the volumes of concrete used, since cement has a high environmental impact in its production phase. The steel consumed by both solutions, and particularly the galvanizing, also represent a large part of the emissions linked to the systems, followed by the production of geosynthetic reinforcements.

Table 4. GWP referring to the production of materials used in the two alternatives.

Material			GWP*	*Boundary: A1-A3 (production)
Fortrac T Geogrids	Reference: Huesker Synthetic GmbH (2021a)	35T	1.11E+00	kgCO2eq./m²
		55T	1.44E+00	
		80T	1.92E+00	
		110T	2.10E+00	
		150T	2.64E+00	
		200T	3.18E+00	
Concrete	Reference: Votorantim Cimentos S.A. (2023) kgCO2eq/t		3.84E+02 kgCO2/m³	5.76E+02
Steel	Reference: Arcelor Mittal Brasil (2018) kgCO2eq/t		7.86E+02 kgCO2eq/kg	7.86E-01
Galvanizing (A2-A3)	Reference: American Galvanizers Association (2022) kgCO2eq/t		3.30E+02 kgCO2eq/kg	3.30E-01
Aggregate	Reference: ICE Database (2011) kgCO2eq/kg		5.20E-03 kgCO2eq/m³	1.04E+01
Geotextile	Reference: Huesker Synthetic GmbH (2021b) kgCO2eq/m²(780g)		3.59E+00 kgCO2eq/m² (137g)	6.31E-01
Sand	Reference: ICE Database (2011) kgCO2eq/kg		5.10E-03 kgCO2eq/m³	7.14E+00

*Global Warming Potential.

Table 5. GWP results per m² of wall face for the two alternatives.

Reinforced Soil with Geogrids H 9 m				Mechanically stabilized soil with face in concrete plates H 9 m			
Material consumption / m² face:			GWP*: [kgCO2eq./m² face]	Material consumption / m² face:			GWP: [kgCO2eq./ m² face]
Sand	0.3	m³	2.142	Concrete	0.156	m³	8.96E+01
Fortrac 55T	7.8	m²	11.23	Sand	0.071	m³	0.5037984
Fortrac 80T	3.9	m²	7.49	Aggregate	0.094	m³	0.98
Basetrac Woven 25	3	m²	1.89	Steel (galvanized)	5.969	kg	6.66
Aggregate	0.8	m³	8.32	Steel (not galvanized) 5/16” 8.0 mm	12.77	m	3.97
Quadratum (galvanized steel)	0.7	un.	21.21				
Total [kgCO2eq./m² face]			52.28	Total [kgCO2eq./m² face]			101.71

Evidently, these GWP values do not represent the totality of the environmental impact of the construction of the structure, however they provide a good indicator of the potential reduction of the environmental impact that can be obtained when replacing traditional solutions with geosynthetics.

12. Final remarks

The reinforced soil Wall 11 was executed with the construction company’s own personnel, with constant guidance and site visits by the supplier of the metallic template and geosynthetics and the construction company’s consultants. Initially, the period allocated for the conclusion of Wall C11 was 4 months, however, with the project optimizations and interactions between the executor, designer and consultants, the work was concluded in only 2 months. The justifications for this were the close collaboration and agility to define and re-evaluate the solution and execution of the work, with real time flow of continuous new information from the field and project revision by those involved from several companies (construction, designer, consultant, material producer, etc.); the use of crushed granular material for the compacted backfill, allowing fast resumption of earthworks even after a period of heavy rainfall; the adoption of the geogrid reinforced soil technique, which basically consists of an earthwork, allowing very fast raising of the backfill and the possibility of executing the services related to the anchors in parallel with the execution of the backfill in reinforced soil.

In other hand, the comparison between GWP values calculated for mechanically stabilized soil with face in concrete plates from the original solution for the next walls of the job and for the alternative geogrid reinforced wall for a 9 m high section provides a good indicator of the potential reduction of the environmental impact that can be obtained when replacing traditional solutions with geosynthetics. In this case, greenhouse gas emissions resulting from the production of materials are reduced by almost half by using the solution in reinforced soil, indicating an additional benefit of a more sustainable construction, in addition to the already known technical advantages.

Declaration of interest

The authors have no conflicts of interest to declare. All co-authors have observed and affirmed the contents of the paper and there is no financial interest to report.

Authors' contributions

Cristina Francischetto Schmidt: conceptualization, supervision, writing – review & editing. Pedro Paulo Monteiro Soares dos Anjos: conceptualization, data curation, project administration, writing. Ivan Steinmeyer: conceptualization, data curation, writing. Mateus Cardoso Reis Cleto: conceptualization, data curation, writing. Emília Mendonça Andrade: conceptualization, data curation, writing.

Data availability

The datasets generated and analyzed in the course of the current study are available from the corresponding author upon request.

References

ABNT NBR 16920-1. (2021). *Walls and slopes in reinforced soils – part 1: reinforced soils in fills*. ABNT - Associação Brasileira de Normas Técnicas, Rio de Janeiro, RJ (in Portuguese).

ABNT NBR 5629. (2018). *Ties anchored in soil – design and execution*. ABNT - Associação Brasileira de Normas Técnicas, Rio de Janeiro, RJ (in Portuguese).

ABNT NBR 6323. (2016). *Hot dip galvanized on steel and cast iron product - specification*. ABNT - Associação Brasileira de Normas Técnicas, Rio de Janeiro, RJ (in Portuguese).

ABNT NBR 6502. (2022). *Soils and rocks – terminology*. ABNT - Associação Brasileira de Normas Técnicas, Rio de Janeiro, RJ (in Portuguese).

American Galvanizers Association. (2022). *Environmental product declaration according to ISO 14025 and ISO 21930:2017*. Hot-Dip Galvanized Steel After Fabrication.

Arcelor Mittal Brasil. (2018). *Environmental product declaration according to ISO 14025 and EM 15804. Reinforced steel bars*. Institut Bauen und Umwelt e.V.

Corney, N., Cox, P., Norgate, S., & Thrower, A. (2010). *Sustainable geosystems in civil engineering applications*. Waste & Resources Action Programme (Geosystems Report).

Huesker Synthetic GmbH. (2021a). *Environmental product declaration as per ISO 14025 and EN 15804 +A1. Fortrac T*. Kiwa BCS Öko-Garantie GmbH - Ecobility Experts.

Huesker Synthetic GmbH. (2021b). *Environmental product declaration as per ISO 14025 and EN 15804 +A1. Stabilenka*. Kiwa BCS Öko-Garantie GmbH - Ecobility Experts.

ICE Database. University of Bath & Carbon Trust, Inventory of Carbon & Energy (ICE). (2011). *Document undertaken by the University of Bath's Department of Engineering, with support from the Carbon Trust and EPSRC (Report)*. Bath: University of Bath's.

Stucki, M., Büsser, S., Itten, R., Frischknecht, R., & Wallbaum, H. (2011). *Comparative life cycle assessment of geosynthetics versus conventional construction materials*. ESU-Services Ltd. Uster/ETH Zürich/European Association for Geosynthetic Manufacturers.

Votorantim Cimentos S.A. (2023). *Environmental product declaration for cement CP, III, 40 [RS in accordance with delines for additional formatting examples]*. Votorantim Cimentos S.A.

Soils and Rocks

An International Journal of Geotechnical and Geoenvironmental Engineering

www.soilsandrocks.com

ISSN 1980-9743
ISSN-e 2675-5475

Alert scenarios for the Metropolitan Region of Recife-PE based on monitoring of rainfall and soil humidity – a case study

Roberto Quental Coutinho[1#], Bruno Diego de Morais[1], Rodolfo Moreda Mendes[2], Marcio Roberto Magalhães de Andrade[2]

Case Study

Keywords
Landslide early warning system
Moisture monitoring
Barreiras Formation
Metropolitan Region of Recife

Abstract

In Brazil, landslides are frequent, causing deaths and property damage, and occur under the influence of natural and/or anthropic conditions. Rain acts as the main non-anthropic agent in triggering this phenomenon. Because of this, the prediction of landslides becomes an essential tool for managing high-risk areas. The Metropolitan Region of Recife (MRR) has a large history with numerous cases of mass movements over the years. Currently, research points out improvements in the quality of forecasts by including hydrological information, such as soil moisture, in warning systems. Given the importance of measuring soil moisture in situ, a network of equipment consisting of rain gauges and capacitive moisture sensors was installed in the MRR, to monitor rainfall and soil moisture in an integrated manner. The objective of this article is to understand the hydrological conditions of the soil in two high-risk areas of the MRR, built over the Barreiras Formation to set the foundations for the development of a Landslide Early Warning System (LEWS) that integrates rain and humidity. The data showed that the variation in soil moisture is very dependent on rainfall and presents sudden variations in moisture with increasing hourly rainfall. The data also revealed that the monitored soils remained wet for approximately six months in the year 2022, highlighting the potential for moderate rainfall during this period to trigger landslides.

1. Introduction

In Brazil, landslides are one of the most frequent hazards, resulting in significant economic and social losses, such as deaths, injured victims, and property destruction (Dias et al., 2021). Rain acts as the main non-anthropic agent in triggering this phenomenon, as it is related to the dynamics of surface and subsurface waters (Augusto Filho et al., 2018).

The Metropolitan Region of Recife (MRR) does not differ from the national scenario and has a large history with numerous cases of mass movements over the years (Bandeira & Coutinho, 2015). According to Macedo & Sandre (2022), between 1988 and 2022, in the city of Recife, 173 deaths caused by landslides were registered.

Due to this background, Bandeira & Coutinho (2015) and Coutinho & Delfino (2022) developed critical precipitation thresholds for several towns in the MRR, to predict landslides, aiming to warn the population residing in high-risk areas. However, many authors point out that, due to simplifications, such as not considering the hydrogeological processes involved in the slope rupture process, those systems that consider only precipitation can generate false alarms (Toll et al., 2011; Abraham et al., 2021).

In the current scenario, research has shown that the quality of forecasts improves when including soil hydrological information (Wicki et al., 2020). According to Pirone et al. (2015), rainwater infiltration is considered a critical factor in the occurrence of landslides, as it reduces matrix suction in soils, which consequently decreases their shear strength resistance. Thus, monitoring soil moisture is an important variable for predicting landslides (Bovolenta et al., 2020).

To monitor the risk of landslides, National Early Warning and Monitoring Centre of Natural Disaster - CEMADEN with technical support from the Group of Geotechnical Engineering of Disasters and Plains - GEGEP installed a network of equipment in the MRR. This network includes rain gauges and capacitive moisture sensors that monitor rainfall and soil moisture in an integrated manner. Therefore, this study aims to understand the hydrological conditions of the soil in two high-risk areas in the MRR during the year 2022. This year was marked by exceptionally intense rains, resulting in landslides and floods (Marengo et al., 2023). In addition,

[#]Corresponding author. E-mail address: roberto.coutinho@ufpe.br
[1]Universidade Federal de Pernambuco, Programa de Pós-graduação em Engenharia Civil, Recife, PE, Brasil.
[2]Centro Nacional de Monitoramento e Alertas de Desastres Naturais, Coordenação Geral de Pesquisa e Desenvolvimento, São José dos Campos, SP, Brasil.

Submitted on June 19, 2023; Final Acceptance on October 25, 2023; Discussion open until February 28, 2024.
https://doi.org/10.28927/SR.2023.008323

the article aims to set the foundations for the development of an early warning system for landslides, which takes into account both rainfall and soil moisture.

2. Description of the study areas

In this article, the study areas cover occupied hillside territories located in the cities of Recife and Jaboatão dos Guararapes, in the State of Pernambuco (PE), Northeastern Brazil, as shown in Figure 1. Area 1 is located in the North zone of Recife and has an approximate area of 25 km^2. Area 2 is located in the south of Recife and part of Jaboatão dos Guararapes municipality, and has an area of approximately 21 km^2. Both areas have a relief characterized by a sharp division between the plain and the hills.

These areas are urban territories, densely occupied, with the construction of houses on slopes that are susceptible to landslides, thus generating a serious socio-environmental problem that requires a series of actions by the public authorities and society (Coutinho et al., 2017). In the field, irregular occupations, steep slopes, cuts, and landfills carried out without technical criteria, waste accumulation, disposal of wastewater and other factors which induce the occurrence of landslides can be identified. Figure 2 illustrates the scenarios found in the study areas and shows the negative impact of anthropic intervention.

3. Climatic aspects

The climate of the city of Recife is characterized as coastal tropical, being strongly influenced by the humid air masses of the Atlantic Ocean and by the Intertropical Convergence Zone. This results in a climate that is generally humid, hot, and influenced by the proximity to the coast. According to Mendonça & Danni-Oliveira (2007), the city has an annual rainfall of about 2500 mm and an average temperature of 26.1 ºC. The wettest period occurs between March and August, with a monthly average of over 200 mm, while the driest season lasts from October to February.

For this paper, data from two automatic rain gauges were analyzed. Data were collected between 2019 and 2022. The rain gauges used were the RG-01, installed in the neighborhood Dois Unidos (Area 1), and the RG-02, installed in the neighborhood Ibura (Area 2). Figure 3 shows the accumulated monthly rainfall. In both areas, it is observed that the rainiest period occurs between March and August,

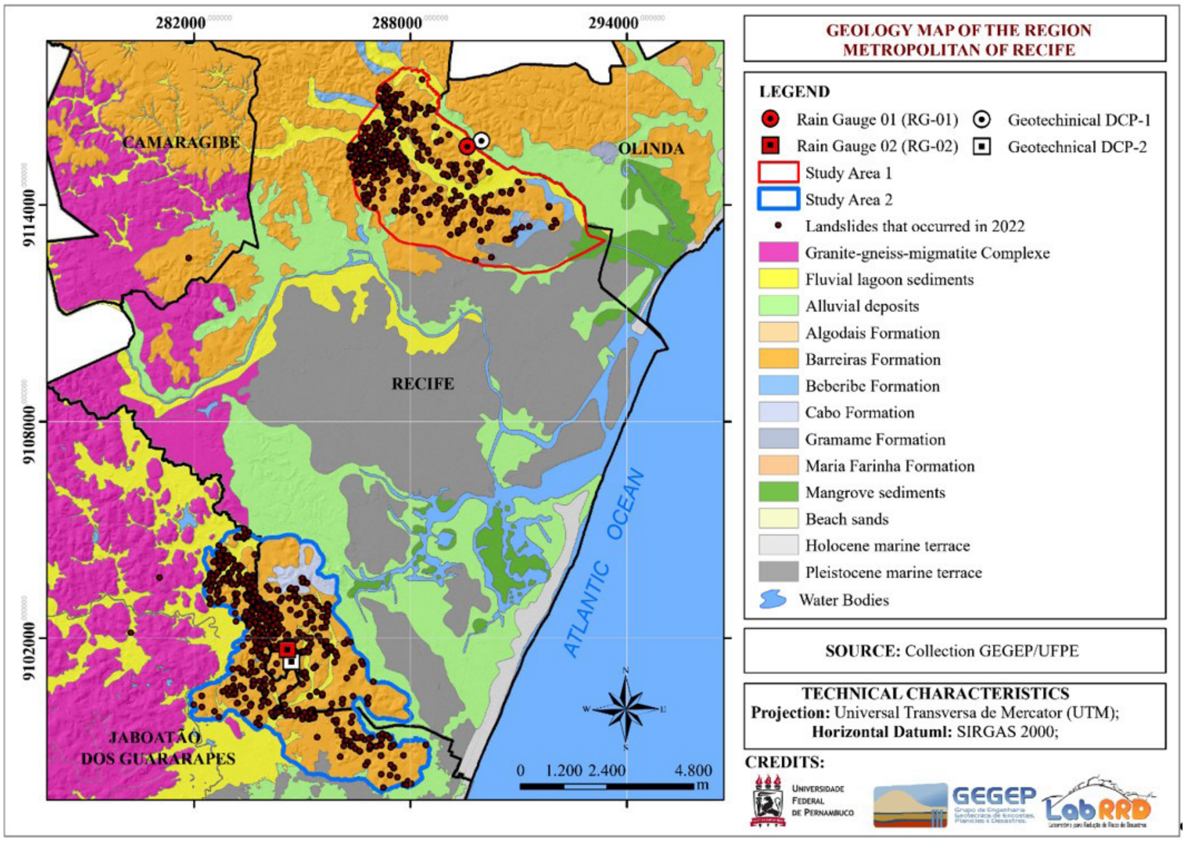

Figure 1. Location of the study areas, rain gauges, Geotechnical DCP, the spatial distribution of geological units in the MRR, and landslides that occurred in the study area in 2022.

Figure 2. Scenarios identified in the study areas: a) steep slopes; b) waste material accumulation on the slopes; c) wastewater discharge on the slope.

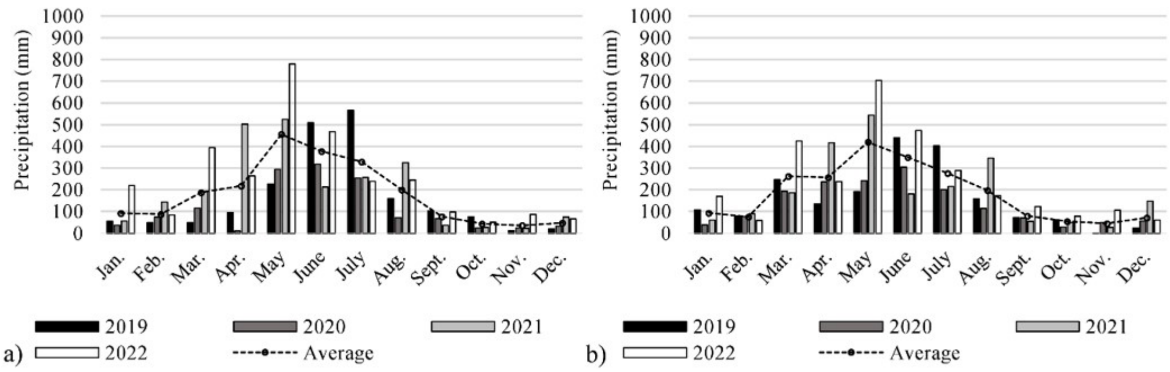

Figure 3. Precipitation recorded monthly between the years 2019 and 2022: a) RG-01 rain gauge; b) RG-02 rain gauge.

with monthly averages equal to or greater than 200 mm. In the analyzed period, May 2022 was the month with the highest monthly rainfall, 780 mm at RG-01 and 703 mm at RG-02.

4. Geological characterization

When analyzing the map in Figure 1, it is observed that the MRR has a complex geology, with several different geological units. However, the two studied areas are mostly located on the Barreiras Formation. This geological unit has continental expression, of great occurrence on the Brazilian coast, being commonly found in the slope areas of the MRR (Bandeira & Coutinho, 2015; Coutinho et al., 2019).

This geological formation has vivid colors, ranging from red and yellow to white, depending on the degree of iron oxidation (Bandeira & Coutinho, 2015). It is lithologically composed of poorly consolidated sand-clay sediments, specifically quartz sands, interspersed with rhythmic strata of fine sand and/or clay (Coutinho & Severo, 2009). Due to these characteristics, the soils of this formation are susceptible to gravitational mass movements and erosion processes (Coutinho et al., 2006).

5. Landslides in the study areas

In the MRR, the main triggering factors for landslides are geology, anthropic action, relief, and precipitation (Coutinho et al., 2019). Currently, the cities of Recife and Jaboatão dos Guararapes occupy the 6th and 10th place, respectively, among the cities with the highest number of deaths caused by landslides in Brazil, between 1988 and 2022 (Macedo & Sandre, 2022). Studies carried out by Bandeira & Coutinho (2015) revealed that 75% and 85% of landslides in these cities, respectively, are directly related to rain.

Between late May and early June of 2022, due to atmospheric disturbances coming from the east, exceptionally heavy rains were recorded in the states of Pernambuco, Alagoas, and Paraíba, causing landslides and flooding (Marengo et al., 2023). In Recife, on May 28, 2022, has accumulated 204 mm, being classified as extreme rain on the scale proposed by Guedes & Silva (2020). Figure 4a and Figure 4b, show that landslides in both areas are closely related to high levels of precipitation.

Most landslides in the MRR are shallow and their failure surfaces are translational (planar) and parallel to

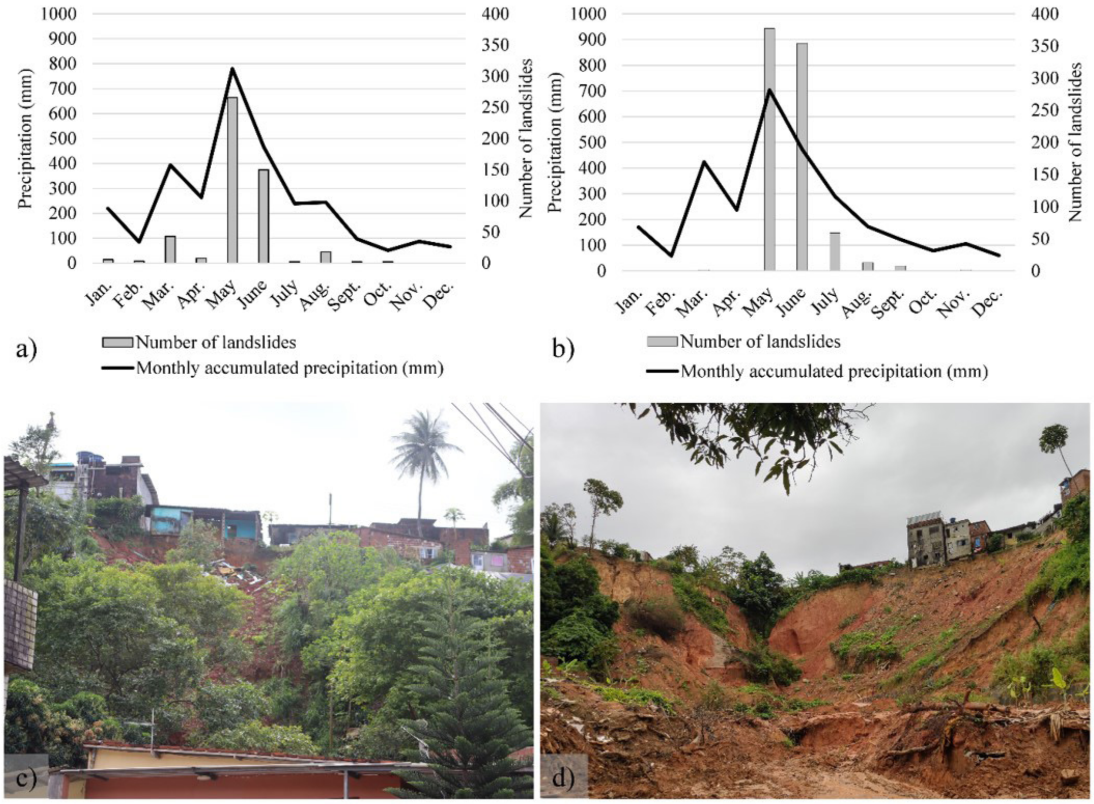

Figure 4. Landslides and monthly rainfall during 2022 in: a) Area 1; b) Area 2. Landslides that occurred on May 28, 2022: c) Córrego do Jenipapo – Area 1; d) Monte Verde – Area 2.

the slope (Gusmão Filho et al., 1997). Figure 4 shows two cases of landslides that occurred in the study areas on May 28, 2022. Figure 4c shows the planar landslide in Córrego do Jenipapo, located in Area 1, which caused fatalities and injuries. Figure 4d shows the landslide at Ave. Chapada do Araripe (Monte Verde), located in Area 2, on the border of Recife and Jaboatão dos Guararapes, which also resulted in fatalities.

Figure 5 presents the proposal for critical rainfall thresholds developed by Coutinho & Delfino (2022) for Area 1. The events were divided into three groups: (i) localized 1 to 3 landslides); (ii) sparse (4 to 9 landslides); and (iii) generalized (above 9 landslides). It is observed in Figure 5 that the dot representing the accidents that occurred in 2022 in Area 1 is outside the trends established by those authors. This discrepancy highlights the need to consider extreme weather events caused by climate change in engineering design and to integrate risk and disaster management strategies.

6. Geotechnical data collection platform

To improve the CEMADEN disaster monitoring and alert system, a geotechnical data collection platform (Geotechnical DCP) network was created in 2019 on MRR. These platforms aim to improve the understanding of rainwater infiltration dynamics into the soil, adding environmental parameters to the system. Each Geotechnical DCP incorporates several devices, including a rain gauge to measure the amount of rainfall, capacitive moisture sensors to determine the in-situ volumetric water content of soil (%), a data logger for collecting and transmitting data, and a photovoltaic panel to provide energy to the system.

Through the collected data, the aim is to predict and identify the conditions in which the maximum moisture values are reached, which indicates soil saturation, the most unfavorable situation for the stability of slopes. At each Geotechnical DCP, moisture sensors were installed every 0.5 m deep, covering a range of 0.5 to 3.0 m. This resulted in a total of 6 moisture sensors per platform. Figure 6 illustrates the equipment that makes up a Geotechnical DCP and shows the arrangement of moisture sensors installed in an access tube implanted in the ground.

7. Methodological aspects

To analyze the effect of rainwater infiltration into the soil, five stages of work were carried out in two study areas in the MRR affected by landslides in 2022. These stages were:

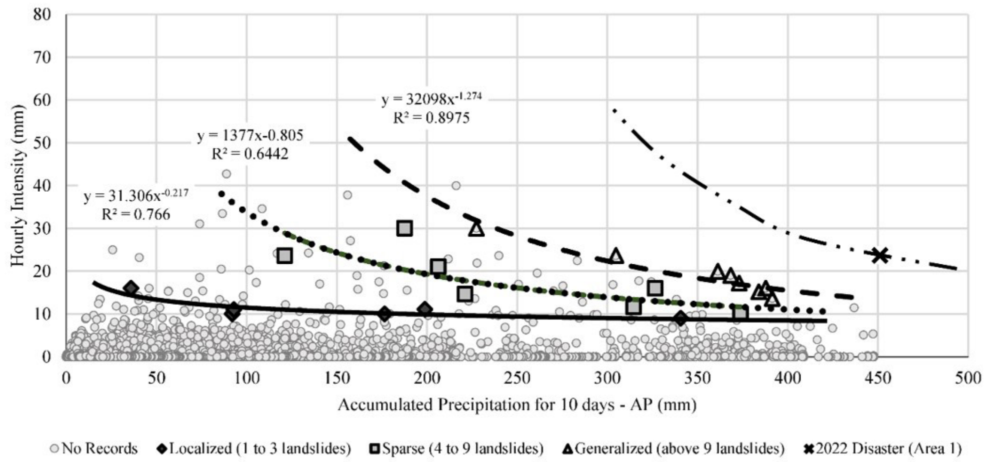

Figure 5. Correlation between hourly intensity by accumulated precipitation for 10 days [adapted from Coutinho & Delfino (2022)].

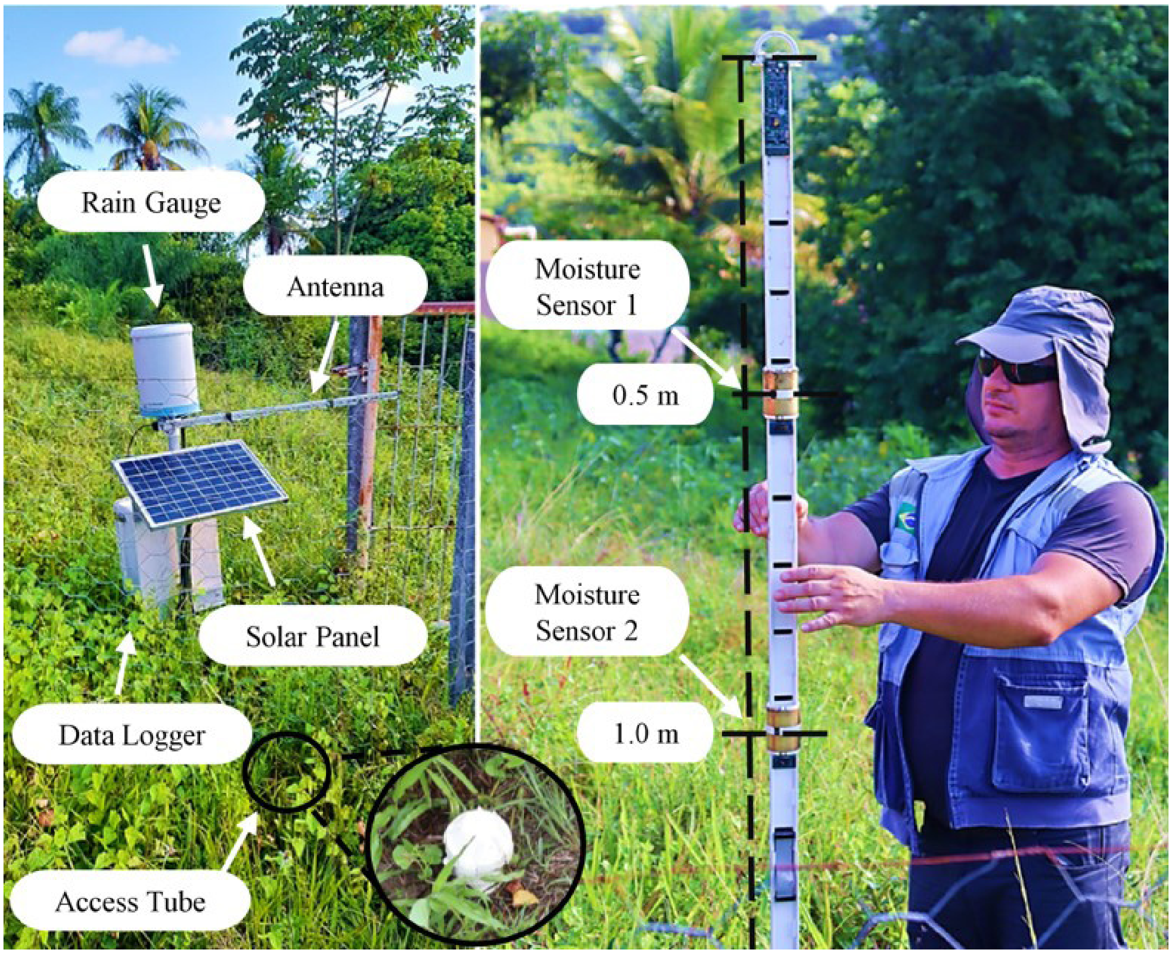

Figure 6. Composition of Geotechnical DCPs and arrangement of moisture sensors.

a) Selection of two Geotechnical DCPs installed near or within the study areas to analyze the variation of soil moisture in response to rainfall.

Geotechnical DCP-1 and Geotechnical DCP-2 were selected, as shown in the map in Figure 1. Geotechnical DCP-1 is close to Area 1, while Geotechnical DCP-2 is located within Area 2. Both the Geotechnical DCPs are located in the Barreiras Formation.

b) Geotechnical studies performed on the soils of the areas monitored by the Geotechnical DCPs.

Soil characterization tests were made: Determination of the liquid limit of the soil (ABNT, 2016a), Determination of the plasticity limit (ABNT, 2016b); and Granulometric analysis (ABNT, 2016c).

c) Gathering of the soil moisture data during the year 2022.

The data collected by Geotechnical DCP-1 covered the interval between January 1 to December 31, 2022. The data collected by the Geotechnical DCP-2 cover the interval between January 1 to December 4, 2022, due to sensor reading failures.

d) Correlation of moisture data with the precipitation information and occurrences of landslides within the study areas.

The data on landslide occurrences for the year 2022 were made available in digital spreadsheet format by the Local Civil Defense of Recife and Jaboatão dos Guararapes, containing the addresses and dates of occurrences. These occurrences were then related to rainfall and humidity data.

e) Data analysis, relating the results found with literature information available.

This step aims to provide a clearer understanding of the effects of infiltration of rainwater and soil moisture on slopes, contributing to the understanding of failure mechanisms and providing useful information for predicting future landslides.

8. Geotechnical characterization

To obtain detailed information about the soil profiles monitored by the Geotechnical DCPs, soil characterization tests were carried out, for which six (06) disturbed samples were collected at each 0.5 m depth in both analyzed areas. The geotechnical characterization, including USCS (Unified Soil Classification System) classification, Atterberg limits, and the granulometry of the soils are shown in Table 1.

The results reveal that the Geotechnical DCP-1 soil profile is predominantly clayey (48-55%) and is classified as low plasticity silt soil according to the USCS, showing an increase in silt fraction with the depth. The soil profile of Geotechnical DCP-2 is sandier (65-78%) and is classified as silty-clayey sand with little plasticity, again it is observed an increase in the silt fraction with depth.

9. Monitoring of Geotechnical DCP

The following results are related to the behavior of moisture sensors with changes induced by rainfall during the year 2022 in two different area.

9.1 Monitoring with the Geotechnical DCP-1

Figure 7a shows the graph of the average daily soil moisture measured by the Geotechnical DCP-1 and the daily precipitation recorded by the RG-01 during the year 2022. The data interval covers January 1 to December 31, 2022, and is divided into five smaller periods. The division criteria were the identification of relatively constant moisture values, to elucidate how the rainwater infiltration alters soil moisture. Table 2 presents the average volumetric soil moisture (%) and the corresponding standard deviation values for each period.

The first period occurred between January 1 to March 5, 2022, lasting 64 days. Since it is part of the driest season, the average moisture values for Period 1 are the lowest, as shown in Table 2. The data reveal that the lowest humidity situations occur at the most superficial depths, specifically between 0.5-1.5 m deep, in response to increased evapotranspiration that occurs in drier periods (Crawford et al., 2019).

The rains of March increased soil moisture levels, thus establishing the second period, characterized by soil wetting (from March 6 to May 22, 2022). The data in Table 2 show

Table 1. Geotechnical characterization of soils monitored by Geotechnical DCP.

Geotechnical DCP	Sample Depth (m)	USCS Classification	Atterberg Limits			Soil Granulometry		
			LL (%)	*PL* (%)	*PI* (%)	Clay (%)	Silt (%)	Sand (%)
Geotechnical DCP-1	0.5	ML	36	27	9	55	3	42
	1.0	CL	47	27	20	54	4	42
	1.5	ML	45	28	17	52	6	42
	2.0	ML	46	32	14	48	8	44
	2.5	MH	51	32	19	49	8	43
	3.0	ML	48	33	15	53	12	35
Geotechnical DCP-2	0.5	SC	20	12	8	20	2	78
	1.0	SM-SC	20	15	5	19	3	78
	1.5	SM-SC	23	19	4	24	4	72
	2.0	SM-SC	25	20	5	23	12	65
	2.5	SM-SC	22	18	4	14	14	72
	3.0	SM-SC	24	16	8	12	21	67

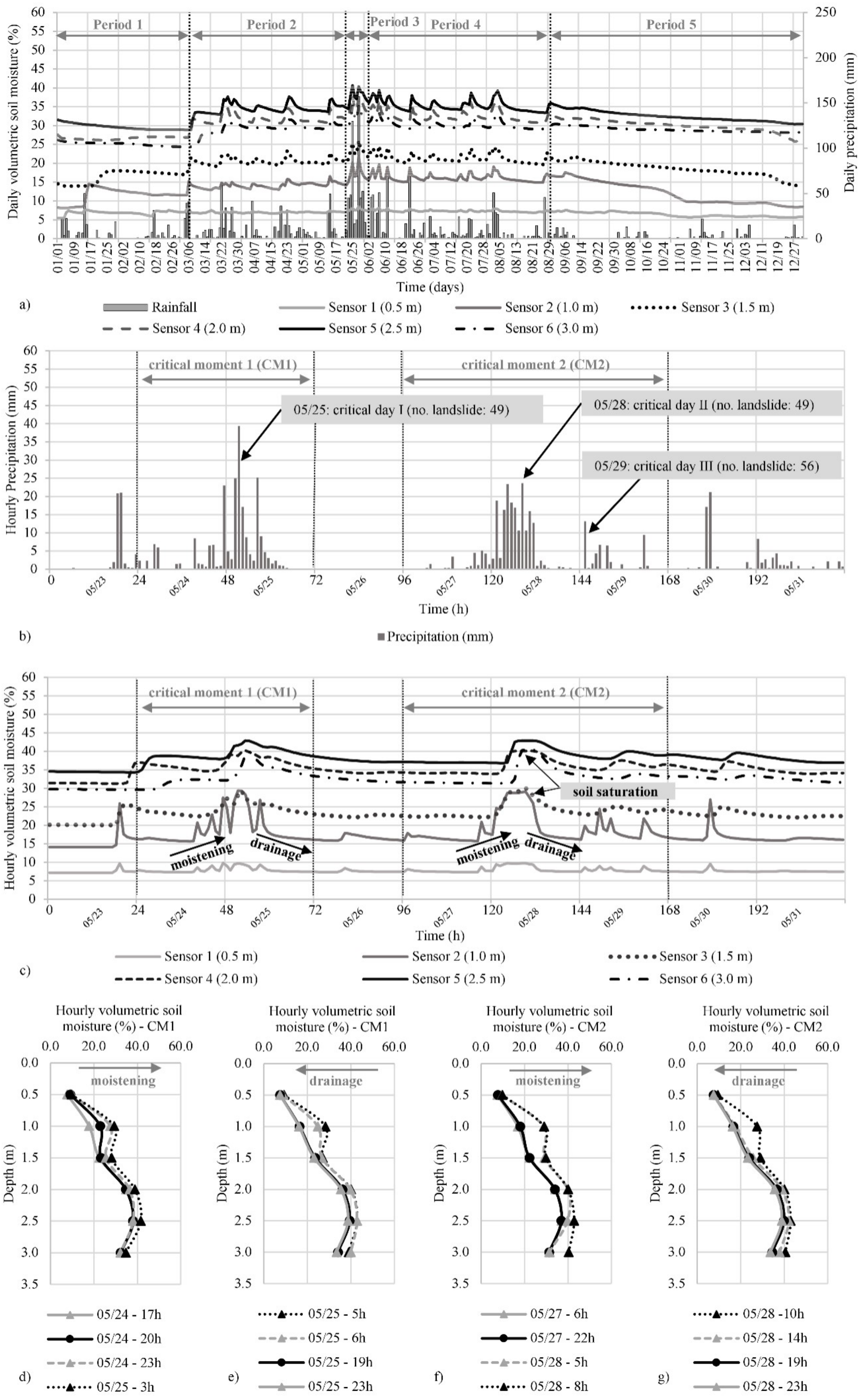

Figure 7. Monitoring data from Area 1: a) rainfall data and the average daily moisture between January 1 to December 31, 2022; b) period 3 hourly precipitation data; c) period 3 hourly average moisture data; d) wetting moisture profile – CM1; e) drainage moisture profile – CM1; f) wetting moisture profile – CM2; g) drainage moisture profile – CM2.

Table 2. Average moisture and standard deviation of the periods in Area 1.

	Sensor 1	Sensor 2	Sensor 3	Sensor 4	Sensor 5	Sensor 6
Period 1	6.89% (0.50)	11.52% (1.87)	16.44% (1.65)	26.65% (0.34)	29.64% (0.75)	25.11% (0.46)
Period 2	6.99% (0.20)	14.13% (0.71)	20.49% (0.88)	31.71% (1.22)	34.44% (1.50)	29.17% (1.59)
Period 3	7.80% (0.35)	17.88% (2.04)	23.53% (1.48)	35.43% (1.87)	38.21% (1.85)	32.74% (1.82)
Period 4	7.33% (0.26)	16.14% (1.00)	21.35% (1.16)	32.59% (1.44)	35.38% (1.46)	30.25% (1.07)
Period 5	6.39% (0.59)	11.98% (2.90)	18.45% (1.89)	29.91% (1.58)	32.42% (1.32)	28.90% (0.63)

Unit: Average volumetric soil moisture (%);
Note: The values presented in parentheses correspond to the standard deviation.

that in Period 2 there was an increase in the average moisture values at all monitored depths, compared to Period 1. In this period, it can be noticed that the humidity at all depths was more sensitive to rain as shown in Figure 7a.

In the third period, lasting eight days (from May 23 to May 30, 2022), an accumulated rainfall of 515 mm was recorded, resulting in the highest peaks of soil moisture, indicating probable soil saturation. According to the data in Table 2, in Period 3 there was an increase in the average moisture in all sensors, about Period 2. The data also show that the deeper layers (1.5-3.0 m) tend to retain the water infiltrated through the profile for a longer time.

The fourth period lasted 93 days (from May 31 to August 31, 2022) and represents the transition from the rainy season to the drier season. During this period, the average moisture values decreased about Period 3 due to the reduction in the amount of rain. The data in Table 2 show that in this period average moisture values are slightly higher than those recorded in Period 2. This shows that the soils in Area 1 remained wet for 179 days.

The fifth period occurred between September 1 to December 31, 2022, lasting 122 days and illustrates the variation in humidity during the return of the driest period. During this period, the data in Table 2 shows that there was a reduction in average moisture compared to Period 4, mainly between 0.5-1.5 m. While in the deeper layers, the humidity decreases more slowly, as shown in Figure 7a.

The Period 3 recorded a large number of landslides. In Area 1, between May 25 and May 31, 262 landslides were registered, according to data provided by Recife's Civil Defense. Thus, for a better understanding of this period, more detailed analyses were carried out, considering precipitation and the average humidity on an hourly scale, as shown in Figures 7b and 7c.

Figure 7b shows two periods of intense precipitation: the first between May 24 and May 25, 2022, and the second between May 27 and May 29, 2022. These two periods were identified as Critical Moments (CM). In general, there is a rapid increase in humidity, followed by drainage due to the cessation of rainfalls. During times of greater precipitation, the formation of 'plateaus' is observed, indicated by arrows, which suggest a possible saturation of the soil.

During the Critical Moment 1 (CM1), 225 mm of rain in 48 h, were recorded, with an hourly peak precipitation registering 40 mm at 3 a.m. on May 25. Moisture profiles during wetting and draining in CM1 are shown in Figures 7d and 7e, respectively. These graphs show that rainwater infiltration occurs faster in surface layers between 0.5 and 1.5 m deep. The percentage change in moisture during wetting, in ascending order of depth, were: 27%, 65%, 25%, 12%, 9%, and 7%.

During Critical Moment 2 (CM2), 254 mm of rain accumulated in 48 h, with the peak hourly precipitation at 8 a.m. on 05/28, registering 24 mm. The CM2 moisture profiles are shown in Figures 7f and 7g. The graphs show a progressive increase in hourly humidity, mainly between 0.5 and 1.5 m depth. The percentage change in humidity during wetting, between 6 a.m. on May 27 and 8 a.m. on May 28, 2022, in ascending order of depth, were: 29%, 72%, 33%, 18%, 16%, and 28%.

9.2 Monitoring with the Geotechnical DCP-2

Figure 8a shows the graph of the average daily soil moisture measured by the Geotechnical DCP-02 and the daily precipitation recorded at RG-02. The analysis interval starts on January 01 and ends on December 4, 2022, being divided into five smaller periods, using the same division criteria applied in Area 1. Table 3 presents the average volumetric soil moisture (%) and the corresponding standard deviation values for each period.

The first period occurred between January 01 and March 4, 2022, lasting 63 days, and is inserted in the driest season. The average values of moisture in period 1 are the lowest, as shown in Table 3. The lowest humidity situations occur at the most superficial depths, specifically between 0.5-1.5 m deep, due to the greater susceptibility of these layers to evapotranspiration. On the other hand, the two deeper sensors registered practically constant moisture values.

In early March, the rain increased soil moisture levels and this humidity remained high due to the increase in rainfall between March 5 and May 22, 2022, thus establishing the second period. The data in Table 3 show that in Period 2 there was an increase in the average moisture values at all monitored depths about Period 1.

In the third period, lasting six days (from May 23 to May 28, 2022), an accumulated rainfall of 497 mm was registered, resulting in the highest soil moisture peaks. Thus, according to the data in Table 3, in Period 3 there was an

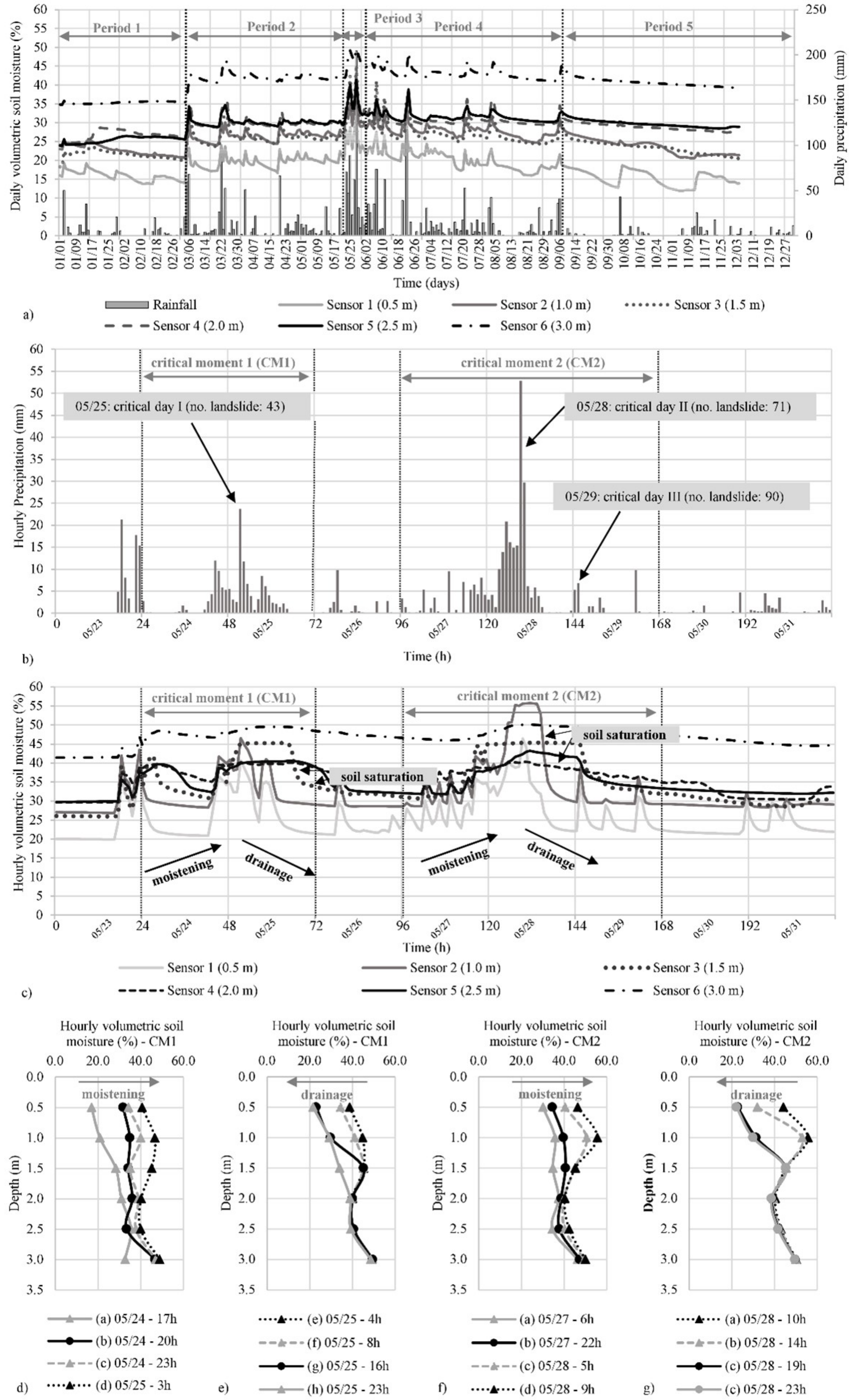

Figure 8. Monitoring data from Area 1: a) rainfall data and average daily moisture between January 01 and December 04, 2022; b) period 3 hourly precipitation data; c) period 3 hourly average moisture data; d) wetting moisture profile – CM1; e) drainage moisture profile – CM1; f) wetting moisture profile – CM2; g) drainage moisture profile – CM2.

Table 3. Average moisture and standard deviation of the periods in Area 2.

	Sensor 1	Sensor 2	Sensor 3	Sensor 4	Sensor 5	Sensor 6
Period 1	15.93% (1.33)	22.71% (1.34)	21.53% (1.06)	26.72% (1.28)	25.46% (0.81)	35.31% (0.28)
Period 2	19.62% (1.56)	26.37% (1.33)	26.21% (1.87)	29.94% (1.52)	30.09% (1.06)	42.03% (1.20)
Period 3	27.21% (2.86)	34.08% (4.41)	36.55% (5.28)	37.39% (1.94)	36.33% (3.36)	47.09% (2.30)
Period 4	20.27% (2.62)	27.90% (1.78)	27.35% (3.02)	31.01% (1.92)	31.61% (1.33)	43.17% (1.62)
Period 5	15.41% (2.06)	23.66% (2.10)	23.45% (1.69)	28.78% (1.01)	29.70% (0.97)	40.70% (1.16)

Unit: Average volumetric soil moisture (%);
Note: The values presented in parentheses correspond to the standard deviation.

increase in average moisture in all sensors, compared to Period 2. However, it was in this period that the highest standard deviations were identified, indicating that the monitored soil is permeable and has a low water holding capacity.

The fourth period lasted 101 days (from May 29 to September 6, 2022), and represents the transition from the rainy season to the drier season. During this period, the average moisture values decreased about Period 3 due to the reduction in the amount of rain. The data in Table 3 show that despite the loss of moisture, Period 4 values are still slightly higher than those recorded in Period 2. This indicates that the soils in Area 2 remained wet for 186 days.

The fifth period occurred between October 09 and December 4, 2022, lasting 89 days. During this period, there was a reduction in average humidity compared to Period 4, mainly between 0.5-1.5 m depth, due to the return of the drier season (Table 3). The graph in Figure 8a illustrates how the decrease in moisture was slow and proportional to depth, especially in the last two sensors, where the average daily moisture values remained relatively high.

Due to the high volume of rainfall and rapid changes in humidity, Period 3 saw a large number of landslides. In Area 2, between May 25 and May 31, 336 landslides were registered, according to data provided by the Local Civil Defenses of Recife and Jaboatão dos Guararapes. Thus, analyses were also carried out considering precipitation and average moisture on an hourly scale, as shown in Figures 8b and 8c. Two Critical Moments (CM) were established: CM1 between May 24 and May 25, 2022, and CM2 between May 27 and May 29, 2022. At the two critical moments, the formation of 'plateaus' indicating soil saturation is highlighted in Figure 8c by arrows.

During the CM1, 90 mm of rain accumulated in 48 h, with the peak hourly precipitation at 3 a.m. on May 25, registering 23 mm. The CM1 moisture profiles are shown in Figures 8d and 8e. These graphs show a progressive increase in hourly humidity, mainly between 0.5 and 2.0 m depth, as the volume of rain increases. The percentage variation of increase in humidity, between 5 p.m. on May 24, 2022 and at 3 a.m. on May 25, 2022, in ascending order of depth were: 94%, 64%, 46%, 13%, 22%, 4%.

In the CM2, an accumulated 298 mm of rain was recorded in 72 hours. The hourly precipitation peak occurred at 9 a.m. on May 28, registering 53 mm. Moisture profiles during the CM2 wetting and draining are shown in Figures 8f and 8g, respectively. These graphs show the increase in hourly humidity, mainly between 0.5 and 2.0 m depth, as the volume of rain increases. The increase in moisture between 6 a.m. on May 27 and 9 a.m. on May 28 was in ascending order of depth: 54%, 55%, 30%, 8%, 22%, and 8%.

10. Discussion of the moisture monitoring results

The data from the Geotechnical DCP-1 and 2 showed consistent behavior in response to rainwater infiltration, with Figures 7 and 8, clearly showing changes in soil water content as a result of rainwater infiltration. The data showed that closer to surface, faster is the sensor response to rainwater infiltration and greater is the magnitude of volumetric water content increase. Similar results were described by Chávez et al. (2016), Crawford et al. (2019), and Bovolenta et al. (2020).

In her studies Pirone et al. (2015), observed a good agreement between the matric suction trend and the volumetric water content, both experiencing fluctuations that depend on the depth of the sensor, being more significant in superficial soils. The results collected from Geotechnical DCP-1 and 2, the deeper layers tend to present more constant values of moisture content and slower drainage in the long term.

The variation in humidity in the deeper layers is more significant during the wettest period of the year (between March and August). During this period the results show that there is variation in moisture at all moisture levels, and the deeper layers respond more pronouncedly to rainwater infiltration. Pirone et al. (2015) observed that the deeper layers were virtually unaffected by individual rainfall events, as these layers generally reflect average seasonal variations.

During period 3, the Geotechnical DCP-2 mostly showed average moisture values and standard deviations higher than the Geotechnical DCP-1, indicating greater permeability and low water retention capacity, especially in the most superficial layers. The different grain sizes of the monitored profiles can explain this behavior since the Geotechnical DCP-1 profile is clayey than the other. Crawford et al. (2019), observed that clayey soils retain moisture for longer times and do not allow large increases in moisture like coarse soils.

In both areas, the soils remained wet for approximately six months. These data revealed a high susceptibility to landslides in this area, since high moisture values indicate lower suctions, and consequently lower shear resistance. In both areas, the sharp increase in soil moisture occurs in response to large hourly rainfall. However, during the CM1 and CM2, even after the reduction of rainfall drainage does not occur immediately at deeper levels, thus explaining the occurrence of some cases of landslides a few hours after the peak of rain.

11. Conclusion

A network of equipment was installed to monitor rainfall and soil moisture in an integrated manner for the development of an early warning system for landslides in high-risk areas of the Metropolitan Region of Recife. The data collected show that soil moisture variation is largely dependent on hourly rainfall. The most superficial layers present greater variation in humidity due to the effects of evapotranspiration. However, during the wettest period, variation in moisture is observed at all levels. The data also reveal that the monitored soils remained wet for approximately six months, indicating that medium rainfall can trigger landslides. This information will allow the improvement of proposals for meteorological thresholds under development for this region.

Acknowledgements

The authors extend their heartfelt gratitude to the Group of Geotechnical Engineering of Disasters and Plains (GEGEP), the Foundation for the Support of Science and Technology of the State of Pernambuco (FACEPE), National Early Warning and Monitoring Centre of Natural Disaster (CEMADEN), and the Federal University of Pernambuco (UFPE) for their generous support.

Declaration of interest

The authors have no conflicts of interest to declare. All co-authors have observed and affirmed the contents of the paper and there is no financial interest to report.

Authors' contributions

Roberto Quental Coutinho: conceptualization, data curation, formal analysis, funding acquisition, methodology, visualization, writing – original draft. Bruno Diego de Morais: conceptualization, data curation, formal analysis, methodology, writing – original draft. Rodolfo Moreda Mendes: conceptualization, formal analysis, funding acquisition, methodology, supervision, writing – review & editing. Marcio Roberto Magalhães de Andrade: conceptualization, funding acquisition, writing – review & editing.

Data availability

The datasets generated and analyzed in the course of the current study are available from the corresponding authors upon request. Data generated and analyzed in the course of the current study are available in the 'Mapa Interativo da Rede Observacional para Monitoramento de Risco de Desastres Naturais do CEMADEN' repository, http://www2.cemaden.gov.br/mapainterativo/.

List of symbols

CEMADEN	National Early Warning and Monitoring Centre of Natural Disaster
CL	Low plasticity clay
CM	Critical moment
DCP	Data collection platform
GEGEP	Group of Geotechnical Engineering of Disasters and Plains
LL	Liquid limit
MH	High plasticity silt
ML	Low plasticity silt
PI	Plasticity index
PL	Plastic limit
RG	Rain gauges
MRR	Metropolitan Region of Recife
SC	Clayey sands
SM-SC	Silty-clayey sand
UFPE	Federal University of Pernambuco
USCS	Unified Soil Classification System

References

ABNT NBR 6459. (2016a). *Soil — liquid limit determination*. ABNT - Associação Brasileira de Normas Técnicas, Rio de Janeiro, RJ (in Portuguese).

ABNT NBR 7180. (2016b). *Soil — plasticity limit determination*. ABNT - Associação Brasileira de Normas Técnicas, Rio de Janeiro, RJ (in Portuguese).

ABNT NBR 7181. (2016c). *Soil — grain size analysis*. ABNT - Associação Brasileira de Normas Técnicas, Rio de Janeiro, RJ (in Portuguese).

Abraham, M.T., Satyam, N., Rosi, A., Pradhan, B., & Segoni, S. (2021). Usage of antecedent soil moisture for improving the performance of rainfall thresholds for landslide early warning. *Catena*, *200*, 105147. http://dx.doi.org/10.1016/j.catena.2021.105147.

Augusto Filho, O., Virgili, J.C., & Diláscio, M.V. (2018). Estabilização de taludes. In A.M.S. Oliveira & J. J. Monticeli (Eds.), *Geologia de engenharia e ambiental* (Vol. 2, pp. 400-420). ABGE (in Portuguese).

Bandeira, A.P.N., & Coutinho, R.Q. (2015). Critical rainfall parameters: proposed landslide warning system for the

Metropolitan Region of Recife, PE, Brazil. *Soils and Rocks*, *38*(1), 27-48. http://dx.doi.org/10.28927/SR.381027.

Bovolenta, R., Iacopino, A., Passalacqua, R., & Federici, B. (2020). Field measurements of soil water content at shallow depths for landslide monitoring. *Geosciences*, *10*(10), 1-26. http://dx.doi.org/10.3390/geosciences10100409.

Chávez, J.A., Landaverde, J., Landaverde, R.L., & Tejnecký, V. (2016). Monitoring and behavior of unsaturated volcanic pyroclastic in the Metropolitan Area of San Salvador, El Salvador. *SpringerPlus*, *5*, 536. http://dx.doi.org/10.1186/s40064-016-2149-x.

Coutinho, R.Q., & Delfino, R.K.R. (2022). Estudo preliminar da pluviometria crítica de deslizamentos dos Morros da Zona Norte do Recife. In Associação Brasileira de Mecânica dos Solos e Engenharia Geotécnica (Org.), *VIII Conferência Brasileira sobre Estabilidade de Encostas* (Vol. 3, pp. 207-214). São Paulo, Brazil: ABMS (in Portuguese).

Coutinho, R.Q., & Severo, R.N.F. (2009). Investigação geotécnica para projeto de estabilidade de encostas. In Associação Brasileira de Mecânica dos Solos e Engenharia Geotécnica (Org.), *V Conferência Brasileira de Estabilidade de Encostas* (pp. 1-55). São Paulo, Brazil: ABMS (in Portuguese).

Coutinho, R.Q., Henrique, H.M., Souza Neto, D.P., & Cavalcanti, M.M. (2017). Mapeamento de áreas de risco de deslizamento na comunidade lagoa encantada, Recife-PE. In Associação Brasileira de Mecânica dos Solos e Engenharia Geotécnica (Org.), *VII Conferência Brasileira sobre Estabilidade de Encostas* (pp. 1-8). São Paulo, Brazil: ABMS (in Portuguese).

Coutinho, R.Q., Silva, M.M., Santos, A.N., & Lacerda, W.A. (2019). Geotechnical characterization and failure mechanism of landslide in granite residual soil. *Journal of Geotechnical and Geoenvironmental Engineering*, *145*(8), 05019004. http://dx.doi.org/10.1061/(ASCE)GT.1943-5606.0002052.

Coutinho, R.Q., Souza Neto, J.B., Santos, L.M., & Lafayette, K.P.V. (2006). Geotechnical characterization of an unsaturated soil in the Barreiras Formation, Pernambuco – Brazil. In G.A. Miller, C.E. Zapata, S.L. Houston & D.G. Fredlund (Eds.), *Unsaturated soils 2006* (Vol. 1, pp. 1627-1638). ASCE.

Crawford, M.M., Bryson, L.S., Woolery, E.W., & Wang, Z. (2019). Long-term landslide monitoring using soil-water relationships and electrical data to estimate suction stress. *Engineering Geology*, *251*, 146-157. http://dx.doi.org/10.1016/j.enggeo.2019.02.015.

Dias, H.C., Hölbling, D., & Grohmann, C.H. (2021). Landslide susceptibility mapping in Brazil: a review. *Geosciences*, *11*(10), 1-15. http://dx.doi.org/10.3390/geosciences11100425.

Guedes, R.V.S., & Silva, T.L.V. (2020). Análise descritiva da precipitação, temperatura, umidade e tendências climáticas no Recife – PE. *Revista Brasileira de Geografia Física*, *13*(7), 3234-3253 (in Portuguese). https://doi.org/10.26848/rbgf.v13.07.p3234-3253.

Gusmão Filho, J.A., Ferreira, S.R.M., & Amorim Junior, W.M. (1997). Escorregamentos em morros urbanos do Recife: o caso do Boleiro. In Associação Brasileira de Mecânica dos Solos e Engenharia Geotécnica (Org.), *Panamerican Symposium on Landslides II* (pp. 985-994). São Paulo, Brazil: ABMS (in Portuguese).

Macedo, E.S., & Sandre, L.H. (2022). Mortes por deslizamentos no Brasil: 1988 a 2022. *Revista Brasileira de Geologia de Engenharia e Ambiental*, *12*(1), 110-117 (in Portuguese).

Marengo, J.A., Alcantara, E., Cunha, A.P., Seluchi, M., Nobre, C.A., Dolif, G., Gonçalves, D., Dias, M.A., Cuartas, L.A., Bender, F., Ramos, A.M., Mantovani, J.R., Alvalá, R.C., & Moraes, O.L. (2023). Flash floods and landslides in the city of Recife, Northeast Brazil after heavy rain on May 25–28, 2022: causes, impacts, and disaster preparedness. *Weather and Climate Extremes*, *39*, 100545. http://dx.doi.org/10.1016/j.wace.2022.100545.

Mendonça, F., & Danni-Oliveira, I.M. (2007). *Climatologia: noções básicas e climas do Brasil*. Oficina de Textos (in Portuguese).

Pirone, M., Papa, R., Nicotera, M.V., & Urciuoli, G. (2015). In situ monitoring of the groundwater field in an unsaturated pyroclastic slope for slope stability evaluation. *Landslides*, *12*, 259-276. http://dx.doi.org/10.1007/s10346-014-0483-z.

Toll, D.G., Lourenço, S.D.N., Mendes, J., Gallipoli, D., Evans, F.D., Augarde, C.E., Cui, Y.J., Tang, A.M., Rojas, J.C., Pagano, L., Mancuso, C., Zingariello, C., & Tarantino, A. (2011). Soil suction monitoring for landslides and slopes. *Quarterly Journal of Engineering Geology and Hydrogeology*, *44*(1), 23-33. http://dx.doi.org/10.1144/1470-9236/09-010.

Wicki, A., Lehmann, P., Hauck, C., Seneviratne, S.I., Waldner, P., & Stähli, M. (2020). Assessing the potential of soil moisture measurements for regional landslide early warning. *Landslides*, *17*, 1881-1896. http://dx.doi.org/10.1007/s10346-020-01400-y.

REVIEW ARTICLES

Soils and Rocks

An International Journal of Geotechnical and Geoenvironmental Engineering

www.soilsandrocks.com

ISSN 1980-9743
ISSN-e 2675-5475

Application of digital technologies in landslide prediction, mapping, and monitoring

Gabriel Raykson Matos Brasil de Araújo[1,2#], Alessandra Cristina Corsi[2], Eduardo Soares de Macedo[2], Marcos Massao Futai[1]

Review Article

Keywords
Landslides
Digital technologies applied to landslides
IoT and AI applied to landslides
Scoping review

Abstract

This paper presents a scoping review on the use of digital technologies for predicting, mapping, or continuously monitoring landslides on natural slopes. Articles and reviews published between 2001 and 2023 indexed by Scopus (Elsevier) were selected. The results showed that the number of publications involving this theme has been growing every year, with two periods of prominence: 2008-2010 and 2015-2021. China, Italy, India, USA and Taiwan are the five countries that published the most on the subject during the studied period. It was also found that remote sensing tools were the most used and showed strong stability, accompanied by artificial intelligence tools. Digital sensors have been widely used in Early Warning Systems, composing Wireless Sensors Network, monitoring terrain or climate variables. There is no doubt that digital technologies are extremely advantageous in relation to traditional technologies and that they already present themselves as a solution and confirm their trend of future consolidation.

1. Introduction

Mass movements on slopes, also called landslides, are movements of blocks of rock, soil, or debris that move down a slope due to natural influences, human-induced factors, or a combination of both. On a geological time scale, mass movements certainly will occur on slopes. These movements have become an object of international political and institutional interest because they are responsible for major socioeconomic impacts at a global level every year. (UNISDR, 2015; UNDRR, 2019).

In 1988, the Centre for Research on the Epidemiology Disasters (CRED) created the Emergency Events Database (EM-DAT) to gather data on adverse events of natural, biological, or industrial origin, including landslides. Using the EM-DAT data available until January 2023, it was found that landslides correspond to about 5.6% of all events reported worldwide between 1900-2022, causing damage of around US$ 23.4 billion, affecting approximately 14.8 million people and fatally hitting 72 thousand. However, it is important to highlight the existence of underreporting, which means that these numbers can be even higher. Figure 1 shows a graph with the number of people affected, injured or dead and the estimated cost of damage caused by landslides using data from 2001-2023 from the EM-DAT database.

In terms of measures for mitigating the effects caused by landslides, solutions can be grouped into two categories: i) structural measures and ii) non-structural measures (MCID/IPT, 2007; IG, 2009). Structural measures involve engineering solutions and can be exemplified by retaining walls, drainage systems, and urban infrastructure works. Conversely, non-structural measures are related to public policies, urban planning, and civil defense plans. These include solutions such as Monitoring Systems (SM), Early Warning Systems (EWS), and Susceptibility Maps (MCID/IPT, 2007; Kong et al., 2020). Non-structural measures indirectly mitigate the effects of landslides. They are less costly and have less impact on the environment compared to structural measures. They can also produce results as satisfactory as structural measures in preventing and mitigating the effects of landslides, especially in irregularly occupied risk areas in urban centers.

In the last decade, Digital Transformation (DX) has caused significant changes, from simple activities in society and economic activities to more complex applications, such as real-time monitoring of industrial and environmental procedures. The outcome of this process has been identified and named as the 4th Industrial Revolution or Industry 4.0 (Frank et al., 2019; Vial, 2019; Tortorella et al., 2020). Vial (2019) defined DX as a process aimed at institutional/social improvement that triggers significant changes through the combination of information, computing, communication, and connectivity technologies. This definition is the result of a review study that included 282 papers involving DX

#Corresponding author. E-mail address: gabrielraykson@usp.br
[1]Universidade de São Paulo, Escola Politécnica, Departamento de Engenharia de Estruturas e Geotécnica, São Paulo, SP, Brasil.
[2]Instituto de Pesquisas Tecnológicas do Estado de São Paulo, Seção de Investigação, Riscos e Gerenciamento Ambiental, São Paulo, SP, Brasil.

Submitted on May 15, 2023; Final Acceptance on October 25, 2023; Discussion open until February 28, 2024.
https://doi.org/10.28927/SR.2023.005823

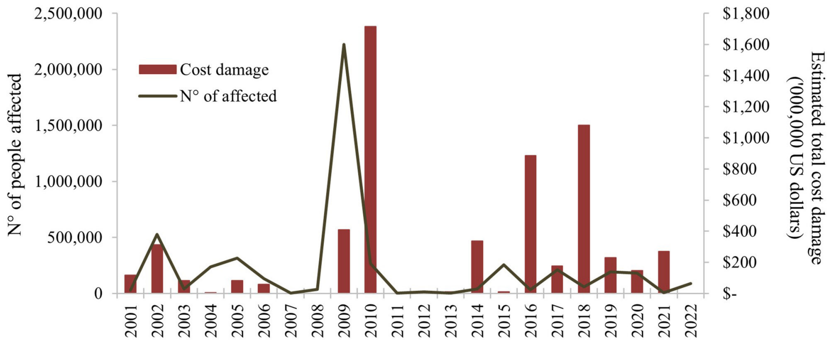

Figure 1. Number of people affected by mass movements per year and their estimated total cost damage adjusted in millions of US dollars caused by the movements.

as a central theme. Traditionally observed in the industrial, technology and information systems environment, mainly due to the digitalization of its processes, products, and organizational strategies (Frank et al., 2019; Nambisan et al., 2019; Tortorella et al., 2020; Vial, 2019), DX is not limited to these fields of application. It also extends to everyday applications in urban centers, enabling the application of the concept of Smart Cities.

The concept of a Smart City was introduced in the 1990s to incorporate solutions based on advanced information and communication technologies into urban planning, and it was closely associated with Digital Transformation. Bellini et al. (2022) highlight that the Internet of Things (IoT) represents one of the main drivers and facilitators of smart innovation and sustainable development linked to the evolution of Smart Cities. IoT is a fundamental part of the digitalization of devices, in addition to the incorporation of Artificial Intelligence (AI) tools, which make data processing more feasible in the face of high acquisition rates that place Smart Cities on the scale of big data.

It is common sense that the Environment is qualified as one of the domains of interest of Smart Cities (Sharif & Pokharel, 2022; Bellini et al., 2022). The monitoring and mapping of susceptibility, danger, and risk of damages events of hydro-geological origin fits in the context of interest of Smart Cities and have suffered the effects of Digital Transformation in recent years (Santos et al., 2020). Several studies have sought to improve the tools and methods for monitoring and managing the risk of movements on slopes. From the point of view of mapping and predicting movements on slopes, Artificial Intelligence tools have been the flagship that leads the advancement of major research and applications (Wang et al., 2019; Bragagnolo et al., 2020; Huang et al., 2020; Catani, 2021; Rodrigues et al., 2021), while the originally digital instruments or the digitalization of traditional instruments are being the main tools for improvement of slope monitoring methods (Giogetti et al., 2016; El Moulat et al., 2018; Mei et al., 2020; Ruzza et al., 2020; Giri et al., 2022; Otero et al., 2022; Marino et al., 2023).

Within the context of IoT, these digital instruments operate interconnected by the same wireless network and transmit data to the same storage center. In recent years, there has been a growth in the amount of use of low-cost sensors and transmitter devices, seeking to reduce the cost of IoT solutions for monitoring movements on slopes. Low-cost sensors have been integrated into so-called Early Warning Systems, composing Wireless Sensors Networks. Sensors are usually used to measure rainfall indices, soil moisture content, seismic vibration, and angular variations (Ruzza et al., 2020; Bagwari et al., 2022; Thirugnanam et al., 2022; Lau et al., 2023; Marino et al., 2023).

As for the use of Artificial Intelligence, Machine Learning has been widely used for prediction or mapping landslides. Machine Learning is a method of data analysis that uses algorithms that seek to simulate human thinking, which would make the machine capable of making decisions based on a set of validated data that would train the algorithm (supervised learning) or discovering patterns in input data using different types of techniques to generate output data (unsupervised learning) (Sreelakshmi et al., 2022; Collini et al., 2022) Deep Learning is a subgroup of Machine Learning, which seeks to simulate, in greater depth, the action of an artificial neural network (Baghbani et al., 2022; Tehrani et al., 2022).

Another alternative to traditional methods for monitoring, remote sensing has also been widely used for mapping areas susceptible to landslides and monitoring movements on natural slopes. Remote sensing uses satellites, radars, and on-board technology to acquire information about a specific area or object. Synthetic aperture radar (SAR) and its variations, light detection and ranging (LiDAR), airborne laser scanning (ALS) are major examples of remote sensing techniques (Thirugnanam et al., 2022).

This paper presents a scoping review of the effects of incorporating new technologies and the DX on natural slope monitoring. It characterizes the process through publications on the subject between 2001-2023, identifying characteristics such as the number of publications over the years, recurrence of keywords used, geographical distribution of the first authors, using Scopus (Elsevier) as a study source. Section 2 presents the methodology protocol applied in the review. Section 3 presents the results obtained and discusses the observations. Section 4 concludes this work.

2. Scoping review protocol

2.1 Review protocol

Review objectives:

i. To characterize the effects of incorporating new technologies for monitoring natural slopes.
ii. To present the gradual growth of the theme throughout the 21st century.
iii. Identify the main features caused by the Digital Transformation in slope mapping, prediction, and monitoring.

PICOC strategy adopted:

- P (Population): Articles written in the English language, published in scientific journals within the Scopus bases (Elsevier).
- I (Intervention): Digital Transformation in slope monitoring, geotechnical instrumentation on slopes, the use of IoT, Big Data and AI as tools for slopes monitoring and warning.
- C (Comparison): Concepts, application limitations of new technologies and spatial distribution of researchers.
- O (Outcome): Evolution of the theme over the last two decades, the regionalization of publications, AI tools and instruments used.
- C (Context): Geological disasters, slope movements and risk assessment.

Research questions:

1. How has the use of digital solutions advanced in the geotechnical environment with a focus on predicting and monitoring movements in natural slopes?
2. What remote sensing, photogrammetry and geodetic tools have been most used?
3. What artificial intelligence tools have been most used?
4. What digital sensors have been most used?
5. Considering the affiliation country of the first author, what are the main countries that are researching and publishing on the subject?

Criteria adopted for acceptance of documents in the review:

- Real case application using IoT, AI, Early Warning System, Remote Sensing, Optical Fibre, MEMS or similar.
- Laboratory simulation using IoT, AI, Optical Fibre, MEMS or similar.
- Monitoring and inspection with UAV, radar, satellites or similar
- State-of-the-art reviews

Criteria adopted for rejection:

- Duplicate
- Outside scope of the review

Search string:

The search was restricted to articles that met the following conditions: i) articles and reviews published between 2001 and May 4, 2023, ii) written in English, iii) in the final stage iv) that contained in the title, abstract or keywords the set of words contained in the groups ‘Phenomenon’, ‘Activity’ and ‘Tools’ shown in Figure 2.

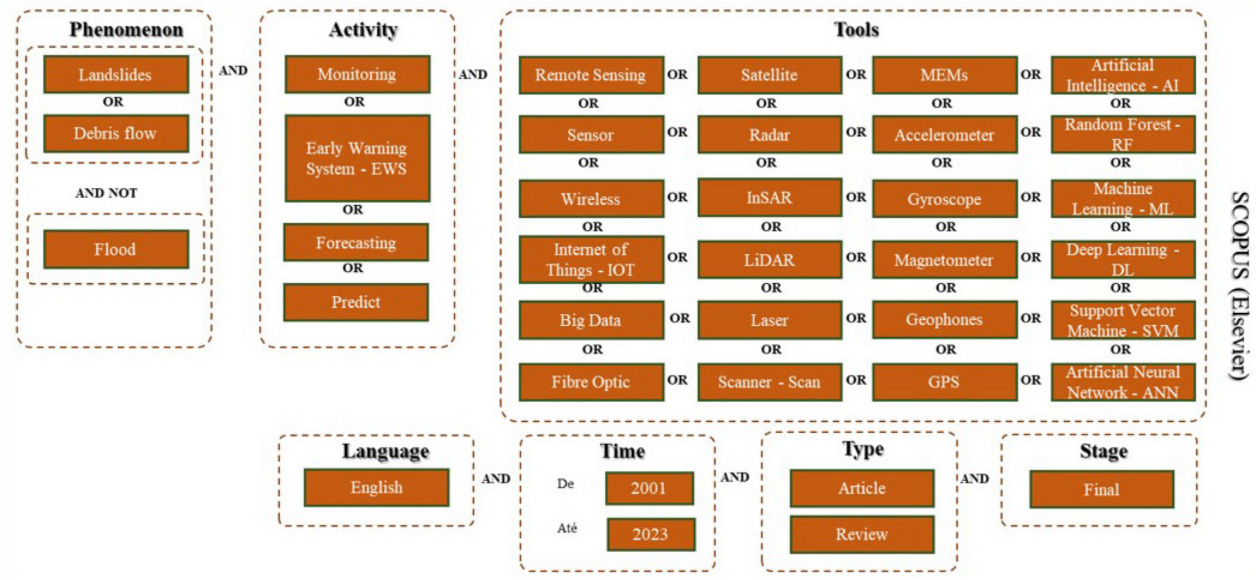

Figure 2. Considerations for constructing the search string.

2.2 Results database

Following the considerations indicated in Figure 2 and described in the previous topic, 2,674 documents were obtained, of which 1,615 were classified as accepted. However, of these, 211 documents lacked some information, be it the country of origin of the publication, source and/or keywords. To maintain a regular analysis of the data, only documents with complete information were admitted, resulting, therefore, in a database with 1,404 articles.

3. Analysis and results

3.1 General observations

By observing Figure 3, clearly use of new technologies as a tool for prediction, forecasting or continuous monitoring of slope stability presents a strong trend growth in the number of publications each year. Analyzing the values individually, note that there is a first strong increase in the number of publications between 2008 and 2010, where the number came close to quadrupling in two years, with oscillations in the following years, but maintaining a certain stability, returning to show growth trend from 2015, with highlights for the period between 2019 and 2021, contemplating the Covid-19 pandemic period, which exceeded the first hundred publications per year and doubled the number in two years. The decrease in the number of publications made in 2022, which was unexpected compared to that of 2021, shows that the resumption of post-pandemic activities directly interfered with the publication process. This should be considered for 2023.

Detailing the contribution of each country in the number of publications considering the affiliation of the first author, Figure 4 presents the individual contribution of the top 5. From the graph, it is evident that China and Italy accompanied the first growth between 2008 and 2010, and remained close until 2008, when China assumed the absolute leadership of annual individual publications. Altogether, the five countries have a total of 902 publications, which represents 64.3% of the total publications surveyed in this study. Of these publications, 494 are attributed to China, 226 to Italy, 80 to India, 58 to USA and 44 to Taiwan. The Figure 5 shows a choropleth map with all the countries identified in this research, revealing a total of 64 countries.

The keywords synthesized in Figure 6 enable a global vision on the interest of researchers. Figure 6a presents the term Landslide as the most frequent phenomenon and the terms Monitoring, Susceptibility as activities of greatest

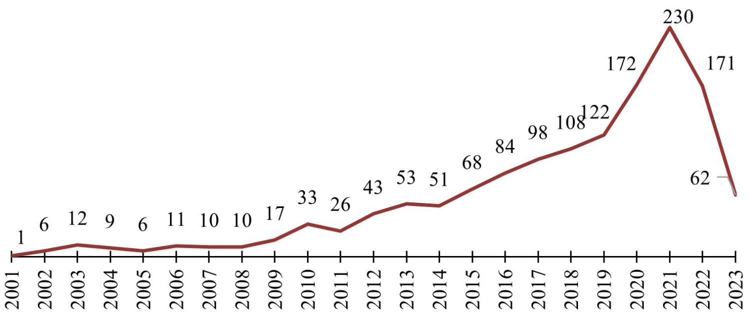

Figure 3. Number of publications per year about digital technologies applied to mass movements on natural slopes from 2001 to May 4, 2023.

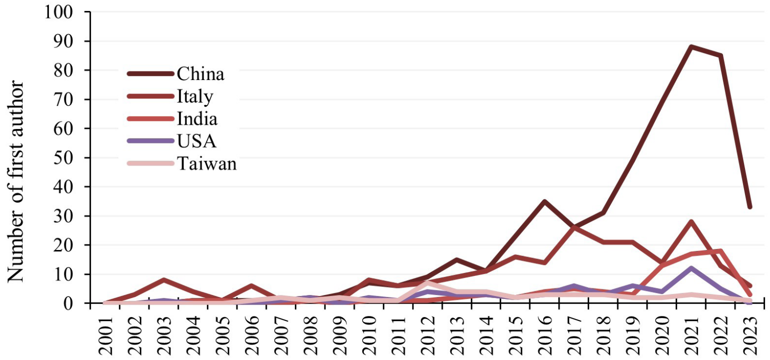

Figure 4. Number of first authors by country affiliation declared in each publication.

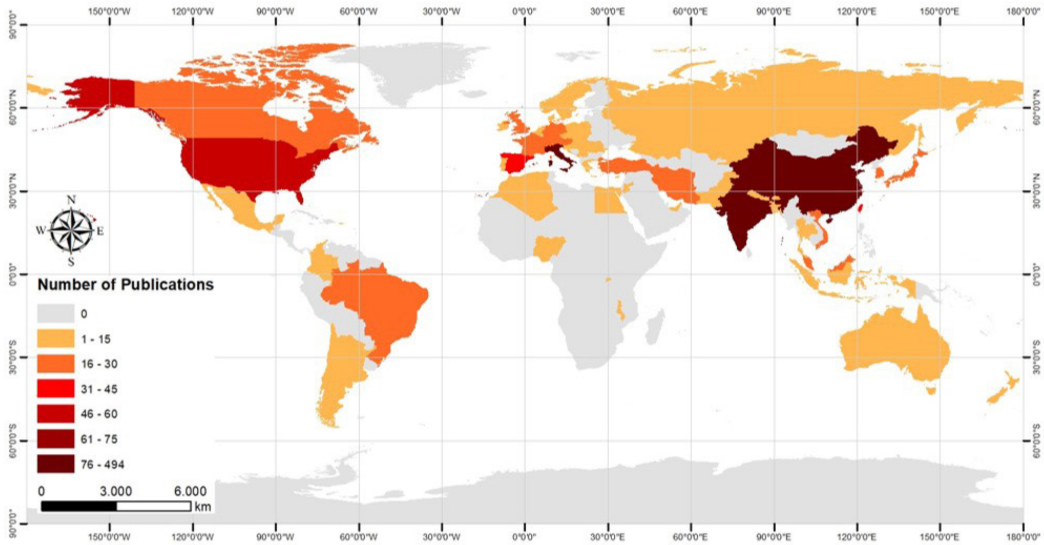

Figure 5. Choropleth map with geographical distribution of the first authors.

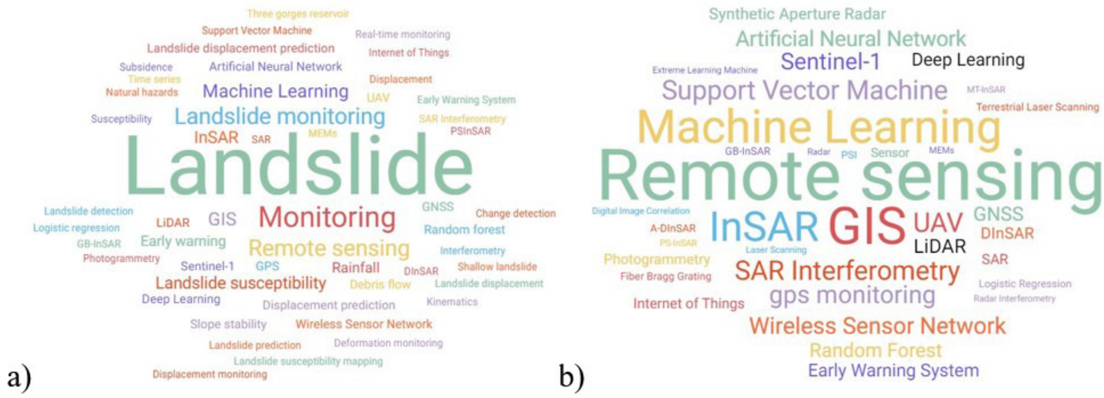

Figure 6. Keyword clouds with a) global and b) tools keywords.

interest for application of the methods. As for the group of tools, Remote Sensing and Machine Learning had greater expression, as well as their respective tools such as SAR and its variations, LiDAR, UAV for Remote Sensing and Support Vector Machine, Artificial Neural Network and Random Forest for Machine Learning.

In the word cloud containing only tools and your groups, it is possible to verify that the tools that work with image acquisition and processing are the most common tools to use. Associated to this fact, the Artificial Intelligence tools, led by the Machine Learning and Deep Learning tool groups are among the main ones adopted. These tools can be used both to optimize image processing, to generate susceptibility, hazard, or risk maps, to identify slope movement patterns or even to identify temporal changes. Moreover, AI tools are fundamental for processing data collected at high acquisition rates of data and stored at Big Data scale, obtained by solutions associated with the Internet of Things.

These high acquisition rates can be exemplified by the Wireless Sensors Network (WSN), also present in Figure 6b. Depending on the duration of monitoring and the acquisition rate, the monitoring system may enter the big data storage scale, raising the level of processing, where it is necessary to use AI tools that carry out filtering processes, identify patterns and use part of the results as a validation set, performing the function of "teaching" the machine what is and that is not of interest to the user, and can be applied to predict events in monitoring and alert systems, or even to evaluate changes in the stability of monitored elements.

Figure 7 shows the journals that published the most about the use of new technologies. It is easy to see that the listed journals are within the context of geology or sensors

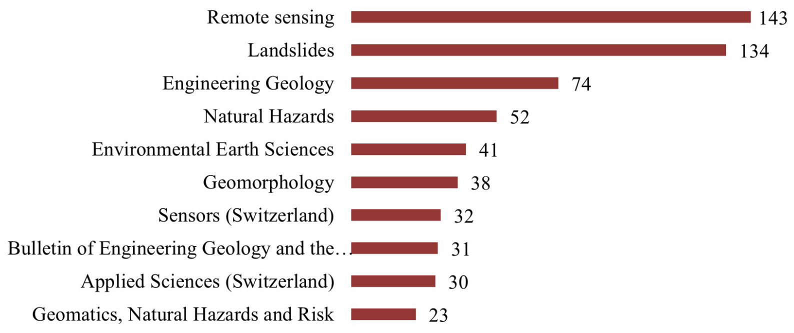

Figure 7. List of the top 10 academic journals that published the most about the theme.

and applied technology, not appearing traditional geotechnical journals. With the study, it was observed that these traditional geotechnical journals have focused their publications either on the application of methods and tools for slope stability analysis or on proposals for solutions applied to the stabilization or containment of movements, with only a small part of the publications focused on methods of movement investigation.

3.2 Answering the research questions

A. How has the use of digital solutions advanced in the geotechnical environment with a focus on predicting and monitoring movements in natural slopes?

The use of new technologies driven by the Digital Transformation began its process slowly between 2001 and 2008, with significant increase in the number of publications between 2008 and 2010. In this first stage, the use of GIS tools predominated for processing data obtained by satellites, radars, or GPS, with strong image processing steps. Initial studies on inertial sensors with wireless transmission and fibre optic applications began to be carried out. From 2010 onwards, in addition to the continuity of GIS, satellite and radar tools, studies on early warning systems were intensified, accompanied by wireless sensor networks and real-time monitoring, and AI for motion prediction and image processing. From 2016, tools such as UAV, IoT, and AI gained greater prominence, still accompanied by GIS, satellite and radar tools, with AI applications for predicting movements, preparing susceptibility maps and processing remotely acquired data at high rates acquisition process, enabling real-time monitoring.

B. What remote sensing, photogrammetry and geodetic tools have been most used?

An expressive presence in the papers evaluated in this research, the most cited tools were:

- Satellite Sentinel-1
- Synthetic Aperture Radar (SAR)
- Interferometric SAR (InSAR)
- Diferencial InSAR (DInSAR)
- Ground Based InSAR (GB-SAR)
- Unmanned Aerial Vehicle (UAV)
- Light Detection and Ranging (LiDAR)
- Global Position System (GPS)

C. What artificial intelligence tools have been most used?

It was observed that Machine Learning and Deep Learning algorithms that work with supervised learning were preferred over unsupervised learning. Below are listed the three tools that were most cited:

- Support Vector Machine (SVM)
- Random Forest (RF)
- Artificial Neural Network (ANN)

D. What digital sensors have been most used?

The digital sensors have been incorporated into Early Warning Systems (EWS), composing the Wireless Sensor Networks. Among the usual sensors, the use of:

- Accelerometer
- Barometer
- Gyroscope
- Soil moisture
- Geophone
- Temperature/humidity
- Optical fibre
- Strain gauge

E. Considering the affiliation country of the first author, what are the main countries that are researching and publishing on the subject?

A total of 64 countries were identified that published at least one publication on the subject. The top 5 positions are occupied China (1st), Italy (2nd), United States of America (3rd), India (4th) and Taiwan (5th), which together represent 65.3% of the total number of publications between 2001-2023.

3.3 Advantages over the traditional methods

- Decreased visits to field monitoring sites.
- The short response time of digitalized instruments.
- The possibility of monitoring readings in real time and remotely.

- The possibility of investigation a greater number of variables at the same instrumentation point, or even different types of measurements at different depths.
- The combination of more than one technological solution in the same monitoring program.

3.4 Projecting the future from the past and present observing

One can expect:

- The continued use of satellites, radars, and on-board technologies, in addition to the increased use of (UAV) for mapping and surface monitoring.
- The digitalization of traditional instruments or, even, the adaptation of new technologies to play the roles of these instruments.
- Greater scope and depth of application of Artificial Intelligence tools, going beyond prediction or simples signal processing.
- Integration of warning systems managed by government agencies, fed in real time by instruments installed in the field.

4. Conclusions

This work conducted a scoping review that presents a study on the effects of incorporating new technologies for monitoring natural slopes. The process was characterized based on publications carried out between 2001-2023 on the subject.

The conclusions can be summarized as follows:

- The use of new technologies applied for predicting, mapping or continuous monitoring slopes shows a strong growth trend, despite the visible decrease in the number of post-pandemic publications.
- The topic grew slowly between 2001 and 2008, with a significant increase between 2008 and 2010, when the number of publications almost quadrupled. As of 2015, the theme again showed a sharp growth trend, with emphasis on the period between 2019 and 2021, with coincided with the Covid-19 pandemic. During this period, publications surpassed the first hundred and doubled in two years.
- China and Italy lead the number of publications on the subject. Until 2018, the two countries were close in the number of publications. From then on, China assumed the absolute leadership of annual individual publications. India, United States, and Taiwan follow as the countries that published the on the subject.
- The journals that have published the most on the subject are linked to geology or sensors and applied technologies.
- It was found that the most recurrent instruments used are satellite imagery or radar and on-board technologies, associated with GIS tools. Instruments for localized use, such as inertial sensors and fibre optics, had their applications intensified from 2010 onwards, mainly for use in monitoring and warning systems.
- The most cited remote sensing, photogrammetry or geodesic tools were: Sentinel-1, SAR, InSAR, DInSAR, GB-InSAR, UAV, LiDAR, GPS.
- It was observed that Machine Learning and Deep Learning algorithms that work with supervised learning were preferred over unsupervised learning.
- The main Artificial Intelligence tools that are being used are: Support Vector Machine, Artificial Neural Network and Random Forest.
- The digital sensors have been incorporated into Early Warning Systems (EWS), composing the Wireless Sensor Networks. Among the most usual sensors, were cited: accelerometer, barometer, gyroscope, soil moisture, geophone, temperature/humidity, optical fibre and strain gauge.
- There is no doubt that the digital technologies driven by the Digital Transformation are already a reality in slope geotechnics, presenting themselves as a present solution and confirming a strong trend towards future consolidation. Studies involving these and new tools should be encouraged in our researchers' centers and the already known use should be improved for possible large-scale applications, favoring the sectors, security, and regional and national economic development.

Acknowledgements

The authors would like to thank FAPESP, Cátedra Under Rail-VALE, and CAPES for the financial support. This research was funded by the Fundação de Amparo à Pesquisa do Estado de São Paulo (FAPESP), process number: 2017/50343-2.

Declaration of interest

The authors have no conflicts of interest to declare. All co-authors have observed and affirmed the contents of the paper and there is no financial interest to report.

Authors' contributions

Gabriel Raykson Matos Brasil de Araújo: conceptualization, methodology, data curation, visualization, software, writing – original draft. Alessandra Cristina Corsi: conceptualization, methodology, visualization, supervision, project administration, funding acquisition, writing – review & editing. Eduardo Soares de Macedo: conceptualization, methodology, supervision, project administration, funding acquisition. Marcos Massao

Futai: conceptualization, methodology, supervision, project administration, funding acquisition, writing – review & editing.

Data availability

The datasets generated analysed in the course of the current study are available from the corresponding author upon request.

References

Baghbani, A., Choudhury, T., Costa, S., & Reiner, J. (2022). Application of artificial intelligence in geotechnical engineering: A state-of-the-art review. *Earth-Science Reviews*, 228, 103991. http://dx.doi.org/10.1016/j.earscirev.2022.103991.

Bagwari, S., Gehlot, A., Singh, R., Priyadarshi, N., & Khan, B. (2022). LoRa based metrics evaluation for real-time landslide monitoring on IoT platform. *IEEE Access: Practical Innovations, Open Solutions*, 10, 46392-46407. http://dx.doi.org/10.1109/ACCESS.2022.3169797.

Bellini, P., Nesi, P., & Pantaleo, G. (2022). IoT-Enabled smart cities: a review of concepts, frameworks and key technologies. *Applied Sciences (Basel, Switzerland)*, 12(3), 1607. http://dx.doi.org/10.3390/app12031607.

Bragagnolo, L., Da Silva, R.V., & Grzybowski, J.M.V. (2020). Landslide susceptibility mapping with r.landslide: A free open-source GIS-integrated tool based on Artificial Neural Networks. *Environmental Modelling & Software*, 123, 104565. http://dx.doi.org/10.1016/j.envsoft.2019.104565.

Catani, F. (2021). Landslide detection by deep learning of non-nadiral and crowdsourced optical image. *Landslides*, 18, 1025-1044. http://dx.doi.org/10.1007/s10346-020-01513-4.

Collini, E., Ipsaro Palesi, L.A., Nesi, P., Pantaleo, G., Nocentini, N., & Rosi, A. (2022). Predicting and understanding landslide events with explainable AI. *IEEE Access: Practical Innovations, Open Solutions*, 10, 31175-31189. http://dx.doi.org/10.1109/ACCESS.2022.3158328.

ElMoulat, M.E., Debauche, O., Mahmoudi, S., Brahim, L.A., Manneback, P., & Lebeau, F. (2018). Monitoring system using internet of things for potential landslides. *Procedia Computer Science*, 134, 26-34. http://dx.doi.org/10.1016/j.procs.2018.07.140.

Frank, A.G., Dalenogare, L.S., & Ayala, N.F. (2019). Industry 4.0 technologies: implementation patterns in manufacturing companies. *International Journal of Production Economics*, 210, 15-26. http://dx.doi.org/10.1016/j.ijpe.2019.01.004.

Giogetti, A., Lucchi, M., Tavelli, E., Barla, M., Gigli, G., Casagli, N., Chiani, M., & Dardari, D. (2016). A robust wireless sensor network for landslide risk analysis: system design, deployment, and field testing. *IEEE Sensors Journal*, 16(16), 6374-6386.

Giri, P., Ng, K., & Phillips, W. (2022). Monitoring soil slide-flow using wireless sensor network-inertial measurement unit system. *Geotechnical and Geological Engineering*, 40, 367-381. http://dx.doi.org/10.1007/s10706-021-01905-w.

Huang, F., Zhang, J., Zhou, C., Wang, Y., Huang, J., & Zhu, L. (2020). A deep learning algorithm using a fully connected sparse autoencoder neural network for landslide susceptibility prediction. *Landslides*, 17, 217-229. http://dx.doi.org/10.1007/s10346-019-01274-9.

Instituto Geológico – IG. (2009). *Desastres naturais: conhecer para prevenir*. IG.

Kong, V.W.W., Kwan, J.S.H., & Pun, W.K. (2020). Hong Kong's landslip warning system – 40 years of progress. *Landslides*, 17, 1453-1463. http://dx.doi.org/10.1007/s10346-020-01379-6.

Lau, Y.M., Wang, K.L., Wang, Y.H., Yiu, W.H., Ooi, G.H., Tan, P.S., Wu, J., Leung, M.L., Lui, H.L., & Chen, C.W. (2023). Monitoring of rainfall-induced landslides at Songmao and Lushan, Taiwan, using IoT and big data-based monitoring system. *Landslides*, 20(2), 271-296.

Marino, P., Quintero, D.C.R., Santonastaso, G.F., & Greco, R. (2023). Prototype of an IoT-based low-cost sensor network for the hydrological monitoring of landslide-prone areas. *Sensors (Basel)*, 23(4), 2299. http://dx.doi.org/10.3390/s23042299.

Ministério das Cidades, Instituto de Pesquisas Tecnológicas – MCID/IPT (2007). *Mapeamento de riscos em encostas e margens de rios.* MCID/IPT.

Mei, G., Xu, N., Qin, J., Wang, B., & Qi, P. (2020). A survey of internet of things (iot) for geohazard prevention: Applications, technologies and challenges. *IEEE Internet of Things Journal*, 7(5), 4371-4386. http://dx.doi.org/10.1109/JIOT.2019.2952593.

Nambisan, S., Wright, M., & Feldman, M. (2019). The digital transformation of innovation and entrepreneurship: Progress, challenges and key themes. *Research Policy*, 48(8), 103773. http://dx.doi.org/10.1016/j.respol.2019.03.018.

Otero, M.D., Abreu, A.E.S., Askarinejad, A., Guimarães, M.P.P., Macedo, E.S., Corsi, A.C., & Almeida, R.Z.H. (2022). Use of low-cost accelerometers for landslides monitoring: results from a flume experiment. *Soils and Rocks*, 45(3), 1-10. http://dx.doi.org/10.28927/SR.2022.078621.

Rodrigues, S.G., Silva, M.M., & Alencar, M.H. (2021). A proposal for an approach to mapping susceptibility to landslides using natural language processing and machine learning. *Landslides*, 18, 2515-2529. http://dx.doi.org/10.1007/s10346-021-01643-3.

Ruzza, G., Guerriero, L., Revellino, P., & Guadagno, F.M. (2020). A multi-module fixed inclinometer for continuous monitoring of landslides: Design, development, and laboratory testing. *Sensors (Basel)*, 20(11), 3318. http://dx.doi.org/10.3390/s20113318.

Santos, A.S., Corsi, A.C., Teixeira, I.C., Gava, V.L., Falcetta, F.A.M., Macedo, E.S., & Braghetto, K.R. (2020). Brazilian natural disasters integrated into cyber-physical systems: computational challenges for landslides and floods in urban ecosystems. In *2020 IEEE International Smart Cities Conference* (1–8). IEE. https://doi.org/10.1109/ISC251055.2020.9239011

Sharif, R.A., & Pokharel, S. (2022). Smart city dimensions and associated risks: review of literature. *Sustainable Cities and Society*, 77, 103542. http://dx.doi.org/10.1016/j.scs.2021.103542.

Sreelakshmi, S., Vinod Chandra, S.S., & Shaji, E. (2022). Landslide identification using machine learning techniques: Review, motivation, and future prospects. *Earth Science Informatics*, 15, 2063-2090. http://dx.doi.org/10.1007/s12145-022-00889-2.

Tehrani, F.S., Calvello, M., Liu, Z., Zhang, L., & Lacasse, S. (2022). Machine learning and landslide studies: recent advances and applications. *Natural Hazards*, 114, 1197-1245. http://dx.doi.org/10.1007/s11069-022-05423-7.

The International Disaster Database – EM-DAT. (2023). *Inventorying hazards & disasters worldwide since 1988*. Retrieved in February 1, 2023, from www.emdat.be.

Thirugnanam, H., Uhlemann, S., Reghunadh, R., Ramesh, M.V., & Rangan, V.P. (2022). Review of landslide monitoring techniques with IoT integration opportunities. *IEEE Journal of Selected Topics in Applied Earth Observations and Remote Sensing*, 15, 5317-5338. http://dx.doi.org/10.1109/JSTARS.2022.3183684.

Tortorella, G.L., Vergara, A., & Mc, (2020). Organizational learning paths based upon industry 4.0 adoption: an empirical study with Brazilian manufacturers. *International Journal of Production Economics*, 219, 284-294. http://dx.doi.org/10.1016/j.ijpe.2019.06.023

United Nations International Strategy for Disaster Reduction – UNISDR. (2015). *Sendai framework for disaster risk reduction 2015-2030*. UNISDR.

United Nations Office for Disaster Risk Reduction – UNDRR. (2019). *Global assessment report on disaster risk reduction*. UNDRR.

Vial, G. (2019). Understanding digital transformation: A review and a research agenda. *The Journal of Strategic Information Systems*, 28(2), 118-144. http://dx.doi.org/10.1016/j.jsis.2019.01.003.

Wang, Y., Tang, H., Wen, T., & Ma, J. (2019). A hybrid intelligent approach for constructing landslide displacement prediction intervals. *Applied Soft Computing*, 81, 105506. http://dx.doi.org/10.1016/j.asoc.2019.105506.

Soils and Rocks

An International Journal of Geotechnical and Geoenvironmental Engineering

www.soilsandrocks.com

ISSN 1980-9743
ISSN-e 2675-5475

Applicability of the InSAR technique for slope monitoring

Roberto Quental Coutinho[1#], Jailson Silva Alves[1], Hanna Barreto de Araújo Falcão Moreira[1], Júlia Isabel Pontes[2], Wilson Ramos Aragão Júnior[1]

Review Article

Keywords
Remote sensing
Synthetic Aperture Radar
Interferometry
Geotechnical monitoring

Abstract

Interferometry is a technique that can be applied to SAR (Synthetic Aperture Radar) images that allow obtaining Digital Elevation Models, displacement measurements and assistance for monitoring large areas and/or engineering constructions. The objective of this paper is to present aspects related to the technique of Interferometry SAR (InSAR) applied to the monitoring of slopes. To do so, a systematic bibliographical review was used, through research platforms in scientific collections, in order to highlight the functioning and method of operation of InSAR. Besides that, the practical experience of the authors contributed to a critical analysis of the remote sensing technique addressed. The results show theoretical aspects related to the operation of SARs on board satellites, highlighting their characteristics, orbital systems, types of imaging geometry, as well as the principles of interferometric processing of SAR images. Practical applications demonstrate the potential of InSAR with an emphasis on slope monitoring, highlighting its ability to acquire topographic information on a millimeter scale, monitoring the long-term temporal evolution of displacements, the possibility of composing a monitoring system allowing directing the implementation of other instruments for evaluating the in situ conditions and some limitations regarding the time interval (satellite revisit time) for the acquisition of the displacement data.

1. Introduction

Extreme events and disasters that occur due to dynamics on the Earth's surface mostly affect the population, especially those who are in a vulnerable situation. Investigating, preventing and mitigating these events/disasters become actions of extreme necessity. Accordingly, there has been a rapid improvement in the techniques and equipment that are used to make land measurements remotely, providing subsidy to ensure effective follow up and monitoring (Zhang et al., 2021).

Remote sensing has been used due to its ability to observe without the need for direct contact with the target to be studied (Novo, 2010). InSAR (Synthetic Aperture Radar Interferometry*)* was developed more than 25 years ago (Gabriel et al., 1989), being an active remote instrumentation technique that measures displacements of the Earth's surface with great spatial coverage and with good precision (Pu et al., 2023). The technique consists of comparing the backscatter of the radar phase at different times to recover phase variations over time and obtain displacement information. It is usually composed of a transmitting antenna and a receiving antenna (Castellazzi et al., 2017).

According to Henderson et al. (1998) interferometry is an alternative to conventional photogrammetric techniques for generating topographic maps with high resolution, having the advantage of using data obtained by SAR (Synthetic Aperture Radar), which have the ability to operate during day and night, and also under any weather condition (Wasowski & Bovenga, 2014). The increasing use of InSAR to analyze geological risks has been evidenced due to the increase of studies that are currently found in the scientific literature (Novellino et al., 2017).

Thus, this article sought to contribute to the technical literature by presenting and discussing case studies that used InSAR as a tool for monitoring displacements in geotechnical applications. The study also aimed to contribute to the understanding of the advantages and limitations of this instrumentation for collecting information that can be used in landslide risk management.

2. Materials and methods

In this paper, a systematic bibliographical review was used in order to verify scientific productions on the aspects of InSAR technology applied to slope monitoring. To define

[#]Corresponding author. E-mail address: roberto.coutinho@ufpe.br
[1]Universidade Federal de Pernambuco, Programa de Pós-graduação em Engenharia Civil, Recife, PE, Brasil.
[2]Universidade Estadual Paulista, Programa de Pós-graduação em Ciências Cartográficas, Presidente Prudente, SP, Brasil.

Submitted on June 13, 2023; Final Acceptance on October 25, 2023; Discussion open until February 28, 2024.
https://doi.org/10.28927/SR.2023.008023

the technical publications to be analyzed in the results of this research, a search was performed on research platforms considering the methodology proposed by Moher et al. (2010) known as Preferred Reporting Items for Systematic Reviews and Meta-Analyses (PRISMA), which consists of four steps: Identification, Selection, Eligibility, and Inclusion.

The identification stage constitutes the initial search for possible papers on the topic of geotechnical monitoring based on InSAR technology. The keywords in English "InSAR" and "Landslide" were applied simultaneously in the Scopus database, present in the titles, abstracts or keywords of the articles. Then, in the selection stage, the most recent publications (2018-2022) and in the final version of publication were filtered. In the third step, eligibility, those articles that were directly related to the subject of study were checked. The last step, inclusion, consisted of reading them to choose the most representative articles in relation to the objective of this paper, considering the fundamental characteristics, advantages and limitations of InSAR, in addition to the presentation of applications of the technique in monitoring slopes.

During the bibliographical research, a theoretical basis was made in order to understand the equipment, procedures and characteristics of the InSAR technology well. The supporting references allowed the conception of theoretical aspects about the study approach, highlighting the basic knowledge to understand the theme. Applications were approached in different contexts, exploring InSAR's potential for slope monitoring. It is also noteworthy that the practical experience of the authors, obtained through the development of technical projects, allowed a critical analysis of the instrumentation method presented, as well as contributions to the proposed discussion.

3. Theoretical aspects

3.1 Remote sensing with SAR

Satellites orbit Earth following solar-synchronized, near-polar paths, with an altitude ranging between 500 and 800 km above the surface. According to Intrieri et al. (2019), the combination of the Earth's rotational movement and their orbits makes satellites capable of collecting information about the same target with two acquisition geometries in opposite directions: ascending (from the South Pole towards the North Pole) and descending (from the North Pole towards the South).

A SAR technology radar operates in the microwave electromagnetic spectrum range ($\lambda = 1$-100 cm) under virtually any meteorological and lighting condition (Hartwig, 2014). SAR has its own light source, regardless of daylight and weather conditions, and can pass through clouds, smoke and haze.

SAR imaging consists of a radar installed on a platform, which can used on land mobile platforms (Bozzano et al., 2011; Nader, 2013; Woods et al., 2020), in aircraft such as airplanes, helicopters and drones (Moreira et al., 2019) and from polar orbit satellites, which is discussed in this study. In the orbital configuration there is a wide variety of options for resolution, coverage and acquisition angles. The temporal density of any InSAR-based monitoring is limited by the satellite's repeated trajectory, which normally varies between 45 and 6 days, depending on its altitude and orbital configuration (Castellazzi et al., 2017).

Orbital systems (satellites) follow synchronous orbits and use electromagnetic waves in different bands, the most common being X ($\lambda \sim 3$ cm), C ($\lambda \sim 6$ cm), and L ($\lambda \sim 23$ cm) (Paradella et al., 2021). In addition to spatial resolution (band type), there are several orbital systems that allow different temporal acquisitions, known as revisit times, which is an important characteristic, as it indicates the time required for the satellite to pass over the same area performing the imaging.

According to Nader (2013) the operation sequence of an imaging radar consists of (1) the antenna transmits a pulse of radiation towards the ground; (2) when the pulse hits the ground it spreads out in all directions; (3) part of the scattering returns towards the radar (backscattering); (4) the antenna captures the backscattered signal and records its amplitude, phase, polarization and return time; (5) the captured signals are subsequently processed, jointly, to form an image of the imaged surface.

Figure 1a shows the fundamental aspects of the imaging system, the azimuth of sight (angle formed between the direction of the flight and the aim of the antenna, in the horizontal plane), the direction in range, the direction in azimuth**,** the range in the terrain that is the sensor-target distance measured on the ground, the inclined range which is the actual sensor-target distance, the height of the platform (H); and the imaging range – swath (total width of the imaged terrain).

The geometry of a SAR is a LOS (Line of Sight) lateral view, with the lightning beam being irradiated at an angle orthogonal to the direction of trajectory of the imaging object (Figure 1a). A two-dimensional image (range x azimuth) of the imaged terrain is obtained by detecting the backscattered signal, by combining the movement of the sensor and the periodic transmission of pulses orthogonally to the satellite trajectory direction (Gama et al., 2015).

Another important aspect related to the acquisition of radar images is connected to the determination of the displacement obtained by interferometry. As the radar is sensitive only to displacements along its line of sight, the components of displacement perpendicular to this direction are not detected (N-S). In addition, the determination of vertical and horizontal displacements (L-W) can be obtained by combining measurements from both orbits (ascending and descending) (Carlà et al., 2016; Paradella et al., 2015). Figure 1b schematically shows the combination of ascending and descending LOS targets (Szucs et al., 2021).

According to Fuhrmann & Garthwaite (2019) it is possible to combine several independent InSAR analyzes if

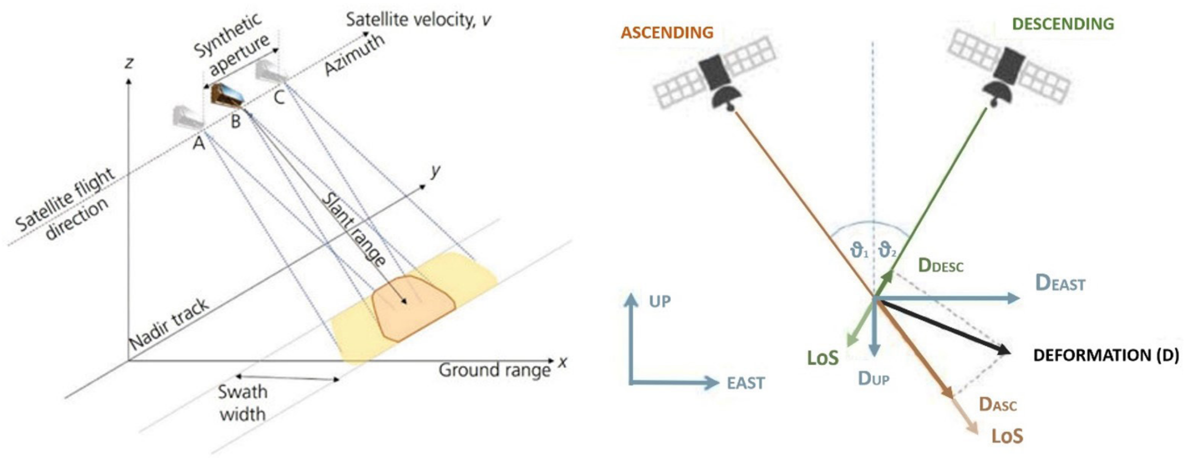

(a) (b)

Figure 1. a) image geometry of the side view radar system (Selvakumaran et al., 2022); b) schematization of the deformations in the ascending LOS and descending LOS views, representing the decomposition of the deformations in the vertical and east-west directions (Szucs et al., 2021).

we have LOS measurements available considering two factors: (i) images from the same location and (ii) in the same period of time. To meet requirement (i), it is necessary to perform spatial interpolation, since the location of selected InSAR pixels usually differs in each set of analyzed images. And to achieve requirement (ii) it is necessary to interpolate in time, considering that the acquisition dates are usually different from each type of image acquisition geometry.

3.2 InSAR

The term interferometry comes from the word interference, which makes use of the principle of superposition of waves of any kind to express some phenomenon and/or property studied. The phase difference ($\Delta\varphi$) is the fundamental information for interferometry.

The fase (φ) is a physical quantity that represents the stage of the cycle that the wave is in at a given moment relating to the distance from the emitting source. In the SAR system, each transmitted signal resembles a sinusoidal function of the type $\sin(\varphi)$. In the case of a target located at a distance r in relation to the SAR, the phase of the return signal is given by (Equation 1), the 4 term being related to the inclined distance (R) of the signal's departure and return (Ferretti et al., 2007):

$$\varphi = \frac{4\pi}{\lambda} R \tag{1}$$

A InSAR is applied to understand changes in the natural relief of the earth's crust and its elements over time (Mura, 2000; Gaboardi, 2002). To obtain an interferogram, at least one pair of SAR images of complex format (Single-Look Complex – SLC) is required to generate a third complex image, called an interferometric image, where the phase of each pixel is formed by the phase difference between the correspondent pixels in the two original images (Paradella et al., 2021).

3.2.1 Interferometric fase

SAR emits radiation that hits the scatterers on the target and returns to the sensor to generate the image. The transmission and reception of radiation on targets with different distances from the radar results in a delay that causes a phase shift between the signals. Using processing techniques, it is possible to calculate the intensity and phase of the backscattering signal for each soil resolution cell (Ulaby, 1982; ESA, 2007; Gama et al., 2013).

The phase difference between pixels at corresponding positions in two images, called an interferogram, is related to the difference in distance between the two trajectories during acquisitions; knowledge about the position of the sensor at the time of acquisitions; the length of the baseline; to the height of the target on the surface and to the wavelength of the sensor system, making it possible to reconstruct the geometry of the SAR system at the time of acquisitions (Taylor et al., 1999).

3.2.2 Interferometric coherence

Interferometric coherence measures the phase correlation between the pixels of a reference image (master) with a repetition image (slave) (Sabater et al., 2011). In an ideal situation of SAR interferometric processing, the obtained phase difference is related to the signal path difference. However, the existing noises in the process of emission and reception of waves affect the phase, interfering with the quality of the interferogram.

According to Hanssen (2001) the viability of the InSAR technique depends on the high interferometric coherence, being calculated by the module of the complex correlation coefficient (Just & Bamler, 1994; Zhou et al., 2009). The coherence image is related to the standard deviation of the interferometric phase, allowing to evaluate whether the two SAR images are suitable for interferometric processing. Thus, high coherence values demonstrate phase stability, representing a similarity in the characteristics of the backscattered energy on the surface target in the two antenna passages through the same location (Victorino, 2016).

3.2.3 Error causes

The interferogram provides information relative to phase 2π, not representing the total number of complete cycles ($2\pi n$) of the wavelength, since the interferogram may contain several 2π cycles (Hanssen, 2001). To remove this ambiguity, the phase unwrapping process is used, which consists of reconstructing the original interferometric phase, determining the absolute phase (unwrapped) of the interferogram.

Speckle is considered a multiplicative noise, inherent to the coherent nature of a SAR image, which reduces the accuracy of the phase shift and can appear as errors in the interferogram (Goldstein et al., 1988).

The loss of coherence between SAR images of a common area acquired at different times can be attributed to three main factors (Nievinski, 2004; Victorino, 2016):

- Temporal Decorrelation: causes the most severe loss of coherence, can be caused by any environmental change (vegetation movement/removal, soil erosion) between the two SAR records that form the interferogram;
- Geometric Decorrelation: indicates a significant change in the spatial baseline length between two SAR images. It causes changes in the angle of incidence and causes geometric differences, leading to decorrelation of the electromagnetic signal; and
- Atmospheric Effects: changes in the behavior of the atmosphere (humidity, pressure, temperature) due to the refractive conditions of the environment, contribute to delaying the propagation of the Radar signal.

3.3 Image processing

3.3.1 Differential Interferometry SAR (DInSAR)

Is a classic and pioneering remote sensing technique for detecting surface changes (deformation) in relation to the satellite's line-of-sight direction (Sansosti et al., 2014). Gabriel et al. (1989) were the first to apply DInSAR to localize small movements (magnitude ≤ 1 cm) of the surface elevation of large regions (50 km ranges), originating from seismic events, via Seasat SAR images. Subsequently, it became more popular in the early 1990s with the studies by Goldstein et al. (1988) and Massonnet et al. (1993).

In a simplified way, the DInSAR technique is based on the calculation, on a pixel-by-pixel basis, of the phase difference relative to, at least, a pair of SAR images, acquired at different times and satellite positions. Assuming that the reflectivity of the target and the behavior of the atmosphere are constant in the analyzed acquisitions, and that the system noise is negligible, the phase values of an interferogram are proportional to the displacement of the target between the two acquisitions.

It is important to point out that the classic DInSAR technique normally employs a Digital Elevation Model (DEM) of good accuracy so that a phase corresponding to the DEM is simulated in the acquisition geometry of the SAR sensor.

Errors induced by atmospheric phase components, residual phase due to orbit errors, and system noise and speckle are disregarded in the DInSAR technique, as a statistical analysis of a temporal series of images is needed to understand these phase components (Paradella et al., 2021). Due to this, the application of DInSAR is limited to detection of deformation in the centimeter to metric order, being recommended to analyze significant surface variations.

3.3.2 Advanced SAR differential interferometry (A-DInSAR)

From the limitations of the DInSAR technique, a series of techniques were developed that use the processing of several SAR acquisitions for the detection and construction of time series of signals with backscattering similar to that of punctual targets, improving accuracy, range coverage and the ability to detect temporal changes of surface deformation phenomena.

These techniques are part of the group named as Advanced Differential SAR Interferometry (A-DInSAR), and can be highlighted: Persistent Scatter Interferometry SAR (PSInSAR) – Ferretti et al. (2000) and Ferretti et al. (2001); Small Baseline Subset (SBAS) – Berardino et al. (2002); and SqueeSAR Technology – Ferretti et al. (2011).

A-DInSAR make use of multi-scenes, at least 15, making it possible to filter out undesirable phase components (decorrelation) and to model the monitoring of surface deformation phenomena with a precision of centimeters to millimeters, using, for the most part, sensors in the bands C and X (Macedo et al., 2011; Gama et al., 2013). The Chart 1 shows the main characteristics of each processing technique and summarizes relevant aspects (Gama et al., 2013).

4. Revelant aspects of InSAR technology

4.1 Advantages

As main advantages of InSAR we can mention the coverage of large areas (images of 250 km by 250 km, in the case of the Sentinel-1A/B satellite, of the European Space Agency); regular image acquisition, that is, high temporal resolution and long-term monitoring; operation under any atmospheric conditions, without the need for sunlight (unlike optical sensors) and allowing to observe most of the structures visible in this image (Patrício, 2018; Lin, 2022).

Chart 1. Comparative between the main InSAR techniques (Gama et al., 2013).

Technique	Main Characteristics
DInSAR	Interferometry with DEM removed; Qualitative information, distributed on soil deformation; Severely affected by atmospheric and noise effects; It does not predict any time series.
PSInSAR	Exploits stable ground targets – Permanent Scatterers (PS); Estimates atmospheric effects and their removal; Provides a time series; It does not provide measurements of the homogeneous distributed scatterers (DS); It needs at least 20 images.
SqueeSAR	Exploits stable ground targets – PS; Provides DS measures; Estimates atmospheric effects and their removal; Provides a time series; It needs at least 20 imagens.
SBAS	Exploits stable ground targets – PS; Estimates atmospheric effects and their removal; Provides a time series; Does not provide DS measures; It needs at least 8 images.

In addition, the possibility of InSAR measuring past displacements, through historical SAR images, allows the performance of studies of surface variations that may not be available through other data sources (Souza, 2022). The space-time capacity of the InSAR data has a larger field of observation, which allows better interpretation of the displacements and areas with different levels of criticality, helping in the implementation of other instruments, in the definition of the best position and in the collaboration of the improvement of the follow-up of the behavior of the region studied (Intrieri & Gigli, 2016).

Allied to these characteristics, the diagnostic analysis obtained through the spatial observables of InSAR data and information from other instruments of a punctual nature, makes decision-making more assertive. As the composition of a monitoring program, in principle, combines different information, such as rainfall data, surface and subsurface displacements, the possibility of integrating this information allows significant gains in understanding the evolution and mechanisms of action of the object of study (McCormack et al., 2011).

New processing techniques have allowed better accuracy of InSAR data. A-DInSAR techniques such as PSInSAR and SBAS are used to monitor surface deformation with an accuracy of centimeters or subcentimeters when using sensors in the C and X band, and accuracy of a few centimeters with sensors in the L band (Gama et al., 2013; Du et al., 2022).

4.2 Limitations

Due to the operating characteristics of the InSAR technology, some limitations are inherent to the system. The operating method of orbital platforms where the image acquisition radars are on board, operate according to predefined orbits. Thus, each satellite mission has a different revisit time. Due to this time, which can take days, monitoring sensitive areas such as unstable slopes, dams and mining environments make it impossible to monitor in real time and create alert systems based only on InSAR data. In addition, the time required to process the SAR images and make the displacement data available directly impacts the observational capacity of the studied phenomena in a monitoring program (Höser, 2018).

Another important factor concerns the aspects related to the operation of the satellites, as the orbits have a polarized nature, it is possible to capture displacements that occur in the east-west direction. However, ground displacements oriented in the north-south direction cannot be perceived in the satellite image direction and, therefore, InSAR is not able to detect them (McCormack et al., 2011).

Factors associated with image acquisition, for example, temporal and geometric miscorrelation, result in loss of coherence and accuracy of the results (Antunes, 2015). Temporal decorrelation has a great impact on interferometric measurements in areas of vegetation or in areas composed of targets whose electrical properties change over time. Also, variations in reflectivity due to the angle of incidence (geometric decorrelation) restrict the number of pairs suitable for interferometric use (Negrão et al., 2017).

5 Applications

Interferometry makes it possible to explore aspects related to the geometry of the relief, such as DEM, displacement measurements and monitoring of large areas and/or engineering constructions. Among the applications some stand out, like the monitoring of slopes (natural slopes, mining slopes, road slopes), land subsidence, constructions such as dams, bridges and highways. In this article, four cases of InSAR applications with emphasis on slope monitoring were analyzed. The review of these examples allows an approach to the characteristics of SAR interferometry, contributing to the discussion of the topic of this article.

5.1 Unoccupied natural slope - Carlà et al. (2019)

The article by Carlà et al. (2019) shows the monitoring of an alpine slope in Bosmatto, alp region in northwest Italy, which suffered a sudden movement reactivation on October 15, 2000, after intense and prolonged rain. Monitoring included InSAR acquisitions from the Sentinel-1 satellite constellation (in the ascending and descending orbits), information from GBInSAR (Ground-Based InSAR) and readings from two GNSS stations (Global Navigation Satellite System) for continuous monitoring and five GNSS stations for campaign measurements (manually operated).

About the analyzed area, the satellite constellation operating in C-band Sentinel-1 acquired 130 IW (wide-band interferometric) scenes in descending orbit, as well as another 130 IW scenes in ascending orbit, between October 10, 2014 and February 22, 2018. InSAR products, with a spatial resolution of 4 × 14 m, were processed using the SqueeSAR algorithm.

As a result, the authors stated that the acquisition of images in the descending orbit presented more satisfactory results than in the ascending orbit, this happened because the movement of the slope studied occurs predominantly in the direction parallel to the displacement of the satellite.

Depending on the ascending and descending orbits, it is possible to decompose the movement into vertical and horizontal. In this case it was calculated the annual velocity measured in both directions. The landslide has comparable values of maximum vertical and east-west velocity (where negative east-west velocity means westward movement), varying from 20 mm/year to 38.5 mm/year in the southeast sector of instability.

Regarding GBInSAR, the results presented were not consistent with those obtained by GNSS and InSAR, which suggests that there was some bias in the acquisition of information. Since it is an alpine slope, subjected to the presence of snow in its different phases, the results showed a sensitivity of GBInSAR to the detection of snow movements, which are not representative of the slope.

The points obtained from the decomposition of the satellites' ascending and descending InSAR datasets were compared with the GNSS measurements, showing remarkably consistent results, especially with regard to the movements of the vertical component. As expected, there are discrepancies between the velocities in the East-West direction of InSAR and the horizontal velocities of the GNSS stations, due to the absence of the North-South component in InSAR.

Carlà et al. (2019) highlighted the importance of GNSS monitoring and conventional techniques, such as topography, to accurately define slope displacements, even if in a rare manner, especially for movements with predominant North-South direction. In the case of alpine slopes, the authors stated that these techniques are relevant for monitoring during the winter months, when interferometric images may show loss of coherence due to the presence of snowe.

Through the better spatial coverage and measurement accuracy, the InSAR satellite technique could therefore be essential for improving the monitoring of landslides similar to those of the Bosmatto Alpines. The authors concluded that the GNSS and InSAR datasets should be used together, overcoming individual limitations, given the different characteristics and acquisition modes.

5.2 Open pit mine slope - Intrieri et al. (2019)

The study deals with the use of InSAR data to show the potential of new generations of satellites in detecting instability limits and predicting failure times in open pit mines. To do this, an analysis was performed using interferometry with C-band SAR images acquired by the Sentinel satellite constellation (revisit time of 6 days) for the period from March 2, 2016 to November 21, 2016, considering the acquisition of ascending (47 images) and descending (49 images) geometry images (Intrieri et al., 2019).

Intrieri et al. (2019) point out that the analysis of the displacement data was based on the respective absolute values, trends, acquisition geometry and spatialization of the data, as well as the geomorphology related to the slope. In the study, the authors also highlight the data analysis according to the inverse velocity method, based on the accelerated creep theory. In this method, it is possible to establish the failure time as the intersection between the inverse of the velocity and the time axis, considering that as the velocity increases and, theoretically, tends to infinity at the moment of collapse, its inverse will tend to zero.

The annual velocity result obtained for the area obtained from the images in ascending orbit show annual velocity ranging from -365 to -100 mm/year, indicative of the zone of higher displacements. According to the authors, in this area, the accelerated creep behavior started in the central portion of the landslide and propagated until the occurrence of the collapse.

According to the authors, the results of the displacement readings obtained over time show a slight linear trend with values close to 34.5 mm of displacement from February 19, 2016 to October 10, 2016. Then, the data presents a accelerated behavior that reaches a total displacement of 110.2 mm on November 15, 2016, the last acquisition before the failure recorded on November 17, 2016. In the analysis, the behavior of the slowed velocity (mm/day) it is possible to identify a change in the behavior pattern of displacement data from October 10, although the reading interval did not allow systematic monitoring of the evolution of displacements in the vicinity of the rupture.

Intrieri et al. (2019) highlight that the linear adjustment formed by the inverse velocity values shows an intersection with the date axis (collapse) around November 26, 2016 (after the collapse). In similar way, the authors highlight that if the last measurement were discarded, the linear adjustment would be better and the predicted failure date would be November 16, 2016, one day before the actual failure. In this sense, the authors draw attention to the fact that even with different adjustments, the analysis clearly identified the ongoing failure process.

Intrieri et al. (2019) concluded that InSAR is effective for monitoring unstable areas, targeting areas where equipment for in loco monitoring should be installed, and reconstructing the geometry of landslide areas surfaces. However, it should be noted that the satellite revisit time may not be enough to observe the beginning of displacement acceleration, compromising the need for quick responses within the framework of an early warning system.

5.3 Natural occupied slope - Ciampalini et al. (2021)

In this case, MT-InSAR (multi-temporal InSAR data) were used to evaluate the displacements that occurred in an area of rugged relief (occupied natural hillside) located in the north-western part of the region of Tuscany (central Italy) between 1992 and 2020 Data from the ERS 1/2 (from 1992 to 2000) satellites of the C band, Envisat (from 2003 to 2010) and COSMO-SkyMed (CSK) satellites of the X band from 2011 to 2014 were used to analyze the conditions of the long displacement term, aiming to identify the best location for the installation of geotechnical instruments (extensometers and inclinometers) (Ciampalini et al., 2021). The authors also used satellite images Sentinel-1A (from 2016 to 2017) and Sentinel-1B (from 2017 to 2020), in a combined analysis, between SAR data and displacements acquired by geotechnical sensors.

The results of the CSK satellite images (2010-2014) were compared with a inventory areas of landslides that occurred over time. The temporal analysis revealed that between 2010 and 2014 there was an increase in the maximum displacement rate with values of around 20.3 mm/year and an average rate of 6.4 mm/year. The highest displacement rates were measured in the southwest part of the village, where seven extensometers and one inclinometer were installed in April 2016.

MT-InSAR data were compared with deformation recorded by geotechnical instruments. Regarding the spatial distribution, there is an agreement between the points of faster movement of the descending data from Sentinel-1 and the movement points registered by the geotechnical sensors, while the extensometers that present stability are surrounded by stable or extremely slow-moving interferometric points.

Sentinel-1 data were compared with deformations recorded by geotechnical monitoring instruments, as well as with rainfall records obtained between 2016 and 2020. The results obtained demonstrate that all geotechnical sensors correctly identified deformation trends and periods of landslide acceleration. The inclinometer recorded a sliding surface at a depth of 23 meters, with a maximum displacement of up to 20 mm between 2017 and 2020, and a second sliding surface at a depth of 5 meters from the ground, resulting in an accumulated surface displacement of about 36 mm during the same period.

According to Ciampalini et al. (2021), the changes observed in the inclinometer confirm that prolonged rainfall increases the displacement rate, a behavior that is recorded by all sensors in the monitoring system.

The authors point out that the spatial and temporal distribution of deformations shows good agreement between both monitoring systems, with a satisfactory correlation. The comparative analysis between deformation and precipitation data suggests that the accelerations identified in the landslide deformation rate can be attributed to rainfalls.

Ciampalini et al. (2021) concluded that InSAR data can be used to select the ideal location for installing in situ sensors, especially when considering the spatial distribution of slope deformations over long periods of time. As they can also be used to confirm and validate measurements of geotechnical instrumentation data. In cases where validation is possible, and there is no need to install warning systems, it is possible to monitor the evolution of deformations, even in the absence of in situ sensors.

5.4 Coastal region slope - Traglia et al. (2018)

The area under study is a volcanic slope in a coastal region, with part of it in an underwater environment. Located in the Aeolian archipelago, it belongs to a large volcanic complex, on the southern coast of Italy. The study employs InSAR for long-term assessment of submarine slope stability in volcanic systems. For this purpose, SAR images were used considering the CSK constellation (84 images, X band) between February 2010 and December 2014 and the Sentinel-1A constellation (47 images, band C) between February 2015 and October 2016.

The authors analyzed a section of the northwest side of the slope, where scars from landslides can be seen up to 700 m below sea level. To characterize the bottom morphology of the study area, Traglia et al. (2018) performed a bathymetric survey with a sonar-type device at depths between -20 and -500 m, in order to obtain a DEM of the underwater part of the area. Since it is a volcanic environment, thermographic surveys were also performed using a thermographic camera, with the aim of analyzing the patterns of thermal behavior and fracturing of the lava delta.

Traglia et al. (2018) highlighted that thermography data indicated rapid cooling since the last eruption and no evidence of fracturing processes related to delta instability. Regarding bathymetry, the authors point out that the lava delta has a difference in level >40º and a rough surface. According to the authors, the InSAR data identified a stable area in the northern portion of the lava delta and instability in the southern portion of the area. The displacement results of the CSK data show the evolution of the displacements, with a pattern of the unstable portion of the order of -200 mm between 2010 and 2014 and Sentinel-1A data with displacement values greater than -200 mm between 2015 and 2016, with a total value towards the end of the period of more than 400 mm of displacement.

The authors also selected four points (CSK and Sentinel-1A data) within the area of the lava delta, in order to show the behavior of the displacement in the period between February 22, 2010 and October 15, 2016. The results of the displacements from the CSK data (February 22, 2010 to December 18, 2014) show a trend change in the final period of the series (period of explosions and occurrence of lava flows in the area), which according to the authors the highest velocity of the order of 70 mm/year.

Traglia et al. (2018) also show LOS displacement results according to Sentinel-1A data (from February 23, 2015 to October 15, 2016) for the same positions of points identified in the CSK dataset. The results show a change in displacement trends in 2016, the points positioned in the central region of the lava delta show a reduction in velocity of 180 mm/year and 70 mm/year, tending towards stability. Some results show small oscillations and their location is outside the central region os the lava delta.

For the authors, the InSAR data made it possible to identify the instability zones of the lava delta, in addition to changes in the patterns of the displacement series demonstrating a relationship with lava flows from previous eruptions, which influenced the behavior of the instability zones along the slope. In addition, the displacement time series along the study region confirmed an internal subdivision of the lava delta, which showed abrupt changes in displacement trends in the unstable portion of the slope.

6 Final considerations

This article has partial results of a master's thesis research, developed by the Geotechnical Engineering Group for Slopes, Plains and Disasters (the acronym in Brazilian Portuguese is GEGEP) of the Federal University of Pernambuco (UFPE) under the supervision of the first author. Characteristics, concepts, principles, some advantages and limitations of the InSAR technique were presented, with emphasis on the potential for applications in the monitoring of slopes (natural and artificial), which can be applied to land subsidence, dams, bridges and highways. The technique has allowed a good contribution in the detection of information about the Earth's surface, such as obtaining DEM, measuring displacements and the possibility of monitoring large areas.

The time series obtained by InSAR are able to provide displacement information with good accuracy, in addition to being able to strategically direct the deployment of traditional monitoring equipment within the area of interest, making it possible to obtain an integrated monitoring network. Furthermore, the InSAR data can be checked and validated using other equipment (GNSS, total station), ensuring better assertiveness in the diagnosis of areas with the presence of movement.

However, there are limitations regarding the acquisition of information by InSAR, especially for short periods of time. Radars on board satellite platforms have a long revisit time, which does not allow for real-time observation of displacements. This condition makes it difficult to make decisions based only on InSAR information, requiring data from other equipment (inclinometers, tiltmeters, extensometers). Although, it should be noted that technology has advanced, with the emergence of new ground-based interferometric radars, which have managed to reduce the acquisition time and increase the accuracy and reliability of the technique.

Declaration of interest

The authors have no conflicts of interest to declare. All co-authors have noted and affirmed the content of the article and there is no financial interest to report.

Authors' contributions

Roberto Quental Coutinho: supervision, guidance, project management. Jailson Silva Alves: research, data analysis, writing of the manuscript. Hanna Barreto de Araújo Falcão Moreira: research, data analysis, writing of the manuscript. Júlia Isabel Pontes: research, conceptualization, writing of the manuscript. Wilson Ramos Aragão Júnior: research, conceptualization, methodology, writing of the manuscript.

Data availability

No data sets were generated in the course of the current study; therefore, data sharing is not applicable.

List of symbols

R	Inclined Distance
φ	Fase
λ	Spectrum Range

References

Antunes, D.P.G. (2015). *Estudo comparativo de diferentes metodologias para extração da altura de edifícios e de infraestruturas com recurso a imagens SAR* [Master's dissertation, University of Lisbon]. University of Lisbon's repository (in Portuguese). https://repositorio.ul.pt/handle/10451/20380.

Berardino, P., Fornaro, G., Lanari, R., & Sansosti, E. (2002). A new algorithm for surface deformation monitoring based on small baseline differential SAR interferograms. *IEEE Transactions on Geoscience and Remote Sensing*, *40*(11), 2375-2383. http://dx.doi.org/10.1109/TGRS.2002.803792.

Bozzano, F., Cipriani, I., Mazzanti, P., & Prestininzi, A. (2011). Displacement patterns of a landslide affected by human activities: insights from ground-based InSAR monitoring. *Natural Hazards*, *59*, 1377-1396. http://dx.doi.org/10.1007/s11069-011-9840-6.

Carlà, T., Raspini, F., Intrieri, E., & Casagli, N. (2016). A simple method to help determine landslide susceptibility from spaceborne InSAR data: the Montescaglio case study. *Environmental Earth Sciences*, *75*, 1492, http://dx.doi.org/10.1007/s12665-016-6308-8.

Carlà, T., Tofani, V., Lombardi, L., Raspini, F., Bianchini, S., Bertolo, D., Thuegaz, P. & Casagli, N. (2019). Combination of GNSS, satellite InSAR, and GBInSAR remote sensing monitoring to improve the understanding of a large landslide in high alpine environment. *Geomorphology*, *335*, 62-75. http://dx.doi.org/10.1016/j.geomorph.2019.03.014.

Castellazzi, P., Garfias, J., Martel, R., Brouard, C., & Rivera, A. (2017). InSAR to support sustainable urbanization over compacting aquifers: the case of Toluca Valley, Mexico. *International Journal of Applied Earth Observation and Geoinformation*, *63*, 33-34. http://dx.doi.org/10.1016/j.jag.2017.06.011.

Ciampalini, A., Farina, P., Lombardi, L., Nocentini, M., Taurino, V., Guidi, R., Pina, F., & Tavarini, D. (2021). Integration of Satellite InSAR with a wireless network of geotechnical sensor for slope monitoring in urban areas: the Pariana landslide case (Massa, Italy). *Remote Sensing*, *13*(13), 2534. http://dx.doi.org/10.3390/rs13132534.

Du, Q., Guo, G., Li, H., Gong, Y., & Wei, T. (2022). The stability analysis method of leveling datum points in mining areas of western china based on SBAS-InSAR technology. *KSCE Journal of Civil Engineering*, *26*(12), 5264-5274.

European Space Agency - ESA. (2007). *ASAR product handbook*. Retrieved in December 30, 2022, from https://earth.esa.int/pub/ESA_DOC/ENVISAT/ASAR/asar.ProductHandbook.2_2.pdf.

Ferretti, A., Ferrucci, F., Prati, C., & Rocca, F. (2000). SAR analysis of building colapse by means of the permanent scatterers technique. In *Proceedings of the IGARSS 2000. IEEE 2000 International Geoscience and Remote Sensing Symposium. Taking the Pulse of the Planet: The Role of Remote Sensing in Managing the Environment* (pp. 3219-3221). Honolulu, HI, USA. http://dx.doi.org/10.1109/IGARSS.2000.860388.

Ferretti, A., Fumagalli, A., Novali, F., Prati, C., Rocca, F., & Rucci, A. (2011). A new algorithm for processing interferometric data-stacks: SqueeSAR. *IEEE Transactions on Geoscience and Remote Sensing*, *49*(9), 3460-3470. http://dx.doi.org/10.1109/TGRS.2011.2124465.

Ferretti, A., Monti-Guarnieri, A., Prati, C., & Rocca, F. (2007). *InSAR principles: guidelines for sar interferometry processing and interpretation* (48 p.). ESA Publications.

Ferretti, A., Prati, C., & Rocca, F. (2001). Permanent scatterers in SAR interferometry. *IEEE Transactions on Geoscience and Remote Sensing*, *39*(1), 8-20. http://dx.doi.org/10.1109/36.898661.

Fuhrmann, T., & Garthwaite, M.C. (2019). Resolving three-dimensional surface motion with InSAR constraints from multi-geometry data fusion. *Remote Sensing*, *11*(3), 241. http://dx.doi.org/10.3390/rs11030241.

Gaboardi, C. (2002). *Utilização de imagem de coerência SAR para classificação do uso da terra: Floresta Nacional do Tapajós* [Master's dissertation, National Institute for Space Research]. National Institute for Space Research's repository (in Portuguese). http://urlib.net/sid.inpe.br/marciana/2003/04.10.08.52.

Gabriel, A.K., Goldstein, R.M., & Zebker, H.A. (1989). Mapping small elevation changes over large areas: differential radar interferometry. *Journal of Geophysical Research: Solid Earth*, *94*(B7), 9183-9191. http://dx.doi.org/10.1029/JB094iB07p09183.

Gama, F.F., Paradella, W.R., Mura, J.C., & Santos, A. (2013). Técnicas de interferometria radar na detecção de deformação superficial utilizando dados orbitais. In *Anais do XVI Simpósio Brasileiro de Sensoriamento Remoto* (pp. 13-18). Foz do Iguaçu.

Gama, F.F., Santos, A.R., Paradella, W.R., Mura, J.C., & Assis, L.M. (2015). Proposta de avaliação de técnicas de interferometria diferencial avançada(A-Dinsar) de dados SAR orbitais dos satélites TerraSAR-X e COSMO-Skymed no monitoramento de instabilidade de minas de ferrso a ceu aberto no Quadrilátero Ferrífero-MG. In *Anais do XVII Simpósio Brasileiro de Sensoriamento Remoto – SBSR* (1539 p). São José dos Campos: INPE.

Goldstein, R.M., Zebker, H.A., & Werner, C.L. (1988). Satellite radar interferometry: twodimensional phase unwrapping. *Radio Science*, *23*(4), 713-720. http://dx.doi.org/10.1029/RS023i004p00713.

Hanssen, R.F. (2001). *Radar interferometry: data interpretation and error analysis*. Kluwer Academic Publishers.

Hartwig, M. E. (2014) *Monitoramento de taludes de mineração por interferometria diferencial com dados Terrasar-X na Amazônia: Mina de N4W, Serra de Carajás, Pará, Brasil* [Doctoral thesis, National Institute for Space Research]. National Institute for Space Research's repository (in Portuguese). http://urlib.net/8JMKD3MGP5W34M/3G5LJSS.

Henderson, F.M., Lewis, J., & Ryerson, R.A. (1998). *Manual of remote sensing: principles and applications of imaging radar* (Vol. 2, 3. ed.). John Wiley & Sons.

Höser, T. (2018). *Analysing the Capabilities and Limitations of InSAR using Sentinel-1 data for Landslide Detection and Monitoring* [Master's dissertation]. University of Bonn.

Intrieri, E., & Gigli, G. (2016). Landslide forecasting and factors influencing predictability. *Natural Hazards and Earth System Sciences*, *16*, 2501-2510. http://dx.doi.org/10.5194/nhess-16-2501-2016.

Intrieri, E., Carlà, T., Farina, P., Bardi, F., Ketizmen, H., & Casagli, N. (2019). Satellite Interferometry as a tool for early warning and aiding decision making in an open-pit mine. *IEEE Journal of Selected Topics in Applied Earth Observations and Remote Sensing*, *12*(12), 5248-5258. http://dx.doi.org/10.1109/JSTARS.2019.2953339.

Just, D., & Bamler, R. (1994). Phase statistics of interferograms with applications to synthetic aperture radar. *Applied Optics*, *33*(20), 4361-4368. http://dx.doi.org/10.1364/AO.33.004361.

Lin, S.-Y. (2022). Urban hazards caused by ground deformation and building subsidence over fossil lake beds: a study from Taipei City. *Geomatics, Natural Hazards & Risk*, *13*(1), 2890-2910.

Macedo, K.A.C., Wimmer, C., Barreto, T.L.M., Lübeck, D., Moreira, J.R., Rabaco, L.M.L., & Oliveira, W.J. (2011). Operacionalização da interferometria diferencial (D-InSAR) para o sistema OrbiSAR – Estudo de caso realização na região de São Sebastião, SP. In *Anais do 15° Simpósio Brasileiro de Sensoriamento Remoto (SBSR)* (pp. 8207-8214). São José dos Campos: INPE. Retrieved in December 8, 2022, from http://urlib.net/3ERPFQRTRW/39UGNS8.

Massonnet, D., Rossi, M., Carmona, C., Adragna, F., Peltzer, G., Feigl, K., & Rabaute, T. (1993). The displacement field of the Landers earthquake mapped by radar interferometry. *Nature*, *364*(6433), 138-142. http://dx.doi.org/10.1038/364138a0.

McCormack, H., Thomas, A., & Solomon, I. (2011). *The capabilities and limitations of satellite InSAR and terrestrial radar interferometry*. Retrieved in January 30, 2023, from https://scholar.googleusercontent.com/scholar?q=cache:Z2Ds-wTKXjgJ:scholar.google.com/+The+capabilities+and+limitations+of+satellite+InSAR+and+terrestrial+radar+interferometry.&hl=pt-BR&as_sdt=0,5&as_vis=1.

Moher, D., Liberati, A., Tetzlaff, J., & Altman, D.G. (2010). Preferred reporting items for systematic reviews and meta-analyses: the PRISMA statement. *International Journal of Surgery*, *8*(5), 336-341. http://dx.doi.org/10.1016/j.ijsu.2010.02.007.

Moreira, L., Castro, F., Góes, J.A., Bins, L., Teruel, B., Fracarolli, J., Castro, V., Alcântara, M., Oré, G., Luebeck, D., Oliveira, L.P., Gabrielli, L., & Hernandez-Figueroa, H.E. (2019). A drone-borne multiband DInSAR: results and applications. In *Proceedings of the IEEE Radar Conference (RadarConf)* (pp. 1-6). Boston, MA, USA. http://dx.doi.org/10.1109/radar.2019.8835653.

Mura, J.C. (2000). *Geocodificação automática de imagens de radar de abertura sintética interferométrico: sistema Geo-InSAR* [Doctoral thesis, National Institute for Space Research]. National Institute for Space Research's repository (in Portuguese). http://urlib.net/sid.inpe.br/deise/2001/08.03.12.24.

Nader, A.S. (2013). *Monitoramento de taludes via radar SSR como indicador chave de desempenho geotécnico integrado às atividades primárias da cadeia de valor mineral* [Doctoral thesis, University of Sao Paulo]. University of São Paulo's repository (in Portuguese). https://teses.usp.br/teses/disponiveis/3/3134/tde-04032013-153034/pt-br.php.

Negrão, P., Gerente, J., Gama, F.F., & Mura, J.C. (2017). Interferometria diferencial com dados SAR: princípios básicos e aplicações em geociência. In *Anais do XXVII Congresso Brasileiro de Cartografia e XXVI Exposicarta* (pp. 659-663). Rio de Janeiro. Retrieved in January 30, 2023, from https://docplayer.com.br/81362348-Interferometria-diferencial-com-dados-sar-principios-basicos-e-aplicacoes-em-geociencias-resumo-abstract.html.

Nievinski, F.G. (2004). *Interferometria por Radar de Abertura Sintética (InSAR)* [Undergraduate thesis, Federal doUniversity of Rio Grande do Sul]. Federal doUniversity of Rio Grande do SulSul's repository (in Portuguese). https://lume.ufrgs.br/handle/10183/75664.

Novellino, A., Cigna, F., Brahmi, M., Sowter, A., Bateson, L., & Marsh, S. (2017). Assessing the feasibility of a national InSAR ground deformation map of great britain with sentinel-1. *Geosciences (Switzerland)*, 7(2), 19. http://dx.doi.org/10.3390/geosciences7020019.

Novo, E. M. L. M. (2010). *Sensoriamento Remoto – Princípios e Aplicações* (4. ed.). Bluncher.

Paradella, W.R., Mura, J.C., & Gama, F.F. (2021). *Monitoramento DInSAR para mineração e geotecnia: a tecnologia DInSAR orbital na mineração e geotecnia: monitoramento do espaço deformações na superfície*. Oficina de Textos.

Paradella, W.R., Mura, J.C., Gama, F.F., Santos, A.R., & Silva, G.G. (2015). Orbital Imaging Radars (SAR): trends in systems and applications. In *Proceedings of the XVII Simpósio Brasileiro de Sensoriamento RemotoBrazilian Symposium on Remote Sensing* (pp. 2506-2513). João Pessoa-PB. Retrieved in June 13, 2023, from https://www.researchgate.net/publication/280716664_Radares_Imageadores_SAR_orbitais_tendencias_em_sistemas_e_aplicacoes.

Patrício, E.G.R. (2018). *Avaliação da Tecnologia InSAR para Monitorização de Grandes Obras* [Doctoral thesis, University of Lisbon]. University of Lisbon's repository (in Portuguese). https://hdl.handle.net/10216/116691.

Pu, C., Xu, Q., Wang, X., Li, Z., Chen, W., Zhao, K., Xiu, D., & Liu, J. (2023). Refined mapping and kinematic trend assessment of potencial landslides associated with large-scale land creation projects with multitemporal InSAR. *International Journal of Applied Earth Observation and*

Geoinformation, *118*, 103266. http://dx.doi.org/10.1016/j.jag.2023.103266.

Sabater, J.R., Duro, J., Arnaud, A., Albiol, D., & Koudogbo, F.N. (2011). Comparative analyses of multi-frequency PSI ground deformation measurements. In *Proceedings of the International Society for Optical Engineering – SPIE* (Vol. 8179, pp. 381-387). Prague: SPIE.

Sansosti, E., Berardino, P., Bonano, M., Calò, F., Castaldo, R., Casu, F., Manunta, M., Manzo, M., Pepe, A., Solaro, G., Tizzani, P., Zeni, G., & Lanari, R. (2014). How second generation SAR systems are impacting the analysis of ground deformation. *International Journal of Applied Earth Observation and Geoinformation*, *28*, 1-11.

Selvakumaran, S., Sadeghi, Z., Collings, M., Rossi, C., Wright, T., & Hooper, A. (2022). Comparison of in situ and interferometric synthetic aperture radar monitoring to assess bridge thermal expansion. *Proceedings of the Institution of Civil Engineers – Smart Infrastructure and Construction*, *175*(2), 73-91. https://doi.org/10.1680/jsmic.21.00008.

Souza, W.O. (2022). *InSAR para avaliação de subsidência do solo devido a ações antrópicas sobre os recursos hídricos subterrâneos e sobre o solo na planície do Recife, Brasil* [Doctoral thesis, Federal deUniversity of Pernambuco]. University of Pernambuco's repository (in Portuguese). https://repositorio.ufpe.br/handle/123456789/46399.

Szucs, E., Gonczy, S., Bozsó, I., Bányai, L., Szakacs, A., Szárnya, C., & Wesztergom, V. (2021). Evolution of surface deformation related to salt-extraction-caused sinkholes in Solotvyno (Ukraine) revealed by Sentinel-1 radar interferometry. *Natural Hazards and Earth System Sciences*, *21*, 977-993. http://dx.doi.org/10.5194/nhess-21-977-2021.

Taylor, S.C., Armour, B., Hughes, W.H., Kult, A., & Nizman, C. (1999). Operational Interferometric SAR data proessing for RADARSAT using distributed computing environment. In *Proceedings of the IV International Conference on GeoComputation Fredericksburg, VA, USA*. Nepean.

Traglia, F., Nicola, T., Lorenzo, S., Ciampalini, A., Frodella, W., Steri, D., Allotta, B., Rindi, A., Marini, L., Monni, N., Galardi, E., & Casagli, N. (2018). Lava delta deformation as a proxy for submarine slope instability. *Earth and Planetary Science Letters*, *488*, 46-58. http://dx.doi.org/10.1016/j.epsl.2018.01.038.

Ulaby, F.T. (1982). Radar signature of terrain: useful monitors of renewable resources. *Proceedings of the IEEE*, *70*(12), 1410-1428.

Victorino, H.S. (2016). *Análise de deformação em pilhas de disposição de estéril (NWI, W e SIV) no Complexo Minerador de Carajás com uso de dados Stripmap do Satélite TerraSAR-X* [Master's dissertation, National Institute for Space Research]. National Institute for Space Research's repository (in Portuguese). http://urlib.net/8JMKD3MGP3W34P/3LAKPKL

Wasowski, J., & Bovenga, F. (2014). Investigating landslides and unstable slopes with satellite Multi Temporal Interferometry: Current issues and future perspectives. *Engineering Geology*, *174*, 103-138. https://doi.org/10.1016/j.enggeo.2014.03.003.

Woods, A., Hendry, M.T., Macciotta, R., Stewart, T., & Marsh, J. (2020). GB-InSAR monitoring of vegetated and snow-covered slopes in remote mountainous environments. *Landslides*, *17*, 1713-1726. http://dx.doi.org/10.1007/s10346-020-01408-4.

Zhang, L., Dai, K., Deng, J., Ge, D., Liang, R., Li, W., & Xu, Q. (2021). Identifying potential landslides by stacking-insar in southwestern china and its performance comparison with sbas-insar. *Remote Sensing*, *13*(18), 3662. http://dx.doi.org/10.3390/rs13183662.

Zhou, X., Chang, N.B., & Li, S. (2009). Applications of SAR interferometry in Earth and environment science research. *Sensors (Basel)*, *9*, 1876-1912.

The Best Solution!

***Tecnilab Portugal, S.A.** will provide you with answers to your Geotechnical engineering needs.*

Tecnilab Portugal, S.A. is a professional Geotechnical engineering company and has a lot of experience as a professional group that mainly engages in measurement engineering in dam, subway(Metro), harbor, power plant, soft ground and structure construction.

WE ARE THE DISTRIBUTOR OF PORTUGAL OF ACE INSTRUMENT CO., LTD. IN KOREA.

ACE INSTRUMENT CO., LTD. is a company that obtains worldwide reputation for supplying high precision, high reliability products in all Geotechnical instruments, data logger and in-situ test equipments. Independently developed automatic monitoring system can be used anywhere in the world, including buildings, bridges, ground and any constructions.

Data Acquisition System & Web Monitoring Program

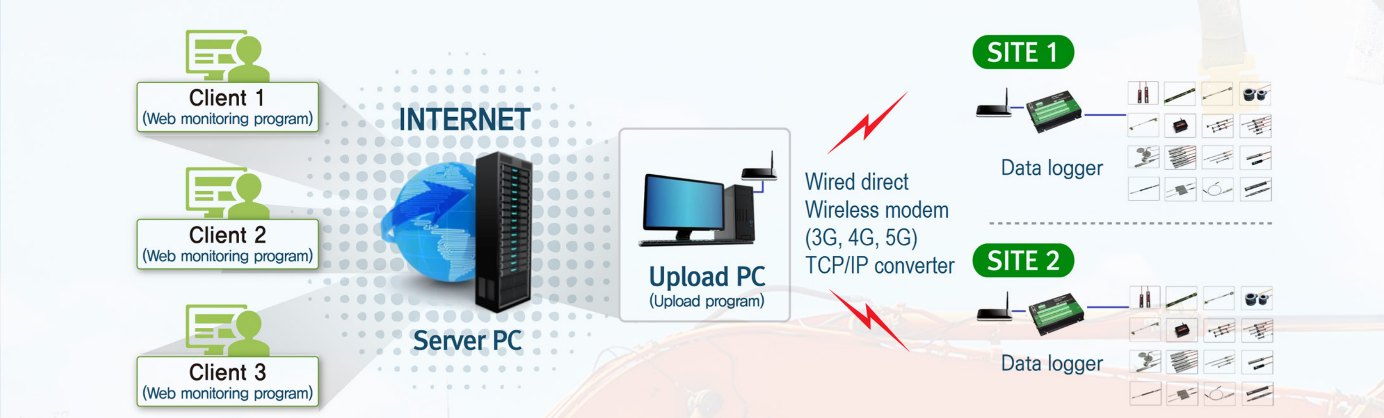

Sales company

Tecnilab Portugal, S.A.
A: Rua Gregorio Lopes, Lote 1512B 1449-041 Lisboa Portugal
T: +351 217 220 870 F: +351 217 264 550
www.tecnilab.pt

Manufacturer

ACE INSTRUMENT CO., LTD.
The first value in Geotechnical & Structural Instrumentation
A: 9, Dangjung-ro 27 beon-gil, Gunpo-si, Gyeonggi-do, Korea
T: +82 31 459 8753-7 F: +82 31 459 8758 E: acens@naver.com
www.aceinstrument.com

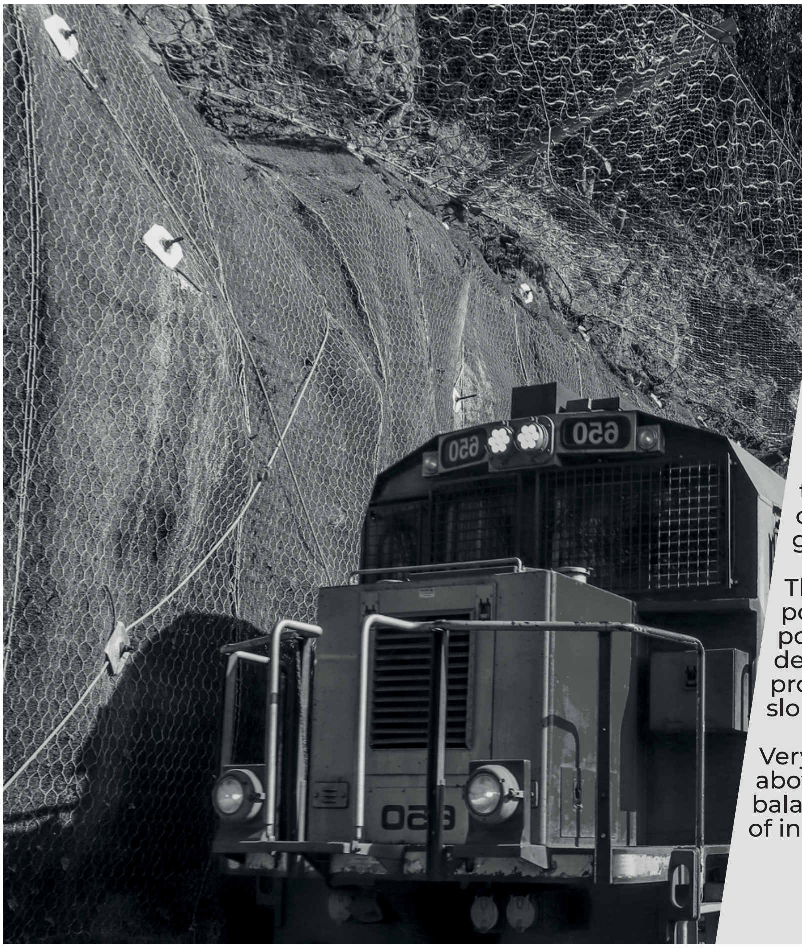


DF+
TRANSFORMATIVE ENGINEERING, MANAGEMENT, AND INNOVATION DELIVERING RESULTS
DF+ IS AN INTEGRATED ENGINEERING CONSULTING FIRM WITH OVER 25 YEARS OF EXPERIENCE IN THE SECTORS OF MINING, INFRASTRUCTURE, AGRIBUSINESS, AND INDUSTRIAL.
WE DEVELOP PROJECTS BASED ON CONSOLIDATED TECHNICAL SOLUTIONS THAT ENCOMPASS THE STATE OF THE ART IN DIGITAL ENGINEERING.
AV. BARÃO HOMEM DE MELO, 4554 - 5th floor
ESTORIL, BELO HORIZONTE/MG
+55 31 2519-1001
dfmais.eng.br
comercial@dfmais.eng.br
DF+ ENGENHARIA

Guide for Authors

Soils and Rocks is an international scientific journal published by the Brazilian Association for Soil Mechanics and Geotechnical Engineering (ABMS) and by the Portuguese Geotechnical Society (SPG). The aim of the journal is to publish original papers on all branches of Geotechnical Engineering. Each manuscript is subjected to a single-blind peer-review process. The journal's policy of screening for plagiarism includes the use of a plagiarism checker on all submitted manuscripts.

Soils and Rocks embraces the international Open Science program and is striving to meet all the recommendations. However, at this moment, the journal is not yet accepting preprints and open data, and has not adopted open peer reviews.

Soils and Rocks provides a manuscript template available at the journal's website.

1. Category of papers

Submissions are classified into one of the following categories:

Article – an extensive and conclusive dissertation about a geotechnical topic, presenting original findings.
Technical Note – presents a study of smaller scope or results of ongoing studies, comprising partial results and/or particular aspects of the investigation.
Case Study – report innovative ways to solve problems associated with design and construction of geotechnical projects. It also presents studies of the performance of existing structures.
Review Article – a summary of the State-of-the-Art or State-of-the-Practice on a particular subject or issue and represents an overview of recent developments.
Discussion – specific discussions about published papers.

Authors are responsible for selecting the correct category when submitting their manuscript. However, the manuscript category may be altered based on the recommendation of the Editorial Board. Authors are also requested to state the category of paper in their Cover Letter.

When submitting a manuscript for review, the authors should indicate the category of the manuscript, and is also understood that they:

a) assume full responsibility for the contents and accuracy of the information in the paper;
b) assure that the paper has not been previously published, and is not being submitted to any other journal for publication.

2. Paper length

Full-length manuscripts (Article, Case Study) should be between 4,000 and 8,000 words. Review articles should have up to 10,000 words. Technical Notes have a word count limit of 3,500 words. Discussions have a word count limit of 1,000 words. These word count limits exclude the title page, notation list (e.g., symbols, abbreviations), captions of tables and figures, acknowledgments and references. Each single column and double column figure or table is considered as equivalent to 150 and 300 words, respectively.

3. Scientific style

The manuscripts should be written in UK or US English, in the third person and all spelling should be checked in accordance with a major English Dictionary. The manuscript should be able to be readily understood by a Civil Engineer and avoid colloquialisms. Unless essential to the comprehension of the manuscript, direct reference to the names of persons, organizations, products or services is not allowed. Flattery or derogatory remarks about any person or organization should not be included.

The author(s) of Discussion Papers should refer to himself (herself/themselves) as the reader(s) and to the author(s) of the paper as the author(s).

The International System (SI) units must be used. The symbols are recommended to be in accordance with Lexicon in 14 Languages, ISSMFE (2013) and the ISRM List of Symbols. Use italics for single letters that denote mathematical constants, variables, and unknown quantities, either in tables or in the text.

4. Submission requirements and contents

A submission implies that the following conditions are met:

- the authors assume full responsibility for the contents and accuracy of the information presented in the paper;
- the manuscript contents have not been published previously, except as a lecture or academic thesis;
- the manuscript is not under consideration for publication elsewhere;
- the manuscript is approved by all authors;
- the manuscript is approved by the necessary authorities, when applicable, such as ethics committees and institutions that may hold intellectual property on contents presented in the manuscript;
- the authors have obtained authorization from the copyright holder for any reproduced material;
- the authors are aware that the manuscript will be subjected to plagiarism check.

The author(s) must upload two digital files of the manuscript to the Soils and Rocks submission system. The size limit for each submission file is 20 MB. The manuscript should be submitted in docx format (Word 2007 or higher) or doc format (for older Word versions). An additional PDF format file of the manuscript is also required upon submission. Currently, the journal is not accepting manuscripts prepared using LaTeX.

The following documents are required as minimum for submission:

- cover letter;
- manuscript with figures and tables embedded in the text (doc or docx format);

manuscript with figures and tables embedded in the text for revision (PDF format);
- permission for re-use of previously published material when applicable, unless the author/owner has made explicit that the image is freely available.

4.1 Cover letter

The cover letter should include: manuscript title, submission type, authorship information, statement of key findings and work novelty, and related previous publications if applicable.

4.2 Title page

The title page is the first page of the manuscript and must include:

- A concise and informative title of the paper. Avoid abbreviations, acronyms or formulae. Discussion Papers should contain the title of the paper under discussion. Only the first letter of the first word should be capitalized.
- Full name(s) of the author(s). The first name(s) should not be abbreviated. The authors are allowed to abbreviate middle name(s).
- The corresponding author should be identified by a pound sign # beside his/her and in a footnote.
- The affiliation(s) of the author(s), should follow the format: Institution, (Department), City, (State), Country.
- Affiliation address and e-mail must appear below each author's name.
- The 16-digit ORCID of the author(s) – mandatory
- Main text word count (excluding abstract and references) and the number of figures and tables

4.3 Permissions

Figures, tables or text passages previously published elsewhere may be reproduced under permission from the copyright owner(s) for both the print and online format. The authors are required to provide evidence that such permission has been granted at the moment of paper submission.

4.4 Declaration of interest

Authors are required to disclose conflicting interests that could inappropriately bias their work. For that end, a section entitled "Declaration of interest" should be included following any acknowledgments and prior to the "Authors' contributions" section. In case of the absence of conflicting interests, the authors should still include a declaration of interest.

4.5 Authors' contributions

Authors are required to include an author statement outlining their individual contributions to the paper according to the CASRAI CRediT roles (as per https://casrai.org/credit). The minimum requirements of contribution to the work for recognition of authorship are: a) Participate actively in the discussion of results; b) Review and approval of the final version of the manuscript. A section entitled "Authors' contributions" should be included after the declaration of interest section, and should be formatted with author's name and CRediT role(s), according to the example:

Samuel Zheng: conceptualization, methodology, validation. Olivia Prakash: data curation, writing - original draft preparation. Fatima Wang: investigation, validation. Kwame Bankole: supervision. Sun Qi: writing - reviewing and editing.

Do not include credit items that do not follow the Taxonomy established by CASRAI CRediT roles.

The authors' contributions section should be omitted in manuscripts that have a single author.

5. Plagiarism checking

Submitted papers are expected to contain at least 50 % new content and the remaining 50 % should not be verbatim to previously published work.

All manuscripts are screened for similarities. Currently, the Editorial Board uses the plagiarism checker Plagius (www.plagius.com) to compare submitted papers to already published works. Manuscripts will be rejected if more than 20 % of content matches previously published work, including self-plagiarism. The decision to reject will be under the Editors' discretion if the percentage is between 10 % and 20 %.

IMPORTANT OBSERVATION: Mendeley software plug-in (suggested in this guide) for MS-Word can be used to include the references in the manuscript. This plug-in uses a field code that sometimes includes automatically both title and abstract of the reference. Unfortunately, the similarity software adopted by the Journal (Plagius) recognizes the title and abstract as an actual written text by the field code of the reference and consequently increases considerably the percentage of similarity. Please do make sure to remove the abstract (if existing) inside Mendeley section where the adopted reference is included. This issue has mistakenly caused biased results in the past. The Editorial Board of the journal is now aware of this tendentious feature.

6. Formatting instructions

The text must be presented in a single column, using ISO A4 page size, left, right, top, and bottom margins of 25 mm, Times New Roman 12 font, and line spacing of 1.5. All lines and pages should be numbered.

The text should avoid unnecessary italic and bold words and letters, as well as too many acronyms. Authors should avoid to capitalize words and whenever possible to use tables with distinct font size and style of the regular text.

Figures, tables and equations should be numbered in the sequence that they are mentioned in the text.

Abstract

Please provide an abstract between 150 and 250 words in length. Abbreviations or acronyms should be avoided. The abstract should state briefly the purpose of the work, the main results and major conclusions or key findings.

Keywords

A minimum of three and a maximum of six keywords must be included after the abstract. The keywords must represent the content of the paper. Keywords offer an opportunity to include synonyms for terms that are frequently referred to in the literature using more than one term. Adequate keywords maximize the visibility of your published paper.

Examples:

Poor keywords – piles; dams; numerical modeling; laboratory testing

Better keywords – friction piles; concrete-faced rockfill dams; material point method; bender element test

List of symbols

A list of symbols and definitions used in the text must be included before the References section. Any mathematical constant, variable or unknown quantity should appear in italics.

6.1 Citations

References to other published sources must be made in the text by the last name(s) of the author(s), followed by the year of publication. Examples:

- Narrative citation: […] while Silva & Pereira (1987) observed that resistance depended on soil density
- Parenthetical citation: It was observed that resistance depended on soil density (Silva & Pereira, 1987).

In the case of three or more authors, the reduced format must be used, e.g.: Silva et al. (1982) or (Silva et al., 1982). Do not italicize "et al."

Two or more citations belonging to the same author(s) and published in the same year are to be distinguished with small letters, e.g.: (Silva, 1975a, b, c.).

Standards must be cited in the text by the initials of the entity and the year of publication, e.g.: ABNT (1996), ASTM (2003).

6.2 References

A customized style for the Mendeley software is available and may be downloaded from this link.

Full references must be listed alphabetically at the end of the text by the first author's last name. Several references belonging to the same author must be cited chronologically.

Some formatting examples are presented here:

Journal Article

Bishop, A.W., & Blight, G.E. (1963). Some aspects of effective stress in saturated and partly saturated soils. *Géotechnique*, 13(2), 177-197. https://doi.org/10.1680/geot.1963.13.3.177

Castellanza, R., & Nova, R. (2004). Oedometric tests on artificially weathered carbonatic soft rocks. *Journal of Geotechnical and Geoenvironmental Engineering*, 130(7), 728-739. https://doi.org/10.1061/(ASCE)1090-0241(2004)130:7(728)

Fletcher, G. (1965). Standard penetration test: its uses and abuses. Journal of the Soil Mechanics Foundation Division, 91, 67-75.

Indraratna, B., Kumara, C., Zhu S-P., Sloan, S. (2015). Mathematical modeling and experimental verification of fluid flow through deformable rough rock joints. *International Journal of Geomechanics*, 15(4): 04014065-1-04014065-11. https://doi.org/10.1061/(ASCE)GM.1943-5622.0000413

Garnier, J., Gaudin, C., Springman, S.M., Culligan, P.J., Goodings, D., Konig, D., ... & Thorel, L. (2007). Catalogue of scaling laws and similitude questions in geotechnical centrifuge modelling. *International Journal of Physical Modelling in Geotechnics*, 7(3), 01-23. https://doi.org/10.1680/ijpmg.2007.070301

Bicalho, K.V., Gramelich, J.C., & Santos, C.L.C. (2014). Comparação entre os valores de limite de liquidez obtidos pelo método de Casagrande e cone para solos argilosos brasileiros. *Comunicações Geológicas*, 101(3), 1097-1099 (in Portuguese).

Book

Lambe, T.W., & Whitman, R.V. (1979). *Soil Mechanics, SI version*. John Wiley & Sons.

Das, B.M. (2012). *Fundamentos de Engenharia Geotécnica*. Cengage Learning (in Portuguese).

Head, K.H. (2006). *Manual of Soil Laboratory Testing - Volume 1*: Soil Classification and Compaction Tests. Whittles Publishing.

Bhering, S.B., Santos, H.G., Manzatto, C.V., Bognola, I., Fasolo, P.J., Carvalho, A.P., ... & Curcio, G.R. (2007). *Mapa de solos do estado do Paraná*. Embrapa (in Portuguese).

Book Section

Yerro, A., & Rohe, A. (2019). Fundamentals of the Material Point Method. In *The Material Point Method for Geotechnical Engineering* (pp. 23-55). CRC Press. https://doi.org/10.1201/9780429028090

Sharma, H.D., Dukes, M.T., & Olsen, D.M. (1990). Field measurements of dynamic moduli and Poisson´s ratios of refuse and underlying soils at a landfill site. In *Geotechnics of Waste Fills - Theory and Practice* (pp. 57-70). ASTM International. https://doi.org/10.1520/STP1070-EB

Cavalcante, A.L.B., Borges, L.P.F., & Camapum de Carvalho, J. (2015). Tomografias computadorizadas e análises numéricas aplicadas à caracterização da estrutura porosa de solos não saturados. In *Solos Não Saturados no Contexto Geotécnico* (pp. 531-553). ABMS (in Portuguese).

Proceedings

Jamiolkowski, M.; Ladd, C.C.; Germaine, J.T., & Lancellotta, R. (1985). New developments in field and laboratory testing of soils. *Proc. 11th International Conference on Soil Mechanics and Foundation Engineering,* San Francisco, August 1985. Vol. 1, Balkema, 57-153.

Massey, J.B., Irfan, T.Y. & Cipullo, A. (1989). The characterization of granitic saprolitic soils. *Proc. 12th International Conference on Soil Mechanics and Foundation Engineering*, Rio de Janeiro. Vol. 6, Publications Committee of XII ICSMFE, 533-542.

Indraratna, B., Oliveira D.A.F., & Jayanathan, M. (2008b). Revised shear strength model for infilled rock joints considering overconsolidation effect. *Proc. 1st Southern Hemisphere International Rock Mechanics Symposium*, Perth. ACG, 16-19.

Barreto, T.M., Repsold, L.L., & Casagrande, M.D.T. (2018). Melhoramento de solos arenosos com polímeros. *Proc. 19º Congresso Brasileiro de Mecânica dos Solos e Engenharia Geotécnica*, Salvador. Vol. 2, ABMS, CBMR, ISRM & SPG, 1-11 (in Portuguese).

Thesis

Lee, K.L. (1965). *Triaxial compressive strength of saturated sands under seismic loading conditions* [Unpublished doctoral dissertation]. University of California at Berkeley.

Chow, F.C. (1997). *Investigations into the behaviour of displacement pile for offshore foundations* [Doctoral thesis, Imperial College London]. Imperial College London's repository. https://spiral.imperial.ac.uk/handle/10044/1/7894

Araki, M.S. (1997). *Aspectos relativos às propriedades dos solos porosos colapsíveis do Distrito Federal* [Unpublished master's dissertation]. University of Brasília (in Portuguese).

Sotomayor, J.M.G. (2018). *Evaluation of drained and non-drained mechanical behavior of iron and gold mine tailings reinforced with polypropylene fibers* [Doctoral thesis, Pontifical Catholic University of Rio de Janeiro]. Pontifical Catholic University of Rio de Janeiro's repository (in Portuguese). https://doi.org/10.17771/PUCRio.acad.36102*

* *official title in English should be used when available in the document.*

Report

ASTM D7928-17. (2017). Standard Test Method for Particle-Size Distribution (Gradation) of Fine-Grained Soils Using the Sedimentation (Hydrometer) Analysis. *ASTM International, West Conshohocken, PA.* https://doi.org/10.1520/D7928-17

ABNT NBR 10005. (2004). Procedure for obtention leaching extract of solid wastes. *ABNT - Associação Brasileira de Normas Técnicas*, Rio de Janeiro, RJ (in Portuguese).

DNIT. (2010). Pavimentação - Base de solo-cimento - Especificação de serviço DNIT 143. *DNIT -Departamento Nacional de Infraestrutura de Transportes*, Rio de Janeiro, RJ (in Portuguese).

USACE (1970). Engineering and Design: Stability of Earth and Rock-Fill Dams, Engineering Manual 1110-2-1902. Corps of Engineers, Washington, D.C.

Web Page

Soils and Rocks. (2020). *Guide for Authors*. Soils and Rocks. Retrieved in September 16, 2020, from http://www.soilsandrocks.com/

6.3 Artworks and illustrations

Each figure should be submitted as a high-resolution image, according to the following mandatory requirements:

- Figures must be created as a TIFF file format using LZW compression with minimum resolution of 500 dpi.
- Size the figures according to their final intended size. Single-column figures should have a width of up to 82 mm. Double-column figures should have a maximum width of 170 mm.
- Use Times New Roman for figure lettering. Use lettering sized 8-10 pt. for the final figure size.
- Lines should have 0.5 pt. minimum width in drawings.
- Titles or captions should not be included inside the figure itself.

Figures must be embedded in the text near the position where they are first cited. Cite figures in the manuscript in consecutive numerical order. Denote figure parts by lowercase letters (a, b, c, etc.). Please include a reference citation at the end of the figure caption for previously published material. Authorization from the copyright holder must be provided upon submission for any reproduced material.

Figure captions must be placed below the figure and start with the term "Figure" followed by the figure number and a period. Example:

Figure 1. Shear strength envelope.

Do not abbreviate "Figure" when making cross-references to figures.

All figures are published in color for the electronic version of the journal; however, the print version uses grayscale. Please format figures so that they are adequate even when printed in grayscale.

Accessibility: Please make sure that all figures have descriptive captions (text-to-speech software or a text-to-Braille hardware could be used by blind users). Prefer using patterns (e.g., different symbols for dispersion plot) rather than (or in addition to) colors for conveying information (then the visual elements can be distinguished by colorblind users). Any figure lettering should have a contrast ratio of at least 4.5:1

Improving the color accessibility for the printed version and for colorblind readers: Authors are encouraged to use color figures because they will be published in their original form in the online version. However, authors must consider the need to make their color figures accessible for reviewers and readers that are colorblind. As a general rule of thumb, authors should avoid using red and green simultaneously. Red should be replaced by magenta, vermillion, or orange. Green should be replaced by an off-green color, such as blue-green. Authors should prioritize the use of black, gray, and varying tones of blue and yellow.

These rules of thumb serve as general orientations, but authors must consider that there are multiple types of color blindness, affecting the perception of different colors. Ideally, authors should make use of the following resources: 1) for more information on how to prepare color figures, visit https://jfly.uni-koeln.de/; 2) a freeware software available at http://www.vischeck.com/ is offered by Vischeck, to show how your figures would be perceived by the colorblind.

6.4 Tables

Tables should be presented as a MS Word table with data inserted consistently in separate cells. Place tables in the text near the position where they are first cited. Tables should be numbered consecutively using Arabic numerals and have a caption consisting of the table number and a brief title. Tables should always be cited in the text. Any previously published material should be identified by giving the original source as a reference at the end of the table caption. Additional comments can be placed as footnotes, indicated by superscript lower-case letters.

When applicable, the units should come right below the corresponding column heading. Horizontal lines should be used at the top and bottom of the table and to separate the headings row. Vertical lines should not be used.

Table captions must be placed above the table and start with the term "Table" followed by the table number and a period. Example:

Table 1. Soil properties.

Do not abbreviate "Table" when making cross-references to tables. Sample:

Table 1. Soil properties

Parameter	Symbol	Value
Specific gravity of the sand particles	G_s	2.64
Maximum dry density (Mg/m³)	$\rho_{d(max)}$	1.554
Minimum dry density (Mg/m³)	$\rho_{d(min)}$	1.186
Average grain-size (mm)	d_{50}	0.17
Coefficient of uniformity	C_u	1.97

6.5 Mathematical equations

Equations must be submitted as editable text, created using MathType or the built-in equation editor in MS Word. All variables must be presented in italics.

Equations must appear isolated in a single line of the text. Numbers identifying equations must be flushed with the right margin. International System (SI) units must be used. The definitions of the symbols used in the equations must appear in the List of Symbols.

Do not abbreviate "Equation" when making cross-references to an equation.